UNIVERSITÄTSKLINIKUM HAMBURG-EPPENDORF

Zentrum für Molekulare Neurobiologie Hamburg
Institute for Synaptic Physiology

Prof. Dr. J. Simon Wiegert

Optimized design and *in vivo* application of optogenetically modified *Drosophila* dopamine receptors to elucidate endogenous functions

Dissertation

zur Erlangung des Doktorgrades PhD

an der Medizinischen Fakultät der Universität Hamburg

vorgelegt von

Fangmin Zhou

aus Fujian, China

Hamburg 2023

Angenommen von der

Medizinischen Fakultät der Universität Hamburg am: 17.01.2024

Veröffentlicht mit Genehmigung der

Medizinischen Fakultät der Universität Hamburg.

Prüfungsausschuss, der/die Vorsitzende: Prof. Dr. J. Simon Wiegert

Prüfungsausschuss, zweite/r Gutachter/in: Prof. Dr. Stefan Bonn

Table of Contents

1 Introduction

G-protein coupled receptors (GPCRs) are one of the largest cell-surface receptors family in the human genome, with broad expression and coupling to specific signaling pathways. GPCRs play a vital role in regulating diverse cellular responses to numerous small molecule neurotransmitters, neuropeptides, and hormones within the human body (Rosenbaum et al., 2009). Due to their widespread presence and physiological significance, GPCRs are very important therapeutic targets, with approximately one-third of the prescribed drugs interacting with members of this superfamily.

1.1 The GPCR family

Based on the sequence and functional similarity of seven transmembrane (7TM) domain receptors (Fredriksson et al., 2003), the majority of GPCRs are categorized into five main families: Class A (Rhodopsin family), Class B (Secretin family), Class C (Glutamate family), Adhesion families and Frizzled/TAS2 Family (Figure 1). Among these five families, the class A family is the largest and most well-known in the research.

GPCRs form a large family of receptors with a 7TM helix architecture which transmit an extracellular signal, initiated by a hormone, neuropeptide, or neurotransmitter into an intracellular response via G proteins (Lefkowitz, 2004). These receptors share a common structure, with an extracellular N-terminus, seven transmembrane helices interconnected by three extracellular and three intracellular loops (ICL1–3), and an intracellular C-terminus (Peeters et al., 2011).

GPCRs can mediate downstream signaling via interaction with heterotrimeric G-proteins. G proteins are mostly composed of three subunits: α, β, and γ. Gα proteins can be classified into four groups based on their signaling properties: $G\alpha_s$, $G\alpha_{i/o}$, $G\alpha_q$, and $G\alpha_{12/13}$ (Gilman, 1987). Upon peptide binding to the GPCR, these Gα subunits regulate various cellular signaling processes, such as cyclic adenosine monophosphate (cAMP) levels ($G\alpha_s$ and $G\alpha_{i/o}$), modifying Ca^{2+} signaling ($G\alpha_q$), impacting motor proteins and the cytoskeleton through Rho GTPases ($G\alpha_{12/13}$).

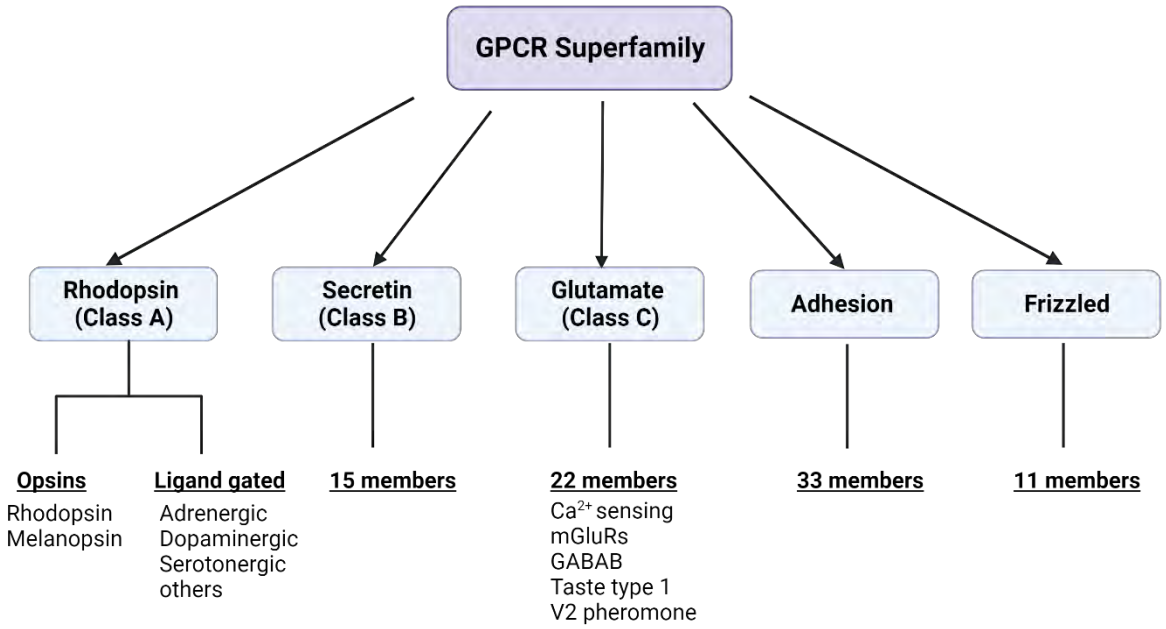

Figure 1. Phylogenetic classification of human GPCRs using the GRAFS system based on sequence homology and functional similarity. GPCRs represent the largest superfamily of receptors in the human genome and are divided into five families, comprising the three classical main classes A, B, and C. as well as adhesion and Frizzled-type (F) receptors. Figure and legend modified from Kleinlogel, 2016, created with BioRender.

1.2 Dopamine receptors

Dopamine (DA) receptors belong to class A GPCRs, with five different DA receptors found in humans. Based on DA's capacity to regulate adenylyl cyclase (AC) activity, they can be categorized into two main groups: the D1-type receptors (D1 and D5) (Tiberi et al., 1991) and D2-type receptors (D2, D3, and D4) (Andersen et al., 1990). DA receptors display broad expression in the central nervous system (CNS) and can also be found in peripheral locations, including blood vessels, kidneys, heart, retina, and adrenals, where they regulate catecholamine release and the renin-angiotensin system (Missale et al,. 1998). Among the DA receptors, D1 and D2 are the ones most prominently expressed in the brain (Baik, 2013; Missale et al,. 1998).

DA receptors are well conserved among phyla and four different receptors are also present in *Drosophila*: two D1-like receptors comprising Dop1R1 (also known as dDA1) and Dop1R2 (known as DAMB), the D2-like receptor Dop2R (also known as DD2R), and Dopamine-Ecdysteroid receptor (DopEcR). In both larval and adult stages, Dop1R1 and Dop1R2 are highly enriched in the mushroom body (MB) in the *Drosophila* brain, which plays pivotal roles in odor learning and memory (Heisenberg 2003). The *Drosophila* MB comprises three principal components: the calyx (input region), pedunculus and lobes (output regions). The acquisition of olfactory memories via

Kenyon cells (KCs), the principal mushroom body neurons, is mediated by the Dop1R1 receptor, while Dop1R2 is essential for the normal forgetting process (Berry et al., 2012). These two receptors are characterized by a preferential and uniform expression pattern along the axonal tracts of all KCs (Han et al., 1996; Kim et al., 2003).

1.2.1 Dopamine Signaling Pathways

The signaling capacities of DA receptors and other GPCRs are highly diverse. In addition to the established GPCR signaling model involving the four distinct G-protein classes ($G\alpha_s$, $G\alpha_{i/o}$, $G\alpha_{q/11}$, $G\alpha_{12/13}$) (Gilman, 1987), GPCR signaling is further regulated by β-arrestins and G-protein coupled receptor kinases (GRKs) (Gurevich et al., 2002; Milner et al., 1998; Reiter & Lefkowitz, 2006). Moreover, it is also influenced by the regulators of G protein signaling (RGS) (Bulenger et al., 2005; Franco et al., 2006).

DA triggers intracellular responses that vary depending on the specific type of DA receptor activated. The downstream signaling of DA primarily involves G proteins. Nonetheless, DA receptor signaling can also trigger G protein-independent signaling pathways (Luttrell & Lefkowitz, 2002). It is widely accepted that D1-like receptors are linked to $G\alpha_{s/olf}$ proteins, $G\alpha_{olf}$ is primarily associated with olfaction and closely related to $G\alpha_s$ with 88% amino acid homology (Herve et al., 2001). Both of them can activate adenylyl cyclase, leading to increased levels of the second messenger cAMP (Figure 2). This, in turn, stimulates the activity of protein kinase A (PKA). Conversely, D2-like receptors, which are coupled to $G\alpha_{i/o}$ proteins, inhibit adenylyl cyclase, resulting in a decrease in the intracellular concentration of cAMP. This reduction in cAMP levels leads to the inhibition of PKA activity (Kebabian & Calne, 1979; Kebabian & Greengard, 1971; Missale et al., 1998). PKA plays a pivotal role in DA signaling and has numerous targets, including cAMP response element-binding protein (CREB), glutamate receptors, GABA receptors, and ion channels (e.g., calcium and potassium) (Greengard, 2001). Furthermore, PKA targets a specific protein known as dopamine and cAMP-regulated phosphoprotein 32-kDa (DARPP-32). This protein serves to enhance and amplify PKA signaling, while also playing a crucial role in integrating and modulating the signaling pathways of various neurotransmitters, including dopamine (Svenningsson et al., 2004).

In addition to their role in regulating adenylyl cyclase activity through $G\alpha_{s/olf}$ or $G\alpha_{i/o}$, dopamine receptors may additionally couple with $G\alpha_q$ proteins to modulate phospholipase C (PLC) (Jose et al., 1995; Margolis et al., 1989; Sahu et al., 2009). PLC is responsible for catalyzing the production of both inositol trisphosphate (IP3) and

diacylglycerol (DAG). These compounds increase intracellular levels of calcium and activate protein kinase C (PKC), respectively. The rise in intracellular calcium levels leads to the activation of various enzymes, which also play a crucial role in regulating multiple signaling pathways (Berridge, 2009, 2016).

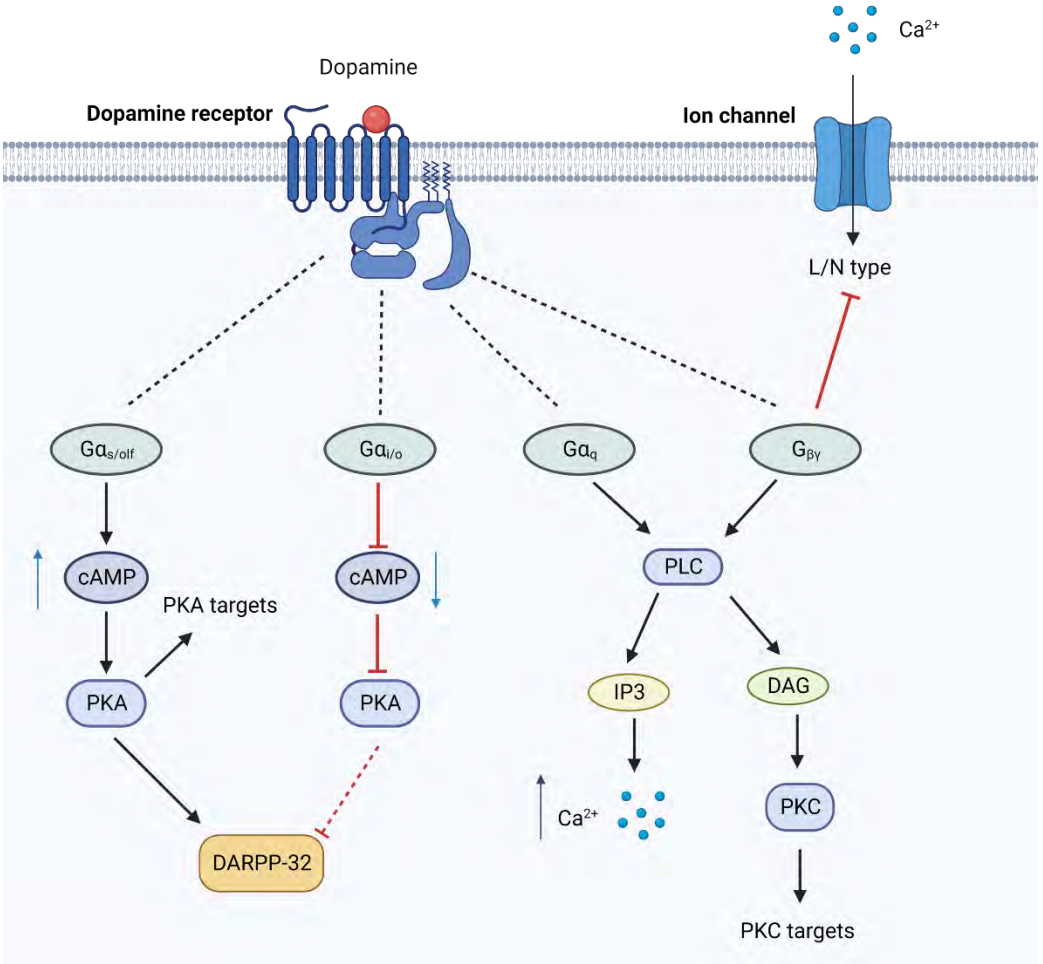

Figure 2. Schematic of dopamine receptor signaling pathways. DA receptors belong to the superfamily of G protein-coupled receptors (GPCRs) and are linked to various types of G proteins. D1-like receptors (D1 and D5) are associated with $G\alpha_{s/olf}$, while D2-like receptors (D2, D3, and D4) are coupled to $G\alpha_{i/o}$, with DARPP-32 serving as their main modulator. These receptors can also activate $G\alpha_q$ and Gβγ, thereby modulating signaling pathways that involve calcium and protein kinase C (PKC). Figure modified from Klein et al., 2018, created with BioRender.

1.2.2 Dopamine

Dopamine functions as a neurotransmitter conserved across species, from Caenorhabditis elegans to humans (Klein et al., 2018). The majority of DA synthesis primarily originates from tyrosine. Tyrosine hydroxylase, which acts as the limiting factor in this process, transforms tyrosine into L-3,4-dihydroxyphenylalanine (L-DOPA) with the assistance of tetrahydrobiopterin, oxygen, and iron as cofactors. Subsequently,

L-DOPA can be converted into DA through the enzymatic action of aromatic DOPA decarboxylase (Christenson et al., 1970).

DA is released at presynaptic sites and can then bind to postsynaptic DA receptors (on the dendrites and soma) or presynaptic auto-receptors (on the presynaptic neuron) (B. Gardner et al., 1996; B. R. Gardner et al., 1997; Levesque et al., 1992). Binding to these DA receptors activates G-protein-dependent pathways including cAMP/PKA/DARPP32. DA plays a central role in the regulation of brain functions like motor control, reward processing, cognitive function, and emotional regulation (Ayano, 2016). The dysfunction of DA signaling is believed to be linked to various medical conditions, including schizophrenia, Parkinson's disease, and attention deficit hyperactivity disorder (ADHD) (Hisahara & Shimohama, 2011; Lou et al., 2004; Seeman, 2013).

1.2 Optogenetics

Due to the varying expression and signaling characteristics of DA receptors, it is able to affect different neural circuits and behaviors. Traditional strategies such as pharmacological approaches can globally modulate the DA signaling pathway leading to numerous undesirable and non-specific side effects. Therefore, it is very important to gain more precise insights into the effects of DA signal transduction and other neuromodulators at the receptor and subcellular compartment level. Pharmacological methods lack cell type specificity and precise temporal control, making it challenging to achieve the level of accuracy and specificity to target specific circuits. Furthermore, most existing genetic tools lack the necessary temporal control and sensitivity to enable direct and efficient manipulation of the corresponding receptors *in vivo*.

A significant breakthrough was achieved by combining genetic engineering with light-sensitive proteins, which allowed precise rapid manipulation of well-defined processes both *in vitro* and *in vivo*. This innovative technology was termed optogenetics and employs the expression of light-sensitive proteins to regulate behavior and physiology (Deisseroth, 2011).

Optogenetics has revolutionized our understanding of distinct neural circuits function by, enabling precise manipulation of specific cell types at the millisecond level. This advancement allows for the examination of their contributions to behavior and physiology through genetic targeting, offering precise control over time and space (Deisseroth, 2011, 2015; Wietek et al., 2017). Over the past decade, optogenetic

approaches have been widely expanded, widening the horizon for biological research and even progressing into clinical trials for vision restoration (Čapek et al., 2019; Scanziani & Häusser, 2009; van Wyk et al., 2015; Yizhar et al., 2011).

1.3.1 Opsins

Opsins are regarded as accurate and adaptable components for photosensitization, which allow conversion of naturally light-insensitive cells into light-sensitive cells for precise optical control over specific cellular processes. Opsin genes are categorized into two distinct groups: microbial opsins (type I) and animal opsins (type II). It is worth noting that each opsin protein relies on the integration of the retinal, an organic cofactor responsible for photon absorption.

Type I opsins are single-component transmembrane proteins commonly found in prokaryotes, algae, and fungi. They serve as transporters for various ions across the membrane in response to light. Light-sensitive channels, which are commonly referred to as Channelrhodopsins (ChRs) (Nagel et al., 2002), constitute the most extensively utilized category of microbial opsins to date (Figure 3 a-c). ChRs can be further categorized into two groups: cation-conducting ChRs (CCRs), which are frequently employed for stimulating neurons; and anion-conducting ChRs (ACRs), which are employed to suppress neuronal spiking (Deisseroth & Hegemann, 2017). Enzyme rhodopsins belong to the category of non-electrogenic type I microbial opsins (Figure 3 c). Within this group, there are various enzymes, including rhodopsin-coupled guanylyl cyclases (RhGCs), phosphodiesterases, and histidine kinases. In particular, RhGCs have been employed to induce depolarization when co-expressed with cyclic nucleotide-gated ion channels (Gao et al., 2015; Rost et al., 2022; Scheib et al., 2018).

Type II opsins are exclusive to higher eukaryotes and are required for vision and modulating circadian rhythms, as well as in pigment regulation (Guru et al., 2015). When Rhodopsins are exposed to light, the bound retinal isomerizes from a 13-*cis* to an all-*trans* configuration, initiating the 2nd messenger signaling cascade underlying visual phototransduction (Rost et al., 2022; Figure 3d). Compared to type I opsins, type II opsins show slower kinetics in affecting cellular changes due to their chromophore turnover and activation of a cascade of downstream biochemical signal transduction partners (Zhang et al., 2011).

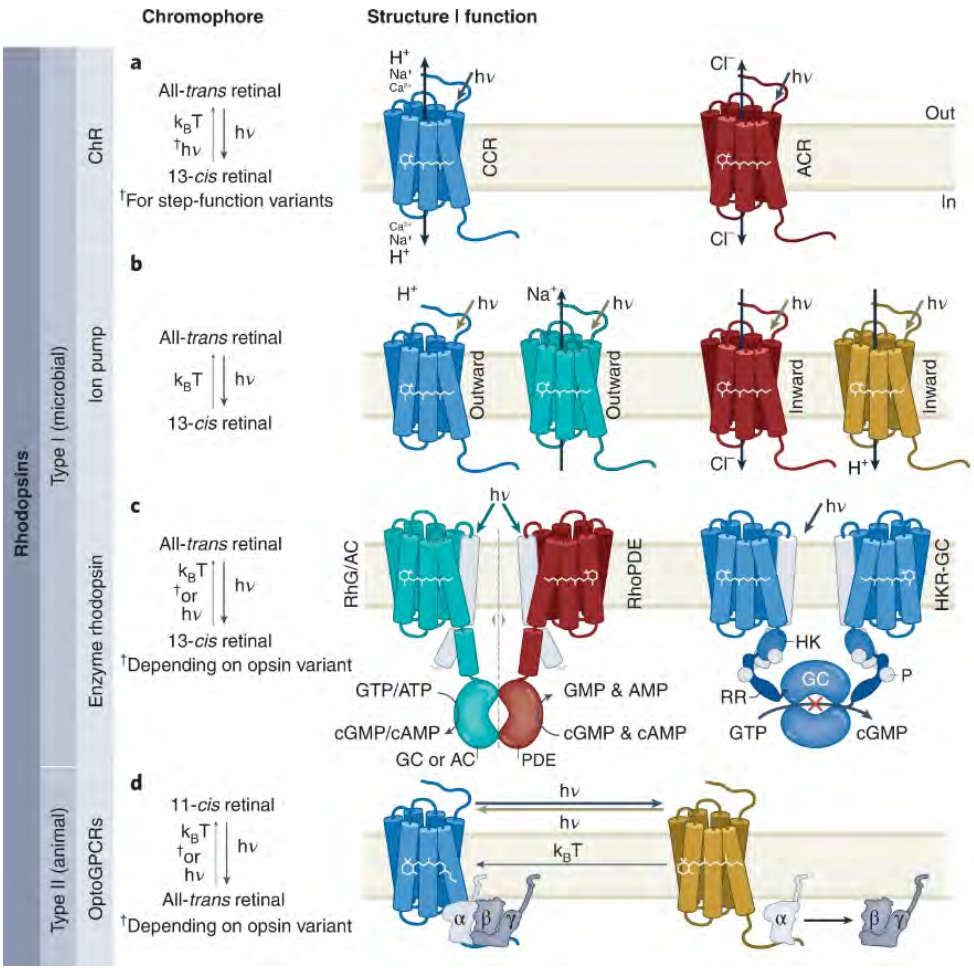

Figure 3. Overview of optogenetic actuators. a–d Left, chromophore photoreaction. Right, schematized architecture and function. cAMP, cyclic adenosine monophosphate; cGMP, cyclic guanosine monophosphate; GC, guanylyl cyclase; GTP, guanosine triphosphate; P, phosphorylation site; PDE, phosphodiesterase; PDE, phosphodiesterase. Figure and legend adapted from Rost et al., 2022.

1.3.2 Optogenetically modified GPCRs

Light-activated chimeric GPCRs, also known as optoXRs (Airan et al., 2009; Tichy et al., 2019), can be used for optical control of intracellular signaling via G-proteins (Figure 4a). This approach involves the creation of chimeric fusions between a vertebrate rhodopsin and conventional ligand-gated GPCRs (Tichy et al., 2019). One notable example is the optogenetically modified β2-adrenergic receptor (Opto-β2AR) (Kim et al., 2005), in which the intracellular domains of a target receptor (β2AR) are placed into a mammalian rhodopsin (Rho) backbone (Figure 4b). Futhermore, researchers have developed and characterized two optoXRs (opto-α1AR and opto-β2AR), where the intracellular loops of rhodopsin have been substituted with those of specific adrenergic receptors: human α1a-adrenergic receptor (α1AR) and hamster β2-adrenergic receptor (β2AR) *in vivo*. These two optoXRs exhibited opposing effects on spike firing within the

nucleus accumbens in mouse (Airan et al., 2009). Additionally, precise and timed optoXR photostimulation in the nucleus accumbens was sufficient to induce conditioned place preference in freely moving mice (Airan et al., 2009). Therefore, the optoXR method serves as a valuable strategy offering an additional dimension of rapid and precise cellular control that is effective in behaving mammals.

Over the last decade, there has been rapid advancement of cell type-specific manipulations of neurons *in vivo* using light-responsive ion channels, such as cation-conducting and anion-conducting ChRs. However, the optical regulation of modulatory GPCR mediated-signaling has encountered certain limitations (Morri et al., 2018; Spangler & Bruchas, 2017). These limitations include the difficulty to mimic endogenous-like localization and signaling pathways.

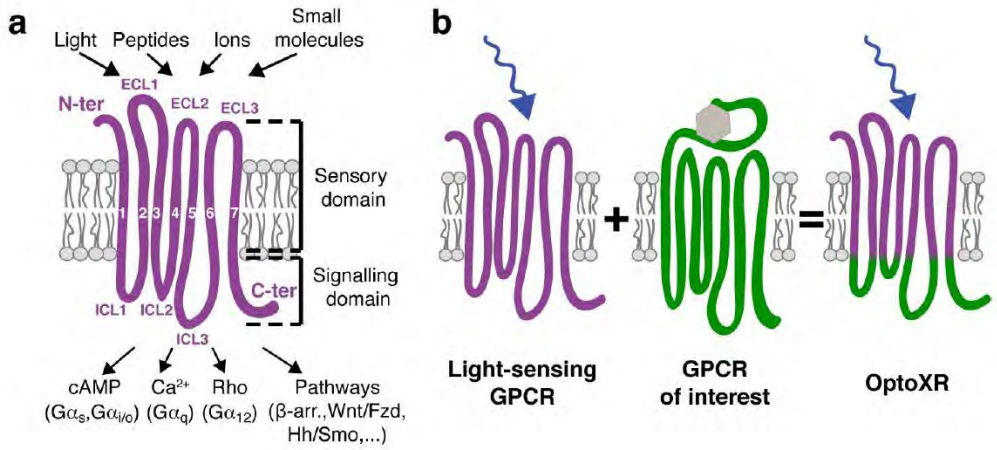

Figure 4. GPCR topology and OptoXR design. **a.** GPCRs sense various extracellular stimuli through extracellular and transmembrane (TM) domains, while the intracellular domains mediate downstream signalling. **b.** Prototypical strategy in which domain swapping is employed to engineer light-activated chimeric GPCRs (OptoXRs). Figure and legend adapted from Tichy et al 2022.

Recently, a systematic strategy for class A GPCRs has led to the development of a library of human optoXRs, demonstrating specific signaling characteristics of known and orphan receptors *in vitro* (Morri et al., 2018). Additionally, chimeric GPCRs have been designed using melanopsin, which have been applied *in vivo* (Cehajic-Kapetanovic et al., 2015; Karunarathne et al., 2013; Mahn et al., 2021). For example, opto-mGluR6 was employed to restore vision through its expression in ON bipolar cells in blind mice mice (Berry et al., 2020). OptoXRs can in principal mimic the activation

kinetics of corresponding native GPCRs by regulating their response levels via the optical stimulation duration and light intensity. Thus, researchers can gain a deeper understanding of how these signals are transmitted over time in genetically defined cell types and neural circuits. Furthermore, a combination with advanced imaging studies of optoXRs signal transduction (e.g., calcium, cAMP) would permit perturbing signaling in a natural system while capturing real-time neuronal ensemble dynamics or GPCR signaling (Kleinlogel, 2016).

Although the prospect of employing optoXRs to replicate GPCR function is appealing, the design and functionality of these receptors remains challenging. Notably, the signaling properties of numerous GPCRs depend on factors such as cell type, receptor localization, activation kinetics, and functional context (Eichel & von Zastrow, 2018; Eickelbeck et al., 2019; Spangler & Bruchas, 2017; Spoida, Eickelbeck, Karapinar, Eckhardt, Mark, Jancke, Ehinger, König, Dalkara, Herlitze, et al., 2016). In addition, optoXRs have been deployed *in vivo* only in a few instances, primarily for acute manipulation of specific G protein signaling pathways (see Table 1). Consequently, there is limited evidence supporting the functional replacement or mimicry of endogenous GPCR function in target tissues by optoXRs.

Chimeric receptor	**Original reference**	***In vivo* applications**	**Cell type-specificity/rescue of endogenous receptor function**
Rho:β_2AR	(Kim et al., 2005)	- virus-mediated overexpression in mouse N. accumbens neurons (Airan et al., 2009) - virus-mediated overexpression in mouse basolateral amygdala, promoting anxiety-like behavior (Siuda et al., 2016; Siuda, McCall, et al., 2015)	partial/no partial/no
Rho:α_1AR	(Airan et al., 2009)	- virus-mediated overexpression in mouse N. accumbens neurons, reward-related preference behavior - virus-mediated overexpression in mouse CA1 astrocytes, memory acquisition(Adamsky et al., 2018) - transgenic overexpression in mouse cortical astrocytes, remote memory acquisition (Iwai et al., 2021) - virus-mediated overexpression in mouse astrocytes in slices, electrophysiology (Gerasimov et al., 2021)	partial/no partial/no partial/no partial/no
Rho:μOR	(Barish et al., 2013)	- virus-mediated overexpression in mouse dorsal root ganglion neurons, preference/aversion behavior (Siuda, Copits, et al., 2015) - Penk-Cre dependent virus-mediated overexpression in dorsal raphe nucleus subset neurons, restoration of consumption behavior (Castro et al., 2021)	partial/no yes/yes

Chimeric receptor	Original reference	*In vivo* applications	Cell type-specificity/rescue of endogenous receptor function
Rho:DRD1	(Gunaydin et al., 2014)	- DRD1-Cre dependent virus-mediated overexpression in mouse N. accumbens; activation of medium spiny neurons to increase social interaction	yes/no
Rho:CXCR4	(Xu et al., 2014)	- virus-mediated overexpression in mouse, T-cell recruitment	yes/no
Rho:$A_{2A}R$	(P. Li et al., 2015)	- virus-mediated overexpression in mouse hippocampus and N. accumbens, spatial memory performance and locomotor activity adora2a-Cre dependent virus-mediated overexpression in mouse striatopallidal neurons, goal-directed behavior (Y. Li et al., 2016)	partial/no yes/no
OPN4:$mGluR_6$	(van Wyk et al., 2015)	- virus-mediated overexpression in retinal ganglion cells, restoration of visually guided behavior - virus-mediated overexpression in bipolar cells, restoration of visually guided behavior (Kralik et al., 2022)	yes/partial (degeneration model) yes/yes (degeneration model)
Rho:Fz7	(Čapek et al., 2019)	- Zebrafish mRNA injection and overexpression, mesoderm cell migration	no/yes

Table 1. Previous optoXRs and their *in vivo* applications.

Only those optoXRs that have been applied *in vivo* are listed here. Abbreviations: Rho: bovine rhodopsin, OPN4: melanopsin. Figure and legend adapted from Zhou et al 2023.

1.4 Animal model of *Drosophila*

Drosophila melanogaster, commonly known as the fruit fly, due to its short generation time, simple nervous system, and availability of excellent genetic tools, has served as a highly productive model organism in neuroscience research. Despite the apparent dissimilarities in appearance between humans and fruit flies, it is widely recognized that the fundamental biological mechanisms and pathways are conserved across evolutionary lines between these two species (Jennings, 2011).

1.4.1 The functions of dopamine receptors in *Drosophila*

In vivo models, including *Drosophila* melanogaster, have made substantial contributions to our understanding of neuromodulatory GPCR signaling in neural circuitry and behavior (Bargmann & Marder, 2013; Nässel, 2018; Nässel & Zandawala, 2019). In particular, *Drosophila* has been extensively studied with regard to DA and its receptors, shedding light on their roles in learning, memory, and goal-directed behaviors (Girault & Greengard, 2004; Kaun & Rothenfluh, 2017; Siju et al., 2021;

Waddell, 2013; Zolin et al., 2021). Dop1R1 is involved in the induction of cAMP signaling, a critical intracellular signaling pathway implicated in many behaviors. Dop1R2 is linked to the release of intracellular calcium stores, which is another crucial aspect of neuronal function underlying olfactory memory processes (Sun et al., 2020). For instance, Dop1R1 and Dop1R2 have established functions in learning and memory int the MB, the insect learning and memory center (Berry et al., 2012; Handler et al., 2019; Himmelreich et al., 2017).

The MB exhibits a three-layered expand-converge architecture, which is a structural pattern found in various learning networks (Stevens 2015). Researchers have identified a MB circuit responsible for both olfactory learning and innate odor avoidance, and the distinct signaling pathways that are mediated by Dop1R1 regulate these behaviors. Moreover, associative learning and learning-induced MB plasticity require adenylyl cyclase activity in the MB (Noyes et al., 2020). Interestingly, Dop1R1 receptor in MB neurons modulates larval locomotion, while other dopaminergic receptors do not to play a significant role in larval motor behavior (Silva et al., 2020). Additionally, Dop1R1-expressing Kenyon cells of the mushroom body can modulate feeding behavior, which promotes a foraging independent satiety state (Landayan et al., 2018). These findings have illuminated some aspects of how specific DA receptors in *Drosophila* contribute to the regulation of complex cognitive behaviors.

1.4.2 The application of optogenetic tools in *Drosophila*

The light- gated channels (for example ChR2), have been instrumental in unraveling the neuronal basis of different behaviors and processes in *Drosophila* (Zhang et al., 2007). These studies have encompassed investigating the nociceptive response (Hwang et al., 2007), and studying the appetitive/aversive odorant learning at both the receptor and neurotransmitter levels (Bellmann-Sickert & Beck-Sickinger, 2010; Schroll et al., 2006). It's worth noting that *Drosophila* has specific requirements for optogenetic applications (Pulver et al., 2009). Unlike mammals, flies lack sufficient levels of endogenous retinal to make exogenously expressed opsins functional .However, retinal can be supplemented in the food to enable the function of these optogenetic tools in flies *in vivo* (Xiang et al., 2010).

While optogenetic approaches have been widely used in flies, there is a lack of optoXRs that can be effectively studied *in vivo*. This is however desirable as, for example, the acute, cell type-specific aspects of DA receptor function, are not well understood. Currently, available tools to not offer the possibility for precise spatiotemporal

dissection of endogenous-like dopaminergic signaling and function. Therefore, there is an urgency to develop optoXR tools to unlock a deeper understanding of the temporal and cell-specific aspects of receptor functions *in vivo*, which will undoubtedly contribute to advancing our knowledge of circuit function and behavior.

1.5 Objective and summary of the project

The aim of this research project was to develop and optimize chimeric optogenetically modified dopamine receptors (optoDopRs) to determine whether they enable precise manipulation of Dopamine receptor signaling *in vitro* and *in vivo*. To get deep insight into the functional specificity and precision of optoDopRs, I further aimed to investigate the localization and signaling properties of optoDopRs in *Drosophila in vivo* and demonstrate their ability to replace or mimic DA receptor functionality in various DA-dependent behaviors.

In this project, firstly, I have optimized chimeric optoDopR design by considering evolutionary conserved GPCR-G protein interactions (Flock et al., 2017) and intracellular loops (Peeters et al., 2011). Adjusting transition sites between the Rhodopsin backbone and the target receptor sequence within the TM7 and C-terminal domain and retaining the Rhodopsin intracellular loop 1 region resulted in more specific and active chimeric optoDopR designs for Dop1R1 and Dop1R2. I showed this by comprehensive assessment of optoDopRs signaling *in vitro* using cellular assays revealing enhanced signaling specificity and light-dependent G protein activation with this optimized design. Secondly, I expressed optoDopRs in *Drosophila* neurons including mushroom body Kenyon cells (KCs) and mushroom body out neurons (MBONs)), which express endogenous DopRs, to compare the subcellular localization of these receptors in axonal and dendritic compartments. The optimized optoDopRs, in particular optoDop1R1, closely resembled the distribution of the endogenous receptor. Furthermore, we demonstrated that optoDopRs can effectively substitute or mimic dopamine receptor functionality in various DA-dependent behaviors, including Dop1R1 function in locomotion and learning behavior, and Dop1R2 function in olfactory and operant feeding behavior. Intriguingly, we could show cell type and receptor-specific functions using optoDopRs in both innate and adaptive behaviors, showing their utility as a specific high precision tool for functional studies of dopamine-dependent behaviors.

2. Materials and Methods

2.1 *Drosophila* melanogaster stocks

All *Drosophila* stocks were raised and maintained in accordance with standard protocols at 25°C and 70% relative humidity, with a 12-hour light and 12-hour dark/light cycle and were provided with standard fly food. Transgenic *UAS-optoDopR* lines were established through phiC31-mediated site-specific transgene integration into the attP2 site on the 3rd chromosome, provided by FlyORF Injection (Zurich, Switzerland). Stocks were obtained from the resources available at the Bloomington *Drosophila* Stock Center (BDSC) unless otherwise indicated. A detailed list of the specific lines used can be found in Table 2.

Line	**label**	**Source**
Dop1R1$^{KO\text{-}Gal4}$	Knockout-Gal4 of Dop1R1	BDSC# 84714
UAS-Dop1R1^{RNAi}	Knockdown of Dop1R1	BDSC# 62193
UAS-Dop1R2^{RNAi}	Knockdown of Dop1R2	BDSC# 51423
Dop1R2$^{KO\text{-}Gal4}$	Knockout-Gal4 of Dop1R2	BDSC# 84715
201y-Gal4	Expresses GAL4 in the mushroom body	BDSC# 64296
H24-Gal4	Expresses GAL4 in the mushroom body	BDSC# 51632
UAS-bPAC	Optogenetic cAMP induction	BDSC# 78788
UAS-optoDop1R1^{V2}	Optogenetic Dop1R1 activation	This study
UAS-optoDop1R2^{V2}	Optogenetic Dop1R2 activation	This study
UAS-optoDop1R1^{V1}	Optogenetic Dop1R1 activation	This study
PPK-Gal4	Expresses GAL4 in C4da neurons	(Han et al., 2011)
UAS-CsChrimson-GFP	Optogenetic activation	BDSC# 55136
UAS-Gflamp1	cAMP reporter	(Wang et al., 2022)
UAS-Gcamp6s	Calcium reporter	(Chen et al., 2013)
MBONg1g2-Gal4	Expresses GAL4 in MBON-g1,g2	(Saumweber et al., 2018)

Line	label	Source
Pdf-Gal4	Expresses GAL4 in I-LN_v	BDSC# 6899
MB011B-Gal4	Expresses GAL4 in valence-encoding MBONs	(Aso et al., 2014)
2U	w^{1118} (isoCJ1) Canton-S derivative	(Tully et al.,1994)
OK107-Gal4	Expresses GAL4 in the mushroom body	BDSC# 854
tub-Gal80^{ts}	Expresses temperature sensitive GAL80 in all cells	BDSC# 7019
R21B06-splitGal4^{DBD}	Expresses $GAL4^{DBD}$ in the mushroom body	(Aso et al., 2014)
6xCRE-splitGal4^{AD}	Expresses $GAL4^{AD}$ in a Cre-dependent manner, VK27 insertion	This study
UAS-myr::tdTomato	Fluorescent reporter line	BDSC# 32223
UAS-Dop1R1GFP$_{11}$, UAS-spGFP$_{1-10}$	Dop1R1 knock-in line with C-terminal GFP_{11} tag	(Kondo et al., 2020)
10xUAS-myr::GFP	Fluorescent reporter line	BDSC# 32197
UAS-BiPOLES	Optogenetic bidirectional modulation	(Vierock et al., 2020)
ok371-Gal4	Expresses GAL4 in motor neurons	(Vierock et al., 2020)
Lgr4$^{T2A-Gal4}$	Expresses GAL4 in Lgr4 expressing cells	BDSC# 77775
A08n-Gal4	Expresses GAL4 in A08n neurons	(Hu et al., 2017)
HuginVNC -Gal4	Expresses GAL4 in Hugin-VNC neurons	(Schoofs et al., 2014)
Ilp7ko	Knockout of Ilp7	(Grönke et al., 2010)
Dp7-Gal4	Expresses GAL4 in Dp7 neurons	(Imambocus et al., 2022)
UAS-Kir2.1	Inhibit neuron activity line	(Baines et al., 2001)

UAS-CD4-tdTom	Morphological marker	BDSC# 35837
UAS-CD4-tdGFP	Morphological marker	BDSC# 35836
Lgr4ko	Knockout of Lgr4	(Deng et al., 2019)

Table 2. Driver lines and transgenes used in this study. *Drosopohila* driver lines and transgenes lines were used in this study, their usage or expression as well as source are shown.

2.2. Solutions and antibodies

The following solutions were used in cellular assay and *in vivo* experiments:

Solution	**Composition**
Phosphate-buffered saline	137 mM NaCl, 2.7 mM KCl, 10 mM Na2HPO4, and 1.8 mM KH2PO4
PBST	0.3% Triton X-100 in PBS buffer
HL3	70 mM NaCl, 5 mM KCl, 4 mM MgCl2, 5 mM trealose, 115 mM sucrose, 5 mM HEPES, 10 mM NaHCO3, pH 7.20-7.25
Physiological saline buffer	108 mM NaCl, 5mM KCl, 2mM $CaCl_2$, 8.2 mM $MgCl_2$, 4 mM $NaHCO_3$, 1 mM NaH_2PO_4, 5 mM trehalose, 10 mM sucrose, 5 mM HEPES, pH 7.5

Table 3. Solution used in this study. The composition of individual solution is shown in the table.

The following table were primary and secondary antibodies used in the study:

Antibody	**Host**	**Dilution**	**Source**
Mouse anti-Rhodopsin	Mouse	1:100	Thermo Fisher, Cat #MA1-722
Rabbit anti-DsRed	Rabbit	1:2,000	Takara Bio Inc., Cat #632496
Mouse anti-GFP	Mouse	1:2,000	Thermo Fisher, Cat #A-11120
Goat anti-chicken, Alexa Fluor 488	Anti-chicken	1:200	Thermo Fisher, Cat # A-11039
Donkey anti-mouse Alexa Fluor 555	Anti- mouse	1:400	Thermo Fisher, Cat # A-31570

Goat anti-rabbit Alexa 594	anti-rabbit	1:1,000	Thermo Fisher, Cat # A-11012
Donkey anti-mouse Alexa 488	Anti- mouse	1:300	Jackson Immunoresearch, Cat# 715-545-150
Goat anti-mouse Alexa 546	Anti- mouse	1:300	Jackson Immunoresearch Cat # A-11030

Table 4. Primary and secondary antibodies used in this study. The host and dilution as well as the source of antibodies are shown in the table.

2.3 The design of OptoDopR

Bovine Rhodopsin (Rho) was used as the acceptor receptor for creating the OptoDopR sequences, and G protein binding sites were replaced with the target receptor. In order to identify the cut sites at the segment boundaries, a multiple protein sequence alignment of Rho and the target receptors was established using the Muscle tool (Edgar, 2004). For optoXRs-V1, the cut sites were determined based on previously published receptor designs(Kim et al., 2005; Morri et al., 2018). As for optoXRs-V2, modifications were made to the cut sites near ICL1 and the C-terminus to align with previously documented G protein binding sites (Flock et al., 2017). Additionally, the C-terminal Rho residues (TETSQVAPA) were appended to the C-terminus of optoXR-V1/V2 chimeric constructs to enable comparative immunolabeling using anti-Rho antibodies.

2.3.1 Plasmids

The cDNAs of the wildtype *Drosophila* Dop1R1 and Dop1R2 were acquired from the *Drosophila* Genomics Resource Center (DGRC, Bloomington, IN, USA), and they were subsequently cloned into the pCDNA3.1 vector (Thermo Fisher, MA, USA). For the constructs of optoDop1R1 and optoDop1R2 chimeric (V1 and V2), custom codon-optimized cDNAs were synthesized by GeneArt (Thermo Fisher). The synthesized constructs were then cloned into both the pCDNA3.1 and pUAttB vectors. Chimeric G protein constructs, which were utilized for the cellular G_{sx} assay (Ballister et al., 2018), were obtained from Addgene (Watertown, MA, USA).

2.4 Cell culture and live-cell G protein coupling assays

G protein coupling of both wild-type and chimeric GPCR constructs was assessed using either HEK293T cells or HEK293-ΔG7 cells (lacking

GNAS/GNAL/GNAQ/GNA11/GNA12/GNA13/GNAZ) obtained from A. Inoue at Tohoku University (Wan et al., 2018). HEK293T cells were cultured in DMEM medium supplemented with 10% FBS (Pan Biotech, Germany), penicillin (100 U/mL), and streptomycin (100 mg/mL) at 37°C with 5% CO_2.

The G_{sx} assay was modified from the original protocol (Ballister et al., 2018). For transfection, white 96-well plates (Greiner Bio-One) coated with 0.1mg/ml poly-L-lysine (Sigma Aldrich, St. Louis, MO, USA) at 37°C for 1 hour, then cells were seeded into these plates. Individual receptor plasmids, G protein chimera, and Glo22F (Promega) were co-transfected using Lipofectamine 2000 (Thermo Fisher, MA, USA) for 24h. After transfection, cells were incubated at 37°C with 5% CO_2 for 24 hours. The culture medium was then replaced with L-15 medium (without phenol-red, with 1% FBS) containing 2 mM beetle luciferin (in 10 mM HEPES pH 6.9) and 10 mM 9-*cis*-retinal (for optoXRs). Subsequently, the cells were incubated at room temperature and dark conditions for 1 hour. The measurement of cAMP-dependent luminescence was conducted using a Berthold Mithras multimode plate reader (Berthold Tech., Germany). Baseline luminescence was recorded three times, and activation of wildtype receptors was induced by adding the respective ligand at various concentrations (diluted in L-15 medium). For optoXRs activation, cells were illuminated with a 1-second light pulse using either a LED light plate (Phlox Corp., Provence, France) or a CoolLED pE-4000 (CoolLED, Andover, UK). The specific light intensities and wavelengths were tailored to individual experiments. Technical duplicates were executed for all experiments, with a minimum of three independent trials. For data quantification each well was normalized to its pre-activation baseline.

In the TRUPATH assay (Olsen et al., 2020), HEK293ΔG7 cells were prepared as described above. They were co-transfected with RLuc8-Gα, Gβ, Gγ-GFP2, and optoDopRs in a 1:1:1:1 ratio (100 ng/well total DNA) using Lipofectamine 2000. Cells were incubated for 24 hours at 37°C with 5% CO_2, followed by incubation in Leibovitz's L-15 medium (without phenol-red, with L-glutamine, 1% FBS, penicillin/streptomycin at 100 mg/mL) and 9-cis retinal (10 μM) in darkness. For the BRET assays, the culture medium was changed to HBBS, supplemented with 20 mM HEPES, 10 μM 9-cis retinal, and 5 μM Coelenterazine 400a, followed by a 5-minute incubation at room temperature. Activation of optoDopRs was achieved by a 1-second, 470 nm light pulse (CoolLED pE4000), while native DopRs were activated by injecting dopamine to reach a final concentration of 1 μM. BRET ratio changes were determined from RLuc8-Gα and Gγ-

GFP2 signals over a 90-second timeframe immediately after light or dopamine treatment.

2.5 Immunochemistry

Larval brains from 3rd instar animals (96 h ± 3h after egg laying (AEL)) of the specified genotypes were dissected in phosphate-buffered saline (PBS) and fixed for 15 minutes at room temperature in a solution containing 4% formaldehyde in PBS. After fixation, samples were washed with PBST (PBS with 0.3% Triton X-100) and then incubated in 5% normal donkey serum in PBST. OptoDopR expression was detected using a mouse anti-Rho antibody (1D4, diluted at 1:100, Thermo Fisher, CA, USA) at 4°C overnight, which recognizes the C-terminal Rho epitope present in all optoXRs. Following first antibody incubation, the samples were washed three times with PBST (wash 5 minutes) and subsequently incubated with secondary antibodies, either donkey anti-mouse Alexa488 or goat anti-mouse Alexa546 (both at a 1:300 dilution) for 1 hour. After washing 3 times, the samples were mounted on poly-L-lysine-coated coverslips using Slow Fade Gold (Thermo Fisher, CA, USA). The native GFP/tdTomato reporter fluorescence was sufficiently bright to be visualized alongside the antibody immunostaining using confocal microscopy (Zeiss LSM900AS2, Zeiss, Oberkochen, Germany). Confocal Z stacks were processed using Fiji (ImageJ, NIH, Bethesda, USA). A detailed list of the solutions used can be found in Table 3.

2.6 Calcium and cAMP imaging in *D. melanogaster* larvae

Third-instar larval brains (96 h ±3h AEL) were partially dissected in physiological HL3 buffer. Dissected brains were subsequently mounted on cover slips coated with poly-L-lysine in HL3 buffer, either without or with the addition of 5 mM 9-*cis*-Retinal for experiments using opto-DopRs. To monitor intracellular cAMP or calcium levels, Gflamp-1 or GCaMP6s was employed, respectively. Live imaging of Kenyon cell somata and medial lobes expressing Gflamp-1 or GCaMP6s within the mushroom body was conducted by confocal microscopy, employing a 40x/NA1.3 objective lens (Zeiss LSM900AS2, Zeiss, Oberkochen, Germany). Activation of OptoDopRs^{V2} or bPAC was achieved using a 470 nm LED light with an intensity of 2.10 mW/cm². Confocal time series were acquired at a frame rate of 7.5 frames per second, with image dimensions set at 128 × 128 pixels (600 frames total or 1000 frames for experiments with repeated light activation). After focusing on KC somata or medial lobes and obtaining a stable imaging period of 100 frames, the 470 nm LED was activated for a duration of 10

seconds. Subsequently, confocal time series data were registered employing the StackReg plugin within ImageJ to correct for XY movement. Quantification of Gflamp-1 signal intensity within the soma and medial lobe was conducted using the Time Series Analyzer V3 plugin (ImageJ). The baseline (F_0) was determined as the average signal intensity over 95 frames acquired prior to activation. The relative maximum intensity change (ΔF_{max}) of Gflamp-1 or GCaMP6s fluorescence was calculated following normalization to the baseline. A detailed list of the buffers used is shown in Table 3.

2.7 cAMP-induced nociceptive behavior in *D. melanogaster* larvae

Larvae expressing *UAS-bPAC*, *UAS-CsChrimson*, or *UAS-optoDopRs* under the control of *ppk-Gal4* were staged and raised in the dark on grape agar plates (2% agar) with yeast paste. The yeast paste contained either 5 mM 9-*cis*-retinal (for optoXRs) or all-*trans*-retinal (for CsChrimson). Staged 3rd instar larvae were placed on a 1% agar film positioned on a FTIR (frustrated total internal reflection) based tracking system (FIM, University of Münster). 1 ml of water was added to the agar, and the experiments were conducted under minimal light conditions similar as previously established (Dannhäuser et al., 2020). After an initial 10-second period, larvae were illuminated with 470 nm light at an intensity of 465 µW/cm² for 3 minutes. Behavioral responses of the larvae during this 3-minute period were recorded and categorized as either "rolling" (indicating a full 360° rotation along the larval body axis) or "no rolling" (indicating incomplete rolling, bending, turning, or no response). Each larva was counted only once, and the cumulative categorized responses were presented in a contingency graph. Staging and experiments were conducted in a blinded and randomized manner.

2.8 Locomotion assays in *D. melanogaste*r larvae

Larvae were staged in darkness on grape agar plates without or with 5 mM 9-cis-retinal. In the indicated experiments, larvae were additionally fed with Rotenone (5µM) for 24 hours at 72 hours after egg laying (AEL) to impair dopaminergic neuron function. Third-instar larvae (96 h ± 4 h AEL) were selected for all experiments. Larvae were carefully chosen and transferred under minimal red-light conditions to a 1% agar film placed on an FTIR-based tracking system (FIM, University of Münster). In each trial, five freely moving larvae were video-captured and stimulated with 525 nm light at an intensity of 130 µW/cm² for the activation of optoDop1R1^{V2} or optoDop1R2^{V2}. The locomotion of the animals was tracked at a rate of 10 frames per second for up to 120 seconds. Locomotion analysis involved the measurement of velocity and bending angles, and it

was conducted using the FIMtrack software (https://github.com/kostasl/FIMTrack). Only animals displaying continuous locomotion before the light stimulus were subjected to analysis. Average locomotion speed and cumulative bending angles were analyzed and plotted for the first 30 seconds under dark or light conditions.

2.9 Innate odor preference and olfactory behavior assays in *D. melanogaster* larva

Groups of 20 carefully staged 3rd instar larvae (96h±4h AEL), were placed at the center of a 2% agar plate, which was divided into two sections. One section contained a receptacle with 10 µl of n-amylacetate (AM, diluted 1:50 in mineral oil; SAFC) or 3-Octanol (3-Oct, Sigma), while the other side with a blank serving as the control. In the context of rescue experiments, the assays were conducted under two distinct conditions: one in complete darkness and the other in the presence of light (at 525 nm, 130 µW/cm²) during the preference behavior assessment. Video recording of the assay duration of 5 minutes, under infrared light illumination, to track the distribution of larvae with a digital camera (Basler ace-2040 gm, Basler, Switzerland). After the 5-minute observation period, the number of larvae present on each side of the divided plate was quantified. Subsequently, the odor preference index was computed as follows: Odor Preference Index = (Number of larvae on the odor side) - (Number of larvae on the blank side) / Total number of larvae

2.10 Learning assays

Odor-fructose reward learning was conducted in accordance with established protocols (Gerber et al., 2013). Groups with 20 larvae were carefully placed within a petri dish coated either with plain 1% agar or 1% agar with 2 M fructose as a reward in the presence of 10 µl n-amylacetate (AM, 1:50). The odor-reward or no reward pairing was done for 3 min (or 5min; as indicated in experiments), alternating 3x between training (odor-reward: odor$^+$), while the unpaired group received reward and no odor during separate 3min (or 5min as indicated) training (blank-reward: blank$^+$). For all optogenetic lines, training was performed under minimum red-light conditions, or with 525nm light activation (130 µW/cm²) during fructose reward training. Reciprocal training was performed for all genotypes and conditions (blank/odor$^+$ and blank$^+$/odor, respectively). After the three training cycles, the larval preference towards the paired odor, specifically AM or blank, was assessed under conditions of darkness by a Basler ace-2040gm camera (same setting as for the olfactory behavior assay), the number of larvae on each side was calculated after a 5-minute interval. Subsequently, the odor preferences

were quantified for both the paired and unpaired groups. The learning index (LI) was then calculated using the following formula: $LI = (Odor\text{-}Pref_{Paired} - Odor\text{-}Pref_{Unpaired})/2$

2.11 Quantification and statistical analysis

All statistical analysis was done with Prism 9 or 10 (Graphpad, San Diego, CA, USA). Boxplots illustrate the median (center line), along with the 25th and 75th percentiles (lower and upper box, respectively), the whiskers extend to the 1st and 99th percentiles. Violin plots with individual data points were employed to illustrate the distribution of the data, particularly for larger sample sizes (high n numbers). For line graphs, the mean±SEM. are shown.

Appropriate statistical tests were chosen depending on the analysis and data. For normal distributed data, an unpaired two-tailed Student's t-test (two groups) was used. Paired two-tailed Student's t-tests were employed for comparisons involving the same individuals under different conditions (e.g. no light vs. light). One-way ANOVA with Dunnett's or Tukey's post-hoc test (more than 2 groups) was utilized for multiple comparisons. Sidak's post-hoc test was performed to compare preselected pairs. Further post-hoc tests (e.g.Bartlett's) were chosen for individual cases, if required for further statistical analysis. Chi-square (χ^2) tests were performed for group comparisons involving categorized data. Mean was used as center measure and standard error of the mean (SEM) or standard deviation (SD) as dispersion measure throughout the study. Statistical significance was defined as follows: $^{*}p < 0.05$, $^{**}p < 0.01$, $^{***}p < 0.001$, $^{****}p < 0.0001$.

3 Included Articles

3.1 Article I

Optimized design and *in vivo* application of optogenetically functionalized *Drosophila* dopamine receptors

Fangmin Zhou[1,2,3], Alexandra-Madelaine Tichy[4,5], Bibi Nusreen Imambocus[2], Shreyas Sakharwade[1,2], Francisco J. Rodriguez Jimenez[6,7], Marco González Martínez[6], Ishrat Jahan[6], Margarita Habib[8], Nina Wilhelmy[9], Vanessa Burre [9], Tatjana Lömker[3], Kathrin Sauter[3], Charlotte Helfrich-Förster[8], Jan Pielage[9], Ilona C. Grunwald Kadow[6,7], Harald Janovjak[4,5,10], Peter Soba[1,2,3,*]

1 Institute of Physiology and Pathophysiology, Friedrich-Alexander-Universität Erlangen-Nürnberg, 91054 Erlangen, Germany
2 LIMES Institute, Department of Molecular Brain Physiology and Behavior, University of Bonn, Carl-Troll-Str. 31, 53115 Bonn, Germany
3 Neuronal Patterning and Connectivity laboratory, Center for Molecular Neurobiology (ZMNH), University Medical Center Hamburg-Eppendorf, 20251 Hamburg, Germany
4 Australian Regenerative Medicine Institute (ARMI), Faculty of Medicine, Nursing and Health Sciences, Monash University, 3800 Clayton, Victoria, Australia
5 European Molecular Biology Laboratory Australia (EMBL Australia), Monash University, 3800 Clayton, Victoria, Australia
6 Institute of Physiology II, University Clinic Bonn (UKB), University of Bonn, 53115 Bonn, Germany
7 ZIEL-Institute of Life and Health, Technical University of Munich, School of Life Sciences, 85354 Freising, Germany
8 Neurobiology and Genetics, Biocenter, University of Würzburg, Am Hubland, 97074 Würzburg
9 Division of Neurobiology and Zoology, RPTU University of Kaiserslautern, 67663 Kaiserslautern, Germany
10 Flinders Health and Medical Research Institute, College of Medicine and Public Health, Flinders University, 5042 Bedford Park, South Australia, Australia

Nature Communications 14, 8434, 2023

DOI: 10.1038/s41467-023-43970-0.

Personal contribution

My contribution to this publication was the following: I performed *in vitro* characterization and analysis of DopRs/optoDopRs, I carried out cAMP signaling, calcium imaging and larval behavior *in vivo*. I discussed, reviewed and commented on the manuscript. In more detail, my results are included in Figures 1-5 and Figure S1-3, S6. In addition, I conducted the experimental investigation during the revision process that resulted in additional figures (Figure S4, S5). I analyzed and plotted these data and wrote the figure legends and methods for the manuscript.

nature communications

Article

https://doi.org/10.1038/s41467-023-43970-0

Optimized design and in vivo application of optogenetically functionalized *Drosophila* dopamine receptors

Received: 18 May 2023

Accepted: 24 November 2023

Published online: 19 December 2023

Check for updates

Fangmin Zhou[1,2,3], Alexandra-Madelaine Tichy[4,5], Bibi Nusreen Imambocus[2], Shreyas Sakharwade[1,2], Francisco J. Rodriguez Jimenez[6,7], Marco González Martínez[6], Ishrat Jahan[6], Margarita Habib[8], Nina Wilhelmy[9], Vanessa Burre[9], Tatjana Lömker[3], Kathrin Sauter[3], Charlotte Helfrich-Förster[8], Jan Pielage[9], Ilona C. Grunwald Kadow[6,7], Harald Janovjak[4,5,10] & Peter Soba[1,2,3]

Neuromodulatory signaling *via* G protein-coupled receptors (GPCRs) plays a pivotal role in regulating neural network function and animal behavior. The recent development of optogenetic tools to induce G protein-mediated signaling provides the promise of acute and cell type-specific manipulation of neuromodulatory signals. However, designing and deploying optogenetically functionalized GPCRs (optoXRs) with accurate specificity and activity to mimic endogenous signaling in vivo remains challenging. Here we optimize the design of optoXRs by considering evolutionary conserved GPCR-G protein interactions and demonstrate the feasibility of this approach using two *Drosophila* Dopamine receptors (optoDopRs). These optoDopRs exhibit high signaling specificity and light sensitivity in vitro. In vivo, we show receptor and cell type-specific effects of dopaminergic signaling in various behaviors, including the ability of optoDopRs to rescue the loss of the endogenous receptors. This work demonstrates that optoXRs can enable optical control of neuromodulatory receptor-specific signaling in functional and behavioral studies.

Behavioral flexibility, learning, as well as goal-directed and state-dependent behavior in animals depend to a large degree on neuromodulatory signaling via G protein-coupled receptors (GPCRs), which tune neuronal network function to the current external sensory environment and the internal state of the animal[1]. Dopamine (DA) is one of the most conserved metabotropic neurotransmitters and modulators, which can activate different G protein-dependent and -independent signaling events via its cognate GPCRs[2,3]. Depending on

[1]Institute of Physiology and Pathophysiology, Friedrich-Alexander-Universität Erlangen-Nürnberg, 91054 Erlangen, Germany. [2]LIMES Institute, Department of Molecular Brain Physiology and Behavior, University of Bonn, Carl-Troll-Str. 31, 53115 Bonn, Germany. [3]Neuronal Patterning and Connectivity laboratory, Center for Molecular Neurobiology (ZMNH), University Medical Center Hamburg-Eppendorf, 20251 Hamburg, Germany. [4]Australian Regenerative Medicine Institute (ARMI), Faculty of Medicine, Nursing and Health Sciences, Monash University, 3800 Clayton, Victoria, Australia. [5]European Molecular Biology Laboratory Australia (EMBL Australia), Monash University, 3800 Clayton, Victoria, Australia. [6]Institute of Physiology II, University Clinic Bonn (UKB), University of Bonn, 53115 Bonn, Germany. [7]ZIEL-Institute of Life and Health, Technical University of Munich, School of Life Sciences, 85354 Freising, Germany. [8]Neurobiology and Genetics, Biocenter, University of Würzburg, Am Hubland, 97074 Würzburg, Germany. [9]Division of Neurobiology and Zoology, RPTU University of Kaiserslautern, 67663 Kaiserslautern, Germany. [10]Flinders Health and Medical Research Institute, College of Medicine and Public Health, Flinders University, 5042 Bedford Park, South Australia, Australia. e-mail: peter.soba@fau.de

23

the receptor subtype, DA signaling can thereby increase or decrease the excitability of the affected neuronal substrates as well as induce synaptic plasticity and long-term transcriptional changes. Typically, activation of D1-like receptors leads to an increase in cyclic adenosine monophosphate (cAMP) levels through activation of adenylate cyclase (AC), while D2-like receptors inhibit AC and thus decrease cAMP levels[2]. Thereby, DA regulates numerous functional processes, including motivation, locomotion, learning and memory via its distinct cognate receptors[2–6]. Dysregulated DA signaling has been linked to several neurological conditions, including schizophrenia, ADHD, and Parkinson's disease[2]. Due to the differential expression and signaling properties of DA receptors affecting distinct circuits and behaviors, systemic DA pathway modulation can result in unwanted and unspecific side effects. Thus, it is highly desirable to obtain more precise insight into the action of DA signaling and that of other neuromodulators on a receptor-specific basis. However, pharmacological approaches are not cell type-specific and difficult to control temporally, thus lacking the precision and specificity to target defined circuits and their regulated behaviors. At the same time, most current genetic tools do not offer the temporal control and sensitivity required to manipulate the corresponding receptors directly and acutely with high efficiency in vivo.

Optogenetics has revolutionized our understanding of the function of specific neural circuits, allowing for investigation of their role in behavior and physiology through genetic targeting and high spatiotemporal precision[7–9]. While cell type-specific manipulation of neurons in vivo using light-controlled ion channels has evolved rapidly, and numerous powerful tools are available, optical control of modulatory GPCR mediated signaling in general, and in circuits endogenous to the modulatory neurotransmitter, has been more limited so far[10–12]. This is in part due to the difficulty of designing functional light-activatable GPCRs showing endogenous-like localization and activity of the target receptor. Previous studies established chimeric receptor designs in which the intracellular domains of a receptor of interest were swapped into a prototypical light-sensitive GPCR, typically bovine Rhodopsin (Rho). In one example, this strategy has been successfully applied to the β2-adrenergic receptor (β2AR) and has yielded a functional optoXR displaying signaling comparable to its native counterpart[13–17]. A systematic approach for class A GPCRs has produced a library of human optoXRs displaying in vitro signaling capacity corresponding to orphan receptors[18]. Similarly, functional class A/F chimera (Rho:Frizzled7) and class A/C chimera (Opn4:mGluR6) were designed and applied in optogenetic cellular migration and vision restoration studies, respectively[19,20]. Additional approaches have used structure-guided design, primary sequence-based empirical methods or native light-sensitive GPCRs with similar signaling properties as the receptor of interest[10,11,17]. While it is appealing to utilize optoXRs to mimic GPCR function, design and functionality remain challenging. Importantly, the signaling properties of many GPCRs depend on the cell type, receptor localization and activation kinetics as well as the functional context[11,21–24]. Only in a few cases have optoXRs been deployed in vivo, and they have so far mostly been used to manipulate G protein signaling pathways without perturbation of the endogenous receptor signaling (see Supplementary Table 1). Thus, there is very limited evidence that optoXRs can functionally replace or mimic endogenous GPCR function in target tissues.

In vivo models, including *Drosophila melanogaster*, have contributed extensively to our understanding of neuromodulatory GPCR signaling in neural circuit function and behavior[1,25–29]. In particular, DA and its receptors have been long studied in *Drosophila* regarding their role in learning, memory and goal-directed behaviors[3,5,6,30–33]. *Drosophila* encodes 4 Dopamine receptors: two D1-like receptors (Dop1R1 and Dop1R2), a D2-like receptor (Dop2R) and Dopamine-Ecdysteroid receptor (DopEcR). Dop1R1 and Dop1R2 display conserved functions in learning and memory in the insect learning center, the mushroom body (MB), by inducing cAMP and intracellular calcium store release, respectively[31,34–40]. Dop1R1 is particularly important for the acquisition of new memories[34], while Dop1R2 is involved in transient and permanent forgetting of learned associations in flies[34,39,41]. In addition, both receptors play opposing roles in directing synaptic and behavioral plasticity in the MB during olfactory association[37], and Dop1R1 has also been implicated in larval locomotion[42]. Yet so far, most acute (i.e., dynamic and short-term) cell type-specific functions of these receptors, such as the timing and duration of their signaling, could not be manipulated due to the lack of suitable tools. OptoXRs that can be readily expressed in vivo and allow precise spatiotemporal dissection of endogenous-like dopaminergic signaling and function would solve these issues but are currently not available.

Here, we generate and optimize chimeric optoXRs of *Drosophila melanogaster* Dop1R1 and Dop1R2 by taking advantage of evolutionary constraints of G protein-coupling specificity. We characterize optoDopR signaling in vitro and find that our optimized design results in improved signaling specificity and light-dependent G protein activation. In vivo, expression and subcellular localization to axonal and dendritic compartments were strongly improved, more closely resembling the endogenous receptor distribution. We then demonstrate that optoDopRs in vivo can replace or mimic dopamine receptor functionality in various DA-dependent behaviors, including locomotion, arousal, learning and operant feeding behavior. Intriguingly, we find cell type and receptor-specific functions using our optoDopRs in innate and adaptive behaviors showing their utility to study DA-dependent function and behavior with high spatiotemporal precision and specificity.

Results

Optimization of sequence-based design for optoDopRs

Previous studies have developed sequence-[14,20,43] or structure-based[17] rules for exchanging regions of GPCRs to generate various chimera that display functional signaling of the target receptor yet altered ligand/sensor specificity. Most optoXRs developed so far were built on Rho as a light-sensitive backbone, mainly due to its well-described structure and function, together with sequence-based rules developed by Kim et al.[14,16,18,44]. In the original design rules, transmembrane (TM) helices and intracellular loop (ICL) regions were exchanged. This resulted in chimeric receptors in which at least two or all three ICLs with proximal TM residues and the C-terminus of Rho were substituted by the corresponding regions of the target receptor. We applied this methodology (termed here 'V1') to *Drosophila* Dop1R1 (Fig. 1a) and Dop1R2 as well as six further *Drosophila* GPCRs (AkhR, 5-HT1B, Lgr3, Lgr4, sNPFR, and TkR99D) and generated corresponding optoXR chimera. To test their functionality in cells, we utilized chimeric $G_{\alpha s}$ proteins ('G_{sx} assay') consisting of the signaling domain of G_s fused to the GPCR binding sequence of a specific G_α protein (s/i/t/o/z/q/12/13/15), thus redirecting all signaling toward cAMP increase (Fig. 1b)[45]. Co-expression of G_{sx} chimera with the GPCR of interest in HEK293T or G protein-deficient cells (HEK293ΔG7)[46] for G_s-coupled receptors thus allows direct comparison of coupling specificity and strength using the cAMP reporter GloSensor[43]. Except for optoDop1R1^{V1}, we failed to detect any major G protein signaling in all other optoXRs, (Fig. 1c, Supplementary Fig. 1a–g). Therefore, we revised the receptor design based on recently computed evolutionary constraints of G protein binding to receptors[47]. It became evident that ICL1 was generally not contributing to major G protein binding contacts, so we reasoned that retaining Rho ICL1 should not limit signaling but may increase the structural integrity of a chimeric optoXR. In addition, we readjusted the TM7/C-terminus exchange site to accommodate additional G-protein contact sites. These sites have been defined in the evolutionary analysis of GPCR-G protein interactions through inspection of multiple GPCR-G-protein complex structures of class A receptors. Using this approach (termed 'V2'), we

https://doi.org/10.1038/s41467-023-43970-0

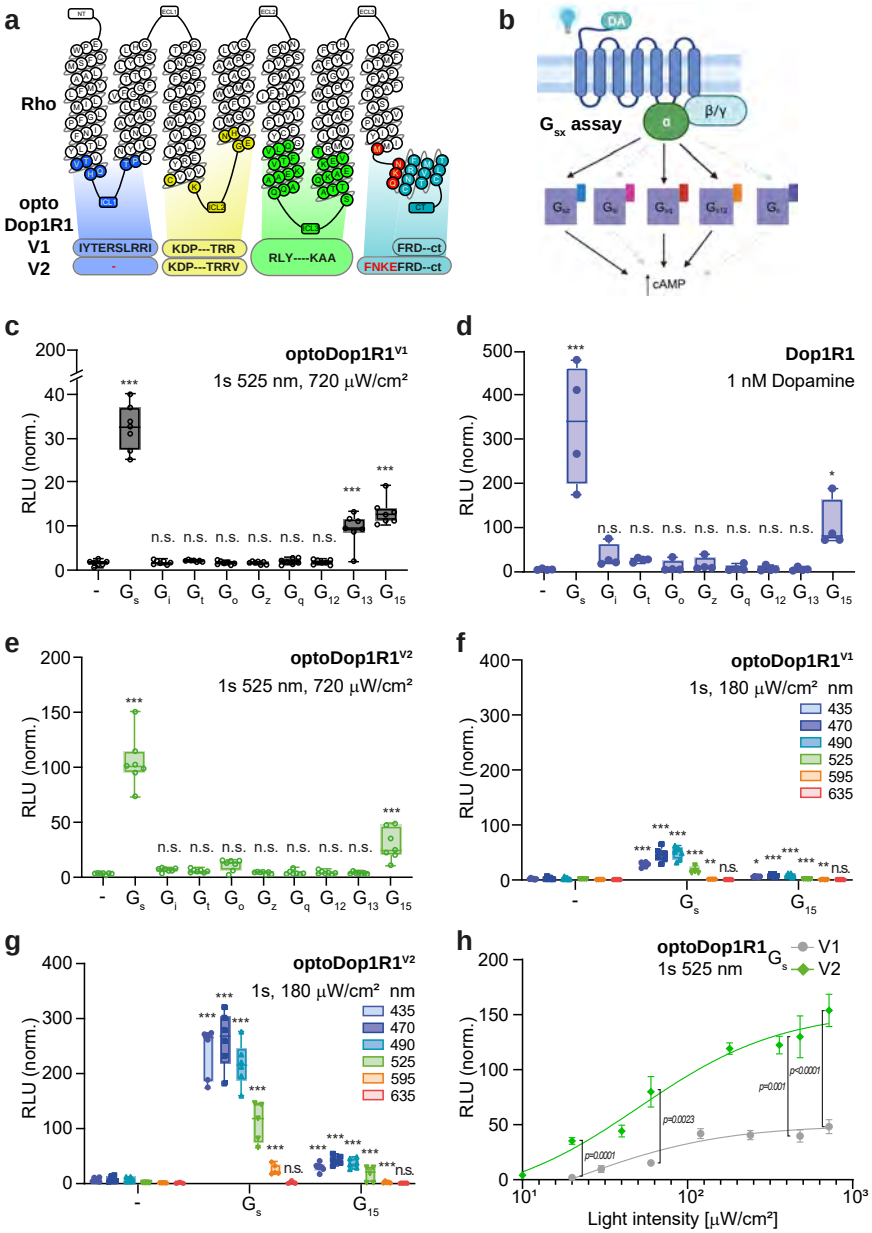

Fig. 1 | Design and characterization of optoDop1R1^{V2}. **a** Schematic overview of optoDop1R1 variants based on the original approach[14] (V1) and the optimized design (V2). **b** Schematic overview of the G_{sX} assay. Coupling to chimeric G_α subunits (G_{sX}) redirects all G protein signaling to the same cellular response (cAMP). Created with BioRender.com. **c** G protein-coupling properties of optoDop1R1^{V1} after activation with light (1 s, 525 nm, 720 µW/cm^2). Maximum normalized responses are shown as relative light units (RLU, $n = 7$, $^{**}p < 0.01$, $^{***}p < 0.001$, one-way ANOVA with Dunnett's post hoc test). **d** G protein-coupling properties of *Drosophila* Dop1R1 with 1nM dopamine. Maximum normalized responses are shown as relative light units (RLU, $n = 4$, $^{*}p < 0.05$, $^{***}p < 0.001$, one-way ANOVA with Dunnett's post hoc test). **e** G protein-coupling properties of improved optoDop1R1^{V2} after activation with light (1 s, 525 nm, 720 µW/cm^2). Maximum normalized responses are shown as relative light units (RLU, $n = 7$, $^{***}p < 0.001$, one-way ANOVA with Dunnett's post hoc test). **f** Wavelength-dependent maximum G protein activation of optoDop1R1^{V1} after activation with light (1 s, 180 µW/cm^2, $n = 7$, $^{*}p < 0.05$ $^{**}p < 0.01$, $^{***}p < 0.001$, one-way ANOVA with Dunnett's post hoc test). **g** Wavelength-dependent maximum G protein coupling of optoDop1R1^{V2} after activation with light (1 s, 180 µW/cm^2, $n = 6$, $^{***}p < 0.001$, one-way ANOVA with Dunnett's post hoc test). **h** Light intensity-dependent maximum of cAMP induction (G_s coupling) of optoDop1R1^{V1} and optoDop1R1^{V2} after activation with light shown as relative light units (RLU, 1 s, 525 nm, mean ± SEM, optoDop1R1^{V1}: 20 µW/cm^2: $n = 6$, 30/240 µW/cm^2: $n = 3$, 60/480/720 µW/cm^2: $n = 4$, 120 µW/cm^2: $n = 8$; optoDop1R1^{V2}: 10/20/40/360 µW/cm^2 $n = 6$, 60/720 µW/cm^2: $n = 8$, 180 µW/cm^2: $n = 4$; 480 µW/cm^2: $n = 10$; p-values as indicated, unpaired two-tailed Student's t-test with Welch's correction). All n indicate the number of independent experiments. All boxplots depict 75th (top), median (central line) and 25th (bottom) percentile, whiskers depict 99th (top) and 1st (bottom) percentile. Source data and statistical details are provided as a Source Data file.

redesigned the optoDop1R1 chimera and studied the effects of these changes.

Characterization of Dop1R1 and optoDop1R1 activation profiles

We compared the activity of the *Drosophila* Dop1R1 receptor with its opto-variants designed with the previous (V1) or optimized (V2) approach. Upon addition of dopamine, Dop1R1 showed strong coupling to G_s as previously described[39], as well as G_{15} and weak, not significant coupling to inhibitory G proteins (Fig. 1c, Supplementary Fig. 2a, b). G_s and G_{15} coupling showed dose-dependent responses in the nanomolar range (Supplementary Fig. 2b). In comparison, optoDop1R1^{V1} activation using a 1 s light pulse (525 nm) resulted in G_s,

https://doi.org/10.1038/s41467-023-43970-0

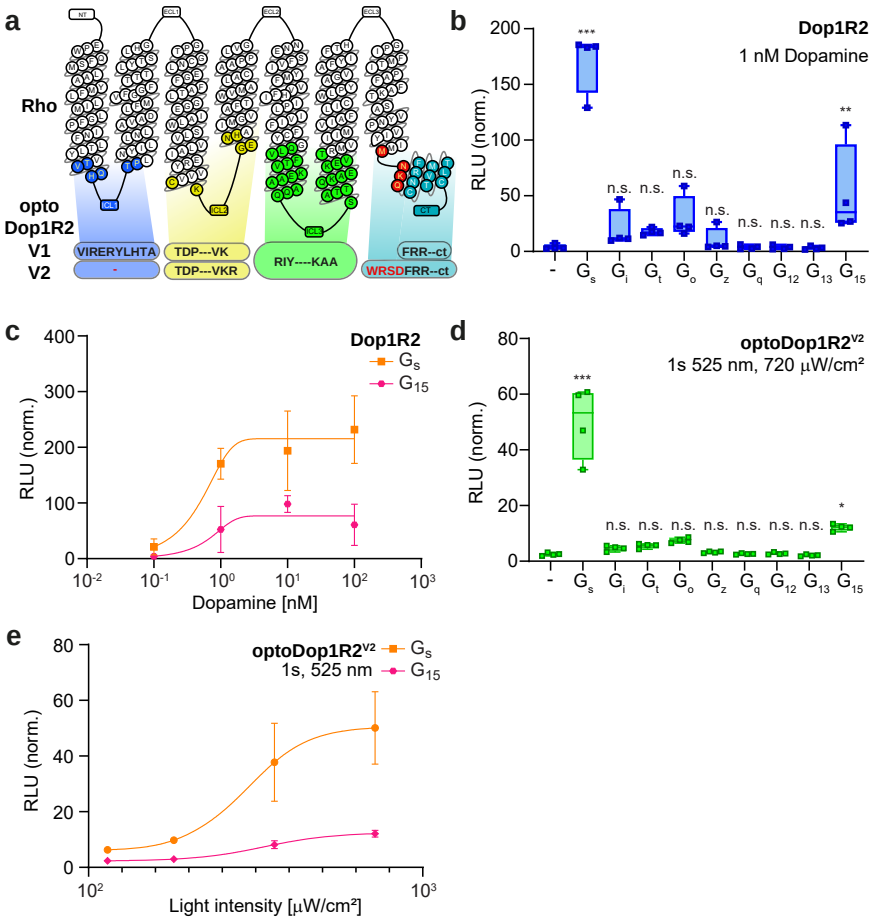

Fig. 2 | Design and characterization of optoDop1R2^{V2}. **a** Schematic overview of optoDop1R2^{V2} design compared to V1. **b** G protein-coupling properties of *Drosophila* Dop1R2 with 1nM dopamine. Maximum normalized responses are shown as relative light units (RLU, $n = 4$, $^{**}p < 0.01$, $^{***}p < 0.001$, one-way ANOVA with Dunnett's post hoc test). **c** DA concentration dependent maximum activation of G_s and G_{15} signaling of Dop1R2 (mean ± SEM, 0.1/10 nM: $n = 3$; 1.0/100 nM: $n = 4$). **d** G protein-coupling properties of optoDop1R2^{V2} after activation with light (1 s, 525 nm, 720 µW/cm²). Maximum normalized responses are shown as relative light units (RLU, $n = 4$, $^{*}p < 0.05$, $^{***}p < 0.001$, one-way ANOVA with Dunnett's post hoc test). **e** Light intensiy-dependent maximum of G_s and G_{15} signaling induced by optoDop1R2^{V2} (1 s, 525 nm, mean ± SEM, $n = 4$). All n indicate the number of independent experiments. All boxplots depict 75th (top), median (central line) and 25th (bottom) percentile, whiskers depict 99th (top) and 1st (bottom) percentile. Source data and statistical details are provided as a Source Data file.

G_{13} and G_{15} coupling with moderate efficiency (Fig. 1c, Supplementary Fig. 2c). While significant induction of G_s signaling was observed, the coupling profile did not match the Dop1R1 receptor profile entirely due to aberrant G_{13} signaling and responses were comparatively small. In contrast, optoDop1R1^{V2} activation more closely resembled the wild-type receptor displaying strong coupling to G_s and G_{15}, as well as weak, not significant coupling to inhibitory G proteins (Fig. 1d, Supplementary Fig. 2d). As a previous report showed coupling of Dop1R1 to G_q[39], which was not observed in our experiments, we utilized the recently developed TRUPATH assay[48] allowing to directly measure G protein complex dissociation after receptor activation (Supplementary Fig. 2e). Using this independent approach, we confirmed the results of the G_{sx} assay and observed G_s and G_{15} but not G_q coupling of Dop1R1 and optoDop1R1^{V2} under our conditions (Supplementary Fig. 2f, g). Of note, however, G_{15} is a promiscuous G_α protein of the G_q family able to induce G_q-type signaling via phospholipase C activation[49].

We then compared the wavelength-dependent G_s and G_{15} activation profiles of the two optoDopR variants. While maximum activation was observed with 470-490 nm light in cells expressing either receptor, optoDop1R1^{V2} induced 5-10-fold higher responses than the corresponding V1 receptor (Fig. 1f, g, Supplementary Fig. 2h). In optoDop1R1^{V2} expressing cells, strong G_s activation was also observed in the green to orange wavelength range up to 595 nm, while it was weak in the case of optoDop1R1^{V1}. Direct comparison of light intensity-dependent G_s signaling induced by the two variants showed half-maximal activation at around 50 µW/cm² (at 525 nm) for both optoXRs (Fig. 1h).

However, responses elicited in the V2-expressing cells excelled in light sensitivity displaying 3- to 20-fold higher G_s responses, particularly at low light intensities below 40 µW/cm². Overall, unlike the classic chimeric sequence-based approach, our optimized optoXR^{V2} design yielded an optoDop1R1 variant exhibiting superior light sensitivity and high signaling specificity comparable to the Dop1R1 wild-type receptor.

Generation and characterization of functional optoDop1R2^{V2}

While for Dop1R1 both designs yielded active optoXRs albeit with different quality, the original approach did not produce a functional optoDop1R2 as no reliable light-dependent responses could be detected in the G_{sx} assay (Supplementary Fig. 1a). We thus again turned to our optimized design and generated optoDop1R2^{V2}, which concordantly contained the Rho ICL1 and the extended C-terminus (Fig. 2a).

We first characterized *Drosophila* Dop1R2 using the G_{sx} assay. Dop1R2 showed dose-dependent coupling to G_s, G_{15} and inhibitory G proteins upon the addition of dopamine in the range of 0.1–100 nM (Fig. 2b, c, Supplementary Fig. 3a, b). Strikingly, in our optimized optoDop1R2^{V2} the implemented changes indeed resulted

in a functional optoXR (Fig. 2d, e, Supplementary Fig. 3c). Similar to the wild-type receptor, optoDop1R2^{V2} coupled to the same G proteins, prominently with G_s and G_{15} showing light-dose-dependent responses in the range of 114–720 μW/cm^2 (Fig. 2d, e). Furthermore, a similar light-dependent profile was also obtained for G_i and G_o responses (Supplementary Fig. 3d). The G protein-coupling profile and dose-dependent activity of optoDop1R2^{V2} closely resembled the wild-type receptor in this assay, yet the maximum activation levels remained consistently lower under these conditions. As for optoDop1R1^{V2}, the rhodopsin-based optoDop1R2^{V2} showed maximum responses to 470-490 nm light (Supplementary Fig. 3e). We also compared Dop1R2 and optoDop1R2^{V2} responses in the TRUPATH assay. For both receptors, we observed comparable activation of G_{15} but only minor induction of G_s for optoDop1R2 suggesting favored activation of G_q-type signaling (Supplementary Fig. 3f, g). Overall, these results show that the optoXR^{V2} design approach allowed the generation of functional and specific optoDopRs not obtainable with the previous strategy.

Characterization of optoDopR localization in vivo

Based on the promising activity of optoDopRs^{V2} in cell culture assays, we generated transgenes to investigate their functionality in vivo. We used the ϕC31 integration method to ensure comparable transgene expression efficiency due to the defined chromosomal integration site[50]. We first tested the expression and localization of optoDopRs in the *Drosophila* mushroom body (MB), the central learning and memory center in insects[51–54]. The principal MB neurons, Kenyon cells (KCs), receive olfactory and other sensory input via dendritic input at the calyx region. This information can then be modulated via compartmentalized dopaminergic innervation along their axonal arbors that are interconnected with MB output neurons (MBONs, Fig. 3a) to relay the information to other connected brain areas[54–57]. The expression of both Dop1R1 and Dop1R2 in KCs is required for learning and memory[34,37,39]. First, we expressed the optoDopRs in larval KCs and specific MBONs involved in odor-fructose association (MBON$^{g1/g2}$)[56] and investigated their cellular localization using immunohistochemistry. In larval KCs, the optoDop1R1^{V1} signal was detectable in the soma and only weakly in axons and the calyx (Fig. 3b, Supplementary Fig. 4a). In comparison, optoDop1R1^{V2} showed more prominent expression and was clearly visible in larval KC axons as well as in the calyx region (Fig. 3b, Supplementary Fig. 4a). Similarly, optoDop1R2^{V2} showed prominent axonal and dendritic localization in larval KCs (Fig. 3b, Supplementary Fig. 4a). Quantitative analysis of axon/soma ratios of optoDopR signals demonstrated that the V2 variants had a more prominent axonal localization, while optoDop1R1^{V1} was mostly confined to KC cell bodies (Fig. 3c). We then compared the localization of optoDop1R1^{V2} in KCs to the localization of endogenous Dop1R1 visualized via a C-terminal split-GFP tag (Dop1R1$^{GFP_{11}}$), enabling cell type-specific endogenous labeling by co-expression of the complementary GFP (GPF_{1-10}) fragment[58]. In both cases, prominent expression was visible in the axonal lobes, calyx, and cell bodies (Fig. 3d). Quantitative analysis of compartmental signal intensity ratios revealed a similar distribution of endogenous Dop1R1 and optoDop1R1^{V2} (Fig. 3e). We further compared their localization at the single cell level in MBON$^{g1/g2}$. We first confirmed the expression of endogenous Dop1R1 in these MBONs using the endogenous GFP tagging method (Fig. 3f). Dop1R1 localized to axon terminals and dendritic compartments in MBON$^{g1/g2}$. Again, unlike optoDop1R1^{V1}, optoDop1R1^{V2} displayed a similar localization, including labeling of axonal varicosities resembling presynaptic sites (Fig. 3f, Supplementary Fig. 4b).

We obtained similar results for optoDopR localization in the adult MB with better expression levels for the V2 variants compared to optoDop1R1^{V1}, indicating more efficient folding, transport and/or stability of the improved versions (Supplementary Fig. 4c, d). Using an activity-induced expression system[59], we next analyzed the expression of endogenous Dop1R1 as well as optoDopRs in individual adult KCs. Endogenous GFP-labeled Dop1R1 localized to somatodendritic compartments and was present within the axonal compartments of the MB lobes (Fig. 3g). Interestingly, Dop1R1 localized to presynaptic varicosities in KC axons, suggesting it exerts part of its function in presynaptic KC compartments (Fig. 3g, arrowheads). optoDop1R1^{V2} again displayed a comparable localization, including labeling of axonal varicosities (Fig. 3h, arrowheads). In contrast, optoDop1R1^{V1} was only weakly localized to axons and dendrites, labeling only a few axonal varicosities (Supplementary Fig. 4e). optoDop1R2^{V2} prominently labeled axons and dendrites, suggesting efficient transport and localization to its site of action (Supplementary Fig. 4f). Overall, these data show that the V2 design yielded optoDopRs that are well expressed and, in case of optoDop1R1^{V2}, closely resemble endogenous receptor localization with prominent localization along KC/MBON axons including presynaptic sites.

Characterization of optoDopR functionality in vivo

We next wanted to assay if 2nd messenger responses can be elicited by our optoDopRs in vivo. Dop1R1 has been reported to be primarily linked to G_s-dependent cAMP production, while Dop1R2 can induce intracellular calcium release via activation of G_q-family signaling that includes G_{15}[37,39,49]. Elevated cAMP and calcium levels in *Drosophila* larval nociceptors can elicit a stereotyped escape response[60], which we chose as a first proxy for functional activation of our optoXRs (Fig. 4a, b). We expressed optoDopRs in larval nociceptors and illuminated freely crawling larvae with blue light for 3 min. Similar to channelrhodopsins, functional optoXR expression requires retinal feeding as *Drosophila* does not produce sufficient amounts of *cis*- or all-*trans*-retinal to support the function of exogenously expressed light-sensitive GPCRs or channelrhodopsins, respectively. We expressed the blue light-activated adenylate cyclase bPAC[61] and the cation channelrhodopsin CsChrimson[62] as positive controls for cAMP and calcium-induced escape responses, respectively. bPAC and our optoXRs induced spontaneous rolling during light illumination, which generally occurred sporadically and with some delay (Fig. 4a, b, Supplementary Movies 1–4). In contrast, activation of CsChrimson resulted in a high percentage of animals rolling immediately after light onset (Supplementary Movie 5). Consistent with the predicted coupling to intracellular calcium stores by optoDop1R2, we also observed fast rolling responses in some cases. Overall, these data indicate that all optoXRs are capable of inducing 2nd messenger signaling in vivo with similarity to cAMP and calcium-induced escape responses.

To measure specific 2nd messenger responses induced by optoDopRs in vivo, we used fluorescent reporters for cAMP and calcium levels (Fig. 4a). Dop1R1 and Dop1R2 were previously shown to primarily regulate cAMP or store-released calcium levels in KC neurons, respectively[37]. We expressed the cAMP reporter Gflamp1[63] together with optoDop1Rs or bPAC in larval KCs and imaged light-induced cAMP changes in the soma and medial lobe regions in dissected live larval brains. bPAC activation with blue light was able to elicit strong cAMP increase, particularly in the KC soma region due to its cytosolic localization, and to a lesser extent also in the medial lobe region (Fig. 4c, d, Supplementary Movie 6). Similarly, activation of optoDop1R1^{V1} resulted in a significant cAMP increase in the soma but not in the medial lobe region (Supplementary Fig. 5a–c). In comparison, activation of optoDop1R1^{V2} resulted in cAMP increase preferentially in the medial lobe and to a lower degree in the soma region, which was largely dependent on the presence of 9-*cis*-retinal during the rearing of the animals (Fig. 4e–g, Supplementary Fig. 5d, Supplementary Movie 7). Axonal cAMP levels in the medial lobe decayed to background levels within approx. 60 s after a 10 s blue light stimulus. Of note, bPAC has been described to exhibit dark activity[64], and baseline fluorescence levels of Gflamp1 were significantly higher than for optoDop1R1^{V2}, suggesting optoDop1R1^{V2} exhibits no or low dark

https://doi.org/10.1038/s41467-023-43970-0

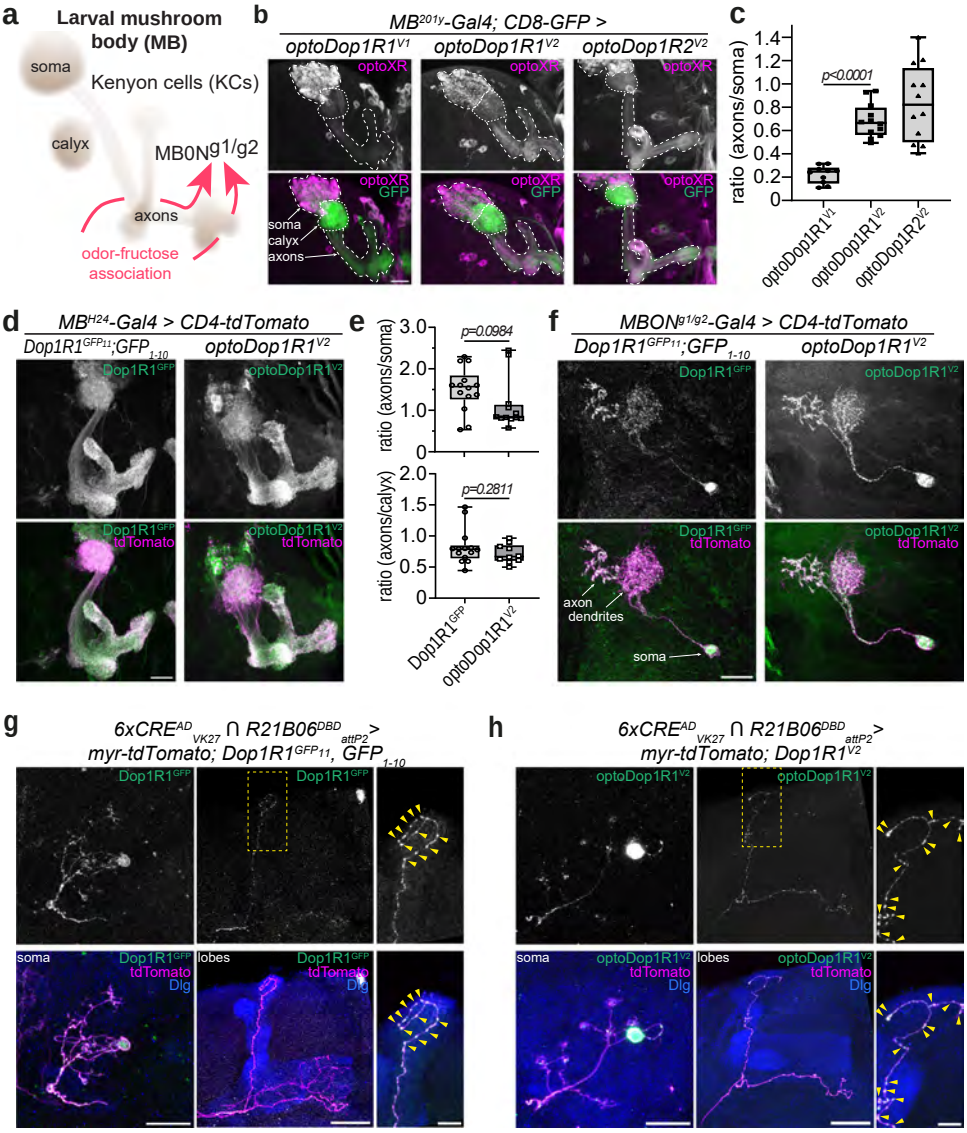

Fig. 3 | In vivo localization of optoDopRs and endogenous Dop1R1. a Schematic model of the larval mushroom body consisting of Kenyon cells (KCs) receiving input from dopaminergic neurons and connecting to output neurons (MBONs). Odor-Fructose association and learning require dopaminergic input and MBON$^{g1/g2}$ (adapted from ref. 56). **b** Immunohistochemistry of optoXRs (anti-Rho labeling) expression in KCs (labeled with CD8-GFP) in the larval mushroom body. Localization of KC somata, calyx (dendrites) and axons are outlined (scale bar: 25 µm). **c** Quantification of the optoDopR signal intensity ratios of axons/soma ($n = 10$, 12, 12 samples from 5, 6, 6 biologically independent animals, respectively, unpaired two-tailed Student's *t*-test). **d** Expression of endogenous Dop1R1 and optoDop1R1^{V2} in the larval mushroom body (scale bars: 25 µm). **e** Quantification of the Dop1R1 and optoDop1R1 signal intensity ratios of axons/soma and axons/calyx. ($n = 14$, 10 samples from 7, 5 biologically independent animals, respectively, unpaired two-tailed Student's *t*-test). **f** Labeling of endogenous GFP-tagged Dop1R1 and expression of optoDop1R1^{V2} (anti-Rho labeling) in MBON$^{g1/g2}$. Axon terminals, dendrites and soma are indicated and co-labeled by CD4-tdTomato expression (representative image from two independent experiments with multiple samples). Scale bar: 20 µm. **g** Single-cell labeling of endogenous GFP-tagged Dop1R1 in adult KCs using activity-dependent induction of Gal4 activity[52]. Example of KC labeled with myristoylated(myr)-tdTomato and endogenous Dop1R1^{GFP} (anti-GFP-labeled) in the somatodendritic region, axonal lobes and enlarged axon region (MB labeled by anti-Dlg). Presynaptic varicosities are indicated by arrowheads (representative images from two independent experiments with multiple samples). Scale bars: 10 µm, 20 µm, 5 µm. **h** Single-cell expression of optoDop1R1^{V2} in adult MB showing a labeled KC expressing myr-tdTomato and optoDop1R1^{V2} (anti-Rho labeled) displaying localization to the somatodendritic compartment, axonal lobes and enlarged axon region (MB labeled by anti-Dlg). Presynaptic varicosities are indicated by arrowheads (representative image from two independent experiments with multiple samples). Scale bars: 10 µm, 20 µm, 5 µm. All boxplots depict 75th (top), median (central line) and 25th (bottom) percentile, whiskers depict 99th (top) and 1st (bottom) percentile. Source data and statistical details are provided as a Source Data file.

activity compared to bPAC. In comparison, optoDop1R2^{V2} activation resulted in weak and not significantly changed cAMP levels suggesting it has a limited capacity to regulate endogenous cAMP levels in KCs (Fig. 4f, g, Supplementary Fig. 5e, f).

We then tested for calcium store release upon optoDop1R^{V2} activation by co-expression of the fluorescent calcium reporter GCaMP6s[65] in larval KCs. Activation of optoDop1R2^{V2} resulted in robust calcium responses in the MB medial lobe and KC soma region (Fig. 4h–j, Supplementary Fig. 5g, Supplementary Movie 8), consistent with the reported role of Dop1R2 in calcium store mobilization[37]. In contrast, optoDop1R1^{V2} activation did not elicit significant calcium responses after blue light exposure suggesting it does not induce G_q-type signaling in KCs in vivo (Fig. 4i, j, Supplementary Fig. 5h, i). We also tested whether optoDopRs can be repeatedly activated under these conditions. optoDop1R1^{V2} and optoDop1R2^{V2} activation induced consistent cAMP and calcium responses during three

https://doi.org/10.1038/s41467-023-43970-0

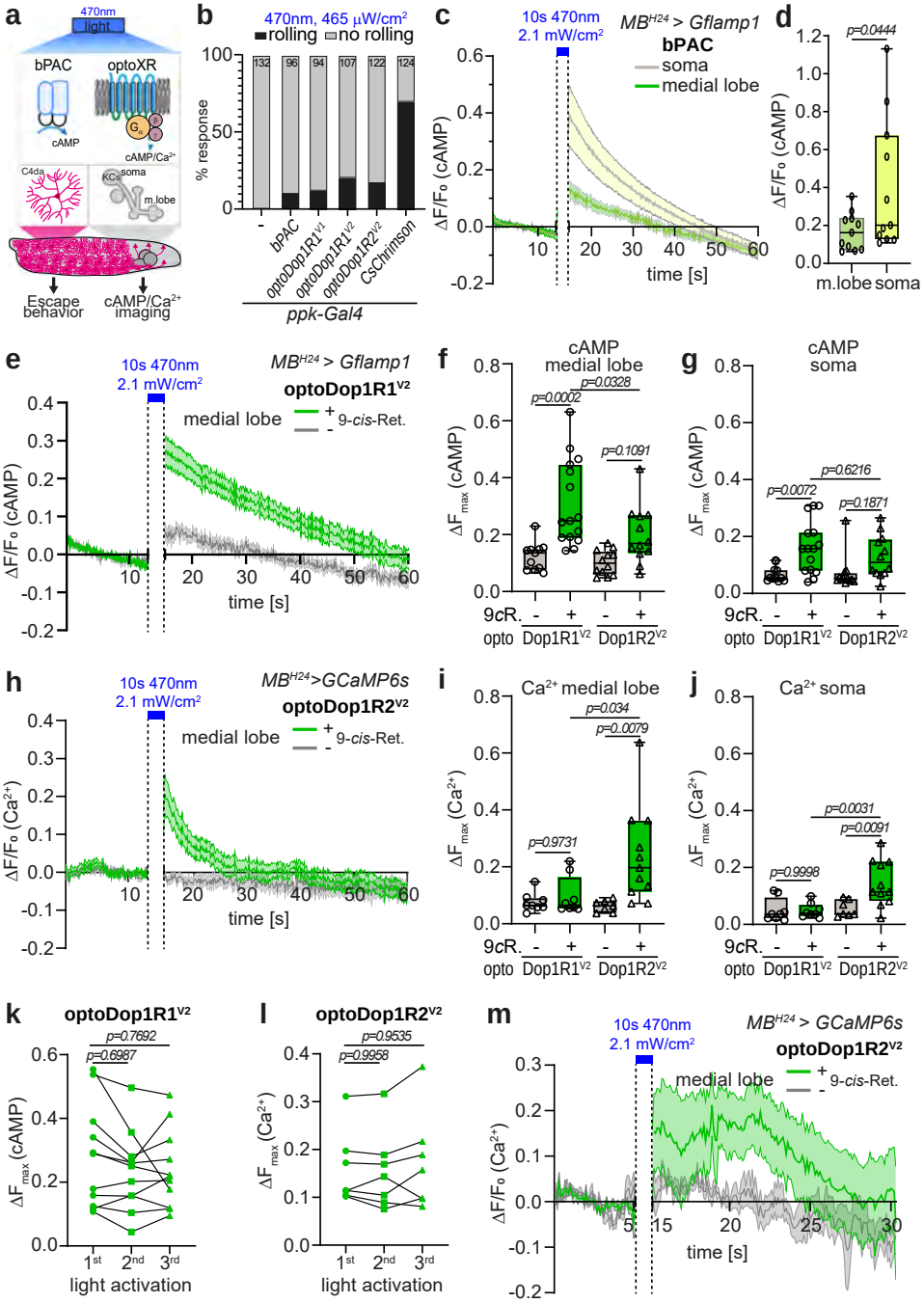

Fig. 4 | In vivo characterization of optoDopR signaling activity. a Schematic of of bPAC and optoXRs activation in larval nociceptors (C4da) or Kenyon cells (KCs). cAMP increase in C4da neurons elicits spontaneous larval escape responses. KC expression of GFlamp1 or GCaMP6s was used to image cAMP or Ca^{2+} responses, respectively. **b** Spontaneous escape responses (rolling) upon blue light illumination in larvae expressing bPAC, optoXRs, or CsChrimson in larval nociceptors (*n* animals as indicated). **c** cAMP responses over time in the larval mushroom body (soma and medial lobe) induced by bPAC activation (mean ± SEM, *n* = 11, 11 biologically independent samples). **d** Maximum cAMP responses in the KC soma and MB medial lobe after light-induced activation of bPAC (*n* = 11, 11 biologically independent samples, unpaired two-tailed Student's *t*-test). **e** cAMP responses in the medial lobe after optoDop1R1^{V2} activation (mean ± SEM, *n* = 11, 15 biologically independent samples). **f** Maximum cAMP responses in the MB medial lobe after light-induced activation of optoDop1R1^{V2} and optoDop1R2^{V2} (*n* = 11, 15, 12, 12 biologically independent samples, one-way ANOVA with Tukey's post hoc test). **g** Maximum cAMP responses in the KC soma region after light-induced activation of optoDop1R1^{V2} and optoDop1R2^{V2} (*n* = 11, 15, 12, 12 biologically independent samples, one-way ANOVA with Tukey's post hoc test). **h** Calcium imaging in the larval mushroom body of isolated brains using GCaMP6s and optoDop1R2^{V2} with and without 9-*cis*-Retinal feeding (mean ± SEM, *n* = 7, 11 biologically independent samples). **i** Maximum calcium responses in the MB medial lobe after light-induced activation of optoDop1R1^{V2} and optoDop1R2^{V2} (*n* = 8, 8, 7, 11 biologically independent samples, one-way ANOVA with Tukey's post hoc test). **j** Maximum calcium responses in the KC soma region after light-induced activation of optoDop1R1^{V2} and optoDop1R2^{V2} (*n* = 8, 8, 7, 11 biologically independent samples, one-way ANOVA with Tukey's post hoc test). **k** Maximum cAMP responses in the MB medial lobe after repeated light-induced activation of optoDop1R1^{V2} (*n* = 9 biologically independent samples, one-way ANOVA with Tukey's post hoc test). **l** Maximum calcium responses in the MB medial lobe after repeated light-induced activation of optoDop1R2^{V2} (*n* = 6 biologically independent samples, one-way ANOVA with Tukey's post hoc test). **m** In vivo calcium imaging of the larval mushroom medial lobe using GCaMP6s and light-induced activation of optoDop1R2^{V2} in animals reared with or without 9-*cis*-retinal (mean ± SEM, *n* = 5, 5 animals). All boxplots depict 75th (top), median (central line) and 25th (bottom) percentile, whiskers depict 99th (top) and 1st (bottom) percentile. Source data and statistical details are provided as a Source Data file.

consecutive activation cycles, respectively (Fig. 4k, l, Supplementary Fig. 5j, k).

We further confirmed optoDop1R2 activity by imaging light-induced changes in calcium levels in live intact larvae. Upon blue light illumination, we could detect calcium responses in the medial lobe as well as in KC somata (Fig. 4m, Supplementary Fig. 5l–n). Interestingly, calcium levels remained elevated for up to 10s after light stimulation, similar to the store release of calcium linked to dopaminergic activation in mammalian neurons[66]. Consistent with our imaging in dissected live larval brains, axonal responses in the medial lobe were overall stronger and more sustained than in the KC somata (Fig. 4i–m, Supplementary Fig. 5i–k), suggesting the local environment of receptor localization affects signaling efficiency.

Taken together, these data show that optoDopRs^{V2} display the expected receptor type-specific signaling in KCs and that they can be repeatedly activated to induce relevant changes in cAMP and calcium levels in vivo.

Functional analysis of dopaminergic signaling in fly larvae

We next wanted to test the functionality of the optoDopRs in relevant behaviors. Dopamine signaling plays a pivotal and conserved role in locomotion, reward, and innate preference behavior[2,3,5,31,67,68]. Dop1R1 function has been implicated in larval locomotion[42], and disruption of dopaminergic neuron function in flies and mammals results in locomotion defects and is a key feature of Parkinson's disease[69–72]. We used Rotenone-induced impairment of dopaminergic neurons in larvae, which resulted in reduced locomotion velocity and increased turning behavior as previously described[70] (Fig. 5a). We reasoned that locomotion deficits might be rescued by triggering dopaminergic signaling in the receiving cells. To this end, we expressed optoDopRs in the endogenous pattern of Dop1R1 using a knock-in Gal4 line (*Dop1R1$^{KO\text{-}Gal4}$*). Locomotion of rotenone-treated larvae was tracked in the dark and subsequently upon green light illumination. We used green light (525 nm) in most of our assays due to strong innate avoidance responses toward blue light, which can interfere with behavioral readouts[73–75]. Expression and activation of optoDop1R1^{V1} did not result in significant changes in locomotion and turning behavior in rotenone-treated larvae, except that green light induced an increase in turning behavior independent of optoDop1R1^{V1} activity (Fig. 5b, Supplementary Fig. 6a). In contrast, we observed clear light-dependent recovery of locomotion using optoDop1R1^{V2} activation (Fig. 5c, Supplementary Movie 9). Optogenetic activation of Dop1R1 signaling using the V2 variant significantly increased larval velocity and reduced the overall turning behavior of the Rotenone-treated animals, but not in control larvae without 9-*cis*-Retinal or Rotenone feeding (Supplementary Fig. 6b, c). This strongly suggests that optoDop1R1^{V2} signaling in DA-receiving neurons can rescue toxin-induced dopaminergic impairment and corresponding locomotion deficits. Interestingly, expression and activation of optoDop1R2^{V2} in the same pattern could also partially but not fully restore larval locomotion after Rotenone treatment (Fig. 5d, Supplementary Fig. 6d).

We next explored another core function of Dop1R1 signaling by addressing its function in learning and memory. *Drosophila* larvae are capable of reward learning, e.g., by forming olfactory preferences through odor-fructose association[38,53]. As in adult flies, the MB plays a key role in this process: KCs receive specific DAergic input and form a tripartite circuit with MB output neurons (MBONs), which together reinforce specific preference behavior[56]. As Dop1R1 signaling and cAMP increase in the MB are essential for learning in flies[33,34], we tested if optoDop1R1 activation during odor-fructose association can replace endogenous Dop1R1 function in KCs. We confirmed that KC-specific knockdown of Dop1R1 reduced learning performance in larvae (Supplementary Fig. 6e). Using optoDop1R1^{V1} or optoDop1R1^{V2} expression in KCs under these conditions partially rescued fructose-odor learning (Supplementary Fig. 6f, g). These results are consistent with the reported function of Dop1R1 in learning and suggest that acute activation of optoDop1R1 signaling in KCs during odor-fructose association is sufficient for learning. Interestingly, even optoDop1R1^{V1} activation could significantly rescue learning despite its weaker expression and predominantly somatic localization. However, as dopaminergic responses in KCs were shown to be compartmentalized within the axons[40,57], activation of optoDopRs in KCs cannot mimic this aspect of endogenous DA signaling. To avoid this issue, we tested for a potential function of Dop1R1 in MBON$^{g1/g2}$, which is specifically required for odor-fructose reward learning[56] and where we have shown endogenous Dop1R1 expression (see Fig. 3f). RNAi-mediated knockdown of Dop1R1 in MBON$^{g1/g2}$ indeed reduced larval reward learning strongly suggesting DA signaling via Dop1R1 has an essential modulatory function in these MBONs (Supplementary Fig. 6h, i). We additionally expressed optoDop1R1^{V2} and activated it specifically during fructose-odor training, which partially rescued preference induction and learning compared to no light conditions (Fig. 5e, Supplementary Fig. 6j). This suggests that acute optoDop1R1^{V2} activation during learning can functionally replace endogenous DA signaling in an MBON essential for odor-fructose association.

As DopR signaling is also involved in state and valence-dependent preference behavior[5], we further tested DopR knockout larvae in naïve odor preference. We focused on Amylacetate (AM) and 3-Octanol (3-OCT), two substances commonly used for larval odor-reward learning[76,77]. Dop1R1 knockout (*Dop1R1$^{ko\text{-}Gal4}$*) and Dop1R2 knockout (*Dop1R2$^{ko\text{-}Gal4}$*) larvae displayed no altered preference toward AM, which we used in our odor-reward learning paradigm (Supplementary Fig. 6k). However, *Dop1R2^{ko}* larvae showed a specific reduction in 3-OCT preference (Fig. 5f). We therefore tested if optoDop1R2^{V2} activation could rescue innate preference behavior. Light exposure during the preference assay indeed was able to restore 3-OCT preference in *Dop1R2$^{ko\text{-}Gal4}$* larvae expressing optoDop1R2^{V2} in an endogenous-like pattern (Fig. 5g). This result confirmed the functionality of optoDop1R2^{V2} by restoring the in vivo function of its corresponding wild-type receptor in naïve odor preference.

Functional analysis of dopaminergic signaling in adult flies

We further investigated the functionality of optoDopRs in adult flies, which requires very high light sensitivity of the optogenetic tools due to the low light penetrance of the fly cuticle, particularly below a wavelength of 530 nm[78]. We first tested the optoDop1R1^{V2} function in the MB in an associative odor-shock learning paradigm, which requires dopaminergic input from PPL1 neurons to KCs[33,79]. We confirmed that Dop1R1 is required in KCs for odor-shock learning using an MB-specific RNAi-mediated knockdown (Fig. 6a, b). We then asked if activation of optoDop1R1^{V2} in KCs can enhance performance when paired with the shock paradigm. We observed a trend toward more robust learning when optoDop1R1^{V2} was activated during shock pairing, but this performance was not significantly enhanced (Fig. 6a, c). Interestingly, optoDop1R1 co-activation reduced trial-dependent variability in this assay, indicating more robust learning. We then asked if activation of DA signaling in KCs via optoDop1R1^{V2} activation could replace the shock stimulus, which would imply that this artificial DA signaling could replace a teaching signal with a negative valence. However, optogenetic activation of DA signaling without the unconditioned stimulus did not confer any preference behavior (Fig. 6d). These results indicate that either activation of Dop1R1 signaling alone is not sufficient for associative preference behavior or that the missing restriction to a distinct KC compartment interferes with memory formation.

We then assayed DopR function in pigment dispersing factor (PDF) neurons, which consist of small (s-LN$_v$s) and large lateral ventral neurons (l-LN$_v$s). In particular, l-LN$_v$s are important for arousal, sleep and light input to the circadian clock[80,81], and previous studies suggested that Dop1R1 but not Dop1R2 has a depolarizing function in

https://doi.org/10.1038/s41467-023-43970-0

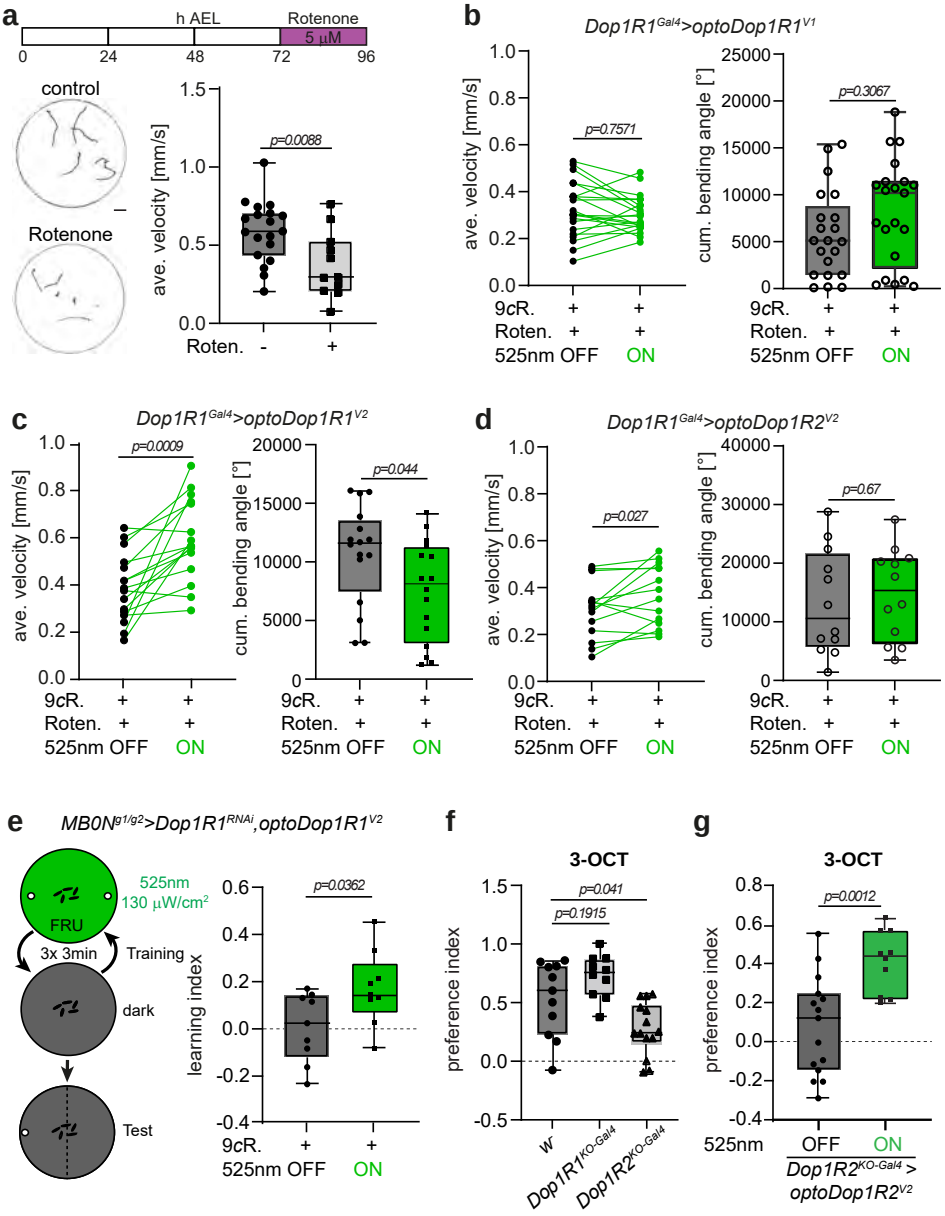

Fig. 5 | Functional validation of optoDopRs in *Drosophila* larvae in vivo. a Larvae were fed with 5 µM Rotenone for 24 h at 72 h after egg laying (AEL), inducing locomotion defects due to impaired dopaminergic neuron function. Representative larval tracks of control or Rotenone-fed animals are shown (1 min, scale bar: 10 mm). Quantification of the average velocity of control or Rotenone-fed animals ($n = 19$, 11 animals, two-tailed unpaired Student's *t*-test). **b** Average velocity and cumulative bending angles of larvae fed with 9-*cis*-Retinal (9cR) and Rotenone expressing optoDop1R1^{V1} in an endogenous Dop1R1 pattern (*Dop1R1*$^{ko\text{-}Gal4}$>*optoDop1R1*^{V2}) before and during 525 nm light illumination (1 min each, $n = 29$, 29 animals, two-tailed paired Student's *t*-test). **c** Average velocity and cumulative bending angles of larvae fed with 9-*cis*-Retinal (9cR) and Rotenone expressing optoDop1R1^{V2} (*Dop1R1*$^{ko\text{-}Gal4}$>*optoDop1R1*^{V2}) before and during 525 nm light illumination (1 min each, $n = 12$, 16 animals, two-tailed paired Student's *t*-test). **d** Average velocity and cumulative bending angles of larvae fed with 9-*cis*-Retinal (9cR) and Rotenone expressing optoDop1R2^{V2} (*Dop1R1*$^{ko\text{-}Gal4}$>*optoDop1R2*^{V2}) before and during 525 nm light illumination (1 min each, $n = 14$, 12 animals, two-tailed paired Student's *t*-test). **e** MBON$^{g1/g2}$ and Dop1R1-dependent single odor-fructose learning in larvae. Animals expressing optoDop1R1^{V2} and Dop1R1^{RNAi} in MBON$^{g1/g2}$ were trained using fructose-odor learning (3x3min) with or without light activation during fructose exposure (3 min 525 nm, 130 µW/cm^2). Learning index of 9cR-fed animals with and without light activation during training are shown ($n = 9$, 9 independent experiments, two-tailed unpaired Student's *t*-test). **f** Innate preference for 3-Octanol (3-OCT) in control (*w*$^-$), *Dop1R1*$^{KO\text{-}Gal4}$ and *Dop1R2*$^{KO\text{-}Gal4}$ 3rd instar larvae ($n = 11$, 10, 14 independent experiments, one-way ANOVA with Tukey's post hoc test). **g** Innate preference for 3-OCT in *Dop1R2*$^{KO\text{-}Gal4}$ 3rd instar larvae expressing optoDop1R1^{V2}. Innate preference for 3-OCT in 9cR-fed 3rd instar animals with and without light activation during the assay ($n = 15$, 10 independent experiments, two-tailed unpaired Student's *t*-test). All boxplots depict 75th (top), median (central line) and 25th (bottom) percentile, whiskers depict 99th (top) and 1st (bottom) percentile. Source data and statistical details are provided as a Source Data file.

I-LN$_v$s affecting the arousal state[82]. We assayed the activity of flies using the *Drosophila* Activity Monitor (DAM) system[83] from TriKinetics (Fig. 6e). Young flies were transferred to constant darkness after they had been reared under a 12 h dark/12 h light cycle. On the third day, darkness was interrupted by 12 arousing blue light pulses of different durations (10 min, 15 min, 20 min) given every hour for a period of 12 h that was in phase with the previous light period. The blue light pulses not only efficiently aroused the flies but additionally activated optoDopRs expressed in PDF neurons. Interestingly, expression and activation of optoDop1R1^{V2} were able to boost activity during the blue light periods compared to isogenic controls not fed with 9-*cis*-Retinal (Fig. 6f, g, Supplementary Fig. 7a, b). We performed a more detailed

https://doi.org/10.1038/s41467-023-43970-0

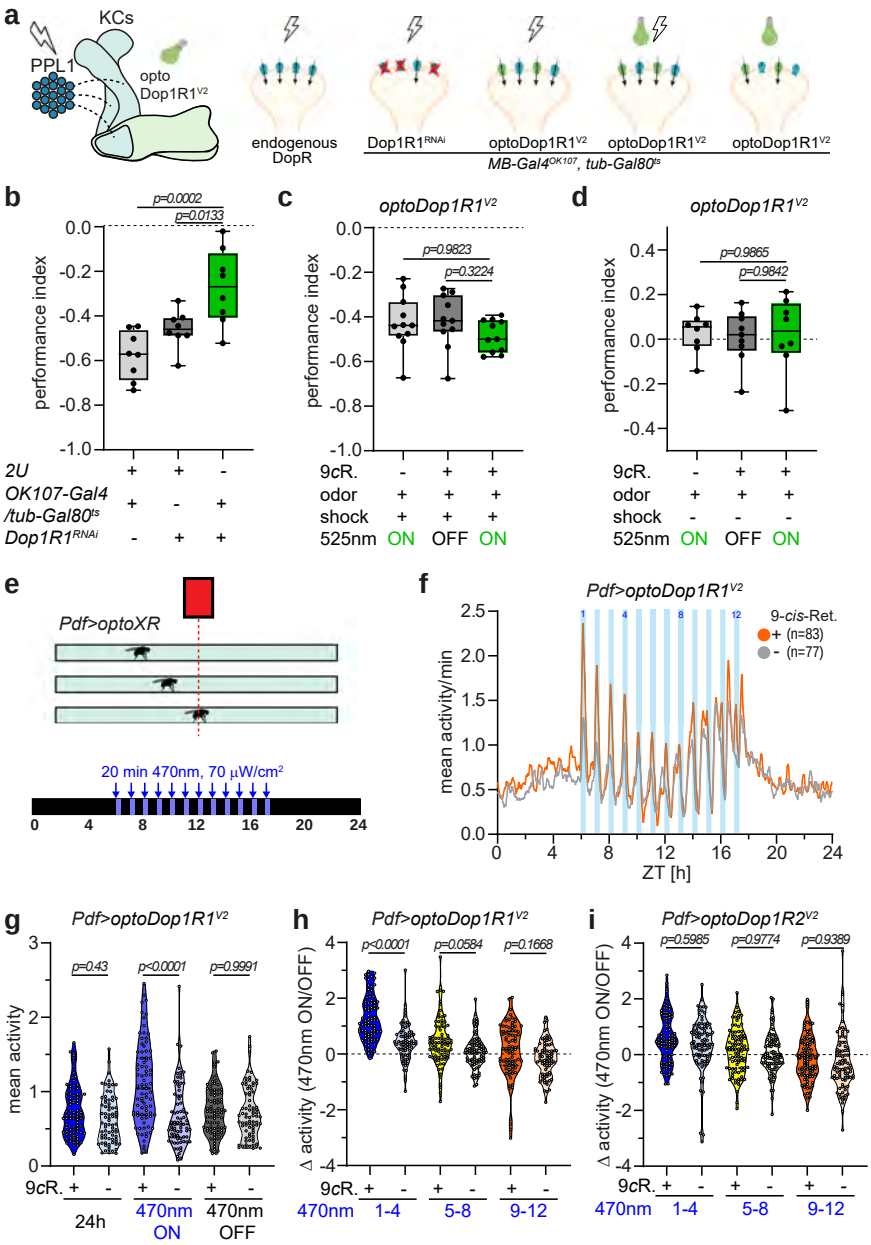

Fig. 6 | Cell type-specific function of acute Dop1R1 activity in adult flies. **a** Schematic of adult mushroom body organization and associative odor-shock learning under different conditions (shock and/or light and altered Dop1R1 activity). Adult flies (*OK107-Gal4; tub-Gal80^{ts}; UAS-RNAi/optoXR*) for experiments (**b**–**d**) were shifted to the permissive temperature (31 °C) 4 days prior to the behavioral assay to induce Gal4 expression. **b** Performance index after aversive odor-shock learning with or without adult-specific RNAi-mediated knockdown of Dop1R1 in Kenyon cells ($n = 8$ independent experiments, one-way ANOVA with Dunnett's post hoc test). **c** Performance index after aversive odor-shock learning with or without additional activation of optoDop1R1^{V2} in Kenyon cells ($n = 11$ independent experiments, one-way ANOVA with Dunnett's post hoc test). **d** Performance index after pairing odor and optoDop1R1^{V2} activation in Kenyon cells without shock ($n = 8$ independent experiments, one-way ANOVA with Dunnett's post hoc test). **e** Schematic of activity monitor with flies expressing optoXRs in PDF neurons with daytime-dependent light activation using a blue light stimulus. The gray bar indicates the flies' subjective day. **f** Mean activity during 24-h monitoring in flies expressing optoDop1R1^{V2} in PDF neurons (mean, $n = 83, 77$ animals). Blue light pulses (12x 20 min, 1/h) during subjective daytime increase fly activity during the morning hours. **g** Mean activity of *Pdf>optoDop1R1^{V2}* -expressing flies during the entire 24 h, all light on and light off phases ($n = 83, 77$ animals, one-way ANOVA with Tukey's post hoc test). **h** Activity difference of flies expressing optoDop1R1^{V2} in PDF neurons during light on/off times in the morning (1–4), midday (5–8) and afternoon (9–12) ($n = 83, 77$ animals, one-way ANOVA with Tukey's post hoc test). **i** Activity difference of flies expressing optoDop1R2^{V2} in PDF neurons during light on/off times in the morning (1–4), midday (5–8) and afternoon (9–12) ($n = 90$ animals, one-way ANOVA with Tukey's post hoc test). All boxplots depict 75th (top), median (central line) and 25th (bottom) percentile, whiskers depict 99th (top) and 1st (bottom) percentile. All violin plots with single data points depict data distribution. Source data and statistical details are provided as a Source Data file.

analysis as the activity peaks were increasingly desynchronized with the blue light pulses (occurring after the light pulses) during the second part of the day. This revealed a significant effect of optoDop1R1^{V2} activation specifically during the first 4h window (Fig. 6h). Next, we also tested optoDop1R2^{V2} activation under the same conditions but did not observe a significant effect on blue light-induced activity (Fig. 6i, Supplementary Fig. 7c–e). We then evaluated the expression of DopRs in I-LN$_v$s using respective Gal4 knock-in lines. We detected strong and specific reporter signal for Dop1R1 only in I-LN$_v$s, consistent with its function in light-induced arousal[82] (Supplementary Fig. 7f). In contrast,

https://doi.org/10.1038/s41467-023-43970-0

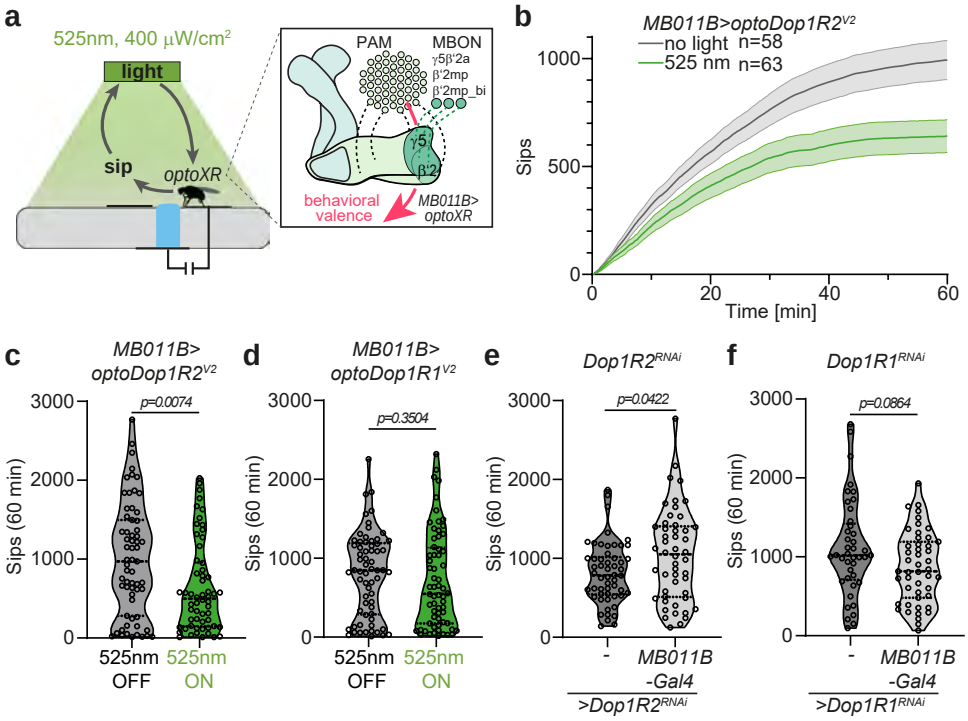

Fig. 7 | Cell type-specific function of operant Dop1R2 activity in adult satiety. **a** OptoPAD setup allowing light stimulation upon feeding action. Flies expressing optoXRs in a subset of MBONs (MBONγ5β′2a,β2mp and β2mp-bilateral) related to behavioral valence receive a light stimulus (1 s 525 nm 400 µW/cm^2) every time they feed on the sucrose drop. **b** Cumulative sips over time for flies expressing optoDop1R2^{V2} using *MB011B-Gal4* without or with light stimulation (mean ± SEM, $n = 58, 63$ animals). **c** Total sips at 60 min for flies expressing optoDop1R2^{V2} using *MB011B-Gal4* without or with light stimulation ($n = 58, 63$ animals, two-tailed Mann-Whitney test). **d** Total sips at 60 min for flies expressing optoDop1R1^{V2} using *MB011B-Gal4* without or with light stimulation ($n = 65, 65$ animals, two-tailed Mann-Whitney test). **e** Total sips at 60 min for flies expressing Dop1R2^{RNAi} control or with *MB011B-Gal4* ($n = 54, 50$ animals, two-tailed Mann-Whitney test). **f** Total sips at 60 min for flies expressing Dop1R1^{RNAi} control or with *MB011B-Gal4* ($n = 41, 47$ animals, two-tailed Mann-Whitney test). All boxplots depict 75th (top), median (central line) and 25th (bottom) percentile, whiskers depict 99th (top) and 1st (bottom) percentile. All violin plots with single data points depict data distribution, dotted lines depict 75th (top) and 25th (bottom) percentile, solid central line the median. Source data and statistical details are provided as a Source Data file.

the Dop1R2 reporter signal was very faint in I-LN$_v$s suggesting limited or no endogenous expression (Supplementary Fig. 7f). Together, these findings suggest a specific role for Dop1R1 signaling in I-LN$_v$s promoting morning activity upon arousal.

Finally, we also addressed a potential function of DopRs in adult MBONs previously implicated in encoding behavioral valence in MB-dependent tasks[52,84]. We chose an optoPAD setup which allows operant optogenetic stimulation of flies during feeding using a closed-loop system[85]. We expressed optoDopRs in relevant MBONs providing output of the γ5/β′2-compartments of the MB and activated DA signaling with green light pulses every time the flies were sipping food (Fig. 7a). Operant activation of optoDop1R2^{V2} resulted in a decreased sipping rate over time suggesting that Dop1R2 signaling reduced the feeding drive and/or preference for the offered food (Fig. 7b, c). In contrast, operant optoDop1R1^{V2} activation during feeding did not result in changed feeding behavior (Fig. 7d, Supplementary Fig. 8a). We further asked if the endogenous DopRs played a role in feeding in valence-encoding MBONs. RNAi-mediated knockdown of Dop1R2 but not Dop1R1 in MBON-γ5/β′2 resulted in an increased feeding rate (Fig. 7e, f, Supplementary Fig. 8b, c), suggesting a specific function for Dop1R2 in these MBONs in feeding-related behavior. Controls without expression of optoDopRs did not show altered feeding with or without operant light exposure (Supplementary Fig. 8d–g).

Taken together, operant optogenetic activation and RNAi-mediated decrease of Dop1R2 signaling in valence-encoding MBONs resulted in specific opposite effects on feeding. In contrast, manipulation of Dop1R1 activity in these MBONs did not alter feeding behavior. These findings strongly suggest that DA signaling in valence-encoding MBONs regulates feeding drive specifically via Dop1R2. Overall, these data show neuron-specific functions of Dop1R1 and Dop1R2 signaling, which can be specifically induced by optoDopR activation.

Discussion

By optimizing the chimeric optoXR approach, we generated highly functional and specific optoDopRs that allowed in vivo analysis of receptor-specific function and behavior in *Drosophila*. optoDop1R1^{V2} showed enhanced and efficient activation in the blue and green spectral range (up to 595 nm) in cellular assays with light-dose-dependent activation properties resembling the wild-type receptor. While Rho-based optoXRs display a broad wavelength range of activation, they are compatible with red-shifted optogenetic tools, including channelrhodopsins like Chrimson that can be activated above 600 nm[62]. This should enable simultaneous optical control of neuronal activity via ion channel-mediated as well as neuromodulatory pathways, providing a way forward toward all-optical access to neuronal network function in vivo. For example, it will be highly interesting to combine optogenetic activation of specific DAergic neurons using CsChrimson as a teaching signal together with activation of Dop1R1 or Dop1R2 in KCs or responding MBONs to investigate timing-dependent synaptic plasticity and learning induced by receptor-specific signaling[37].

The high light sensitivity of the Rho backbone enables the activation of our optoXRs with blue or green light in adult flies in vivo despite less than 6% light penetrance of the adult cuticle in this spectral range[78,86]. Although Rho is known to inactivate after its light cycle and only slowly being recycled[87], we did not observe a run-down in

functionality in vitro or in vivo, possibly due to the abundance of the expressed optoXRs and the supplemented 9-*cis*-retinal.

Localization, cell type-specific and subcellular signaling dynamics are key to understanding endogenous GPCR signaling[24,88,89]. Recent evidence showed that 2nd messenger signaling can occur in nanodomains with receptor-specific profiles[90], emphasizing the importance of proper subcellular localization. Our optoDopR^{V2}s display localization in the fly mushroom body in somatic and axonal compartments similar to their endogenous counterparts[58]. In contrast, the previous design did not yield a functional optoDop1R2^{V1} receptor, and an optoDop1R1^{V1} mostly localizing to the somatic compartment with a signaling profile different from the wild-type receptor. While some functional complementation was obtained with optoDop1R1^{V1} in larval learning assays, unlike the V2 variants, it was not able to restore locomotion in animals with impaired DAergic neurons. This suggests that careful chimeric design is necessary to mimic endogenous receptor localization, signaling and function. This notion is consistent with optoDopR^{V2}s mirroring the specific localization and signaling properties of their corresponding wild-type receptors. Dop1R1 has been shown to be required for cAMP responses in KCs, while Dop1R2 is required for calcium store release during olfactory conditioning[37]. Therefore, these tools will be beneficial to further unravel their temporal activation requirements to induce functional associations during learning or goal-directed behavior.

DA signaling plays a complex role in innate and adaptive behaviors. We used a wide range of behavioral paradigms showing that our optoDopRs exhibit cell type, receptor, and behavioral paradigm-specific functions in vivo. We showed that both optoDopR^{V2}s are functional and can at least partially replace endogenous DopRs in several assays, including odor preference, locomotion and learning. At the same time, we uncovered a cell type-specific requirement of DopR signaling: only optoDop1R1^{V2} but not optoDop1R2^{V2} activation promoted LN_v-mediated arousal; vice versa, operant activation of optoDop1R2^{V2} but not optoDop1R1^{V2} in valence-encoding MBONs was able to control feeding. DopR function has been extensively studied in KCs but has so far not been investigated in MBONs. Our findings therefore strongly suggest that corresponding MB outputs are also under the control of DA signaling. Thus, our optoXRs provide an entry point to gain insight into temporal and cell type-specific DA signaling requirements of the insect learning center, enabling detailed studies of the temporospatial requirement of DA signaling for learning, valence encoding, goal-directed and innate behavior in one of the most developed and heavily used model systems.

Although our improved optoXR design allowed the generation of optoDopRs that are functional in vivo, the complexity of GPCR signaling and the high sequence diversity of class A receptors make a general rational design of such tools difficult. Our incorporated adjustments provide an improved starting point that could be useful to generate optoXRs from other target receptors. Recently used approaches using structure-based design allowed improving the functionality of optoβ2AR, significantly increasing its light-induced signaling properties[17]. However, experimental structures of opto-DopRs are currently not available. Similarly, the implementation of spectrally tuned or bistable rhodopsin backbones, as for example, shown for mouse Opn4[20,91], lamprey parapinopsin or mosquito Opn3[92], yields further promise to extend the optoXR toolbox. Combinations of these complementary methods could further improve optoXR design and functionality to enable efficient chimera generation allowing in vivo studies of other receptors in the future.

Methods

OptoDopR design

OptoDopR sequences were designed using Rho as the acceptor receptor, with segments containing G protein binding sites exchanged for those of the target receptor. To determine cut sites at the segment edges, a multiple protein sequence alignment of Rho and the target receptors was generated using Muscle[93]. Macros written in IgorPro were then used to cut and combine the aligned protein sequences in an automated fashion. V1 cut sites were based on previously published receptor designs[14,18]. For V2, cut sites around ICL1 and the C-terminus were amended to reflect previously published G protein binding sites[47]: residues in ICL1 were shown to not contribute to G protein binding, thus exchanges in ICL1 were omitted to retain the intact Rho ICL1. Conversely, the C-terminal cut sites were moved further toward the TM domains as these residues were shown to contribute to G protein binding. C-terminal Rho residues (TETSQVAPA) were added to the C-terminus of optoXRs V1/V2 chimeric constructs to enable comparative immunolabeling using anti-Rho antibodies. Protein sequences of chimeric GPCRs generated in this study are shown in Supplementary Table 2.

Plasmids

cDNAs of wild-type *Drosophila* Dop1R1 and Dop1R2 were obtained from the *Drosophila* Genomics Resource Center (DGRC, Bloomington, IN, USA) and cloned into pCDNA3.1 (Thermo Fisher). optoDop1R1 and optoDop1R2 chimera (V1 and V2) were synthesized as codon-optimized cDNAs (Thermo Fisher) and cloned into pCDNA3.1 and pUAttB. Chimeric G proteins for the G_{sx} assay[45] and the TRUPATH assay plasmids were obtained from Addgene (Watertown, MA, USA).

Cell culture and live-cell G protein-coupling assays

G protein coupling of wild-type and chimeric GPCR constructs was tested in HEK293T cells (gift from M. Karsak, ZMNH, University Medical Center Hamburg-Eppendorf, Germany) or HEK293-ΔG7[46] (lacking GNAS/GNAL/GNAQ/GNA11/GNA12/GNA13/GNAZ; gift from A. Inoue, Tohoku University, Japan) using the G_{sx} assay[45]. The GPCR constructs were subcloned into pcDNA3.1 (Thermo Fisher). HEK293T cells were incubated in DMEM medium containing 10% FBS (PAN Tech.) with penicillin (100 U/mL) and streptomycin (100 mg/mL) at 37 °C and 5% CO_2. For transfection, cells were seeded into white 96-well plates (Greiner Bio One) coated with poly-L-lysine (Sigma Aldrich). On the next day, the medium was changed to DMEM/FBS containing 10 mM 9-*cis*-Retinal.

Cells were then transfected with individual opto- or wild-type receptors, G protein chimera (G_{sx}) and Glo22F (Promega) using Lipofectamine 2000 (Thermo Fisher). Cells were incubated at 37 °C and 5% CO_2 for 24 h and the medium was replaced with Leibovitz's L-15 media (without phenol-red, 1% FBS) containing 2 mM beetle luciferin (in 10 mM HEPES pH 6.9) and 10 mM 9-*cis*-retinal (for optoXRs) and cells were incubated at room temperature for 1h. For optoXR experiments, the plates were kept in the dark at all times before illumination and cAMP-dependent luminescence was measured using a Berthold Mithras multimode plate reader (Berthold Tech., Germany). Baseline luminescence was measured three times, and activation of DopRs was induced by ligand addition (dopamine at various concentrations diluted in L-15). For optoDopR activation, cells were illuminated with a 1-s light pulse using an LED light plate (Phlox Corp., Provence, France) or a CoolLED pE-4000 (CoolLED, Andover, UK). Specific light intensities and wavelengths are indicated in individual experiments. Technical duplicates were performed for all experiments with a minimum of three independent trials. For data quantification, each well was normalized to its pre-activation baseline.

For the TRUPATH assay[48], HEK293ΔG7 cells were seeded as described above, co-transfected with RLuc8-G_α, G_β, G_γ-GFP2 and wild-type or opto-DopRs in a 1:1:1:1 ratio (100 ng/well total DNA) using Lipofectamine 2000. Cells were incubated for 24 h at 37 °C, 5% CO_2 and subsequently, in Leibovitz's L-15 media (without phenol-red, with L-glutamine, 1% FBS, penicillin/streptomycin 100 mg/ml) and 9-*cis*

Table 1 | Transgenic *Drosophila* lines used in this study

Line	Label	Source
Dop1R1$^{KO\text{-}Gal4}$	Knockout-Gal4 of Dop1R1	BDSC# 84714
UAS-Dop1R1^{RNAi}	Knockdown of Dop1R1	BDSC# 62193
UAS-Dop1R2^{RNAi}	Knockdown of Dop1R2	BDSC# 51423
Dop1R2$^{KO\text{-}Gal4}$	Knockout-Gal4 of Dop1R2	BDSC# 84715
201y-Gal4	Expresses GAL4 in the mushroom body	BDSC# 64296
H24-Gal4	Expresses GAL4 in the mushroom body	BDSC# 51632
UAS-bPAC	Optogenetic cAMP induction	Stierl et al. (ref. 61), BDSC# 78788
UAS-optoDop1R1^{V2}	Optogenetic Dop1R1 activation	This study
UAS-optoDop1R2^{V2}	Optogenetic Dop1R2 activation	This study
UAS-optoDop1R1^{V1}	Optogenetic Dop1R1 activation	This study
ppk-Gal4	Expresses GAL4 in C4da neurons	Han et al. (ref. 99)
UAS-CsChrimson-GFP	Optogenetic activation	Klapoetke et al. (ref. 62), BDSC# 55136
UAS-Gflamp1	cAMP reporter	Wang et al. (ref. 63)
UAS-Gcamp6s	calcium reporter	Chen et al. (ref. 65)
MBONg1g2-Gal4	Expresses GAL4 in MBON-g1,g2	Saumweber et al. (ref. 56)
Pdf-Gal4	Expresses GAL4 in l-LN$_v$ and s-LN$_v$	BDSC# 6899
MB011B-Gal4	Expresses GAL4 in valence-encoding MBONs	Aso et al. (ref. 84)
2U	w^{1118} (isoCJ1) Canton-S derivative	Tully et al. (ref. 100)
OK107-Gal4	Expresses GAL4 in the mushroom body	BDSC# 854
tub-Gal80^{ts}	Expresses temperature sensitive GAL80 in all cells	BDSC# 7019
R21B06-splitGal4^{DBD}	Expresses GAL4^{DBD} in the mushroom body	Aso et al. (ref. 52)
6xCRE-splitGal4^{AD}	Expresses GAL4^{AD} in a Cre-dependent manner, VK27 insertion	This study, see Siegenthaler et al. (ref. 59)
UAS-myr::tdTomato	Fluorescent reporter line	Pfeiffer et al. (ref. 101), BDSC# 32223
UAS-Dop1R1GFP$_{11}$, *UAS-spGFP*$_{1\text{-}10}$	Dop1R1 knock-in line with C-terminal GFP$_{11}$ tag	Kondo et al. (ref. 58)
10xUAS-myr::GFP	Fluorescent reporter line	Pfeiffer et al. (ref. 101), BDSC# 32197

retinal (10 µM) and kept in the dark. For performing BRET assays, the medium was changed to HBBS, supplemented with 20 mM HEPES, 10 µM 9-*cis*-retinal and 5 µM Coelenterazine 400a, and incubated for 5 min at RT. optoDopRs were activated using a 1 s,470 nm light pulse (collimated CoolLED pE4000, Andover, UK). Native DopRs were activated by injection of DA with a final concentration of 1 µM. BRET ratio changes were determined from RLuc8-G$_\alpha$ and G$_\gamma$-GFP2 emission using a Berthold Mithras multimode plate reader with BRET2 filters (410m80/515m40, Berthold Tech.) over a 90s timeframe directly after light or DA application.

Drosophila melanogaster stocks

All *Drosophila* stocks were raised and treated under standard conditions at 25 °C and 70% relative humidity with a 12 h light/dark cycle on standard fly food unless stated otherwise. Transgenic UAS-optoDopR lines were generated by phiC31-mediated site-specific transgene using the attP2 site on the 3rd chromosome (FlyORF Injection Service, Zurich, Switzerland). Stocks were obtained from the Bloomington (BDSC) *Drosophila* stock centers unless otherwise noted. We used the lines as shown in Table 1.

Immunochemistry

Larval brains from 3rd instar animals (96 h ± 3 h AEL) of the indicated genotypes were dissected in phosphate-buffered saline (PBS) and fixed for 15 min at room temperature in 4% paraformaldehyde/PBS, washed in PBST (PBS with 0.3% Triton X-100) and incubated in 5% normal donkey serum in PBST. OptoDopR expression was analyzed using a mouse anti-Rho antibody detecting the C-terminal Rho epitope present in all optoXRs (1D4, Cat #MA1-722, 1:1000, Thermo Fisher, CA, USA) at 4 °C overnight, washed in PBST 3 times (5 min in each time) and incubated with secondary antibodies (donkey anti-mouse Alexa 488 Cat #715-545-150, Jackson Immunoresearch, or goat anti-mouse Alexa 546 Cat # A-11030, Thermo Fisher, CA, USA, 1:300) for 1h. After washing, samples were mounted on poly-L-lysine coated coverslips in Slow Fade Gold (Thermo Fisher, CA, USA). Native reporter fluorescence was sufficiently bright to be visualized together with antibody immunostaining by confocal microscopy (Zeiss LSM900AS2, Zeiss, Oberkochen, Germany). Confocal Z-stacks were processed in Fiji (ImageJ, NIH, Bethesda, USA).

Adult brains of 3- to 7-day-old flies of the indicated genotypes were dissected in hemolymph-like saline (HL3) and fixed for 1 h at room temperature in 2% paraformaldehyde/HL3. After washing in PBST (PBS with 0.5% Triton X-100) and incubation in 5% normal goat serum in PBST, samples were incubated with mouse anti-Rhodopsin (1D4, Cat #MA1-722, 1:1000, Thermo Fisher) to detect optoDopR expression, rabbit anti-DsRed (1:2000, Cat #632496, Takara Bio Inc.), mouse anti-GFP (1:2000, Cat #A-11120, Thermo Fisher), rabbit or guinea pig anti-Discs large (Dlg, 1:30000 and 1:1000;[94]) antibodies for 4 h at room temperature, followed by 2 nights at 4 °C. For DopR/PDF co-expression analysis in adult brains, mouse anti-PDF (Cat #PDF C7, 1:1000, DSHB) and chicken anti-GFP (Cat #ab13970, Abcam, 1:2000) were incubated for 24h at 4 °C. Samples were subsequently washed in PBST (3 x 30 min) and incubated with secondary antibodies (goat anti-mouse Alexa 488 Cat # A-11001, goat anti-rabbit Alexa 594 Cat # A-11012, goat anti-guinea pig Alexa 647 Cat # A-21450, 1:1000, Thermo Fisher) for 4 h at room temperature, followed by 2 nights at 4 °C. For DopR/PDF co-expression analysis, secondary antibodies (donkey anti-mouse Alexa 555 Cat # A-31570, 1:400; goat anti-chicken Alexa 488 Cat

A-11039, 1:200, Thermo Fisher) were incubated for 6h at room temperature. After washing, a pre-embedding fixation in 4% paraformaldehyde/PBS was performed for 4 h at room temperature. Samples were washed in PBST (4 × 15 min) followed by 10 min in PBS. Brains were mounted on poly-L-lysine coated coverslips. An ethanol dehydration series and a xylene clearing series were performed and the samples were mounted in DPX[95]. Images were taken on a Leica STELLARIS 8 confocal microscope using a 20x (NA 0.75) and 93x (NA 1.3) glycerol immersion objective. Confocal z-stacks were processed in Fiji (ImageJ, NIH, Bethesda, USA).

Calcium and cAMP imaging in *D. melanogaster* larvae

3rd instar larval brains (96 h ± 3 h AEL) were partially dissected in physiological saline buffer (108 mM NaCl, 5mM KCl, 2mM $CaCl_2$, 8.2 mM $MgCl_2$, 4 mM $NaHCO_3$, 1 mM NaH_2PO_4, 5 mM trehalose, 10 mM sucrose, 5 mM HEPES, pH 7.5) and mounted on poly-L-lysine-coated cover slips in the saline buffer with or without 5mM 9-*cis*-Retinal (for opto-Dop1R1 and opto-Dop1R2). Gflamp-1 or GCaMP6s was utilized to monitor cAMP or calcium levels, respectively. Live imaging of Kenyon cell somata and medial lobes expressing Gflamp-1 or GCaMP6s in the mushroom body was performed using confocal microscopy with a 40x/NA1.3 objective (Zeiss LSM900AS2, Zeiss, Oberkochen, Germany). OptoDopR^{V2} or bPAC activation was achieved using a 470 nm LED light with an intensity of 2.10 mW/cm². Confocal time series were recorded at 7.5 frames/s (128 × 128 pixels, 600 frames total or 1000 frames total for repeated light activation). KC somata or medial lobes were focused, and after a stable imaging period of 100 frames, the 470 nm LED was activated for 10 s. Confocal time series were analyzed using image registration (StackReg plugin, ImageJ) to correct for XY movement, and Gflamp-1 signal intensity in the soma and medium lobe was quantified using the Time Series Analyzer V3 plugin (ImageJ). Baseline (F_0) was determined as the average of 95 frames before activation. The relative maximum intensity change (ΔF_{max}) of Gflamp-1/GCaMP6s fluorescence was calculated after normalization to baseline.

Live imaging of calcium responses in intact 3rd instar larvae was performed under low light conditions. Larvae were mounted in 90% glycerol, sandwiched between a coverslip and the slide with the aid of silicon paste. Calcium responses were recorded from the soma/calyx region and the medial lobe of the mushroom body using *UAS-GCaMP6s* and *UAS-OptoDop1R2* ^{V2} under the control of H*24-Gal4*. Animals were reared in the dark on grape agar plates supplemented with yeast paste and 9-*cis*-retinal. The soma, as well as the medial lobe of the mushroom body, were live imaged using a Zeiss LSM 780 2-photon microscope and a 25x/NA1.0 water immersion objective. For activation of the optoDop1R2^{V2}, larvae were subjected to 10s blue light stimulation (470 nm, 720 µW/cm², CoolLED) twice with an interval of 30s between each pulse. Only datasets without significant Z-drift were used for analysis. Analysis of the time series was performed using Fiji (ImageJ, NIH, Bethesda, USA) as described above. Normalized calcium responses were obtained by subtracting the amplitude of the pre-stimulation baseline (average of 50 frames) from the stimulation evoked amplitude. The calcium response was recorded before and after the light stimulus due to PMT overexposure during the light pulse. Graphs showing the mean ± s.e.m were generated with GraphPad Prism (GraphPad, San Diego, CA, USA). Boxplots were used to show the comparison between the maximum responses ($\Delta F_{max}/F_0$) and analyzed with unpaired Student's *t*-test with Welch's correction.

cAMP-induced nociceptive behavior in *D. melanogaster* larvae

For cAMP-induced nociceptive behavior, larvae expressing UAS-bPAC, UAS-CsChrimson or UAS-optoDopRs under the control of *ppk-Gal4* were staged and fed in the dark on grape agar plates (2% agar) with yeast paste containing 5 mM 9-*cis*-retinal (optoXRs) or all-*trans*-retinal (CsChrimson). Staged 3rd instar larvae were placed on a 1% agar film on an FTIR (frustrated total internal reflection) based tracking system (FIM, University of Münster) with 1ml water added. Experiments were performed under minimum light conditions (no activation). After 10 s, larvae were illuminated with 470 nm light (465 µW/cm²) for 3 min. Behavioral responses during the 3 min were recorded and categorized as rolling (full 360° rotation along the larval body axis) or no rolling (incomplete rolling, bending, turning, or no response). Each animal was counted only once, and the cumulated categorized responses were plotted as a contingency graph. Staging and experiments were performed in a blinded and randomized manner.

Locomotion assays in *D. melanogaster* larvae

D. melanogaster larvae were staged in darkness on grape agar plates containing yeast paste with or without 5 mM 9-*cis*-retinal. For the indicated experiments, larvae were additionally fed with Rotenone for 24 h at 72 h after egg laying (AEL) to impair dopaminergic neuron function. Third instar larvae (96 h ± 4 h AEL) were used for all experiments. Animals were carefully selected and transferred under minimum red-light conditions to a 1% agar film on an FTIR (frustrated total internal reflection) based tracking system (FIM, University of Münster). Five freely moving larvae per trial were video-captured and stimulated with 525 nm light (130 µW/cm²) for activation of optoDop1R1^{V2}. Animal locomotion was tracked with 10 frames/s for up to 120s. For locomotion analysis, velocity and bending angles were analyzed using the FIMtrack software (https://github.com/kostasl/FIMTrack). Only animals displaying continuous locomotion before the light stimulus were analyzed. Average locomotion speed and cumulative bending angles were analyzed and plotted for the first 30 s under dark or light conditions.

Innate odor preference and olfactory behavior assays in *D. melanogaster* larvae

Groups of 20 staged mid-3rd instar larvae (96 h ± 4 h AEL) were placed in the middle of a 2% agar plate containing a container with 10 µl n-amylacetate (AM, diluted 1:50 in mineral oil; SAFC) or 3-Octanol (3-Oct, Sigma) on one side and a blank on the other side. For rescue experiments, assays were performed either in the dark or using light conditions (525 nm, 130 µW/cm²) during the preference behavior. Assays were video-captured for 5 min under infrared light illumination to monitor larval distribution with a digital camera (Basler ace-2040 gm, Basler, Switzerland). After 5 min, the number of larvae on each side was determined and the odor preference was calculated as (*n*(larvae) on odor side − *n*(larvae) on blank side)/total n(larvae).

Odor-fructose reward learning assays in *D. melanogaster* larvae

Odor-fructose reward learning was performed essentially as described[77]. Groups of 20 larvae each were placed in a petri dish coated either with plain 1% agar or 1% agar with 2 M fructose as a reward in the presence of 10 µl n-amylacetate (AM, 1:50). The odor-reward or no reward pairing was done for 3 min (or 5 min; as indicated in experiments), alternating 3x between training (odor$^+$), while the unpaired group received odor and reward during separate 3 min (or 5 min as indicated) training (blank$^+$). For all optogenetic lines, training was performed under minimum red-light conditions or with 525 nm light activation (130 µW/cm²) during fructose reward training. Reciprocal training was performed for all genotypes and conditions (blank/odor$^+$ and blank$^+$/odor, respectively).

After three training cycles, larval preference toward the trained odor (AM or blank) was recorded in darkness using a Basler ace-2040gm camera (same setting as for the olfactory behavior assay). The number of larvae on each side was calculated after 5 min, and odor preferences were calculated for the paired and unpaired groups. The learning index (LI) was then calculated using the following formula:

$$LI = (Odor - Pref_{Paired} - Odor - Pref_{Unpaired})/2 \quad (1)$$

Odor-shock learning behavior assays in *D. melanogaster* adult flies

Aversive olfactory conditioning of adult flies was performed as described before[77]. Conditioning was performed in the dark at 21 °C and 75% humidity using 3- to 7-day-old flies. Groups of flies were loaded into custom-made copper grid tubes with high-power LEDs mounted at the end of the tube (525 nm, Ø 37 μW/mm²). Flies were exposed to a constant air stream or the odorized air stream (750 ml/min).

Experimental flies were raised at 20 °C and shifted to 31 °C four days prior to the experiments to induce Gal80^{ts}/Gal4-dependent gene expression. Flies were transferred to 0.4 mM 9-*cis*-retinal food ~48 h prior to the experiment and kept in the dark.

For conditioning the odors 4-MCH (1:250, Merck, Darmstadt, Germany, CAS #589-91-3) and 3-OCT (1:167, Merck, Darmstadt, Germany, CAS #589-98-0) were diluted in mineral oil (Thermo Fisher, Waltham, MA, CAS #8042-47-5). Flies were conditioned following a five times spaced training paradigm. After a resting period of 3 min with only airflow the flies were exposed to the stimuli as indicated in the figure. The CS$^+$, electric shocks (twelve 1.5-s 90 V shocks with 3.5-s intervals) (Fig. 5b) and pulsed green light (4 Hz, 0.125 s on and 0.125 s off) (Fig. 5c, d) were applied simultaneously for 60 s. After 45 s of airflow, the CS$^-$ was presented for 60 s. This training cycle was repeated five times with 15-min breaks in between cycles. Odors for CS$^+$ and CS$^-$ were interchanged for each *n*.

Learning behavior was subsequently analyzed in the T-Maze. At the decision point of the T-Maze, flies could choose for 2 min between the CS$^+$ and the CS$^-$ (OCT 1:670, MCH 1:1000). The performance index was calculated for MCH and OCT individually:

$$\text{Performance index} = (\#\text{ of flies}(CS^+) - \#\text{ of flies}(CS^-))/\text{total}\#\text{ of flies} \quad (2)$$

For each n the two data points obtained with MCH and OCT as CS+ were averaged.

DopR function in I-LNv neurons of *D. melanogaster* adults

Flies were raised under 12 h:12 h light-dark cycles at 20 °C on standard fly food. One- to four-day-old male flies were placed individually in DAM (TriKinetics) monitors[83] containing 2% agar with 4% sucrose and 5mM 9-*cis*-Retinal solved in ethanol (for opto-Dop1R1 and opto-Dop1R2) or only ethanol (for controls). The activity of the flies was recorded in complete darkness for 2 days before the flies were subjected to light pulses of 470 nm LED light with an intensity of 70 ± 10 μW/cm². The light pulses were administered 12 times during the previous light period of the 12 h:12 h light-dark cycle (one pulse every hour for 10 min, 15 min or 20 min). Experiments were performed 3 times with 32 experimental and control flies, respectively. Activity data were plotted as individual and average actograms using the ImageJ plug-in actogramJ[96], and individual and average activity profiles of the 24 h day with light pulses were calculated for each fly group as described in[97].

Feeding behavior assays in *D. melanogaster* adults

Flies used in the flyPAD were reared and maintained in standard cornmeal food, with the composition described before[98] in incubators at 28 °C, 60% humidity and cycles of light/dark of 12 h each. After hatching, male flies of 4–8 days old were collected. Then, 5 μl of 10% sucrose solution containing 1% low gelling temperature agarose were placed in wells of the flyPAD containing electrodes to detect the capacitance change when the flies physically interacted with the food. The flies, following starvation for 24 h in the presence of a wet tissue with 3 ml of water, were transferred to the flyPAD individually using a pump. The experiments were all performed in a climate chamber at 25 °C, at 60% humidity. The recording of each session of flyPAD lasted 60 min, during which the flies could freely interact with the food.

For the optoPAD experiments[85], flies were reared and maintained in standard cornmeal food as explained above, with supplementation of all-*trans*-retinal at 0.2 mM concentration, in incubators at 25 °C, 60% humidity and blue light/dark cycles of 12/12 h. The chimeric dopaminergic receptors were activated using 523 nm green light at 3 V, which was automatically activated once the fly started to sip food. All flies were wet starved for 24 h prior to the experiment. The acquisition of the data was done using scripts (https://github.com/ribeiro-lab/optoPAD-software) based on Bonsai, an open-source program. The data analysis was done using Matlab (2022b).

Statistics and reproducibility

No statistical method was used to predetermine the sample size. No data were excluded from the analyses except if samples did not meet sufficient quality standards, including sufficient cellular expression levels (HEK293 cell assays) or physically damaged samples after dissection. For functional imaging experiments, we excluded samples that showed significant z-drift during imaging. For analysis of larval locomotion, we excluded animals that could not be continuously tracked by the tracking software due to loss of signal. The experiments were randomized, and the investigators were blinded to allocation during experiments and outcome assessment whenever possible.

Statistical analysis was performed using Prism 8 (Graphpad, San Diego, CA, USA). All boxplots depict the median (center line) with 25th and 75th percentile (lower and upper box, respectively), and whiskers represent the 1st and 99th percentile. For line graphs, the mean ±SEM is shown. For high *n* numbers, violin plots with individual data points were used depicting the distribution of the data, including the 75th-percentile (upper dotted line), median (solid center line), and 25th-percentile (lower dotted line).

For the comparison of two groups, an unpaired two-tailed Student's *t*-test with Welch correction was used for normally distributed data, or, alternatively, a Mann-Whitney U-test for non-normally distributed data. A paired two-tailed Student's *t*-test was used for the comparison of the same individuals under different conditions (no light vs. light). One-way ANOVA with Dunnett's or Tukey's post hoc test was used for multiple comparisons. Statistical significance is defined as: $^*p < 0.05$, $^{**}p < 0.01$, $^{***}p < 0.001$.

Representative images were obtained from experiments that were repeated independently at least twice.

Reporting summary

Further information on research design is available in the Nature Portfolio Reporting Summary linked to this article.

Data availability

The raw data generated in this study are provided in the Source Data file. Due to the large size, raw imaging data (calcium imaging and immunohistochemistry) generated in this study can be obtained by request from the corresponding author. Requests will be fulfilled within 3 weeks. Source data are provided with this paper.

References

1. Bargmann, C. I. & Marder, E. From the connectome to brain function. *Nat. Methods* **10**, 483–490 (2013).
2. Klein, M. O. et al. Dopamine: functions, signaling, and association with neurological diseases. *Cell. Mol. Neurobiol.* **39**, 31–59 (2018).
3. Girault, J. A. & Greengard, P. The neurobiology of dopamine signaling. *Arch. Neurol.* **61**, 641–644 (2004).
4. Beaulieu, J. M. & Gainetdinov, R. R. The physiology, signaling, and pharmacology of dopamine receptors. *Pharmacol. Rev.* **63**, 182–217 (2011).

5. Siju, K. P., De Backer, J. F. & Grunwald Kadow, I. C. Dopamine modulation of sensory processing and adaptive behavior in flies. *Cell Tissue Res.* **383**, 207–225 (2021).
6. Karam, C. S., Jones, S. K. & Javitch, J. A. Come fly with me: an overview of dopamine receptors in *Drosophila melanogaster*. *Basic Clin. Pharmacol. Toxicol.* **1**, 1–10 (2019).
7. Deisseroth, K. Optogenetics: 10 years of microbial opsins in neuroscience. *Nat. Neurosci.* **18**, 1213–1225 (2015).
8. Deisseroth, K. Optogenetics. *Nat. Methods* **8**, 26–29 (2011).
9. Wiegert, J. S., Mahn, M., Prigge, M., Printz, Y. & Yizhar, O. Silencing neurons: tools, applications, and experimental constraints. *Neuron* **95**, 504–529 (2017).
10. Tichy, A.-M., Gerrard, E. J., Sexton, P. M. & Janovjak, H. Light-activated chimeric GPCRs: limitations and opportunities. *Curr. Opin. Struct. Biol.* **57**, 196–203 (2019).
11. Spangler, S. M. & Bruchas, M. R. Optogenetic approaches for dissecting neuromodulation and GPCR signaling in neural circuits. *Curr. Opin. Pharmacol.* **32**, 56–70 (2017).
12. Rost, B. R., Schneider-Warme, F., Schmitz, D. & Hegemann, P. Optogenetic tools for subcellular applications in neuroscience. *Neuron* **96**, 572–603 (2017).
13. Siuda, E. R. et al. Optodynamic simulation of β-adrenergic receptor signalling. *Nat. Commun.* **6**, 8480 (2015).
14. Kim, J.-M. et al. Light-driven activation of β_2-adrenergic receptor signaling by a chimeric rhodopsin containing the β_2-adrenergic receptor cytoplasmic loops. *Biochemistry* **44**, 2284–2292 (2005).
15. Bailes, H. J., Zhuang, L.-Y. & Lucas, R. J. Reproducible and sustained regulation of gαs signalling using a metazoan opsin as an optogenetic tool. *PLoS ONE* **7**, e30774 (2012).
16. Airan, R. D., Thompson, K. R., Fenno, L. E., Bernstein, H. & Deisseroth, K. Temporally precise in vivo control of intracellular signalling. *Nature* **458**, 1025–1029 (2009).
17. Tichy, A. M., So, W. L., Gerrard, E. J. & Janovjak, H. Structure-guided optimization of light-activated chimeric G-protein-coupled receptors. *Structure* **30**, 1075–1087.e4 (2022).
18. Morri, M. et al. Optical functionalization of human Class A orphan G-protein-coupled receptors. *Nat. Commun.* **9**, 1950 (2018).
19. Čapek, D. et al. Light-activated Frizzled7 reveals a permissive role of non-canonical wnt signaling in mesendoderm cell migration. *Elife* **8**, e42093 (2019).
20. van Wyk, M., Pielecka-Fortuna, J., Löwel, S. & Kleinlogel, S. Restoring the ON switch in blind retinas: opto-mGluR6, a next-generation, cell-tailored optogenetic tool. *PLoS Biol.* **13**, 1–30 (2015).
21. Eichel, K. & von Zastrow, M. Subcellular organization of GPCR signaling. *Trends Pharmacol. Sci.* **39**, 200–208 (2018).
22. Spoida, K., Masseck, O. A., Deneris, E. S. & Herlitze, S. Gq/5-HT2c receptor signals activate a local GABAergic inhibitory feedback circuit to modulate serotonergic firing and anxiety in mice. *Proc. Natl Acad. Sci. USA* **111**, 6479–6484 (2014).
23. Eickelbeck, D. et al. CaMello-XR enables visualization and optogenetic control of Gq/11 signals and receptor trafficking in GPCR-specific domains. *Commun. Biol.* **2**, 1–16 (2019).
24. Lohse, M. J. & Hofmann, K. P. Spatial and temporal aspects of signaling by G-protein–coupled receptors. *Mol. Pharmacol.* **88**, 572–578 (2015).
25. Nässel, D. R. Substrates for neuronal cotransmission with neuropeptides and small molecule neurotransmitters in *Drosophila*. *Front. Cell Neurosci.* **12**, 1–26 (2018).
26. Nässel, D. R., Pauls, D. & Huetteroth, W. Neuropeptides in modulation of *Drosophila* behavior: how to get a grip on their pleiotropic actions. *Curr. Opin. Insect Sci.* **36**, 1–8 (2019).
27. Bargmann, C. I. Beyond the connectome: how neuromodulators shape neural circuits. *BioEssays* **34**, 458–465 (2012).
28. Taghert, P. H. & Nitabach, M. N. Peptide neuromodulation in invertebrate model systems. *Neuron* **76**, 82–97 (2012).
29. Nässel, D. R. & Zandawala, M. Endocrine cybernetics: neuropeptides as molecular switches in behavioural decisions. *Open Biol.* **12**, 24–26 (2022).
30. Zolin, A. et al. Context-dependent representations of movement in *Drosophila* dopaminergic reinforcement pathways. *Nat. Neurosci.* **24**, 1555–1566 (2021).
31. Kaun, K. R. & Rothenfluh, A. Dopaminergic rules of engagement for memory in *Drosophila*. *Curr. Opin. Neurobiol.* **43**, 56–62 (2017).
32. Waddell, S. Reinforcement signalling in *Drosophila*; dopamine does it all after all. *Curr. Opin. Neurobiol.* **23**, 324–329 (2013).
33. Adel, M. & Griffith, L. C. The role of dopamine in associative learning in *Drosophila*: an updated unified model. *Neurosci. Bull.* **37**, 831–852 (2021).
34. Berry, J. A., Cervantes-Sandoval, I., Nicholas, E. P. & Davis, R. L. Dopamine is required for learning and forgetting in *Drosophila*. *Neuron* **74**, 530–542 (2012).
35. Keleman, K. et al. Dopamine neurons modulate pheromone responses in *Drosophila* courtship learning. *Nature* **489**, 145–149 (2012).
36. Burke, C. J. et al. Layered reward signalling through octopamine and dopamine in *Drosophila*. *Nature* **492**, 433–437 (2012).
37. Handler, A. et al. Distinct dopamine receptor pathways underlie the temporal sensitivity of associative learning. *Cell* **178**, 60–75.e19 (2019).
38. Rohwedder, A. et al. Four individually identified paired dopamine neurons signal reward in larval *Drosophila*. *Curr. Biol.* **26**, 661–669 (2016).
39. Himmelreich, S. et al. Dopamine receptor DAMB signals via Gq to mediate forgetting in *Drosophila*. *Cell Rep.* **21**, 2074–2081 (2017).
40. Boto, T., Louis, T., Jindachomthong, K., Jalink, K. & Tomchik, S. M. Dopaminergic modulation of cAMP drives nonlinear plasticity across the *Drosophila* mushroom body lobes. *Curr. Biol.* **24**, 822–831 (2014).
41. Sabandal, J. M., Berry, J. A. & Davis, R. L. Dopamine-based mechanism for transient forgetting. *Nature* **591**, 426–430 (2021).
42. Silva, B., Hidalgo, S. & Campusano, J. M. Dop1R1, a type 1 dopaminergic receptor expressed in Mushroom Bodies, modulates *Drosophila* larval locomotion. *PLoS ONE* **15**, 1–15 (2020).
43. Hickey, D. G. et al. Chimeric human opsins as optogenetic light sensitisers. *J. Exp. Biol.* **224**, jeb240580 (2021).
44. Gunaydin, L. A. et al. Natural neural projection dynamics underlying social behavior. *Cell* **157**, 1535–1551 (2014).
45. Ballister, E. R., Rodgers, J., Martial, F. & Lucas, R. J. A live cell assay of GPCR coupling allows identification of optogenetic tools for controlling Go and Gi signaling. *BMC Biol.* **16**, 10 (2018).
46. Bowin, C. F., Inoue, A. & Schulte, G. WNT-3A-induced β-catenin signaling does not require signaling through heterotrimeric G proteins. *J. Biol. Chem.* **294**, 11677–11684 (2019).
47. Flock, T. et al. Selectivity determinants of GPCR-G-protein binding. *Nature* **545**, 317–322 (2017).
48. Olsen, R. H. J. et al. TRUPATH, an open-source biosensor platform for interrogating the GPCR transducerome. *Nat. Chem. Biol.* **16**, 841–849 (2020).
49. Yang, W., Hildebrandt, J. D. & Schaffer, J. E. G-proteins | Gq family. *Encyclopedia of Biological Chemistry* 3rd edn, Vol. 6, 450–455 (Elsevier, 2021).
50. Groth, A. C., Fish, M., Nusse, R. & Calos, M. P. Construction of transgenic *Drosophila* by using the site-specific integrase from phage phiC31. *Genetics* **166**, 1775–1782 (2004).
51. Heisenberg, M. Mushroom body memoir: from maps to models. *Nat. Rev. Neurosci.* **4**, 266–275 (2003).

52. Aso, Y. et al. The neuronal architecture of the mushroom body provides a logic for associative learning. *Elife* **3**, e04577 (2014).
53. Thum, A. S. & Gerber, B. Connectomics and function of a memory network: the mushroom body of larval *Drosophila*. *Curr. Opin. Neurobiol.* **54**, 146–154 (2019).
54. Eichler, K. et al. The complete connectome of a learning and memory centre in an insect brain. *Nature* **548**, 175–182 (2017).
55. Eschbach, C. et al. Recurrent architecture for adaptive regulation of learning in the insect brain. *Nat. Neurosci.* **23**, 544–555 (2020).
56. Saumweber, T. et al. Functional architecture of reward learning in mushroom body extrinsic neurons of larval Drosophila. *Nat. Commun.* **9**, 1104 (2018).
57. Cohn, R., Morantte, I. & Ruta, V. Coordinated and compartmentalized neuromodulation shapes sensory processing in *Drosophila*. *Cell* **163**, 1742–1755 (2015).
58. Kondo, S. et al. Neurochemical organization of the *Drosophila* brain visualized by endogenously tagged neurotransmitter receptors. *Cell Rep.* **30**, 284–297.e5 (2020).
59. Siegenthaler, D., Escribano, B., Bräuler, V. & Pielage, J. Selective suppression and recall of long-term memories in Drosophila. *PLoS Biol.* **17**, e3000400 (2019).
60. Dannhäuser, S. et al. Antinociceptive modulation by the adhesion GPCR CIRL promotes mechanosensory signal discrimination. *Elife* **9**, e56738 (2020).
61. Stierl, M. et al. Light modulation of cellular cAMP by a small bacterial photoactivated adenylyl cyclase, bPAC, of the soil bacterium *Beggiatoa*. *J. Biol. Chem.* **286**, 1181–1188 (2011).
62. Klapoetke, N. C. et al. Independent optical excitation of distinct neural populations. *Nat. Methods* **11**, 338–346 (2014).
63. Wang, L. et al. A high-performance genetically encoded fluorescent indicator for in vivo cAMP imaging. *Nat. Commun.* **13**, 5363 (2022).
64. Yang, S. et al. PACmn for improved optogenetic control of intracellular cAMP. *BMC Biol.* **19**, 1–17 (2021).
65. Chen, T.-W. et al. Ultrasensitive fluorescent proteins for imaging neuronal activity. *Nature* **499**, 295–300 (2013).
66. Glovaci, I. & Chapman, C. A. Dopamine induces release of calcium from internal stores in layer II lateral entorhinal cortex fan cells. *Cell Calcium* **80**, 103–111 (2019).
67. Sayin, S. et al. A neural circuit arbitrates between persistence and withdrawal in hungry *Drosophila*. *Neuron* **104**, 544–558.e6 (2019).
68. Lewis, L. P. C. et al. A higher brain circuit for immediate integration of conflicting sensory information in *Drosophila*. *Curr. Biol.* **25**, 2203–2214 (2015).
69. Montgomery, E. B. Basal ganglia pathophysiology in Parkinson's disease. *Ann. Neurol.* **65**, 618 (2009).
70. Berardelli, A., Rothwell, J. C., Thompson, P. D. & Hallett, M. Pathophysiology of bradykinesia in Parkinson's disease. *Brain* **124**, 2131–2146 (2001).
71. Braak, H. et al. Staging of brain pathology related to sporadic Parkinson's disease. *Neurobiol. Aging* **24**, 197–211 (2003).
72. Riemensperger, T. et al. A single dopamine pathway underlies progressive locomotor deficits in a *Drosophila* model of Parkinson disease. *Cell Rep.* **5**, 952–960 (2013).
73. Lazopulo, S., Lazopulo, A., Baker, J. D. & Syed, S. Daytime colour preference in *Drosophila* depends on the circadian clock and TRP channels. *Nature* **574**, 108–111 (2019).
74. Imambocus, B. N. et al. A neuropeptidergic circuit gates selective escape behavior of *Drosophila* larvae. *Curr. Biol.* **32**, 149–163.e8 (2022).
75. Xiang, Y. et al. Light-avoidance-mediating photoreceptors tile the *Drosophila* larval body wall. *Nature* **468**, 921–926 (2010).
76. Gerber, B. & Stocker, R. F. The *Drosophila* larva as a model for studying chemosensation and chemosensory learning: a review. *Chem. Senses* **32**, 65–89 (2007).
77. Gerber, B., Biernacki, R. & Thum, J. Odor-taste learning assays in *Drosophila* larvae. *Cold Spring Harb. Protoc.* **2013**, 212–223 (2013).
78. Inagaki, H. K. et al. Optogenetic control of *Drosophila* using a red-shifted channelrhodopsin reveals experience-dependent influences on courtship. *Nat. Methods* **11**, 325–332 (2014).
79. Boto, T., Stahl, A. & Tomchik, S. M. Cellular and circuit mechanisms of olfactory associative learning in *Drosophila*. *J. Neurogenet.* **34**, 36–46 (2020).
80. Sheeba, V. et al. Large ventral lateral neurons modulate arousal and sleep in *Drosophila*. *Curr. Biol.* **18**, 1537–1545 (2008).
81. Shang, Y., Griffith, L. C. & Rosbash, M. Light-arousal and circadian photoreception circuits intersect at the large PDF cells of the *Drosophila* brain. *Proc. Natl Acad. Sci. USA* **105**, 19587–19594 (2008).
82. Fernandez-Chiappe, F. et al. Dopamine signaling in wake-promoting clock neurons is not required for the normal regulation of sleep in *Drosophila*. *J. Neurosci.* **40**, 9617–9633 (2020).
83. Pfeiffenberger, C., Lear, B. C., Keegan, K. P. & Allada, R. Locomotor activity level monitoring using the *Drosophila* Activity Monitoring (DAM) system. *Cold Spring Harb. Protoc.* **2010**, pdb.prot5518 (2010).
84. Aso, Y. et al. Mushroom body output neurons encode valence and guide memory-based action selection in *Drosophila*. *Elife* **3**, e04580 (2014).
85. Moreira, J.-M. et al. optoPAD, a closed-loop optogenetics system to study the circuit basis of feeding behaviors. *Elife* **8**, e43924 (2019).
86. Ingles-Prieto, A. et al. Optogenetic delivery of trophic signals in a genetic model of Parkinson's disease. *PLoS Genet.* **17**, e1009479 (2021).
87. Koyanagi, M. & Terakita, A. Diversity of animal opsin-based pigments and their optogenetic potential. *Biochim. Biophys. Acta* **1837**, 710–716 (2014).
88. Muntean, B. S. et al. Interrogating the spatiotemporal landscape of neuromodulatory GPCR signaling by real-time imaging of cAMP in intact neurons and circuits. *Cell Rep.* **22**, 255–268 (2018).
89. Lobingier, B. T. & von Zastrow, M. When trafficking and signaling mix: how subcellular location shapes G protein-coupled receptor activation of heterotrimeric G proteins. *Traffic* **20**, 130–136 (2019).
90. Anton, S. E. et al. Receptor-associated independent cAMP nanodomains mediate spatiotemporal specificity of GPCR signaling. *Cell* **185**, 1130–1142.e11 (2022).
91. Spoida, K. et al. Melanopsin variants as intrinsic optogenetic on and off switches for transient versus sustained activation of G protein pathways. *Curr. Biol.* **26**, 1206–1212 (2016).
92. Koyanagi, M. et al. High-performance optical control of GPCR signaling by bistable animal opsins MosOpn3 and LamPP in a molecular property-dependent manner. *Proc. Natl Acad. Sci. USA* **119**, e2204341119 (2022).
93. Edgar, R. C. MUSCLE: a multiple sequence alignment method with reduced time and space complexity. *BMC Bioinformatics* **5**, 1–19 (2004).
94. Pielage, J., Bulat, V., Zuchero, J. B., Fetter, R. D. & Davis, G. W. Hts/Adducin controls synaptic elaboration and elimination. *Neuron* **69**, 1114–1131 (2011).
95. Nern, A., Pfeiffer, B. D. & Rubin, G. M. Optimized tools for multicolor stochastic labeling reveal diverse stereotyped cell arrangements in the fly visual system. *Proc. Natl Acad. Sci. USA* **112**, E2967-76 (2015).
96. Schmid, B., Helfrich-Förster, C. & Yoshii, T. A new ImageJ plug-in 'ActogramJ' for chronobiological analyses. *J. Biol. Rhythms* **26**, 464–467 (2011).
97. Schlichting, M. & Helfrich-Förster, C. Photic entrainment in *Drosophila* assessed by locomotor activity recordings. *Methods Enzymol.* **552**, 105–123 (2015).

98. Kobler, J. M., Rodriguez Jimenez, F. J., Petcu, I. & Grunwald Kadow, I. C. Immune receptor signaling and the mushroom body mediate post-ingestion pathogen avoidance. *Curr. Biol.* **30**, 4693–4709.e3 (2020).
99. Han, C., Jan, L. Y. & Jan, Y.-N. Enhancer-driven membrane markers for analysis of nonautonomous mechanisms reveal neuron-glia interactions in *Drosophila*. *Proc. Natl Acad. Sci. USA* **108**, 9673–9678 (2011).
100. Tully, T., Preat, T., Boynton, S. C. & Del Vecchio, M. Genetic dissection of consolidated memory in *Drosophila*. *Cell* **79**, 35–47 (1994).
101. Pfeiffer, B. D. et al. Refinement of tools for targeted gene expression in *Drosophila*. *Genetics* **186**, 735–755 (2010).

Acknowledgements

We thank A. Thum for *H24-Gal4* and *MBON*$^{g1/g2}$*-Gal4*, M. Schwärzel for *UAS-bPAC*, J. Chu and Y. Li for *UAS-Gflamp1* fly lines. E. Kostenis and A. Inoue for HEK293ΔG7 cell lines. A. Schoofs for technical help with 2-Photon imaging. cDNA was obtained from the *Drosophila* Genomics Resource Center, supported by NIH grant 2P40OD010949. Stocks obtained from the Bloomington *Drosophila* Stock Center (NIH P40OD018537) were used in this study. This work was supported by grants from the Deutsche Forschungsgemeinschaft (DFG SO 1337/2-2 and SO 1337/7-1 to P.S., INST 248/293-1 to J.P., DFG FO207/14-1 to C.H.F., DFG GR-4310/11-1, DFG FOR2705 TP3, and INST 95/1419-1 to I.G.K.), the DFG Heisenberg program (SO1337/6-1 to P.S.). F.Z. was supported by a Chinese Scholarship Council (CSC) scholarship.

Author contributions

F.Z. performed in vitro characterization and analysis of DopRs/optoDopRs, cAMP signaling and larval behavior; A.M.T. and H.J. designed optoDopRs; B.N.I. performed and analyzed functional in vivo imaging; S.S. performed larval locomotion experiments and analysis; F.J.R.J., M.G.M., I.J. and I.G.K. designed, performed and analyzed flyPAD/optoPAD experiments; M.H. and C.H.F. designed, performed and analyzed locomotor activity experiments; N.W., V.B. and J.P. designed, performed and analyzed adult learning and immunhistochemical experiments; T.L. and K.S. contributed to in vitro characterization of DopRs/optoDopRs; P.S. designed the study and wrote the manuscript with input from all authors.

Funding

Open Access funding enabled and organized by Projekt DEAL.

Competing interests

The authors declare no competing interests.

Additional information

Supplementary information The online version contains supplementary material available at https://doi.org/10.1038/s41467-023-43970-0.

Correspondence and requests for materials should be addressed to Peter Soba.

Peer review information *Nature Communications* thanks Milena Anna Damulewicz, Sandra Siegert and the other anonymous reviewer(s) for their contribution to the peer review of this work

Supplementary Information

Optimized design and in vivo application of optogenetically functionalized Drosophila dopamine receptors

Fangmin Zhou, Alexandra-Madelaine Tichy, Bibi Nusreen Imambocus, Shreyas Sakharwade, Francisco J. Rodriguez Jimenez, Marco González Martínez, Ishrat Jahan, Margarita Habib, Nina Wilhelmy, Vanessa Burre, Tatjana Lömker, Kathrin Sauter, Charlotte Helfrich-Förster, Jan Pielage, Ilona C. Grunwald Kadow, Harald Janovjak, Peter Soba

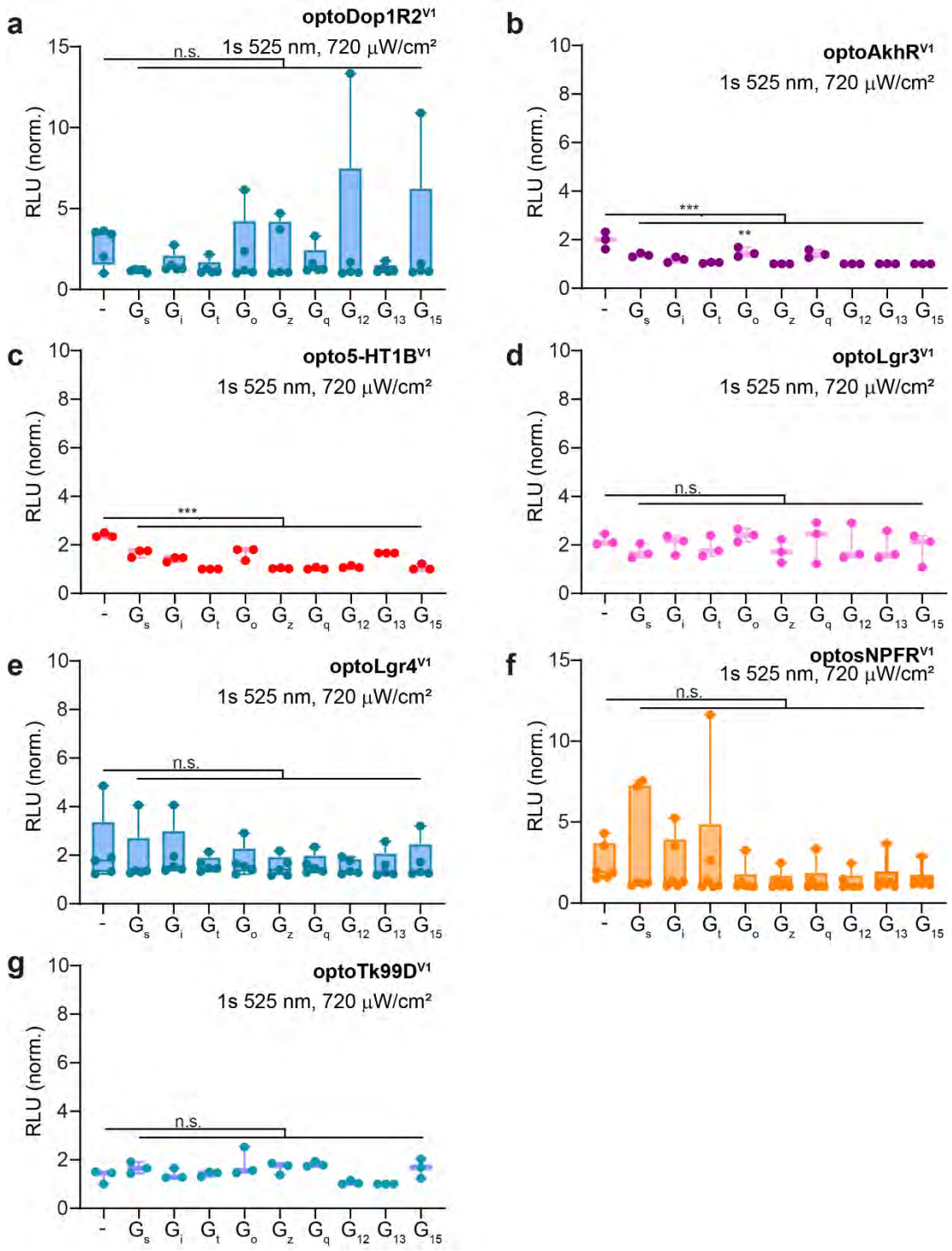

Supplementary Figure 1. Validation of optoXR^{V1} function in the G_{sx} assay.

a-g. Analysis of optoXR^{V1} function in live HEK293 cells using the G_{sx} assay to probe specific G protein activation. **a.** G protein coupling properties of optoDop1R2^{V1} after activation with light (1 s, 525 nm, 720 µW/cm^2). Maximum normalized responses are shown as relative light units (RLU, n=5 independent experiments, n.s. p>0.05). **b.** G protein coupling properties of optoAkhR^{V1} after activation with light (1s 525 nm, 720 µW/cm^2). Maximum normalized responses are shown as relative light units (RLU, n=3 independent experiments, **p<0.01, ***p<0.001, one-way ANOVA with Dunnett's *post-hoc* test). **c.** G protein coupling properties of opto5HT1B^{V1} after activation with light (1 s, 525 nm, 720 µW/cm^2). Maximum normalized responses are shown as relative light units (RLU, n=3 independent experiments, ***p<0.001, one-way ANOVA with Dunnett's *post-hoc* test). **d.** G protein coupling properties of optoLgr3

^{V1} after activation with light (1 s, 525 nm, 720 μW/cm^2). Maximum normalized responses are shown as relative light units (RLU, n=3 independent experiments, n.s. p>0.05, one-way ANOVA with Dunnett's *post-hoc* test). **e.** G protein coupling properties of optoLgr4^{V1} after activation with light (1s 525 nm, 720μW/cm^2). Maximum normalized responses are shown as relative light units (RLU, n=5, n.s. p>0.05, one-way ANOVA with Dunnett's *post-hoc* test). **f.** G protein coupling properties of optosNPFR ^{V1} after activation with light (1 s, 525 nm, 720μW/cm^2). Maximum normalized responses are shown as relative light units (RLU, n=6 independent experiments, n.s. p>0.05, one-way ANOVA with Dunnett's *post-hoc* test). **g.** G protein coupling properties of optoTk99D^{V1} after activation with light (1 s, 525 nm, 720μW/cm^2). Maximum normalized responses are shown as relative light units (RLU, n=3 independent experiments, n.s. p>0.05, one-way ANOVA with Dunnett's *post-hoc* test). All boxplots depict 75th (top), median (central line) and 25th (bottom) percentile, whiskers depict 99th (top) and 1st (bottom) percentile. Source data and statistical details are provided as a Source Data file.

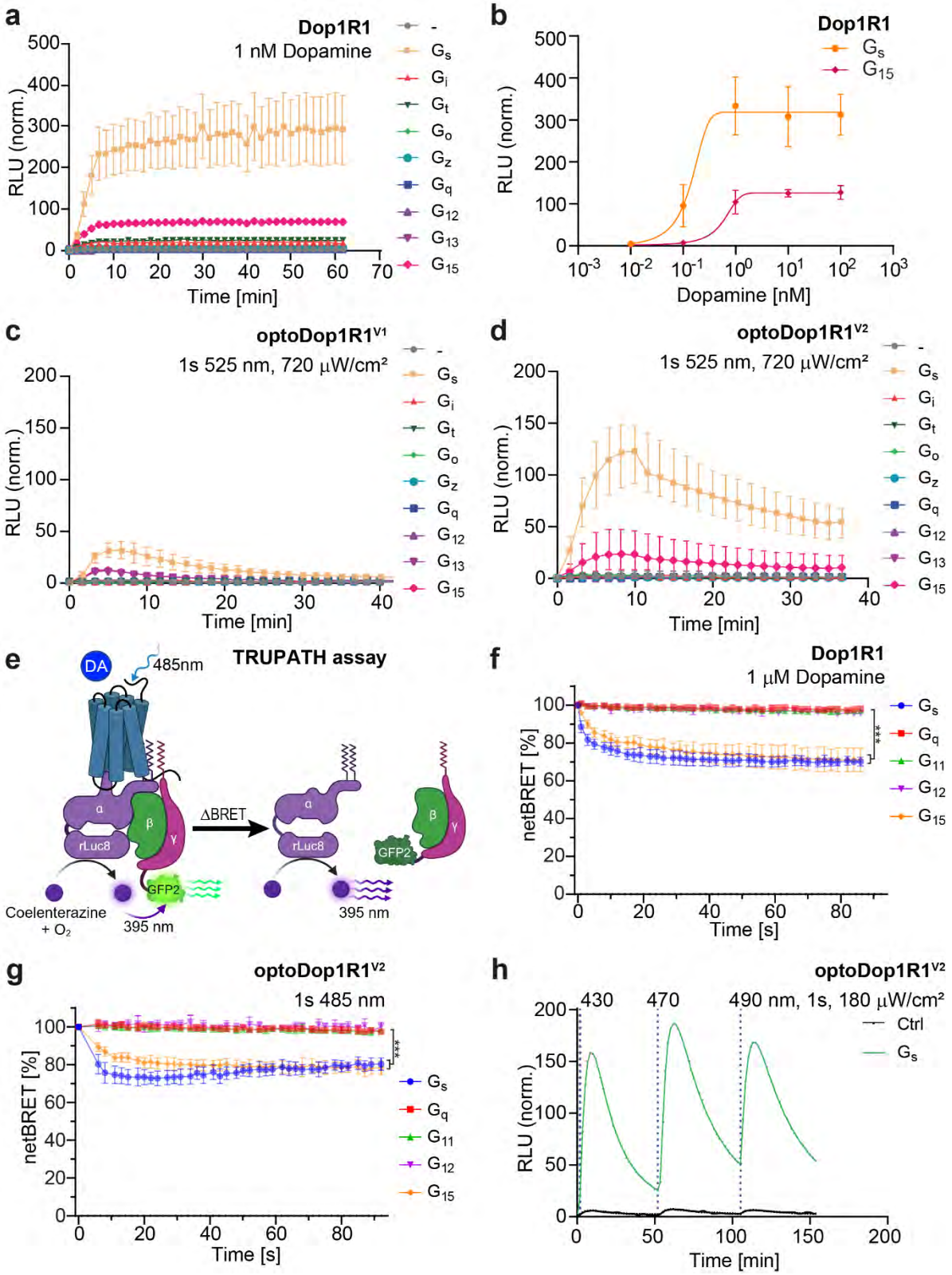

Supplementary Figure 2. Validation of optoDop1R1^{V2} function in G_{sx} and TRUPATH assays.

a-d. G protein coupling properties of *Drosophila* Dop1R1 and optoDop1R1 in the G_{sx} assay (shown as relative light units (RLU)). **a.** G protein coupling responses over time of *Drosophila* Dop1R1 with 1nM DA (mean ± SEM, n=4 independent experiments). **b.** DA concentration dependent maximum activation of G_s and G_{15} signaling of Dop1R1 (n=4 independent experiments). **c.** G protein coupling of optoDop1R1^{V1} after activation with light (1 s, 525 nm, 720 µW/cm^2). Normalized response kinetics are shown as relative light units (RLU, mean ±

SEM, n=7 independent experiments). **d.** G protein coupling properties of improved optoDop1R1^{V2} after activation with light (1s 525 nm, 720 μW/cm^2). Normalized response kinetics are shown as relative light units (RLU, mean ± SEM, n=7 independent experiments). **e.** Schematic of the TRUPATH assay. Bioluminescence resonance energy transfer (BRET) between Gα subunits fused to RLuc8 and Gγ subunits fused to GFP2 is diminished upon receptor activation and G protein subunit dissociation, resulting in lower BRET efficiency. Changes in the BRET emission ratio (netBRET: 515 nm/410 nm) represent G protein activation kinetics. Created with BioRender.com. **f.** Kinetic G protein coupling properties of *Drosophila* Dop1R1 after activation with 1μM DA assayed using TRUPATH (mean ± SEM, n=3 independent experiments, ***p<0.001, one-way ANOVA with Dunnett's *post-hoc* test). **g.** G protein coupling properties of optoDop1R1^{V2} after activation with light (1 s, 485 nm) using the TRUPATH assay. Normalized response kinetics are shown (mean ± SEM, n=4 independent experiments, ***p<0.001, one-way ANOVA with Dunnett's *post-hoc* test). **h.** Mean response of wavelength-dependent induction of G_s-mediated cAMP production after optoDop1R1^{V2} activation with light (1 s, 180 μW/cm^2, 430-490 nm, n=3 independent experiments). All boxplots depict 75th (top), median (central line) and 25th (bottom) percentile, whiskers depict 99th (top) and 1st (bottom) percentile. Source data and statistical details are provided as a Source Data file.

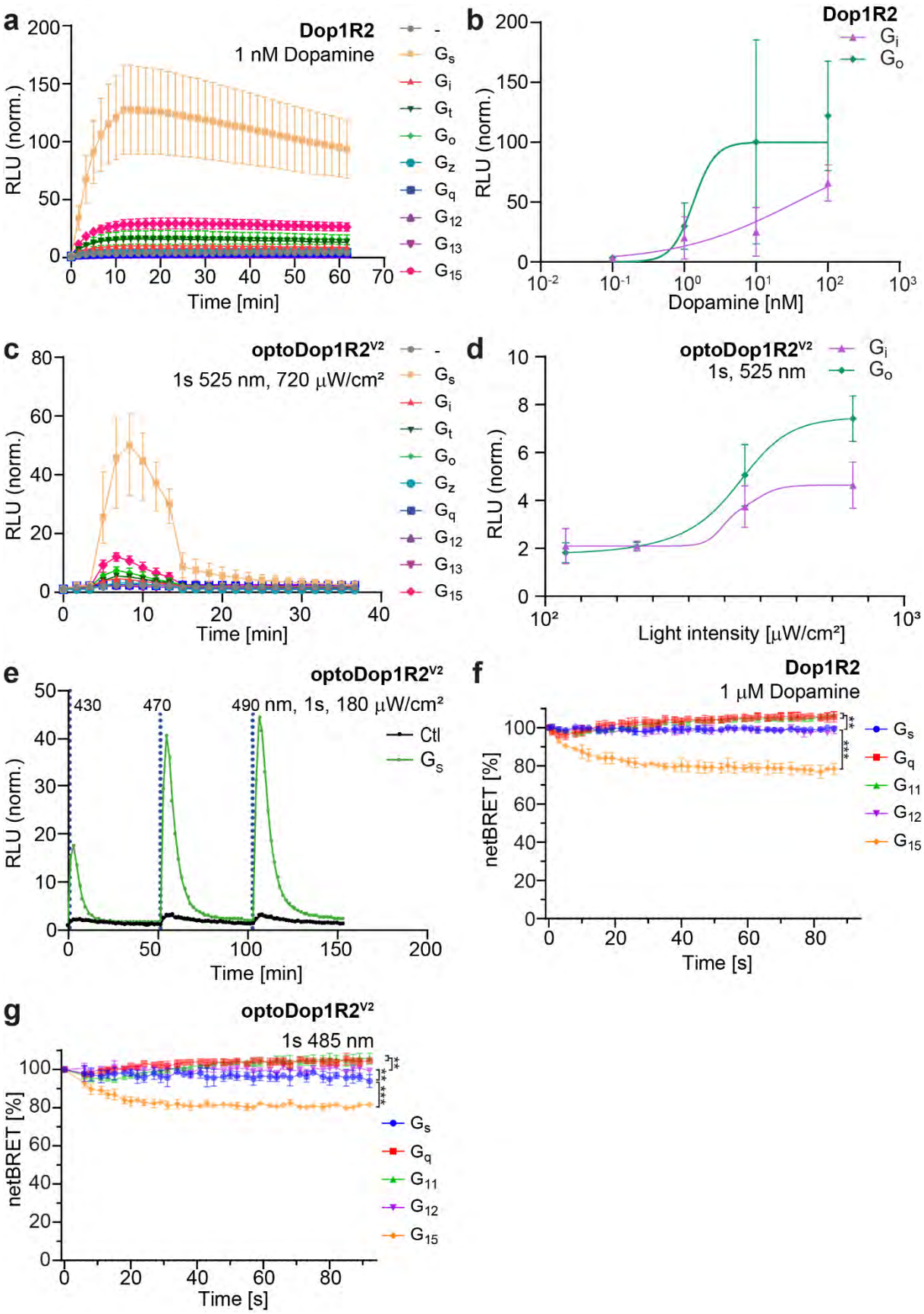

Supplementary Figure 3. Validation of optoDop1R2^{V2} function in G_{sx} and TRUPATH assays.

a-e. G protein coupling properties of *Drosophila* Dop1R2 and optoDop1R2^{V2} in the G_{sx} assay (shown as relative light units (RLU)). **a.** G protein coupling responses over time of Drosophila

Dop1R2 with 1nM DA (mean ± SEM, n=4 independent experiments). **b.** DA concentration dependent maximum activation of G_i and G_o signaling of Dop1R2 (mean ± SEM, 0.1/10 nM: n=3 independent experiments; 1.0/100 nM: n=4 independent experiments). **c.** G protein coupling responses over time of optoDop1R2^{V2} after activation with light (1s 525 nm, 720 μW/cm^2). Normalized response kinetics are shown (mean ± SEM, n=4 independent experiments). **d.** Light intensity-dependent maximum of G_i and G_o signaling induced by optoDop1R2^{V2} (1 s, 525 nm, n=4 independent experiments). **e.** Wavelength-dependent induction of G_s-mediated cAMP production after optoDop1R2^{V2} activation with light (1s 180 μW/cm^2, 430-490 nm, n=3 independent experiments). **f.** Kinetic G protein coupling properties of wild type Dop1R2 after activation with 1μM DA assayed with TRUPATH (mean ± SEM, n=3 independent experiments, one-way ANOVA with Dunnett's *post-hoc* test). **g.** G protein coupling properties of optoDop1R2^{V2} after activation with light (1 s, 485 nm) using TRUPATH. Normalized response kinetics are shown (mean ± SEM, n=4 independent experiments, one-way ANOVA with Dunnett's *post-hoc* test). All boxplots depict 75th (top), median (central line) and 25th (bottom) percentile, whiskers depict 99th (top) and 1st (bottom) percentile. Source data and statistical details are provided as a Source Data file.

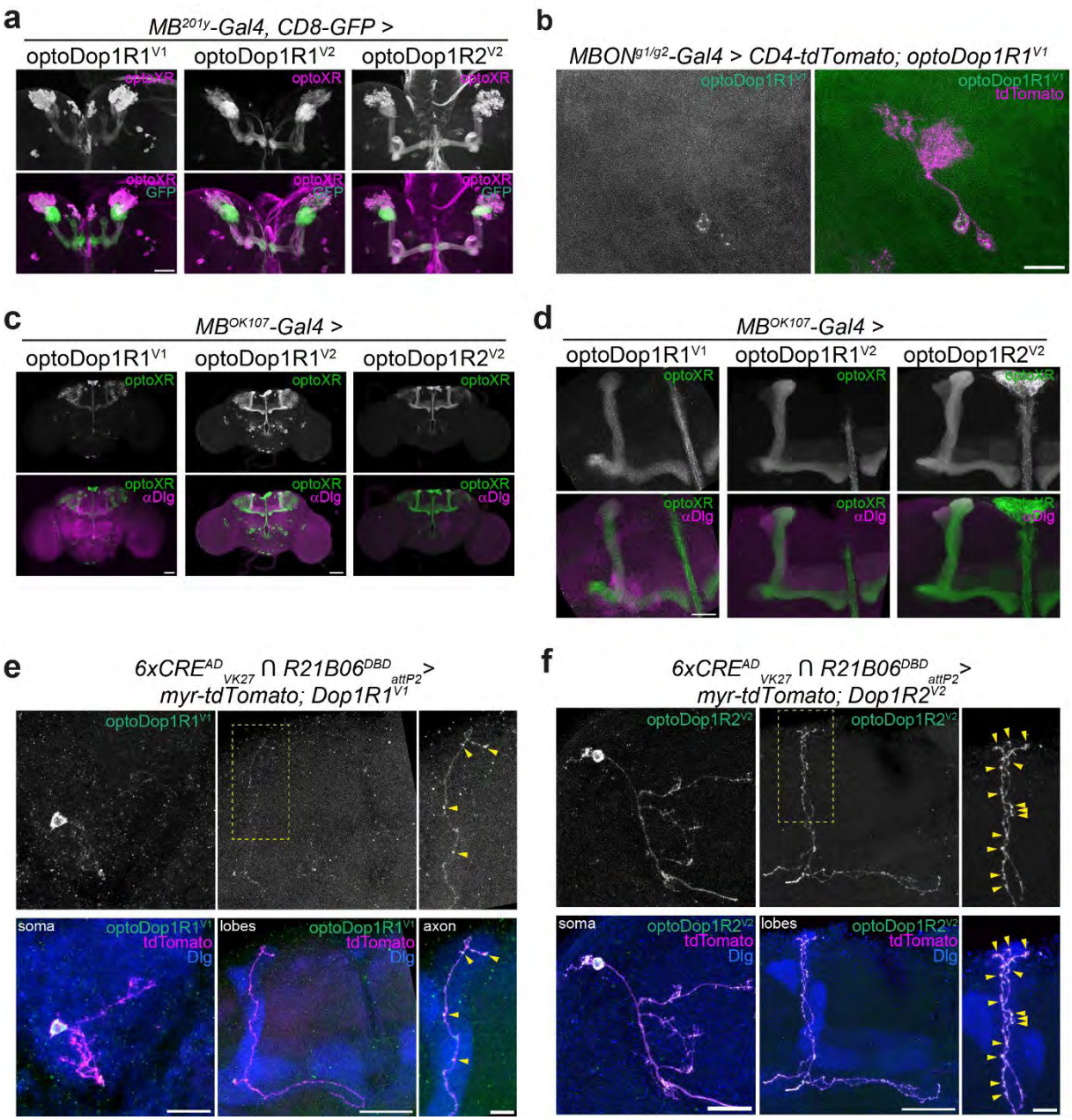

Supplementary Figure 4. *In vivo* localization of optoDopRs.

a. Overview of immunolabeled optoDopR expression in the larval mushroom body (*201y-Gal4, CD8-GFP,* scale bars: 50 μm). **b.** Single cell expression of immunolabeled optoDop1R1^{V1} in larval MBONs co-labeled with membrane bound CD4-tdTomato (*MBON$^{g1/g2}$-Gal4, CD4-tdTomato*). Scale bar 20 μm. Expression was mostly detected in the soma, with low expression in the axon and dendrites. **c.** Immunolabeling of optoDopRs in the adult mushroom body (all KCs, *OK107-Gal4, myr-tdTomato*) co-labeled with anti-Dlg marking the MB (scale bars: 50 μm). **d.** Enlarged view of optoDopR expression in the adult mushroom body (all KCs, *OK107-Gal4, myr-tdTomato*) co-labeled with anti-Dlg marking the MB (scale bars: 25 μm). **e.** Single cell immunolabeling of optoDop1R1^{V1} expressed in an adult mushroom body KC together with membrane-bound tdTomato and Dlg outlining the MB (scale bar: 10, 20, 5 μm). Prominent labeling is only seen in the KC soma with low dendritic and axonal signal. Arrowheads indicate axonal varicosities. **f.** Single cell expression of optoDop1R2^{V2} in the adult mushroom body showing a KC labeled with membrane bound tdTomato and immunostained for opto Dop1R2^{V2} and Dlg outlining the MB (scale bar: 10, 20, 5 μm). Prominent axonal and somatodendritic

localization can be detected, with arrowheads indicating axonal varicosities. All panels show representative images from at least two independent experiments with multiple samples.

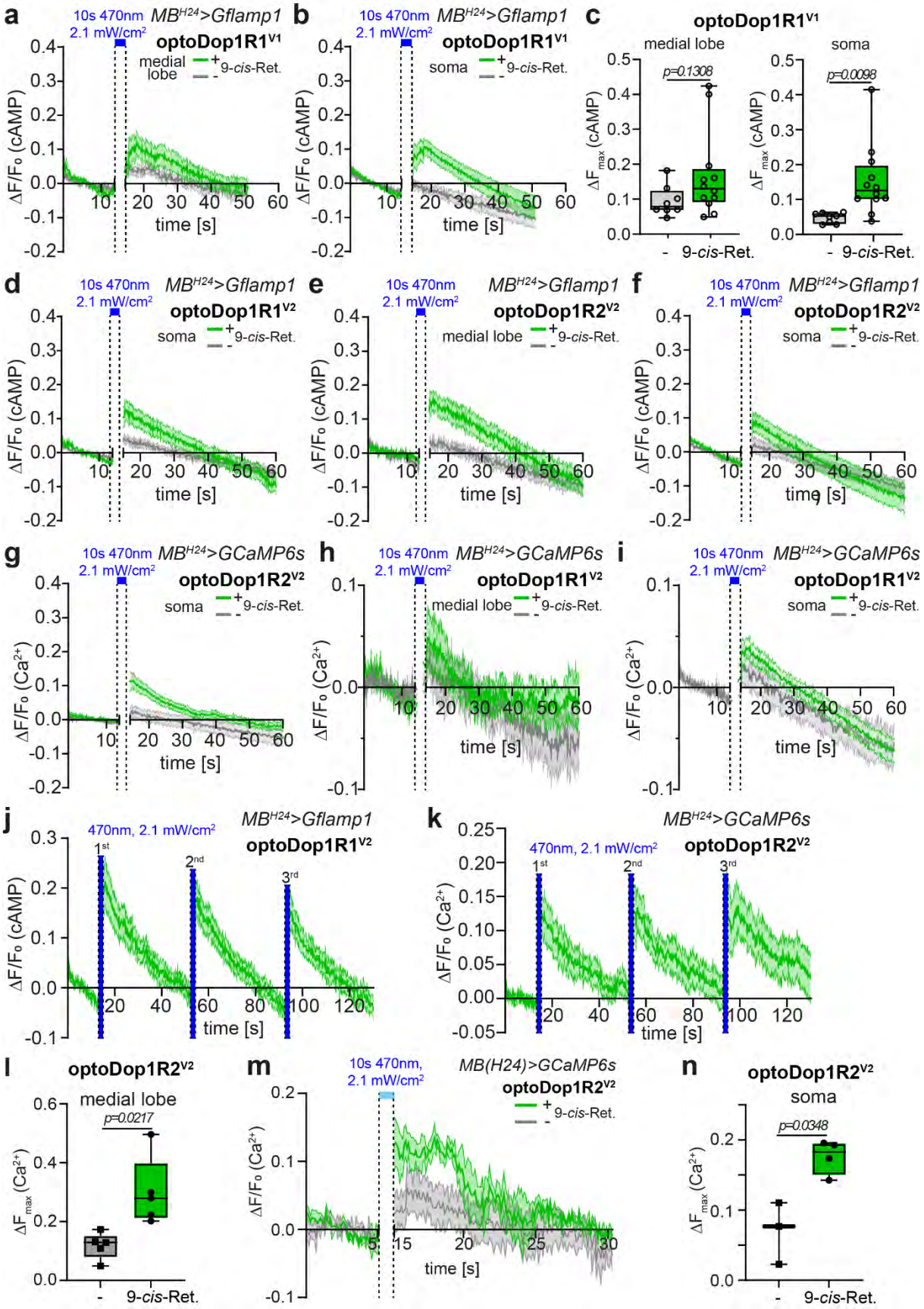

Supplementary Figure 5. *In vivo* validation of optoDopR activity.

a-c. cAMP imaging in the larval mushroom body using Gflamp1 and optoDop1R1^{V1} expression with and without 9-*cis*-Retinal feeding. Responses in the medial lobe (**a**) and soma (**b**) after 10s blue light illumination are shown over time. Maximum cAMP responses in the medial lobe

and soma (**c**) after optoDop1R1^{V1} activation (n=8,12 biologically independent samples, two-tailed unpaired Student's *t*-test). **d.** cAMP imaging in the larval mushroom body using Gflamp1 and optoDop1R1^{V2} expression (*H24-Gal4>G-Flamp1, optoDop1R1^{V2}*, 10s 470 nm, n=11, 15). Responses in the soma after 10s blue light illumination are shown over time. **e-f.** cAMP imaging in the larval mushroom body using Gflamp1 and optoDop1R2^{V2} expression with and without 9-*cis*-Retinal feeding (10s 470 nm, n=7,8 biologically independent samples). Responses in the medial lobe (**e**) and soma (**f**) after 10s blue light illumination are shown over time. **g-i.** Calcium imaging in the mushroom body using GCaMP6s and optoDop1R2^{V2} or optoDop1R1^{V2} expression in isolated larval brains (10s 470 nm, optoDop1R2^{V2}: n=11,7 biologically independent samples; optoDop1R1^{V2}: n=8,8 biologically independent samples). Responses in the soma upon optoDop1R2^{V2} activation (**g**), and for optoDop1R1^{V2} activation in the medial lobe (**h**) and soma (**i**) are shown over time. **j-k.** cAMP or calcium imaging in the larval mushroom body in isolated brains with repeated light activation of optoDopRs (each light pulse: 10 s, 470 nm). Medial lobe cAMP responses upon optoDop1R1^{V2} activation (n=10 biologically independent samples) (**j**) and calcium responses upon optoDop1R2^{V2} activation (n=6 biologically independent samples) (**k**) are shown over time. **l-n.** *In vivo* calcium imaging in intact larvae using GCaMP6s and optoDop1R2^{V2} expressed in the larval mushroom body (*H24-Gal4>GCaMP6s, optoDop1R2^{V2}*). Maximum calcium responses in the MB medial lobe after light-induced activation of optoDop1R2^{V2} with or without 9-*cis*-retinal feeding (10s 470 nm, n=5,5 animals, two-tailed unpaired Student's *t*-test) (**l**). Calcium responses in KC somata with or without 9-*cis*-retinal over time (**m**) and maximum responses (**n**) after light-induced activation of optoDop1R2^{V2} (10s 470 nm, n=3, 4 animals, two-tailed unpaired Student's *t*-test).

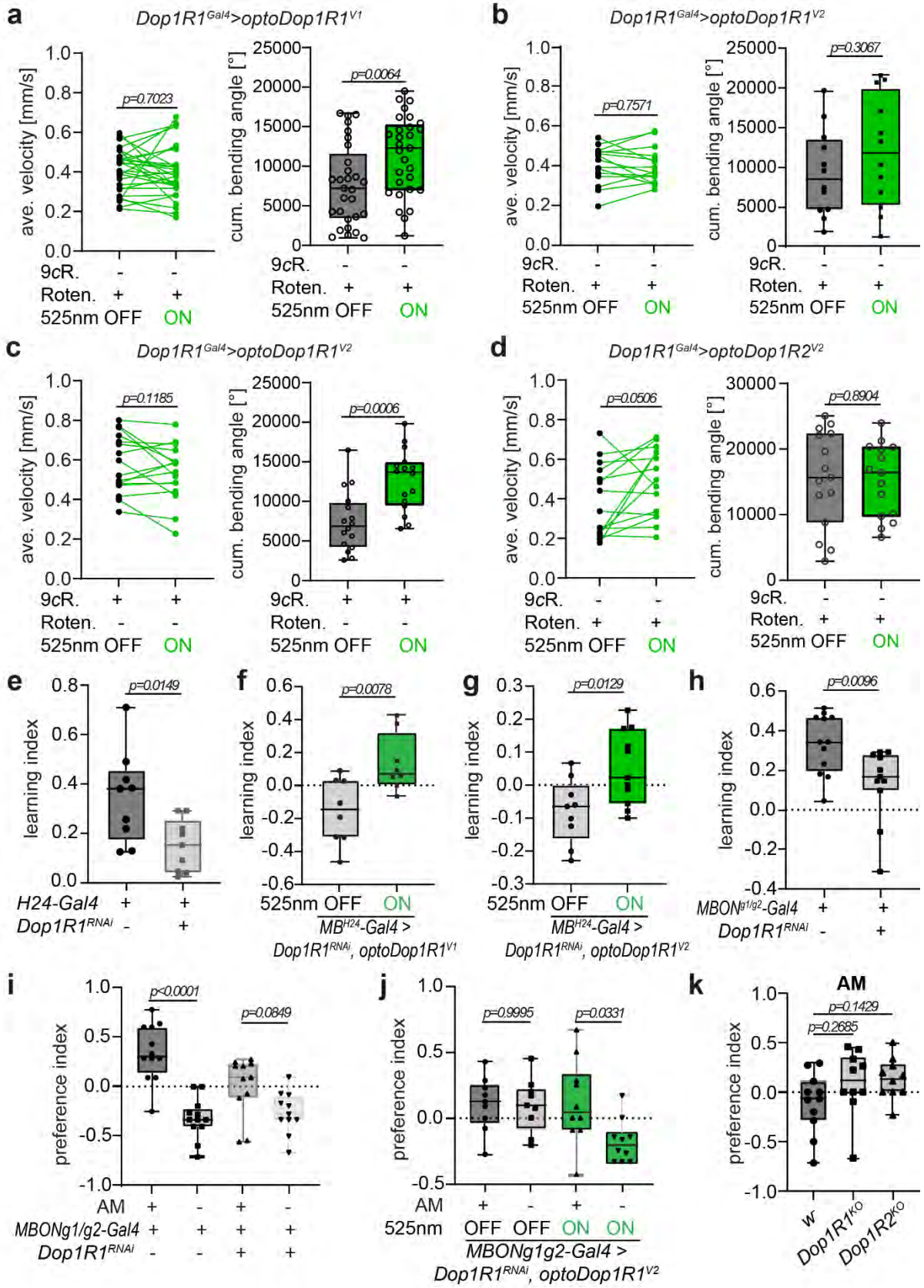

Supplementary Figure 6. Functional validation of optoDopRs in Drosophila larvae *in vivo*.

a-b. Average velocity and bending angles of Rotenone-fed animals expressing optoDop1R1^{V1}(**a**) or optoDop1R1^{V2} (**b**) in an endogenous Dop1R1-like pattern without 9-*cis*-

Retinal feeding. Animals were tracked without light for 1min and with 525 nm light illumination for 1 min. Average velocity (left) or cumulative bending angles (right) in the dark (OFF) and during light activation (ON) are shown (optoDop1R1^{V1}: n=29, 29 animals, optoDop1R1^{V2}: n=12,12 animals, two-tailed paired Student's *t*-test). **c.** Average velocity and bending angles of 9-*cis*-Retinal fed larvae without Rotenone treatment expressing optoDop1R1^{V2} in an endogenous Dop1R1-like pattern. Larvae were tracked without light for 1min and with 525 nm light illumination for 1 min. Average velocity (left) or cumulative bending angles (right) in the dark and during light activation are shown (n=16,16, ** $p<0.01$, paired Student's *t*-test). **d.** Average velocity and bending angles of Rotenone-fed animals expressing optoDop1R2^{V2} in an endogenous Dop1R1-like pattern without 9-*cis*-Retinal feeding. Larvae were tracked without light for 1min and with 525 nm light illumination for 1 min. Average velocity (left) or cumulative bending angles (right) in the dark and during light activation are shown (n=15,15, n.s. $p>0.05$, two-tailed paired Student's t-test). **e.** Larval learning after fructose-odor training is impaired upon Dop1R1^{RNAi} expression in the MB (n=9, 9 independent experiments, two-tailed unpaired Student's *t*-test). **f.** Dop1R1-dependent single odor-fructose learning in larvae. Animals expressing optoDop1R1^{V1} and Dop1R1^{RNAi} in KCs were trained using fructose-odor learning (3x3min) with or without light activation during fructose exposure (3 min 525 nm, 720 μW/cm^2). Learning index of 9-*cis*-Retinal fed animals with and without light activation during training is shown (n=8, 8 independent experiments, unpaired two-tailed Student's *t*-test). **g.** Single odor-fructose learning in larvae expressing optoDop1R1^{V2} and Dop1R1^{RNAi} in KCs. Fructose-odor learning (3x3min) with or without light activation during fructose exposure (3 min 525 nm, 720 μW/cm^2). Learning index of 9-*cis*-retinal fed animals with and without light activation during training is shown (n=9, 11 independent experiments, two-tailed unpaired Student's *t*-test). **h.** Larval learning after fructose-odor training is impaired upon Dop1R1^{RNAi} expression in MBON$^{g1/g2}$ (n=12, 11 independent experiments, two-tailed unpaired Student's *t*-test). **i** Fructose reward-dependent induction of odor preference (AM or blank) for Dop1R1-dependent data from (**h**) (n=12, 11 independent experiments, One-way ANOVA with Tukey's *post-hoc* test). **j.** Fructose and optoDop1R1^{V2}-dependent induction of odor preference (amylacetate (AM) or blank) with (green bars) or without (gray bars) light illumination during fructose pairing in Dop1R1^{RNAi} larvae (n=9, 9 independent experiments, One-way ANOVA with Tukey's *post-hoc* test, data from Fig. 5e). **k.** Innate preference index for AM in control (w$^-$), *Dop1R1^{KO}* and *Dop1R2^{KO}* 3rd instar larvae (n=11, 10, 9 independent experiments, One-way ANOVA with Tukey's *post-hoc* test). All boxplots depict 75th (top), median (central line) and 25th (bottom) percentile, whiskers depict 99th (top) and 1st (bottom) percentile. Source data and statistical details are provided as a Source Data file.

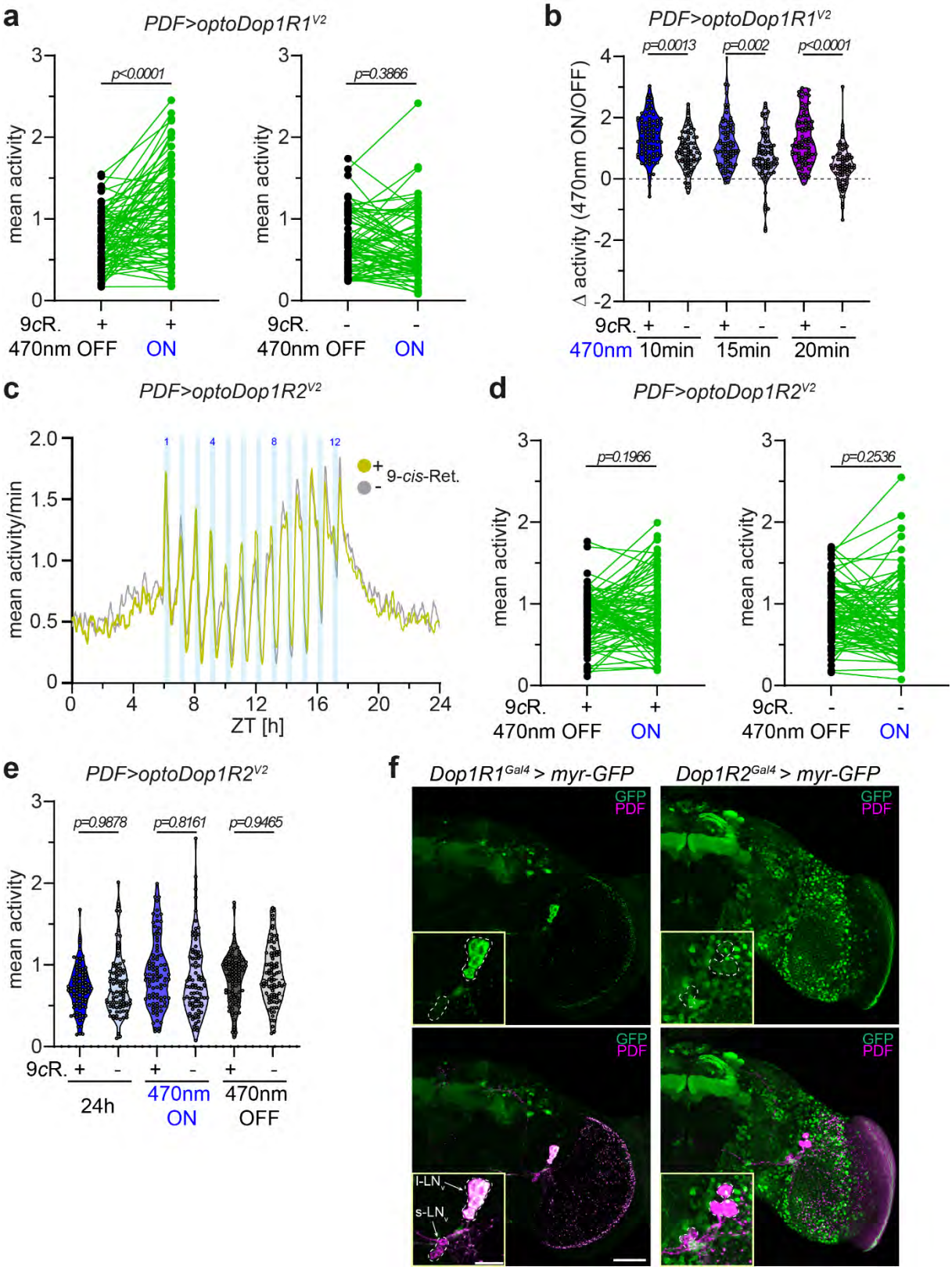

Supplementary Figure 7. Cell type-specific function of Dop1R1 activity in blue light induced arousal.

a. Activity difference of flies expressing optoDop1R1^{V2} in PDF neurons with (left) and without 9-*cis*-Retinal (9cR) feeding (right) before and during blue light pulse exposure (24h activity data from Fig. 6g, n=83,77 animals, two-tailed paired *t*-test). **b.** Activity difference of flies expressing optoDop1R1^{V2} in PDF neurons (with and without 9-*cis*-Retinal feeding) during light on times using different duration of blue light pulse exposure (1/h, 10, 15 or 20min,

n=83,77 animals, one-way ANOVA with Tukey's *post-hoc* test). **c.** Mean activity during 24h monitoring in flies expressing optoDop1R2^{V2} in pdf neurons with and without 9cR feeding (n=90 animals). Blue light pulses (12x 20min, 1/h) during daytime increase fly activity independently of optoDop1R1^{V2} activation. **d.** Activity difference of flies expressing optoDop1R2^{V2} in PDF neurons with (left) and without 9-*cis*-Retinal (9cR) feeding (right) before and during blue light pulse exposure (24h activity data from Fig. S6e, (n=90 animals, two-tailed paired *t*-test). **e.** Mean activity of *pdf>optoDop1R2*^{V2} -expressing flies during the entire 24h, all light on and light off phases (n=90 animals, one-way ANOVA with Tukey's *post-hoc* test). **f.** myristoylated (myr-)GFP reporter expression using Dop1R1 (left panel) or Dop1R2 (right panel) knock-in Gal4 lines together with immunolabeling of PDF-expressing s-LN$_v$s and l-LN$_v$s (somata are indicated by dotted lines). Note that Dop1R1 reporter expression is specific for l-LN$_v$s, while Dop1R2 reporter expression is weak in all LN$_v$s. Scale bar: 50μm, inset 10μm. All violin plots with single data points depict data distribution, dotted lines depict 75th (top) and 25th (bottom) percentile, solid central line the median. Source data and statistical details are provided as a Source Data file.

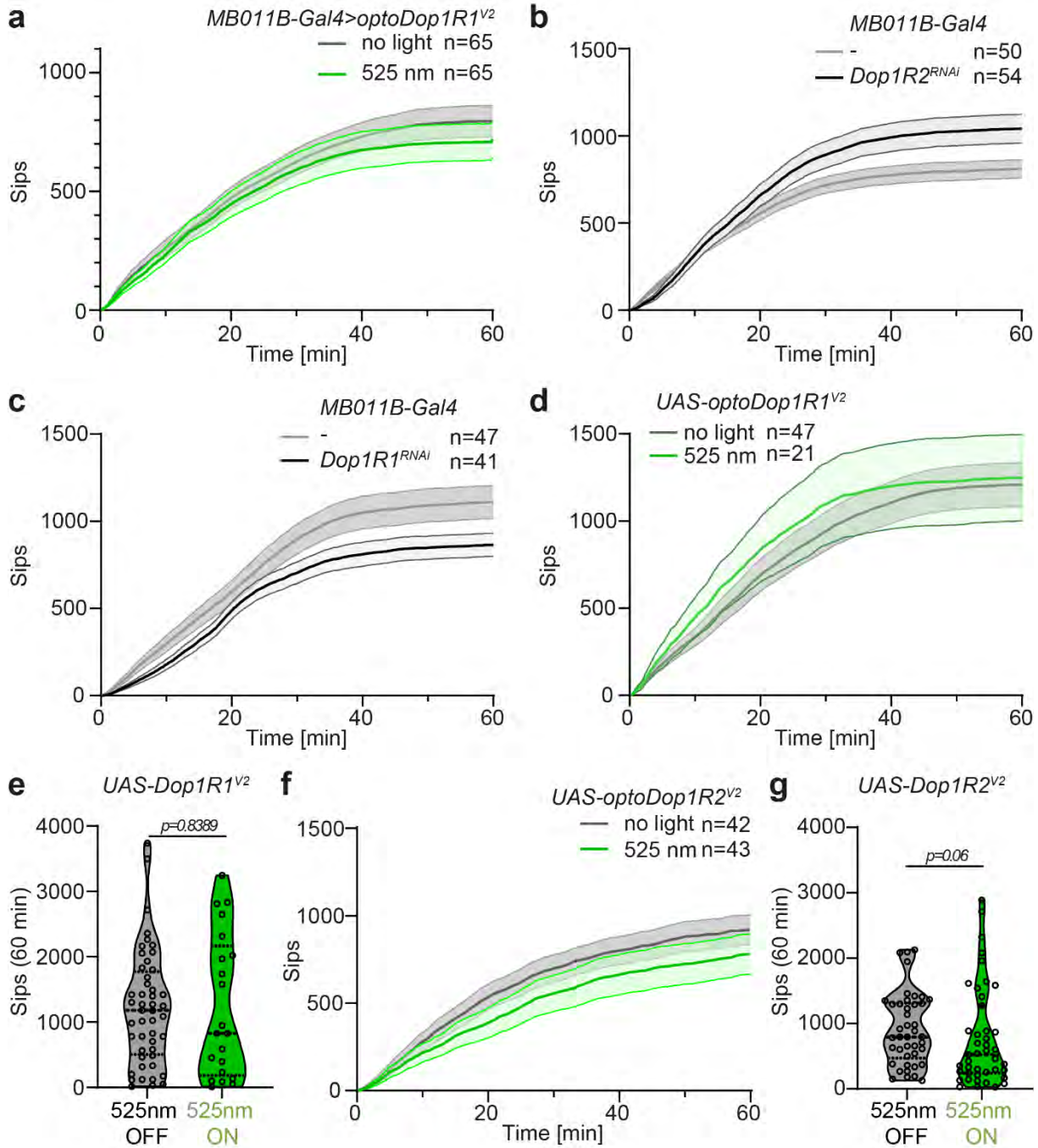

Supplementary Figure 8: Cell type-specific function of Dop1R2 activity in satiety.
a. Cumulative sips over time in flies expressing optoDop1R1^{V2} with *MB011B-Gal4* with or without light stimulation (mean ± SEM, n=65,65 animals). **b.** Cumulative sips over time in flies expressing Dop1R2^{RNAi} with *MB011B-Gal4* compared to control (mean ± SEM, n=50,54 animals). **c.** Cumulative sips over time in flies expressing Dop1R1^{RNAi} with *MB011B-Gal4* (mean ± SEM, n=47,41 animals). **d.** Cumulative sips over time in optoDop1R1^{V2} transgenes without Gal4 expression and without or with light stimulation (mean ± SEM, n=48,21 animals). **e.** Total sips at 60min for optoDop1R1^{V2} transgenes without Gal4 expression and without or with light stimulation (n=48,21 animals, two-tailed Mann-Whitney test). **f.** Cumulative sips over time in optoDop1R2^{V2} transgenes without Gal4 expression and without or with light stimulation (mean ± SEM, n=42,43 animals). **g.** Total sips at 60min for optoDop1R2^{V2} transgenes without Gal4 expression and without or with light stimulation (n=42,43 animals, two-tailed Mann-Whitney test). All violin plots with single data points depict

data distribution, dotted lines depict 75th (top) and 25th (bottom) percentile, solid central line the median. Source data and statistical details are provided as a Source Data file.

Supplementary Table 1. Previous optoXRs and their *in vivo* applications. Only optoXRs that have been applied *in vivo* are listed here. Abbreviations: Rho: bovine Rhodopsin, OPN4: melanopsin

Chimeric receptor	**Original reference**	***In vivo* applications**	**Cell type-specificity/rescue of endogenous receptor function**
Rho:β_2AR	[1]	- virus-mediated overexpression in mouse N. accumbens neurons [2] - virus-mediated overexpression in mouse basolateral amygdala, promoting anxiety-like behavior [3,4]	partial/no partial/no
Rho:α_1AR	[2]	- virus-mediated overexpression in mouse N. accumbens neurons, reward-related preference behavior - virus-mediated overexpression in mouse CA1 astrocytes, memory acquisition[5] - transgenic overexpression in mouse cortical astrocytes, remote memory acquisition [6] - virus-mediated overexpression in mouse astrocytes in slices, electrophysiology [7]	partial/no partial/no partial/no partial/no
Rho:μOR	[8]	- virus-mediated overexpression in mouse dorsal root ganglion neurons, preference/aversion behavior [9] - Penk-Cre dependent virus-mediated overexpression in dorsal raphe nucleus subset neurons, restoration of consumption behavior [10]	partial/no yes/yes
Rho:DRD1	[11]	- DRD1-Cre dependent virus-mediated overexpression in mouse N. accumbens; activation of medium spiny neurons to increase social interaction	yes/no
Rho:CXCR4	[12]	- virus-mediated overexpression in mouse, T-cell recruitment	yes/no
Rho:A_{2A}R	[13]	- virus-mediated overexpression in mouse hippocampus and N. accumbens, spatial memory performance and locomotor activity - adora2a-cre dependent virus-mediated overexpression in mouse striatopallidal neurons, goal-directed behavior [14]	partial/no yes/no
OPN4:mGluR$_6$	[15]	- virus-mediated overexpression in retinal ganglion cells, restoration of visually guided behavior - virus-mediated overexpression in bipolar cells, restoration of visually guided behavior [16]	yes/partial (degeneration model) yes/yes (degeneration model)
Rho:Fz7	[17]	- Zebrafish mRNA injection and overexpression, mesoderm cell migration	no/yes

Supplementary Table 2. optoXR variants generated in this study.

GPCR source sequence	Opto variant	Protein sequence of generated optoXR chimera (Rho/target receptor residues)
A0A0B4KHI2.1/ 145-431 Dopamine 1-like receptor 1 isoform E ECO:0000313 EMBL:AGB959 44.1	**Opto Dop1R1 V1**	MKTIIALSYIFCLVFAMYTDIEMNRLGKDSLMNGTEGPNFYVPFSNKTGVVR SPFEAPQYYLAEPWQFSMLAAYMFLLIMLGFPINFLTLYV**IYTERSLRR**ILNYI LLNLAVADLFMVFGGFTTTLYTSLHGYFVFGPTGCNLEGFFATLGGEIALWS LVVLAIERYVVV**KDPLRYGRWVTRR**AIMGVAFTWVMALACAAPPLVGWSR YIPEGMQCSCGIDYYTPHEETNNESFVIYMFVVHFIIPLIVIFFCYG**RLYCYAQ KHVKSIKAVTRPGEVAEKQRYKSIRRPKNQPKKFKVRNLHTHSSPYHVSD HKAA**RMVIIMVIAFLICWLPYAGVAFYIFTHQGSDFGPIFMTIPAFFAKTSAVY NPVIYIMMNKQ**FRDAFKRILTMRNPWCCAQDVGNIHPRNSDRFITDYAAKN VVVMNSGRSSAELEQVSAI**TETSQVAPA
A0A0B4KHI2.1/ 145-431 Dopamine 1-like receptor 1 isoform E ECO:0000313 EMBL:AGB959 44.1	**Opto Dop1R1 V2**	MKTIIALSYIFCLVFAMYTDIEMNRLGKDSLMNGTEGPNFYVPFSNKTGVVR SPFEAPQYYLAEPWQFSMLAAYMFLLIMLGFPINFLTLYVTVQHKKLRTPLN YILLNLAVADLFMVFGGFTTTLYTSLHGYFVFGPTGCNLEGFFATLGGEIAL WSLVVLAIERYVVV**KDPLRYGRWVTRRV**AIMGVAFTWVMALACAAPPLVG WSRYIPEGMQCSCGIDYYTPHEETNNESFVIYMFVVHFIIPLIVIFFCYG**RLYC YAQKHVKSIKAVTRPGEVAEKQRYKSIRRPKNQPKKFKVRNLHTHSSPYH VSDHKAA**RMVIIMVIAFLICWLPYAGVAFYIFTHQGSDFGPIFMTIPAFFAKTS AVYNPVIYIM**FNKEFRDAFKRILTMRNPWCCAQDVGNIHPRNSDRFITDYA AKNVVVMNSGRSSAELEQVSAI**TETSQVAPA
A0A0B4KI18.1/ 125-474 Dopamine 1-like receptor 2 isoform CECO:0000313 EMBL:AGB964 52.1	**Opto Dop1R2 V1**	MKTIIALSYIFCLVFAMYTDIEMNRLGKDSLMNGTEGPNFYVPFSNKTGVVR SPFEAPQYYLAEPWQFSMLAAYMFLLIMLGFPINFLTLYV**VIRERYLHTA**LNY ILLNLAVADLFMVFGGFTTTLYTSLHGYFVFGPTGCNLEGFFATLGGEIALW SLVVLAIERYVVV**TDPFSYPMRMTVK**AIMGVAFTWVMALACAAPPLVGWSR YIPEGMQCSCGIDYYTPHEETNNESFVIYMFVVHFIIPLIVIFFCYG**RIYRAAVI QTRSLKIGTKQVLMASGELQLTLRIHRGGTTRDQQNQVSGGGGGGGGGG GGGGSLSHSHSHSHHHHHNHGGGTTTSTPEEPDDEPLSALHNNGLARHR HMGKNFSLSRKLAKFAKEKKAA**RMVIIMVIAFLICWLPYAGVAFYIFTHQGS DFGPIFMTIPAFFAKTSAVYNPVIYIMMNKQ**FRRAFVRLLCMCCPRKIRRKY QPTMRSKSQCHVAAAMVAASTSFGYHSVNQIDRTLM**TETSQVAPA
A0A0B4KI18.1/ 125-474 Dopamine 1-like receptor 2 isoform C ECO:0000313 EMBL:AGB964 52.1	**Opto Dop1R2 V2**	MKTIIALSYIFCLVFAMYTDIEMNRLGKDSLMNGTEGPNFYVPFSNKTGVVR SPFEAPQYYLAEPWQFSMLAAYMFLLIMLGFPINFLTLYVTVQHKKLRTPLN YILLNLAVADLFMVFGGFTTTLYTSLHGYFVFGPTGCNLEGFFATLGGEIAL WSLVVLAIERYVVV**TDPFSYPMRMTVKR**AIMGVAFTWVMALACAAPPLVG WSRYIPEGMQCSCGIDYYTPHEETNNESFVIYMFVVHFIIPLIVIFFCYG**RIYR AAVIQTRSLKIGTKQVLMASGELQLTLRIHRGGTTRDQQNQVSGGGGGGG GGGGGGGSLSHSHSHSHHHHHNHGGGTTTSTPEEPDDEPLSALHNNGLA RHRHMGKNFSLSRKLAKFAKEKKAA**RMVIIMVIAFLICWLPYAGVAFYIFTH QGSDFGPIFMTIPAFFAKTSAVYNPVIYIM**WSRDFRRAFVRLLCMCCPRKIR RKYQPTMRSKSQCHVAAAMVAASTSFGYHSVNQIDRTLM**TETSQVAPA
Q0IGY0.1/480-738 Leucine-rich repeat-containing G protein-coupled receptor 4 isoform B ECO:0000313 EMBL:ABW094 04.2	**Opto Lgr4 V1**	MKTIIALSYIFCLVFAMYTDIEMNRLGKDSLMNGTEGPNFYVPFSNKTGVVR SPFEAPQYYLAEPWQFSMLAAYMFLLIMLGFPINFLTLYV**RYFYKSRSNVE**L NYILLNLAVADLFMVFGGFTTTLYTSLHGYFVFGPTGCNLEGFFATLGGEIAL WSLVVLAIERYVVV**TRPLKPRDTEKVR**AIMGVAFTWVMALACAAPPLVGWS RYIPEGMQCSCGIDYYTPHEETNNESFVIYMFVVHFIIPLIVIFFCYG**RMLQAI RDSGGGMRSTHSGRENVVA**RMVIIMVIAFLICWLPYAGVAFYIFTHQGSDF GPIFMTIPAFFAKTSAVYNPVIYIMMNKQ**FRQQLRRYCHTLPSCSLVNNETR SQTQTAYESGLSVSLAHLGGGVGGGSGRKRMSHRQMSYL**TETSQVAPA
E1JJ17.1/118-381 Tachykinin-like receptor at 99D isoform B ECO:0000313 EMBL:ACZ950 66.1	**Opto Tk99D V1**	MKTIIALSYIFCLVFAMYTDIEMNRLGKDSLMNGTEGPNFYVPFSNKTGVVR SPFEAPQYYLAEPWQFSMLAAYMFLLIMLGFPINFLTLYV**VMTTKRMRTV**LN YILLNLAVADLFMVFGGFTTTLYTSLHGYFVFGPTGCNLEGFFATLGGEIAL WSLVVLAIERYVVV**IRPLQPRMSKRC**AIMGVAFTWVMALACAAPPLVGWSR YIPEGMQCSCGIDYYTPHEETNNESFVIYMFVVHFIIPLIVIFFCYG**RVGIELW GSKTIGECTPRQVENVRSKRRVV**RMVIIMVIAFLICWLPYAGVAFYIFTHQGS DFGPIFMTIPAFFAKTSAVYNPVIYIMMNKQ**FRYGFKMVFRWCLFVRVGTEP FSRRENLTSRYSCSGSPDHNRIKRNDTQKSILYTCPSSPKSHRISHSGRSA TLRNSLPAESLSSGGSGGGGHRKRLSYQQEMQQRWSGPNSATAVTNSS STANTTQLLS**TETSQVAPA

GPCR source sequence	Opto variant	Protein sequence of generated optoXR chimera (Rho/target receptor residues)
E1JGM2.2/107-533 5-hydroxytryptamine (Serotonin) receptor 1B isoform D ECO:0000313 EMBL:ACZ94473.2	**Opto 5-HT1B V1**	MKTIIALSYIFCLVFAMYTDIEMNRLGKDSLMNGTEGPNFYVPFSNKTGVVR SPFEAPQYYLAEPWQFSMLAAYMFLLIMLGFPINFLTLYV**IILERNLQNV**LNYI LLNLAVADLFMVFGGFTTTLYTSLHGYFVFGPTGCNLEGFFATLGGEIALWS LVVLAIERYVVV**TNIDYNNLRTPR**AIMGVAFTWVMALACAAPPLVGWSRYIP EGMQCSCGIDYYTPHEETNNESFVIYMFVVHFIIPLIVIFFCYG**KIYIIARKRIQ RRAQKSFNVTLTETDCDSAVRELKKERSKRRAERKRLEAGERTPVDGDG TGGQLQRRTRKRMRICFGRNTNTANVYRTSNANEIITLSQQVAHATQHHLI ASHLNAITPLAQSIAMGGVGCLTTTTPSEKALSGAGTVAGAVAGGSGSGS GEEGAGTEGKNAGVGLGGVLASIANPHQKLAKRRQLLEAKRERKAAR**MV IIMVIAFLICWLPYAGVAFYIFTHQGSDFGPIFMTIPAFFAKTSAVYNPVIYIMM NKQ**FRRAFKRILFGRKAAARARSAKI**TETSQVAPA
Q7KTL9.1/55-319 Adipokinetic hormone receptor isoform C ECO:0000313 EMBL:AAS64647.1	**Opto AkhR V1**	MKTIIALSYIFCLVFAMYTDIEMNRLGKDSLMNGTEGPNFYVPFSNKTGVVR SPFEAPQYYLAEPWQFSMLAAYMFLLIMLGFPINFLTLYV**LTKRRLRGPLR**L NYILLNLAVADLFMVFGGFTTTLYTSLHGYFVFGPTGCNLEGFFATLGGEIAL WSLVVLAIERYVVV**LKPLKRSYNRGR**AIMGVAFTWVMALACAAPPLVGWS RYIPEGMQCSCGIDYYTPHEETNNESFVIYMFVVHFIIPLIVIFFCYG**AIYLEIY RKSQRVLKDVIAERFRRSNDDVLSRAKKRTL**RMVIIMVIAFLICWLPYAGVA FYIFTHQGSDFGPIFMTIPAFFAKTSAVYNPVIYIMMNKQ**FRMNNNNPSVNN RHTSLSNRLDSSNQLMQKQLTNNSLLNGRGQVMAAAVSATTKLANVVSL KGTANGNGSAAAAGTVPITPPLTVTIAPLATDDEANDDSCLSAVTIRCQDQ SPIRQKCGDSIELTSVVK**TETSQVAPA
Q9VBP0.2/447-704 Leucine-rich repeat containing G protein-coupled receptor 3 ECO:0000313 EMBL:AAF56490.2	**Opto Lgr3 V1**	MKTIIALSYIFCLVFAMYTDIEMNRLGKDSLMNGTEGPNFYVPFSNKTGVVR SPFEAPQYYLAEPWQFSMLAAYMFLLIMLGFPINFLTLYV**RFIYRDENVA**LNY ILLNLAVADLFMVFGGFTTTLYTSLHGYFVFGPTGCNLEGFFATLGGEIALW SLVVLAIERYVVV**ADPFRGHRSIGNR**AIMGVAFTWVMALACAAPPLVGWSR YIPEGMQCSCGIDYYTPHEETNNESFVIYMFVVHFIIPLIVIFFCYG**ALLISIWR TRSATPLTLLDCEFA**RMVIIMVIAFLICWLPYAGVAFYIFTHQGSDFGPIFMTI PAFFAKTSAVYNPVIYIMMNKQ**FRNQIFLRGWKKITSRKRAEAGNGNVATT TTGTATGSSQHPDDFTIFAKAAMRCH**TETSQVAPA
Q9VW75.2/80-236 Short neuropeptide F receptor isoform B EMBL:AGB94779.1	**Opto sNPFR V1**	MKTIIALSYIFCLVFAMYTDIEMNRLGKDSLMNGTEGPNFYVPFSNKTGVVR SPFEAPQYYLAEPWQFSMLAAYMFLLIMLGFPINFLTLYV**VLRNRAMQTVTN IFITNLALSD**LNYILLNLAVADLFMVFGGFTTTLYTSLHGYFVFGPTGCNLEG FFATLGGEIALWSLVVLAIERYVVV**IYPFHPRMKLST**AIMGVAFTWVMALAC AAPPLVGWSRYIPEGMQCSCGIDYYTPHEETNNESFVIYMFVVHFIIPLIVIFF CYG**WISVKLNQRARAKPGSKSSRREEADRDRKKRTN**RMVIIMVIAFLICWL PYAGVAFYIFTHQGSDFGPIFMTIPAFFAKTSAVYNPVIYIMMNKQFR**YAWL NENFRKEFKHVLPCFNPSNNNIINITRGYNRSDRNTCGPRLHHGKGDGGM GGGSLDADDQDENGITQETCLPKEKLLIIPREPTYGNGTGAVSPILSGRGIN AALVHGGDHQMHQLQPSHHQQVELTRRIRRRTDETDGDYLDSGDEQTVE VRFSETPFVSTDNTTGISILETSTSHCQDSDVMVELGEAIGAGGGAELGRRI N**TETSQVAPA

Supplementary References

1. Kim, J.-M. *et al.* Light-Driven Activation of β 2 -Adrenergic Receptor Signaling by a Chimeric Rhodopsin Containing the β 2 -Adrenergic Receptor Cytoplasmic Loops †. *Biochemistry* **44**, 2284–2292 (2005).

2. Airan, R. D., Thompson, K. R., Fenno, L. E., Bernstein, H. & Deisseroth, K. Temporally precise in vivo control of intracellular signalling. *Nature* **458**, 1025–1029 (2009).

3. Siuda, E. R. *et al.* Optodynamic simulation of β-adrenergic receptor signalling. *Nat Commun* **6**, 8480 (2015).

4. Siuda, E. R., Al-Hasani, R., McCall, J. G., Bhatti, D. L. & Bruchas, M. R. Chemogenetic and Optogenetic Activation of Gαs Signaling in the Basolateral Amygdala Induces Acute and Social Anxiety-Like States. *Neuropsychopharmacology* **41**, 2011–2023 (2016).

5. Adamsky, A. *et al.* Astrocytic Activation Generates De Novo Neuronal Potentiation and Memory Enhancement. *Cell* **174**, 59-71.e14 (2018).

6. Iwai, Y. *et al.* Transient Astrocytic Gq Signaling Underlies Remote Memory Enhancement. *Front Neural Circuits* **15**, (2021).

7. Gerasimov, E. *et al.* Optogenetic Activation of Astrocytes—Effects on Neuronal Network Function. *International Journal of Molecular Sciences 2021, Vol. 22, Page 9613* **22**, 9613 (2021).

8. Barish, P. A. *et al.* Design and functional evaluation of an optically active μ-opioid receptor. *Eur J Pharmacol* **705**, 42–48 (2013).

9. Siuda, E. R. *et al.* Spatiotemporal Control of Opioid Signaling and Behavior. *Neuron* **86**, 923–935 (2015).

10. Castro, D. C. *et al.* An endogenous opioid circuit determines state-dependent reward consumption. *Nature 2021 598:7882* **598**, 646–651 (2021).

11. Gunaydin, L. A. *et al.* Natural Neural Projection Dynamics Underlying Social Behavior. *Cell* **157**, 1535–1551 (2014).

12. Xu, Y. *et al.* Optogenetic control of chemokine receptor signal and T-cell migration. *Proc Natl Acad Sci U S A* **111**, 6371–6376 (2014).

13. Li, P. *et al.* Optogenetic activation of intracellular adenosine A2A receptor signaling in the hippocampus is sufficient to trigger CREB phosphorylation and impair memory. *Mol Psychiatry* **20**, 1481 (2015).

14. Li, Y. *et al.* Optogenetic Activation of Adenosine A2A Receptor Signaling in the Dorsomedial Striatopallidal Neurons Suppresses Goal-Directed Behavior. *Neuropsychopharmacology* **41**, 1003–1013 (2016).

15. van Wyk, M., Pielecka-Fortuna, J., Löwel, S. & Kleinlogel, S. Restoring the ON Switch in Blind Retinas: Opto-mGluR6, a Next-Generation, Cell-Tailored Optogenetic Tool. *PLoS Biol* **13**, 1–30 (2015).

16. Kralik, J., van Wyk, M., Stocker, N. & Kleinlogel, S. Bipolar cell targeted optogenetic gene therapy restores parallel retinal signaling and high-level vision in the degenerated retina. *Communications Biology 2022 5:1* **5**, 1–15 (2022).

17. Čapek, D. *et al.* Light-activated Frizzled7 reveals a permissive role of non-canonical wnt signaling in mesendoderm cell migration. *Elife* **8**, (2019).

3.2 Article II

BiPOLES is an optogenetic tool developed for bidirectional dual-color control of neurons

Johannes Vierock [1,8], Silvia Rodriguez-Rozada [2,8], Alexander Dieter[2], Florian Pieper [3], Ruth Sims[4], Federico Tenedini[5], Amelie C. F. Bergs [6], Imane Bendifallah[4], **Fangmin Zhou** [5], Nadja Zeitzschel[6], Joachim Ahlbeck[3], Sandra Augustin[1], Kathrin Sauter[2,5], Eirini Papagiakoumou [4], Alexander Gottschalk [6], Peter Soba [5,7], Valentina Emiliani [4], Andreas K. Engel[3], Peter Hegemann [1] & J. Simon Wiegert[2]

1 Institute for Biology, Experimental Biophysics, Humboldt University Berlin, Berlin, Germany.
2 Research Group Synaptic Wiring and Information Processing, Center for Molecular Neurobiology Hamburg, University Medical Center Hamburg-Eppendorf, Hamburg, Germany.
3 Department of Neurophysiology and Pathophysiology, University Medical Center Hamburg-Eppendorf, Hamburg, Germany.
4 Wavefront-Engineering Microscopy Group, Photonics Department, Institut de la Vision, Sorbonne Université, INSERM, CNRS, Institut de la Vision, Paris, France.
5 Research Group Neuronal Patterning and Connectivity, Center for Molecular Neurobiology Hamburg, University Medical Center Hamburg-Eppendorf, Hamburg, Germany.
6 Buchmann Institute for Molecular Life Sciences and Institute of Biophysical Chemistry, Goethe University, Frankfurt, Germany.
7 LIMES Institute, University of Bonn, Bonn, Germany.
8These authors contributed equally:

Nature Communications volume 12, Article number: 4527 (2021), doi.org/10.1038/s41467-021-24759-5

Personal contribution

My contribution to this publication was the following: I performed the experiments showing BiPOLES-mediated bidirectional control of body contraction and relaxation in *Drosophila* larvae. Besides, I was involved in the analysis and methodology of the locomotion assay. These data are shown in Figure 6c, 6d. In addition, I wrote the related methods part and added comments to the manuscript during the revision process.

64
nature COMMUNICATIONS

ARTICLE

https://doi.org/10.1038/s41467-021-24759-5 OPEN

BiPOLES is an optogenetic tool developed for bidirectional dual-color control of neurons

Johannes Vierock[1,8], Silvia Rodriguez-Rozada[2,8], Alexander Dieter[2], Florian Pieper[3], Ruth Sims[4], Federico Tenedini[5], Amelie C. F. Bergs[6], Imane Bendifallah[4], Fangmin Zhou[5], Nadja Zeitzschel[6], Joachim Ahlbeck[3], Sandra Augustin[1], Kathrin Sauter[2,5], Eirini Papagiakoumou[4], Alexander Gottschalk[6], Peter Soba[5,7], Valentina Emiliani[4], Andreas K. Engel[3], Peter Hegemann[1] & J. Simon Wiegert[2]✉

Optogenetic manipulation of neuronal activity through excitatory and inhibitory opsins has become an indispensable experimental strategy in neuroscience research. For many applications bidirectional control of neuronal activity allowing both excitation and inhibition of the same neurons in a single experiment is desired. This requires low spectral overlap between the excitatory and inhibitory opsin, matched photocurrent amplitudes and a fixed expression ratio. Moreover, independent activation of two distinct neuronal populations with different optogenetic actuators is still challenging due to blue-light sensitivity of all opsins. Here we report BiPOLES, an optogenetic tool for potent neuronal excitation and inhibition with light of two different wavelengths. BiPOLES enables sensitive, reliable dual-color neuronal spiking and silencing with single- or two-photon excitation, optical tuning of the membrane voltage, and independent optogenetic control of two neuronal populations using a second, blue-light sensitive opsin. The utility of BiPOLES is demonstrated in worms, flies, mice and ferrets.

[1] Institute for Biology, Experimental Biophysics, Humboldt University Berlin, Berlin, Germany. [2] Research Group Synaptic Wiring and Information Processing, Center for Molecular Neurobiology Hamburg, University Medical Center Hamburg-Eppendorf, Hamburg, Germany. [3] Department of Neurophysiology and Pathophysiology, University Medical Center Hamburg-Eppendorf, Hamburg, Germany. [4] Wavefront-Engineering Microscopy Group, Photonics Department, Institut de la Vision, Sorbonne Université, INSERM, CNRS, Institut de la Vision, Paris, France. [5] Research Group Neuronal Patterning and Connectivity, Center for Molecular Neurobiology Hamburg, University Medical Center Hamburg-Eppendorf, Hamburg, Germany. [6] Buchmann Institute for Molecular Life Sciences and Institute of Biophysical Chemistry, Goethe University, Frankfurt, Germany. [7] LIMES Institute, University of Bonn, Bonn, Germany. [8] These authors contributed equally: Johannes Vierock, Silvia Rodriguez-Rozada. ✉email: simon.wiegert@zmnh.uni-hamburg.de

To prove the necessity and sufficiency of a particular neuronal population for a specific behavior, a cognitive task, or a pathological condition, faithful activation, and inhibition of this population of neurons are required. In principle, optogenetic manipulations allow such interventions. However, excitation and inhibition of the neuronal population of interest are commonly done in separate experiments, where either an excitatory or inhibitory microbial opsin is expressed. Alternatively, if both opsins are co-expressed in the same cells, it is essential to achieve efficient membrane trafficking of both opsins, equal subcellular distributions, and a tightly controlled ratio between excitatory and inhibitory action at the specific wavelengths and membrane potentials, so that neuronal activation and silencing can be controlled precisely and predictably in all transduced cells. Precise co-localization of the two opsins is important when local, subcellular stimulation is required, or when control of individual neurons is intended, for example with two-photon holographic illumination[1]. Meeting these criteria is particularly challenging in vivo, where the optogenetic actuators are either expressed in transgenic lines or from viral vectors that are exogenously transduced. Ideally, both opsins are expressed from the same gene locus or delivered to the target neurons by a single viral vector. Moreover, for expression with fixed stoichiometry, the opsins should be encoded in a single open reading frame (ORF).

Previously, two strategies for stoichiometric expression of an inhibitory and an excitatory opsin from a single ORF were reported using either a gene fusion approach[2] or a 2A ribosomal skip sequence[3,4]. In both cases, a blue-light sensitive cation-conducting channel for excitation was combined with a red-shifted rhodopsin pump for inhibition. The gene fusion approach was used to systematically combine the inhibitory ion pumps halorhodopsin (NpHR), bacteriorhodopsin (BR), or archaerhodopsin (Arch) with a number of channelrhodopsin-2 (ChR2) mutants to generate single tandem-proteins[2]. While this strategy ensured co-localized expression of the inhibitory and excitatory opsins at a one-to-one ratio and provided important mechanistic insights into their relative ion-transport rates, membrane trafficking was not as efficient as with individually expressed opsins, thus limiting the potency of these fusion constructs for reliable control of neuronal activity.

The second strategy employed a 2A ribosomal skip sequence[3] to express the enhanced opsins ChR2(H134R)[5] and eNpHR3.0 as independent proteins at a fixed ratio from the same mRNA[4]. These bicistronic constructs, termed eNPAC, and eNPAC2.0[6], were used for bidirectional control of neuronal activity in various brain regions in mice[6–9]. While membrane trafficking of the individual opsins is more efficient compared to the gene fusion strategy, the expression ratio might still vary from cell to cell. Moreover, subcellular targeted co-localization (e.g., at the soma) is not easily achieved. Finally, functionality is limited in some model organisms such as *D. melanogaster*, since rhodopsin pumps are not efficient in these animals[10,11].

In addition to activation and inhibition of the same neurons, also independent optogenetic activation of two distinct neuronal populations is still challenging. Although two spectrally distinct opsins have been combined previously to spike two distinct sets of neurons[12–15], careful calibration and dosing of blue light were required to avoid activation of the red-shifted opsin. This typically leaves only a narrow spectral and energetic window to activate the blue-light but not the red-light-sensitive rhodopsin. Thus, dual-color control of neurons is particularly challenging in the mammalian brain where irradiance decreases by orders of magnitude over a few millimeters in a wavelength-dependent manner[16,17].

In order to overcome current limitations for bidirectional neuronal manipulations and to facilitate spiking of neuronal populations with orange-red light exclusively, in this work we systematically explore the generation of two-channel fusion proteins that combine red-light activated cation-channels and blue-light activated anion-channels enabling neuronal spiking and inhibition with red and blue light, respectively. With respect to previous bidirectional tools, inversion of the excitatory and inhibitory action spectra restricts depolarization to a narrow, orange-red spectral window since the inhibitory opsin compensates the blue-light-activated currents of the excitatory red-shifted channel. We show that among all tested variants, a combination of *Gt*ACR2[18] and Chrimson[12] termed BiPOLES (for Bidirectional Pair of Opsins for Light-induced Excitation and Silencing) proves most promising and allows (1) potent and reliable blue-light-mediated silencing and red-light-mediated spiking of pyramidal neurons in hippocampal slices; (2) bidirectional control of single neurons with single-photon illumination and two-photon holographic stimulation; (3) dual-color control of two distinct neuronal populations in combination with a second blue-light-sensitive ChR without cross-talk at light intensities spanning multiple orders of magnitude; (4) precise optical tuning of the membrane voltage between the chloride and cation reversal potentials; (5) bidirectional manipulations of neuronal activity in a wide range of invertebrate and vertebrate model organisms including worms, fruit flies, mice, and ferrets.

Results

Engineering of BiPOLES and biophysical characterization in HEK cells. To identify suitable combinations of opsins for potent membrane voltage shunting or depolarization with blue and red light, respectively, we combined the blue-light or green-light sensitive anion-conducting channelrhodopsins (ACRs) Aurora[11], iC++[19], *Gt*ACR1, and *Gt*ACR2[18] with the red-light sensitive cation-conducting channelrhodopsin (CCR) Chrimson[12]; or conversely, the blue-light sensitive *Gt*ACR2 with the red-light sensitive CCRs bReaChES[20], f-Chrimson, vf-Chrimson[21], and ChRmine[22] (Fig. 1a). We fused these opsin-pairs with different linkers, expanding previous rhodopsin fusion strategies[2,23] to obtain optimal expression and membrane targeting. The linkers were composed of the Kir2.1 membrane trafficking signal (TS)[4], different arrangements of a cyan or yellow fluorescent protein, and the transmembrane β helix of the rat gastric H^+/K^+ ATPase (βHK) to maintain the correct membrane topology of both opsins[2] (Fig. 1a).

For a detailed biophysical evaluation, we expressed all ACR-CCR tandems in human embryonic kidney (HEK) cells and recorded blue-light and red-light evoked photocurrents in the presence of a chloride gradient. In all constructs, except the one lacking the βHK-subunit (L3, Fig. 1a), blue-light-activated currents were shifted towards the chloride Nernst potential whereas red-light-activated currents were shifted towards the Nernst potential for protons and sodium (Fig. 1b–d, Supplementary Fig. 1), indicating functional membrane insertion of both channels constituting the tandem constructs. Reversal potentials (Fig. 1d) and photocurrent densities (Fig. 1e) varied strongly for the different tandem variants indicating considerable differences in their wavelength-specific anion/cation conductance ratio and their membrane expression. Photocurrent densities were not only dependent on the identity of the fused channels, but also on the sequence of both opsins in the fusion construct, as well as the employed fusion linker. In contrast to a previous study[2], the optimized linker used in this study did not require a fluorescent protein to preserve the functionality of both channels (L4, Fig. 1a, d, e). Direct comparison of red-light and blue-light evoked photocurrent densities with those of ßHK-Chrimson and *Gt*ACR2 expressed alone indicated that most tandem constructs

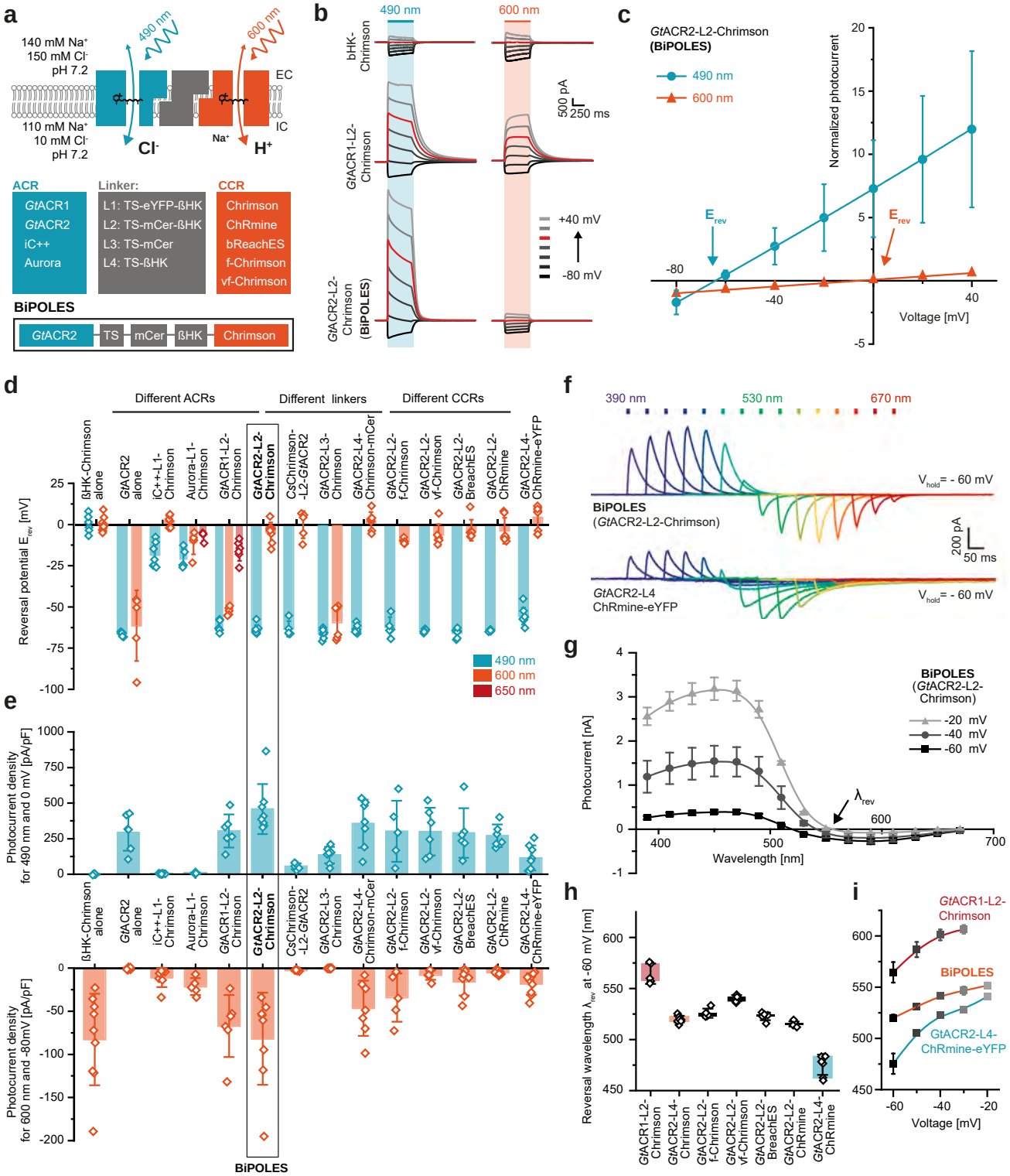

harboring a *Gt*ACR reached similar membrane expression efficacy as the individually expressed channels (Fig. 1e).

At membrane potentials between the Nernst potentials for chloride and protons, blue and red light induced outward and inward currents, respectively, in all *Gt*ACR-fusion constructs. (Fig. 1e–g, Supplementary Fig. 1). The specific wavelength of photocurrent inversion (λ_{rev}) was dependent on the absorption spectra and relative conductance of the employed channels, as well as on the relative ionic driving forces defined by the membrane voltage and the respective ion gradients (Fig. 1g–i). The red-shift of λ_{rev} for the vf-Chrimson tandem compared to BiPOLES reflects the reduced conductance of this Chrimson mutant (Fig. 1h, Supplementary Fig. 1c), as already previously shown[21,24], whereas the blue-shift of λ_{rev} for the ChRmine tandem with L4 (Fig. 1f, h) is explained by the blue-shifted activation spectrum of ChRmine compared to Chrimson[25] and its

Fig. 1 Development of BiPOLES and biophysical characterization. a Molecular scheme of BiPOLES with the extracellular (EC) and intracellular (IC) ionic conditions used for HEK293-cell recordings. The blue-green-light-activated natural anion channels *Gt*ACR1 and *Gt*ACR2 or the engineered ChR-chimeras iC++ and Aurora were fused to the red-light-activated cation channels Chrimson, ChRmine, bReaChES, f-Chrimson, or vf-Chrimson by different linker regions consisting of a trafficking signal (ts), a yellow or cyan fluorescent protein (eYFP, mCerulean3) and the βHK transmembrane fragment. The fusion construct termed BiPOLES is indicated by a black frame. **b** Representative photocurrents of βHK-Chrimson-mCerulean (top), *Gt*ACR1-ts-mCerulean-βHK-Chrimson (middle) *Gt*ACR2-ts-mCerulean-βHK-Chrimson (BiPOLES, bottom) in whole-cell patch-clamp recordings from HEK293 cells at 490 nm and 600 nm illumination. **c** Normalized peak photocurrents of BiPOLES at different membrane voltages evoked at either 490 or 600 nm (see panel **b**, mean ± SD; $n = 8$ independent cells; normalized to the peak photocurrent at −80 mV and 600 nm illumination). **d** Reversal potential of peak photocurrents during 500-ms illumination with 490, 600, or 650 nm light as shown in **b** (mean ± SD). **e** Peak photocurrent densities for 490 nm and 600 nm excitation at 0 mV (close to the reversal potential of protons and cations) and −80 mV (close to the reversal potential for chloride) measured as shown in **b** (mean ± SD; for both **d** and **e** $n = 5$ biological independent cells for Aurora-L1-Chrimson, *Cs*Chrimson-L2-*Gt*ACR2 and *Gt*ACR2-L2-f-Chrimson; $n = 6$ for *Gt*ACR2, *Gt*ACR1-L2-Chrimson and *Gt*ACR2-L2-vf-Chrimson; $n = 7$ for iC++-L1-Chrimson, *Gt*ACR2-L3-Chrimson, *Gt*ACR2-L4-Chrimson-mCer, *Gt*ACR2-L2-BreachES, and *Gt*ACR2-L2-ChRmine; $n = 8$ for *Gt*ACR2-L2-Chrimson and $n = 9$ for ßHK-Chrimson and *Gt*ACR2-L4-ChRmine-ts-eYFP-er). **f** Representative photocurrents of BiPOLES (top) and *Gt*ACR2-L4-ChRmine-ts-eYFP-er (bottom) with 10 ms light pulses at indicated wavelengths and equal photon flux at −60 mV. **g** Action spectra of BiPOLES at different membrane voltages (λ_{rev} = photocurrent reversal wavelength, mean ± SEM, $n = 9$ independent cells for −60 mV, $n = 4$ for −40 mV and $n = 2$ for −20 mV). **h** Photocurrent reversal wavelength λ_{rev} at −60 mV (mean ± SD, $n = 5$ independent cells for *Gt*ACR1-L2-Chrimson and *Gt*ACR2-L2-f-Chrimson, $n = 6$ for *Gt*ACR2-L2-vf-Chrimson and *Gt*ACR2-L2-ChRmine, $n = 7$ for *Gt*ACR2-L4-ChRmine-ts-eYFP-er, $n = 8$ for *Gt*ACR2-L2-BreachES and $n = 9$ for *Gt*ACR2-L2-Chrimson). **i** λ_{rev} of *Gt*ACR1-L2-Chrimson, BiPOLES, and *Gt*ACR2-L4-ChRmine-TS-eYFP-ER at different membrane voltages (mean ± SD; $n = 5$ biological independent cells for *Gt*ACR1-L2-Chrimson, $n = 7$ for *Gt*ACR2-L4-ChRmine-ts-eYFP-er and $n = 9$ for *Gt*ACR2-L2-Chrimson).

presumably large single-channel conductance. Switching the L4 linker to L2 shifted λ_{rev} to longer wavelengths for the ChRmine fusion constructs at the expense of ChRmine photocurrents (Fig. 1e, h), pointing to a stronger impact of the protein linker on the ChRmine photocurrent compared to other red-shifted CCRs (Fig. 1e).

Among all tested combinations, *Gt*ACR2-L2-Chrimson—from here on termed BiPOLES—was the most promising variant. First, it showed the largest photocurrent densities of all tested fusion constructs (Fig. 1e,f), second, reversal potentials for blue or red light excitation were close to those of individually expressed channels (−64 ± 3 mV and −5 ± 6 mV for BiPOLES compared to −66 ± 2 mV and 0 ± 5 mV of *Gt*ACR2 and βHK-Chrimson expressed alone, Fig. 1c, d, Supplementary Fig. 1b) and third, peak activity of the inhibitory anion and excitatory cation current had the largest spectral separation among all tested variants (150 ± 5 nm, Fig. 1f, g). Thus, BiPOLES enables selective activation of large anion and cation currents with spectrally well-separated wavelengths (Fig. 1e). BiPOLES was remarkably better expressed in HEK-cells than the previously reported ChR2-L1-NpHR fusion construct[2] and featured larger photocurrents at −60 mV than the bicistronic construct eNPAC2.0[6] (Supplementary Fig. 2a–c). Moreover, employing an anion channel with high conductance instead of a chloride pump, which transports one charge per absorbed photon and is weak at a negative voltage, yielded chloride currents in BiPOLES expressing cells at irradiances 2 orders of magnitude lower than with eNPAC2.0 (Supplementary Fig. 2d–f). Anion conductance in BiPOLES was sufficiently large to compensate inward currents of Chrimson even at high irradiance, driving the cell back to the chloride Nernst potential, which is close to the resting membrane voltage (Supplementary Fig. 2d–f). We further verified the implementation of an anion-conducting channel by testing whether sufficient blue-light hyperpolarization could be achieved with a rhodopsin pump[26] instead of a channel. Replacing *Gt*ACR2 with a blue-light sensitive proton pump led to barely detectable outward currents at the same irradiance due to low ion turnover of the ion pump under the given voltage and ion conditions (Supplementary Fig. 2d, g).

Evaluation of BiPOLES in CA1 pyramidal neurons. Next, we validated BiPOLES as an optogenetic tool for bidirectional control of neuronal activity. In CA1 pyramidal neurons of rat hippocampal slice cultures, illumination triggered photocurrents with biophysical properties similar to those observed in HEK cells (Fig. 2a, b, Supplementary Fig. 3a–c). We observed membrane-localized BiPOLES expression most strongly in the somatodendritic compartment (Fig. 2c, Supplementary Fig. 3d). However, some fraction of the protein accumulated inside the cell in the periphery of the cell nucleus, indicating sub-optimal membrane trafficking of BiPOLES. To enhance membrane trafficking, we generated a soma-targeted variant (somBiPOLES) by attaching a C-terminal Kv2.1-trafficking sequence[27]. Soma targeting has the additional benefit of avoiding the expression of the construct in axon terminals, where the functionality of BiPOLES might be limited due to an excitatory chloride reversal potential and subsequent depolarizing action of *Gt*ACR2[28,29]. somBiPOLES showed strongly improved membrane localization restricted to the cell soma and proximal dendrites with no detectable intracellular accumulations (Fig. 2c, Supplementary Fig. 3d). Compared to BiPOLES, blue-light and red-light mediated photocurrents were enhanced and now similar in magnitude to those in neurons expressing either Chrimson or soma-targeted *Gt*ACR2 (som*Gt*ACR2), alone (Fig. 2d, Supplementary Fig. 4a, 5a, b). Passive and active membrane parameters of BiPOLES-expressing and somBiPOLES-expressing neurons were similar to non-transduced, wild-type neurons (Supplementary Fig. 6), indicative of good tolerability in neurons.

To verify the confinement of somBiPOLES to the somatodendritic compartment despite the improved expression, we virally transduced area CA3 in hippocampal slice cultures with somBiPOLES and recorded optically evoked EPSCs in postsynaptic CA1 cells. Local illumination with red light in CA3 triggered large excitatory postsynaptic currents (EPSCs), while local red illumination of axon terminals in CA1 (635 nm, 2 pulses of 5 ms, 40 ms ISI, 50 mW mm^{-2}), did not trigger synaptic release, indicating the absence of somBiPOLES from axonal terminals (Supplementary Fig. 3e,f). Thus, despite enhanced membrane trafficking, somBiPOLES remained confined to the somatodendritic compartment.

Having shown that somBiPOLES is efficiently expressed in CA1 pyramidal cells, we next systematically benchmarked light-evoked spiking and inhibition parameters for somBiPOLES by direct comparison to Chrimson or som*Gt*ACR2 expressed in

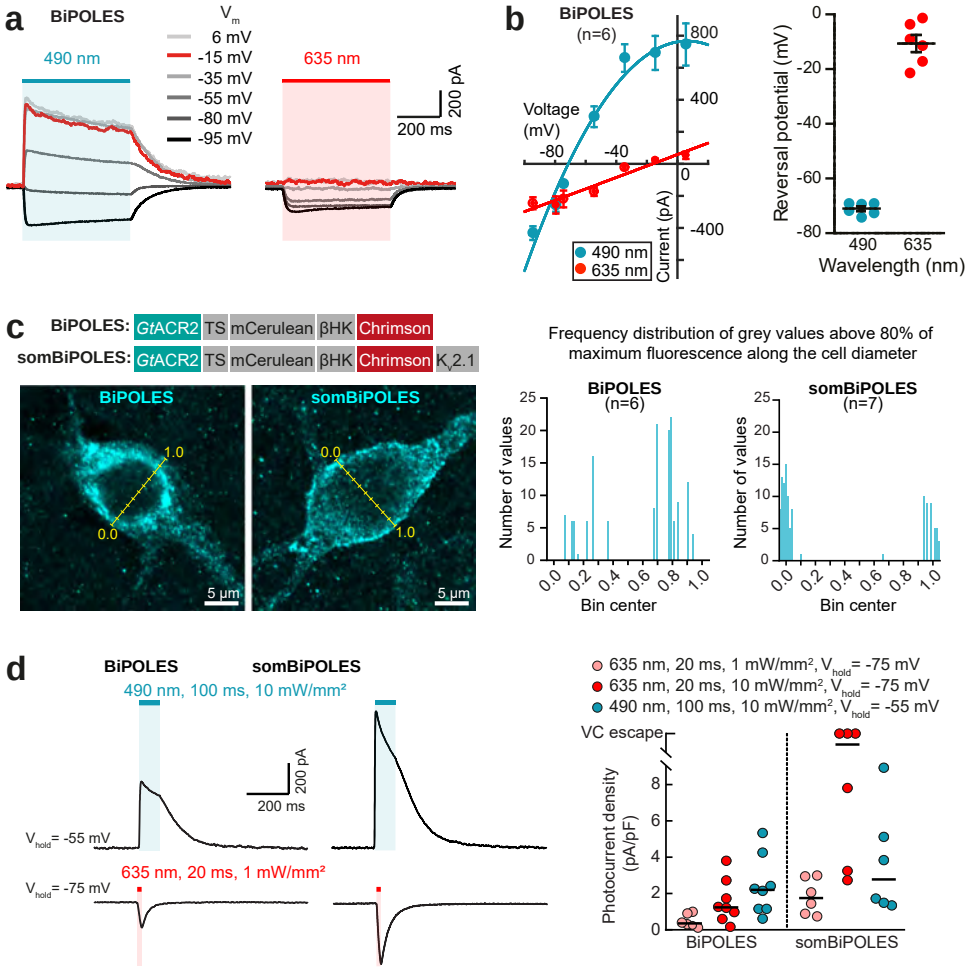

Fig. 2 Expression and functional characterization of BiPOLES and somBiPOLES in hippocampal neurons. a Representative photocurrent traces of BiPOLES in CA1 pyramidal neurons at indicated membrane voltages (V_m: from −95 to +6 mV) upon illumination with 490 or 635 nm (500 ms, 10 mW mm^{-2}). **b** Left: quantification of photocurrent-voltage relationship (symbols: mean ± SEM, $n = 6$ cells, lines: polynomial regression fitting, $R^2 = 0.98$ and 0.94, for 490 and 635 nm, respectively). Right: reversal potential under 490 or 635 nm illumination (black lines: mean ± SEM, $n = 6$ cells). **c** Left: Molecular scheme of BiPOLES and somBiPOLES as used in neurons. Representative maximum-intensity projection images of immunostainings showing expression of BiPOLES or soma-targeted BiPOLES (somBiPOLES) in CA3 pyramidal neurons of organotypic hippocampal slices. Yellow lines indicate the bins used to measure fluorescence intensity along the cell equator. Right: Frequency distribution of gray values above 80% of the maximum fluorescence intensity measured along the cell diameter in BiPOLES-expressing ($n = 6$ cells) and somBiPOLES-expressing CA3 cells ($n = 7$ cells). Note improved trafficking of somBiPOLES to the cell membrane, shown by the preferential distribution of brighter pixels around bins 0.0 and 1.0. **d** Left: Representative photocurrent traces measured in BiPOLES-expressing or somBiPOLES-expressing CA1 pyramidal neurons. Inward cationic photocurrents evoked by a 635 nm light pulse (20 ms, 1 mW mm^{-2}) were recorded at a membrane voltage of −75 mV, and outward anionic photocurrents evoked by a 490 nm light pulse (100 ms, 10 mW mm^{-2}) were recorded at a membrane voltage of −55 mV. Right: Quantification of photocurrent densities evoked under the indicated conditions. Note that photocurrent densities were strongly enhanced for somBiPOLES compared to BiPOLES (black horizontal lines: medians, $n_{BiPOLES} = 8$ cells, $n_{somBiPOLES} = 6$ cells.

hippocampal CA1 pyramidal neurons, respectively (Fig. 3, Supplementary Figs. 4, 5). To compare spiking performance in somBiPOLES or Chrimson expressing CA1 pyramidal cells, we delivered trains of 5-ms blue (470 nm), orange (595 nm), or red (635 nm) light pulses at irradiances ranging from 0.1 to 100 mW mm^{-2}. Action potential (AP) probability in somBiPOLES neurons reached 100% at 0.5 mW mm^{-2} with 595 nm and 10 mW mm^{-2} with 635 nm light, similar to neurons expressing Chrimson alone (Fig. 3b,c). In pyramidal cells, action potentials (APs) could be reliably driven up to 10-20 Hz with somBiPOLES (Supplementary Fig. 7c) similar to Chrimson alone, as shown previously[12]. Delivering the same number of photons in a time range of 1–25 ms did not alter the AP probability, but longer pulses increased sub-threshold depolarization (Supplementary Fig. 7d).

In contrast to orange or red light, blue light did not evoke APs at any irradiance in somBiPOLES neurons due to the activity of the blue-light sensitive anion channel. On the contrary, neurons expressing Chrimson alone reached 100% AP firing probability at 10 mW mm^{-2} with 470 nm (Fig. 3b, c). Using light ramps with gradually increasing irradiance enabled us to precisely determine the AP threshold and to quantitatively compare the spiking efficacy of different excitatory opsins. The irradiance threshold for the first AP was similar for somBiPOLES and Chrimson at 595 nm (0.74 ± 0.06 mW mm^{-2} for somBiPOLES and 0.68 ± 0.05 mW mm^{-2} for Chrimson) reflecting that the functional expression levels were similar. In contrast, blue light triggered APs at 0.95 ± 0.09 mW mm^{-2} in Chrimson expressing cells, but never in somBiPOLES or BiPOLES neurons (Fig. 3d, e, Supplementary Fig. 7a, b). Thus, somBiPOLES enables neuronal excitation

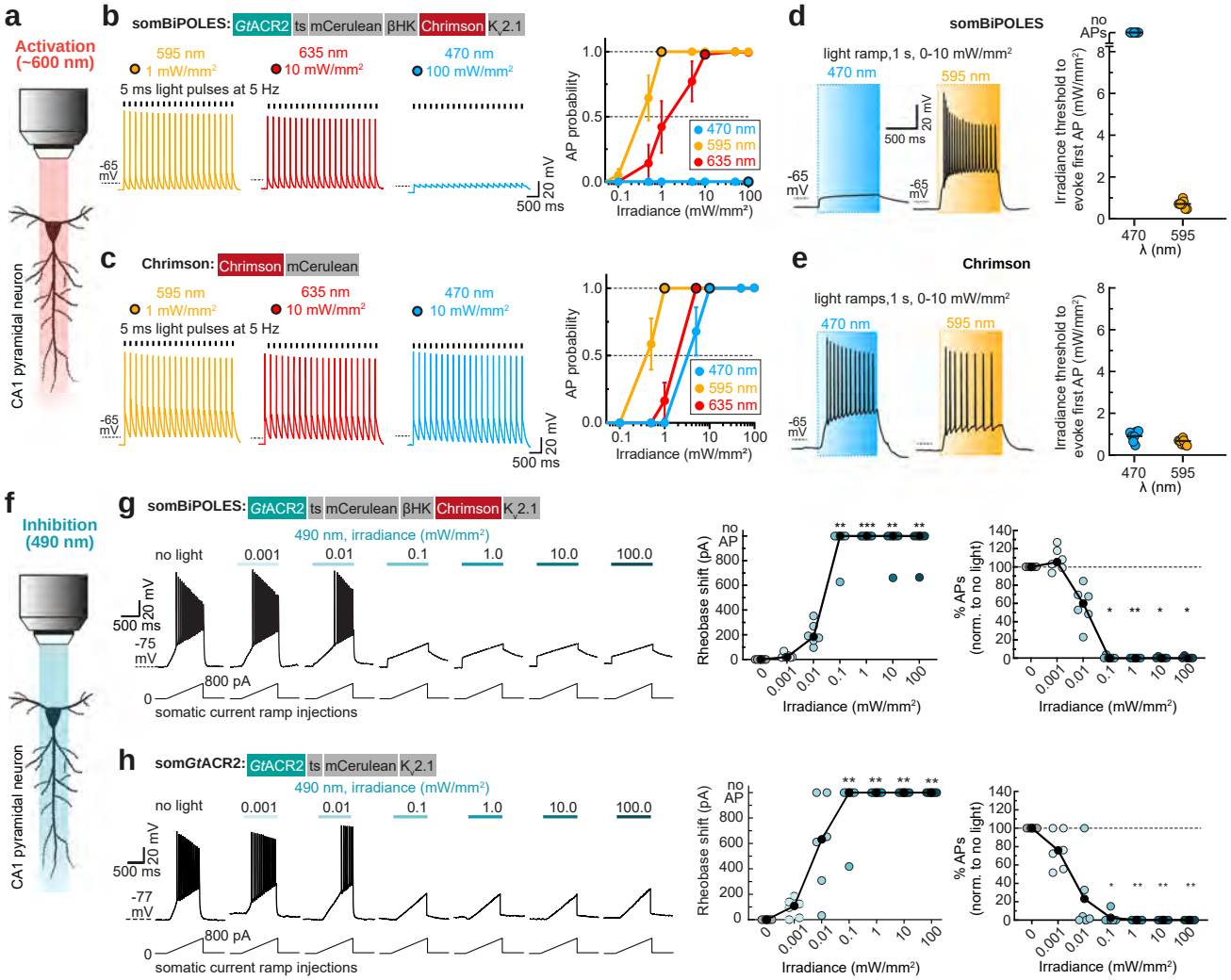

Fig. 3 somBiPOLES allows potent dual-color spiking and silencing of the same neurons using red and blue light, respectively. a Quantification of neuronal excitation with somBiPOLES or Chrimson only**. b** Optical excitation is restricted exclusively to the orange/red spectrum in somBiPOLES-expressing neurons. Left: Example traces of current-clamp (IC) recordings in somBiPOLES-expressing CA1 pyramidal cells to determine light-evoked action potential (AP)-probability at different wavelengths. Right: quantification of light-mediated AP probability at indicated wavelengths and irradiances (symbols correspond to mean ± SEM, $n = 8$ cells). Black outlined circles correspond to irradiance values shown in example traces on the left. **c** Same experiment as shown in **b**, except that CA1 neurons express Chrimson only (symbols correspond to mean ± SEM, $n = 7$ cells) Note blue-light excitation of Chrimson, but not somBiPOLES cells. **d** Light-ramp stimulation to determine the AP threshold irradiance. Left: Representative membrane voltage traces measured in somBiPOLES-expressing CA1 pyramidal neurons. The light was ramped linearly from 0 to 10 mW mm^{-2} over 1 s. Right: Quantification of the irradiance threshold at which the first AP was evoked (black horizontal lines: medians, $n = 7$ cells). **e** Same experiment as shown in (**b**), except that CA1 neurons express Chrimson only (black horizontal lines: medians, $n = 7$ cells). The threshold for action potential firing with 595 nm was similar between somBiPOLES-expressing and Chrimson-expressing neurons, while somBiPOLES cells were not sensitive to blue light. **f** Quantification of neuronal silencing with somBiPOLES or som*Gt*ACR2 only. **g** somBiPOLES mediates neuronal silencing upon illumination with blue light. Left: Current ramps (from 0–100 to 0–900 pA) were injected into somBiPOLES-expressing CA1 pyramidal cells to induce APs during illumination with blue light at indicated intensities (from 0.001 to 100 mW mm^{-2}). The injected current at the time of the first action potential was defined as the rheobase. Right: Quantification of the rheobase shift and the relative change in the number of ramp-evoked action potentials. Illumination with 490 nm light of increasing intensities activated somBiPOLES-mediated Cl^- currents shifting the rheobase to higher values and shunting action potentials. **h** Same experiment is shown in **g**, except that CA1 neurons express som*Gt*ACR2 only. Note similar silencing performance of somBiPOLES and *Gt*ACR2. In **h**, **g** black circles correspond to medians, $n_{somBiPOLES} = 6$ cells, $n_{somGtACR2} = 6$ cells, one-way Friedman test, $^*p < 0.05$, $^{**}p < 0.01$, $^{***}p < 0.001$.

exclusively within a narrow spectral window restricted to orange-red light, avoiding inadvertent blue-light mediated spiking.

Next, we quantified the silencing capacity of somBiPOLES and compared it to som*Gt*ACR2 alone—the most potent opsin for blue-light mediated somatic silencing[28,29]—by measuring the capacity to shift the threshold for electrically evoked APs (i.e., rheobase, see "Methods" section). Both variants similarly shifted the rheobase towards larger currents starting at an irradiance of 0.1 mW mm^{-2} with 490 nm light, leading to a complete block of APs in most cases (Fig. 3g, h). Neuronal silencing was efficient under 490 nm-illumination, even at high irradiances (up to 100 mW mm^{-2}, Fig. 3g), showing that blue light cross-activation of Chrimson in somBiPOLES did not compromise neuronal shunting.

We compared somBiPOLES with eNPAC2.0, the most advanced optogenetic tool currently available for dual-color

excitation and inhibition[4,6,7]. In eNPAC2.0 expressing CA1 pyramidal neurons, depolarizing and hyperpolarizing photocurrents were present under blue and yellow/orange light, respectively (Supplementary Fig. 8a), consistent with its inverted action spectrum compared to BiPOLES (Supplementary Fig. 2). Compared to BiPOLES (Supplementary Fig. 3c) peak photocurrent ratios were more variable between cells (Supplementary Fig. 8a), indicative of different stoichiometries between ChR2(HR) and eNpHR3.0 in different neurons, probably because membrane trafficking and degradation of both opsins occur independently. Moreover, blue-light-evoked spiking with eNPAC2.0 required approx. 10-fold higher irradiance compared to somBiPOLES and did not reach 100% reliability (Supplementary Fig. 8c), which might be explained by cross-activation of eNpHR3.0 under high blue irradiance (see also Supplementary Fig. 2d). Blue-light-triggered APs could not be reliably blocked with concomitant yellow illumination at 10 mW mm^{-2} (Supplementary Fig. 8b). Further on, activation of eNPAC2.0 (i.e., eNpHR3.0) with yellow light (580 nm) caused strong membrane hyperpolarization followed by rebound spikes in some cases (Supplementary Fig. 8d). Finally, and consistent with photocurrent measurements in HEK cells (Supplementary Fig. 2e, f), silencing of electrically evoked APs required 100-fold higher irradiance with eNPAC2.0, compared to somBiPOLES, until a significant rheobase-shift was observed (Supplementary Fig. 8e).

In summary, somBiPOLES is suitable for potent, reliable neuronal activation exclusively with orange-red light and silencing with blue light. somBiPOLES displays similar potency for neuronal excitation and inhibition as Chrimson and som*Gt*ACR2 alone.

BiPOLES allows various neuronal manipulations with visible light. We evaluated BiPOLES and somBiPOLES in the context of three distinct neuronal applications: bidirectional control of neuronal activity, optical tuning of the membrane voltage, and independent spiking of two distinct neuronal populations.

We first tested the suitability of BiPOLES and somBiPOLES for all-optical excitation and inhibition of the same neurons (Fig. 4a). Red light pulses (635 nm, 20 ms, 10 mW mm^{-2}) reliably triggered APs in somBiPOLES expressing neurons (Fig. 4b), while APs were triggered only in approx. 50% of BiPOLES expressing neurons under these stimulation conditions (Supplementary Fig. 7e), due to a higher irradiance threshold to evoke APs in those cells (Supplementary Fig. 7a, b). Concomitant blue illumination (490 nm, 10 mW mm^{-2}) for 100 ms reliably blocked red-light evoked APs in all cases. As expected from an anion conducting channel, blue light alone had only a minor impact on the resting membrane voltage, due to the close proximity of the chloride reversal potential to the resting potential of the cell (Fig. 4b, Supplementary Fig. 7e) In contrast, neurons expressing Chrimson alone showed APs both under red and blue illumination (Supplementary Fig. 4b).

Aside from dual-color spiking and inhibition, a major advantage of the fixed 1:1 stoichiometry between an anion and cation channel with different activation spectra in BiPOLES is the ability to precisely tune the ratio between anion-conductance and cation-conductance with light (Fig. 1f,g, Supplementary Fig. 3c). In neurons, this allows to optically tune the membrane voltage between the chloride reversal potential and the action potential threshold (Fig. 4c). Optical membrane voltage tuning was achieved either by a variable ratio of blue and orange light at the absorption peak wavelengths of *Gt*ACR2 and Chrimson (Fig. 4d) or by using a single color with fixed irradiance over a wide spectral range (Fig. 4e). Both approaches yielded reliable and reproducible membrane voltage shifts. Starting from the chloride Nernst potential when only *Gt*ACR2 was activated with blue light at 470 nm, the membrane depolarized steadily with an increasing 595/470 nm ratio, eventually passing the action potential threshold (Fig. 4d). Similarly, tuning a single wavelength between 385 nm and 490 nm clamped the cell near the Nernst potential for chloride, while shifting the wavelength peak further towards red led to gradual depolarization, eventually triggering action potentials at 580 nm (Fig. 4e). Depending on the available light source both methods allow precise control of anion and cation fluxes at a fixed ratio and might be applied for locally defined subthreshold membrane depolarization in single neurons or to control the excitability of networks of defined neuronal populations.

Since BiPOLES permits neuronal spiking exclusively within the orange-red light window, it facilitates two-color excitation of genetically distinct but spatially intermingled neuronal populations using a second, blue-light-activated ChR (Fig. 4f). To demonstrate this, we expressed somBiPOLES in CA1 VIP interneurons and CheRiff, a blue-light-sensitive ChR (λ_{max} = 460 nm)[30] in CA1 pyramidal neurons (Fig. 4g, see "Methods" section for details). Both CA1 and VIP neurons innervate Oriens-Lacunosum-Moleculare (OLM) interneurons. Therefore, exclusive excitation of CA1 pyramidal cells or VIP interneurons is expected to trigger excitatory (EPSCs) and inhibitory (IPSCs) postsynaptic currents, respectively. CheRiff-expressing pyramidal cells were readily spiking upon blue, but not orange-red illumination up to 10 mW mm^{-2} (Fig. 4h, Supplementary Fig. 9). Conversely, as expected, red light evoked APs in somBiPOLES-expressing VIP neurons, while blue light up to 100 mW mm^{-2} did not evoke APs (Fig. 4h). Next, we recorded synaptic inputs from these two populations onto VIP-negative GABAergic neurons in stratum-oriens (Fig. 4i). As expected, blue light triggered EPSCs (CheRiff) and red light triggered IPSCs (somBiPOLES), evident by their respective reversal potentials at 8.8 ± 10.4 mV and −71.4 ± 13.1 mV (Fig. 4i). Thus, somBiPOLES, in combination with the blue-light sensitive CheRiff enabled independent activation of two distinct populations of neurons in the same field of view.

Bidirectional neuronal control using dual-laser two-photon holography. Two-photon holographic excitation enables spatially localized photostimulation of multiple neurons with single-cell resolution in scattering tissue[1]. We evaluated the feasibility of bidirectional control of single neurons by two-photon holographic excitation (Supplementary Fig. 10a) in hippocampal organotypic slices virally transduced with somBiPOLES expressed from a CaMKII promoter. Single-photon excitation confirmed the high potency of somBiPOLES using this expression strategy (Supplementary Fig. 11). The two-photon action spectrum of somBiPOLES was explored by measuring the peak photocurrents (I_p) at a range of holding potentials (−80 to −55 mV) and excitation wavelengths (850 to 1100 nm). Similar to single-photon excitation, blue-shifted wavelengths (λ_{ex} < 980 nm) generated large photocurrents, apparently dominated by the flow of chloride ions (outward chloride currents below the chloride Nernst potential and inward chloride currents above the chloride Nernst potential, Fig. 5a–c, Supplementary Fig. 10b). Red-shifted wavelengths (λ_{ex} > 980 nm) generated photocurrents, which appeared to be dominated by the flow of protons and cations across the membrane (inward currents at physiological neuronal membrane potentials, Fig. 5a–c, Supplementary Fig. 10b). Since 920 nm and 1100 nm illumination generated the largest magnitudes of inhibitory and excitatory photocurrents, respectively, these wavelengths were used to evaluate whether the neuronal activity could be reliably suppressed or evoked in neurons expressing

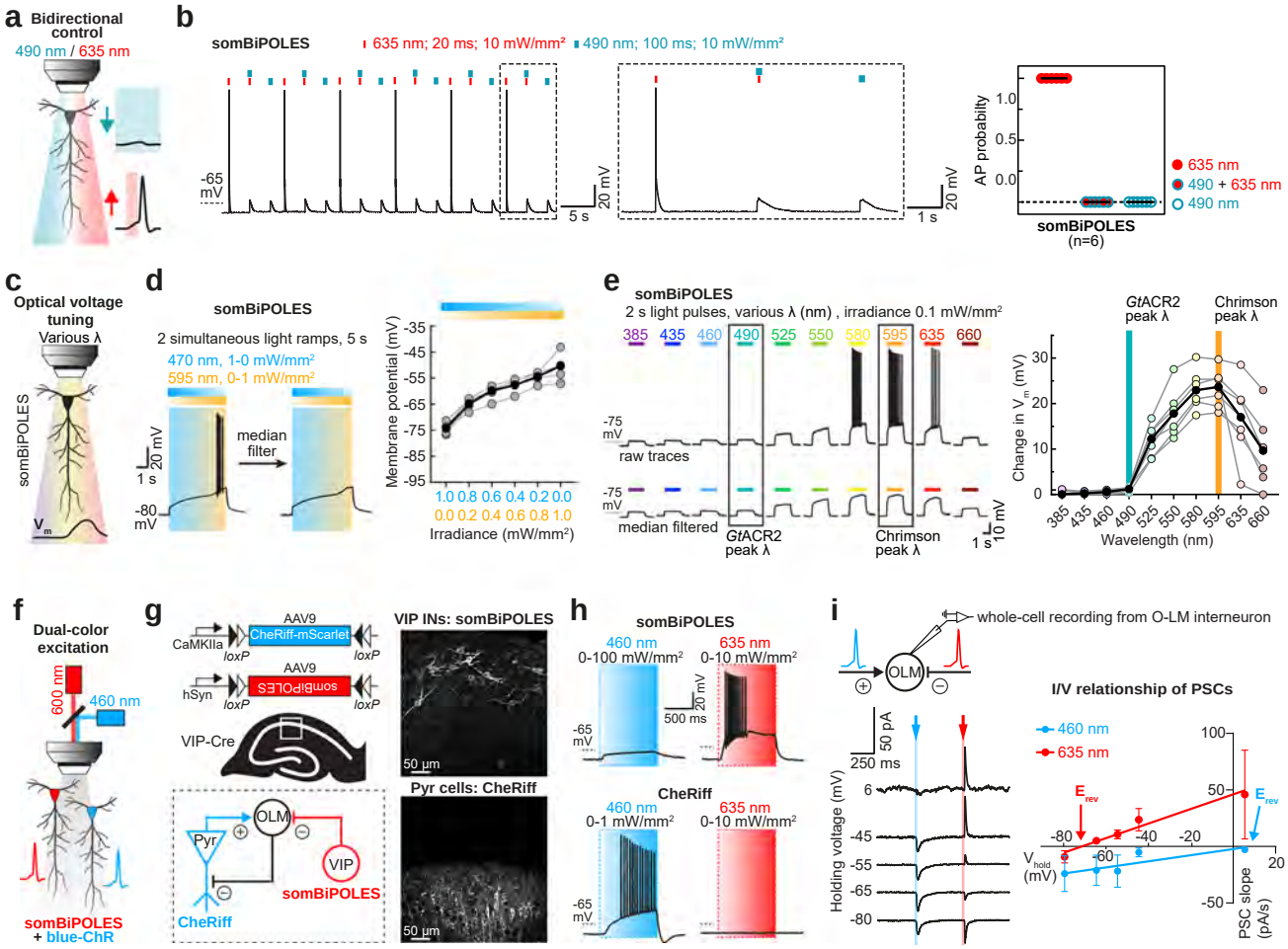

Fig. 4 Applications of BiPOLES: bidirectional control of neuronal activity, optical voltage tuning, and independent dual-color excitation of two distinct neuronal populations. a Schematic drawing illustrating bidirectional control of neurons with blue and red light. **b** Current-clamp characterization of bidirectional optical spiking-control with somBiPOLES. Left: Voltage traces showing red-light-evoked APs, which were blocked by a concomitant blue light pulse. Right: quantification of AP probability under indicated conditions (black horizontal lines: medians, $n = 6$ cells). **c** Schematic drawing illustrating control of membrane voltage with somBiPOLES. **d** Left: Representative membrane voltage traces from a somBiPOLES-expressing CA1 pyramidal cell during simultaneous illumination with 470-nm and 595-nm light ramps of the opposite gradient. Voltage traces were median-filtered to reveal the slow change in membrane voltage during the ramp protocol. Right: Quantification of membrane voltage at different 595/470 nm light ratios (black circles: medians, $n = 5$ cells). **e** Left: Representative membrane voltage traces of somBiPOLES in CA1 pyramidal neurons upon illumination with different wavelengths and equal photon flux. As in **d** voltage traces were median-filtered to eliminate action potentials and reveal the slow changes in membrane voltage during the light protocol. Right: Quantification of membrane potential along the spectrum showing optical voltage tuning at the indicated wavelengths. (black circles: medians, an irradiance of 0.1 mW mm^{-2} was kept constant for all wavelengths, $n = 6$ cells). **f** Schematic drawing illustrating control of 2 neurons expressing either somBiPOLES (red) or a blue-light-sensitive ChR (blue). **g** Left: Cre-On/Cre-Off strategy to achieve mutually exclusive expression of CheRiff-mScarlet in CA1 pyramidal neurons and somBiPOLES in VIP-positive GABAergic neurons. Both cell types innervate OLM interneurons in CA1. Right: Example maximum-intensity projection images of two-photon stacks showing expression of somBiPOLES in VIP-interneurons (top) and CheRiff-mScarlet in the pyramidal layer of CA1 (bottom). **h** IC-recordings demonstrating mutually exclusive spiking of somBiPOLES-expressing and CheRiff-expressing neurons under red or blue illumination. **i** Postsynaptic whole-cell voltage-clamp recordings from an OLM cell at indicated membrane voltages showing EPSCs and IPSCs upon blue-light and red-light pulses, respectively. Right: quantification of blue-light and red-light-evoked PSCs and their reversal potential. Symbols show mean ± SEM, $n_{460\ nm} = 8$ cells, $n_{635\ nm} = 7$ cells, lines: linear regression fit, $R^2 = 0.06$ and 0.20 for a blue and red light, respectively.

somBiPOLES. Action potentials could be reliably evoked using short (5 ms) exposure to 1100 nm light (power density: 0.44 mW/µm²), with latency (19.9 ± 6.3 ms) and jitter (2.5 ± 1.5 ms) (Fig. 5d, Supplementary Fig. 10c) comparable to literature values for Chrimson[31]. 5 ms pulses were also able to induce high-fidelity trains of APs with frequencies up to 20 Hz (Supplementary Fig. 10d). It is likely that shorter latency and jitter (and consequently higher rates of trains of APs) could be achieved by replacing the stimulation laser with one with optimized pulse parameters, in particular, higher peak energy[32]. 920 nm excitation effectively inhibited neural activity, increasing the rheobase of AP firing at power densities above 0.1 mW µm^{-2} (Fig. 5e). It further enabled temporally precise elimination of single electrically evoked APs (Supplementary Fig. 10e) and silencing of neuronal activity over sustained (200 ms) periods (Fig. 5f). Finally, we demonstrate two-photon, bidirectional control of neurons by coincident illumination of appropriately titrated 920 nm and 1100 nm light (Fig. 5g). Thus, somBiPOLES is suitable for dual-color

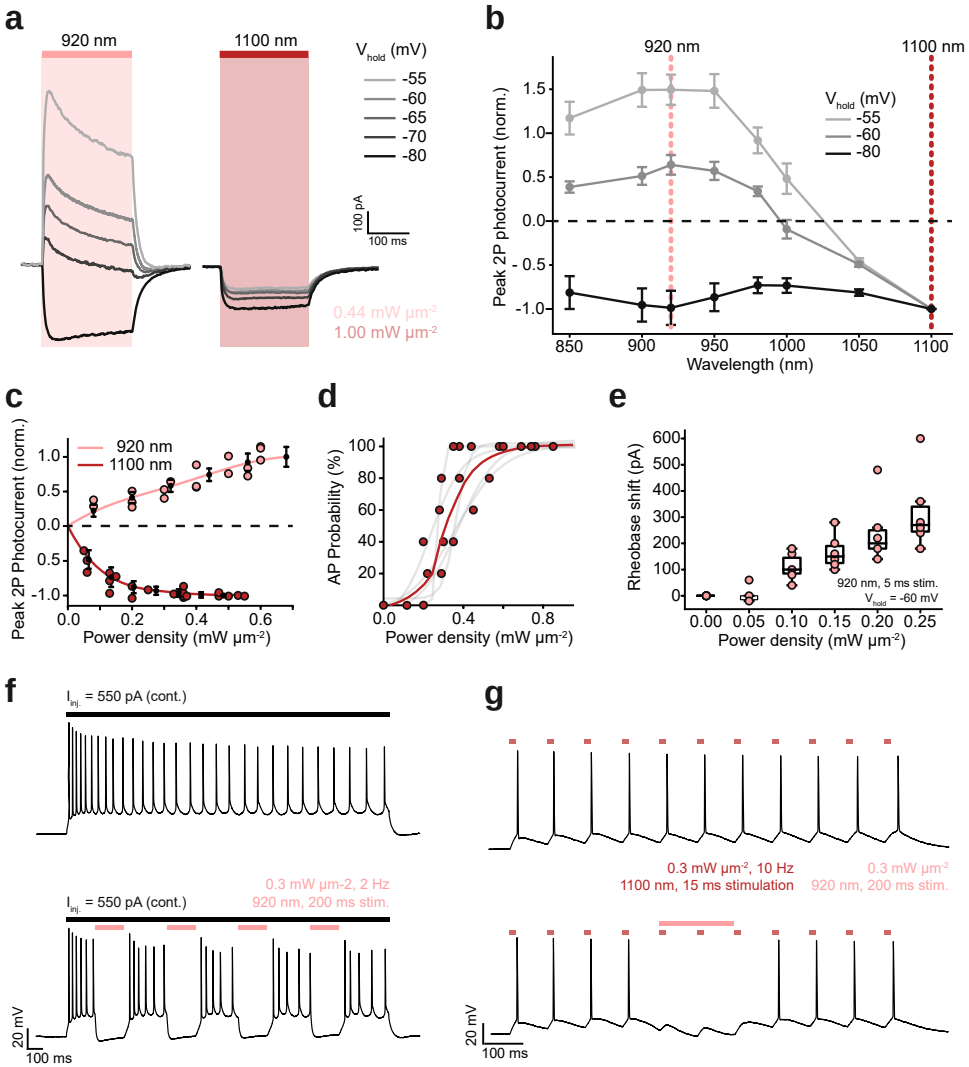

Fig. 5 Bidirectional control of neuronal activity with somBiPOLES using dual-color two-photon holography. a–c Voltage clamp (VC) characterization of somBiPOLES in CA1 pyramidal cells. **a** Representative photocurrent traces at different holding potentials, obtained by continuous 200 ms illumination of 920 and 1100 nm at constant average power density (0.44 and 1.00 mW μm^{-2}). **b** Peak photocurrent as a function of wavelength at different holding potentials (mean ± SEM, $n = 5$). Data acquired with a constant photon flux of 6.77×10^{26} photons $s^{1}m^{-2}$. Dashed lines indicate 920 and 1100 nm respectively; the wavelengths subsequently utilized for photo-stimulation and inhibition. **c** Peak photocurrent as a function of incident power density at a holding potential of −60 mV (mean ± SEM, 920 nm, $n = 4$; 1100 nm, $n = 5$). **d–g** Current clamp (IC) characterization of somBiPOLES in CA1 pyramidal cells. **d** Probability of photo evoked action potentials under 1100 nm illumination for 5 ms ($n = 5$, red: average, gray: individual trials). **e** Characterization of the efficacy of silencing somBiPOLES expressing neurons under 920-nm illumination by co-injection of current (Box: median, 1st–3rd quartile, whiskers: 1.5x inter quartile range, $n = 5$). **f** Representative voltage traces demonstrating sustained neuronal silencing of neurons by two-photon excitation of somBiPOLES at 920 nm. Upper trace (control): 550 pA current injected (illustrated by the black line), no light. Lower trace: continuous injection of 550 pA current, 0.3 mW μm^{-2}, 920 nm, 2 Hz, 200 ms illumination. **g** Two-photon, bidirectional, control of single neurons demonstrated by co-incident illumination of 920 nm and 1100 nm light. Upper trace: 10 Hz spike train evoked by 15 ms pulses of 1100 nm light. Lower trace: optically induced action potentials shunted using a single, 200 ms pulse of 920 nm light.

two-photon holographic manipulation of neuronal activity with a cellular resolution with standard lasers typically used for two-photon imaging.

Considering the reliable performance of BiPOLES in pyramidal neurons we next tested its applicability in the invertebrate model systems *C. elegans* and *D. melanogaster*, as well as mice and ferrets, representing vertebrate model systems.

Bidirectional control of motor activity in *C. elegans*. We expressed BiPOLES in cholinergic motor neurons of *C. elegans* to optically control body contraction and relaxation. Illumination with red light resulted in body-wall muscle contraction and effective body shrinkage, consistent with motor neuron activation. Conversely, blue light triggered body extension, indicative of muscle relaxation and thus, cholinergic motor neuron inhibition (Fig. 6b). Maximal body length changes of +3% at 480 nm and −10% at 560–600 nm and reversal of the effect between 480 and 520 nm were consistent with the inhibitory and excitatory action spectrum of BiPOLES (Fig. 6b, Supplementary Fig. 12a). The light effects on body length required functional BiPOLES as the light did not affect body length in the absence of all-*trans*-retinal (ATR, Fig. 6b). Previous strategies for bidirectional motor control in *C. elegans* using ChR2(HR) and NpHR did not show body contraction and elongation in the same

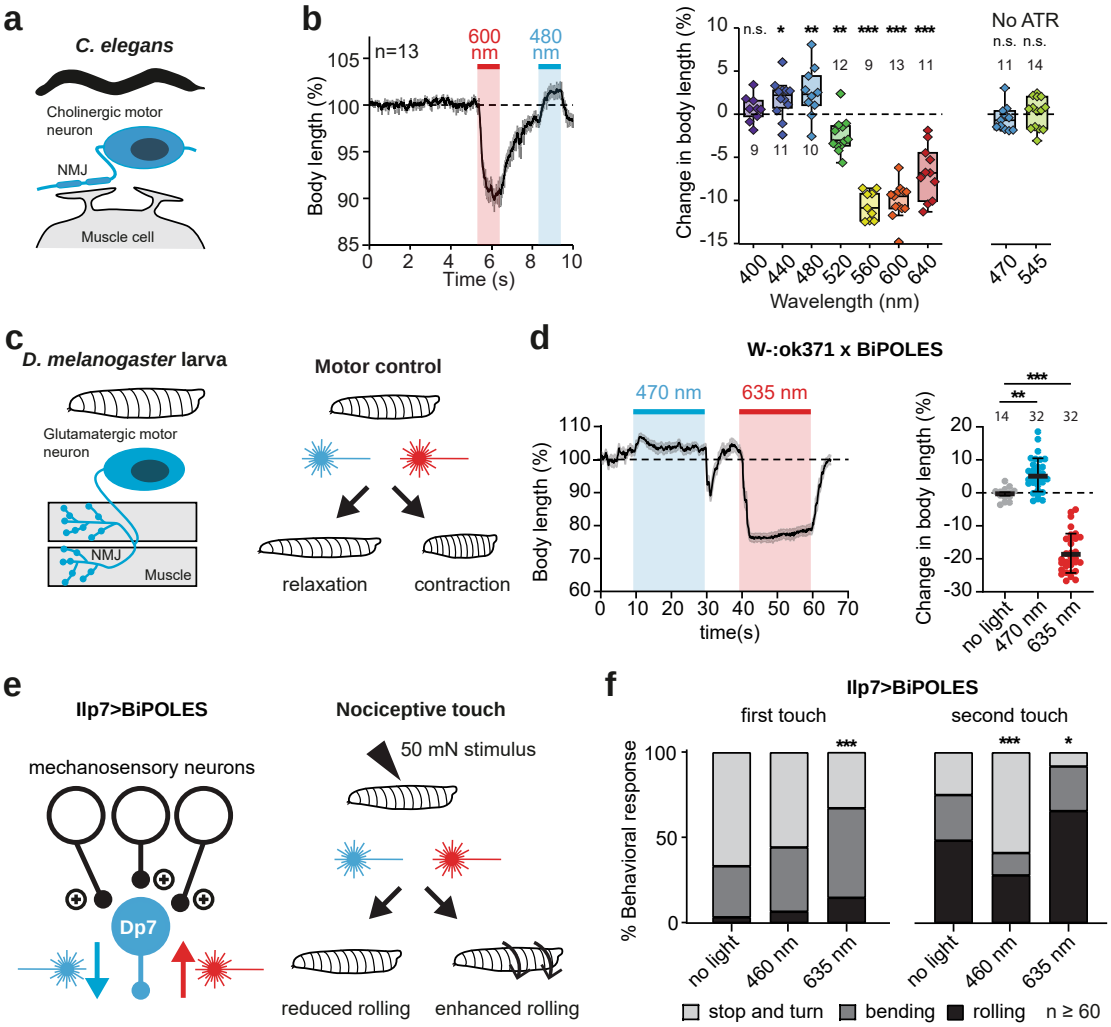

Fig. 6 BiPOLES allows bidirectional modulation of neuronal activity in *C. elegans* and *D. melanogaster*. a BiPOLES expressed in cholinergic neurons of *C. elegans* enables bidirectional control of body contraction and relaxation. Scheme of BiPOLES-expressing cholinergic motor neuron innervating a muscle cell. **b** Left: Temporal dynamics of relative changes in body length upon illumination with 600 and 480 nm light (mean ± SEM, 1.1 mW mm^{-2}, $n = 13$ animals). Right: Spectral quantification of maximal change in body length, compared is the body length before to during light stimulation (seconds 0–4 vs. seconds 6–9, see Supplementary fig. 12a; Box: median, 1st–3rd quartile, whiskers: 1.5x interquartile range, two-way ANOVA (Sidak's multiple comparisons test), p values: 400 nm ($n = 9$ animals): 0.99, 440 nm ($n = 12$): 0.049, 480 nm ($n = 10$): 0.007, 520 nm ($n = 12$): 0.002, 560 nm ($n = 9$): <0.0001, 600 nm ($n = 13$): <0.0001, 640 nm ($n = 11$): <0.0001, no ATR 470 nm ($n = 11$): 0.24, no ATR 545 nm ($n = 14$): 0.78). Experiments in absence of all-*trans*-retinal were done with 470/40 nm and 545/30 nm bandpass filters. **c** BiPOLES expressed in glutamatergic neurons of *D. melanogaster* larvae enables bidirectional control of body contraction and relaxation. Scheme of BiPOLES-expressing glutamatergic motor neuron innervating muscle fibers. **d** Left: Temporal dynamics of relative changes in body length upon illumination with 470 (17 µW mm^{-2}, $n = 32$ animals) and 635 nm light (25 µW mm^{-2}, $n = 32$). Right: Quantification of maximal change in body length (mean ± SEM, no light = 14, 470 nm = 32, 635 nm = 32, $^{**}p = 0.0152$, $^{***}p = 0.0005$, one-way ANOVA with Dunnett's multiple comparisons test). **e** BiPOLES-dependent manipulation of Dp7 neurons in the Drosophila larval brain (Ilp7-Gal4>UAS-BiPOLES) and the resulting change in nociceptive escape behavior following a 50 mN noxious touch. **f** Behavioral response after the first and second mechanical stimulus under blue light (470 nm, 1.7 mW mm^{-2}) or red light (635 nm, 2.5 mW mm^{-2}) illumination compared to no light. $n = 61$ animals $^{*}p = 0.034$, $^{***}p = 0.0005$ (first touch) and 0.0007 (second touch), X^2-test.

animal[33]. Therefore, we tested this directly with light conditions similar to those used for BiPOLES activation. Excitation with blue light resulted in a 5% body length decrease, while activation of NpHR at its peak wavelength (575 nm) failed to induce significant changes in body length (Supplementary Fig. 12b). Thus, BiPOLES expands the possibilities for bidirectional control of neuronal activity in *C. elegans* beyond what is achievable with currently available tools.

Bidirectional control of motor activity and nociception in *D. melanogaster*. Next, we demonstrate bidirectional control of circuit function and behavior with BiPOLES in *Drosophila melanogaster*. *Gt*ACR2 and *Cs*Chrimson were previously used in separate experiments to silence and activate neuronal activity, respectively[10]. In contrast, rhodopsin pump functionality is strongly limited in this organism[10,11], and bidirectional control of neuronal activity has not been achieved. We, therefore, expressed BiPOLES in glutamatergic motor neurons of *D. melanogaster* larvae (Fig. 6c). Illumination with blue light led to muscle relaxation and concomitant elongation (Fig. 6d). The change in body length was similar to animals expressing *Gt*ACR2 alone (Supplementary Fig. 12c). Importantly, *Gt*ACR2 activation in BiPOLES overrides blue-light evoked Chrimson activity and

thereby eliminates blue-light excitation of neurons, as observed with *Cs*Chrimson alone (Supplementary Fig. 12c). Conversely, red illumination of BiPOLES expressing larvae triggered robust muscle contraction and corresponding body length reduction (Fig. 6d). Thus, BiPOLES facilitates bidirectional optogenetic control of neuronal activity in *D. melanogaster* which was not achieved previously.

We further tested BiPOLES functionality in a more sophisticated in vivo paradigm expressing it in key modulatory neurons (dorsal pair Ilp7 neurons, Dp7) of the mechanonociceptive circuit. Dp7 neurons naturally exert bidirectional control of the larval escape response to noxious touch depending on their activation level[34] (Fig. 6e). Acute BiPOLES-dependent silencing of Dp7 neurons with blue light strongly decreased the rolling escape (Fig. 6f), consistent with previously shown chronic silencing of these neurons[34]. In turn, red light illumination of the same animals enhanced escape responses upon noxious touch showing that BiPOLES activation in Dp7 neurons can acutely tune their output and thus the corresponding escape response (Fig. 6f). BiPOLES activation in Dp7 neurons showed a similar ability to block or enhance nociceptive behavior as *Gt*ACR2 or *Cs*Chrimson, respectively, while preventing Chrimson-dependent activation with blue light (Supplementary Fig. 12d, e). Taken together, BiPOLES allows robust, acute, and bidirectional manipulation of neuronal output and behavior in *Drosophila melanogaster* in vivo.

All-optical, bidirectional control of pupil size in mice. To further extend the applications of BiPOLES to vertebrates, we generated various conditional and non-conditional viral vectors, in which the expression of the fusion construct is regulated by different promoters (see "Methods" section, Table 1). Using these viral vectors, we sought to test BiPOLES and somBiPOLES in the mammalian brain. To this end, we conditionally expressed somBiPOLES in TH-Cre mice, targeting Cre-expressing neurons in the Locus Coeruleus (LC) (Fig. 7a). Orange illumination (594 nm) through an optical fiber implanted bilaterally above LC reliably triggered transient pupil dilation, indicative of LC-mediated arousal[35] (Fig. 7b–d). Pupil dilation was evident already at 0.7 mW at the fiber tip and gradually increased with increasing light power (Supplementary Fig. 13a). Light-mediated pupil dilation was reverted immediately by additional blue light (473 nm) during the orange-light stimulation or suppressed altogether when blue-light delivery started before orange-light application (Fig. 7b–d), suggesting that orange-light-induced spiking of somBiPOLES-expressing neurons in LC was efficiently shunted. Illumination of the LC in wt-animals did not influence pupil dynamics (Supplementary Fig. 13b). Thus, LC neurons were bidirectionally controlled specifically in somBiPOLES expressing animals.

We estimated the brain volume accessible to reliable activation and inhibition with somBiPOLES using Monte-Carlo simulations of light propagation[16] under the experimental settings used for the LC-manipulations described above (Supplementary Fig. 14). Based on the light parameters required for neuronal excitation and inhibition determined in Fig. 3, and assuming 1 mW of 473 nm and 10 mW of 593 nm at the fiber tip, we estimate that reliable bidirectional control of neuronal activity can be achieved over a distance of >1.5 mm in the axial direction below the fiber tip (Supplementary Fig. 14c).

Manipulation of neocortical excitation/inhibition ratio in ferrets. Finally, we applied BiPOLES to bidirectionally control the excitation/inhibition (E/I) ratio in the mammalian neocortex. Therefore, we generated a viral vector using the minimal *Dlx* promoter[36] (mDlx) to target GABAergic neurons in the ferret secondary visual cortex (V2). Functional characterization in GABAergic neurons in vitro confirms all-optical spiking and inhibition of GABAergic neurons with mDlx-BiPOLES (Supplementary Fig. 15). Thus, we injected mDlx-BiPOLES in ferret V2 to modulate E/I-ratio during sensory processing (Fig. 7e). Extracellular recordings obtained from linear silicon probes in V2 of isoflurane-anesthetized ferrets provided evidence for modulation of cortical activity by shifts in the E/I ratio (Fig. 7f, g). Blue light led to an increase in baseline activity, consistent with the deactivation of inhibitory, GABAergic neurons (Fig. 7f, g). Activation of GABAergic cells by red light did not further decrease the low cortical baseline activity, but significantly reduced cortical responses triggered by sensory stimuli (Fig. 7f, g). Although effects of blue light on evoked spiking were not significant in the average data, we obtained clear evidence in individual recordings that blue light could enhance late response components (Fig. 7f), confirming a disinhibitory effect. Overall, these data suggest that BiPOLES is efficient in bidirectional control of inhibitory mechanisms, demonstrating its applicability for the control of E/I shifts in the cortical microcircuit in vivo.

Discussion

In summary, BiPOLES is a performance-optimized fusion construct composed of a red-light-activated cation- and a blue-light-activated anion-selective ChR. BiPOLES serves as an optogenetic tool for potent excitation and inhibition of the same neurons with red and blue light, respectively. In addition, it can be applied for exclusive red-light activation of a neuronal subpopulation in multicolor experiments, and for locally defined optical tuning of the membrane voltage between the Nernst potential for chloride and the action potential threshold.

BiPOLES performs reliably in invertebrate and vertebrate model systems, showing potent, bidirectional modulation in the *C. elegans* motor system, the *D. melanogaster* motor and nociceptive systems, and the ferret visual cortex. The addition of the soma-targeting signal from the mammalian potassium channel Kv2.1 yielded somBiPOLES, leading to further enhancement of trafficking to the plasma membrane at the soma and proximal dendrites while avoiding localization to distal dendrites and axons, as previously shown for individually expressed microbial rhodopsins[27–29]. Thus, eliminating the risk of inadvertent blue-light mediated depolarization of axons[28,37] while improving bidirectional optogenetic manipulation of the somatodendritic compartment somBiPOLES is optimized for applications in mammalian systems.

Combining cation and anion channels of overlapping action spectra requires careful consideration of the electrochemical conditions of the neuronal membrane. Since the resting membrane potential is close to the Nernst potential of chloride, anion channels displaying large unitary conductance are needed in order to efficiently shunt depolarizing currents of the red-shifted cation channel, which, in turn, needs to be potent enough to reliably trigger action potentials. Thus, photocurrent amplitudes and spectral sensitivity of the two opsins need to match the aforementioned conditions in order to both reliably silence and drive neuronal activity. If the red-shifted excitatory opsin shows too large, blue-light sensitive photocurrents, it may compromise the silencing capacity of the anion channel. Conversely, if the action spectrum of the blue-light sensitive anion channel extends too far towards longer wavelengths, efficient red-light evoked spiking may get impaired. For the molecular engineering of BiPOLES we focused on a large spectral separation of the anion and the cation conductance. Minimizing the optical cross-talk of both channels favors inhibitory conductance under blue light

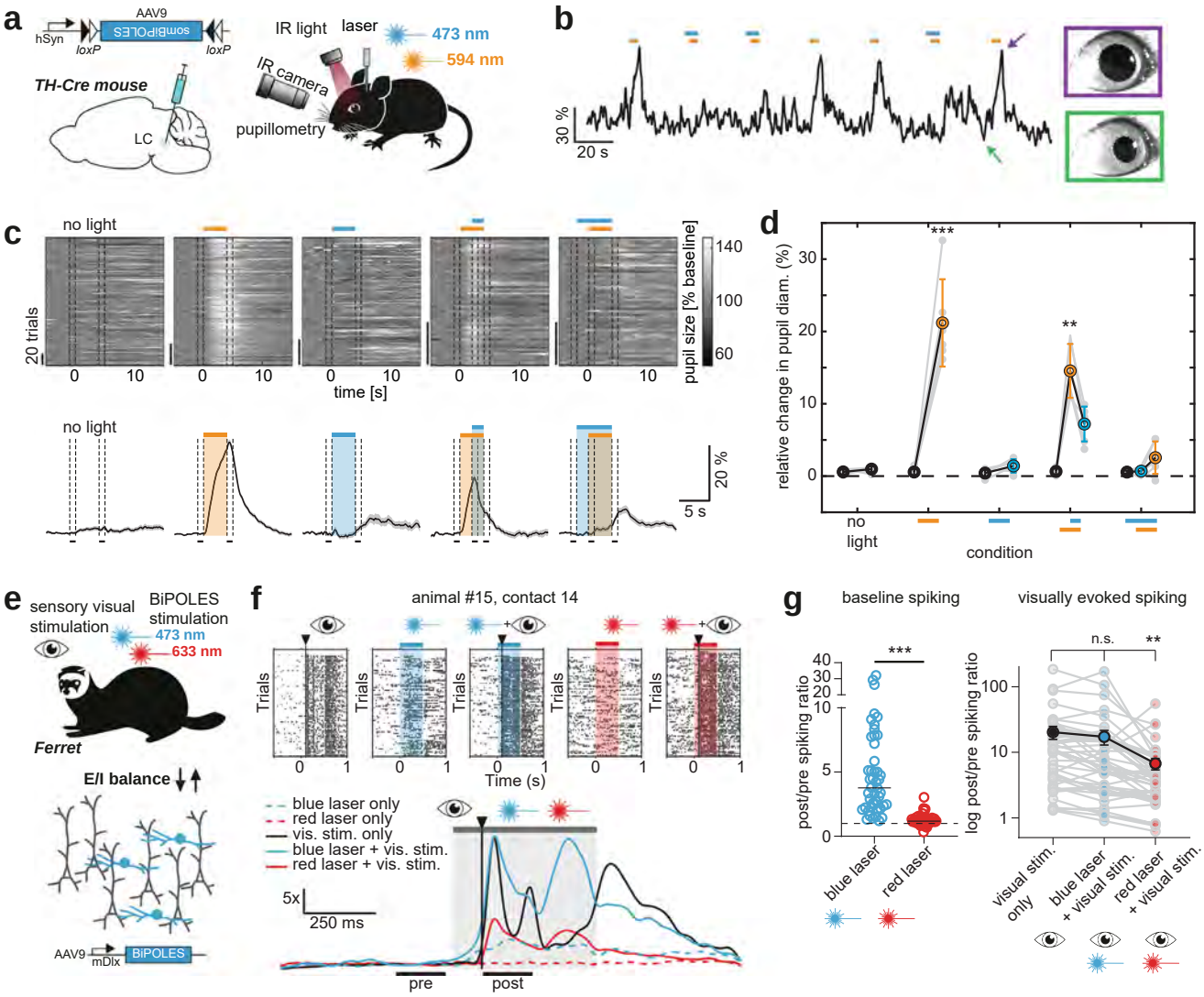

Fig. 7 BiPOLES and somBiPOLES allow bidirectional modulation of neuronal activity in mice and ferrets. a Conditional expression of somBiPOLES in Cre-positive neurons of the TH-Cre mouse to modulate pupil dilation. **b** Relative pupil diameter in single trials. Orange and blue bars indicate the time of illumination with 594 (orange) and 473 nm (blue), respectively. Arrows indicate positions of the two example images of the eye. **c** Quantification of normalized pupil size in one animal under various stimulation conditions for somBiPOLES as indicated. Top: single trials. Bottom: mean ± SEM. Dashed lines show time windows used for quantification in the plot on the right. **d** Quantification of relative pupil size ($n = 6$ mice; One-way analysis of variance; $F = 61.67$, $p = 1.36 \times 10^{-12}$; Tukey's multiple comparison test: $^{**}p = 0.0028$, $^{***}p < 0.0001$). **e** Modulation of GABAergic neurons (blue) in ferret secondary visual cortex (area 18) with mDlx-BiPOLES. Red (633 nm) or blue (473 nm) laser light was used to (de-)activate interneurons with or without a following 10-ms visual flash (white LED; Osram OSLON Compact) to the ferret's right eye. **f** Example neuronal spiking responses at one contact of the linear probe (~700 µm depth) under indicated stimulation conditions Top: Raster-plots of the visual stimulus alone, blue laser (+visual), red laser (+visual) conditions. Bottom: Normalized to 'pre'-phase averaged spike-density plot (sigma = 20 ms) of each indicated condition. Gray area: laser-on epoch; black vertical line: visual stimulus onset. Black horizontal lines indicate the 200 ms pre-stim and post-stim analysis epochs to compute the results in **g**. Note the rate increase after the onset of the blue laser before the onset of the visual stimulus and the reduced answer after red laser illumination. **g** Spike-rate ratio of post vs. pre-laser-stimulus epoch. Left: quantification of laser-mediated impact on baseline spiking rate (no visual stim.). Right: quantification of the spike-rate change of the same units during only visual and laser + visual stimulation ($n = 46$ contacts showing visual responses from 3 animals, $^{**}p = 0.0046$, $^{***}p < 0.0001$).

illumination and increases both the light intensity range and the spectral range that allows exclusive activation of the red-shifted cation channel. Due to the large spectral separation, BiPOLES can be controlled with two simple light sources, such as LEDs, without the requirement of sophisticated spectral control, making its use straightforward. The *Gt*ACR2-L4-ChRmine-construct might be an interesting alternative if spectrally narrow light sources, such as lasers, are available, because it reaches peak depolarizing currents 60 nm blue-shifted compared to BiPOLES. Thus, inhibition and excitation can be achieved with 430–470 nm and 530–550 nm (Fig. 1f) providing an additional spectral window in the red, that can be used for a third optogenetic actuator or sensor. Finally, a seemingly trivial but equally important advantage of all the tandem systems we present here is their modular architecture allowing easy tailoring of fusion constructs fulfilling specific future experimental requirements.

Noteworthy, BiPOLES does not represent the first optogenetic tool for bidirectional control of neuronal activity. Different combinations of the excitatory blue-light-sensitive ChR2 and orange-light-sensitive inhibitory ion pumps such as NpHR, bR, or

Arch3.0 were generated previously[2,4,6]. However, among all these variants, only the combination of ChR2 and NpHR (i.e., eNPAC and eNPAC2.0) was successfully used to address neuroscientific questions in mice[6–9]. BiPOLES will significantly expand the possibilities of bidirectional neuronal manipulations, since, aside from efficient expression in a wide array of different model systems, it also features a number of additional advantages: First, combining two potent channels, rather than a pump and a channel, provides a more balanced ionic flux per absorbed photon for the inhibitory and excitatory rhodopsin. This results in a high operational light sensitivity for both excitation and inhibition by orange and blue light, respectively. In contrast, high irradiance and expression levels are required for the ion pumps that only transport one charge per absorbed photon. Second, due to the use of two channels, BiPOLES-mediated photocurrents do not actively move ions against their gradients, which can cause adverse side-effects[37], but rather fixes the neuronal membrane voltage anywhere between the reversal potential of *Gt*ACR2 and Chrimson. The membrane voltage can be tuned depending on the ratio of blue/red light or a single light source tuned to wavelengths between the absorption peaks of *Gt*ACR2 and Chrimson. Third, inverting the color of the excitatory and inhibitory opsin, compared to previous tools, restricts optical excitation in BiPOLES-expressing cells exclusively to the orange/red spectrum. The inverted color scheme enables scale-free and mutually exclusive spiking of two neuronal populations in combination with a second, blue-light-sensitive ChR, expressed in the second population of neurons, as the blue-light-activated, inhibitory channel *Gt*ACR2 potently shunts Chrimson-mediated, blue-light-activated excitatory photocurrents. Other applications could employ multiplexing with blue-light sensitive cyclases[38] or genetically encoded activity-indicators that require blue light for photoconversion[39,40]. Fourth, compared to the first generation of tandem constructs, BiPOLES was optimized for membrane trafficking and especially the somBiPOLES variant shows strongly improved membrane expression in mammalian neurons, enabling reliable and potent optogenetic spiking and inhibition even in deep brain regions in vivo. One additional reason for the superior membrane expression of BiPOLES compared to other rhodopsin-tandems might be the absence of N-terminal, extracellular cysteine residues, which are involved in disulfide bond formation and thus dimerization in all structurally described ChRs[41–44]. The absence of N-terminal cysteines may avoid heteromeric protein networks and undesired clustering of the fused tandem rhodopsins. Fifth, soma-targeted BiPOLES allows efficient and reliable bidirectional control of neuronal spiking over a wide range of light intensities. This is important for in vivo applications in the mammalian brain, where light scattering and absorption lead to an exponential fall-off of the irradiance over distance[17]. The color scheme in somBiPOLES in combination with the large-conductance of *Gt*ACR2 and its absence from axon terminals enables potent and reliable silencing with blue light over a wide range of intensities. Potential cross-activation of Chrimson by high blue light intensities did not compromise neuronal silencing in pyramidal neurons. Similarly, due to the red-shifted absorption of Chrimson, neuronal spiking can be efficiently achieved with orange light. somBiPOLES reliably mediates silencing and activation at modest intensities of blue and orange light far away from the fiber tip, while maintaining its wavelength-specificity under high-intensity irradiance, as typically present directly under the fiber tip. Thus, somBiPOLES holds the potential to manipulate neuronal activity in large brain areas with single-photon illumination (Supplementary Fig. 14c). Finally, a fusion protein of two potent channels with opposite charge selectivity targeted to the somatodendritic compartment and displaying a local one-to-one expression ratio in the plasma membrane enables temporally precise bidirectional control of neuronal activity at single-cell resolution using two-photon excitation. In contrast to widefield illumination with visible light, two-photon excitation in combination with soma-targeted opsins allows optogenetic control with single-cell resolution[45–47]. Bidirectional optogenetic control in the same cells has not been achieved with two-photon excitation, so far; partially due to the low quantum efficiency of rhodopsin pumps, which limits their two-photon activation. In contrast, the large conductance of the two channels improves their efficacy with respect to the number of transported ions per absorbed photon, and their presence at equal stoichiometry anywhere on the membrane ensures the reliable and reproducible generation of anion currents and/or cation currents, which is particularly important under locally confined two-photon excitation.

In principle, also multicistronic vectors encoding both opsins under a single promoter using either an internal ribosomal entry site (IRES)[48] or a 2A ribosomal skip sequence allow expression of both ion channels at a fixed ratio from a single AAV vector[3,7]. However, with both of these strategies, neither co-localized nor stoichiometric membrane expression of both channels is guaranteed since both channels might get differentially targeted and distributed in the plasma membrane. This may not pose a limitation for experiments that require bidirectional control of large numbers of cells where precise control of a single-cell activity or sub-cellular ion gradients is not so crucial. BiPOLES as a covalently linked fusion protein displays a fixed expression of both opsins at a 1:1 stoichiometry anywhere in the membrane and membrane trafficking or degradation of both opsins occur at identical rates, preserving excitatory and inhibitory currents at a fixed ratio in all expressing cells. A fixed stoichiometry anywhere in the cell membrane is important if local, subcellular activation of the opsins is required, such as during two-photon excitation or when a fixed ratio of cation and anion conductance is desired between different neurons or in particular neuronal compartments, such as single dendrites or dendritic spines.

Notably, BiPOLES employs an anion channel for optogenetic silencing and therefore relies on the extracellular and intracellular chloride concentration. In the case of a depolarized chloride Nernst potential, the opening of the anion channel may produce depolarizing currents, which can trigger action potentials or neurotransmitter release[49]. Unlike for rhodopsin pumps, efficient silencing consequently requires low cytosolic chloride concentrations and is therefore limited in neurons or cellular compartments with a depolarized Nernst potential for chloride, such as immature neurons or axon terminals. Given these caveats, BiPOLES may not be suitable for bidirectional control of developing neurons or presynaptic boutons. In this case, silencing may be more efficient with rhodopsin pumps, despite their own limitations[37,49] or with G-protein coupled rhodopsins[50,51]. As with any optogenetic application, neurophysiological parameters need to be considered by the experimenter, guiding the appropriate choice of the tool suitable to address the specific experimental requirements.

Since BiPOLES can be used to spike or inhibit the same population of mature neurons in vivo, a number of previously inaccessible questions can be addressed. During extracellular recordings, BiPOLES may be useful for optogenetic identification (optotagging) with red light[52] and optogenetic silencing of the same neurons. This will permit verification of the identity of silenced neurons by their spiking profiles. Moreover, in combination with a second, blue-light sensitive ChR, BiPOLES can be used to map local networks of spatially intermingled neurons. For example, expressed in distinct types of molecularly defined GABAergic neurons, connectivity of these neurons to a postsynaptic target cell can be evaluated. Additional applications of

BiPOLES may encompass bidirectional control of engram neurons[53] to test both necessity and sufficiency of a particular set of neurons for memory retrieval or switching the valence of a particular experience by inhibiting or activating the same or even two distinct populations of neuromodulatory neurons. In principle, this could even be achieved with cellular resolution using two-photon holography. Due to its utility for a wide range of research questions, its versatile functionality, and its applicability in numerous model systems, as demonstrated in this study, BiPOLES fills an important gap in the optogenetic toolbox and might become the tool of choice to address a number of yet inaccessible problems in neuroscience.

Methods

Molecular biology. For HEK-cell expression, the coding sequences of Chrimson (KF992060.1), CsChrimson (KJ995863.2) from *Chlamydomonas noctigama*[12], ChRmine from *Rhodomonas lens* although initially attributed to *Tiarina fusus*[22,25] (Addgene #130997), bReaChES[20], iC++ (Addgene #98165)[19], Aurora (Addgene #98217)[11], *Gt*ACR1 (KP171708) and *Gt*ACR2 (KP171709) from *Guillardia theta*[18], as well as the blue-shifted Arch3.0 mutant M128A/S151A/A225T herein described as ArchBlue[26] were cloned together with mCerulean3[54] and a trafficking signal (ts) from the Kir 2.1 channel[4] into a pCDNA3.1 vector containing the original opsin tandem cassette[2] with a linker composed of eYFP and the first 105 N-terminal amino acids of the rat gastric H+/K+-ATPase beta subunit (βHK, NM_012510.2), kindly provided by Sonja Kleinlogel (University of Bern, CH). For direct comparison also the bicistronic tool eNPAC2.0[6]—kindly provided by Karl Deisseroth (Stanford University, CA)—was cloned into the same backbone. Site-directed mutagenesis to introduce the f-Chrimson and vf-Chrimson mutations Y261F, S267M, and K176R[21] was performed using the QuickChange Site-Directed Mutagenesis Kit (Agilent Technologies, Santa Clara, CA) according to the manufacturers' instructions.

For neuronal expression, the insert consisting of *Gt*ACR2-ts-mCerulean3-βHK-Chrimson was cloned into an AAV2-backbone behind human synapsin (hSyn) promoter (pAAV-hSyn-BiPOLES-mCerulean; Addgene #154944). A soma-targeted, membrane-trafficking optimized variant was generated by fusing an additional trafficking signal from the potassium channel Kv2.1[27] to the C-terminus of Chrimson (pAAV-hSyn-somBiPOLES-mCerulean; Addgene #154945). For expression in GABAergic neurons, BiPOLES was cloned into an AAV2-backbone behind the minimal Dlx (mDlx) promoter[36] resulting in pAAV-mDlx-BiPOLES-mCerulean (Addgene #154946). For expression in projection neurons, somBiPOLES was cloned into an AAV2-backbone behind the minimal CaMKII promoter[55] resulting pAAV-CaMKII-somBiPOLES-mCerulean (Addgene #154948). Double-floxed inverted open reading frame variants of BiPOLES and somBiPOLES were generated by cloning these inserts in antisense direction behind the hSyn promoter, flanked by two loxP and lox2272 sites (hSyn-DIO-BiPOLES-mCerulean, Addgene #154950; hSyn-DIO-somBiPOLES-mCerulean, Addgene #154951). Note that in all constructs the mCerulean3-tag is fused between *Gt*ACR2-ts and βHK-Chrimson and therefore part of BiPOLES. We nonetheless chose to add "mCerulean" to the plasmid names to remind the reader of the presence of a cyan fluorophore in BiPOLES. BiPOLES stands for "Bidirectional Pair of Opsins for Light-induced Excitation and Silencing". Sequences of all primers used for cloning and sequences of DNA inserts used in this study are provided in a separate list (Supplementary Data 1).

Patch-Clamp experiments in HEK293 cells. Fusion constructs were expressed under the control of a CMV-promotor in HEK293 cells that were cultured in Dulbecco's Modified Medium (DMEM) with stable glutamine (Biochrom, Berlin, Germany), supplemented with 10% (v/v) fetal bovine serum (FBS Superior; Biochrom, Berlin, Germany), 1 µM all-*trans*-retinal, and 100 µg ml^{-1} penicillin/streptomycin (Biochrom, Berlin, Germany). Cells were seeded on poly-lysine coated glass coverslips at a concentration of 1×10^5 cell ml^{-1} and transiently transfected using the FuGENE® HD Transfection Reagent (Promega, Madison, WI). two days before measurement.

Patch-clamp experiments were performed in transgene expressing HEK293 cells two days after transfection[56]. Patch pipettes were prepared from borosilicate glass capillaries (G150F-3; Warner Instruments, Hamden, CT) using a P-1000 micropipette puller (Sutter Instruments, Novato, CA) and subsequently fire-polished. Pipette resistance was between 1.2 and 2.5 MΩ. Single fluorescent cells were identified using an Axiovert 100 inverted microscope (Carl Zeiss, Jena, Germany). Monochromatic light (± 7 nm) was provided by a Polychrome V monochromator (TILL Photonics, Planegg, Germany) or by a pE-4000 CoolLED system (CoolLED, Andover, UK) for light titration experiments. Light intensities were attenuated by a motorized neutral density filter wheel (Newport, Irvine, CA) for equal photon flux during action spectra recordings. Light pulses of the Polychrome V were controlled by a VS25 and VCM-D1 shutter system (Vincent Associates, Rochester, NY). Recordings were done with an AxoPatch 200B amplifier (Molecular Devices, Sunnyvale, CA) or an ELV-03XS amplifier (npi Electronics, Tamm, Germany), filtered at 2 kHz, and digitized using a DigiData 1440 A digitizer (Molecular Devices, Sunnyvale, CA) at a sampling rate of 10 kHz. The reference bath electrode was connected to the bath solution via a 140 mM NaCl agar bridge. Bath solutions contained 140 mM NaCl, 1 mM KCl, 1 mM CsCl, 2 mM $CaCl_2$, 2 mM $MgCl_2$ and 10 mM HEPES at pH_e 7.2 (with glucose added up to 310 mOsm). Pipette solution contained 110 mM NaGluconate, 1 mM KCl, 1 mM CsCl, 2 mM $CaCl_2$, 2 mM $MgCl_2$, 10 mM EGTA and 10 mM HEPES at pH_i 7.2 (glucose added up to 290 mOsm). All light intensities were measured in the object plane using a P9710 optometer (Gigahertz-Optik, Türkenfeld, Germany) and normalized to the water Plan-Apochromat ×40/1.0 differential interference contrast (DIC) objective illuminated field (0.066 mm^2). The irradiance was 2.7 mW mm^{-2} at 650 nm, 3.5 mW mm^{-2} at 600 nm, 4.2 mW mm^{-2} at 530 nm, 5.7 mW mm^{-2} at 490 nm, and 5.2 mW mm^{-2} at 450 nm. All electrical recordings were controlled by the pCLAMP™ software (Molecular Devices, Sunnyvale, CA). All whole-cell recordings had a membrane resistance of at least 500 MΩ (usual >1 GΩ) and an access resistance below 10 MΩ.

Preparation of organotypic hippocampal slice cultures. All procedures were in agreement with the German national animal care guidelines and approved by the independent Hamburg state authority for animal welfare (Behörde für Justiz und Verbraucherschutz). They were performed in accordance with the guidelines of the German Animal Protection Law and the animal welfare officer of the University Medical Center Hamburg-Eppendorf.

Organotypic hippocampal slices were prepared from Wistar rats or VIP-IRES-Cre mice of both sexes (Jackson-No. 031628) at post-natal days 5–7[57]. Dissected hippocampi were cut into 350 µm slices with a tissue chopper and placed on a porous membrane (Millicell CM, Millipore). Cultures were maintained at 37 °C, 5% CO_2 in a medium containing 80% MEM (Sigma M7278), 20% heat-inactivated horse serum (Sigma H1138) supplemented with 1 mM L-glutamine, 0.00125% ascorbic acid, 0.01 mg ml^{-1} insulin, 1.44 mM $CaCl_2$, 2 mM $MgSO_4$ and 13 mM D-glucose. No antibiotics were added to the culture medium.

Transgene delivery for single-photon experiments. For transgene delivery in organotypic slices, individual CA1 pyramidal cells were transfected by single-cell electroporation[58] between DIV 14–16. Except for pAAV-hSyn-eNPAC2.0, which was used at a final concentration of 20 ng $µl^{-1}$, all other plasmids, namely pAAV-hSyn-BiPOLES-mCerulean, pAAV-hSyn-somBiPOLES-mCerulean, pAAV-hSyn-Chrimson-mCerulean, and pAAV-hSyn-som*Gt*ACR2-mCerulean were used at a final concentration of 5 ng $µl^{-1}$ in K-gluconate-based solution consisting of (in mM): 135 K-gluconate, 10 HEPES, 4 Na_2-ATP, 0.4 Na-GTP, 4 $MgCl_2$, 3 ascorbate, 10 Na_2-phosphocreatine (pH 7.2). A plasmid encoding hSyn-mKate2 or hSyn-mCerulean (both at 50 ng $µl^{-1}$) was co-electroporated with the opsin-mCerulean or eNPAC2.0 plasmids, respectively, and served as a morphology marker. An Axoporator 800 A (Molecular Devices) was used to deliver 50 hyperpolarizing

Table 1 List of recombinant adeno-associated viral vectors used for experiments in organotypic hippocampal slices.

Recombinant adeno-associated virus (rAAV2/9)	Titer used for transduction of hippocampal organotypic slice cultures (vg/ml)	Addgene plasmid reference
mDlx-BiPOLES-mCerulean	2.8×10^{13}	154946
hSyn-DIO-BiPOLES-mCerulean	7.0×10^{13}	154950
hSyn-DIO-somBiPOLES-mCerulean	3.4×10^{13}	154951
CaMKIIa(0.4)-somBiPOLES-mCerulean	2.5×10^{13}	154948
CaMKIIa(0.4)-DO-CheRiff-ts-mScarlet-ER	8.15×10^{11}	n.a.
mDlx-H2B-EGFP	2.8×10^{10}	n.a.
CaMKIIa-Cre	3.0×10^{12}	n.a.

Viruses were transduced at the indicated titers. *n.a.*: not applicable.

pulses (−12 V, 0.5 ms) at 50 Hz. During electroporation, slices were maintained in pre-warmed (37 °C) HEPES-buffered solution (in mM): 145 NaCl, 10 HEPES, 25 D-glucose, 2.5 KCl, 1 $MgCl_2$, and 2 $CaCl_2$ (pH 7.4, sterile filtered). In some cases, slice cultures were transduced with recombinant adeno-associated virus (see Table 1 for details) at DIV 3–5[59]. The different rAAVs were locally injected into the CA1 region using a Picospritzer (Parker, Hannafin) by a pressurized air pulse (2 bar, 100 ms) expelling the viral suspension into the slice. During virus transduction, membranes carrying the slices were kept on pre-warmed HEPES-buffered solution.

Preparation of organotypic hippocampal slice cultures for two-photon holographic stimulation of somBiPOLES. All experimental procedures were conducted in accordance with guidelines from the European Union and institutional guidelines on the care and use of laboratory animals (council directive 2010/63/EU of the European Union). Organotypic hippocampal slices were prepared from mice (Janvier Labs, C57Bl6J) at postnatal day 8 (P8). Hippocampi were sliced into 300 µm thick sections in a cold dissecting medium consisting of GBSS supplemented with 25 mM D-glucose, 10 mM HEPES, 1 mM Na-Pyruvate, 0.5 mM α-tocopherol, 20 nM ascorbic acid, and 0.4% penicillin/streptomycin (5000 U ml^{-1}).

Slices were placed onto a porous membrane (Millicell CM, Millipore) and cultured at 37 °C, 5% CO2 in a medium consisting of 50% Opti-MEM (Fisher 15392402), 25% heat-inactivated horse serum (Fisher 10368902), 24% HBSS, and 1% penicillin/streptomycin (5000 U ml^{-1}). This medium was supplemented with 25 mM D-glucose, 1 mM Na-Pyruvate, 20 nM ascorbic acid, and 0.5 mM α-tocopherol. After three days in-vitro, the medium was replaced with one containing 82% neurobasal-A, 15% heat-inactivated horse serum (Fisher 11570426), 2% B27 supplement (Fisher, 11530536), 1% penicillin/streptomycin (5000 U ml^{-1}), which was supplemented with 0.8 mM L-glutamine, 0.8 mM Na-Pyruvate, 10 nM ascorbic acid and 0.5 mM α-tocopherol. This medium was removed and replaced once every 2-3 days.

Slices were transduced with rAAV9-CaMKII-somBiPOLES-mCerulean at DIV 3 by bulk application of 1 µl of virus (final titer: 2.5×10^{13} vg ml^{-1}) per slice. Experiments were performed between DIV 13 and 17.

Slice culture electrophysiology with singe-photon stimulation. At DIV 19-21, whole-cell patch-clamp recordings of transfected or virus-transduced CA1 pyramidal or GABAergic neurons were performed. Experiments were done at room temperature (21–23 °C) under visual guidance using a BX 51WI microscope (Olympus) equipped with Dodt-gradient contrast and a Double IPA integrated patch amplifier controlled with SutterPatch software (Sutter Instrument, Novato, CA). Patch pipettes with a tip resistance of 3–4 MΩ were filled with an intracellular solution consisting of (in mM): 135 K-gluconate, 4 $MgCl_2$, 4 Na_2-ATP, 0.4 Na-GTP, 10 Na_2-phosphocreatine, 3 ascorbate, 0.2 EGTA, and 10 HEPES (pH 7.2). Artificial cerebrospinal fluid (ACSF) consisted of (in mM): 135 NaCl, 2.5 KCl, 2 $CaCl_2$, 1 $MgCl_2$, 10 Na-HEPES, 12.5 D-glucose, 1.25 NaH_2PO_4 (pH 7.4). In experiments where synaptic transmission was blocked, 10 µM CPPene, 10 µM NBQX, and 100 µM picrotoxin (Tocris, Bristol, UK) were added to the recording solution. In experiments analyzing synaptic inputs onto O-LM interneurons, ACSF containing 4 mM $CaCl_2$ and 4 mM $MgCl_2$ was used to reduce the overall excitability. Measurements were corrected for a liquid junction potential of −14,5 mV. Access resistance of the recorded neurons was continuously monitored and recordings above 30 MΩ were discarded. A 16 channel LED light engine (CoolLED pE-4000, Andover, UK) was used for epifluorescence excitation and delivery of light pulses for optogenetic stimulation (ranging from 385 to 635 nm). Irradiance was measured in the object plane with a 1918 R power meter equipped with a calibrated 818 ST2 UV/D detector (Newport, Irvine CA) and divided by the illuminated field of the Olympus LUMPLFLN 60XW objective (0.134 mm^2).

For photocurrent density measurements in voltage-clamp mode CA1 cells expressing BiPOLES, somBiPOLES, Chrimson or som*Gt*ACR2 were held at −75 or −55 mV to detect inward (cationic) or outward (anionic) currents elicited by red (635 nm, 20 ms, 1 and 10 mW mm^{-2}) and blue light (490 nm, 100 ms, 10 mW mm^{-2}), respectively. For each cell, the peak photocurrent amplitude (in pA) was divided by the cell membrane capacitance (in pF) which was automatically recorded by the SutterPatch software in voltage-clamp mode ($V_{hold} = -75$ mV).

In current-clamp experiments holding current was injected to maintain CA1 cells near their resting membrane potential (−75 to −80 mV). To assess the suitability of BiPOLES and somBiPOLES as dual-color neuronal excitation and silencing tools, alternating pulses of red (635 nm, 20 ms, 10 mW mm^{-2}), blue (490 nm, 100 ms, 10 mW mm^{-2}), and a combination of these two (onset of blue light 40 ms before red light) were delivered to elicit and block action potentials. For eNPAC2.0 alternating pulses of blue (470 nm, 20 ms, 10 mW mm^{-2}), yellow (580 nm, 100 ms, 10 mW mm^{-2}), and a combination of these two (onset of yellow light 40 ms before blue light) were used.

In experiments determining the spiking probability of somBiPOLES and Chrimson under illumination with light of different wavelengths (470, 595, and 635 nm), a train of 20 light pulses (5 ms pulse duration) was delivered at 5 Hz. For each wavelength, irradiance values from 0.1 to 100 mW mm^{-2} were used. For comparisons with eNPAC2.0, only light of 470 nm was used, which is the peak activation wavelength of ChR2(HR). AP probability was calculated by dividing the number of light-triggered APs by the total number of light pulses.

To compare the irradiance threshold needed to spike CA1 cells with BiPOLES, somBiPOLES, eNPAC2.0, Chrimson, and CheRiff across different wavelengths, 470, 525, 595, and 635 nm light ramps going from 0 to 10 mW mm^{-2} over 1 s were delivered in current-clamp mode. In the case of BiPOLES and somBiPOLES the blue light ramp went up to 100 mW mm^{-2} to rule out that very high blue-light irradiance might still spike neurons. The irradiance value at the time of the first spike was defined as the irradiance threshold (in mW mm^{-2}) needed to evoke action potential firing.

To measure the ability of BiPOLES, somBiPOLES, and som*Gt*ACR2 to shift the rheobase upon blue-light illumination, depolarizing current ramps (from 0–100 to 0–900 pA) were injected into CA1 neurons in the dark and during illumination with 490 nm light at irradiance values ranging from 0.001 to 100 mW mm^{-2}. The injected current at the time of the first spike was defined as the rheobase. The relative change in the number of ramp-evoked APs was calculated counting the total number of APs elicited during the 9 current ramp injections (from 0–100 to 0–900 pA) for each irradiance and normalized to the number of APs elicited in the absence of light. The same experiment was conducted for eNPAC2.0, but using 580 nm light ranging from 0.01 to 100 mW mm^{-2}. Statistical significance was calculated using the Friedman test.

To optically clamp the neuronal membrane potential using somBiPOLES, simultaneous illumination with blue and orange light at varying ratios was used. In current-clamp experiments, 470 and 595 nm light ramps (5 s) of opposite gradients (1 to 0 mW mm^{-2} and 0 to 1 mW mm^{-2}, respectively) were applied. Alternatively, optical clamping of the membrane potential was achieved by tuning a single wavelength between 385 and 660 nm (2 s light pulses, 0.1 mW mm^{-2}). Voltage traces were median-filtered to remove orange/red-light-mediated spikes and reveal the slow change in membrane voltage during illumination.

For independent optogenetic activation of two distinct populations of neurons, organotypic slice cultures from VIP-Cre mice were transduced with two rAAVs: 1, a double-floxed inverted open reading frame (DIO) construct encoding somBiPOLES (hSyn-DIO-somBiPOLES-mCerulean, see Table 1 for details) to target VIP-positive interneurons, and 2, a double-floxed open reading frame (DO) construct encoding CheRiff (hSyn-DO-CheRiff-ts-mScarlet-ER, see Table 1 for details) to target CA1 pyramidal neurons and exclude expression in VIP-positive cells. Synaptic input from these two populations was recorded in VIP-negative stratum-oriens GABAergic neurons (putative O-LM cells). In CA1, O-LM neurons receive innervation both from local CA1 pyramidal cells and VIP-positive GABAergic neurons[60]. To facilitate the identification of putative GABAergic postsynaptic neurons in stratum oriens, slices were transduced with an additional rAAV encoding mDlx-H2B-EGFP. In the absence of synaptic blockers light-evoked EPSCs and IPSCs were recorded while holding the postsynaptic cell at different membrane potentials (−80, −65, −55, −45, and 6 mV) in whole-cell voltage-clamp mode. A blue (460 nm, 0.03–84.0 mW mm^{-2}) and a red (635 nm, 6.0–97.0 mW mm^{-2}) light pulse were delivered 500 ms apart from each other through a Leica HC FLUOTAR L ×25/0.95 W VISIR objective.

To functionally assess the putative expression of somBiPOLES in the axon terminals of CA3 pyramidal cells, slice cultures were transduced with an rAAV9 encoding for CaMKIIa(0.4)-somBiPOLES-mCerulean (see Table 1 for details). Red-light evoked EPSCs were recorded in postsynaptic CA1 cells during local illumination either in CA3 at the somata (two light pulses of 5 ms delivered 40 ms apart using a fiber-coupled LED (400 µm fiber, 0.39 NA, 625 nm, Thorlabs) controlled by a Mightex Universal 4-Channel LED Driver (1.6 mW at fiber tip), or in CA1 at axon terminals of somBiPOLES-expressing CA3 cells (two light pulses of 5 ms delivered 40 ms apart through the ×60 microscope objective, 635 nm, 50 mW mm^{-2}). Axonal light stimulation was done in the presence of tetrodotoxin (TTX, 1 µM) and 4-aminopyridine (4-AP, 100 µM) to avoid antidromic spiking of CA3 cells.

To determine the high-frequency spiking limit with somBiPOLES, action potentials were triggered in CA1 cells at frequencies ranging from 10 to 100 Hz using 40 light pulses (595 nm, 3 ms pulse width, 10 mW mm^{-2}). AP probability was calculated by dividing the number of light-triggered APs by the total number of light pulses.

To characterize the spectral activation of BiPOLES, eNPAC2.0. and som*Gt*ACR2, photocurrents were recorded from CA1 cells in a voltage-clamp mode in response to 500 ms illumination with various wavelengths (from 385 to 660 nm, 10 mW mm^{-2}). BiPOLES-expressing and som*Gt*ACR2-expressing cells were held at a membrane voltage of −55 mV, more positive than the chloride Nernst potential, to measure light-mediated outward chloride currents. Photocurrent recordings from eNPAC2.0-expressing cells were done at a holding voltage of −75 mV. For BiPOLES and eNPAC2.0 the photocurrent ratio between excitatory and inhibitory photocurrents was calculated in each cell by diving the amplitude of the photocurrents evoked by 490/595 nm (for BiPOLES) and 460/580 nm (for eNPAC2.0).

Passive and active membrane parameters were measured in somBiPOLES-expressing and non-transduced, wild-type CA1 pyramidal cells. Resting membrane potential, membrane resistance, and capacitance were automatically recorded by the SutterPatch software in voltage-clamp mode ($V_{hold} = -75$ mV) in response to a voltage test pulse of 100 ms and −5 mV. The number of elicited action potentials were counted in response to a somatic current injection of 300 pA in current-clamp mode (0 pA holding current). For the 1st elicited AP, the voltage threshold, peak, and amplitude were measured.

Slice culture immunohistochemistry and confocal imaging. The subcellular localization of BiPOLES and somBiPOLES in hippocampal neurons was assessed 20 days after virus transduction (rAAV9-hSyn-DIO-BiPOLES-mCerulean + CaMKIIa-Cre, and CaMKIIa(0.4)-somBiPOLES-mCerulean, respectively. See Table 1 for details). Hippocampal organotypic slice cultures were fixed in a solution of 4% (w/v) paraformaldehyde (PFA) in PBS for 30 min at room temperature (RT). Next, slices were washed in PBS (3 × 10 min), blocked for 2 h at RT (10% [v/v] normal goat serum [NGS] in 0.3% [v/v] Triton X-100 containing PBS) and subsequently incubated for 48 h at 4 °C with a primary antibody against GFP to amplify the mCerulean signal (chicken, anti-GFP, Invitrogen, A10262, Lot 1972783) at 1:1000 in carrier solution (2% [v/v] NGS, in 0.3% [v/v] Triton X-100 containing PBS). Following 3 rinses of 10 min with PBS, slices were incubated for 3 h at RT in carrier solution (same as above) with an Alexa Fluor® dye-conjugated secondary antibody (goat, anti-chicken Alexa-488, Invitrogen; A11039, Lot 2079383, 1:1000). Slices were washed again, transferred onto glass slides, and mounted for visualization with Shandon Immu-Mount (Thermo Scientific; 9990402).

Confocal images were acquired using a laser-scanning microscope (Zeiss, LSM 900) equipped with a ×40 oil-immersion objective lens (Zeiss EC Plan-Neofluar ×40/1.3 oil). Excitation/emission filters were appropriately selected for Alexa 488 using the dye selection function of the ZEN software. The image acquisition settings were optimized once and kept constant for all images within an experimental data set. Z-stack images were obtained using a 1 µm z-step at a 1024 × 1024-pixel resolution scanning at 8 µs per pixel. Fiji[61] was used to quantify fluorescence intensity values along a line perpendicular to the cell equator and spanning the cell diameter. For each cell, gray values above 80% of the maximum intensity were distributed in 10 bins according to their location along the line.

Slice culture two-photon imaging. Neurons in organotypic slice cultures (DIV 19-21) were imaged with two-photon microscopy to check for the live expression of hSyn-DIO-somBiPOLES-mCerulean, CaMKIIa(0.4)-DO-CheRiff-ts-mScarlet-ER, mDlx-BiPOLES-mCerulean and CaMKIIa(0.4)-somBiPOLES-mCerulean. The custom-built two-photon imaging setup was based on an Olympus BX-51WI upright microscope upgraded with a multiphoton imaging package (DF-Scope, Sutter Instrument), and controlled by ScanImage 2017b software (Vidrio Technologies). Fluorescence was detected through the objective (Leica HC FLUOTAR L 25x/0.95 W VISIR) and through the oil immersion condenser (numerical aperture 1.4, Olympus) by two pairs of GaAsP photomultiplier tubes (Hamamatsu, H11706-40). Dichroic mirrors (560 DXCR, Chroma Technology) and emission filters (ET525/70m-2P, ET605/70m-2P, Chroma Technology) were used to separate cyan and red fluorescence. Excitation light was blocked by short-pass filters (ET700SP-2P, Chroma Technology). A tunable Ti:Sapphire laser (Chameleon Vision-S, Coherent) was set to 810 nm to excite mCerulean on BiPOLES and somBiPOLES. An Ytterbium-doped 1070-nm pulsed fiber laser (Fidelity-2, Coherent) was used at 1070 nm to excite mScarlet on CheRiff. Maximal intensity projections of z-stacks were generated with Fiji[61].

Electrophysiology for two-photon photostimulation of somBiPOLES. At DIV 13–17, whole-cell patch-clamp recordings of somBiPOLES-infected excitatory neurons were performed at room temperature (21– 23 °C). An upright microscope (Scientifica, SliceScope) was equipped with an infrared (IR) source (Thorlabs, M1050L4), oblique condenser, microscope objective (Nikon, CFI APO NIR, ×40, 0.8 NA), tube lens (Thorlabs, AC508-300-B), and a CMOS camera (Point Grey, CM3-U3-31S4M-CS) to collect IR light transmitted through the sample. Recordings were performed using an amplifier (Molecular Devices, Multiclamp 700B), a digitizer (Molecular Devices, Digidata 1550B) at a sampling rate of 10 kHz and controlled using pCLAMP11 (Molecular Devices). During experimental sessions, slice cultures were perfused with artificial cerebrospinal fluid (ACSF) comprised of 125 mM NaCl, 2.5 mM KCl, 1.5 mM $CaCl_2$, 1 mM $MgCl_2$, 26 mM $NaHCO_3$, 0.3 mM ascorbic acid, 25 mM D-glucose, 1.25 mM NaH_2PO_4. Synaptic transmission was blocked during all experiments by the addition of 1 µM AP5 (Abcam, ab120003), 1 µM NBQX (Abcam, ab120046), and 10 µM picrotoxin (Abcam, ab120315) to the extracellular (recording) solution. Continuous aeration of the recording solution with 95% O_2 and 5% CO_2, resulted in a final pH of 7.4. Patch pipettes with a tip resistance of 4–6 MΩ were filled with an intracellular solution consisting of 135 mM K-gluconate, 4 mM KCl, 4 mM Mg-ATP, 0.3 mM Na-GTP, 10 mM Na_2-phosphocreatine, and 10 mM HEPES (pH 7.35). Only recordings with an access resistance below 30 MΩ were included in the subsequent analysis.

During experiments performed using whole-cell voltage clamp, neurons were held at −60 mV (the average resting potential of neurons in hippocampal organotypic slices). The soma of each patched neuron was precisely positioned in the center of the field of view. When recording the photocurrent as a function of membrane potential (holding potentials: −80, −70, −65, −60, −55 mV), neurons were temporarily held at each holding potential 5 s before and after photostimulation. For data presented in Fig. 5a–d, two-photon photoactivation was performed by continuous, 200 ms, illumination of each patched neuron using a 12-µm-diameter holographic spot (wavelengths: 850, 900, 920, 950, 980, 1000, 1050, 1100 nm), which was precisely positioned in the center of the field of view.

Data presented in Fig. 7d–g was acquired in current-clamp experiments. Where necessary, the current was injected to maintain neurons at the resting membrane potential (−60 mV).

The ability of two-photon holographic excitation to evoke action potentials was first assessed using a protocol consisting of 5, 5 ms pulses of 1100 nm light for power densities ranging between 0.16 and 1.00 mW μm^{-2}. The latency and jitter of light-evoked action potentials, respectively defined as the mean and standard deviation of the time between the onset of stimulation to the peak of the action potential, were measured using an identical protocol. Trains of light pulses with frequencies between (2–30 Hz) were used to verify that trains of action potentials could be reliably induced using 5 ms 1100 nm illumination.

The potency of two-photon inhibition was evaluated by measuring the rheobase shift induced by 920 nm illumination. The depolarizing current was injected for 5 ms into recorded neurons (from 0 to 1.2 nA in steps of 20 pA). The protocol was stopped when action potentials were observed for 3 consecutive current steps. The rheobase was defined as the amount of current injected to evoke the first of these 3 action potentials. The rheobase shift was measured by repeating the protocol with co-incident, 5 ms, illumination of the neuron with a 920 nm holographic spot (power densities between 0.05 and 0.25 mW μm^{-2}). Co-incident trains of light pulses (15 ms) and injected current (10 ms) with frequencies between (2–30 Hz) were used to verify that two-photon inhibition could precisely and reliably eliminate single spikes.

Sustained neuronal silencing by two-photon excitation of somBiPOLES under 920 nm illumination was characterized by continuously injecting current above the rheobase for 1 s. The protocol was repeated with 200 ms co-incident illumination using a 920 nm holographic spot (power densities between 0.05 and 0.3 mW μm^{-2}).

Two-photon, bidirectional, control of single neurons was demonstrated by co-incident illumination of titrated 920 nm and 1100 nm light. A 10-Hz train of 15 ms pulses of 1100 nm light was used to evoke a train of action potentials which were shunted using a continuous 200 ms pulse of 920 nm light.

Two-photon photostimulation of somBiPOLES in hippocampal organotypic slices. Two-photon photostimulation was performed using a tunable femtosecond laser (Coherent Discovery, 80 MHz, 100 fs, tuned between 850 and 1100 nm). A schematic diagram of the experimental setup is presented in Supplementary Fig. 10. A telescope formed of two lenses (L1 (Thorlabs, AC508-100-B) and L2 (Thorlabs, AC508-400-B)) expanded the beam onto a Spatial Light Modulator (SLM, Hamamatsu, LCOS 10468-07, 600 × 800 pixels, 20 µm pitch). In the schematic diagram, the reflective SLM is shown as transmissive for illustrative purposes. The SLM, controlled using custom-built software[62], was used to modulate the phase of the beam. Holograms designed to generate 12 µm holographic spots at the focal plane of the microscope were computed using an iterative Gerchberg-Saxton algorithm[63]. The zeroth diffraction order from the SLM was removed using a physical beam block. The modulated field was relayed and de-magnified using a pair of telescopes (formed of lenses L3 (Thorlabs, AC508-750-B), L4 (Thorlabs, AC508-750-B), L5 (Thorlabs, AC508-500-B) and L6 (Thorlabs, AC508-300-B)) to fill the back-aperture of the microscope objective (Nikon, CFI APO NIR, ×40, 0.8 NA) which projected the holograms onto the focal plane. Phase masks were calculated such that holographic spots for the light of different wavelengths overlapped laterally and axially. The anti-reflective coating of the lenses used are optimized for wavelengths 650–1050 nm, and losses incurred at 1100 nm result in the system being power limited at this wavelength. Hence, spectral characterization was performed by normalizing the power density at all wavelengths to the maximum transmitted at 1100 nm. The power incident on the sample plane was adjusted using a high-speed modulator (Thorlabs, OM6NH/M), which was calibrated for each experimental session for each wavelength used, to ensure a photon flux of 6.77×10^{26} photons s^{-1} m^{-2} for all data presented in Fig. 5a. All powers were measured in the object plane using a power meter (Thorlabs, S121C). This experimental configuration was used for all data presented in Fig. 5a, along with all data acquired using 1100 nm illumination. Two-photon inhibition was performed using a femtosecond laser with a fixed wavelength (Spark Alcor, 80 MHz, 100 fs, 920 nm) which was combined with the beam from the tunable laser using a dichroic mirror (Thorlabs, DMLP950R). A liquid crystal variable retarder (Thorlabs, LCC1111-B) and a polarizing beam splitter (Thorlabs, PBS253) were combined to modulate the maximum power of the fixed 920 nm beam independently of that of the tunable laser. The power densities used in each experiment are specified alongside the relevant data in Fig. 5 and Supplementary Fig. 10.

Transgenic *C. elegans* lines and transgenes. The strain ZX417 (*zxEx34[punc17::NpHR-ECFP;punc17::CHOP-2(H134R)::eYFP;rol-6]*) was generated by injection of plasmid DNA (plasmids pRF4 (*rol-6d*), punc-17::NpHR-eCFP, and punc-17::ChR2 (H134R)-eYFP; each at 80 ng/µl) into the germline of *C. elegans* wild-type hermaphrodites. Transgenic animals were picked from the F1 generation and one line (ZX417) was selected out of several transgenic F2 lines for further experiments[33]. For expression in cholinergic neurons of *C. elegans*, BiPOLES (*Gt*ACR2::ts::mCerulean3::βHK::Chrimson) was subcloned into the *punc*-17 vector RM#348p (a gift from Jim Rand) via Gibson Assembly based on the plasmid CMV_*Gt*ACR2_mCerulean_βHK_Chrimson, using the restriction enzyme *Nhe*I and the primers ACR2_Chrimson_fwd (5'-attttcaggaggacccttggATGGCATCACAGGTCGTC-3') and ACR2_Chrimson_rev (5'-ataccatggtaccgtcgacgTCACACTGTGTCCTCGTC-3'), resulting in the construct

pAB26. The respective transgenic strain ZX2586 (wild type; *zxEx1228[punc-17::GtACR2::ts::mCerulean3::βHK::Chrimson; pelt-2::GFP]*), was generated via microinjection[64] of both 30 ng μl^{-1} plasmid and co-marker plasmid DNA *pelt-2::GFP*. Animals were cultivated on nematode growth medium (NGM), seeded with *E. coli* OP-50 strain, in 6 cm Petri dishes. To obtain functional rhodopsins in optogenetic experiments, the OP-50 bacteria were supplemented with all-*trans*-retinal ATR (0.25 μl of a 100 mM stock (in ethanol) mixed with 250 μl OP-50 bacterial suspension).

***C. elegans* stimulation and behavioral experiments**. For body-length measurements, L4 stage transgenic animals were cultivated on ATR plates overnight. Video analysis of light-stimulation protocols provided information on depolarized and hyperpolarized states, based on contracted or relaxed body-wall muscles (BWMs)[65]. Prior to experiments, animals were singled on plain NGM plates to avoid imaging artefacts. They were manually tracked with an Axio Scope.A1 microscope (Zeiss, Germany), using a ×10 objective (Zeiss A-Plan 10x/0,25 Ph1 M27) and a Powershot G9 digital camera (Canon, USA). For light-stimulation of optogenetic tools, transgenic worms were illuminated with 5 s light pulses at 1.1 mW mm^{-2} of different wavelengths as indicated in Fig. 6d (monochromatic light source, Polychrome V, Till Photonics or 100 W HBO mercury lamp with 470/40 ET Bandpass or 575/40 ET Bandpass filters, AHF Analysentechnik), controlled via an Arduino-driven shutter (Sutter Instrument, USA). Videos were processed and analyzed using a custom-written MATLAB script[66] (MathWorks, USA). For the analysis of data, the animals' body length was normalized to the recording period prior to illumination.

Transgenic *D. melanogaster* lines and transgenes. BiPOLES-mCerulean cDNA was cloned via blunt-end ligation into pJFRC7[67]. BILOES was cut with BamHI/HindIII and the vector was cut with NotI/XbaI. A transgenic line inserted into the attP2 site on the 3rd chromosome[68] was generated by phiC31-mediated site-specific transgenesis (FlyORF Injection Service, Zurich, Switzerland). A Gal4 line expressing in glutamatergic neurons including motor neurons (*OK371-Gal4*[11]) was used for locomotion experiments, a Dp7-expressing line (Ilp7-Gal4[34]) was used for mechanonociception experiments.

Locomotion and mechanonociception assays in *D. melanogaster* larvae. *D. melanogaster* larvae were staged in darkness on grape agar plates and fed with yeast paste containing 5 mM all-trans-retinal. Third instar larvae (96 h ± 2 h after egg laying) were used for all experiments.

For locomotion and body length analyses, animals were carefully transferred under minimum red light conditions to a 2% agar film on an FTIR (frustrated total internal reflection) based tracking system (FIM, University of Münster)[69]. Five freely moving larvae/trials were video-captured and stimulated with 470 nm (17 μW mm^{-2}) or 635 nm (25 μW mm^{-2}) light (CoolLED PE4000) for activation of BiPOLES. Animal locomotion was tracked with 10 frames per s for up to 70 s and then body length was analyzed using the FIMtracking software (FIM, University of Münster). For analysis, only animals displaying continuous locomotion before the light stimulus were kept. Larval body length was analyzed over time and was displayed with a 1 s moving average. The body length was normalized to the average of the first 5 s of recording. Relative body length changes during the experiment were then analyzed and plotted.

For mechanonociception, staged larvae were placed on 2% agar plates with a 1 ml water film added. Experiments were performed under minimum light conditions (no activation) with calibrated von-Frey-filaments (50 mN). For activation of BiPOLES, larvae were illuminated during the assay with either 470 nm (17 μW mm^{-2}) or 635 nm (25 μW mm^{-2}). Larvae were stimulated twice on mid-abdominal segments (a3–a6) within 2 s. Behavioral responses (stop and turning, bending, rolling) were noted, analyzed, and plotted. Staging and experiments were done in a blinded and randomized fashion.

Modulation of noradrenergic neurons in the mouse locus coeruleus

Animals. All procedures were in agreement with the German national animal care guidelines and approved by the Hamburg state authority for animal welfare (Behörde für Justiz und Verbraucherschutz) and the animal welfare officer of the University Medical Center Hamburg-Eppendorf. Experiments were performed on mice of either sex between 2.5 and 4 months of age at the start of the experiment. Mice were obtained from The Jackson Laboratory, bred, and maintained at our own colony (12/12 h light-dark cycle, 22 °C room temperature, ~40% relative humidity, food, and water ad libitum). Transgenic mice expressing Cre recombinase in tyrosine hydroxylase positive neurons (TH-Cre, Stock No: 008601)[70] were injected with a suspension of rAAV2/9 viral particles encoding hSyn-DIO-somBiPOLES to target Cre-expressing neurons in the locus coeruleus. Control experiments were performed in non-injected wild-type littermates.

Virus injection and implantation of optic fibers. General anesthesia and analgesia were achieved by intraperitoneal injections of midazolam/medetomidine/fentanyl (5.0/0.5/0.05 mg kg^{-1}, diluted in NaCl). After confirming anesthesia and analgesia by the absence of the hind limb withdrawal reflex, the scalp of the animal was trimmed and disinfected with Iodide solution (Betaisodona; Mundipharma, Germany). The animal was placed on a heating pad to maintain body temperature, fixed in a stereotactic frame, and eye ointment (Vidisic; Bausch + Lomb, Germany) was applied to prevent drying of the eyes. To bilaterally access the LC, an incision (~1 cm) was made along the midline of the scalp, the skull was cleaned, and small craniotomies were drilled −5.4 mm posterior and ±1 mm lateral to Bregma. 0.4 μl of virus suspension were injected into each LC (−3.6 mm relative to Bregma) at a speed of ~100–200 nl min^{-1} using a custom-made air pressure system connected to a glass micropipette. After each injection, the micropipette was left in place for a minimum of 5 min before removal. After virus injection, cannulas housing two ferrule-coupled optical fibers (200 μm core diameter, 0.37 NA, 4 mm length) spaced 2 mm apart (TFC_200/245-0.37_4mm_TS2.0_FLT; Doric Lenses, Canada) were inserted just above the injection site to a depth of −3.5 mm relative to Bregma using a stereotactic micromanipulator. The implant, as well as a headpost for animal fixation during the experiment, were fixed to the roughened skull using cyanoacrylate glue (Pattex; Henkel, Germany) and dental cement (Super Bond C&B; Sun Medical, Japan). The incised skin was glued to the cement to close the wound. Anesthesia was antagonized by intraperitoneally injecting a cocktail of atipamezole/flumazenil/buprenorphine (2.5/0.5/0.1 mg kg^{-1}, diluted in NaCl). Carprofen (4 mg kg^{-1}) was given subcutaneously for additional analgesia and to avoid inflammation. In addition, animals received meloxicam mixed into softened food for 3 days after surgery.

Optogenetic stimulation. Four to six weeks after surgery, mice were habituated to head fixation and placement in a movement-restraining plastic tube for at least one session. Bilateral optogenetic stimulation of LC neurons was achieved by connecting the fiber implant to a 1 × 2 step-index multimode fiber optic coupler (200 μm core diameter, 0.39 NA; TT200SL1A, Thorlabs, Germany) in turn connected to a laser combiner system (LightHUB; Omicron, Germany) housing a 473 nm (LuxX 473-100; Omicron, Germany) and a 594 nm diode laser (Obis 594 nm LS 100 mW; Coherent, Germany) for activation the *Gt*ACR2 and Chrimson components of somBiPOLES, respectively. Coupling to the implant was achieved with zirconia mating sleeves (SLEEVE_ZR_1.25; Doric lenses, Canada) wrapped with black tape to avoid light emission from the coupling interface. Following a habituation period of ~3 min after placing mice in the setup, stimuli were generated and presented using custom-written MATLAB scripts (MathWorks, US) controlling a NI-DAQ-card (PCIe-6323; National Instruments, US) to trigger the lasers via digital input channels. For activation of Chrimson, pulse trains (594 nm, ~10 mW at each fiber end, 20 ms pulse duration, 20 Hz repetition rate) of 4 s duration were presented, while *Gt*ACR2 was activated by continuous illumination (473 nm, ~10 mW at each fiber end) of 2–6 s duration. 30–40 trials of 473 nm pulses, 594 nm pulse trains, and combinations thereof, were presented at an inter-train-interval of 20–30 s in each session.

Data acquisition. A monochrome camera (DMK 33UX249; The Imaging Source, Germany) equipped with a macro objective (TMN 1.0/50; The Imaging Source, Germany) and a 780 nm long-pass filter (FGL780; Thorlabs, Germany) was pointed towards one eye of the mouse. Background illumination was provided with an infrared spotlight (850 nm), while a UV LED (395 nm; Nichia, Japan) was adjusted to maintain pupil dilation of the mouse at a moderate baseline level. Single frames were triggered at 30 Hz by an additional channel of the NI-DAQ-card that controlled optogenetic stimulation, and synchronization was achieved by simultaneous recording of all control voltages and their corresponding timestamps.

Data analysis. Pupil diameter was estimated using a custom-modified, MATLAB-based algorithm developed by McGinley et al.[71]. In short, an intensity threshold was chosen for each recording to roughly separate between pupil (dark) and non-pupil (bright) pixels. For each frame, a circle around the center of mass of putative pupil pixels and with an area equivalent to the number of pupil pixels was then calculated, and putative edge pixels were identified by canny edge detection. Putative edge pixels that were more than 3 pixels away from pixels below the threshold (putative pupil) or outside an area of ±0.25–1.5 times the diameter of the fitted circle were neglected. Using least-squares regression, an ellipse was then fit on the remaining edge pixels, and the diameter of a circle of the equivalent area to this ellipse was taken as the pupil diameter. Noisy frames (e.g., no visible pupil due to blinking or blurry pupil images due to saccades of the animal) were linearly interpolated, and the data was low-passed filtered (<3 Hz; 3rd order Butterworth filter). Pupil data was segmented from 5 s before to 15 s after the onset of each stimulus and normalized to the median pupil diameter of the 5 s preceding the stimulus onset, before individual trials were averaged. Randomly chosen segments of pupil data of the same duration served as a control. The difference in median pupil diameter one second before and after stimulation (as indicated in Fig. 7c) was used to calculate potential changes in pupil diameter for each condition. Statistical significance was calculated using one-way analysis of variance and Tukey's post-hoc multiple comparison tests.

In-vivo recordings from ferret visual cortex. Data were collected from 3 adult female ferrets (*Mustela putorius*). All experiments were approved by the independent Hamburg state authority for animal welfare (Behörde für Justiz und Verbraucherschutz) and were performed in accordance with the guidelines of the German Animal Protection Law and the animal welfare officer of the University Medical Center Hamburg-Eppendorf.

Table 2 Photon flux given as a number of photons s^{-1} m^{-2}.

	Irradiance ($mW\ mm^{-2}$)					
	0.001	**0.01**	**0.1**	**1**	**10**	**100**
Wavelength (nm)						
365	1.84E + 18	1.84E + 19	1.84E + 20	1.84E + 21	1.84E + 22	1.84E + 23
385	1.94E + 18	1.94E + 19	1.94E + 20	1.94E + 21	1.94E + 22	1.94E + 23
405	2.04E + 18	2.04E + 19	2.04E + 20	2.04E + 21	2.04E + 22	2.04E + 23
435	2.19E + 18	2.19E + 19	2.19E + 20	2.19E + 21	2.19E + 22	2.19E + 23
460	2.32E + 18	2.32E + 19	2.32E + 20	2.32E + 21	2.32E + 22	2.32E + 23
470	2.37E + 18	2.37E + 19	2.37E + 20	2.37E + 21	2.37E + 22	2.37E + 23
490	2.47E + 18	2.47E + 19	2.47E + 20	2.47E + 21	2.47E + 22	2.47E + 23
525	2.65E + 18	2.65E + 19	2.65E + 20	2.65E + 21	2.65E + 22	2.65E + 23
550	2.77E + 18	2.77E + 19	2.77E + 20	2.77E + 21	2.77E + 22	2.77E + 23
580	2.92E + 18	2.92E + 19	2.92E + 20	2.92E + 21	2.92E + 22	2.92E +;23
595	3E + 18	3E + 19	3E + 20	3E + 21	3E + 22	3E + 23
630	3.18E + 18	3.18E + 19	3.18E + 20	3.18E + 21	3.18E + 22	3.18E + 23
660	3.33E + 18	3.33E + 19	3.33E + 20	3.33E + 21	3.33E + 22	3.33E + 23

For injection of rAAV2/9 viral particles encoding mDlx-BiPOLES-mCerulean (see Table 2) animals were anesthetized with an injection of ketamine (15 mg kg^{-1}), medetomidine (0.02 mg kg^{-1}), midazolam (0.5 mg kg^{-1}) and atropine (0.15 mg kg^{-1}). Subsequently, they were intubated and respiration with a mixture of 70:30 N_2/O_2 and 1–1.5% isoflurane. A cannula was inserted into the femoral vein to deliver a bolus injection of enrofloxacin (15 mg kg^{-1}) and Rimadyl (4 mg kg^{-1}) and, subsequently, continuous infusion of 0.9% NaCl and fentanyl (0.01 mg kg^{-1} h^{-1}). Body temperature, heart rate, and end-tidal CO_2 were constantly monitored throughout the surgery. Before fixing the animal's head in the stereotaxic frame, a local anesthetic (Lidocaine, 10%) was applied to the external auditory canal. The temporalis muscle was folded back, such that a small craniotomy (ø: 2.5 mm) could be performed over the left posterior cortex and the viral construct was slowly (0.1 µl min^{-1}) injected into the secondary visual cortex (area 18). The excised piece of bone was put back in place and fixed with tissue-safe silicone (Kwikcast; WPI). Also, the temporalis muscle was returned to its physiological position and the skin was closed. After the surgery, the animals received preventive analgesics (Metacam, 0.1 mg) and antibiotics (Enrofloxacin, 15 mg kg^{-1}) for ten days.

After an expression period of at least 4 weeks, recordings of cortical signals were carried out under isoflurane anesthesia. Anesthesia induction and maintenance were similar to the procedures described above, except for a tracheotomy performed to allow for artificial ventilation of the animal over an extended period. The i.v. infusion was supplemented with pancuronium bromide (6 µg kg^{-1} h^{-1}) to prevent slow ocular drifts. To keep the animal's head in a stable position throughout the placement of recording electrodes and the measurements, a headpost was fixed with screws and dental acrylic to the frontal bone of the head. Again, the temporalis muscle was folded back and a portion of the cranial bone was resected. The dura was removed before introducing an optrode with 32 linearly distributed electrodes (A1x32-15mm-50(100)-177, NeuroNexus Technologies) into the former virus-injection site (area 18). The optrode was manually advanced via a micromanipulator (David Kopf Instruments) under visual inspection until the optic fiber was positioned above the pial surface and the uppermost electrode caught a physiological signal, indicating that it had just entered the cortex.

During electrophysiological recordings, the isoflurane level was maintained at 0.7%. To ensure controlled conditions for sensory stimulation, all experiments were carried out in a dark, sound-attenuated anechoic chamber (Acoustair, Moerkapelle, Netherlands). Visual stimuli were created via an LED placed in front of the animal's eye. In separate blocks, 150 laser stimuli of different colors ('red', 633 nm LuxXplus and 'blue', 473 nm LuxXplus, LightHub-4, Omicron) were applied through the optrode for 500 ms, each, at a variable interval of 2.5–3 s. Randomly, 75 laser stimuli were accompanied by a 10 ms LED flash, starting 100 ms after the respective laser onset. For control, one block of 75 LED flashes alone was presented at comparable interstimulus intervals.

Electrophysiological signals were sampled with an AlphaLab SnR recording system (Alpha Omega Engineering, Nazareth, Israel) or with a self-developed neural recording system based on INTAN digital head-stages (RHD2132, Intantech). Signals recorded from the intracortical laminar probe were band-pass filtered between 0.5 Hz and 7.5 kHz and digitized at 22–44 kHz or 25 kHz, respectively. All analyses of neural data presented in this study were performed offline after the completion of experiments using MATLAB scripts (MathWorks). To extract multiunit spiking activity (MUA) from broadband extracellular recordings, we high-pass filtered signals at 500 Hz and detected spikes at negative threshold (>3.5 SD)[72].

Reporting summary. Further information on research design is available in the Nature Research Reporting Summary linked to this article.

Data availability

Source data are provided with this paper. All data generated in this study are provided in the Source Data file. Source data are provided with this paper.

Received: 2 May 2021; Accepted: 29 June 2021;
Published online: 26 July 2021

References

1. Chen, I. W., Papagiakoumou, E. & Emiliani, V. Towards circuit optogenetics. *Curr. Opin. Neurobiol.* **50**, 179–189 (2018).
2. Kleinlogel, S. et al. A gene-fusion strategy for stoichiometric and co-localized expression of light-gated membrane proteins. *Nat. Methods* **8**, 1083–1088 (2011).
3. Tang, W. et al. Faithful expression of multiple proteins via 2A-peptide self-processing: a versatile and reliable method for manipulating brain circuits. *J. Neurosci.* **29**, 8621–8629 (2009).
4. Gradinaru, V. et al. Molecular and cellular approaches for diversifying and extending optogenetics. *Cell* **141**, 154–165 (2010).
5. Gradinaru, V. et al. Targeting and readout strategies for fast optical neural control in vitro and in vivo. *J. Neurosci.* **27**, 14231–14238 (2007).
6. Carus-Cadavieco, M. et al. Gamma oscillations organize top-down signalling to hypothalamus and enable food seeking. *Nature* **542**, 232–236 (2017).
7. Rashid, A. J. et al. Competition between engrams influences fear memory formation and recall. *Science* **353**, 383–387 (2016).
8. Vesuna, S. et al. Deep posteromedial cortical rhythm in dissociation. *Nature* **586**, 87–94 (2020).
9. Heikenfeld, C. et al. Prefrontal-subthalamic pathway supports action selection in a spatial working memory task. *Sci. Rep.* **10**, 10497 (2020).
10. Mohammad, F. et al. Optogenetic inhibition of behavior with anion channelrhodopsins. *Nat. Methods* **14**, 271–274 (2017).
11. Wietek, J. et al. Anion-conducting channelrhodopsins with tuned spectra and modified kinetics engineered for optogenetic manipulation of behavior. *Sci. Rep.* **7**, 14957 (2017).
12. Klapoetke, N. C. et al. Independent optical excitation of distinct neural populations. *Nat. Methods* **11**, 338–346 (2014).
13. Yizhar, O. et al. Neocortical excitation/inhibition balance in information processing and social dysfunction. *Nature* **477**, 171–178 (2011).
14. Akerboom, J. et al. Genetically encoded calcium indicators for multi-color neural activity imaging and combination with optogenetics. *Front. Mol. Neurosci.* **6**, 2 (2013).
15. Erbguth, K., Prigge, M., Schneider, F., Hegemann, P. & Gottschalk, A. Bimodal activation of different neuron classes with the spectrally red-shifted channelrhodopsin chimera C1V1 in Caenorhabditis elegans. *PLoS ONE* **7**, e46827 (2012).

16. Stujenske, J. M., Spellman, T. & Gordon, J. A. Modeling the spatiotemporal dynamics of light and heat propagation for in vivo optogenetics. *Cell Rep.* **12**, 525–534 (2015).
17. Yizhar, O., Fenno, L. E., Davidson, T. J., Mogri, M. & Deisseroth, K. Optogenetics in neural systems. *Neuron* **71**, 9–34 (2011).
18. Govorunova, E. G., Sineshchekov, O. A., Janz, R., Liu, X. & Spudich, J. L. NEUROSCIENCE. Natural light-gated anion channels: A family of microbial rhodopsins for advanced optogenetics. *Science* **349**, 647–650 (2015).
19. Berndt, A. et al. Structural foundations of optogenetics: determinants of channelrhodopsin ion selectivity. *Proc. Natl Acad. Sci. USA* **113**, 822–829 (2016).
20. Rajasethupathy, P. et al. Projections from neocortex mediate top-down control of memory retrieval. *Nature* **526**, 653–659 (2015).
21. Mager, T. et al. High frequency neural spiking and auditory signaling by ultrafast red-shifted optogenetics. *Nat. Commun.* **9**, 1750 (2018).
22. Marshel, J. H. et al. Cortical layer-specific critical dynamics triggering perception. *Science* **365**, https://doi.org/10.1126/science.aaw5202 (2019).
23. Batabyal, S., Cervenka, G., Ha, J. H., Kim, Y. T. & Mohanty, S. Broad-band activatable white-opsin. *PLoS ONE* **10**, e0136958 (2015).
24. Bansal, H., Gupta, N. & Roy, S. Theoretical analysis of low-power bidirectional optogenetic control of high-frequency neural codes with single spike resolution. *Neuroscience* **449**, 165–188 (2020).
25. Sineshchekov, O. A. et al. Conductance mechanisms of rapidly desensitizing cation channelrhodopsins from cryptophyte algae. *mBio* **11**, https://doi.org/10.1128/mBio.00657-20 (2020).
26. Sudo, Y. et al. A blue-shifted light-driven proton pump for neural silencing. *J. Biol. Chem.* **288**, 20624–20632 (2013).
27. Lim, S. T., Antonucci, D. E., Scannevin, R. H. & Trimmer, J. S. A novel targeting signal for proximal clustering of the Kv2.1 K+ channel in hippocampal neurons. *Neuron* **25**, 385–397 (2000).
28. Mahn, M. et al. High-efficiency optogenetic silencing with soma-targeted anion-conducting channelrhodopsins. *Nat. Commun.* **9**, 4125 (2018).
29. Messier, J. E., Chen, H., Cai, Z. L. & Xue, M. Targeting light-gated chloride channels to neuronal somatodendritic domain reduces their excitatory effect in the axon. *eLife* **7**, https://doi.org/10.7554/eLife.38506 (2018).
30. Hochbaum, D. R. et al. All-optical electrophysiology in mammalian neurons using engineered microbial rhodopsins. *Nat. Methods* **11**, 825–833 (2014).
31. Mardinly, A. R. et al. Precise multimodal optical control of neural ensemble activity. *Nat. Neurosci.* **21**, 881–893 (2018).
32. Ronzitti, E. et al. Submillisecond optogenetic control of neuronal firing with two-photon holographic photoactivation of Chronos. *J. Neurosci.* **37**, 10679–10689 (2017).
33. Zhang, F. et al. Multimodal fast optical interrogation of neural circuitry. *Nature* **446**, 633–639 (2007).
34. Hu, C. et al. Sensory integration and neuromodulatory feedback facilitate Drosophila mechanonociceptive behavior. *Nat. Neurosci.* **20**, 1085–1095 (2017).
35. Breton-Provencher, V. & Sur, M. Active control of arousal by a locus coeruleus GABAergic circuit. *Nat. Neurosci.* **22**, 218–228 (2019).
36. Dimidschstein, J. et al. A viral strategy for targeting and manipulating interneurons across vertebrate species. *Nat. Neurosci.* **19**, 1743–1749 (2016).
37. Mahn, M., Prigge, M., Ron, S., Levy, R. & Yizhar, O. Biophysical constraints of optogenetic inhibition at presynaptic terminals. *Nat. Neurosci.* **19**, 554–556 (2016).
38. Stierl, M. et al. Light modulation of cellular cAMP by a small bacterial photoactivated adenylyl cyclase, bPAC, of the soil bacterium Beggiatoa. *J. Biol. Chem.* **286**, 1181–1188 (2011).
39. Moeyaert, B. et al. Improved methods for marking active neuron populations. *Nat. Commun.* **9**, 4440 (2018).
40. Perez-Alvarez, A. et al. Freeze-frame imaging of synaptic activity using SynTagMA. *Nat. Commun.* **11**, 2464 (2020).
41. Kato, H. E. et al. Crystal structure of the channelrhodopsin light-gated cation channel. *Nature* **482**, 369–374 (2012).
42. Volkov, O. et al. Structural insights into ion conduction by channelrhodopsin 2. *Science* **358**, https://doi.org/10.1126/science.aan8862 (2017).
43. Oda, K. et al. Crystal structure of the red light-activated channelrhodopsin Chrimson. *Nat. Commun.* **9**, 3949 (2018).
44. Kim, Y. S. et al. Crystal structure of the natural anion-conducting channelrhodopsin GtACR1. *Nature* **561**, 343–348 (2018).
45. Baker, C. A., Elyada, Y. M., Parra, A. & Bolton, M. M. Cellular resolution circuit mapping with temporal-focused excitation of soma-targeted channelrhodopsin. *eLife* **5**, https://doi.org/10.7554/eLife.14193 (2016).
46. Forli, A. et al. Two-photon bidirectional control and imaging of neuronal excitability with high spatial resolution in vivo. *Cell Rep.* **22**, 3087–3098 (2018).
47. Shemesh, O. A. et al. Temporally precise single-cell-resolution optogenetics. *Nat. Neurosci.* **20**, 1796–1806 (2017).
48. Douin, V. et al. Use and comparison of different internal ribosomal entry sites (IRES) in tricistronic retroviral vectors. *BMC Biotechnol.* **4**, 16 (2004).
49. Wiegert, J. S., Mahn, M., Prigge, M., Printz, Y. & Yizhar, O. Silencing neurons: tools, applications, and experimental constraints. *Neuron* **95**, 504–529 (2017).
50. Mahn, M. et al. Efficient optogenetic silencing of neurotransmitter release with a mosquito rhodopsin. *Neuron* **109**, 1621–1635 e1628 (2021).
51. Copits, B. A. et al. A photoswitchable GPCR-based opsin for presynaptic inhibition. *Neuron* https://doi.org/10.1016/j.neuron.2021.04.026 (2021).
52. Lima, S. Q., Hromadka, T., Znamenskiy, P. & Zador, A. M. PINP: a new method of tagging neuronal populations for identification during in vivo electrophysiological recording. *PLoS ONE* **4**, e6099 (2009).
53. Ramirez, S. et al. Creating a false memory in the hippocampus. *Science* **341**, 387–391 (2013).
54. Markwardt, M. L. et al. An improved cerulean fluorescent protein with enhanced brightness and reduced reversible photoswitching. *PLoS ONE* **6**, e17896 (2011).
55. Dittgen, T. et al. Lentivirus-based genetic manipulations of cortical neurons and their optical and electrophysiological monitoring in vivo. *Proc. Natl Acad. Sci. USA* **101**, 18206–18211 (2004).
56. Grimm, C., Vierock, J., Hegemann, P. & Wietek, J. Whole-cell patch-clamp recordings for electrophysiological determination of ion selectivity in Channelrhodopsins. *J. Vis. Exp.* https://doi.org/10.3791/55497 (2017).
57. Gee, C. E., Ohmert, I., Wiegert, J. S. & Oertner, T. G. Preparation of slice cultures from rodent Hippocampus. *Cold Spring Harb. Protoc.* **2017**, pdb prot094888 (2017).
58. Wiegert, J. S., Gee, C. E. & Oertner, T. G. Single-cell electroporation of neurons. *Cold Spring Harb. Protoc.* **2017**, pdb prot094904 (2017).
59. Wiegert, J. S., Gee, C. E. & Oertner, T. G. Viral vector-based transduction of slice cultures. *Cold Spring Harb. Protoc.* **2017**, pdb prot094896 (2017).
60. Booker, S. A. & Vida, I. Morphological diversity and connectivity of hippocampal interneurons. *Cell Tissue Res.* **373**, 619–641 (2018).
61. Schindelin, J. et al. Fiji: an open-source platform for biological-image analysis. *Nat. Methods* **9**, 676–682 (2012).
62. Lutz, C. et al. Holographic photolysis of caged neurotransmitters. *Nat. Methods* **5**, 821–827 (2008).
63. Gerchberg, R. W. & Saxton, W. O. Practical algorithm for determination of phase from image and diffraction plane pictures. *Optik* **35**, 237–+ (1972).
64. Fire, A. Integrative transformation of Caenorhabditis elegans. *Embo J.* **5**, 2673–2680 (1986).
65. Liewald, J. F. et al. Optogenetic analysis of synaptic function. *Nat. Methods* **5**, 895–902 (2008).
66. Stephens, G. J., Johnson-Kerner, B., Bialek, W. & Ryu, W. S. Dimensionality and dynamics in the behavior of C. elegans. *PLoS Comput. Biol.* **4**, e1000028 (2008).
67. Pfeiffer, B. D. et al. Refinement of tools for targeted gene expression in Drosophila. *Genetics* **186**, 735–755 (2010).
68. Groth, A. C., Fish, M., Nusse, R. & Calos, M. P. Construction of transgenic Drosophila by using the site-specific integrase from phage phiC31. *Genetics* **166**, 1775–1782 (2004).
69. Risse, B. et al. FIM, a novel FTIR-based imaging method for high throughput locomotion analysis. *PLoS ONE* **8**, e53963 (2013).
70. Savitt, J. M., Jang, S. S., Mu, W., Dawson, V. L. & Dawson, T. M. Bcl-x is required for proper development of the mouse substantia nigra. *J. Neurosci.* **25**, 6721–6728 (2005).
71. McGinley, M. J., David, S. V. & McCormick, D. A. Cortical membrane potential signature of optimal states for sensory signal detection. *Neuron* **87**, 179–192 (2015).
72. Quiroga, R. Q., Nadasdy, Z. & Ben-Shaul, Y. Unsupervised spike detection and sorting with wavelets and superparamagnetic clustering. *Neural Comput.* **16**, 1661–1687 (2004).

Acknowledgements

We thank Stefan Schillemeit and Tharsana Tharmalingam for excellent technical assistance, Mathew McGinley and Peter Murphy for help with pupil analysis, and Sonja Kleinlogel for providing plasmids carrying the original opsin tandem. We also thank Karl Deisseroth and Charu Ramakrishnan for providing the plasmids and coding sequences of bReaChES and eNPAC2.0, as well as for providing the ChRmine plasmid and coding sequence in advance of publication. We further thank Jonas Wietek for providing ACR plasmids and for discussions at an early phase of the project. Ingke Braren of the UKE Vector Facility produced AAV vectors. This work was supported by the German Research Foundation, DFG (SPP1926, FOR2419/P6, SFB936/B8 to J.S.W., SFB936/A2 and SPP2041/EN533/15-1 to A.K.E., SPP1926 and SFB1315 to P.H., SFB807/P11 to A.C.F.B. and A.G.), the 'Agence Nationale de la Recherche' (CE16-2019 HOLOPTOGEN, CE16-0021 SLALLOM, ANR-10-LABX-65 LabEx LIFESENSES, and ANR-18-IAHU-01 *IHU FOReSIGHT to V.E.), the AXA research foundation and the European Research Council (ERC2016-StG-714762 to J.S.W., HOLOVIS-AdG to V.E., Stardust H2020 767092 to P.H.). Peter Hegemann is a Hertie Professor and supported by the Hertie Foundation.

Author contributions

Conceptualization: J.V., S.R.R., P.H., J.S.W.; investigation: J.V., S.R.R., A.D., F.P., R.S., F.T., A.C.F.B., I.B., F.Z., N.Z., J.A., S.A., K.S., J.S.W.; data curation: J.V., S.R.R., A.D., F.P.,

R.S., F.T., A.C.F.B., J.A.; analysis: J.V., S.R.R., A.D., F.P., R.S., F.T., A.C.F.B., I.B., F.Z., J.A., J.S.W.; software: A.D., F.P.; supervision: E.P., A.G., P.S., V.E., A.K.E., P.H., J.S.W.; funding acquisition: E.P., A.G., P.S., V.E., A.K.E., P.H., J.S.W.; project administration: P.H., J.S.W.; writing: J.V., S.R.R., F.P., R.S., J.S.W. with contributions from all authors.

Funding
Open Access funding enabled and organized by Projekt DEAL.

Competing interests
The authors declare no competing interests.

Additional information
Supplementary information The online version contains supplementary material available at https://doi.org/10.1038/s41467-021-24759-5.

Correspondence and requests for materials should be addressed to J.S.W.

Peer review information *Nature Communications* thanks Ute Hochgeschwender, Adam Packer and the other, anonymous, reviewer(s) for their contribution to the peer review of this work. Peer reviewer reports are available.

BiPOLES is an optogenetic tool developed for bidirectional dual-color control of neurons

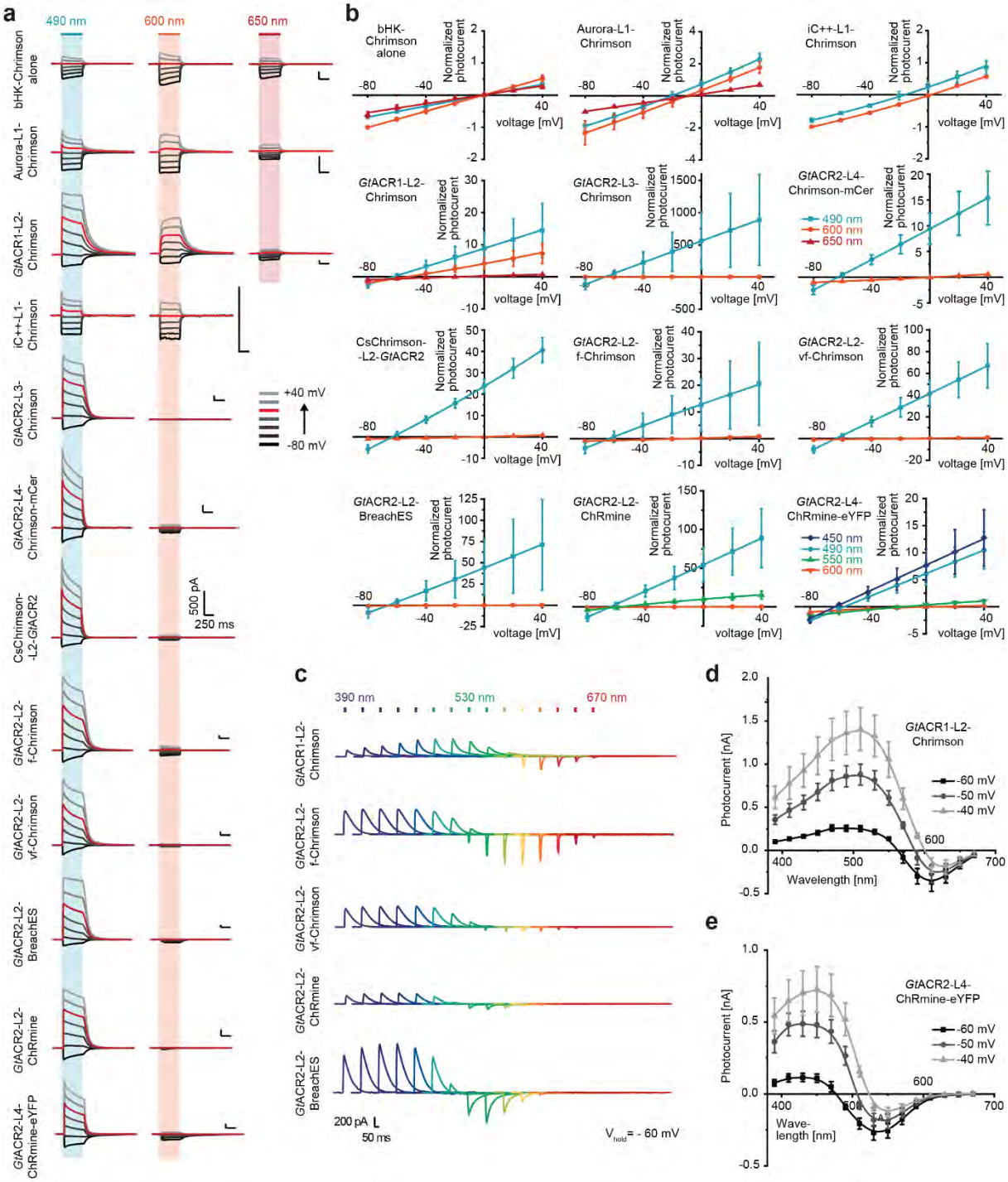

Supplementary Fig. 1. Biophysical characterization of different ACR-CCR tandem constructs. (a) Representative photocurrents of ßHK-Chrimson and different tandem constructs as described in Fig. 1a. **(b)** Normalized peak photocurrents of ßHK-Chrimson and tandem constructs at different membrane voltages evoked at 450 nm, 490 nm, 530 nm or 600 nm (see panel (a), mean ± SD; n indicates number of independent cells. n = 4 for ßHK-Chrimson; n = 5 for Aurora-L1-Chrimson, *Cs*Chrimson-L2-*Gt*ACR2 and *Gt*ACR2-L2-f-Chrimson; n = 6 for *Gt*ACR2, *Gt*ACR1-L2-Chrimson and *Gt*ACR2-L2-vf-Chrimson; n = 7 for iC++-L1-Chrimson, *Gt*ACR2-L3-Chrimson, *Gt*ACR2-L4-Chrimson-mCer, *Gt*ACR2-L2-BreachES and *Gt*ACR2-L2-ChRmine; n = 8 for *Gt*ACR2-L2-Chrimson and n = 9 for *Gt*ACR2-L4-ChRmine-ts-eYFP-er); normalized to the peak photocurrent at -80 mV and 600 nm illumination). **(c)** Representative photocurrents of different ACR-CCR tandems with 10 ms light pulses at indicated wavelengths and equal photon flux at -60 mV. **(d, e)** Action spectra of *Gt*ACR1-L2-Chrimson and *Gt*ACR2-L4-ChRmine-

TS-eYFP-ER at different membrane voltages (mean ± SEM, n = 6 for *Gt*ACR1-L2-Chrimson and n = 8 for *Gt*ACR2-L4-ChRmine-TS-eYFP-ER). The data presented in this figure are provided in the Source Data file.

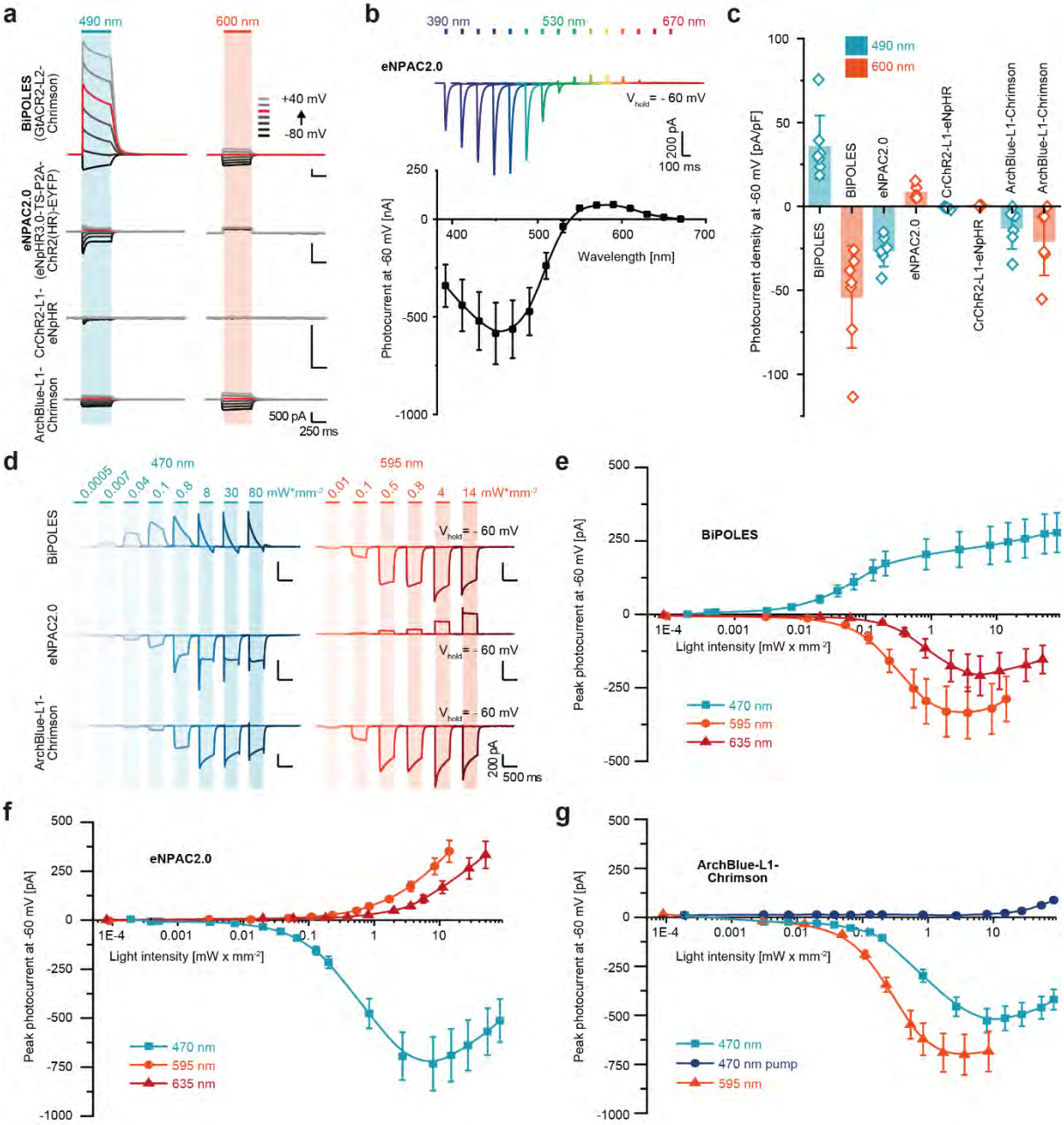

Supplementary Fig. 2. Comparison of BiPOLES to established bidirectional optogenetic tools in HEK293 cells. (a) From top to bottom: representative photocurrents of BiPOLES, eNPAC2.0 (eNpHR3.0-TS-p2A-*Cr*ChR2(H134R)-EYFP), *Cr*ChR2-L1-eNpHR[2] and ArchBlue-L1-Chrimson in whole-cell patch clamp recordings from HEK293 cells at 490 nm and 600 nm illumination. ArchBlue stands for the blue shifted mutant of Arch3.0[26]. **(b)** Top: Representative photocurrents of eNPAC2.0 with 10 ms light pulses at indicated wavelengths and equal photon flux at -60 mV. Bottom: Action spectrum of eNPAC2.0 at -60 mV (mean ± SEM, n = 5). **(c)** Peak photocurrent densities for 490 nm and 600 nm excitation at -60 mV (close to the neuronal resting potential) as shown in (a) (Mean ± SD; n indicates number of independent cells. n = 5 for *Cr*ChR2-L1-NpHR; n = 6 for ArchBlue-L1-Chrimson and eNPAC2.0, n = 7 for BiPOLES). **(d)** Representative photocurrents of BiPOLES (top), eNPAC2.0(middle) and ArchBlue-L1-Chrimson (bottom) at -60 mV and different irradiances and wavelengths. **(e-g)** Peak photocurrents at different irradiances, different excitation wavelength and -60 mV according to (d). (mean ± SEM, n = 4 for ArchBlue-L1-Chrimson and n = 6 for BiPOLES and eNPAC2.0) 6). Pump currents at 470 nm in (g) describe the initial outward currents observed directly after blue light switching in (d). The data presented in this figure are provided in the Source Data file.

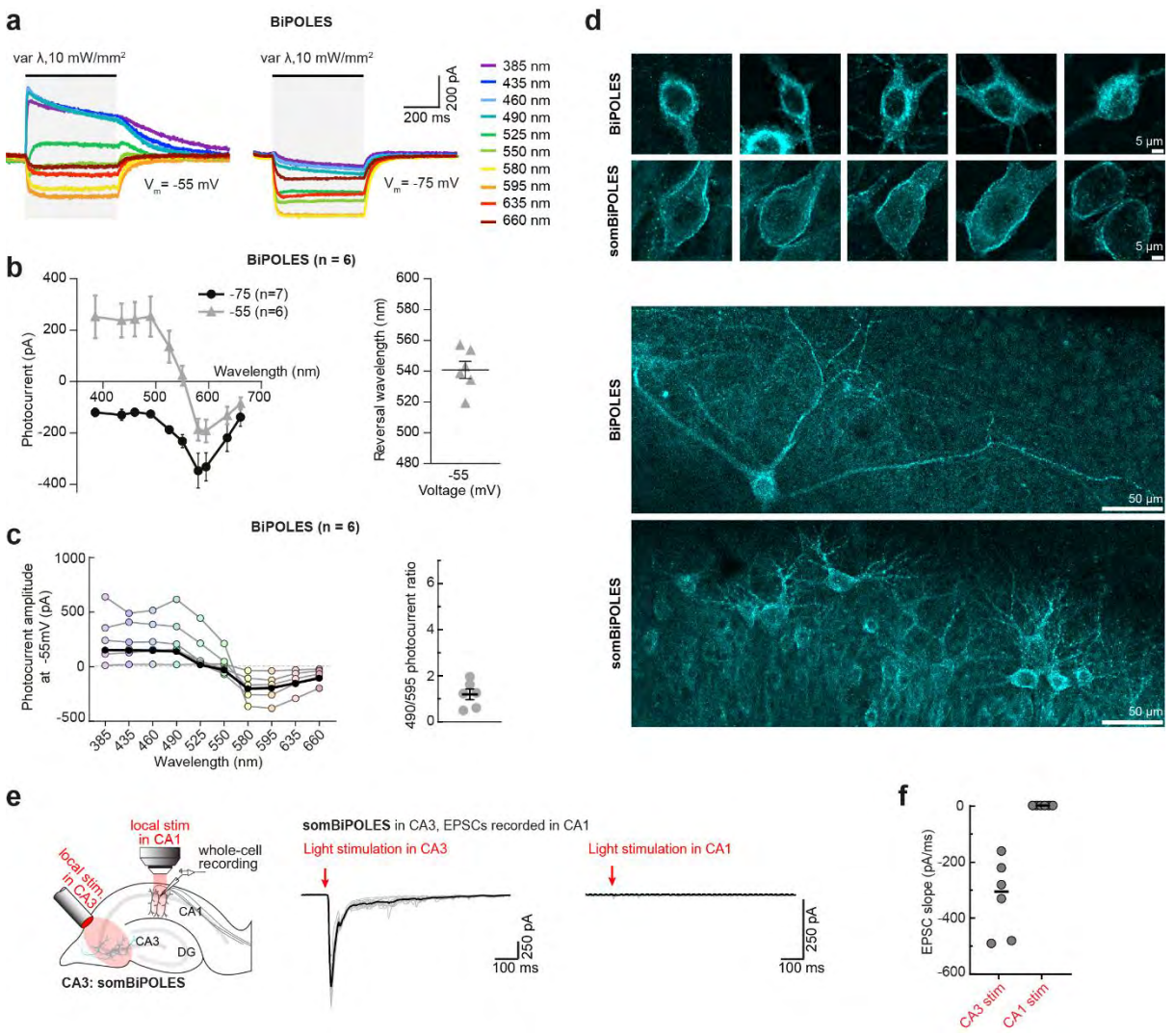

Supplementary Fig. 3. Biophysical characterization of BiPOLES and differential expression of BiPOLES and somBiPOLES in CA1 pyramidal neurons. (a) Representative photocurrent traces of BiPOLES in CA1 pyramidal neurons upon illumination with different wavelengths and equal photon flux at membrane voltages above (left) and below (right) the chloride Nernst potential. **(b)** Left: Quantification of photocurrent amplitude along the spectrum at a membrane voltage of -55 mV (grey) and -75 mV (black). Symbols indicate mean ± SEM and lines are interpolations of data points ($n_{-55\ mV}$ = 6 cells, $n_{-75\ mV}$ = 7 cells). Similar to HEK-cell measurements, inward and outward photocurrents were evoked with 635 nm and 490 nm at a membrane voltage between the chloride and proton Nernst potentials, respectively, indicative of independently evoked Chrimson- and *Gt*ACR2-photocurrents. Right: Quantification of photocurrent reversal wavelength at -55 mV (mean ± SEM, n = 6 cells). **(c)** Left: Quantification of photocurrent amplitudes at -55 mV (same data as in (b) but showing individual data points for each wavelength, black circles: medians, n = 6 cells). Right: Ratio of inhibitory (490 nm) over excitatory (595 nm) photocurrents (mean ± SEM, n = 6 cells). Note that, unlike for eNPAC2.0 (Supplementary Fig. 8a) the photocurrent ratio shows little variability between cells, indicating a reproducible stoichiometry of Chrimson and *Gt*ACR2 currents. **(d)** Maximum-intensity projections of confocal images showing expression of BiPOLES or soma-targeted BiPOLES (somBiPOLES) in CA3 pyramidal neurons of organotypic hippocampal slices. For each opsin 5 representative neurons from 5 organotypic slices are shown (top rows).. Bottom: lower-magnification example images of CA3 neurons in *stratum oriens* show confinement of somBiPOLES to soma and proximal dendrites. These images were not used for quantitative analysis. CA3 cells were transduced with an AAV9 encoding for either BiPOLES or somBiPOLES and fixed after 20 days. Fluorescence was enhanced by an antibody staining against the fluorophore mCerulean. **(e)** Left: Schematic drawing depicting the experiment used to verify

absence of somBiPOLES-expression in axon terminals of CA3 cells. Whole-cell voltage-clamp recordings were done in postsynaptic CA1 cells to determine red-light evoked EPSCs. Illumination was done locally either in CA3 at the somata or in CA1 at axon terminals of somBiPOLES-expressing CA3 cells. Axon stimulation was done in the presence of TTX to avoid antidromic spiking of CA3 cells and 4-AP to inhibit K^+-mediated fast repolarization. Middle: Example voltage-clamp recordings from CA1 cells upon red-light stimulation in CA3. Right: example voltage-clamp recordings from CA1 cells upon red-light stimulation of axon terminals in CA1. Black lines show average response of 10 repetitions (grey lines). **(f)** Quantification of experiment shown in (e) (black lines: medians, no error bars shown, n = 6 cells). The absence of somBiPOLES-mediated EPSCs upon local illumination in CA1, indicates efficient exclusion of somBiPOLES from the axon terminals, despite strong membrane expression in the somatodendritic compartment, which was evident from large EPSCs upon local illumination in CA3. The data presented in this figure are provided in the Source Data file.

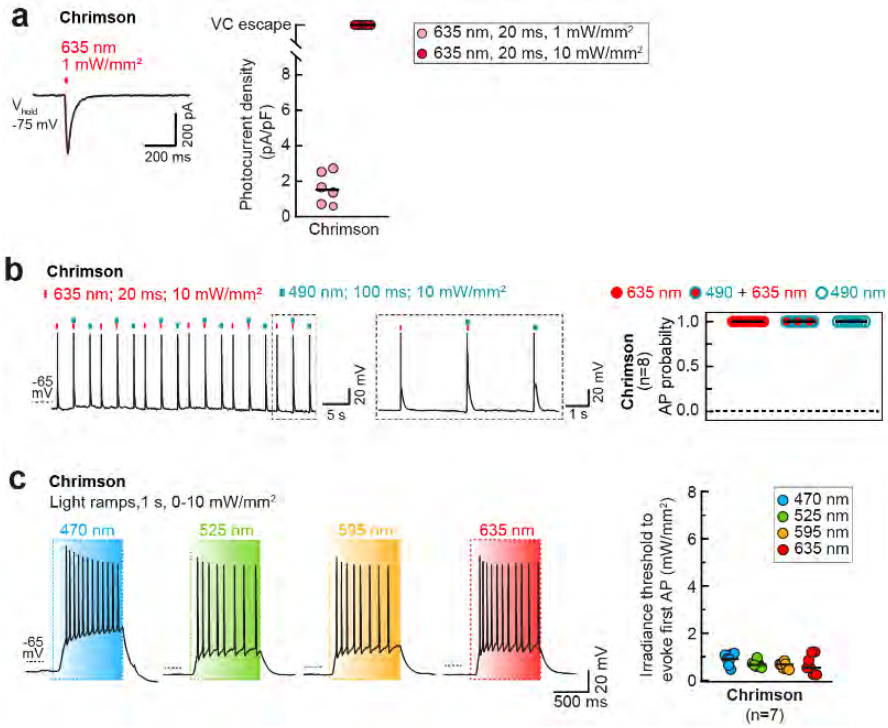

Supplementary Fig. 4. Characterization of Chrimson-mediated currents and spiking in CA1 pyramidal cells. (a) Left: Representative photocurrent trace evoked by a 635 nm light pulse (20 ms, 1 mW mm^{-2}) recorded in a Chrimson-expressing CA1 pyramidal neuron at a membrane voltage of -75 mV. Right: Quantification of photocurrent densities evoked under the indicated conditions (black horizontal lines: medians, n = 6 cells). **(b)** Left: Voltage traces showing red- and blue-light-evoked APs. Right: Quantification of AP probability under indicated conditions (black horizontal lines: medians, n = 8 cells). Note that blue light does not elicit APs in somBiPOLES-expressing cells due to *Gt*ACR2-mediated shunting (see Fig. 4b). **(c)** Spectral quantification of the irradiance threshold for AP generation with Chrimson. Left: Representative membrane voltage traces during light ramps at indicated wavelengths with irradiance increasing linearly from 0 to 10 mW mm^{-2}. Right: Quantification of the irradiance threshold at which the first AP was evoked (black horizontal lines: medians, n = 7 cells). Datasets for 470 and 595 nm are the same as shown in Fig. 3e. The data presented in this figure are provided in the Source Data file.

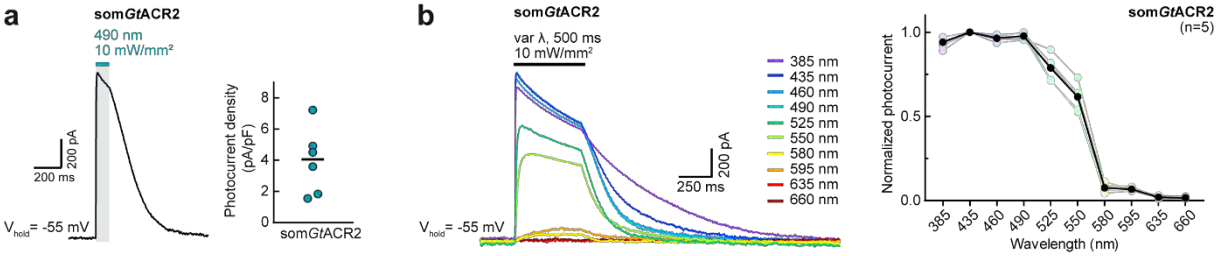

Supplementary Fig. 5. Quantification of som*Gt*ACR2-mediated photocurrents in CA1 pyramidal cells. (a) Left: Representative photocurrent trace evoked by a 490 nm light pulse (100 ms, 10 mW mm^{-2}) recorded in a som*Gt*ACR2-expressing CA1 pyramidal neuron at -55 mV, 20 mV more positive than the chloride Nernst potential. Right: Quantification of photocurrent densities evoked under the indicated conditions (black horizontal lines: medians, n = 6 cells). **(b)** Left: Representative photocurrent traces upon illumination with different wavelengths and equal photon flux at a membrane voltage of -55 mV. Right: Normalized photocurrent amplitude along the spectrum (black circles: medians, n = 5 cells). The data presented in this figure are provided in the Source Data file.

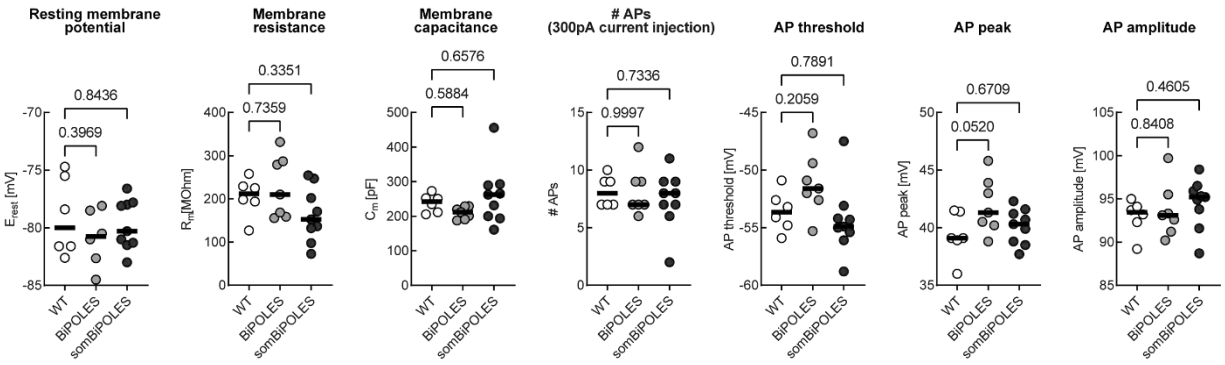

Supplementary Fig. 6: Basic neuronal parameters of WT, BiPOLES- and somBiPOLES-expressing CA1 pyramidal cells. The following parameters were measured to asses cell viability and tolerability of BiPOLES and somBiPOLES: resting membrane potential, membrane resistance, membrane capacitance, number of APs evoked by somatic current injection (300 pA, 500 ms), voltage threshold, peak voltage and AP amplitude of the 1st AP elicited by somatic current injection (black lines: medians, WT n = 6 cells, BiPOLES n = 7 cells, somBiPOLES n = 9 cells, one-way ANOVA, exact P-values are shown). The data presented in this figure and details on the statistical analysis are provided in the Source Data file.

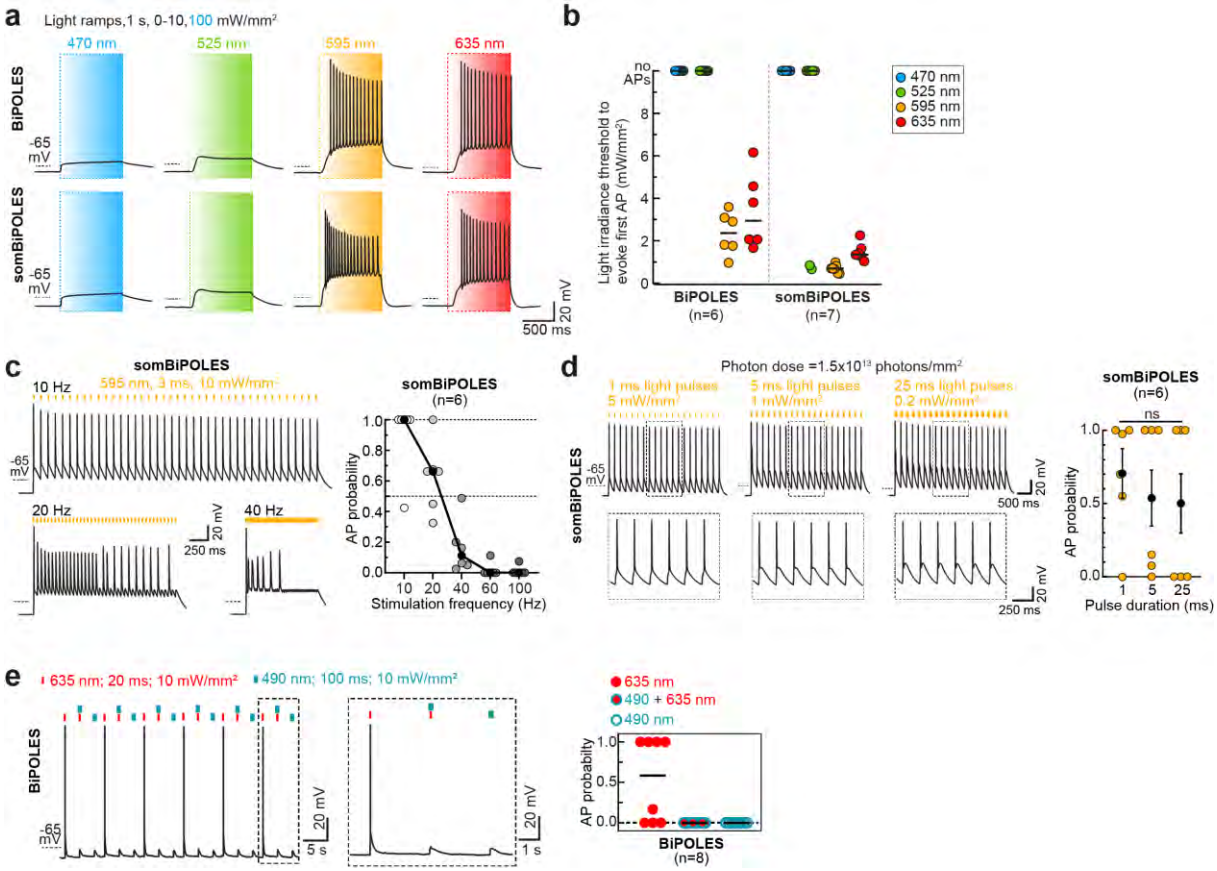

Supplementary Fig. 7. Optical spiking parameters for BiPOLES and somBiPOLES. (a,b) Spectral quantification of action potential threshold for BiPOLES and somBiPOLES. **(a)** Representative membrane voltage traces measured in BiPOLES- (top), or somBiPOLES-expressing CA1 pyramidal neurons (bottom). In IC experiments, light ramps of different wavelengths were applied as indicated. The irradiance was ramped linearly from 0 to 10 mW mm^{-2} over 1 s, except for 470-nm ramps, which were ranging to 100 mW mm^{-2} to rule out the possibility that high-intensity blue light might still evoke action potentials. **(b)** Quantification of the irradiance threshold at which the first action potential was evoked. 470-nm light up to 100 mW mm^{-2} did not evoke action potentials in BiPOLES or somBiPOLES-expressing cells. The irradiance threshold for 595 and 635 nm illumination was lower in somBiPOLES-expressing cells compared to BiPOLES-expressing cells indicating higher light sensitivity in the former (black horizontal lines: medians, $n_{BiPOLES}$ = 6 cells, $n_{somBiPOLES}$ =7 cells). somBiPOLES data for 470 and 595 nm are the same as in Fig. 3d. **(c)** Left: membrane voltage traces at different light-pulse frequencies in CA1 cells expressing somBiPOLES. APs were triggered by 40 pulses (λ = 595 nm, pulse width = 3 ms, 10 mW mm^{-2}). Right: Quantification of AP probability at increasing stimulation frequencies (from 10 to 100 Hz, black circles: medians, n = 6 cells). To determine AP probability, the number of light-triggered APs was divided by the total number of light pulses. **(d)** Left: membrane voltage traces at different light-pulse widths (1, 5 and 25 ms) and irradiances (5, 1, and 0.2 mW mm^{-2}, respectively). In all conditions the photon dose was kept constant at 1.5x10^{13} photons/mm^2. Magnified views of the traces are shown below. Note the different shapes of the sub-threshold membrane voltages evoked by the respective combination of parameters. Right: Quantification of AP probability at indicated light stimulation condition (black circles: mean ± SEM, n = 6 cells). **(e)** All-optical excitation and inhibition with BiPOLES. Current-clamp characterization of bidirectional optical spiking-control with BiPOLES. Left: Voltage traces showing red-light-evoked action potentials (APs), which were blocked by a concomitant blue light pulse. Right: quantification of AP probability under indicated conditions (black horizontal lines: medians, n = 8 cells). The data presented in this figure and details on the statistical analysis are provided in the Source Data file.

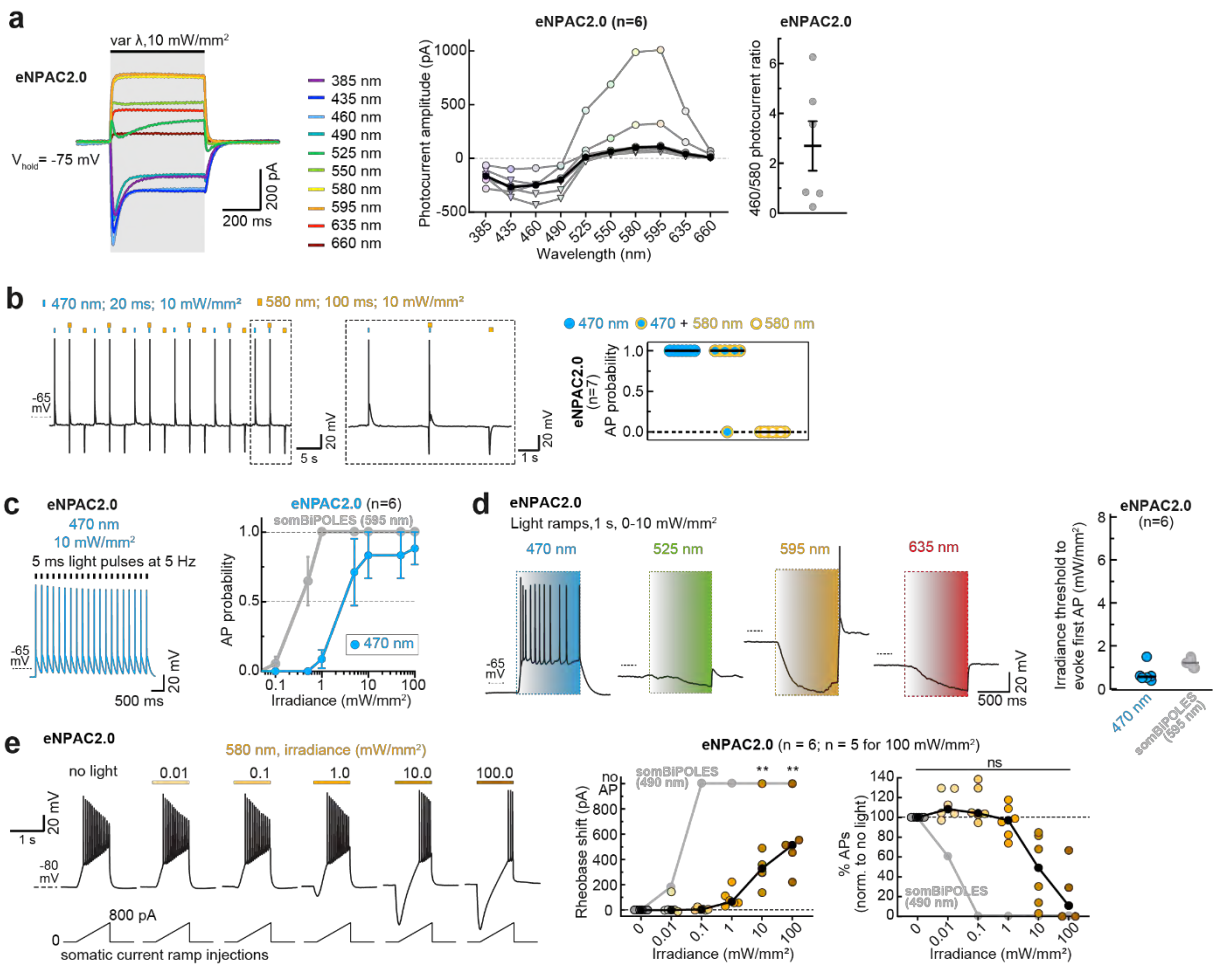

Supplementary Fig. 8. Characterization of bidirectional optogenetic manipulation of neuronal activity with eNPAC2.0. (a) Left: Representative eNPAC2.0 photocurrent traces in CA1 pyramidal neurons upon illumination with different wavelengths and equal photon flux at a membrane voltage of -75 mV. Middle: Quantification of photocurrent amplitude along the spectrum (black circles: medians, colored circles: photocurrents elicited by an irradiance of 10 mW mm^{-2}, colored triangles: photocurrents elicited by an irradiance of 1 mW mm^{-2}, n = 6 cells). Similar to HEK-cell measurements (see Supplementary Fig. 2b), inward and outward photocurrents were evoked with blue and orange light, respectively, indicative of independently evoked ChR2(H134R)- and eNpHR3.0-photocurrents. Right: Quantification of the ratio of excitatory (460 nm) over inhibitory (580 nm) photocurrents (black line: mean ± SEM, n = 6 cells). Note that this ratio is more scattered compared to BiPOLES (see Supplementary Fig. 3c), indicating variability in the stoichiometry of excitatory and inhibitory opsins between cells. This is likely explained by the different expression strategies for eNPAC2.0 (bi-cistronic, p2A construct) and BiPOLES (fusion protein and 1:1 stoichiometric expression of both tandem partners). **(b)** Characterization of all-optical spiking and silencing with eNPAC2.0. Left: Voltage traces showing blue-light-evoked APs, which, under the indicated conditions, could not be blocked by stimulation of eNpHR3.0 with a concomitant yellow light pulse. Yellow light alone led to a hyperpolarization of membrane voltage, indicating chloride loading of the cell by eNpHR3.0. Right: quantification of AP probability under indicated conditions (black horizontal lines: medians, n = 7 cells). **(c)** Left: Example traces of voltage clamp recordings of eNPAC2.0 to determine light-evoked AP probability with 470 nm. Right: quantification of light-mediated AP probability at indicated irradiances (symbols represent mean ± SEM, n = 6 cells). Note that even at an irradiance of 100 mW mm^{-2} not all cells achieved 100% spiking probability. This contrasts with CA1 cells expressing somBiPOLES or Chrimson alone, where 100% spiking probability is achieved with 595-nm light (their peak activation wavelength) at irradiances around 1 mW mm^{-2} (see Fig. 3b,c). **(d)** Spectral quantification of the irradiance threshold for AP generation with

eNPAC2.0. Left: Representative membrane voltage traces during light ramps at indicated wavelengths with irradiance increasing linearly from 0 to 10 mW mm^{-2}. Note that a rebound spike was triggered after applying a 595-nm light ramp. Right: Quantification of the irradiance threshold at which the first AP was evoked (black horizontal lines: medians, n = 6 cells). **(e)** eNPAC2.0 mediates neuronal membrane voltage hyperpolarization upon illumination with yellow light. Left: Current ramps (from 0–100 to 0–900 pA) were injected into eNPAC2.0-expressing CA1 pyramidal cells to induce APs during illumination with yellow light at indicated intensities (from 0.01 to 100 mW mm^{-2}). Right: Quantification of the rheobase shift and the relative change in the number of ramp-evoked action potentials. The injected current at the time of the first action potential was defined as the rheobase. Illumination with 580 nm light of increasing intensities activated eNpHR3.0-mediated Cl^- pumping, which strongly hyperpolarized the membrane voltage, shifting the rheobase to higher values and shunting APs. Note that the ability of eNPAC2.0 to silence neurons is smaller compared to somBiPOLES (see Fig. 3g). eNPAC2.0 required 2 orders of magnitude higher irradiance to achieve a significant shift of the rheobase (black circles: medians, n = 6, one-way Friedman test, *p < 0.05, **p < 0.01, ***p < 0.001). Grey symbols and lines in (c), (d) and (e) are somBiPOLES values from Fig. 3 plotted for comparison. The data presented in this figure and details on the statistical analysis are provided in the Source Data file.

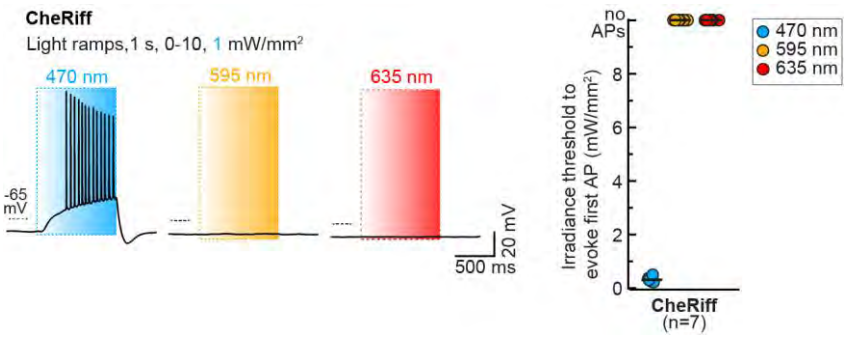

Supplementary Fig. 9. CheRiff exhibits optical excitation restricted to the blue spectrum. (a) Left: Representative membrane voltage traces measured in CheRiff-expressing CA1 pyramidal neurons. In IC experiments, light ramps of different wavelengths were applied as indicated. Light was ramped linearly from 0 to 10 mW mm^{-2} over 1 s. 470-nm ramps were ranging only up to 1 mW mm^{-2}, which was already sufficient to evoke APs. Right: Quantification of the irradiance threshold at which the first AP was evoked. Orange/red light up to 10 mW mm^{-2} did not evoke action potentials in CheRiff-expressing cells (black horizontal lines: medians, n = 7 cells). The data presented in this figure are provided in the Source Data file.

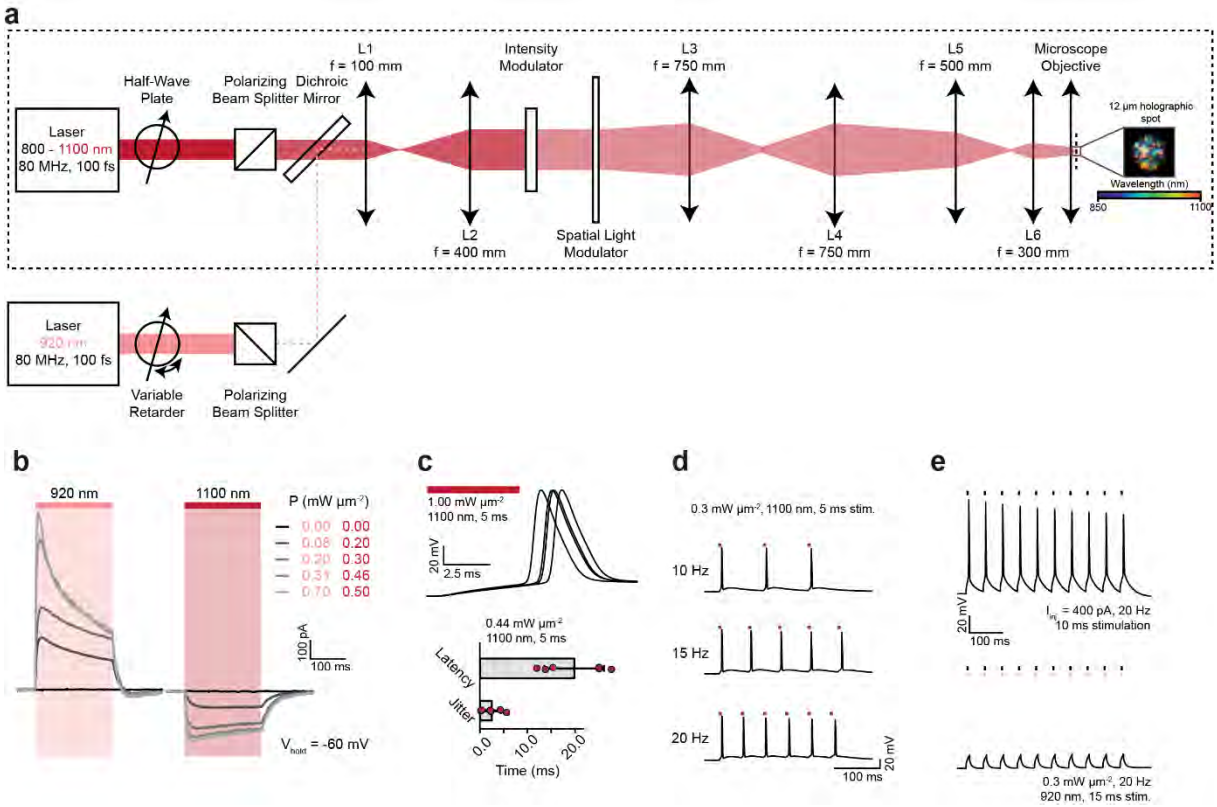

Supplementary Fig. 10. Design of the dual-laser 2-photon holography setup. (a) A schematic diagram of the experimental setup used for two-photon photo-stimulation and inhibition using holography. The optical path indicated by the black, dashed rectangle was used to acquire all data presented in Fig. 5. The system was aligned at the central wavelength (980 nm), but holograms at all wavelengths were co-aligned laterally and axially as demonstrated in the inset. Double-headed arrows are used to illustrate lenses, denoted by L, with focal lengths denoted by f. The reflective Spatial Light Modulator (SLM) is shown as transmissive for illustrative purposes. The photoinhibition beam (920 nm) was combined with the beam from the tunable laser using a dichroic mirror. The precise details of each optical component can be found in the main text. **(b)** Representative photocurrent traces at a range of different average power densities, obtained by continuous 200 ms illumination of 920 and 1100 nm at a holding potential of -60 mV. **(c)** Top: Representative traces of photo-evoked action potentials. Bottom: Mean latency and jitter calculated as the average of 5 trials in different neurons. Error bars represent the standard deviation across trials. **(d)** Representative photo evoked trains of action potentials under 1100-nm illumination at different stimulation frequencies. **(e)** Demonstration of precise elimination of single action potentials using short (15 ms) pulses of 920 nm light. Upper trace (control): electrically induced 20 Hz spike train by 10 ms injection of 400 pA current. Lower trace: suppression of electrically induced action potentials by co-incident illumination of 15 ms pulses of 920 nm light. The data presented in this figure are provided in the Source Data file.

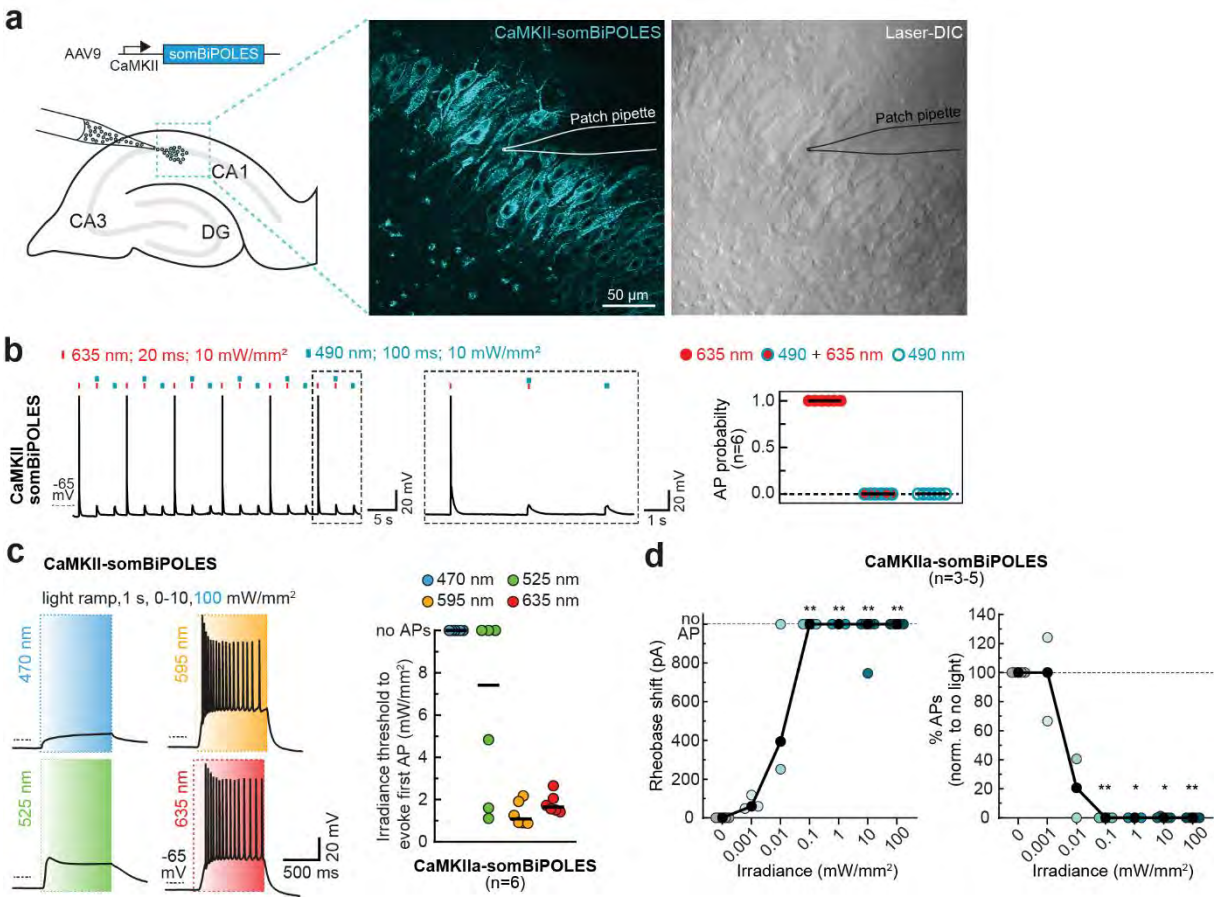

Supplementary Fig. 11. Virally expressed CaMKII-somBiPOLES enables bidirectional control of activity in projection neurons. (a) Viral transduction of CaMKII-somBiPOLES in hippocampal organotypic slice cultures. Right: Single-plane 2-photon fluorescence (cyan) and laser-DIC (gray) example images showing expression of somBiPOLES in pyramidal cells of *stratum pyramidale* and cellular morphology, respectively. The position of the patch pipette is depicted by a drawing of its outline. **(b)** IC characterization of bidirectional optical spiking-control with CaMKII-somBiPOLES. Left: Voltage traces showing red-light-evoked APs, which were blocked by a concomitant blue-light pulse. Blue light alone did not trigger APs. Right: quantification of AP probability under indicated conditions (black horizontal lines: medians, n = 6 cells). **(c)** Left: Representative membrane voltage traces measured in CaMKII-somBiPOLES-expressing pyramidal neurons. In IC experiments, light ramps were applied as indicated. Light was ramped linearly from 0 to 10 mW mm^{-2} over 1 s, except for 470 nm ramps, which were ranging to 100 mW mm^{-2} to rule out the possibility that high-irradiance blue light might still evoke APs. Right: Quantification of the irradiance threshold at which the first AP was evoked (black horizontal lines: medians, n = 6 cells). **(d)** Quantification of CaMKII-somBiPOLES-mediated neuronal silencing. Current ramps (from 0–100 to 0–900 pA) were injected into CaMKII-somBiPOLES-expressing cells to induce APs. The injected current at the time of the first AP was defined as the rheobase. Illumination with blue light of increasing irradiance (from 0.001 to 100 mW mm^{-2}) activated *Gt*ACR2-mediated Cl^- currents shifting the rheobase to higher values (black circles: medians, n = 5 cells (in 3 cells rheobase shift and %APs were measured for all light irradiances, in 1 cell for 0.0 0.1, 10 and 100 mW mm^{-2}; and in 1 cell only for 0.0 and 0.1 mW mm^{-2}) , one-way Kruskal-Wallis test, $^{**}p < 0.01$, $^{**}p < 0.001$). The data presented in this figure and details on the statistical analysis are provided in the Source Data file.

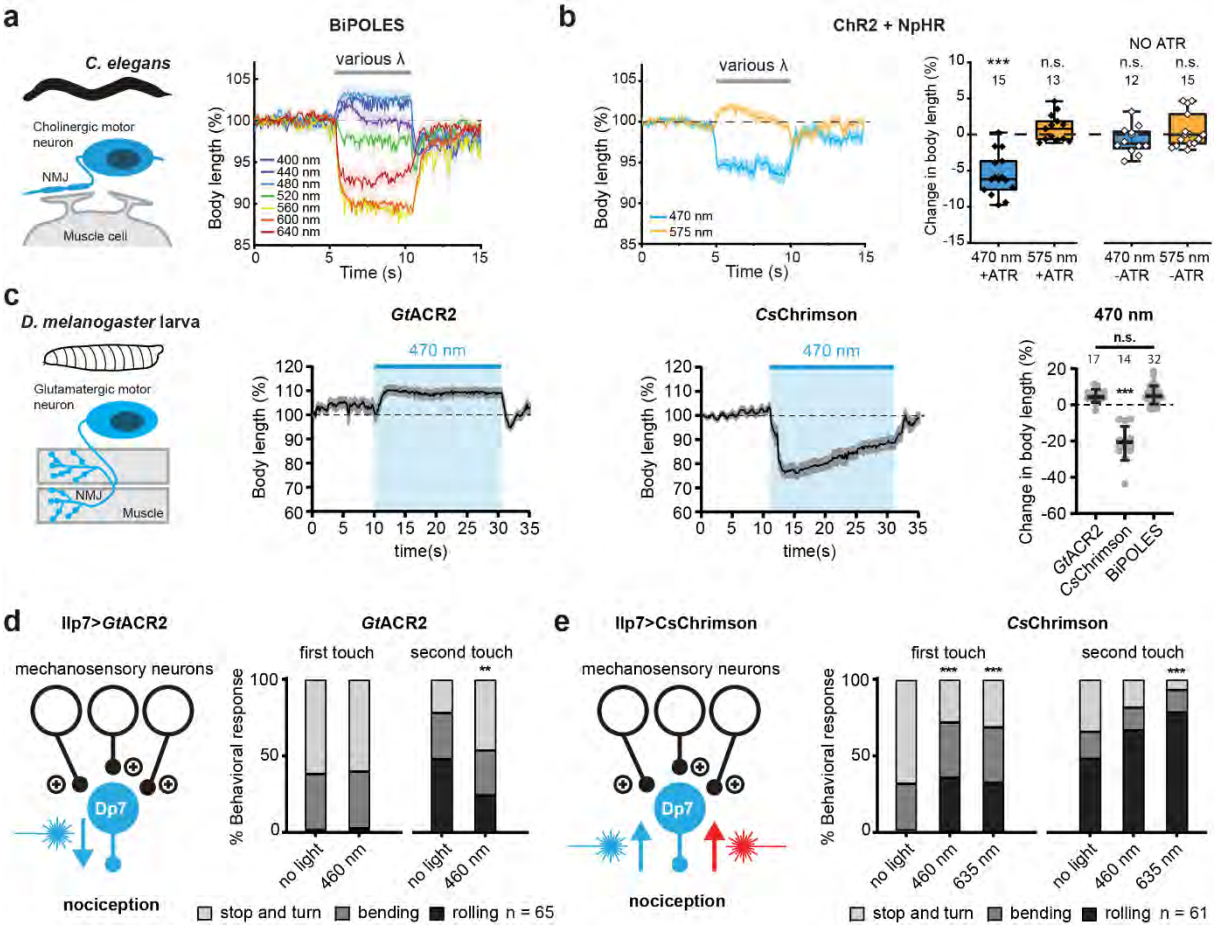

Supplementary Fig. 12. BiPOLES and controls in *C. elegans* and *D. melanogaster*. (a) Precise timing of bidirectional control of cholinergic motor neurons in *C. elegans*. Temporal dynamics of relative changes in body length upon illumination with light at wavelengths ranging from 400 to 640 nm in *C. elegans* expressing BiPOLES in cholinergic motor neurons (mean ± SEM, 1.1 mW mm^{-2}, 400 nm, n = 9; 440 nm, n = 12; 480 nm, n = 10; 520 nm, n = 12; 560 nm, n= 9; 600 nm, n = 13; 640 nm, n = 11). **(b)** Left: temporal dynamics of relative changes in body length upon illumination with light at 470 and 575 nm in *C. elegans* expressing ChR2(HR) and NpHR in cholinergic motor neurons (mean ± SEM, 1.1 mW mm^{-2}, 400 nm, n = 9; 440 nm, n = 12; 480 nm, n = 10; 520 nm, n = 12; 560 nm, n= 9; 600 nm, n = 13; 640 nm, n = 11). Right: quantification of maximal change in body length (Box: median, 1st – 3rd quartile, whiskers: 1.5x inter quartile range, ***p < 0.0001, paired, two-sided t-test, p values of comparisons of the stimulated condition (seconds 6-9 against the non-stimulated condition (seconds 0-4): 470 nm with ATR (n = 15): 6.4E-8, 575 nm with ATR (n = 13): 0.11, 470 nm without ATR (n = 12): 0.21, 575 nm without ATR (n = 15): 0.73). Note that NpHR stimulation did not lead to significant body relaxation. **(c)** *Gt*ACR2 or *Cs*Chrimson expressed alone in glutamatergic neurons of *D. melanogaster* larvae (*OK371-Gal4>UAS-GtACR2* or *UAS-CsChrimson*) result in opposite responses upon blue light stimulation. Schematic of *Gt*ACR2- or *Cs*Chrimson-expressing glutamatergic motor neuron innervating muscle fibers. Middle: Temporal dynamics of relative changes in body length upon illumination with 470 nm light (mean ± SEM, 17 μW/mm^2, n = 32). Right: Quantification of maximal change in body length (mean ± SEM, *Gt*ACR2, n = 17; *Cs*Chrimson, n = 14; BiPOLES, n = 32, ***p < 0.0001). Note that similar to BiPOLES, blue light illumination of animals expressing *Gt*ACR2 alone leads to body relaxation (BiPOLES dataset from Fig. 6d). In contrast, *Cs*Chrimson alone induces body constriction under blue light. **(d)** *Gt*ACR2 expression in Dp7 neurons in *Drosophila* larvae (*Ilp7-Gal4>UAS-GtACR2*) and behavioral response after the first and second mechanical stimulus under blue light (470 nm) compared to no light shows comparable inhibition of rolling as BiPOLES. n = 60 **p = 0.0057, X^2-test. **(e)** *Cs*Chrimson expression in Dp7 neurons (*Ilp7-Gal4>UAS-CsChrimson*) and behavioral response after the first and second mechanical stimulus under blue light (470 nm, 1.7 μmW mm^{-2}) or red light (635 nm, 2.5 μW/mm^2) illumination compared to no light. Note that unlike with BiPOLES, blue light and red light

increased rolling responses with *Cs*Chrimson. n = 61, ***p < 0.0001, X^2-test. The data presented in this figure and details on the statistical analysis are provided in the Source Data file.

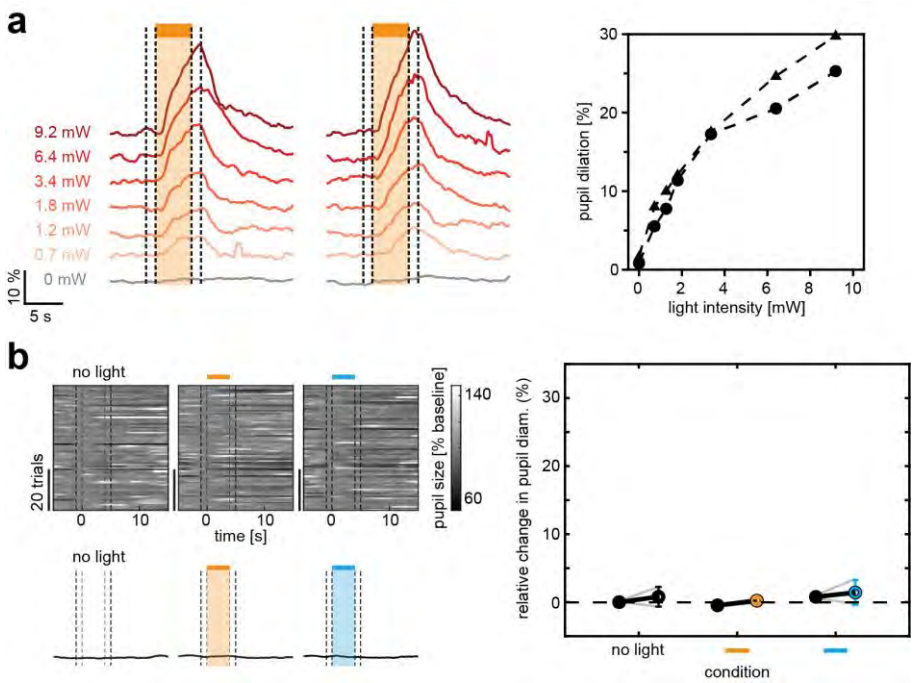

Supplementary Fig. 13. somBiPOLES controls in LC neurons. (a) The magnitude of pupil dilation scales with the red-light irradiance. Quantification of normalized pupil size in two animals under indicated light powers per fiber (594 nm). Dashed lines show regions used for quantification in the plot on the right. **(b)** Pupil dilation is not altered by light applied to the LC in fiber-implanted, non-injected wild-type animals. Quantification of normalized pupil size in one wild-type animal under various stimulation conditions as indicated. Orange and blue bars indicate time of illumination with 594 (orange) and 473 nm (blue), respectively. Top left: single trials. Bottom left: mean ± SEM. Dashed lines show time points used for quantification in the plot on the right. Right: quantification of relative pupil size (n = 3 mice; One-way analysis of variance; F = 0.01, p = 0.99). The data presented in this figure and details on the statistical analysis are provided in the Source Data file.

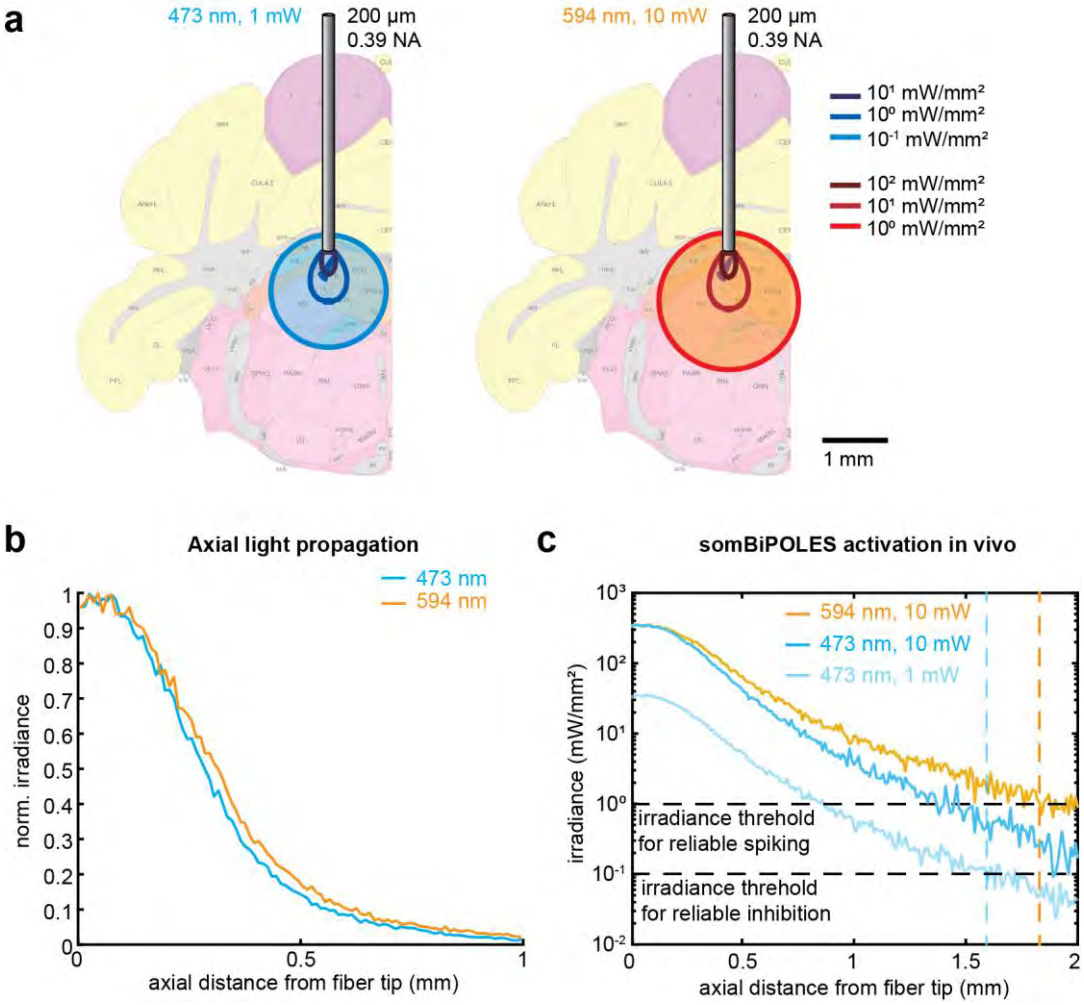

Supplementary Fig. 14. Monte-Carlo simulation of light propagation in the mouse brain to estimate somBiPOLES performance in vivo. **(a)** Simulation of light propagation (473 nm, left and 594 nm, right) from the tip of an optical fiber implanted above Locus Coeruleus in the mouse brain. Contour lines indicate interval of one log unit. **(b)** Simulation of the axial irradiance perpendicular to the fiber tip. Note the minimal differences in attenuation of blue light vs. orange light. **(c)** Estimation of reliable somBiPOLES performance under indicated light conditions. Reliable spiking of neurons can be achieved up to ~1.8 mm away from the fiber tip with 10 mW of 594 nm light. Similarly, efficient shunting of neuronal activity is achieved up to ~1.6 mm from the fiber tip with 1 mW of 473 nm light. The blue and orange irradiance thresholds required for reliable silencing and spiking are derived from Fig. 3. The data presented in this figure are provided in the Source Data file.

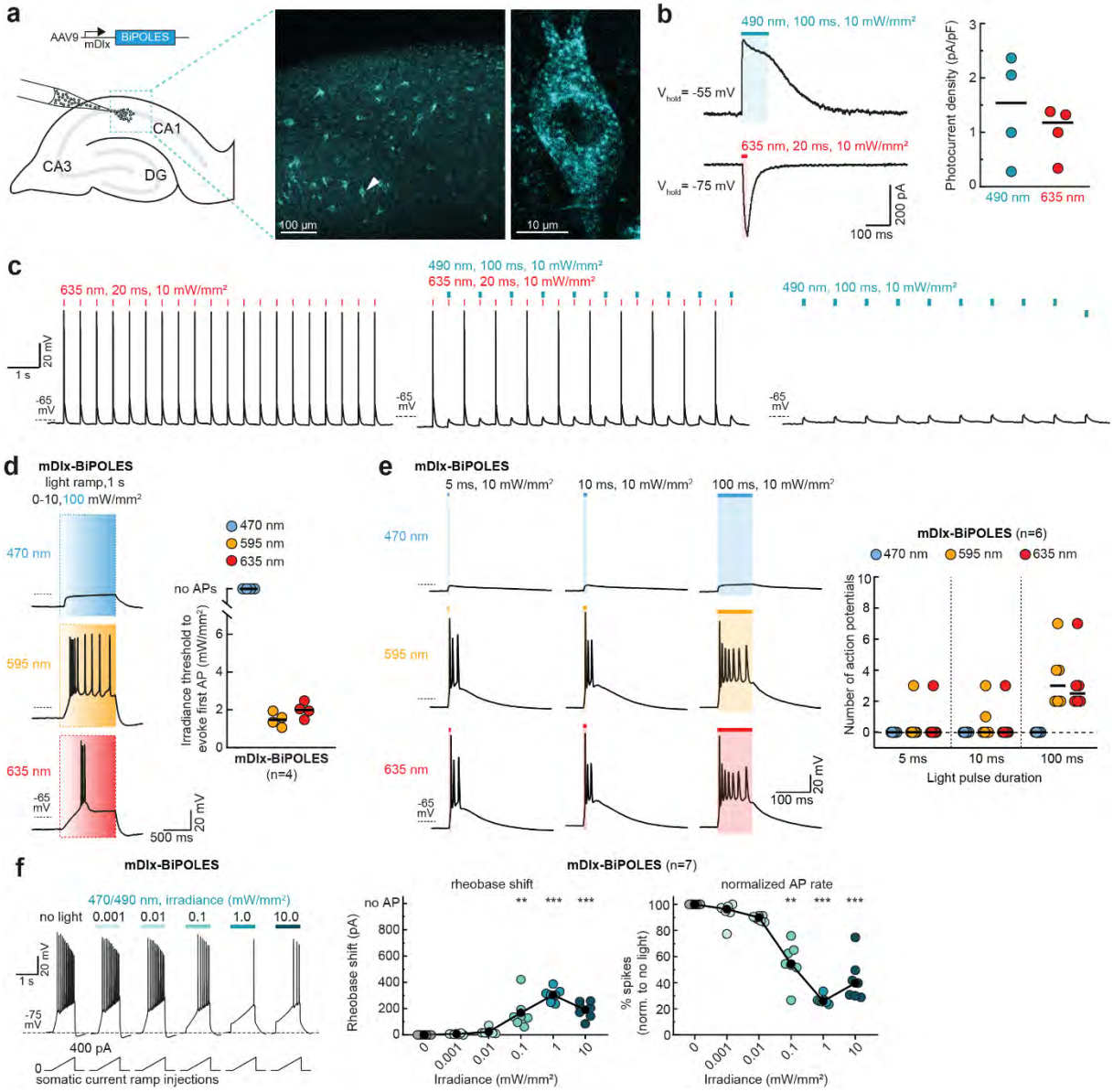

290

291 **Supplementary Fig. 15. Virally expressed mDlx-BiPOLES enables bidirectional control of**
292 **GABAergic neuronal activity. (a)** Viral transduction of mDlx-BiPOLES in hippocampal organotypic
293 slice cultures. Right: Representative maximum-intensity projection image of a 2-photon stack showing
294 expression of BiPOLES in GABAergic neurons in CA1. Magnified view of a single neuron indicated by
295 white arrowhead is shown on the right. **(b)** Left: Representative photocurrent traces measured in an
296 mDlx-BiPOLES-expressing CA1 GABAergic neuron. Photocurrents evoked by a 490 nm light pulse (100
297 ms, 10 mW mm^{-2}) were recorded at a membrane voltage of -55 mV and photocurrents evoked by a 635
298 nm light pulse (20 ms, 10 mW mm^{-2}) were recorded at a membrane voltage of -75 mV. Right:
299 Quantification of photocurrent densities evoked under the indicated conditions (black horizontal lines:
300 medians, n = 4 cells). **(c)** IC characterization of bidirectional optical spiking-control with mDlx-BiPOLES.
301 Voltage traces showing red-light-evoked APs (left), which were blocked by a concomitant blue-light
302 pulse (middle). Blue light alone did not trigger APs (right). **(d)** Left: Representative IC membrane voltage
303 traces measured in mDlx-BiPOLES-expressing neurons. In IC experiments, light ramps were applied as
304 indicated. Irradiance was ramped linearly over 1 s from 0 to 10 mW mm^{-2} or to 100 mW mm^{-2} for 470
305 nm to rule out the possibility that high-irradiance blue light might still evoke action potentials. Right:
306 Quantification of the irradiance threshold at which the first AP was evoked (black horizontal lines:
307 medians, n = 4 cells) 470-nm light up to 100 mW mm^{-2} did not evoke APs in mDlx-BiPOLES-expressing
308 cells, while 595 and 635 nm light evoked APs at irradiance levels comparable to pyramidal cells
309 expressing BiPOLES (see Supplementary Fig. 7a,b). **(e)** Extended duration of illumination increased the

probability and number of action potentials. Left: Representative IC membrane voltage traces measured in mDlx-BiPOLES-expressing neurons illuminated as indicated. Right: quantification of the number of action potentials evoked by the different illumination protocols (black horizontal lines: medians, n = 6 cells). **(f)** Quantification of mDlx-BiPOLES-mediated neuronal silencing. Current ramps (from 0–100 to 0–900 pA) were injected into mDlx-BiPOLES-expressing cells to induce action potentials. The injected current at the time of the first action potential was defined as the rheobase. Illumination with blue light of increasing irradiance (from 0.001 to 10.0 mW mm^{-2}) activated *Gt*ACR2-mediated Cl^- currents shifting the rheobase to higher values. Middle: Quantification of the rheobase shift at different light intensities. Right: Relative change in the number of ramp-evoked action potentials upon illumination with blue light at indicated irradiance values (black circles: medians, n = 7 cells, one-way Friedman test, $^{**}p < 0.01$, $^{***}p < 0.001$). The data presented in this figure and details on the statistical analysis are provided in the Source Data file.

3.3 Article III

Efficient optogenetic silencing of neurotransmitter release with a mosquito rhodopsin

Mathias Mahn [1 2 11], Inbar SarafSinik [1 11], Pritish Patil [1 11], Mauro Pulin [3 11], Eyal Bitton [1], Nikolaos Karalis [2], Felicitas Bruentgens [5], Shaked Palgi [1], Asaf Gat [1], Julien Dine [1], Jonas Wietek [1], Ido Davidi [1], Rivka Levy [1], Anna Litvin [1], **Fangmin Zhou** [3], Kathrin Sauter [3], Peter Soba [3 4], Dietmar Schmitz [5 6 7 8 9 10], Andreas Lüthi [2], Benjamin R. Rost [6], J. Simon Wiegert [3], Ofer Yizhar [1 12]

1 Department of Neurobiology, Weizmann Institute of Science, Rehovot 76100, Israel
2 Friedrich Miescher Institute for Biomedical Research, Basel, 4058, Switzerland
3 Center for Molecular Neurobiology Hamburg, Hamburg 20251, Germany
4 LIMES Institute, University of Bonn, Bonn 53115, Germany
5 Charité-Universitätsmedizin Berlin, Berlin 10117, Germany
6 German Center for Neurodegenerative Diseases (DZNE), Berlin 10117, Germany
7 Bernstein Center for Computational Neuroscience, Berlin 10115, Germany
8 Cluster of Excellence NeuroCure, Berlin 10117, Germany
9 Einstein Center for Neurosciences Berlin, Berlin 10117, Germany
10 Max-Delbrück Center for Molecular Medicine, Berlin 13125, Germany
11These authors have equally contributed to this work

Neuron 2021, DOI: 10.1016/j.neuron.2021.03.013

Personal contribution

My contribution to this publication was the following: I performed the Gsx assays to charcterize light-dependent G protein activation by eOPN3 and wrote the respective methods part. The results are displayed in Figure 1F, Figure S1C and Figure S2. In addition, I contributed to the revision of the manuscript.

Neuron

NeuroResource

Efficient optogenetic silencing of neurotransmitter release with a mosquito rhodopsin

Highlights

- eOPN3 is a mosquito-derived rhodopsin that inhibits neurotransmission in neurons
- Activation of eOPN3 activates the $G_{i/o}$ pathway and reduces Ca^{2+} channel activity
- eOPN3 can suppress neurotransmission in a variety of cell types *in vitro* and *in vivo*
- Activation of eOPN3 in nigrostriatal dopamine axons modulates locomotor behavior

Authors

Mathias Mahn, Inbar Saraf-Sinik, Pritish Patil, ..., Benjamin R. Rost, J. Simon Wiegert, Ofer Yizhar

Correspondence

ofer.yizhar@weizmann.ac.il

In brief

This study describes the engineering, validation, and application of a novel optogenetic tool, eOPN3, based on a mosquito homolog of encephalopsin. Illumination of eOPN3-expressing synaptic terminals leads to robust and stable suppression of synaptic transmission through activation of inhibitory G protein signaling.

Mahn et al., 2021, Neuron *109*, 1621–1635
May 19, 2021
https://doi.org/10.1016/j.neuron.2021.03.013

CellPress

Neuron

CellPress

NeuroResource

Efficient optogenetic silencing of neurotransmitter release with a mosquito rhodopsin

Mathias Mahn,[1,2,11] Inbar Saraf-Sinik,[1,11] Pritish Patil,[1,11] Mauro Pulin,[3,11] Eyal Bitton,[1] Nikolaos Karalis,[2] Felicitas Bruentgens,[5] Shaked Palgi,[1] Asaf Gat,[1] Julien Dine,[1] Jonas Wietek,[1] Ido Davidi,[1] Rivka Levy,[1] Anna Litvin,[1] Fangmin Zhou,[3] Kathrin Sauter,[3] Peter Soba,[3,4] Dietmar Schmitz,[5,6,7,8,9,10] Andreas Lüthi,[2] Benjamin R. Rost,[6] J. Simon Wiegert,[3] and Ofer Yizhar[1,12,*]

[1]Department of Neurobiology, Weizmann Institute of Science, Rehovot 76100, Israel
[2]Friedrich Miescher Institute for Biomedical Research, Basel, 4058, Switzerland
[3]Center for Molecular Neurobiology Hamburg, Hamburg 20251, Germany
[4]LIMES Institute, University of Bonn, Bonn 53115, Germany
[5]Charité-Universitätsmedizin Berlin, Berlin 10117, Germany
[6]German Center for Neurodegenerative Diseases (DZNE), Berlin 10117, Germany
[7]Bernstein Center for Computational Neuroscience, Berlin 10115, Germany
[8]Cluster of Excellence NeuroCure, Berlin 10117, Germany
[9]Einstein Center for Neurosciences Berlin, Berlin 10117, Germany
[10]Max-Delbrück Center for Molecular Medicine, Berlin 13125, Germany
[11]These authors contributed equally
[12]Lead contact
*Correspondence: ofer.yizhar@weizmann.ac.il
https://doi.org/10.1016/j.neuron.2021.03.013

SUMMARY

Information is carried between brain regions through neurotransmitter release from axonal presynaptic terminals. Understanding the functional roles of defined neuronal projection pathways requires temporally precise manipulation of their activity. However, existing inhibitory optogenetic tools have low efficacy and off-target effects when applied to presynaptic terminals, while chemogenetic tools are difficult to control in space and time. Here, we show that a targeting-enhanced mosquito homolog of the vertebrate encephalopsin (eOPN3) can effectively suppress synaptic transmission through the $G_{i/o}$ signaling pathway. Brief illumination of presynaptic terminals expressing eOPN3 triggers a lasting suppression of synaptic output that recovers spontaneously within minutes *in vitro* and *in vivo*. In freely moving mice, eOPN3-mediated suppression of dopaminergic nigrostriatal afferents induces a reversible ipsiversive rotational bias. We conclude that eOPN3 can be used to selectively suppress neurotransmitter release at presynaptic terminals with high spatiotemporal precision, opening new avenues for functional interrogation of long-range neuronal circuits *in vivo*.

INTRODUCTION

Neurons form local and long-range synaptic connections, through which they interact with neighboring neurons and with distant neuronal circuits, respectively. Long-range neuronal communication is crucial for synchronized activity across the brain and for the transmission of information between brain regions with distinct information processing capabilities. For example, dopaminergic neurons in the substantia nigra project to the dorsal striatum via the nigrostriatal pathway and play a critical role in movement control as part of the basal ganglia circuitry (Alcaro et al., 2007). Manipulating the activity of such long-range projection pathways allows a detailed evaluation of their functional contribution to cognitive and behavioral processes. However, while optogenetics allows robust and temporally precise excitation of long-range projecting axons (Yizhar et al., 2011), silencing such long-range connections with existing optogenetic tools has proven difficult (Wiegert et al., 2017a). We have previously shown that the light-driven chloride pump halorhodopsin (eNpHR3.0) only partially suppresses neurotransmitter release. The proton-pumping archaerhodopsin (eArch3.0) triggers off-target effects, including an increase in intracellular pH and elevated spontaneous neurotransmission (Mahn et al., 2016), potentially leading to off-target behavioral consequences (Lafferty and Britt, 2020). While halorhodopsin-mediated inhibition has no effect on intra-synaptic pH (Mahn et al., 2016), it does temporarily shift the chloride reversal potential and can lead to GABA-mediated excitation (Raimondo et al., 2012). Furthermore, both halorhodopsin and archaerhodopsin require continuous delivery of high light power to sustain their ion

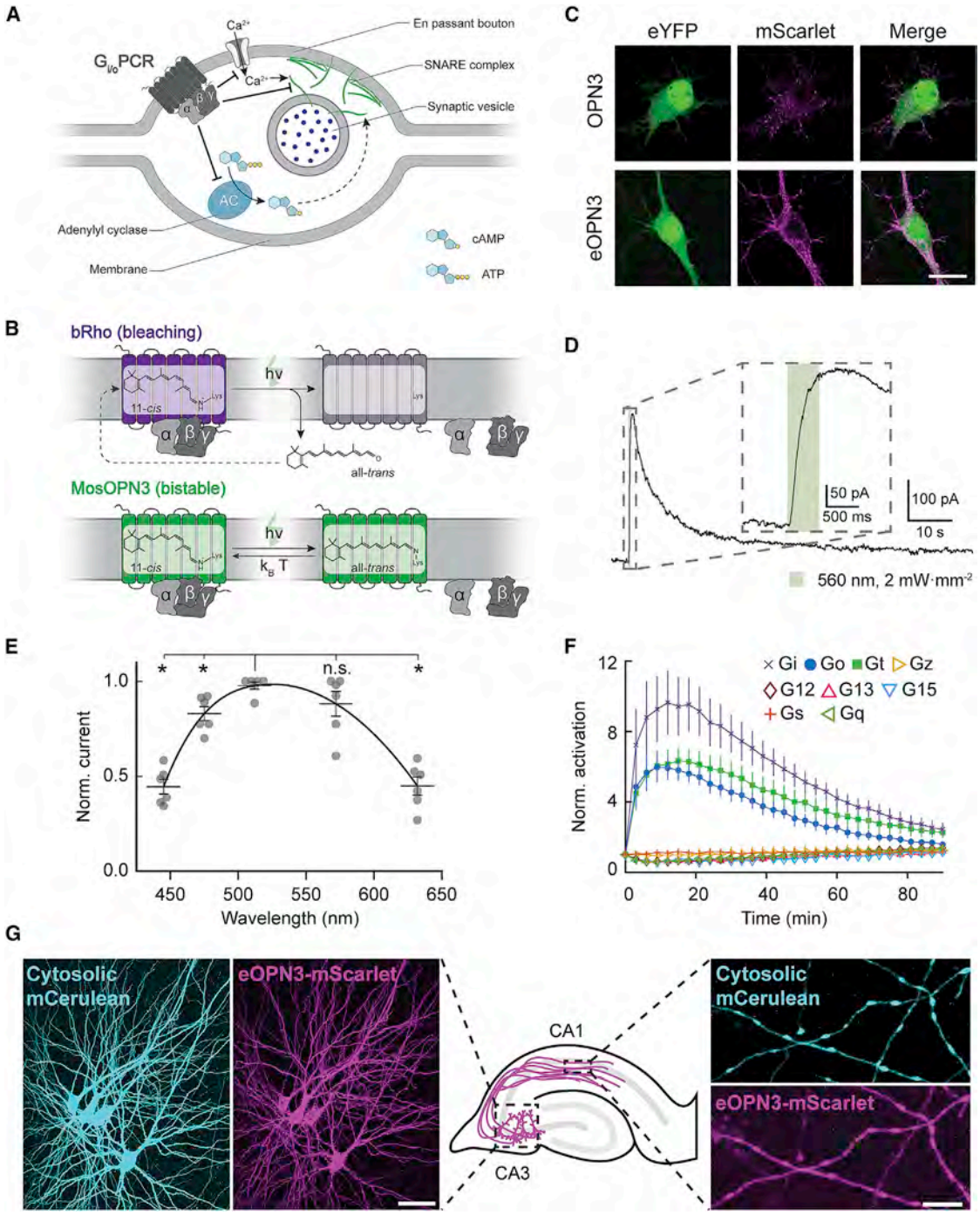

Figure 1. $G_{i/o}$-coupled rhodopsins for light-mediated presynaptic inhibition

(A) Schematic diagram depicting the mechanism through which $G_{i/o}$ signaling reduces the synaptic vesicle release probability. An activated GPCR leads to inhibition of voltage-gated Ca^{2+} channels as well as reduced cAMP levels, both leading directly (solid arrow) and indirectly (dashed arrow) to a reduction of Ca^{2+}-dependent vesicle release.

(B) Schematic diagram of distinct retinal binding mechanisms in bleaching (top) and bistable (bottom) rhodopsins. Bleaching rhodopsins release all-*trans*-retinal following photon absorption ($h \cdot v$) and need to bind a new 11-*cis*-retinal before being able to enter the next photocycle. Bistable rhodopsins sustain their covalent bond with retinal independent of its configuration, removing the influence of 11-*cis*-retinal tissue availability. In bistable rhodopsins, all-*trans*-retinal switches back to 11-*cis*-retinal either by absorbing another photon or spontaneously in the dark with a probability depending on the kinetic energy of the molecule ($k_B \cdot T$). k_B = Boltzmann constant; T = thermodynamic temperature; h = Planck constant; ν = photon frequency.

(legend continued on next page)

pumping activity (Zhang et al., 2007). Alternative approaches, such as optogenetic induction of synaptic plasticity (Creed et al., 2015; Klavir et al., 2017; Nabavi et al., 2014), or inhibition by disruption of the release machinery (InSynC [Lin et al., 2013]; photo-uncaging of botulinum toxin-B [Liu et al., 2019]), can effectively decrease synaptic transmission but are not as temporally precise as direct optogenetic manipulations.

Chemogenetic tools (Armbruster et al., 2007; Magnus et al., 2011) can effectively suppress presynaptic terminal function upon delivery of the cognate ligands of these engineered receptors (Basu et al., 2016; Stachniak et al., 2014). However, these approaches depend on infusion of the ligand to the location of the targeted presynaptic terminals, and their temporal specificity is fundamentally limited by the binding affinity to and clearance of the ligand. The designer receptor activated by designer drug (DREADD) hM4Di inhibits synaptic transmission (Stachniak et al., 2014) through a mechanism used by native inhibitory GPCRs, presumably through suppression of Ca^{2+} channel activity (Herlitze et al., 1996) and inhibition of the vesicle release machinery downstream of Ca^{2+} influx (Gerachshenko et al., 2005; Zhu and Roth, 2014; Zurawski et al., 2019a). We reasoned that a light-activated $G_{i/o}$-coupled rhodopsin could potentially trigger the same type of synaptic suppression (Figure 1A). However, while many known vertebrate rhodopsins couple to the $G_{i/o}$ pathway, these proteins are difficult to utilize as optogenetic tools since they undergo photobleaching after G protein dissociation as part of their natural phototransduction cycle (Bailes et al., 2012) (Figure 1B). Previous studies have revealed that bistable type-II rhodopsins are abundant across vertebrates and invertebrates (Tsukamoto and Terakita, 2010). These photoreceptors form a stable association with both the cis- and trans-configuration of the retinal chromophore (similar to the microbial type-I rhodopsin family including channelrhodopsin) and are therefore often referred to as bistable photopigments (Koyanagi et al., 2004; Terakita, 2005). Importantly, bistable type-II rhodopsins show reduced photobleaching (Bailes et al., 2012) (Figure 1B). We reasoned that members of the bistable type-II rhodopsin family that couple to $G_{i/o}$ signaling would be suitable candidates for light-mediated silencing of neurotransmitter release from presynaptic terminals.

Here, we tested several bistable rhodopsin variants for use as optogenetic tools, specifically addressing their expression in mammalian neurons and their capacity for $G_{i/o}$ pathway activation and light-driven inhibition of presynaptic release. While many of these invertebrate opsins failed to express in mammalian neurons, we were able to optimize the expression of a mosquito-derived homolog of the mammalian encephalopsin/panopsin protein (OPN3). The mosquito OPN3 is a bistable photopigment that, upon activation, allows efficient and specific recruitment of the $G_{i/o}$ signaling cascade (Koyanagi et al., 2013). Using a targeting-enhanced OPN3 (eOPN3) protein, we were able to suppress synaptic release in rodent hippocampal, cortical, thalamic, and mesencephalic neurons. In behaving mice, eOPN3 triggered robust pathway-specific behavioral effects. These findings suggest that eOPN3, and potentially other members of the bistable rhodopsin family, can be utilized as optogenetic tools for potent G protein-mediated modulation of the activity of presynaptic terminals with high spatiotemporal precision.

RESULTS

Expression of naturally occurring and engineered $G_{i/o}$-coupled bistable rhodopsins in mammalian neurons

We reasoned that the efficient suppression of presynaptic function by the DREADD hM4Di (Figure 1A; Stachniak et al., 2014) arises from the stable binding of the engineered ligands of these receptors (Sternson and Roth, 2014) and the subsequent, stable $G_{i/o}$-mediated signal transduction. We therefore hypothesized that rhodopsins coupling to the $G_{i/o}$ pathway could serve as potent presynaptic silencing tools provided that persistent activation of such a tool can be achieved with light. While vertebrate visual rhodopsins, which dissociate from their retinal chromophore upon illumination (Figure 1B, bRho), can in principle be used for presynaptic silencing (Li et al., 2005), it remains unclear whether these rhodopsins can provide sufficiently robust activation of the $G_{i/o}$ pathway at presynaptic terminals to support potent and sustained effects. Recent work has identified several new members of the encephalopsin subfamily of ciliary opsins, which couple to the $G_{i/o}$ pathway. Encephalopsins exist in a wide range of organisms, including the pufferfish teleost multi-tissue opsin 3a (PufTMT3a) and the mosquito opsin 3 (OPN3). These rhodopsins are intrinsically bistable, as they retain the covalent bond between the retinal chromophore and the protein moiety (Figure 1B) and display prolonged signal transduction following activation (Koyanagi et al., 2013). We tested several photoreceptors of this family for expression in mammalian neurons.

Generation and characterization of a targeting-enhanced OPN3

We previously showed that addition of an ER export signal (ER) along with a Golgi trafficking signal (ts) to the light-gated chloride

(C) Representative confocal images of neurons co-transfected with expression vectors for eYFP and OPN3 or eOPN3. Images show fluorescence in the eYFP channel (left), the mScarlet channel (middle) and the merged images (right). See Figure S2 for all tested rhodopsin variants and quantifications. Scale bar, 15 μm.
(D) Sample whole-cell voltage-clamp recording of a cultured hippocampal neuron co-expressing eOPN3 and GIRK2-1, held at −70 mV. Inset shows an expanded view of the GIRK current onset during the light pulse.
(E) Action spectrum of endogenous GIRK-mediated currents in neurons expressing eOPN3, normalized to peak activation per cell ($n = 6$, $p = 3.45 \cdot 10^{-4}$ Friedman rank sum test followed by pairwise comparisons using Conover's test). Peak excitation occurred at 512 nm ($p < 4.24 \cdot 10^{-3}$ Holm corrected pairwise comparisons to all other wavelengths except 572 nm).
(F) Light-dependent G protein activation by eOPN3, assayed as in Figure S3. eOPN3 specifically and strongly activated inhibitory G proteins (G_i, G_o, G_t) in a light-dependent manner ($n = 5$). See Figure S3 for complete assay and statistics.
(G) Two-photon maximum-intensity projections of CA3 neurons co-expressing the cytosolic fluorophore mCerulean (cyan) and eOPN3-mScarlet (magenta). Shown are the somatodendritic compartment of neurons electroporated with the two plasmids (left; scale bar, 50 μm) and their axons projecting into *stratum radiatum* of CA1 (right; scale bar, 5 μm). Plots depict individual data points and average ± SEM.

channel GtACR2 (eGtACR2) (Mahn et al., 2018) leads to an increase in axonal membrane localization. Applying this modification to OPN3, yielding the enhanced OPN3-ts-mScarlet-ER (eOPN3), led to an increased overall expression and enhanced membrane targeting in cultured hippocampal neurons (Figures 1C and S2A). Green light pulses delivered to neurons co-expressing eOPN3 and G protein-coupled inwardly rectifying potassium (GIRK2-1) channels triggered robust GIRK-mediated currents (Figures 1D and S2B). Activation of GIRK currents was maximal at 512 nm (Figure 1E), consistent with previous characterization of light absorption by OPN3 protein (Koyanagi et al., 2013).

We confirmed that eOPN3 retained its capacity to specifically activate the $G_{i/o}$ pathway using the GsX assay. Light-activation of GsX-expressing HEK cells yielded selective and strong activation of G_i-, G_o-, and G_t-mediated signal transduction, but not of other G proteins (Figures 1F, S2C, and S3B). To rule out undesired consequences of heterologous rhodopsin overexpression, such as impaired cell health or light-independent effects on the physiological activity of expressing neurons, we examined the intrinsic excitability of cultured hippocampal neurons expressing eOPN3-mScarlet. Whole-cell patch-clamp recordings revealed no significant difference in intrinsic properties between neurons expressing eOPN3-mScarlet and neighboring, non-expressing neurons from the same neuronal culture (Figure S4). We therefore conclude that expression of eOPN3 is well tolerated in mammalian neurons and does not result in significant light-independent physiological changes in neuronal excitability.

Next, we tested eOPN3 in pyramidal neurons of organotypic hippocampal slice cultures, a preparation that preserves the anatomical and functional connectivity between neurons in the CA3 and CA1 regions. Light delivery directly to the somatodendritic region of cells co-expressing eOPN3-mScarlet with cytoplasmic mCerulean (Figure 1G) triggered long-lasting photocurrents reversing at -105.1 ± 0.9 mV (Figure S5A), close to the calculated K^+ reversal potential of -102.5 mV, indicating activation of endogenous GIRK channels. This eOPN3-dependent K^+-conductance led to a lower input resistance (Figure S5B), a decrease in electrically evoked action potential firing (Figure S5C), a slight hyperpolarization of the resting membrane potential (Figure S5D), and an increased rheobase (Figure S5E).

Activation of eOPN3 leads to suppression of neurotransmitter release

Our findings demonstrated that eOPN3 reliably couples to the $G_{i/o}$-signaling pathway and evokes GIRK-mediated currents. Axons and boutons of mCerulean-expressing CA3 pyramidal neurons in the *stratum radiatum* in CA1 of hippocampal slice cultures (Figure 1G) showed expression of eOPN3-mScarlet, indicating that the rhodopsin is present at presynaptic terminals as well. We therefore used the autaptic neuron preparation (Bekkers and Stevens, 1991) to ask whether activation of eOPN3 triggers changes in neurotransmission via G-protein activation, similar to the DREADD hM4Di (Figure S6). Light delivery to eOPN3-expressing autaptic neurons resulted in a robust and long-lasting decrease of excitatory postsynaptic currents (EPSCs; Figure 2A) and led to an increase in the paired-pulse ratio (Figure 2B), consistent with a decrease in release probability (Dobrunz et al., 1997). Light-triggered suppression of release was also found in autaptic hippocampal interneurons and was similarly accompanied by an increase in the paired-pulse ratio of the inhibitory postsynaptic currents (Figure 2C). To determine the light sensitivity of eOPN3, we varied the light exposure between 0.2 $\mu W \cdot s \cdot mm^{-2}$ and 20 $mW \cdot s \cdot mm^{-2}$ (Figure 2D). The half-maximal effect size was reached at 2.90 $mW \cdot s \cdot mm^{-2}$, meaning that 1 s continuous illumination at 2.9 $mW \cdot mm^{-2}$ was sufficient to reach half maximal inhibition of synaptic vesicle release. The onset of eOPN3-mediated suppression of release was rapid, with a time constant (t_{on}) of 0.24 s, and saturated after 1 s (Figure 2E). Furthermore, activation of eOPN3 significantly decreased the frequency of AP-independent miniature EPSCs (Figure 2F), but not their amplitude (Figure 2G). Together, these results are consistent with a presynaptic action of this photoreceptor on neurotransmission.

The effect of eOPN3 activation on synaptic transmission was similar to the effect of the $GABA_B$ agonist baclofen, a potent modulator of neurotransmitter release (Figures 3A and 3B; Rost et al., 2011; Scanziani et al., 1992), indicating that they both act through the $G_{i/o}$ signaling pathway. Accordingly, preincubating the neurons with the $G\alpha_{i/o}$ subunit blocker pertussis toxin (PTX) blocked both the eOPN3- and the baclofen-mediated effects (Figures 3A and 3B), indicating that eOPN3 acts through the PTX-sensitive $G_{i/o}$ protein signaling cascade. To examine whether the effects on synaptic transmission are dependent on GIRK channel activation, we applied SCH23390, which blocks GIRK channel currents (Kuzhikandathil and Oxford, 2002). Bath application of SCH23390 abolished the outward currents evoked by green light at the somatic compartment (Figure 3C) but had no detectable impact on the light-activated suppression of synaptic release in the same neurons (Figure 3D). These results suggest that the synaptic effects of eOPN3 are not mediated by blocking the propagation of APs, but rather by direct G protein-mediated effects at the presynaptic compartment (Wu and Saggau, 1994; Zurawski et al., 2019b).

We next tested whether presynaptically expressed eOPN3 can be used to inhibit synaptic transmission in organotypic slices, where axon terminals can be locally illuminated independently of the neuronal soma (Figure 4A). In whole-cell recordings from pairs of CA3 and CA1 neurons, local illumination of the axonal terminals in CA1 induced a potent, long-lasting, and reversible reduction of the evoked EPSC amplitude (Figures 4B–4E and S7). Light application in CA1 neither induced AP failure nor GIRK-mediated hyperpolarization in the recorded presynaptic neurons (Figure S7), suggesting that activation of eOPN3 in the axonal compartment does not reduce somatic excitability. In accordance with a reduction in evoked release and thus a direct effect of eOPN3 on neurotransmitter release, we found that both the coefficient of variation (CV, Figure 4F) and the paired-pulse ratio (PPR, Figure 4G) increased following illumination in nearly all recorded pairs. The time until 50% EPSC recovery was 6.58 ± 1.78 min (Figures S7C–S7F). Synaptic transmission in non-expressing CA3-CA1 control pairs was unaffected by light stimulation (Figures 4E–4G). We therefore conclude that eOPN3 robustly activates the $G_{i/o}$ pathway in neurons, leading to efficient

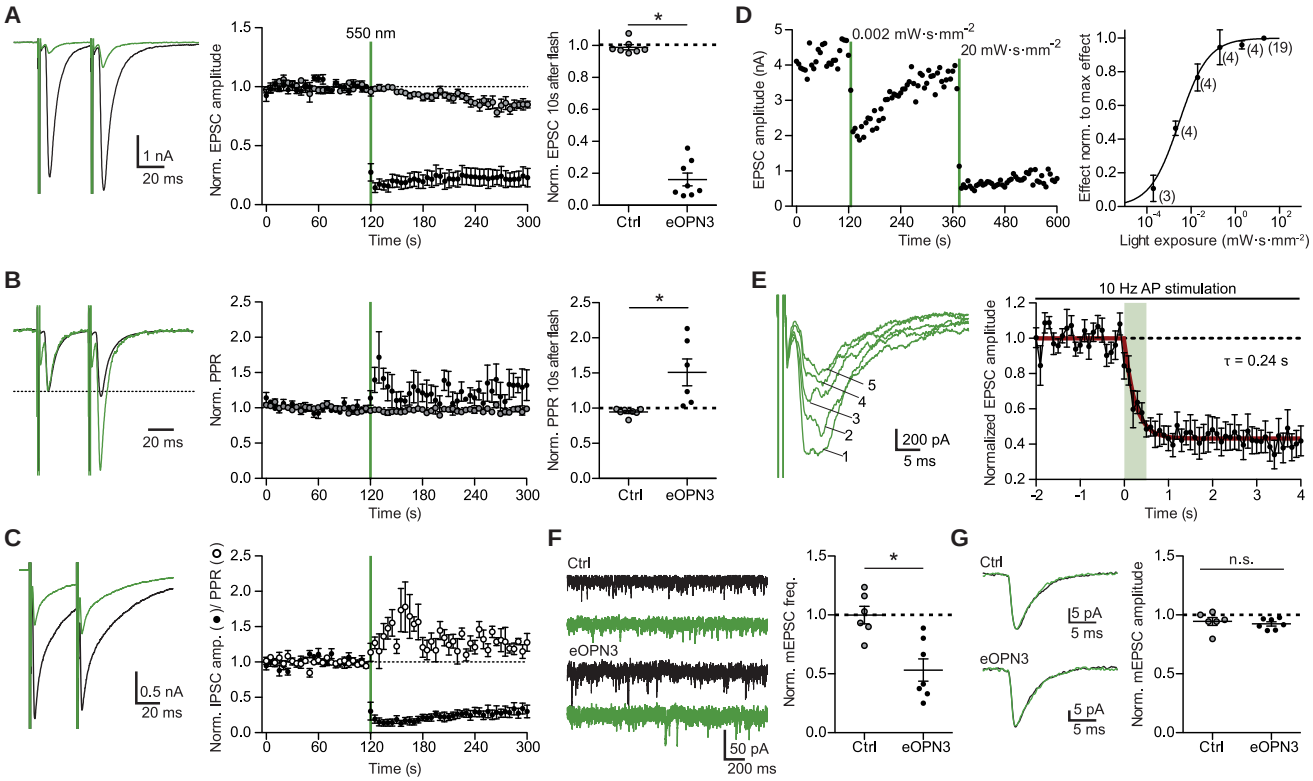

Figure 2. Light-induced inhibition of neurotransmitter release in autaptic hippocampal neurons expressing eOPN3

(A) Typical autaptic EPSCs evoked by a pair of 1 ms depolarizing current injections (40 ms inter-stimulus interval, injected currents clipped for presentation) before (black) and after (green) illumination with 550 nm light (40 mW·mm^{-2}, unless otherwise indicated). Traces are averages of 6 sweeps. A 500 ms light pulse caused sustained suppression of EPSCs in eOPN3-expressing neurons. EPSCs decreased to 16 ± 4% of baseline (n = 8), while EPSCs in control neurons were not affected by illumination (open circles, n = 7, p = $3 \cdot 10^{-4}$ two-tailed Mann-Whitney test).

(B) Traces from (A) scaled to the amplitude of the first EPSC (dashed line). Illumination increased the paired-pulse ratio ($EPSC_2/EPSC_1$) in the eOPN3-positive neurons (n = 6) compared to controls (p = $1.2 \cdot 10^{-3}$ unpaired, two-tailed Student's t test).

(C) Amplitudes and PPR of evoked autaptic IPSCs in GABAergic neurons, compared to the pre-light baseline (IPSCs: n = 7; PPR: n = 5).

(D) Quantification of light exposure required for half maximal synaptic inhibition. Normalized effect size was fit as a sigmoidal dose-response curve (n is reported next to the measurement points, EC_{50} = 2.895 μW·s·mm^{-2}).

(E) Time-course of the eOPN3 activation on EPSC amplitudes evoked by APs triggered at 10 Hz. Traces show five consecutive EPSCs of the train following the onset of a single 500 ms light pulse. EPSCs decreased with a time constant t_{on} of 240 ms (n = 6).

(F) Representative traces of mEPSCs (left) and quantification (right). eOPN3 activation decreased mEPSC frequency to 53 ± 9% compared to baseline (n = 7), significantly different from controls (n = 6, p = $3 \cdot 10^{-3}$, two-tailed Mann-Whitney test).

(G) Quantal EPSC amplitude in eOPN3-expressing and control neurons after illumination (p = 0.3 unpaired, two-tailed Student's t test). Plots show individual data points and average (black) ± SEM.

suppression of presynaptic vesicle release that recovers spontaneously within minutes.

To predict the effects of eOPN3-mediated inhibition *in vivo*, we virally transduced CA3 pyramidal cells in organotypic hippocampal slice cultures, emulating the most commonly used method for gene transfer *in vivo* (Figures 4H–4M). To avoid both recurrent polysynaptic activity of the CA3 network and contribution of somatic eOPN3 activation, CA3 axons were dissected from their somata at the boundary of CA3 to CA1 (Figure 4H). The PSC amplitude evoked by electrical stimulation of isolated Schaffer collateral axons was attenuated by 56 ± 5% following a single 500 ms light pulse to the terminal field in the CA1 (Figures 4I–4L) and recovered to baseline levels with a time constant of 4.57 min (95% CI: 4.19 to 4.97; R^2: 0.90; Figure 4M). As before, the CV of synaptic responses increased in the 5 min following light stimulation, and eventually returned to baseline values. The lower efficacy of PSC amplitude reduction recorded in this experimental setup (Figure 4K) compared with the efficacy observed in paired recordings (81 ± 4%, Figure 4E) is likely due to the contribution of non-expressing axons to the PSCs evoked by field stimulation.

GPCRs may act at presynaptic terminals as canonical or non-canonical modulators of synaptic transmission (Zurawski et al., 2019a). It has been reported that canonical GPCR-mediated presynaptic inhibition decreases neurotransmission by altering the probability of vesicle release and changing the short-term plasticity profile of modulated synapses (Chalifoux and Carter, 2011), leading in some cases to suppression of initial release

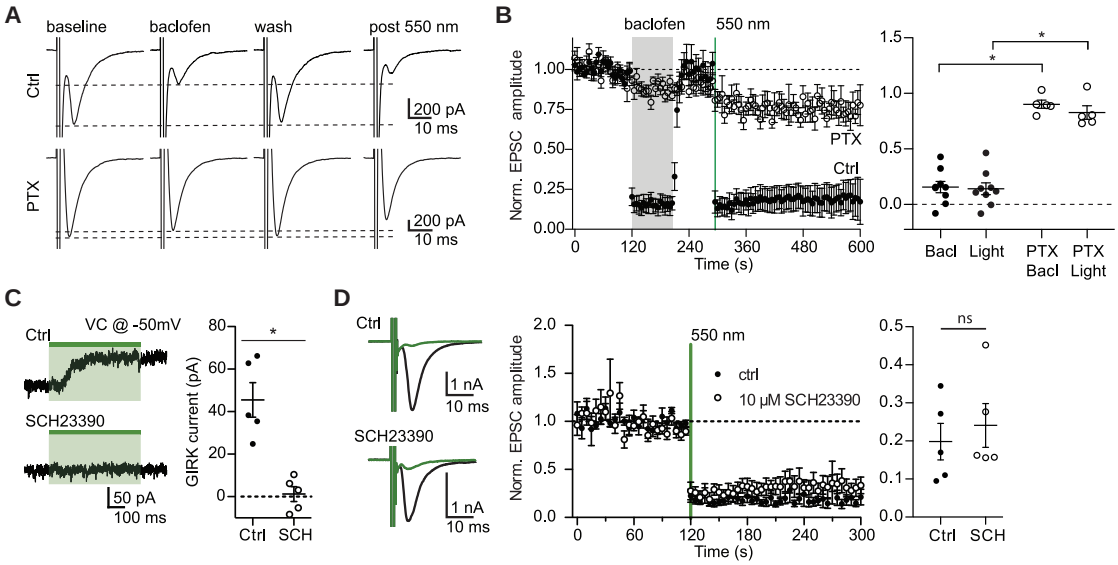

Figure 3. The effect of eOPN3 on neurotransmitter release is sensitive to pharmacological inhibition of $G_{i/o}$-protein signaling but is not affected by a GIRK channel blocker

(A) Action potential-evoked EPSCs in control neurons (upper row) were suppressed both by the $GABA_BR$ agonist baclofen (30 μM) and by subsequent activation of eOPN3 with 550 nm light (500 ms, 40 mW·mm^{-2}). In pertussis toxin (PTX)-treated neurons (20–26 h pre-treatment, 0.5 μg·mL^{-1}, bottom row), both baclofen and eOPN3 largely failed to suppress release.

(B) Averaged time-course of EPSCs recorded in neurons treated with PTX (open circles; n = 5) and neurons not treated with PTX (filled circles; n = 9; $p = 3 \cdot 10^{-4}$ Kruskal-Wallis test followed by Dunn's multiple comparison tests: $p < 0.05$ for Bacl versus PTX Bacl, Light versus PTX Bacl and Light versus PTX Light).

(C) Illumination of eOPN3-expressing neurons evokes robust outward currents (45.5 ± 8.1 pA, n = 5), which are abolished in the presence of the GIRK channel blocker SCH23390 (10 μM, 1.2 ± 3.5 pA; n = 5; $p = 1 \cdot 10^{-3}$ unpaired, two-tailed Student's t test).

(D) The extent and time-course of EPSC suppression by eOPN3 activation is not affected by the GIRK channel blocker SCH23390 (filled circles: ctrl recordings, n = 5; open circles: SCH23390, n = 5; p = 0.59 unpaired, two-tailed Student's t test). Plots show individual data points and average ± SEM.

but facilitation of subsequent responses. To better characterize the efficacy of eOPN3-mediated synaptic inhibition during higher firing rates, we applied trains of 10 stimulations at 25 Hz (Figures 4N–4P). Postsynaptic responses in the dark showed facilitation for the initial pulses while displaying depression toward the end of the train. In accordance with our previous single-pulse field stimulation results, light activation of eOPN3 inhibited the first pulse by an almost identical amount (single pulse stimulation: 44 ± 5% versus train stimulation: 47 ± 5% of initial strength). Consistent with our paired recording data, eOPN3 increased the PPR of the initial two pulses (PSC 2 / PSC 1) and maintained facilitation throughout the train. Nonetheless, light activation of eOPN3 robustly suppressed the entire sequence of PSCs in the stimulus train, albeit to a slightly lower degree for all the consecutive pulses relative to the initial one (suppression of the 10th pulse was 43 ± 2% of the initial strength).

Integration of eOPN3-based manipulation with two-photon Ca^{2+} imaging

To assess whether eOPN3 can be combined with two-photon imaging, we tested eOPN3 activation by two-photon absorption. In CA3 pyramidal cells of organotypic hippocampal cultures expressing eOPN3 and GIRK2-1, we compared green light-evoked GIRK channel currents to fast spiral scanning on the soma or slow raster scanning across the somatodendritic compartment with a femtosecond-pulsed infrared laser at wavelengths ranging from 800 to 1070 nm and at intensities ranging from 10 to 100 mW (Figures 5A–5C). Spiral scans did not evoke any detectable photocurrents (Figure 5B). Only slow raster scans at wavelengths above 980 nm and intensities above 30 mW resulted in very small photocurrents of less than 10 pA on average (Figure 5C). In contrast, green-light activation of eOPN3 in the same cells evoked more than 20-fold larger photocurrents (Figure 5B). Thus, eOPN3 can be combined with two-photon imaging of blue-shifted sensors with minimal cross-activation.

Based on this characterization, we used two-photon imaging to determine whether eOPN3 alters Ca^{2+} influx through presynaptic voltage-gated Ca^{2+} channels, as shown for different neuromodulators (Wu and Saggau, 1994; Ikeda, 1996; Herlitze et al., 1996; Chalifoux and Carter, 2011; Burke et al., 2018). G_i-coupled GPCRs can suppress neurotransmitter release via $G_{\beta\gamma}$-mediated inhibition of voltage-gated Ca^{2+} channels (Herlitze et al., 1996; Kajikawa et al., 2001), possibly by delaying the time of first opening or by shifting the voltage-dependency of channel activation (Bean, 1989). We therefore tested whether eOPN3 activation in presynaptic terminals reduces AP-evoked Ca^{2+} influx. We evoked single APs in CA3 cells co-expressing eOPN3 and jGCaMP7f (Dana et al., 2019) while imaging the corresponding presynaptic Ca^{2+} transients in CA3 cell axonal boutons in CA1 *stratum radiatum* (Figures 5D and 5E). The GIRK channel blocker SCH23390 was added to exclude potentially confounding GIRK channel-mediated hyperpolarization effects. Green light pulses

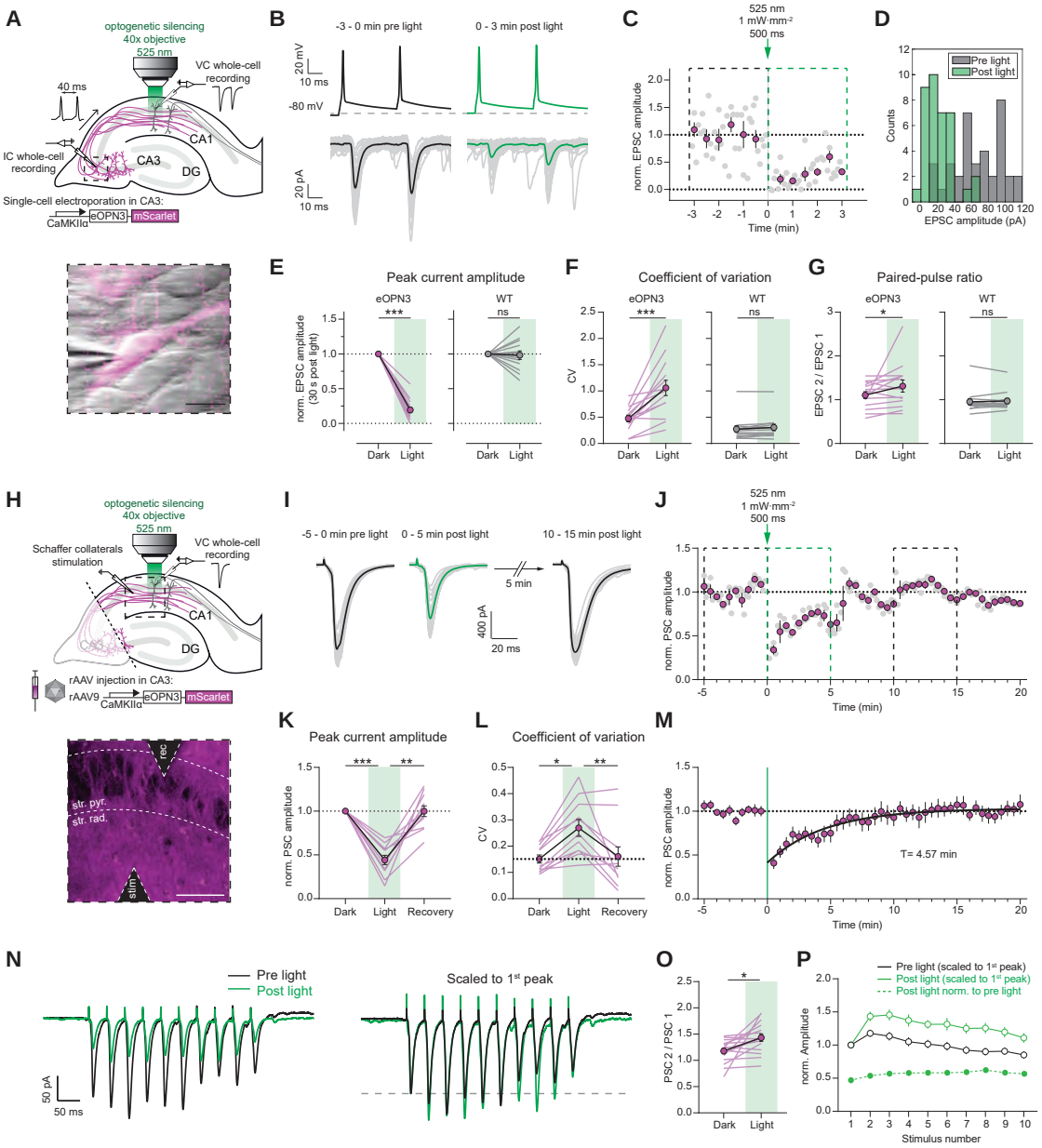

Figure 4. eOPN3 activation induces long-lasting, reversible inhibition of synaptic transmission at Schaffer collateral synapses

(A) Schematic diagram of experimental setup for whole-cell paired-recordings in organotypic hippocampal slices (see STAR Methods for details). Inset: IR-scanning gradient contrast image overlaid with the fluorescence image of patch-clamped, eOPN3 expressing CA3 neuron. Scale bar, 20 μm.

(B) Top: representative voltage traces of electrically induced APs from an eOPN3 expressing CA3 neuron, before and after light delivery to the CA1 region (dashed line shows the resting membrane potential at the beginning of the experiment. Note that APs were still reliably evoked after light stimulation). Bottom: corresponding current traces from a postsynaptic CA1 neuron in response to the paired-pulse stimulation, before and after light delivery (gray: single trials, black and green: averaged trials).

(C) Time course of the normalized EPSCs peak amplitudes from the example shown in (B) (gray circles: single trials, magenta: means of 30 s time bins ± SEM).

(D) Histogram count of peak current amplitudes of the example shown in (B).

(E) Normalized EPSC amplitudes in the eOPN3 group (left) and wild-type (WT) control group (right) (eOPN3: 0.19 ± 0.04, n = 14 pairs from 14 slices, $p = 1 \cdot 10^{-4}$, Wilcoxon test; WT: 0.98 ± 0.06, n = 13 pairs from 13 slices, p = 0.5, Wilcoxon test).

(F) Coefficient of variation of EPSCs in the dark and after light application for the eOPN3 (left) and control group (right) (eOPN3 dark: 0.48 ± 0.06, eOPN3 light: 1.06 ± 0.15, n = 14 pairs from 14 slices, $p = 4 \cdot 10^{-4}$, paired t test; WT dark: 0.27 ± 0.06, WT light: 0.31 ± 0.06, n = 13 pairs from 13 slices, p = 0.11, Wilcoxon test).

(G) Paired-pulse ratio change in the dark compared to after light application for the eOPN3 (left) and control group (right) (eOPN3 dark: 1.11 ± 0.08, eOPN3 light: 1.32 ± 0.14, n = 14 pairs from 14 slices, p = 0.02, Wilcoxon test; WT dark: 0.95 ± 0.07, WT light: 0.97 ± 0.06, n = 13 pairs from 13 slices, p = 0.59, Wilcoxon test). Circles in (E–G): mean ± SEM.

(legend continued on next page)

locally applied to the CA1 region before each trial significantly reduced presynaptic Ca^{2+} influx in a GIRK-independent manner (Figures 5F–5G), indicating that eOPN3 acts directly at voltage-dependent Ca^{2+} channels at presynaptic terminals similar to native G_i-coupled receptors.

In vivo characterization of eOPN3-mediated terminal inhibition

Next, we examined the efficacy and kinetics of eOPN3-mediated presynaptic silencing using *in vivo* electrophysiology. We chose to modulate the visual thalamocortical pathway, since the visual responses of V1 neurons depend on input from the lateral geniculate nucleus of the thalamus (LGN), which constitutes the main feed-forward projection from the retina to V1 (Niell and Stryker, 2008; Froudarakis et al., 2019). Using multi-shank silicon probes, we recorded bilaterally from V1 in mice expressing eOPN3 in the LGN (Figure 6A). Visual stimulation (4 s compound visual stimulus every 30 s) led to reliable evoked responses in V1 (Figures 6C and 6D left). A subset of units showed an increase in their average firing rates during visual stimulus presentation (Figure 6D). After 10 trials of visual stimulus presentation, we activated eOPN3 in LGN terminals unilaterally by 30 s continuous illumination (2 mW at the fiber tip) directed at V1. eOPN3 activation resulted in a reduced impact of visual stimulation on evoked network activity in V1 (Figures 6C and 6D), with responsive units reducing their response amplitude (Figure 6E). In units that showed a strong suppression of visually evoked responses (more than 50% during eOPN3 activation; 14 of 54 units), the average response amplitude recovered with a time constant of 5.17 min (95% CI: 1.12 to 7.20 min; R^2: 0.82; Figure 6F). By contrast, units recorded simultaneously at the contralateral (non-illuminated) side did not show a change in their visual stimulus presentation response after eOPN3 activation on the ipsilateral hemisphere (Figure 6F), demonstrating the spatial specificity of the manipulation.

To examine the efficacy and kinetics of eOPN3-mediated presynaptic silencing *in vivo* on the behavioral level, we used eOPN3 to inhibit dopaminergic (DA) input to the dorsomedial striatum (DMS) of mice during free locomotion. Previous work has demonstrated the important role of nigrostriatal DA projections in the control of animal locomotion (Alcaro et al., 2007; Kravitz et al., 2010; Grealish et al., 2010; Tecuapetla et al., 2014; Barter et al., 2015; Borgkvist et al., 2015; da Silva et al., 2018). Briefly, striatal D1-expressing medium spiny neurons (D1-MSNs) facilitate motion upon selective, bilateral activation and induce a contralateral rotation upon unilateral stimulation. Conversely, D2-expressing MSNs (D2-MSNs) decrease motion and, upon unilateral stimulation, induce ipsilateral rotation. While D1 and D2 neurons drive motion in opposite directions, their common substantia nigra pars compacta (SNc) dopaminergic input stimulate D1-MSNs while inhibiting D2-MSNs. Overall, these studies suggest that unilateral inhibition of SNc DA projections would introduce an ipsiversive bias in free locomotion (Figure 7A). We thus expressed an eOPN3- or an eYFP-expressing control vector unilaterally in SNc DA neurons and implanted an optical fiber above the ipsilateral DMS to allow illumination of nigrostriatal DA projections (Figure 7B). Activation of eOPN3 in DA terminals (500 ms light pulses at 0.1 Hz, 540 nm, 10 mW at the fiber tip) triggered an ipsiversive bias in locomotion (Figures 7C and 7D). The rotational preference was not observed during the baseline period, became evident within the first minute following light onset, and recovered within <10 min of the last light pulse (Figure 7E), in line with the recovery kinetics of eOPN3 observed in our experiments *in vitro* and *in vivo* (Figures 4M, 6F, and S7C–S7F). Control eYFP-expressing mice did not show such side bias or light-induced equivalent dynamics (Figures 7C–7E). Apart from their strong side preference, eOPN3 mice did not differ from control mice in distance traveled ($p = 0.54$, Kruskal-Wallis test), center entries ($p = 0.99$, Kruskal-Wallis test), or time in center ($p = 0.69$, Kruskal-Wallis test). The magnitude of the observed behavioral effect of eOPN3 activation, quantified as the rotation index (Figure 7D, *insets*; see STAR Methods), was positively correlated with expression levels across individual mice ($p = 6.1 \cdot 10^{-3}$, $R^2 = 0.81$) during the light activation period, but not before light delivery or after its termination (Figure 7F). No significant correlation was found with the average velocity before, during, or after eOPN3 activation (Figure 7F). Finally, one week after the initial test, we repeated the test using the same parameters. We found a high correlation in the light evoked rotational bias between the first and second trial in each mouse (Pearson's correlation coefficient: 0.8147; $p = 0.0256$). Taken together, our results demonstrate that eOPN3 can be used for synaptic terminal inhibition in behaving animals, with high

(H) Schematic diagram of experimental setup for field stimulation (see STAR Methods for details). Inset: two-photon single-plane image of the CA1 region with the stimulating and recording electrodes. eOPN3-expressing axons (magenta) surround CA1 pyramidal neurons (dark shadows). Scale bar, 50 μm.
(I) Representative voltage traces (PSCs) before, immediately and 10 min after light (gray: single trials, black and green: average trials).
(J) Time course of the normalized PSC peak amplitudes from the example shown in (I). Dashed boxes indicate the time periods shown in (I) (gray circles: single trials, magenta: 30 s time bins ± SEM).
(K) Quantification of eOPN3 effect on PSC peak amplitudes ("Dark": 5 min period before light; "Light": maximal eOPN3 effect during first 30 s post light, 0.44 ± 0.05, $p < 1 \cdot 10^{-4}$; "Recovery": 10–15 min period after light, 0.99 ± 0.06, $p = 1.9 \cdot 10^{-3}$; n = 11 slices, Friedman test with Dunn's multiple comparison test).
(L) Quantification of the effect of eOPN3 activation on the coefficient of variation. "Light" refers to the 5 min post light application matching the duration of the two other conditions ("Dark": 0.15 ± 0.02; "Light": 0.27 ± 0.03, p = 0.02; "Recovery": 0.16 ± 0.04, $p = 8.5 \cdot 10^{-3}$, n = 11 slices, Friedman test with Dunn's multiple comparison test).
(M) Summary of all field stimulation experiments. Mono-exponential fit is shown in black.
(N) Left: representative voltage traces in response to a 10-pulse stimulus train (25 Hz). Traces are averages of 5 sweeps each. Right: same traces as on the left, each scaled to its 1st PSC peak amplitude.
(O) Quantification of the PPR (PSC 2 / PSC 1 of the train), showing increased facilitation (Dark: 1.18 ± 0.05, Light: 1.43 ± 0.07, p = 0.01, n = 16 slices, Paired t test).
(P) Summary of all train stimulation experiments.
Circles in (K–P): mean ± SEM.

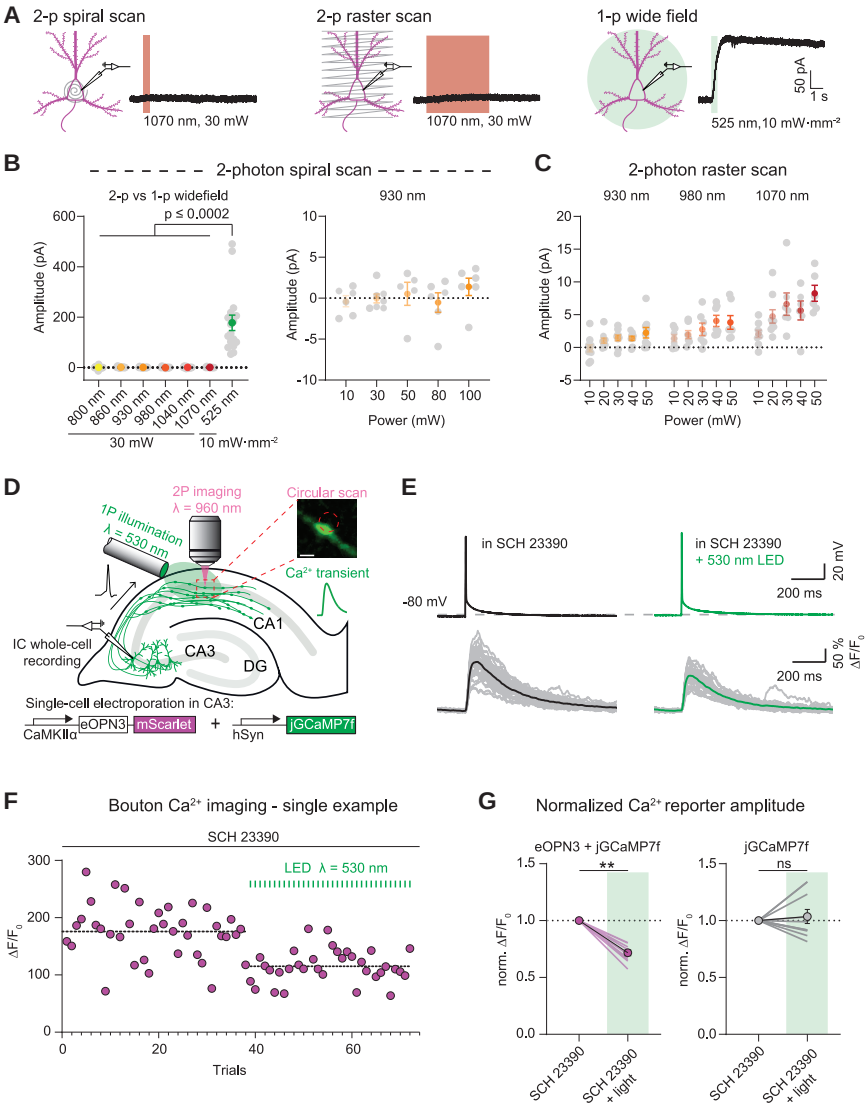

Figure 5. eOPN3 two-photon activation properties and modulation of presynaptic voltage-gated Ca^{2+} channels

(A) Two-photon (left, middle) versus single-photon (right) activation of eOPN3 in CA3 pyramidal neurons in organotypic hippocampal slice cultures expressing eOPN3-mScarlet and GIRK2-1. Somatic 500 Hz spiral scans (2 ms/spiral, 250 cycles, 500 ms total duration) or raster scans (FOV = 106*106 μm, 512x512 pixels, 1.8 ms/line, 5 frames, 4.6 s total duration) at 1.09 Hz over the somatodendritic compartment were used for two-photon activation characterization. Example voltage-clamp traces show photocurrents obtained by the different stimulation modalities in the same cell.

(B) Quantification of the photocurrents elicited by two-photon versus single-photon illumination. Left: GIRK-mediated currents in eOPN3 expressing neurons stimulated with two-photon spiral scanning at wavelengths from 800 nm to 1070 nm at 30 mW, or with full-field 525 nm light (Kruskal-Wallis test, Dunn's multiple comparisons test). Right: Increasing laser intensity during spiral scans at 930 nm did not result in significant photocurrent.

(C) Slower and longer raster scanning over a larger field of view resulted in minimal outward currents and was wavelength and laser-intensity dependent (Linear regression indicated positive slopes. Bonferroni-Holm corrected p values: wavelength: $p = 6.1 \cdot 10^{-4}$; laser power: 930 nm: $p = 0.01$; 980 nm: $p = 7.2 \cdot 10^{-3}$; 1070 nm: $p = 1.2 \cdot 10^{-3}$).

(D) Schematic diagram of presynaptic Ca^{2+} imaging experiments (see STAR Methods for details). Inset shows a single-plane jGCaMP7f image of an en passant bouton and the circular imaging-laser scanning path (red dashed circle, scale bar, 1 μm). A fiber-coupled LED was used to locally activate eOPN3 in CA1 the presence of the GIRK channel blocker SCH 23390.

(E) Top: representative voltage traces of electrically evoked APs in a transfected CA3 pyramidal neuron in the dark and after a green light pulse (dashed line shows the resting membrane potential at the beginning of the experiment). Bottom: corresponding Ca^{2+} responses from a presynaptic bouton. Single trials are shown in gray; black and green traces represent the averaged responses before and after light, respectively.

(F) Peak jGCaMP7f transients in the dark and after green light pulses in a single experiment, indicating a light-dependent decrease in presynaptic Ca^{2+} influx. Dashed lines show the average for the two conditions.

(G) Quantification of normalized eOPN3-jGCaMP7f transients (left) (SCH 23390 + light = 0.72 ± 0.026, $p = 2 \cdot 10^{-3}$, Wilcoxon-test, n = 10 slices) and jGCaMP7f alone (right) (SCH 23390 + light = 1.04 ± 0.06, p = 0.89, paired t test, n = 10 slices). Plots show individual data points (lines), and average (circles) ± SEM.

light-sensitivity, precisely timed onset, and behaviorally relevant recovery time.

DISCUSSION

Optogenetic silencing is a powerful tool for functionally dissecting neuronal circuits and understanding the contribution of defined neuronal populations to behavioral processes. However, silencing of long-range axonal projections has posed a formidable challenge. Our results demonstrate that a mosquito homolog of encephalopsin (OPN3) can selectively recruit $G_{i/o}$ signaling in mammalian neurons. Optimization of this rhodopsin (yielding eOPN3) led to enhanced membrane targeting and improved expression in long-range axons. Activation of eOPN3 in four different neuronal preparations (autaptic hippocampal neurons, organotypic hippocampal slices, thalamocortical afferents, and nigrostriatal DA fibers) led to effects that are consistent with robust suppression of neurotransmitter release. In autaptic neurons, eOPN3 activation led to an inhibitory effect that was similar in its magnitude to the effect of activating endogenous $GABA_B$ receptors and was blocked by pertussis toxin, consistent with $G_{i/o}$-mediated inhibition. One potential caveat to the use of $G_{i/o}$-mediated inhibition for the manipulation of neuronal and synaptic activity is that the biochemical signaling pathways and

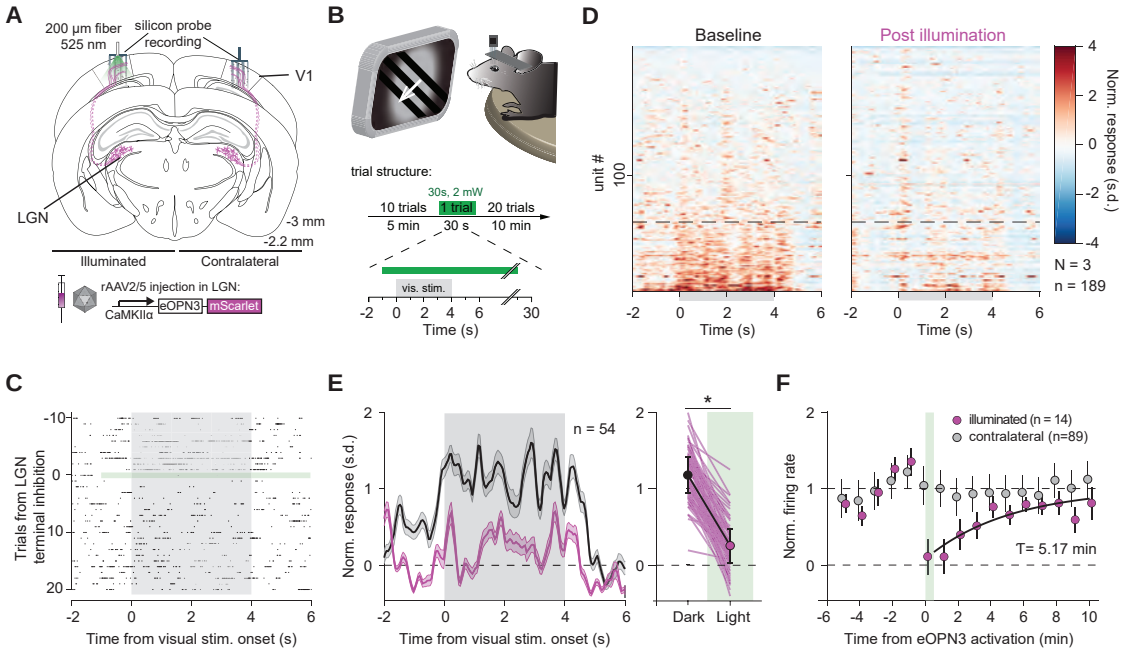

Figure 6. eOPN3 mediated suppression of thalamocortical inputs in awake head-fixed mice

(A) Schematic diagram of the investigated circuit. Lateral geniculate nucleus (LGN) neurons were bilaterally transduced with eOPN3. Acute silicon probe recordings were performed bilaterally in primary visual cortex (V1) before and after unilateral illumination of LGN terminals in V1.

(B) During recordings, head-fixed mice were presented with a compound drifting grating stimulus (4 s duration) every 30 s for 21 trials (top). Ten baseline trials were followed by a single trial paired with 30 s of light delivery (525 nm at ~2 mW from a 200 µm, 0.5 NA optical fiber) to V1, and 20 post-light trials.

(C) Raster plot of a representative V1 unit with reduced firing rate induced by eOPN3 activation.

(D) Heat plot of the population response to visual stimulus presentation of all recorded units (189 units from 3 mice) on the hemisphere of eOPN3 activation before (left) and after (right) eOPN3 activation. Units were sorted by their response magnitude to visual stimulus presentation during baseline condition. Units below the dashed line (n = 54) show a positive average response during the 4 s visual stimulus presentation.

(E) Left: Average peristimulus time histogram of the visual stimulus responsive units (below dashed line in D). Each unit's activity was normalized to the average firing rate in the 15 s prior to stimulus presentation during the two trials before eOPN3 activation. Right: Quantification of the average response during 4 s visual stimulus presentation in the two trials before (Dark) and first two trials after eOPN3 activation onset (Light). Dark: 1.17 ± 0.23, Light: 0.25 ± 0.22, $p < 1 \cdot 10^{-3}$, Wilcoxon test, n = 54 units. Plot shows individual units (lines), and population average (circles) ± SEM.

(F) Kinetics of the recovery of visual stimulus response amplitude for units that showed a reduction >50% in their visual stimulus response (magenta), fitted with a mono-exponential function (black line). Units recorded simultaneously from the contralateral hemisphere (gray) did not change their response following ipsilateral eOPN3 activation. During the baseline and post light period, the plot shows the averages of two consecutive trials (circles) ± SEM.

the effector proteins might differ among cell types and subcellular compartments. Furthermore, $G_{i/o}$-mediated inhibition is known to be activity-dependent to some extent (Brenowitz et al., 1998), and its efficacy might be dependent on the initial firing patterns and short-term synaptic plasticity features of the targeted neurons. We therefore recommend that eOPN3 effects are rigorously characterized using electrophysiology before this tool is applied in a behavioral setting.

Although we detected eOPN3-mediated GIRK currents, the effect of eOPN3 activation on the intrinsic excitability of expressing neurons was relatively weak. This suggests that activation of eOPN3 in the somatodendritic compartment induces a less efficient inhibition of neuronal spiking compared to other K^+ channel-mediated optogenetic silencing approaches (Bernal Sierra et al., 2018; Beck et al., 2018). In contrast, silencing of synaptic transmission with eOPN3 was highly efficient and independent of GIRK channel activity, suggesting that eOPN3-mediated synaptic inhibition occurs through direct activity on the highly conserved presynaptic release apparatus and on Ca^{2+} channel function (Dittman and Regehr, 1996; Kajikawa et al., 2001; Sakaba and Neher, 2003; Zurawski et al., 2019b). This is consistent with our observation of GIRK-channel-independent suppression of spike-evoked Ca^{2+} transients after eOPN3 activation. Thus, if locally activated at synaptic terminals, eOPN3 is a robust and broadly applicable optogenetic tool for inhibition of synaptic neurotransmission, similar to the DREADD receptor hM4Di, which has been successfully used for presynaptic silencing in a variety of neuronal cell types and systems (Stachniak et al., 2014; Evans et al., 2018; Malvaez et al., 2019).

The effects of GPCRs on presynaptic neurotransmitter release have been partially attributed to G-protein modulation of presynaptic Ca^{2+} influx (Herlitze et al., 1996). Meanwhile, non-canonical presynaptic GPCR modulators have been shown to decrease the vesicle release probability without a concomitant change in short term plasticity, through Ca^{2+}-dependent and independent mechanisms (Hamid et al., 2014; Burke et al., 2018). Our paired-pulse facilitation results suggest that eOPN3 acts as a canonical presynaptic GPCR modulator, suppressing the initial synaptic

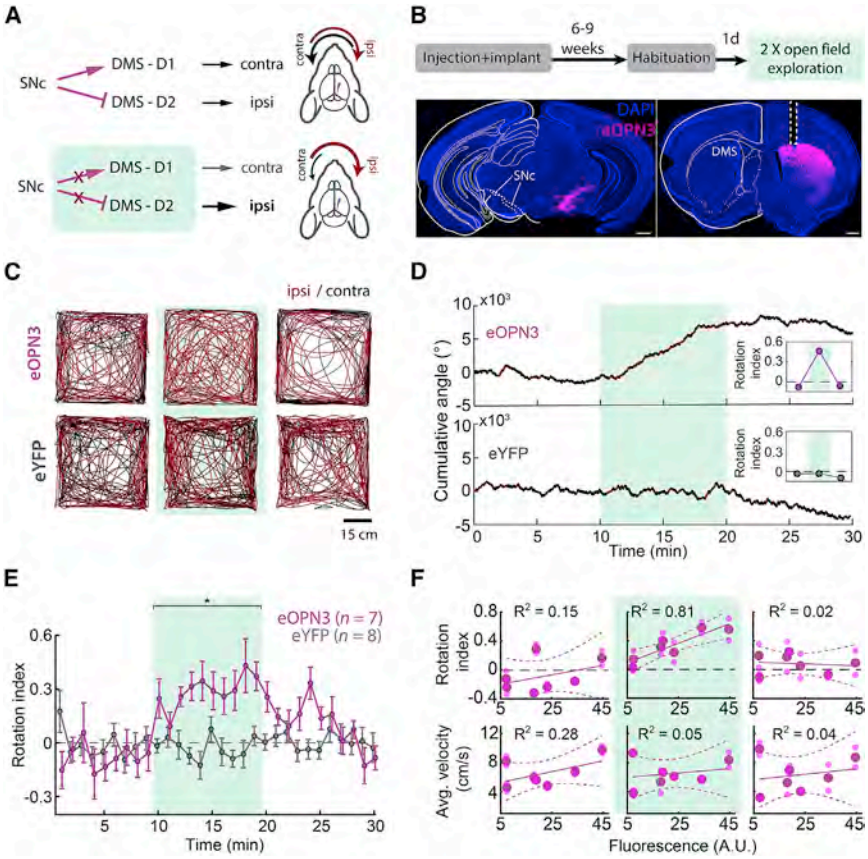

Figure 7. eOPN3-mediated suppression of dopaminergic projections from the substantia nigra to the dorsomedial striatum leads to ipsiversive bias during free locomotion

(A) Schematic diagram of the experimental setup and hypothesis. Unilateral expression of eOPN3 in SNc dopaminergic neurons and light-mediated suppression of their striatal projections would induce an ipsiversive side bias during free locomotion.

(B) Top: experimental timeline. Bottom: Representative images of neurons expressing eOPN3-mScarlet in the SNc (left) and their striatal projections (right) in DAPI-stained brain sections. Scale bars, 500 μm.

(C) Locomotion trajectories of representative eOPN3 (top) and eYFP (bottom) mice, over successive 10-min periods: (left to right) before, during and after light delivery (540 nm, 500 ms pulses at 0.1 Hz, 10 mW from the fiber tip), together covering continuous 30 min sessions. Red and black color code trajectory segments where the mice showed ipsilateral or contralateral angle gain, respectively.

(D) Representative cumulative angle traces of individual eOPN3-expressing (top) and eYFP-expressing (bottom) mice, over 30 min of free locomotion in an open field arena. Red and black colors depict ipsilateral or contralateral segments, respectively. Green shaded region marks the light delivery period.

(E) The rotation index (mean ± SEM), calculated as the difference between cumulative ipsilateral and contralateral rotations, divided by their sum, over 1-min bins for eOPN3-expressing mice (magenta, n = 7) and eYFP controls (gray, n = 8). Green shaded region marks the light delivery period, where eOPN3 demonstrate significant ipsiversive bias ($p = 1.3 \cdot 10^{-3}$ Kruskal-Wallis test followed by Bonferroni-Holm corrected pairwise comparisons using Wilcoxon rank sum tests. Baseline: ctrl versus eOPN3 p = 1; light: ctrl versus eOPN3 $p = 1.9 \cdot 10^{-3}$; post light: ctrl versus eOPN3 p = 0.09).

(F) Top: rotation index, calculated for individual mice before (left), during (middle), and after (right) light-induced activation of eOPN3, plotted against eOPN3 expression levels measured at the DMS projections (symbols). Solid and dashed lines are linear regression fit with 95% confidence intervals, respectively. Bottom: average velocity of individual mice, plotted against expression levels in the same manner shown above. R^2 values are indicated separately for each plot.

response more strongly than it does the consecutive pulses (Figures 4N–4P). This could be due to presynaptic Ca^{2+} accumulation (Jackman and Regehr, 2017) and a depolarization-triggered relief of the G-protein interaction with voltage-gated Ca^{2+} channels (Currie, 2010). Thus, eOPN3 activation biases short-term synaptic plasticity toward short-term facilitation.

We have previously shown that current approaches utilizing ion pumps for vesicle release inhibition are not suitable for suppressing presynaptic release for extended time periods (Mahn et al., 2016; Wiegert et al., 2017a; Lafferty and Britt, 2020). Although bistable rhodopsins such as eOPN3 cannot replace ion-pumping type-I rhodopsins in the sub-second range, eOPN3 can be used for experiments that require modulation in the range of minutes to hours. For even longer inhibition periods, tools such as the photoactivatable botulinum neurotoxin are likely also suitable (Liu et al., 2019). Silencing synaptic transmission using hM4Di with local agonist infusion at the terminal field (Stachniak et al., 2014) should in principle allow for similar efficiency compared to eOPN3. However, eOPN3 has the advantage of more precise temporal control and reduced problems with agonist microinfusion such as potential off-site effects due to leakage to the cerebrospinal fluid. The time course of recovery after eOPN3 activation that we observed *in vitro* (Figures 4M and S7C–S7F) and *in vivo* (Figures 6F and 7E) is consistent across the four preparations and three cell types used. However, we would like to emphasize that the exact time constants will depend on cell type and expression level and should ideally be determined experimentally in every preparation.

Our *in vitro* experiments showed that eOPN3 is highly light sensitive (Figure 2D), likely due to its recovery kinetics. By relaxing the limitations imposed by tissue heating *in vivo*, eOPN3 allows for optical access to large brain volumes, a major constraint of type-I rhodopsins such as NpHR and Arch (Stujenske et al., 2015; Owen et al., 2019). In our single-photon excitation experiments, we used light exposures above 0.5 $mW \cdot s \cdot mm^{-2}$, leading to complete eOPN3 activation. This approach was aimed at achieving the maximal effect, making the effect of light exposures comparable as long as they are beyond saturation while not leading to tissue heating. However, for experiments where subsets of postsynaptic targets need to be specifically inhibited, light exposure should be minimized to prevent inadvertent eOPN3 activation in neighboring areas. Furthermore, the high

light sensitivity of eOPN3 necessitates working in light shielded conditions when using *in vitro* preparations or transparent organisms. For behavioral experiments, we used single light pulses spaced at 0.1 Hz. The exact irradiance and duty cycle in such experiments should be calibrated based on the volume of the targeted terminal field and the distance from other projections and somata that should remain unaffected.

We also show that eOPN3 has a small two-photon absorption cross section at the typical wavelength ranges used for two-photon Ca^{2+} indicator imaging (Figure 5B). Even continuous raster scanning on the soma and proximal dendrites of neurons expressing eOPN3 and GIRK2-1 only led to a mild somatic hyperpolarization, indicating that eOPN3 is not effectively activated. A potential use case would be to image the activity of a local network before and during inhibition of a given afferent via eOPN3 activation. Here, one potential concern is that the slow recovery kinetics of eOPN3 might lead to an accumulation of $G_{i/o}$ signaling over time, even with the low two-photon absorption properties of eOPN3. This certainly warrants careful controls, but we do not expect this to represent a major constraint in classical raster scanning two-photon imaging. Typical experiments in which network activity is continuously imaged typically involve a larger field of view (1×1 mm versus 106×106 μm used here). This effectively reduces the irradiance per illuminated presynaptic terminal. Second, whatever activation of eOPN3 molecules does take place, it will be limited to the imaging plane, meaning that out-of-focus eOPN3 molecules will not be affected. In contrast, combination of eOPN3-mediated inhibition with scanless two-photon approaches, such as temporal focusing or holographic imaging, might lead to an increased crosstalk. Although we did not observe such an effect in our experiments, one should also take into account that eOPN3 can potentially be activated by the emission light of the imaged indicator. In both types of experiments, the imaging parameters should be optimized to minimize such cross-activation.

To the best of our knowledge, this study along with the adjoining manuscript from the Bruchas and Gereau labs using the lamprey parapinopsin (PPO; Copits et al., 2021) are the first to describe an optogenetic application of bistable nonvisual rhodopsins for efficient light-gated silencing of synaptic transmission. The unique spectral features of eOPN3 and PPO, particularly in their two-photon cross sections, will potentially allow them to be utilized in concert for dual-channel optogenetic control of intracellular signaling. These two rhodopsins are part of a widespread family of non-visual rhodopsins, some of which have been shown to similarly couple to $G_{i/o}$ signaling when expressed heterologously (Koyanagi and Terakita, 2014). Thus, additional members of this rhodopsin family could potentially serve as effective tools for controlling the activity of presynaptic terminals and might be further engineered for spectral tuning or G-protein coupling specificity. Further work is needed to examine the functional properties of these little-explored photoreceptors and adapt them for optogenetic applications. Nevertheless, eOPN3-mediated silencing of transmitter release constitutes a much-needed experimental approach for light-triggered suppression of neuronal communication in the target area of long-range projections, and we expect its application will facilitate research in a variety of neurobiological studies.

STAR★METHODS

Detailed methods are provided in the online version of this paper and include the following:

- KEY RESOURCES TABLE
- RESOURCE AVAILABILITY
  - Lead contact
  - Materials availability
  - Data and code availability
- EXPERIMENTAL MODEL AND SUBJECT DETAILS
  - Animals
  - Cell lines
  - Primary cell cultures
- METHOD DETAILS
  - Molecular cloning of bistable rhodopsin constructs
  - Production of recombinant AAV vectors
  - Primary hippocampal neuron culture
  - Confocal imaging and quantification
  - Histology, imaging, and quantification
  - Cell culture and live-cell cAMP assay
  - Slice culture preparation and transgene delivery
  - Electrophysiology in cultured neurons
  - Slice culture electrophysiology and two-photon microscopy
  - *In vivo* electrophysiological recordings
  - *In vivo* optogenetic silencing of the nigrostriatal pathway
- QUANTIFICATION AND STATISTICAL ANALYSIS

SUPPLEMENTAL INFORMATION

Supplemental information can be found online at https://doi.org/10.1016/j.neuron.2021.03.013.

ACKNOWLEDGMENTS

We thank the members of the Yizhar, Wiegert, Soba, and Schmitz labs for ideas, criticism, and discussions throughout this project. We thank Bryan Copits, Michael Bruchas, and Robert Gereau for insightful comments on the manuscript. We would also like to thank Thomas Oertner for generous sharing of equipment and Eitan Reuveny for the GIRK expression plasmids. This work was supported by funding from the European Research Commission (ERC CoG PrefrontalMap 819496 to O.Y., ERC StG LIFE synapses 714762 to J.S.W., and ERC BrainPlay to D.S.), the Israel Science Foundation (COEX 3131/20), the Adelis Brain Research Award, the Ilse Katz Institute for Material Sciences and Magnetic Resonance Research (to O.Y.), EMBO (ALTF 352-2019 to M.M., ALTF 914-2018 to N.K., and ALTF 378-2019 to J.W.), the Achar Research Fellow Chair in Electrophysiology (to J.D.), the Minerva Foundation (to J.W.), and the German Research Foundation (DFG FOR2419 and SFB936 to J.S.W., DFG EXC-2049, SFB 958, SFB 1315, and SFB 1665 to D.S., and DFG SPP 1926 jointly to O.Y., P.S., B.R.R., and J.S.W.).

AUTHOR CONTRIBUTIONS

Contributions of the authors, according to CRediT, are as follows: conceptualization (M.M., O.Y.), formal analysis (M.M., I.S.-S., P.P., M.P., E.B., N.K., J.D., J.W., B.R.R.), investigation (M.M., I.S.-S., P.P., M.P., E.B., N.K., F.B., S.P., A.G., J.D., J.W., R.L., A. Litvin, F.Z., B.R.R., O.Y.), methodology (M.M., I.S.-S., P.P., M.P., E.B., N.K., R.L., F.Z., K.S., J.S.W.), resources (R.L., P.S., D.S., A. Lüthi, B.R.R., J.S.W., O.Y.), supervision (P.S., D.S., A. Lüthi, B.R.R., J.S.W., O.Y.), writing the original draft (M.M., I.S.-S., M.P., B.R.R., J.S.W., O.Y.), review and editing (M.M., I.S.-S., P.P., M.P., N.K., B.R.R., J.W., D.S.,

A. Lüthi, J.S.W., O.Y.), funding acquisition (P.S., J.S.W., O.Y.), overall project administration (O.Y.).

DECLARATION OF INTERESTS

O.Y. and M.M. have disclosed these findings to Yeda, the Weizmann Institute Technology Transfer Arm, which is filing a patent application on these developments. The constructs and viral vectors remain freely available from the authors and through Addgene.

Received: February 2, 2021
Revised: March 2, 2021
Accepted: March 9, 2021
Published: May 11, 2021

SUPPORTING CITATIONS

The following references appear in the supplemental information: Edgar et al. (2004); Lesage et al. (1994).

REFERENCES

Alcaro, A., Huber, R., and Panksepp, J. (2007). Behavioral functions of the mesolimbic dopaminergic system: an affective neuroethological perspective. Brain Res. Brain Res. Rev. *56*, 283–321.

Armbruster, B.N., Li, X., Pausch, M.H., Herlitze, S., and Roth, B.L. (2007). Evolving the lock to fit the key to create a family of G protein-coupled receptors potently activated by an inert ligand. Proc. Natl. Acad. Sci. USA *104*, 5163–5168.

Bailes, H.J., Zhuang, L.-Y., and Lucas, R.J. (2012). Reproducible and sustained regulation of Gαs signalling using a metazoan opsin as an optogenetic tool. PLoS ONE *7*, e30774.

Ballister, E.R., Rodgers, J., Martial, F., and Lucas, R.J. (2018). A live cell assay of GPCR coupling allows identification of optogenetic tools for controlling Go and Gi signaling. BMC Biol. *16*, 10.

Barter, J.W., Li, S., Lu, D., Bartholomew, R.A., Rossi, M.A., Shoemaker, C.T., Salas-Meza, D., Gaidis, E., and Yin, H.H. (2015). Beyond reward prediction errors: the role of dopamine in movement kinematics. Front. Integr. Nuerosci. *9*, 39.

Basu, J., Zaremba, J.D., Cheung, S.K., Hitti, F.L., Zemelman, B.V., Losonczy, A., and Siegelbaum, S.A. (2016). Gating of hippocampal activity, plasticity, and memory by entorhinal cortex long-range inhibition. Science *351*, aaa5694.

Bean, B.P. (1989). Neurotransmitter inhibition of neuronal calcium currents by changes in channel voltage dependence. Nature *340*, 153–156.

Beck, S., Yu-Strzelczyk, J., Pauls, D., Constantin, O.M., Gee, C.E., Ehmann, N., Kittel, R.J., Nagel, G., and Gao, S. (2018). Synthetic Light-Activated ion channels for optogenetic activation and inhibition. Front. Neurosci. *12*, 643.

Bekkers, J.M., and Stevens, C.F. (1991). Excitatory and inhibitory autaptic currents in isolated hippocampal neurons maintained in cell culture. Proc. Natl. Acad. Sci. USA *88*, 7834–7838.

Bernal Sierra, Y.A., Rost, B.R., Pofahl, M., Fernandes, A.M., Kopton, R.A., Moser, S., Holtkamp, D., Masala, N., Beed, P., Tukker, J.J., et al. (2018). Potassium channel-based optogenetic silencing. Nat. Commun. *9*, 4611.

Bindels, D.S., Haarbosch, L., van Weeren, L., Postma, M., Wiese, K.E., Mastop, M., Aumonier, S., Gotthard, G., Royant, A., Hink, M.A., and Gadella, T.W.J., Jr. (2017). mScarlet: a bright monomeric red fluorescent protein for cellular imaging. Nat. Methods *14*, 53–56.

Borgkvist, A., Avegno, E.M., Wong, M.Y., Kheirbek, M.A., Sonders, M.S., Hen, R., and Sulzer, D. (2015). Loss of Striatonigral GABAergic Presynaptic Inhibition Enables Motor Sensitization in Parkinsonian Mice. Neuron *87*, 976–988.

Brenowitz, S., David, J., and Trussell, L. (1998). Enhancement of synaptic efficacy by presynaptic GABA(B) receptors. Neuron *20*, 135–141.

Burke, K.J., Jr., Keeshen, C.M., and Bender, K.J. (2018). Two Forms of Synaptic Depression Produced by Differential Neuromodulation of Presynaptic Calcium Channels. Neuron *99*, 969–984.e7.

Chalifoux, J.R., and Carter, A.G. (2011). GABAB receptor modulation of voltage-sensitive calcium channels in spines and dendrites. J. Neurosci. *31*, 4221–4232.

Copits, B.A., Gowrishankar, R., O'Neill, P.R., Li, J.-N., Girven, K.S., Yoo, J.J., Meshik, X., Parker, K.E., Spangler, S.M., Elerding, A.J., et al. (2021). A photoswitchable GPCR-based opsin for presynaptic inhibition. Neuron *109*. Published online May 11, 2021. https://doi.org/10.1016/j.neuron.2021.04.026.

Creed, M., Pascoli, V.J., and Lüscher, C. (2015). Addiction therapy. Refining deep brain stimulation to emulate optogenetic treatment of synaptic pathology. Science *347*, 659–664.

Currie, K.P.M. (2010). G protein modulation of CaV2 voltage-gated calcium channels. Channels (Austin) *4*, 497–509.

da Silva, J.A., Tecuapetla, F., Paixão, V., and Costa, R.M. (2018). Dopamine neuron activity before action initiation gates and invigorates future movements. Nature *554*, 244–248.

Dana, H., Sun, Y., Mohar, B., Hulse, B.K., Kerlin, A.M., Hasseman, J.P., Tsegaye, G., Tsang, A., Wong, A., Patel, R., et al. (2019). High-performance calcium sensors for imaging activity in neuronal populations and microcompartments. Nat. Methods *16*, 649–657.

Dittman, J.S., and Regehr, W.G. (1996). Contributions of calcium-dependent and calcium-independent mechanisms to presynaptic inhibition at a cerebellar synapse. J. Neurosci. *16*, 1623–1633.

Dobrunz, L.E., Huang, E.P., and Stevens, C.F. (1997). Very short-term plasticity in hippocampal synapses. Proc. Natl. Acad. Sci. USA *94*, 14843–14847.

Edgar, R.C. (2004). MUSCLE: multiple sequence alignment with high accuracy and high throughput. Nucleic Acids Res. *32*, 1792–1797.

Evans, D.A., Stempel, A.V., Vale, R., Ruehle, S., Lefler, Y., and Branco, T. (2018). A synaptic threshold mechanism for computing escape decisions. Nature *558*, 590–594.

Froudarakis, E., Fahey, P.G., Reimer, J., Smirnakis, S.M., Tehovnik, E.J., and Tolias, A.S. (2019). The Visual Cortex in Context. Annu Rev Vis Sci *5*, 317–339.

Gee, C.E., Ohmert, I., Wiegert, J.S., and Oertner, T.G. (2017). Preparation of Slice Cultures from Rodent Hippocampus. Cold Spring Harb. Protoc. *2017*, https://doi.org/10.1101/pdb.prot094888.

Gerachshenko, T., Blackmer, T., Yoon, E.-J., Bartleson, C., Hamm, H.E., and Alford, S. (2005). Gbetagamma acts at the C terminus of SNAP-25 to mediate presynaptic inhibition. Nat. Neurosci. *8*, 597–605.

Graham, F.L., and van der Eb, A.J. (1973). A new technique for the assay of infectivity of human adenovirus 5 DNA. Virology *52*, 456–467.

Grealish, S., Mattsson, B., Draxler, P., and Björklund, A. (2010). Characterisation of behavioural and neurodegenerative changes induced by intranigral 6-hydroxydopamine lesions in a mouse model of Parkinson's disease. Eur. J. Neurosci. *31*, 2266–2278.

Grimm, D., Kay, M.A., and Kleinschmidt, J.A. (2003). Helper virus-free, optically controllable, and two-plasmid-based production of adeno-associated virus vectors of serotypes 1 to 6. Mol. Ther. *7*, 839–850.

Hamid, E., Church, E., Wells, C.A., Zurawski, Z., Hamm, H.E., and Alford, S. (2014). Modulation of neurotransmission by GPCRs is dependent upon the microarchitecture of the primed vesicle complex. J. Neurosci. *34*, 260–274.

Herlitze, S., Garcia, D.E., Mackie, K., Hille, B., Scheuer, T., and Catterall, W.A. (1996). Modulation of Ca2+ channels by G-protein beta gamma subunits. Nature *380*, 258–262.

Ikeda, S.R. (1996). Voltage-dependent modulation of N-type calcium channels by G-protein beta gamma subunits. Nature *380*, 255–258.

Jackman, S.L., and Regehr, W.G. (2017). The mechanisms and functions of synaptic facilitation. Neuron *94*, 447–464.

Kajikawa, Y., Saitoh, N., and Takahashi, T. (2001). GTP-binding protein β γ subunits mediate presynaptic calcium current inhibition by GABA(B) receptor. Proc. Natl. Acad. Sci. USA *98*, 8054–8058.

Klavir, O., Prigge, M., Sarel, A., Paz, R., and Yizhar, O. (2017). Manipulating fear associations via optogenetic modulation of amygdala inputs to prefrontal cortex. Nat. Neurosci. *20*, 836–844.

Koyanagi, M., and Terakita, A. (2014). Diversity of animal opsin-based pigments and their optogenetic potential. Biochim. Biophys. Acta *1837*, 710–716.

Koyanagi, M., Kawano, E., Kinugawa, Y., Oishi, T., Shichida, Y., Tamotsu, S., and Terakita, A. (2004). Bistable UV pigment in the lamprey pineal. Proc. Natl. Acad. Sci. USA *101*, 6687–6691.

Koyanagi, M., Takada, E., Nagata, T., Tsukamoto, H., and Terakita, A. (2013). Homologs of vertebrate Opn3 potentially serve as a light sensor in nonphotoreceptive tissue. Proc Natl Acad Sci U S A *110*, 4998–5003.

Kravitz, A.V., Freeze, B.S., Parker, P.R., Kay, K., Thwin, M.T., Deisseroth, K., and Kreitzer, A.C. (2010). Regulation of parkinsonian motor behaviours by optogenetic control of basal ganglia circuitry. Nature *466*, 622–626.

Kuzhikandathil, E.V., and Oxford, G.S. (2002). Classic D1 dopamine receptor antagonist R-(+)-7-chloro-8-hydroxy-3-methyl-1-phenyl-2,3,4,5-tetrahydro-1H-3-benzazepine hydrochloride (SCH23390) directly inhibits G protein-coupled inwardly rectifying potassium channels. Mol Pharmacol *62*, 119–126.

Lafferty, C.K., and Britt, J.P. (2020). Off-Target Influences of Arch-Mediated Axon Terminal Inhibition on Network Activity and Behavior. Front. Neural Circuits *14*, 10.

Lesage, F., Duprat, F., Fink, M., Guillemare, E., Coppola, T., Lazdunski, M., and Hugnot, J.P. (1994). Cloning provides evidence for a family of inward rectifier and G-protein coupled K+ channels in the brain. FEBS Lett. *353*, 37–42.

Li, X., Gutierrez, D.V., Hanson, M.G., Han, J., Mark, M.D., Chiel, H., Hegemann, P., Landmesser, L.T., and Herlitze, S. (2005). Fast noninvasive activation and inhibition of neural and network activity by vertebrate rhodopsin and green algae channelrhodopsin. Proc. Natl. Acad. Sci. USA *102*, 17816–17821.

Lin, J.Y., Sann, S.B., Zhou, K., Nabavi, S., Proulx, C.D., Malinow, R., Jin, Y., and Tsien, R.Y. (2013). Optogenetic inhibition of synaptic release with chromophore-assisted light inactivation (CALI). Neuron *79*, 241–253, https://doi.org/10.1016/j.neuron.2013.05.022.

Liu, Q., Sinnen, B.L., Boxer, E.E., Schneider, M.W., Grybko, M.J., Buchta, W.C., Gibson, E.S., Wysoczynski, C.L., Ford, C.P., Gottschalk, A., et al. (2019). A Photoactivatable Botulinum Neurotoxin for Inducible Control of Neurotransmission. Neuron *101*, 863–875.

Magnus, C.J., Lee, P.H., Atasoy, D., Su, H.H., Looger, L.L., and Sternson, S.M. (2011). Chemical and genetic engineering of selective ion channel-ligand interactions. Science *333*, 1292–1296.

Mahn, M., Prigge, M., Ron, S., Levy, R., and Yizhar, O. (2016). Biophysical constraints of optogenetic inhibition at presynaptic terminals. Nat Neurosci *19*, 554–556.

Mahn, M., Gibor, L., Patil, P., Cohen-Kashi Malina, K., Oring, S., Printz, Y., Levy, R., Lampl, I., and Yizhar, O. (2018). High-efficiency optogenetic silencing with soma-targeted anion-conducting channelrhodopsins. Nat Commun *9*, 4125.

Malvaez, M., Shieh, C., Murphy, M.D., Greenfield, V.Y., and Wassum, K.M. (2019). Distinct cortical-amygdala projections drive reward value encoding and retrieval. Nat Neurosci *22*, 762–769.

Mathis, A., Mamidanna, P., Cury, K.M., Abe, T., Murthy, V.N., Mathis, M.W., and Bethge, M. (2018). DeepLabCut: markerless pose estimation of user-defined body parts with deep learning. Nat. Neurosci. *21*, 1281–1289.

Nabavi, S., Fox, R., Proulx, C.D., Lin, J.Y., Tsien, R.U., and Malinow, R. (2014). Engineering a memory with LTD and LTP. Nature *511*, 348–352.

Niell, C.M., and Stryker, M.P. (2008). Highly selective receptive fields in mouse visual cortex. J. Neurosci. *28*, 7520–7536.

Owen, S.F., Liu, M.H., and Kreitzer, A.C. (2019). Thermal constraints on in vivo optogenetic manipulations. Nat. Neurosci. *22*, 1061–1065.

Pachitariu, M., Steinmetz, N., Kadir, S., Carandini, M., and Harris, K.D. (2016). Kilosort: realtime spike-sorting for extracellular electrophysiology with hundreds of channels. bioRxiv. Published online June 30, 2016. https://doi.org/10.1101/061481.

Pologruto, T.A., Sabatini, B.L., and Svoboda, K. (2003). ScanImage: Flexible software for operating laser scanning microscopes. BioMed Eng Online *2*, https://doi.org/10.1186/1475-925X-2-13.

Raimondo, J.V., Kay, L., Ellender, T.J., and Akerman, C.J. (2012). Optogenetic silencing strategies differ in their effects on inhibitory synaptic transmission. Nat Neurosci *15*, 1102–1104.

Rizzo, M.A., Springer, G.H., Granada, B., and Piston, D.W. (2004). An improved cyan fluorescent protein variant useful for FRET. Nat. Biotechnol. *22*, 445–449.

Rost, B.R., Breustedt, J., Schoenherr, A., Grosse, G., Ahnert-Hilger, G., and Schmitz, D. (2010). Autaptic cultures of single hippocampal granule cells of mice and rats. Eur J Neurosci *32*, 939–947.

Rost, B.R., Nicholson, P., Ahnert-Hilger, G., Rummel, A., Rosenmund, C., Breustedt, J., and Schmitz, D. (2011). Activation of metabotropic GABA receptors increases the energy barrier for vesicle fusion. J. Cell Sci. *124*, 3066–3073.

Rost, B.R., Schneider, F., Grauel, M.K., Wizny, C., Bentz, C., Blessing, A., Rosenmund, T., Jentsch, T.J., Schmitz, D., Hegemann, P., and Rosenmund, C. (2015). Optogenetic acidification of synaptic vesicles and lysosomes. Nat Neurosci *18*, 1845–1852.

Sakaba, T., and Neher, E. (2003). Direct modulation of synaptic vesicle priming by GABA(B) receptor activation at a glutamatergic synapse. Nature *424*, 775–778.

Scanziani, M., Capogna, M., Gähwiler, B.H., and Thompson, S.M. (1992). Presynaptic inhibition of miniature excitatory synaptic currents by baclofen and adenosine in the hippocampus. Neuron *9*, 919–927.

Schindelin, J., Arganda-Carreras, I., Frise, E., Kaynig, V., Longair, M., Pietzsch, T., Preibisch, S., Rueden, C., Saalfeld, S., and Schmid, B. (2012). Fiji: an open-source platform for biological-image analysis. Nat Methods *9*, 676–682.

Stachniak, T.J., Ghosh, A., and Sternson, S.M. (2014). Chemogenetic synaptic silencing of neural circuits localizes a hypothalamus→midbrain pathway for feeding behavior. Neuron *82*, 797–808.

Sternson, S.M., and Roth, B.L. (2014). Chemogenetic tools to interrogate brain functions. Annu. Rev. Neurosci. *37*, 387–407.

Stujenske, J.M., Spellman, T., and Gordon, J.A. (2015). Modeling the Spatiotemporal Dynamics of Light and Heat Propagation for In Vivo Optogenetics. Cell Rep. *12*, 525–534.

Suter, B.A., O'Connor, T., Iyer, V., Petreanu, L.T., Hooks, B.M., Kiritani, T., Svoboda, K., and Shepherd, G.M. (2010). Ephus: multipurpose data acquisition software for neuroscience experiments. Front. Neural Circuits *4*, 100.

Tecuapetla, F., Matias, S., Dugue, G.P., Mainen, Z.F., and Costa, R.M. (2014). Balanced activity in basal ganglia projection pathways is critical for contraversive movements. Nat. Commun. *5*, 4315.

Terakita, A. (2005). The opsins. Genome Biol. *6*, 213.

Tsukamoto, H., and Terakita, A. (2010). Diversity and functional properties of bistable pigments. Photochem Photobiol Sci *9*, 1435–1443.

Wiegert, J.S., Mahn, M., Prigge, M., Printz, Y., and Yizhar, O. (2017a). Silencing Neurons: Tools, Applications, and Experimental Constraints. Neuron *95*, 504–529.

Wiegert, J.S., Gee, C.E., and Oertner, T.G. (2017b). Single-Cell Electroporation of Neurons. Cold Spring Harb Protoc *2017*, https://doi.org/10.1101/pdb.prot094904.

Wiegert, J.S., Gee, C.E., and Oertner, T.G. (2017c). Viral Vector-Based Transduction of Slice Cultures. Cold Spring Harb Protoc *2017*, https://doi.org/10.1101/pdb.prot094896.

Wimmer, V.C., Nevian, T., and Kuner, T. (2004). Targeted *in vivo* expression of proteins in the calyx of Held. Pflugers Arch. *449*, 319–333, https://doi.org/10.1007/s00424-004-1327-9.

Wu, L.G., and Saggau, P. (1994). Adenosine inhibits evoked synaptic transmission primarily by reducing presynaptic calcium influx in area CA1 of hippocampus. Neuron *12*, 1139–1148.

Yang, L., Lee, K., Villagracia, J., and Masmanidis, S.C. (2020). Open source silicon microprobes for high throughput neural recording. J Neural Eng *17*, 016036.

Yizhar, O., Fenno, L.E., Davidson, T.J., Mogri, M., and Deisseroth, K. (2011). Optogenetics in neural systems. Neuron *71*, 9–34.

Zhang, F., Wang, L.P., Brauner, M., Liewald, J.F., Kay, K., Watzke, N., Wood, P.G., Bamberg, E., Nagel, G., Gottschalk, A., and Deisseroth, K. (2007). Multimodal fast optical interrogation of neural circuitry. Nature *446*, 633–639.

Zhu, H., and Roth, B.L. (2014). Silencing synapses with DREADDs. Neuron *82*, 723–725.

Zurawski, Z., Thompson Gray, A.D., Brady, L.J., Page, B., Church, E., Harris, N.A., Dohn, M.R., Yim, Y.Y., Hyde, K., Mortlock, D.P., et al. (2019a). Disabling the Gβγ-SNARE interaction disrupts GPCR-mediated presynaptic inhibition, leading to physiological and behavioral phenotypes. Science *12*, eaat8595.

Zurawski, Z., Yim, Y.Y., Alford, S., and Hamm, H.E. (2019b). The expanding roles and mechanisms of G protein-mediated presynaptic inhibition. J Biol Chem *294*, 1661–1670.

STAR★METHODS

KEY RESOURCES TABLE

REAGENT or RESOURCE	SOURCE	IDENTIFIER
Bacterial and virus strains		
rAAV2/1&2.CamKIIα(0.4).OPN3-mScarlet	This paper	N/A
rAAV2/1&2.CamKIIα.eYFP.WPRE	This paper	N/A
rAAV2/1&2.CamKIIα(0.4).eOPN3-mScarlet	This paper	www.addgene.org/125712/
rAAV2/1&2.hSyn.SIO-eOPN3-mScarlet	This paper	www.addgene.org/125713/
Chemicals, peptides, and recombinant proteins		
(R)-baclofen	Tocris	Cat#0796
Clozapine-N-Oxide	Enzo Life Science	Cat#-BML-NS105
CPPene	Tocris	Cat#1265
Gabazine	Tocris	Cat#1262
NBQX	Tocris	Cat#1044
Pertussis toxin	Sigma-Aldrich	Cat#516560
Picrotoxin	Tocris	Cat#1128
SCH23390	Tocris	Cat#0925
Critical commercial assays		
GloSensor cAMP Assay	Promega	Cat#E1171
Experimental models: Cell lines		
HEK293T	Sigma-Aldrich	Cat#12022001 RRID:CVCL_0063
Experimental models: Organisms/strains		
Mouse: C57BL/6JRccHsd	Envigo	Cat#043
Mouse: C57BL/6NHsd	Envigo	Cat#044
Mouse: DAT-IRES-Cre	The Jackson Laboratory	Strain #006660
Rattus norvegicus: Sprague-Dawley	Envigo	Cat#002
Rattus norvegicus: Wistar	Charles River, bred in the animal facility, UKE Hamburg	Cat#003
Recombinant DNA		
pAAV-CaMKIIa(0.4)-OPN3-mScarlet	This Paper	N/A
pAAV-CaMKIIa(0.4)-PufTMT3a-mScarlet	This Paper	N/A
pAAV-CaMKIIa(0.4)-OPN3-M4-mScarlet	This Paper	N/A
pAAV-CaMKIIa(0.4)-PufTMT3a-M4-mScarlet	This Paper	N/A
pAAV-CamKIIα-eYFP	Karl Deisseroth	RRID:Addgene_105622; www.addgene.org/105622
pcDNA3.1-GIRK2-1	Eitan Reuveny	GenBank: NM_001025584.2
pcDNA3.1-mCerulean	Dave Piston; Rizzo et al.,2004	RRID:Addgene_15214; www.addgene.org/15214/
pAAV-CaMKIIa(0.4)-eOPN3-mScarlet	This Paper	RRID:Addgene_125712; www.addgene.org/125712/
pAAV-hSyn-SIO-eOPN3-mScarlet	This Paper	RRID:Addgene_125713; www.addgene.org/125713/
Software and algorithms		
Fiji	Schindelin et al., 2012	RRID:SCR_002285; http://imagej.net/Fiji
MATLAB 2018b	Mathworks	RRID:SCR_001622; www.mathworks.com
Prism 8.2.1	Graphpad	RRID:SCR_002798; https://www.graphpad.com
RStudio Desktop	RStudio	RRID:SCR_000432; https://www.rstudio.com
Ephus	Suter et al., 2010	https://doi.org/10.3389/fncir.2010.00100
WaveSurfer	Janelia	https://wavesurfer.janelia.org

(*Continued on next page*)

Continued

REAGENT or RESOURCE	SOURCE	IDENTIFIER
ScanImage	Vidrio Technologies	RRID:SCR_014307; v2017b http://www.scanimage.org/
EthoVision XT 11.5	Noldus	RRID:SCR_000441; https://www.noldus.com/ethovision-xt
DeepLabCut	Mathis et al., 2018	www.mackenziemathislab.org/deeplabcut

RESOURCE AVAILABILITY

Lead contact

Further information and requests for resources and reagents should be directed to and will be fulfilled by the lead contact, Ofer Yizhar (ofer.yizhar@weizmann.ac.il).

Materials availability

Plasmids and viral vectors for expression of eOPN3 are available from Addgene (https://www.addgene.org/Ofer_Yizhar/).

Data and code availability

The datasets and the code that support the findings of this study are available from the lead contact upon reasonable request.

EXPERIMENTAL MODEL AND SUBJECT DETAILS

Animals

Animal experiments were carried out according to the guidelines stated in directive 2010/63/EU of the European Parliament on the protection of animals used for scientific purposes. Animal experiments at the Weizmann Institute were approved by the Weizmann Institute Institutional Animal Care and Use Committee (IACUC); experiments in Berlin were approved by local authorities in Berlin and the animal welfare committee of the Charité – Universitätsmedizin Berlin, Germany. Experiments in Hamburg were done in accordance with the guidelines of local authorities and Directive 2010/63/EU. Experiments in Basel were done in accordance with institutional guidelines at the Friedrich Miescher Institute for Biomedical Research and were approved by the Veterinary Department of the Canton of Basel-Stadt. For *in vivo* electrophysiological recordings male mice (C57BL/6JRccHsd; Envigo, Cat#043) at 8-9 weeks old were used. Mean weight at the day of surgery was 23.8 g. Experimental mice were individually housed. All mice were assigned to the same experimental group. For *in vivo* behavioral experiments male and female mice (DAT-IRES-Cre; The Jackson Laboratory, Strain #006660) were used. Mice were housed in single gender groups, 2-4 littermates/cage. Littermates from single cages underwent surgery on the same day and were assigned to the eOPN3 or control group such that cages always included mixed groups. The control group included 8 mice (3 males and 5 females). Age at day of surgery was 9-14 weeks (mean = 12 weeks). Mean weight at the day of surgery was 19.6 g for females and 24.6 g for males. The eOPN3 group included 7 mice (3 males and 4 females). Age at day of surgery was 9-14 weeks (mean = 11.9 weeks). Mean weight at the day of surgery was 19.2 g for females and 24.75 g for males. The room temperature was set at 22°C (±2°C) and room humidity was set at 55% (±10%). Mice were kept in a 12-h light/dark cycle with access to food and water *ad libitum*. Mice were checked daily by animal caretakers.

Cell lines

HEK293T cells (RRID:CVCL_0063) were incubated at 37°C (5% CO2) in DMEM containing 4500 mg/L glucose, L-glutamine, (Sigma) with penicillin (100 U/mL), streptomycin (100 mg/mL), and 10% FBS. The cell line is authenticated by the European collection of authenticated cell cultures. Sex of these cells is female, and the cell line is derived from fetal human tissue.

Primary cell cultures

Primary cultured hippocampal neurons were prepared from post-natal day 0 Sprague-Dawley rat pups (Envigo, Cat#002) of either sex.

Autaptic cultures of primary hippocampal neurons on glia cell micro-islands were prepared from newborn mice (C57BL/6NHsd; Envigo, Cat#044) of either sex.

Organotypic hippocampal slices were prepared from post-natal day 5-7 Wistar rats (Charles River Cat#003 bred in the animal facility, UKE Hamburg) of either sex.

METHOD DETAILS

Molecular cloning of bistable rhodopsin constructs

The genes encoding mScarlet (Bindels et al., 2017), OPN3, PufTMT3a, OPN3-M4 and PufTMT3a-M4 were synthesized using the Twist gene synthesis service (Twist Bioscience, USA). The Rho1D4 sequence (TETSQVAPA) was added at the C terminus of all rhodopsins. All genes were subcloned into pAAV vectors under the CamKIIa promoter and in-frame with mScarlet at the C terminus. The eOPN3 plasmid was generated by adding the Kir2.1 membrane trafficking signal (KSRITSEGEYIPLDQIDINV) between the OPN3 and the mScarlet coding sequences and the Kir2.1 ER export signal (FCYENEV) following the C terminus of mScarlet. eOPN3 constructs and viruses are available from Addgene: https://www.addgene.org/Ofer_Yizhar/

Production of recombinant AAV vectors

HEK293T cells were seeded at 25%–35% confluence. The cells were transfected 24 h later with plasmids encoding AAV rep, cap of AAV1 and AAV2 and a vector plasmid for the rAAV cassette expressing the relevant DNA using the PEI method (Grimm et al., 2003). Cells and medium were harvested 72 h after transfection, pelleted by centrifugation (300 g), resuspended in lysis solution ([mM]: 150 NaCl, 50 Tris-HCl; pH 8.5 with NaOH) and lysed by three freeze-thaw cycles. The crude lysate was treated with 250 U benzonase (Sigma) per 1 mL of lysate at 37°C for 1.5 h to degrade genomic and unpackaged AAV DNA before centrifugation at 3,000 g for 15 min to pellet cell debris. The virus particles in the supernatant (crude virus) were purified using heparin-agarose columns, eluted with soluble heparin, washed with phosphate buffered saline (PBS) and concentrated by Amicon columns. Viral suspension was aliquoted and stored at –80°C. Viral titers were measured using real-time PCR. In experiments that compared between different constructs, viral titers were matched by dilution to the lowest concentration. AAV vectors used for neuronal culture transduction were added 4 days after cell seeding. Recordings were carried out between 4-20 days after viral transduction. The following viral vectors were used in this study:

AAV2/1&2.CamKIIa(0.4).OPN3-mScarlet, AAV2/1&2.CamKIIa(0.4).eOPN3-mScarlet, AAV2/5.CamKIIa(0.4).eOPN3-mScarlet, AAV2/9.CamKIIa(0.4).eOPN3-mScarlet AAV2/1&2.CamKIIa.eYFP.WPRE, AAV2/1&2.hSyn.SIO-eOPN3-mScarletAAV2/1&2.EF1a.DIO.eYFP.WPRE.

Primary hippocampal neuron culture

Primary cultured hippocampal neurons were prepared from male and female P0 Sprague-Dawley rat pups (Envigo). CA1 and CA3 were isolated, digested with 0.4 mg ml^{-1} papain (Worthington), and plated into a 24-well plate at a density of 65,000 cells per well, onto glass coverslips pre-coated with 1:30 Matrigel (Corning). Cultured neurons were maintained in a 5% CO_2 humidified incubator in Neurobasal-A medium (Invitrogen) containing 1.25% fetal bovine serum (FBS, Biological Industries), 4% B-27 supplement (GIBCO), and 2 mM Glutamax (GIBCO). To inhibit glial overgrowth, 200 μM fluorodeoxyuridine (Sigma) was added after 4 days of *in vitro* culture (DIV).

Neurons were transfected using the Ca^{2+} phosphate method (Graham and van der Eb, 1973). Briefly, the medium of primary hippocampal neurons cultured in a 24 well plate was collected and replaced with 400 μl serum-free modified eagle medium (MEM, Thermo Fisher Scientific). 30 μl transfection mix (2 μg plasmid DNA and 250 μM $CaCl_2$ in HBS at pH 7.05) were added per well. After 1 h incubation the cells were washed 2 times with MEM and the medium was changed back to the collected original medium. Cultured neurons were used between 14 – 17 DIV for experiments. The following plasmids were used in this study: pAAV-CamKIIa(0.4)-OPN3-mScarlet, pAAV-CamKIIa(0.4)-eOPN3-mScarlet, pAAV-CamKIIa(0.4)-PufTMT3a-mScarlet, pAAV-CamKIIa(0.4)-OPN3-M4-mScarlet, pAAV-CamKIIa-(0.4)PufTMT3a-M4-mScarlet, pAAV-CamKIIa(0.4)-eYFP. The pcDNA3.1-GIRK2-1 plasmid was a gift from Eitan Reuveny.

Autaptic cultures of primary hippocampal neurons on glia cell micro-islands were prepared from newborn mice (C57BL/6NHsd; Envigo, Cat#044) of either sex as previously described (Rost et al., 2010). Briefly, 300 μm diameter spots of growth permissive substrate consisting of 0.7 mg ml^{-1} collagen and 0.1 mg ml^{-1} poly-D-lysine was applied with a custom-made stamp on coverslips coated with a thin film of agarose. Astrocytes were seeded onto the glass coverslips and were allowed to proliferate in Dulbecco's modified eagle medium (DMEM) supplemented with 10% fetal calf serum and 0.2% penicillin/streptomycin (Invitrogen) for one more week to form glia micro-islands. After changing the medium to Neurobasal-A supplemented with 2% B27 and 0.2% penicillin/streptomycin, hippocampal neurons prepared from P0 mice were added at a density of 370 cells cm^{-2}. Neurons were infected with AAVs at DIV 1–3 and recorded between DIV 14 and DIV 21.

Confocal imaging and quantification

Primary cultured hippocampal neurons were transfected at 5 DIV with plasmids encoding a rhodopsin protein (mScarlet, OPN3, PufTMT3a, OPN3-M4, PufTMT3a-M4, eOPN3) along with pAAV-CamKIIa-eYFP. Four days after transfection, cells were fixed and permeabilized, washed 4 times with PBS and stained for 3 min with DAPI (5 mg/mL solution diluted 1:30,000 prior to staining). Coverslips were then mounted using PVA-DABCO (Sigma) and allowed to dry. Images of mScarlet and EYFP fluorescence were acquired using a Zeiss LSM 700 confocal microscope with a 20X magnification objective. Fluorescence was quantified using ImageJ (Schindelin et al., 2012) by marking a region containing the somatic cytoplasm using the EYFP fluorescence and then measuring the average pixel intensity in the red imaging channel.

Histology, imaging, and quantification

Mice were deeply anesthetized using pentobarbital (130 mg per kg, intraperitoneally) and then transcardially perfused with ice-cold PBS (pH 7.4, 10 ml) followed by 4% paraformaldehyde (PFA, 10 ml) solution. Heads were removed and post-fixed overnight at 4 °C in 4% PFA. Then, brains were extracted and transferred to 30% sucrose solution for at least 24 h. Coronal sections (40 μm) were acquired using a microtome (Leica Microsystems) and stained with a nucleic acid dye (4,6-diamidino-2-phenylindole (DAPI), 1:10,000). Slices were then mounted on gelatin-coated slides, dehydrated, and embedded in DABCO mounting medium (Sigma). Slices were imaged using a VS120 microscope (Olympus), at 10x magnification with two channels: 1) DAPI, to identify brain structures, the corresponding anterior-posterior coordinates and sites of lesions created by the optic fiber. 2) Either Cy3 (mScarlet - eOPN3 mice) or FITC (eYFP - control mice), to measure expression levels in cells and projections. The resulting images were then analyzed using ImageJ to measure the fluorescence of DAPI and additional fluorophores within specific target regions. For each slice, a rectangle outlining the target site was defined and copied to the contralateral (non-expressing) hemisphere. Mean fluorescence values were measured separately for each channel and compared between hemispheres, demonstrating differences in fluorophore expression but not in DAPI staining. Imaging acquisition parameters and the ensuing analysis pipeline were kept constant across mice to allow comparison between the eOPN3 and the control groups.

Cell culture and live-cell cAMP assay

Optical activation and G protein coupling of mosOPN3-mScarlett and chimeric GPCR constructs was tested in HEK293T cells using a live cell assay (Ballister et al., 2018). Briefly, GPCR constructs were subcloned into pcDNA3.1 (ThermoFisher). HEK293T cells were incubated at 37°C (5% CO_2) in DMEM containing 4500 mg/L glucose, L-glutamine (Sigma Aldrich) with penicillin (100 U/mL), streptomycin (100 mg/mL), and 10% FBS. For transfection, cells were seeded into solid white 96-well plates (Greiner) coated with poly-L-Lysine (Sigma Aldrich) and transfected with Lipofectamine 2000 (ThermoFisher) together with individual G protein chimera (GsX) and Glo22F (Promega). Cells were incubated for 24 h at 37°C, 5% CO2 and, subsequently, in L-15 media (without phenol-red, with L-glutamine, 1% FBS, penicillin, streptomycin (100 mg/mL)) and 9-*cis* retinal (10 mM) and beetle luciferin (2 mM in 10 mM HEPES pH 6.9) for 1 h at RT. Cells were kept in the dark throughout the entire time. Baseline luminescence was measured 3 times and opto-GPCR activation was then induced by illuminating cells for 1 s with an LED plate (530 nm, 5.5 $\mu W \cdot mm^{-2}$, Phlox Corp.) Changes in cAMP levels were measured over time using GloSensor luminescence. For the assay quantification each technical repeat was normalized to its pre-light baseline.

Slice culture preparation and transgene delivery

Organotypic hippocampal slices were prepared from Wistar rats at postnatal day 5-7 as described (Gee et al., 2017). Briefly, dissected hippocampi were cut into 400 μm slices with a tissue chopper and placed on a porous membrane (Millicell CM, Millipore). Cultures were maintained at 37°C, 5% CO2 in a medium containing 80% MEM (Sigma M7278), 20% heat-inactivated horse serum (Sigma H1138) supplemented with 1 mM L-glutamine, 0.00125% ascorbic acid, 0.01 mg/mL insulin, 1.44 mM $CaCl_2$, 2 mM $MgSO_4$ and 13 mM D-glucose. No antibiotics were added to the culture medium.

For transgene delivery in organotypic slices, individual CA3 pyramidal cells were transfected by single-cell electroporation between DIV 15-20 as previously described (Wiegert et al., 2017b). The plasmids pAAV-CKIIa(0.4)-eOPN3-mScarlet, pCI-hSyn-mCerulean, CAG-GIRK2-1 and pGP-AAV-hSyn-jGCaMP7f-WPRE were all diluted to 50 ng/μl in K-gluconate-based solution consisting of (in mM): 135 K-gluconate, 10 HEPES, 0.2 EGTA, 4 Na_2-ATP, 0.4 Na-GTP, 4 $MgCl_2$, 3 ascorbate, 10 Na_2- phosphocreatine, pH 7.2, 295 mOsm/kg. An Axoporator 800A (Molecular Devices) was used to deliver 25 hyperpolarizing pulses (−12 V, 0.5 ms) at 50 Hz. During electroporation slices were maintained in pre-warmed (37°C) HEPES-buffered solution in (mM): 145 NaCl, 10 HEPES, 25 D-glucose, 2.5 KCl, 1 $MgCl_2$ and 2 $CaCl_2$ (pH 7.4, sterile filtered).

For targeted viral vector-based transduction of organotypic hippocampal slice cultures (Wiegert et al., 2017c), adeno-associated viral particles encoding AAV2/9.CamKIIa(0.4).eOPN3-mScarlet were pressure injected (20 PSI/2-2.5 bar, 50 ms duration) using a Picospritzer III (Parker) under visual control (oblique illumination) into CA3 *stratum pyramidale* between DIV 2-5. Slice cultures were then maintained in the incubator for 2-3 weeks allowing for virus payload expression.

Electrophysiology in cultured neurons

Whole-cell patch clamp recordings in dissociated cultures were performed under visual control using differential interference contrast infrared (DIC-IR) illumination on an Olympus IX-71 microscope equipped with a monochrome scientific CMOS camera (Andor Neo). Borosilicate glass pipettes (Sutter Instrument BF100-58-10) with resistances ranging from 3–7 MΩ were pulled using a laser micropipette puller (Sutter Instrument Model P-2000). For hippocampal neuron cultures, electrophysiological recordings from neurons were obtained in Tyrode's medium ([mM] 150 NaCl, 4 KCl, 2 $MgCl_2$, 2 $CaCl_2$, 10 D-glucose, 10 HEPES; 320 mOsm; pH adjusted to 7.35 with NaOH). The recording chamber was perfused at 0.5 mL min^{-1} and maintained at 29°C or 23°C (Figure S4A). Pipettes were filled using a potassium gluconate-based intracellular solution ([mM] 135 K-gluconate, 4 KCl, 2 NaCl, 10 HEPES, 4 EGTA, 4 MgATP, 0.3 NaGTP; 280 mOsm kg^{-1}; pH adjusted to 7.3 with KOH). Whole-cell voltage clamp recordings were performed using a MultiClamp 700B amplifier, filtered at 8 kHz and digitized at 20 kHz using a Digidata 1440A digitizer (Molecular Devices). Light was delivered using a Lumencor SpecraX light engine, using band-pass filters at 445/20, 475/28, 512/25, 572/35 and 632/22 nm

(peak wavelength/bandwidth). Photon flux was calibrated to be similar for all five wavelengths at the sample plane to allow comparison of activation efficiency. Remaining photon flux differences were less than 6%.

Whole-cell recordings in autaptic neurons were performed on an Olympus IX73 microscope using a Multiclamp 700B amplifier (Molecular Devices) under control of Clampex 10 (Molecular Devices). Data was acquired at 10 kHz and filtered at 3 kHz. Extracellular solution contained (in mM): 140 NaCl, 2.4 KCl, 10 HEPES, 10 glucose, 2 $CaCl_2$, and 4 $MgCl_2$ (pH adjusted to 7.3 with NaOH, 300 mOsm). Internal solution contained the following (in mM): 136 KCl, 17.8 HEPES, 1 EGTA, 0.6 $MgCl_2$, 4 MgATP, 0.3 Na_2GTP, 12 Na_2 phosphocreatine, 50 U ml^{-1} phosphocreatine kinase (300 mOsm); pH adjusted to 7.3 with KOH. Fluorescence light from a TTL-controlled LED system (pE4000, CoolLED) was filtered using single band-pass filters (AHF F66-415), coupled into the back port of the microscope by a liquid light guide, and delivered through an Olympus UPLSAPO 20×, 0.75 NA objective. Membrane potential was set to −70 mV, and series resistance and capacitance were compensated by 70%. To obtain strong GIRK currents, cells were voltage clamp briefly to −50 mV for the light flash only, while EPSCs were recorded at −70 mV. Synaptic transmitter release was elicited by 1 ms depolarization to 0 mV, causing an unclamped AP in the axon. To estimate the onset time course of the eOPN3-mediated effect on synaptic release, trains of APs were evoked at 10 Hz. Light was applied after 200 such APs, when EPSC amplitudes reached a steady state. Baclofen and SCH23390 were applied via a rapid perfusion system (Rost et al., 2010). Pertussis toxin was applied to the cultures 24 h before the recordings, at a concentration of 0.5 μg ml^{-1}. Cells were excluded from the analysis of the paired-pulse ratio if eOPN3 activation completely abolished the first EPSC, and mEPSCs were not analyzed when noise-events detected by an inverted template occurred at > 1 Hz, as previously described (Rost et al., 2015).

Slice culture electrophysiology and two-photon microscopy

To characterize the effects of eOPN3-activation on neuronal cell parameters, targeted whole-cell recordings of transfected CA3 pyramidal neurons were performed at room temperature (21-23°C), between 1-2 weeks after electroporation or viral transduction, under visual guidance using a BX 51WI microscope (Olympus) and a Multiclamp 700B amplifier (Molecular Devices) controlled by either Ephus (Suter et al., 2010) or WaveSurfer software (https://www.janelia.org/open-science/wavesurfer), both written in MATLAB. Patch pipettes with a tip resistance of 3-4 MΩ were filled with (in mM): 135 K-gluconate, 4 $MgCl_2$, 4 Na_2-ATP, 0.4 Na-GTP, 10 Na_2-phosphocreatine, 3 ascorbate, 0.2 EGTA, and 10 HEPES (pH 7.2). Artificial cerebrospinal fluid (ACSF) consisted of (in mM): 135 NaCl, 2.5 KCl, 4 $CaCl_2$, 4 $MgCl_2$, 10 Na-HEPES, 12.5 D-glucose, 1.25 NaH_2PO_4 (pH 7.4). To block synaptic transmission, 10 μM CPPene, 10 μM NBQX, and 100 μM picrotoxin (Tocris, Bristol, UK) were added to the recording solution. Measurements were corrected for a liquid junction potential of −14 mV.

In dual patch-clamp experiments (Figure 4), we recorded from pairs of synaptically connected CA3 pyramidal cells expressing eOPN3 and non-expressing CA1 pyramidal cells. CA3 pyramidal neurons were stimulated in current clamp to elicit 2 action potentials (40 ms Inter Stimulus Interval, 0.2 Hz) by brief somatic current injection (2 - 3 ms, 3 - 4 nA) in the absence of synaptic blockers while recording EPSCs by holding the CA1 cell at −60 mV in voltage clamp mode. A brief light pulse (500 ms, 525 nm, 1 $mW \cdot mm^{-2}$) through the objective (illuminated area = 0.322 mm^2) in CA1 was used to activate eOPN3 locally at axon terminals innervating the postsynaptic CA1 pyramidal cell. For extracellular stimulation, afferent Schaffer collateral axons were stimulated (0.2 ms, 20-70 μA every 10 s) with a monopolar glass electrode connected to a stimulus isolator (IS4 stimulator, Scientific Devices). For train stimulation, 10 pulses were delivered every 40 ms. Access resistance of the recorded non-transfected CA1 neuron was continuously monitored and recordings above 20 MΩ and/or with a drift > 30% were discarded. A 16-channel pE-4000 LED light engine (CoolLED, Andover, UK) was used for epifluorescence excitation and light activation of eOPN3 (500 ms, 525 nm, 1 mW mm^{-2}). Light intensity was measured in the object plane with a 1918 R power meter equipped with a calibrated 818 ST2 UV/D detector (Newport, Irvine CA) and divided by the illuminated field of the Olympus LUMPLFLN 60XW objective (0.134 mm^2) or of the Olympus LUMPLFLN 40XW objective (0.322 mm^2). All the electrophysiological synaptic measurements in organotypic hippocampal slice cultures were performed at 33 ± 1°C.

For the eOPN3 two-photon stimulation experiments (Figure 5), a custom-built two-photon imaging setup was used based on an Olympus BX51WI microscope controlled by ScanImage 2017b (Vidrio Technologies). Electrophysiological recordings were acquired using a Multiclamp 700B amplifier controlled by the WaveSurfer software written in MATLAB (https://www.janelia.org/open-science/wavesurfer). A tunable, pulsed Ti:Sapphire laser (MaiTai DeepSee, Spectra Physics) controlled by an electro-optic modulator (350-80, Conoptics) tuned to 1040 nm was used to excite the mScarlet-labeled eOPN3. Red fluorescence was detected through the objective (LUMPLFLN 60XW, 60x, 1.0 NA, Olympus) and through the oil immersion condenser (numerical aperture 1.4, Olympus) by photomultiplier tubes (H7422P-40SEL, Hamamatsu). 560 DXCR dichroic mirrors and 525/50 and 607/70 emission filters (Chroma Technology) were used to separate green and red fluorescence. Excitation light was blocked by short-pass filters (ET700SP-2P, Chroma). In addition, the forward-scattered IR laser light was collected through the condenser, spatially filtered by a Dodt contrast tube (Luigs&-Neumann) attached to the trans-illumination port of the microscope and detected with a photodiode connected to a detection channel of the laser scanning microscope. This generated an IR-scanning gradient contrast image (IR-SGC) synchronized with the fluorescence images(Wimmer et al., 2004). This approach was used for targeted patch-clamp recordings avoiding prior activation of the ultrasensitive eOPN3 with epifluorescence illumination. The two-photon laser scanning pattern used for stimulation was either a spiral scan with a repetition rate of 500 Hz above the soma (2 ms/spiral, 250 cycles, 500 ms total duration) or standard raster scans at 1.09 Hz over the somatodendritic compartment (FOV = 106×106 μm, 512×512 pixels, 1.8 ms/line, 5 frames, 4.6 s total duration). The laser wavelengths used for stimulation were 800 nm, 860 nm, 930 nm, 980 nm and 1040 nm, all at 30 mW, measured at the back focal aperture of the objective. Wide field illumination at 525 nm (10 mW/mm^2) was done with a 16 channel pE-4000 LED light engine

(CoolLED, Andover, UK) for 500 ms. An additional set of experiments was performed on a second custom-modified two-photon imaging setup (DF-Scope, Sutter) based on an Olympus BX51WI microscope controlled by ScanImage 2017b (Vidrio Technologies) and equipped with an Ytterbium-doped 1070-nm pulsed fiber laser (Fidelity-2, Coherent) for far infrared stimulation. Electrophysiological recordings were performed using a Double IPA integrated patch amplifier controlled with SutterPatch software (Sutter Instrument).

The same microscope was used to acquire images of eOPN3-expressing CA3 cells co-transfected with the cyan cell-filler fluorophore mCerulean (Rizzo et al., 2004) and their projecting axons in *stratum radiatum* of CA1 (Figure 1). The 1070-nm laser was used to excite fluorescence of mScarlet-labeled eOPN3. mCerulean was excited by a pulsed Ti:Sa laser (Vision-S, Coherent) tuned to 810 nm. Laser power was controlled by electro-optic modulators (350-80, Conoptics). Red and cyan fluorescence were detected through the objective (Olympus LUMPLFLN 60XW, 1.0 NA, or Leica HC FLUOTAR L 25x/0.95 W VISIR) and through the oil immersion condenser (numerical aperture 1.4, Olympus) by GaAsP photomultiplier tubes (Hamamatsu, H11706-40). Dichroic mirrors (560 DXCR, Chroma Technology) and emission filters (ET525/70 m-2P, ET605/70 m-2P, Chroma Technology) were used to separate cyan and red fluorescence. Excitation light was blocked by short-pass filters (ET700SP-2P, Chroma Technology). All electrophysiology recordings were analyzed using custom written scripts in MATLAB except for recordings acquired with the Double IPA integrated patch amplifier, which were analyzed with the SutterPatch software.

For presynaptic Ca^{2+} imaging experiments (Figure 5), single action potentials were triggered via a patch pipette in a CA3 pyramidal neuron co-expressing eOPN3 and jGCaMP7f or jGCaMP7f alone as control while evoked Ca^{2+} influx at distal presynaptic terminals in *stratum radiatum* of CA1 was monitored by two-photon microscopy. A custom-modified version of ScanImage 3.8 (Pologruto et al., 2003) was used to allow user-defined arbitrary line scans. jGCaMP7f was excited at 960 nm. Similar to the two-photon stimulation experiments, targeted patch-clamp recordings were achieved using IR-scanning gradient contrast image (IR-SGC) synchronized with the fluorescence images. Action potentials were triggered by brief somatic current injection (2 - 3 ms, 3 - 4 nA) in the absence of synaptic blockers while monitoring fluorescent transients at single Schaffer collateral terminals in CA1 (70-80 trials on average at 0.1 Hz). User-defined circular scans at 500 Hz across the bouton were used to repeatedly sample the fluorescent changes. During each trial (3 s), laser exposure was restricted to the periods of expected Ca^{2+} response (~1.3 s) to minimize bleaching. To activate eOPN3 selectively at the terminals, we used a fiber-coupled LED (400 μm fiber, NA 0.39, M118L02, ThorLabs) to deliver 500 ms green light pulses (l = 530 nm, 83 μW at the fiber tip) 1 s prior to the onset of electrical stimulation. During the LED pulses, upper and lower PMTs were protected by TTL triggered shutters (NS45B, Uniblitz). GIRK channels were blocked by SCH 23390 (10 μM, Tocris, Bristol, UK) throughout the entire experiment to exclude hyperpolarization-mediated effects on action potential propagation and presynaptic Ca^{2+} influx.

The photon shot-noise subtracted relative change in jGCaMP7f fluorescence ($\Delta F/F_0$) was measured by using a template-based fitting algorithm. The characteristic fluorescence time constant was extracted for every bouton by fitting a double exponential function (t_{rise}, t_{decay}) to the average jGCaMP7f signal. To estimate the Ca^{2+} transient amplitude for every trial, we fitted the bouton-specific template to every response, amplitude being the only free parameter. Response amplitude was defined as the value of the fit function at its maximum.

In vivo electrophysiological recordings

8-9 weeks old male C75/Bl6 mice were pressure injected (Picospritzer III; Parker) bilaterally into LGN (AP: - 2.2 mm; ML: +/− 2.3 mm; DV: −3.1 mm) at 50 nL/min with 200 nL adeno-associated viral particles encoding eOPN3 (AAV2/5.CKIIa(0.4).eOPN3-mScarlet) diluted to 2.5×10^{12} viral genomes per ml using a pulled glass capillary. Following 5-6 weeks of recovery, mice underwent 3-4 head fixation habituation sessions starting with 15 min and gradually increasing to 25 min. 7-12 weeks after virus injection, craniotomies were performed bilaterally to provide access to V1 spanning from −2.3 mm to −4.7 mm in the anterior posterior direction and 2 mm at its widest part (at AP: −3.8 mm) from ± 1.3 mm to ± 3.3 mm along the medio-lateral axis. Craniotomies were covered with Kwik-Cast (WPI Inc) to protect the brain surface from mechanical impact, dehydration, and light exposure between the silicon probe recording sessions.

For the electrophysiological recordings, two 4-shank, 128 channel silicon microprobes (128DN; 4 shanks, 150 μm shank spacing, 25 μm channel spacing, 100 μm^2 electrode area, 7 mm x 65 μm x 23 μm shank dimensions) (Yang et al., 2020) (kindly provided by Dr. S. Masmanidis, UCLA) were inserted bilaterally in the V1 at a depth of approximately 1 mm, with an insertion speed of 100 μm/min. Before each recording session, silicon probe recording sites were electroplated in a PEDOT solution to an impedance of ~100 kOhm. Each silicon probe was connected to an RHD2000 chip-based 128 channel amplifier board (Intan Technologies). Broadband (0.1 Hz-7.5 kHz) signals were acquired at 30 kHz. Signals were digitized at 16 bit and transmitted to an OpenEphys recording controller (OEPS).

Raw data were processed to detect spikes and extract single-unit activity. Briefly, the wide-band signals were band-pass filtered (0.6 kHz-6 kHz), spatially whitened across channels and thresholded for isolation of putative spikes. Clustering was performed using template matching implemented in Kilosort2 (Pachitariu et al., 2016) and computed cluster metrics were used to pre-select units for later manual curation using custom-written software.

For the optogenetic inhibition of LGN axons, the silicon probe inserted in one of the two craniotomies was coupled with a 200 μm 0.5 NA optic fiber (Thorlabs, FP200URT), placed between the two middle shanks and at ~300 μm above the top-most channel of the

silicon probe, thus the optic fiber remained just outside the surface of the cortex during the recordings. This fiber was coupled with a 525 nm LED (PlexBright, Plexon), controlled using a Cyclops 3.6 LED driver and a custom Teensy3.2-based stimulation system, calibrated to deliver ~2 mW of light at the tip of the fiber.

Following a long baseline period, the paradigm used to investigate the effect of eOPN3 on the synaptic vesicle release *in vivo* consisted of 31 presentations of a visual stimulus every 30 s. The 10 first trials were used to establish the baseline of the visual response and the 11th trial was coupled with optogenetic stimulation, starting 1 s before the visual stimulation and lasting for a total of 30 s. Each visual stimulus presentation trial consisted of 8 repeats of a 500 ms visual drifting grating presentations in the cardinal and intercardinal directions. The stimuli were presented on a 23.5'' monitor placed 20 cm centrally in front of the mouse, so that the monitor was visible to both eyes. The stimulus presentation was controlled using a custom-written Python program and utilized PsychoPy3.0. For the accurate detection of the stimulus onset to allow for alignment with electrophysiological data, a photodetector was mounted in one corner of the monitor. The mouse was gradually habituated to head-fixation over multiple sessions and was running freely on a horizontal wheel. Each mouse was recorded for 1 or 2 identical sessions on different days and data were pooled for the subsequent analyses. Recording sessions in which no units showed visual stimulus-evoked activity were excluded from the analysis.

For visual stimulus response characterization, the spike rates were calculated in 50 ms bins. Each unit's activity was normalized to the average firing rate in the 15 s prior to stimulus presentation during the baseline period. The baseline period in Figure 6D was defined as the activity during the two trials before eOPN3 activation. For clarity, the peristimulus time histograms shown in Figure 6E were low pass filtered using a Gaussian function (window: 250 ms, $\sigma = 100$ ms). The recovery time constant shown in Figure 6F was calculated by fitting the post eOPN3 activation visual stimulus response to $f(t) = 1 - a \cdot \exp(-t/tau)$, with the effect size (a) and recovery time constant (tau) as free parameters.

In vivo optogenetic silencing of the nigrostriatal pathway

AAV vectors encoding a Cre-dependent eOPN3-mScarlet transgene (AAV2/1&2.hSyn.SIO-eOPN3-mScarlet; 6×10^{12} viral genomes / ml) or eYFP (AAV2/1&2.EF1a.DIO.eYFP; 2×10^{13} viral genomes / ml) were unilaterally injected into the substantia nigra (AP: - 3.5 mm, ML: + or - 1.4 mm DV: - 4.25 mm; 500 nL per mouse) of DAT-Cre transgenic mice. Optical fibers (200 μm diameter, NA 0.5) were unilaterally implanted above the ipsilateral dorsomedial striatum (AP: + 0.6 mm, ML: + or – 1.5 mm DV: - 2.1 mm). Left and right implanted mice were counterbalanced among the eOPN3 and control groups. Mice were allowed to recover for 6-9 weeks to allow for viral expression. Following recovery, mice underwent a single 10-min habituation session, to habituate to handling, patch cord attachment and the open field arena. In experimental sessions, we attached individual mice to a patch cord and video recorded their free locomotion continuously in the open field under near-infrared illumination.

To measure eOPN3 induced bias in locomotion, we video recorded the free locomotion of single mice in an open field arena (50× 50×50 *cm*) continuously over 30 min. After a 10-min baseline no-light period, we delivered 500 ms light pulses (540 nm, 10 mW at the fiber tip), at 0.1 Hz for 10 min, followed by an additional 10-min no-light period. Offline video processing and mouse tracking was done using DeepLabCut (DLC; (Mathis et al., 2018)). Briefly, we trained DLC to detect 6 features on the mouse body (nose, head center, left and right ears, center of mass, tail) and 3 bottom corners of the arena. X-Y coordinates of each feature were then further processed to complete missing or noisy values (high amplitude and short duration changes in X or Y dynamics) using linear interpolation (*interp1*) of data from neighboring frames. This was followed by a low pass filtering of the signals (*malowess*, with 50 points span and of linear order). Finally, a pixel to cm conversion was done based on the video-detected arena features and its physical measurements. A linear fit to the nose, head, center and tail features defined the mouse angle with respect to the south arena wall at each frame. Following its dynamics over the session, we identified direction shifts as a direction change in angle that exceeds 20° and 1 s. To achieve a comparable measurement between right- and left- hemisphere injected mice, we measured motion in the ipsilateral direction as positive and contralateral motion as negative from the cumulative track of angle. The net angle gain was calculated as the sum of ipsilateral and contralateral angle gained over each time bin (1- or 10-min bins as indicated). For each time bin we then calculated a rotation index, based on angle gains, as follows:

$$Rotation\ index = \frac{(ipsilateral - contralateral)}{ipsilateral + contralateral}$$

For each mouse, rotation index scores were calculated for two complete sessions on different days. Individual scores were plotted for each mouse against the expression levels measured in that mouse (see section: Histology, imaging, and quantification). Results were then averaged across individual sessions, and used for all statistical comparisons, and linear regressions analysis. Mouse positions and velocities were measured by the ''center of mass'' feature.

QUANTIFICATION AND STATISTICAL ANALYSIS

Mean was used as center measure and standard error of the mean (SEM) as dispersion measure throughout the manuscript. The data was tested for violations of assumptions of parametric tests (Gaussian distribution of the residuals was assessed using the Kolmogorov-Smirnov test; Equality of variances was assessed using the Levene's test), and non-parametric tests were utilized where assumptions were violated. The statistical details for the specific experiments, including the statistical tests used, exact value of n, what n represents (e.g., number of animals, number of brain slices, number of cells, or number of trials), can be found in the figures, figure

legends or Results text. Significance was determined at a level of 0.05 using the statistical test as reported in the figure legend or Results. P values were corrected for multiple comparison as reported in the figure legends or Results. For fitting results, confidence intervals are reported. No statistical tests were run to predetermine sample size, but sample sizes were similar to those commonly used in the field. Blinding and randomization were performed only in the behavioral experiments (Figure 7); in other experiments, automated analysis was used whenever possible. For autaptic neuron recordings (Figure 2), cells were excluded from the analysis of the paired-pulse ratio if eOPN3 activation completely abolished the first EPSC, and mEPSCs were not analyzed when noise-events detected by an inverted template occurred at > 1 Hz, as previously described (Rost et al., 2015). For organotypic slice culture recordings the access resistance of the recorded non-transfected CA1 neuron was continuously monitored and recordings with access resistance above 20 MΩ and/or with a drift > 30% were discarded. For *in vivo* electrophysiology (Figure 6), recording sessions in which no units showed visual stimulus-evoked activity were excluded from the analysis. Statistical analysis was performed using MATLAB (Mathworks), RStudio Desktop (RStudio), and Prism (Graphpad).

Neuron, Volume *109*

Supplemental information

Efficient optogenetic silencing of neurotransmitter release with a mosquito rhodopsin

Mathias Mahn, Inbar Saraf-Sinik, Pritish Patil, Mauro Pulin, Eyal Bitton, Nikolaos Karalis, Felicitas Bruentgens, Shaked Palgi, Asaf Gat, Julien Dine, Jonas Wietek, Ido Davidi, Rivka Levy, Anna Litvin, Fangmin Zhou, Kathrin Sauter, Peter Soba, Dietmar Schmitz, Andreas Lüthi, Benjamin R. Rost, J. Simon Wiegert, and Ofer Yizhar

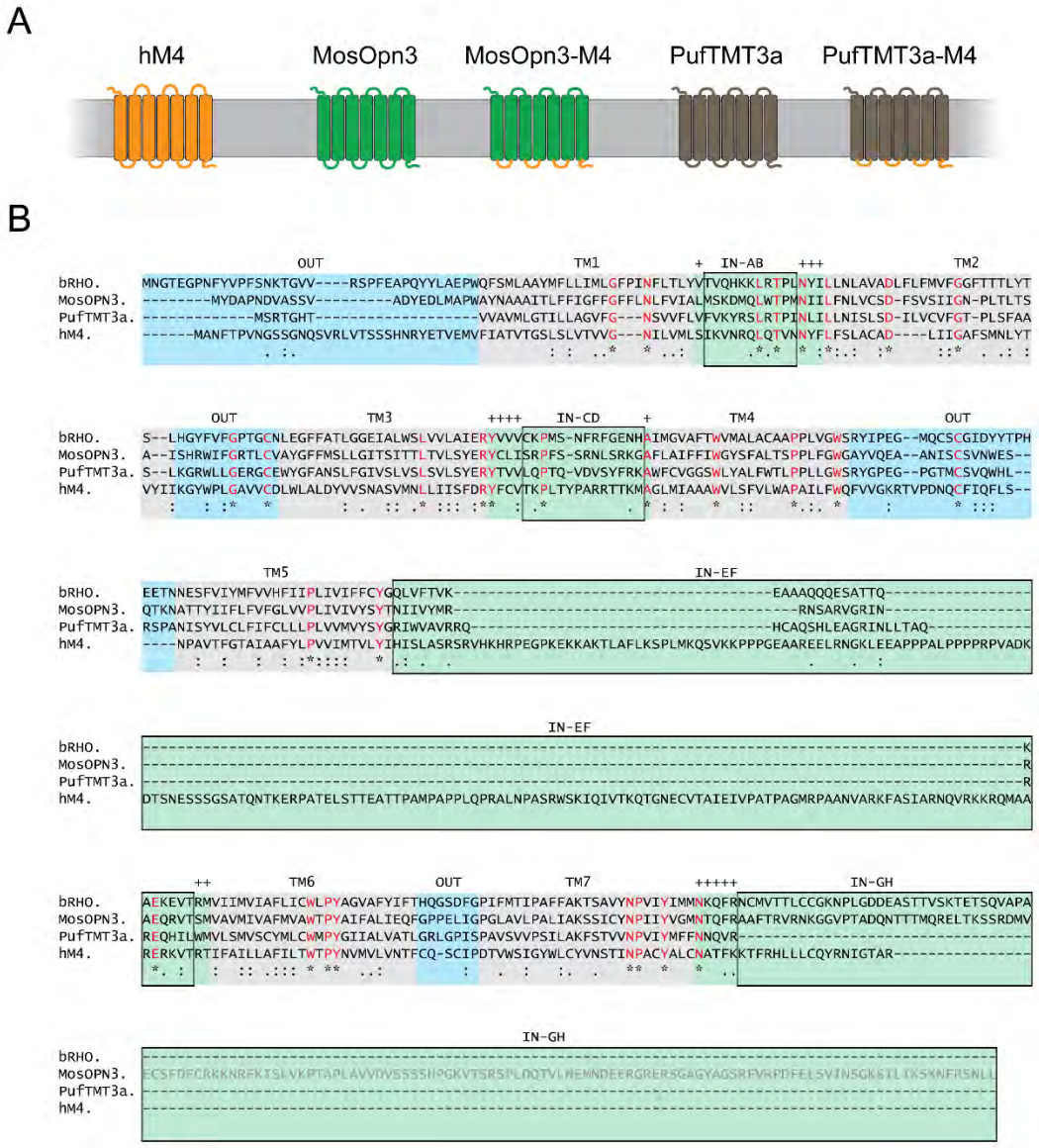

Figure S1. hM4 chimera design. Related to Figure 1. To maximally recapitulate the signaling pathway of the M4 acetylcholine receptor, as utilized by hM4Di, we also generated chimeric photoreceptors composed of bistable invertebrate rhodopsins and the intracellular domains of the M4 receptor. **(A)** Schematic diagrams of chimeric proteins comprising transmembrane and extracellular domains from the bistable mosquito OPN3 opsin (OPN3, GenBank: AB753162.1) or the teleost multiple tissue opsin 3a from pufferfish (PufTMT3a, UniParc: UPI00016E4442) and intracellular domains of the human muscarinic receptor 4 (hM4, GenBank: NM_000741). **(B)** Multiple sequence alignment (Edgar, 2004) of the amino acid sequences of visual and non-visual rhodopsins, along with hM4. Shown are sequences of the bovine rhodopsin (bRho), OPN3, PufTMT3a, and hM4. Intracellular domains are labeled with green background, extracellular domains are labeled with blue background and the transmembrane domains are in gray. "*" indicates an identical amino acid in all sequences in the alignment (red letters), ":" indicates conserved amino acid substitutions according to the COLOUR table (http://www.jalview.org/help/html/colourSchemes/clustal.html), and "." indicates semi-conserved substitutions. Intracellular regions that were replaced by the hM4 sequence to create chimeric proteins are indicated by black boxes. Non-replaced amino acids within the intracellular region are indicated by a + above the column. The 99 amino acid deletion in OPN3, introduced to improve expression in neurons, is indicated by gray amino acid letters (bottom row).

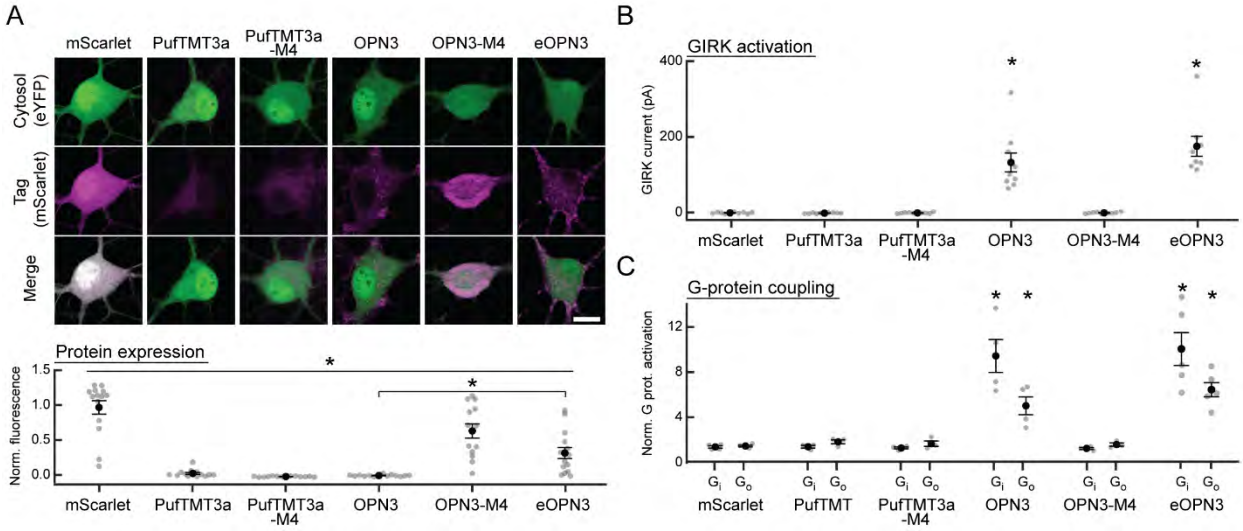

Figure S2. In vitro characterization of bistable rhodopsins and their M4 chimeras. Related to Figure 1. To evaluate the utility of the bistable rhodopsins PufTMT3a, wild-type mosquito OPN3 (referred to as OPN3 hereafter), and their M4 chimeras, we first characterized their expression and membrane targeting in neurons. We transfected primary cultured hippocampal neurons with mammalian codon-optimized versions of these rhodopsins, with C-terminal mScarlet fusions for direct visualization. **(A)** Representative confocal images of neurons co-transfected with expression vectors for eYFP and the indicated rhodopsin variant. Images show fluorescence in the eYFP channel (*top*), the mScarlet channel (*middle*) and the merged images (*bottom*). Bottom: Expression level of each of the displayed rhodopsin-mScarlet constructs, quantified as the average pixel intensity in n > 13 neurons for each construct normalized to cells expressing only mScarlet. The amount of measured fluorescence differed between all conditions ($p = 1.34 \cdot 10^{-12}$ Kruskal-Wallis test followed by Bonferroni-Holm corrected pairwise comparisons using Wilcoxon rank sum tests: OPN3 vs. eOPN3 fluorescence n = 14, $p = 1.3 \cdot 10^{-4}$. The expression of OPN3 was low, punctate, and mostly intracellular. The OPN3-M4 chimera, containing the intracellular loops of the M4 acetylcholine receptor, expressed at higher levels in comparison to OPN3, but showed a predominantly intracellular localization. Scale bar, 15 µm. Images in the mScarlet channel are individually scaled for visualization of low fluorescence levels. Fluorescence measurements were taken under matched imaging conditions for all variants tested. **(B)** Characterization of the ability of the rhodopsins to evoke G protein-coupled inwardly-rectifying potassium channel-mediated (GIRK) currents in cultured neurons as a readout for functional activation of the $G_{i/o}$ pathway. Co-expressing one of each of the rhodopsin variants along with a GIRK2-1 channel (Lesage, et al., 1994) allowed us to quantify and compare the magnitude of $G_{i/o}$ pathway activity through the measurement of GIRK2-1-mediated hyperpolarizing K^+-currents. GIRK currents evoked by a 500 ms pulse of 560 nm light at 2 $mW \cdot mm^{-2}$ in hippocampal neurons during a voltage clamp recording, held at -70 mV. Both the wild-type PufTMT3a opsin and the PufTMT3a-M4 chimera did not yield light-activated GIRK currents, in contrast to OPN3 and eOPN3 expressing neurons ($p = 1.71 \cdot 10^{-6}$ Kruskal-Wallis test followed by Bonferroni-Holm corrected pairwise comparisons using Wilcoxon rank sum tests). OPN3-M4 did not evoke any detectable GIRK currents. **(C)** We determined the interactions between the rhodopsin variants and specific G proteins using a HEK cell-based GPCR screening assay that couples the opsin to a Gs-chimera (GsX assay, see fig. S3 for complete assay and statistics, (Ballister, et al., 2018)). This approach allowed us to analyze their interaction with all major G proteins (Gi, Go, Gt, Gq, Gs, Gz, G12, G13, G15). Only OPN3 and eOPN3 showed G_i and G_o activation. PufTMT3a-expressing cells only activated G_z (see also Fig. S3B). In combination, these results show that PufTMT3a cannot be used to fully recapitulate the efficient inhibition of vesicle release induced by hM4Di. Plots depict individual data points and average ± SEM.

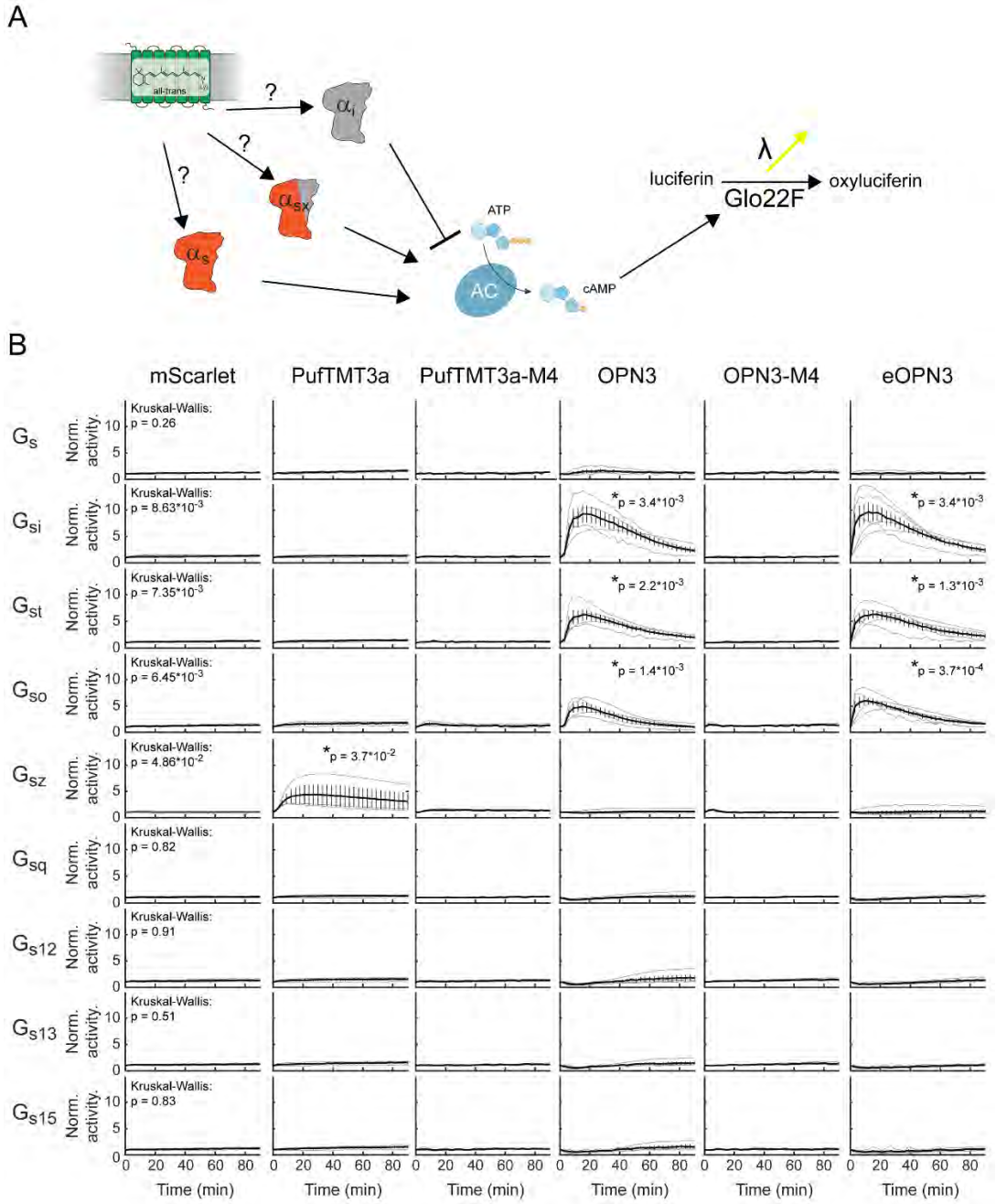

Figure S3. G protein activation assay. Related to Figure 1. Light-dependent G protein activation by several opto-GPCR constructs, assayed in HEK293T cells. **(A)** Essay scheme. HEK293T cells are transfected with chimeras of G_α proteins and the $G_{\alpha s}$ C-terminus. cAMP levels in live cells are measured through the cAMP reporter (Glo22F). This allows for measuring cAMP levels as readout of chimera activation by the co-expressed opto-GPCR. **(B)** opto-GPCRs were activated with a green LED pulse (1s, 530nm, 5.5 $\mu W \cdot mm^{-2}$) and luminescence was measured over time. Graphs show the light-induced response, normalized to pre-activation baseline, for mScarlet (control, n = 4), PufTMT3a-mScarlet (n = 3), PufTMT3a-M4-mScarlet (n = 3), OPN3-mScarlet (n = 4), OPN3-M4-mScarlet (n = 3), and eOPN3-mScarlet (n = 5). Only OPN3-mScarlet and eOPN3-mScarlet specifically and strongly activated inhibitory G proteins (G_i, G_t, G_o) in a light-dependent manner (Kruskal-Wallis tests of the maximal measured values per G protein, followed by Bonferroni-Holm corrected pairwise comparisons using Conover–Iman tests; reported p-values describe the comparison against the mScarlet control). Single trials are depicted in gray, mean ± SEM are in black.

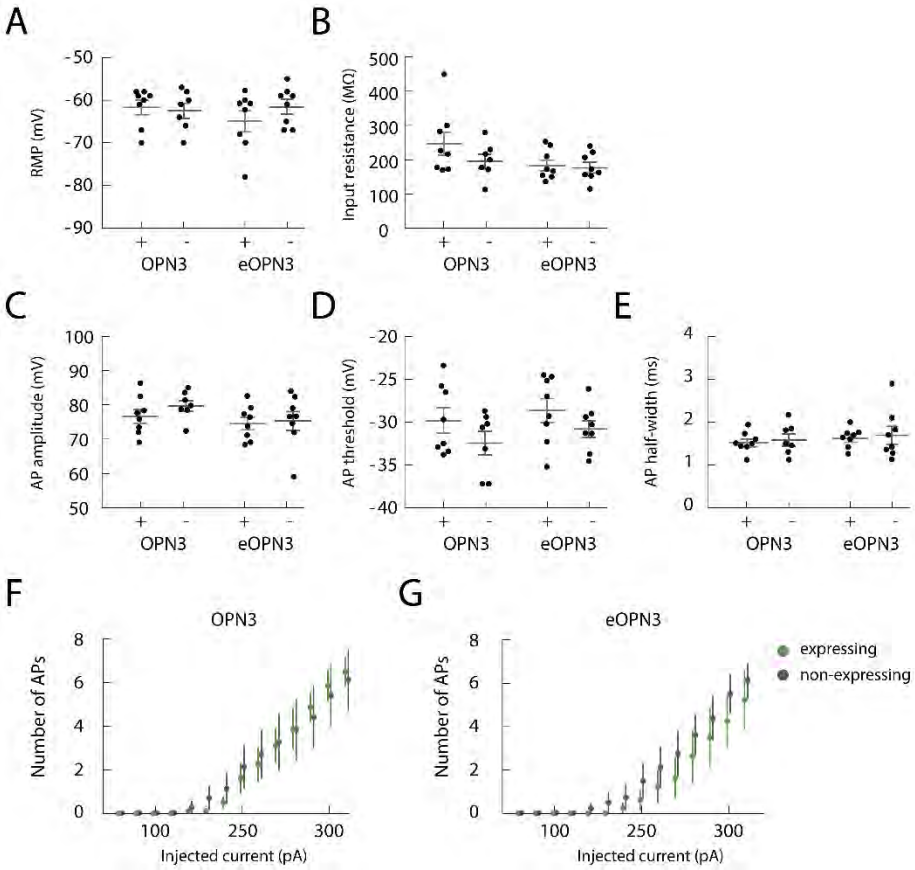

Figure S4. No change in the intrinsic excitability of cultured hippocampal neurons expressing OPN3-mScarlet or eOPN3-mScarlet in the absence of light. Related to Figure 1. The following intrinsic properties were characterized in cultured hippocampal neurons: **(A)** resting membrane potential (RMP, OPN3 vs. ctrl: p = 0.79; eOPN3 vs. ctrl: 0.27; two-tailed Mann-Whitney tests), **(B)** membrane input resistance (OPN3 vs ctrl: p = 0.35; eOPN3 vs. ctrl: 0.82; two-tailed Mann-Whitney tests), **(C)** action potential (AP) amplitude (OPN3 vs. ctrl: p = 0.19; eOPN3 vs. ctrl: 0.57; two-tailed Mann-Whitney tests), **(D)** AP threshold (OPN3 vs. ctrl: p = 0.38; eOPN3 vs. ctrl: 0.23; two-tailed Mann-Whitney tests), and **(E)** AP half-width (OPN3 vs. ctrl: p = 0.85; eOPN3 vs. ctrl: 0.94; two-tailed Mann-Whitney tests). No differences between neurons expressing OPN3-mScarlet (n = 7) or eOPN3-mScarlet (n = 8) and neighboring non-transfected control cells (n = 7 and n = 8, respectively) were detected. **(F-G)** The number of evoked APs in response to current injection were not different in neurons expressing OPN3 or eOPN3 and non-expressing controls (p = 0.91 and 0.46, respectively; two-way repeated measures ANOVA). Plots show individual data points and average ± SEM.

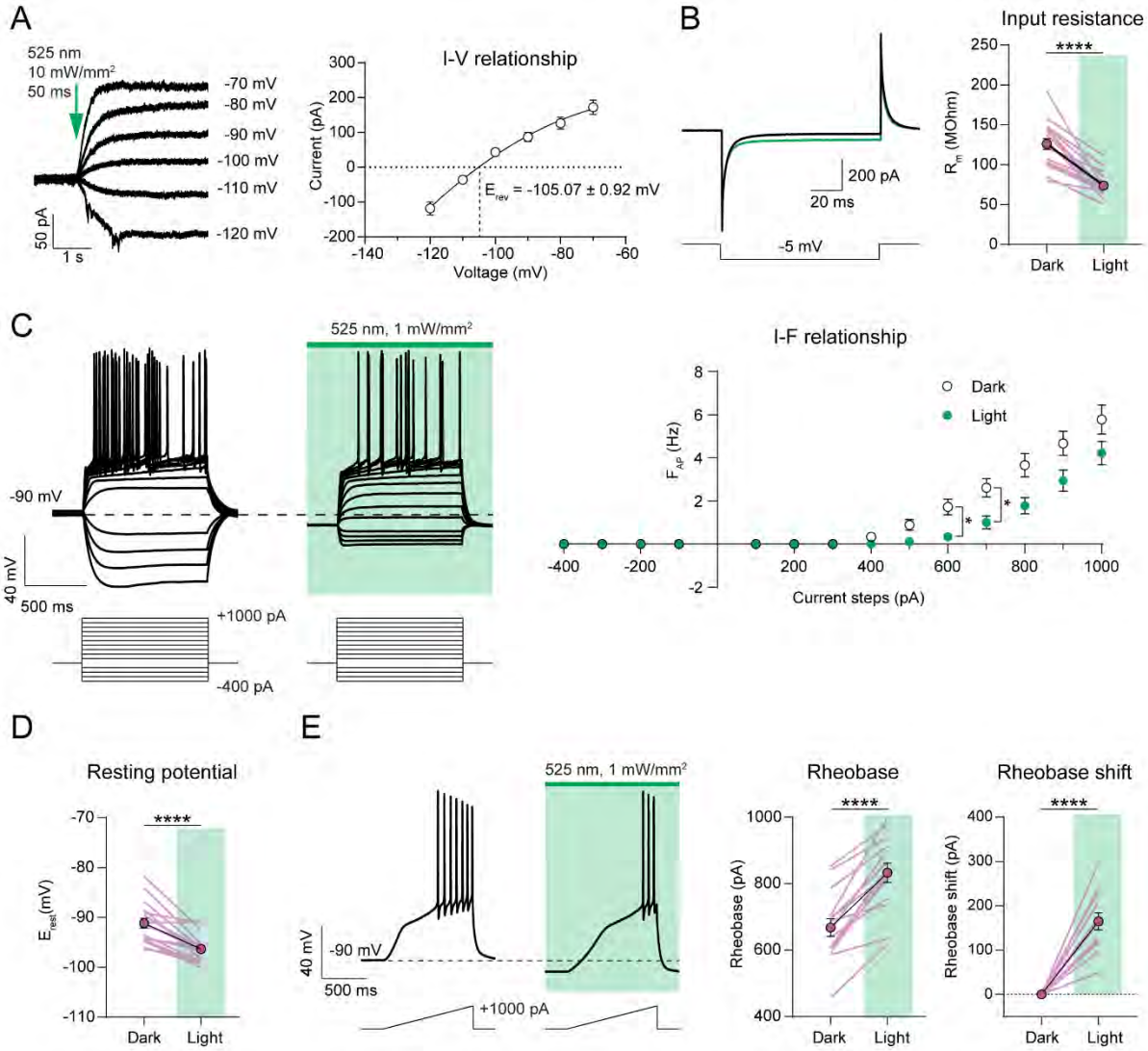

Figure S5: Passive and active membrane properties of eOPN3-expressing CA3 pyramidal neurons in organotypic hippocampal slices. Related to Figure 4. **(A)** Light-evoked (putative GIRK) currents evoked by 50-ms green-light pulses (525 nm, 10 mW·mm^{-2}) at different holding potentials, ranging from -70 to -120 mV. Values are baseline-subtracted and corrected for a liquid junction potential of -14 mV. Representative traces are shown on the *left*, quantification of the current-voltage relationship is shown on the *right* (n = 6). The photocurrent reversal potential of -105.07 ± 0.92 mV (determined with a non-linear fit) is close to the calculated K^+ equilibrium potential of -102.5 mV. **(B)** *Left*: Representative current traces in response to a negative voltage step (-5 mV, 100 ms) in the dark (black traces) and during continuous green light (525 nm, 1 mW·mm^{-2}). Note the drop of the stationary current resulting from a decreased input resistance due to increased GIRK channel conductance under illumination. *Right*: Quantification of input resistance. (Dark: 126 ± 6.79 MΩ, Light: 73 ± 3.46 MΩ, $p < 1 \cdot 10^{-4}$, Wilcoxon-test, n = 18). **(C)** *Left*: representative voltage responses to somatic current injections ranging from -400 pA to +1000 pA in the dark and during illumination (525 nm, 1 mW·mm^{-2}). *Right*: I-F plot showing decreased spike frequency in response to positive current injections, likely due to $G_{i/o}$-mediated GIRK channel opening ($p < 0.05$, n = 18, two-way ANOVA with Sidak's multiple comparisons test). **(D)** Quantification of the resting membrane potential from the current step experiments shown in C (Dark: -91.18 ± 0.96 mV; Light: -96.34 ± 0.62 mV; $p < 1 \cdot 10^{-4}$, paired t-test, n = 18). **(E)** *Left*: representative voltage traces in response to depolarizing current ramps to assess the eOPN3-mediated rheobase shift (0 - 1000 pA). Injected current at the time of the first spike was defined as the rheobase. Green light (525 nm, 1 mW·mm^{-2}) raised the rheobase of current-ramp-evoked APs. *Right*: quantification of the absolute rheobase (dark: 667.9 ± 26.79 pA, light: 832.7 ± 28.69 pA; $p < 1 \cdot 10^{-4}$, paired t-test, n = 15) and the rheobase shift (light: 164.8 ± 19.30 pA, $p < 1 \cdot 10^{-4}$, paired t-test, n = 15).

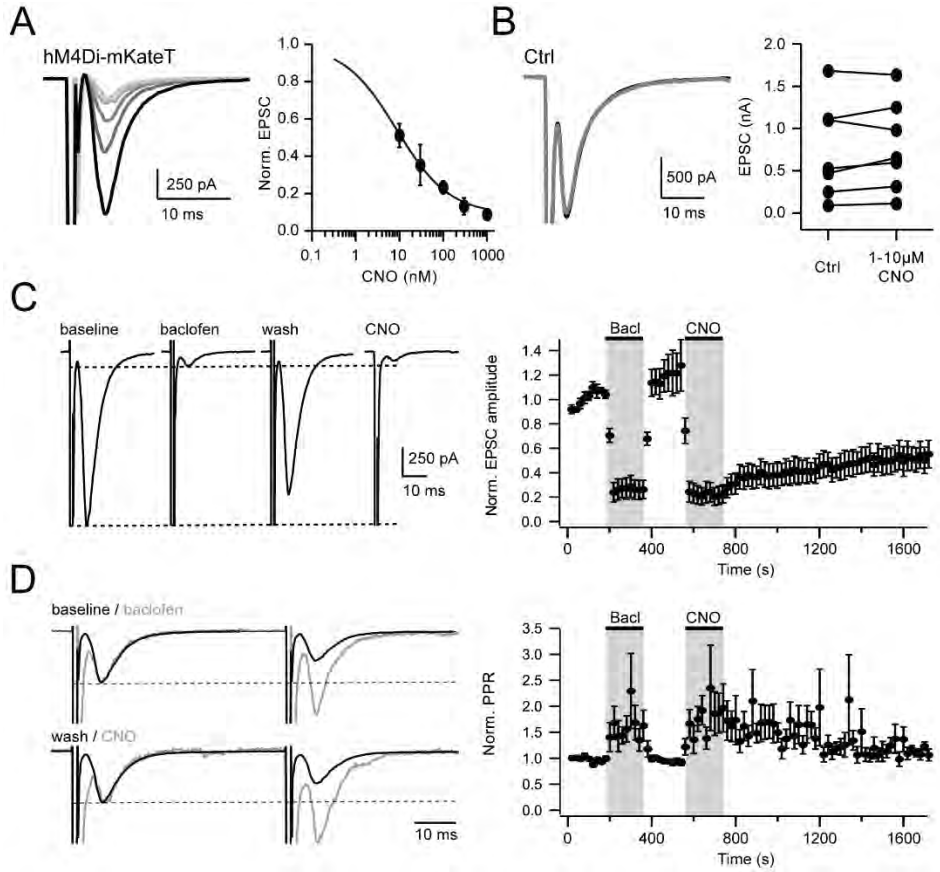

Figure S6. Presynaptic inhibition of neurotransmitter release by hM4Di expressed in autaptic cultures of hippocampal neurons. Related to Figure 2. **(A)** Application of increasing concentrations of clozapine-N-oxide (CNO; 10, 30, 100, 300, 1000 nM, from black to light gray) leads to reduction in EPSC amplitude (IC_{50} = 8.6 nM, n = 3-12). **(B)** CNO (1-10 µM) has no effect on EPSC amplitude in neurons not expressing hM4Di (ctrl 0.746 ± 0.215 nA; CNO: 0.79 ± 0.201 nA; p = 0.3, paired t-test, n = 7). **(C-D)** Comparison of presynaptic inhibition by $GABA_BR$ and presynaptic inhibition by hM4Di. After 30 µM baclofen application for 180 s and washout, 100 nM CNO was added for 180 s to the same cells. Action potentials were evoked by depolarization to 0 mV for 1 ms at 0.2 Hz. Data were binned by 2. **(C)** Both types of GPCRs suppress EPSC amplitudes to a similar extent (Baclofen: to 0.267 ± 0.083 of Baseline, CNO: to 0.218 ± 0.076; p = 0.06, paired t-test, n = 6). However, washout kinetics of CNO is dramatically slower compared to baclofen. **(D)** Increased paired-pulse ratio in response to both $GABA_B$ and hM4Di receptor activation ($GABA_BR$: 1.776 ± 0.329; hM4D: 1.864 ± 0.355; p = 0.2, paired t-test, n = 6), indicating a presynaptic action. Example traces are scaled to the peak of the first EPSC under control conditions for both baclofen and CNO applications.

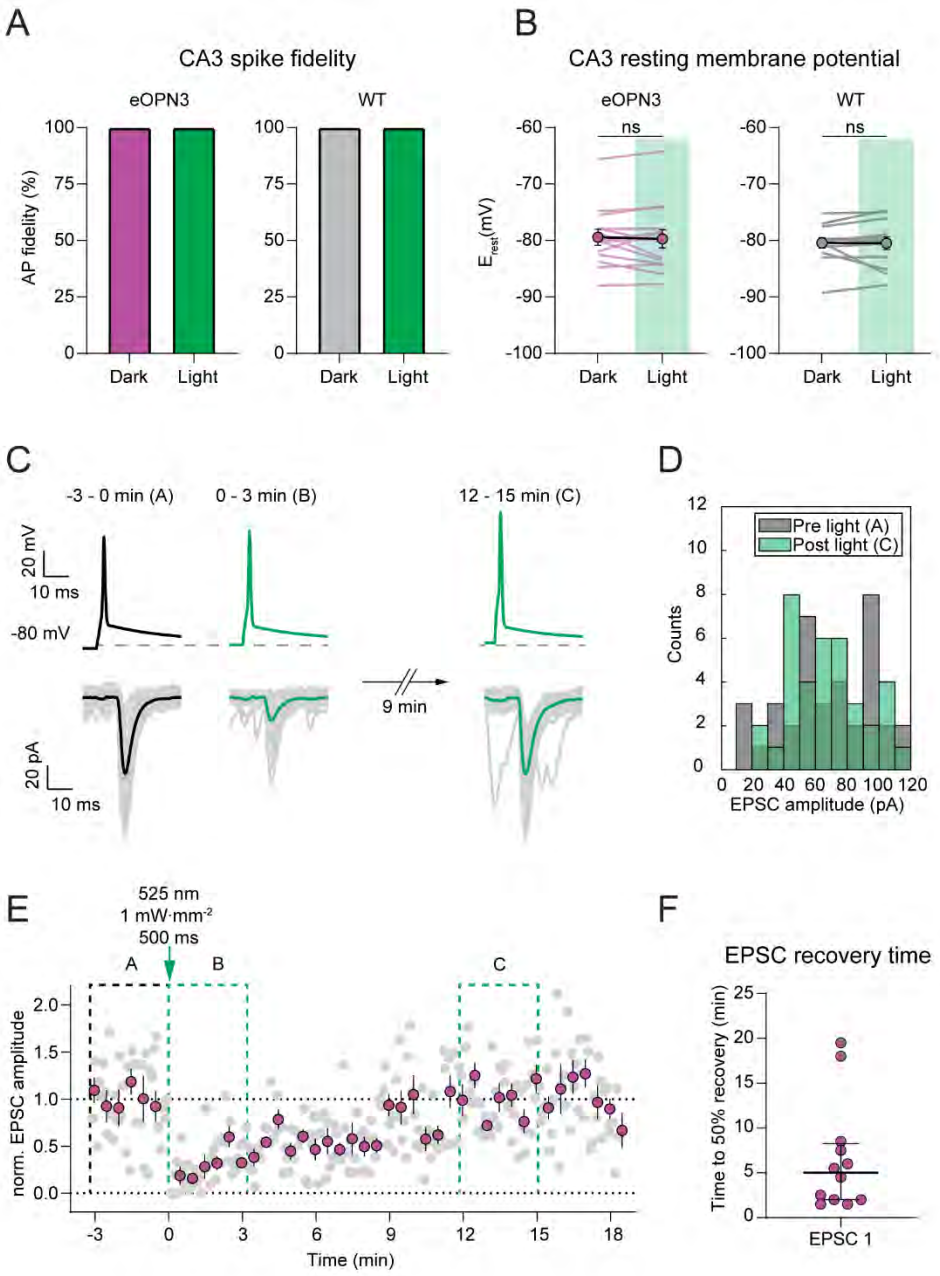

Figure S7: Excitability of CA3 neurons and EPSC recovery in paired-recording experiments. Related to Figure 4. **(A)** Comparison of action potential success rate in CA3 in the dark and in the 30 s after light stimulation in CA1 (eOPN3 dark, eOPN3 light = 100%, n = 14; WT dark, WT light = 100%, n = 13). **(B)** Quantification of the resting membrane potential of CA3 pyramidal cells used in paired recordings in the dark and in the 30 s after light stimulation in CA1 (500 ms of 525 nm light at 1 mW·mm^{-2}; eOPN3 dark: -79.41 ± 1.43, eOPN3 light: -79.71 ± 1.62, p = 0.9032, Wilcoxon test, n = 14; WT dark: -80.41 ± 0.94, WT light: -80.47 ± 1.14, p = 0.3396, Wilcoxon test, n = 13). Plots show individual data points (lines), and average (circles) ± SEM. Note absence of effects of local CA1 illumination on CA3-cell somatic properties. **(C)** Representative voltage (*top*) and current (*bottom*) traces from the example shown in E. For display purposes "pulse 2" of the paired-pulse stimulation was omitted. Note the EPSC recovery within minutes after light application. **(D)** Histogram count of peak current amplitudes of the example shown in C. **(E)** Quantification of the normalized EPSC peak amplitude shown in C (gray: individual trials, magenta: 30 s bins). **(F)** The EPSC recovery time was defined as the first 30 s-bin post light reaching at least 50% recovery of the EPSC peak amplitude compared to the average baseline EPSC peak amplitude (EPSC 1: 6.58 ± 1.78 min, mean + SEM, n = 12). Each circle represents an individual paired recording experiment.

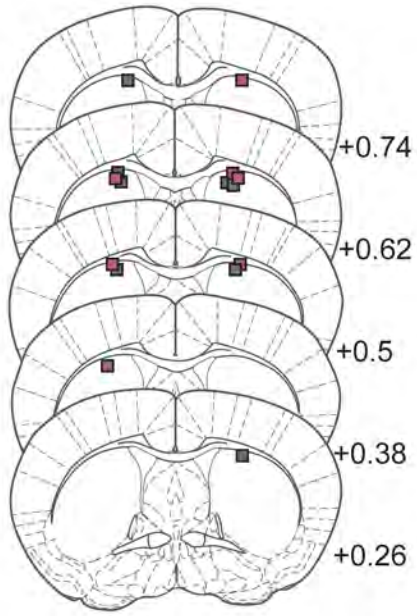

Figure S8: Histological analysis of optic fiber placements in nigrostriatal projection inhibition experiments. Related to Figure 7. Each point represents the fiber tip position of mice expressing eYFP (N = 8 mice, gray squares) or eOPN3-mScarlet (N = 7 mice, magenta squares). Numbers indicate anterior – posterior position relative to Bregma.

3.4 Article IV

A neuropeptidergic circuit gates selective escape behavior of *Drosophila* larvae

Bibi Nusreen Imambocus,[1,2] **Fangmin Zhou**,[1,2] Andrey Formozov,[2] Annika Wittich,[2] Federico M. Tenedini,[2] Chun Hu,[2,11] Kathrin Sauter,[2] Ednilson Macarenhas Varela,[3] Fabiana Herédia,[3] Andreia P. Casimiro,[3] André Macedo,[3] Philipp Schlegel,[1,12] Chung-Hui Yang,[4] Irene Miguel-Aliaga,[5,6] J. Simon Wiegert,[2] Michael J. Pankratz,[1] Alisson M. Gontijo,[3,7] Albert Cardona,[8,9,10] and Peter Soba[1,2,13]

1 LIMES Institute, Department of Molecular Brain Physiology and Behavior, University of Bonn, Carl-Troll-Str. 31, 53115 Bonn, Germany
2 Center for Molecular Neurobiology (ZMNH), University Medical Center Hamburg-Eppendorf, Falkenried 94, 20251 Hamburg, Germany
3 Integrative Biomedicine Laboratory, CEDOC, Chronic Diseases Research Center, NOVA Medical School, Faculdade de Ciências Médicas, Universidade Nova de Lisboa, Rua do Instituto Bacteriológico 5, 1150-082 Lisbon, Portugal
4 Department of Neurobiology, Duke University Medical School, 427E Bryan Research, Durham, NC 27710, USA
5 MRC London Institute of Medical Sciences, Du Cane Road, London W12 0NN, UK
6 Institute of Clinical Sciences, Faculty of Medicine, Imperial College London, Du Cane Road, London W12 0NN, UK
7 The Discoveries Centre for Regenerative and Precision Medicine, Lisbon Campus, Av. Rovisco Pais, 1049-001 Lisbon, Portugal
8 HHMI Janelia Research Campus, 19700 Helix Drive, Ashburn, VA 20147, USA
9 MRC Laboratory of Molecular Biology, Francis Crick Avenue, Cambridge CB2 0QH, UK
10 Department of Physiology, Development, and Neuroscience, University of Cambridge, Downing Street, Cambridge CB2 3EJ, UK
13 Lead contact

Current Biology 2021 doi.org/10.1016/j.cub.2021.10.069

Personal contribution

My contribution to this publication was the following: I performed the experiments on locomotion and chemotaxis as well as analysis of the data. I was also involved in performing a subset of the light-avoidance assays. These data are displayed in Figure S1E-F and Figure S4D-G, and parts of Figure 1F-G. In addition, I was involved in writing the behavioral methods part for the manuscript and added comments during the revision process.

Article

Current Biology

A neuropeptidergic circuit gates selective escape behavior of *Drosophila* larvae

Graphical abstract

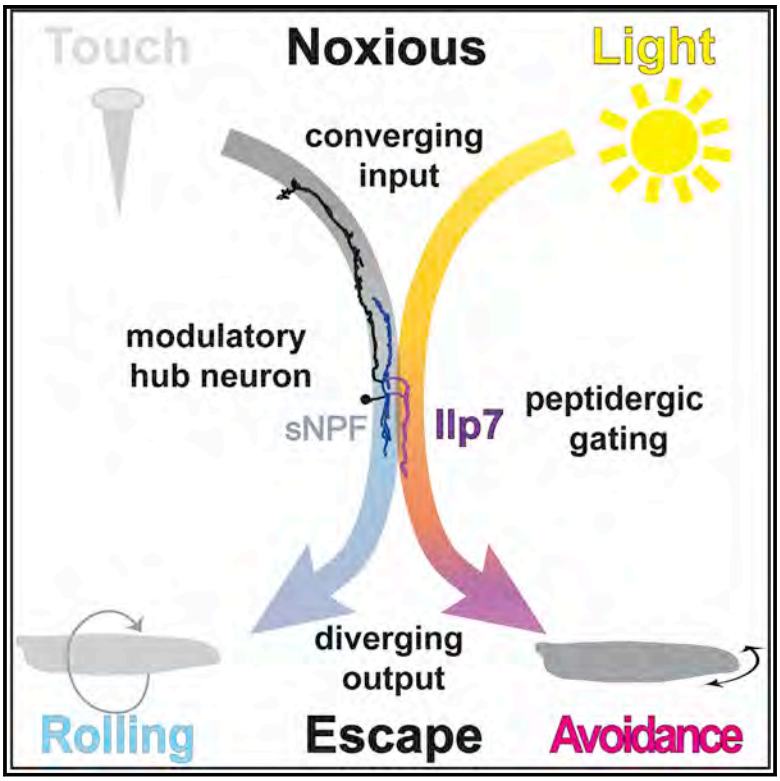

Highlights

- Connectome of a neuromodulatory circuit required for noxious light avoidance
- Domain-specific input of noxious light and touch circuits on modulatory hub neurons
- Acute neuropeptide release from hub neurons gates noxious light avoidance
- Noxious light and touch are differentiated by selective peptide-responsive circuits

Authors

Bibi Nusreen Imambocus, Fangmin Zhou, Andrey Formozov, ..., Alisson M. Gontijo, Albert Cardona, Peter Soba

Correspondence

psoba@uni-bonn.de

In brief

Animals escape from danger using stimulus-specific responses. Imambocus et al. show that in *Drosophila* larvae, neuromodulatory hub neurons help to discriminate noxious stimuli and facilitate specific behavioral responses by acute neuropeptide release to promote avoidance of noxious light.

Imambocus et al., 2022, Current Biology *32*, 149–163
January 10, 2022
https://doi.org/10.1016/j.cub.2021.10.069

Current Biology

CellPress

Article

A neuropeptidergic circuit gates selective escape behavior of *Drosophila* larvae

Bibi Nusreen Imambocus,[1,2] Fangmin Zhou,[1,2] Andrey Formozov,[2] Annika Wittich,[2] Federico M. Tenedini,[2] Chun Hu,[2,11] Kathrin Sauter,[2] Ednilson Macarenhas Varela,[3] Fabiana Herédia,[3] Andreia P. Casimiro,[3] André Macedo,[3] Philipp Schlegel,[1,12] Chung-Hui Yang,[4] Irene Miguel-Aliaga,[5,6] J. Simon Wiegert,[2] Michael J. Pankratz,[1] Alisson M. Gontijo,[3,7] Albert Cardona,[8,9,10] and Peter Soba[1,2,13,*]

[1]LIMES Institute, Department of Molecular Brain Physiology and Behavior, University of Bonn, Carl-Troll-Str. 31, 53115 Bonn, Germany
[2]Center for Molecular Neurobiology (ZMNH), University Medical Center Hamburg-Eppendorf, Falkenried 94, 20251 Hamburg, Germany
[3]Integrative Biomedicine Laboratory, CEDOC, Chronic Diseases Research Center, NOVA Medical School, Faculdade de Ciências Médicas, Universidade Nova de Lisboa, Rua do Instituto Bacteriológico 5, 1150-082 Lisbon, Portugal
[4]Department of Neurobiology, Duke University Medical School, 427E Bryan Research, Durham, NC 27710, USA
[5]MRC London Institute of Medical Sciences, Du Cane Road, London W12 0NN, UK
[6]Institute of Clinical Sciences, Faculty of Medicine, Imperial College London, Du Cane Road, London W12 0NN, UK
[7]The Discoveries Centre for Regenerative and Precision Medicine, Lisbon Campus, Av. Rovisco Pais, 1049-001 Lisbon, Portugal
[8]HHMI Janelia Research Campus, 19700 Helix Drive, Ashburn, VA 20147, USA
[9]MRC Laboratory of Molecular Biology, Francis Crick Avenue, Cambridge CB2 0QH, UK
[10]Department of Physiology, Development, and Neuroscience, University of Cambridge, Downing Street, Cambridge CB2 3EJ, UK
[11]Present address: Key Laboratory of Brain, Cognition, and Education Sciences, Ministry of Education, and Institute for Brain Research and Rehabilitation, South China Normal University, 510631 Guangzhou, China
[12]Present address: Department of Zoology, University of Cambridge, Downing Street, Cambridge CB2 3EJ, UK
[13]Lead contact
*Correspondence: psoba@uni-bonn.de
https://doi.org/10.1016/j.cub.2021.10.069

SUMMARY

Animals display selective escape behaviors when faced with environmental threats. Selection of the appropriate response by the underlying neuronal network is key to maximizing chances of survival, yet the underlying network mechanisms are so far not fully understood. Using synapse-level reconstruction of the *Drosophila* larval network paired with physiological and behavioral readouts, we uncovered a circuit that gates selective escape behavior for noxious light through acute and input-specific neuropeptide action. Sensory neurons required for avoidance of noxious light and escape in response to harsh touch, each converge on discrete domains of neuromodulatory hub neurons. We show that acute release of hub neuron-derived insulin-like peptide 7 (Ilp7) and cognate relaxin family receptor (Lgr4) signaling in downstream neurons are required for noxious light avoidance, but not harsh touch responses. Our work highlights a role for compartmentalized circuit organization and neuropeptide release from regulatory hubs, acting as central circuit elements gating escape responses.

INTRODUCTION

Animals use stimulus-specific, optimized strategies to deal with acute threats and noxious stimuli, including escape or avoidance behaviors.[1–3] In the somatosensory system of vertebrates and invertebrates, noxious stimuli are sensed by nociceptive neurons, and their activation results in acute escape or avoidance.[4–7] A specific noxious stimulus thereby elicits a stereotyped response with high fidelity (e.g., jumping in mice, corkscrew-like rolling in *Drosophila* larvae in response to noxious heat).[6,8] Selection of the appropriate behavioral response minimizes risk and increases the likelihood of survival.

The neuronal networks underlying escape responses range from simple reflex to extensive circuits.[8–13] Recent reconstruction of such networks at the synaptic level and neuronal circuit mapping have revealed extensive integration and interaction of circuits mediating distinct responses.[8–10,14] Integration and processing of sensory information starts at the sensory level, where different types of sensory neurons are converging on common second-order neurons, which are in turn part of the interconnected circuits providing feedback and feedforward information. How such circuits can specifically gate stimulus-specific information to support selected actions is not fully understood and difficult to deduce from pure anatomical network connectivity. Selection of behavior can occur probabilistically in a "winner takes all" fashion, for example, by reciprocal inhibition of circuits regulating mutually exclusive behaviors.[10,15] Differences in the activation pattern of sensory neuron subsets can result in different sensations and behavioral responses, as shown for combinatorial coding in mechanosensation and olfaction, suggesting extensive integration and processing in such networks.[16–19] Adding to the complexity of circuit computation are neuropeptides, which are expressed by many neurons across species.[20–23] They can be released in parallel to small synaptic

neurotransmitters to exert modulatory functions.[24–27] In most cases, their precise role, site of release, and action remain unclear, although they strongly contribute to network function and behavior.

To achieve detailed insight into the encoding of discrete escape responses at the circuit and neuromodulatory levels, we took advantage of the escape behavior of *Drosophila* larva, given its experimental accessibility and the ability to map the neuronal wiring diagram with nanometer resolution. The recent reconstruction of *Drosophila* larval brain circuits[14,28,29] has revealed a complex somatosensory network capable of processing different mechanical and noxious stimuli[14,30–32] comparable to its vertebrate counterpart.[33–35] At the sensory level, class IV dendritic arborization (C4da) neurons are polymodal neurons able to detect noxious touch, heat, and UV/blue light, which generate two different escape behaviors[6,36,37]: heat and harsh mechanical touch (mechanonociception) cause corkscrew-like rolling, while exposure to UV or blue light results in reorientation, avoidance, and dark preference. *Drosophila* larvae can sense UV, blue, and green light via different light-sensitive cells: Bolwig's organ (BO) consists of a group of cells in the larval head region and is sensitive to all of these wavelengths;[38] C4da neurons detect only noxious short-wavelength light in the UV and blue spectral range, presumably via the light-sensitive Gr28b receptor.[37] Avoidance responses to noxious light in acute and two-choice light-avoidance assays have been shown to rely on both BO and C4da neuron function.[36,37] While the circuit mechanism for light avoidance has not been studied in detail thus far, mechanonociception requires the integration of three mechanosensory subtypes (namely C2da, C3da, and C4da) by dorsal pair insulin-like peptide 7 (Dp7) neurons,[39] which provide neuropeptidergic feedback via short neuropeptide F (sNPF). sNPF action in turn promotes C4da and downstream partner (A08n) neuron responses, thus facilitating rolling escape behavior.[30] As Dp7 neurons integrate input from the mechanosensitive and light-sensitive C4da neurons and have neuromodulatory functions, we reasoned that they are potential candidates for computing distinct behavioral outputs, depending on the type of sensory input.

RESULTS

Neuromodulatory Dp7 neurons integrate sensory input required for noxious light avoidance

To explore the larval somatosensory escape circuit for noxious light avoidance (Figures 1A and 1B), we sought to confirm the noxious effect of short-wavelength light on development by rearing freshly hatched larvae either under blue or green light (470 or 525 nm at 2.5 μW/mm^2). Only blue light exposure resulted in lethality during development at larval or white pupal stages (Figure 1C). Thus, *Drosophila* larvae may have evolved avoidance behaviors to avoid short-wavelength light (e.g., bright sunlight) during their development. We therefore explored the circuits underlying escape behavior in response to noxious light using a two-choice preference assay[36,40] in which larvae in an arena were allowed to choose between darkness or white light of physiological relevance (365–600 nm with 6.9–3.3 μW/mm^2, respectively). After placing larvae close to the dark/light boundary, controls (w^{1118}) preferentially redistributed to the dark side within <5 min and maintained this preference for at least 15 min (Figures S1A and S1B; Video S1). This allowed us to reliably assess light avoidance by analyzing larval distribution after 15 min as previously described[36] (see STAR Methods for details).

To test for a potential function of Dp7 neurons in noxious light avoidance, we genetically hyperpolarized them by expressing the inward rectifying potassium channel Kir2.1 (*Dp7-LexA*[30]). In contrast to controls, silencing of Dp7 neurons strongly impaired larval light avoidance (Figures 1D, S1C, and S1D). We next tested whether Dp7 neurons were functionally activated in response to noxious light by expressing the calcium sensor GCaMP7s.[41] To prevent crosstalk of the stimulus with excitation/emission of the sensor, we used a narrow 365-nm light pulse (10 s, 60 μW/mm^2). We found that UV light exposure gave rise to robust calcium responses in the soma of Dp7 neurons in live larvae (Figure 1E; Video S2), strongly suggesting that Dp7 neurons are part of an innate noxious light-sensing circuit.

We next asked whether Dp7 neuron-derived neuropeptides are involved in noxious light avoidance. Dp7 neurons express multiple neuropeptides, including sNPF and insulin-like peptide 7 (Ilp7), of which sNPF, but not Ilp7, is required for mechanonociception.[30,42] Interestingly, we found that light avoidance was impaired in *Ilp7^{ko}*, but not *sNPF* mutant animals (Figure 1F). Temporal analysis showed that larvae eventually distributed almost evenly across the arena, suggesting that they are not able to maintain dark preference (Figures S1A and S1B). We analyzed light-dependent changes in larval locomotion in the dark or during exposure to noxious blue light. Control larvae displayed mildly elevated locomotion speed in blue light conditions, with a concomitant reduction in turning rates, presumably to escape the uniform noxious stimulus (Figures S1E and S1F). In contrast, *Ilp7^{ko}* animals displayed comparable speed, but lower turning rates in darkness, while slowing down and increasing turning under noxious light conditions. This suggests that in the absence of Ilp7, noxious light is still inducing locomotion changes, but responses are virtually inverted compared to controls. *Drosophila* larvae maintain light avoidance throughout development and preferentially pupariate in the dark.[36] *Ilp7^{ko}* animals formed pupae slightly earlier than controls (median *Ilp7^{ko}*: 119 h AEL, w^{1118}: 121 h AEL), but displayed reduced preference for pupariation in the dark (Figures S1G and S1H), suggesting that Ilp7 is required for light avoidance throughout development. Lastly, we rescued Ilp7 expression in *Ilp7^{ko}* animals using a Dp7 neuron-specific line, which completely restored light avoidance (*Dp7-Gal4* > *UAS-Ilp7*; Figures 1G and S1I). These data show that Dp7 neuron function and Ilp7 are required and that Dp7 neuron-derived Ilp7 is sufficient for noxious light avoidance.

Dp7 neurons integrate noxious light input from multiple somatosensory subcircuits

To gain more insight into the larval noxious light circuit, we identified the partially reconstructed Dp7 neurons from the electron microscopy (EM) brain volume of the first-instar larva.[14,24] To confirm dendritic and axonal compartments of Dp7 neurons, we expressed a dendritic marker (DenMark[43]) that labeled its medial and lateral arbors within the ventral nerve cord (VNC), but not the ascending arbor projecting to the brain lobes (Figure S2A). We then reconstructed Dp7 neurons and traced all of their synaptic partners (Figures 1H and S2B–S2F). Dp7 neurons

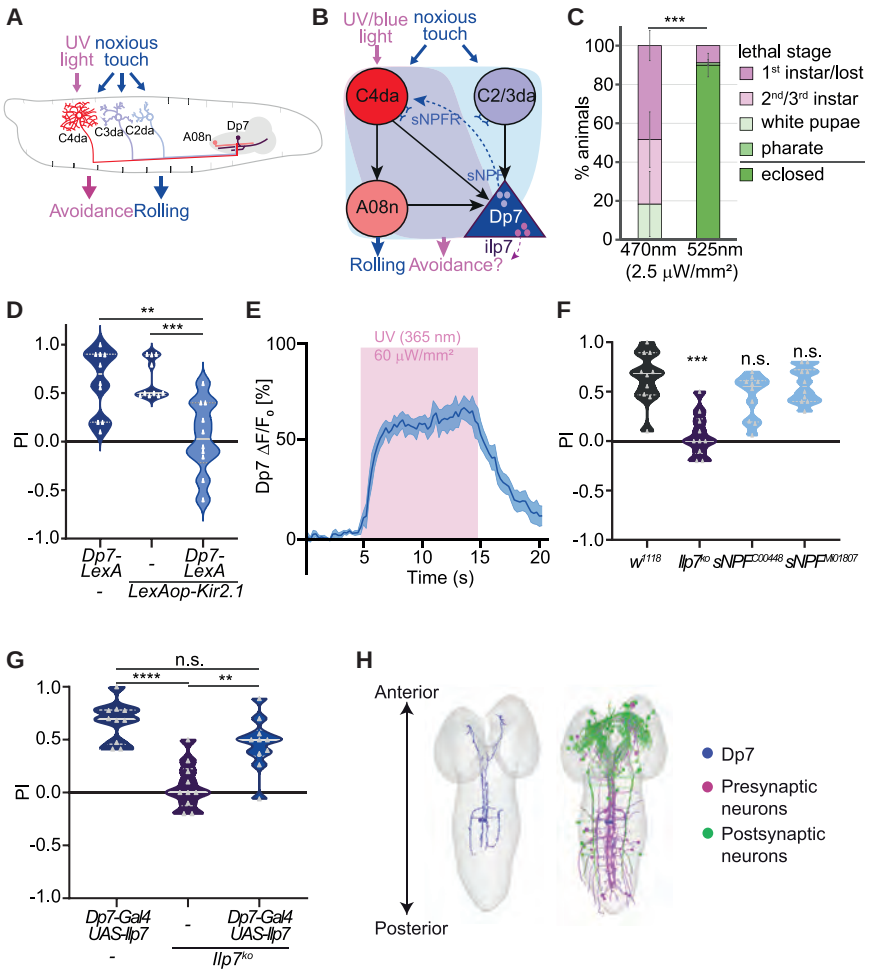

Figure 1. Ilp7-releasing Dp7 neurons are required for light avoidance

(A) Schematic representation of escape behaviors in *Drosophila* larvae. Noxious touch requires C2da, C3da, and C4da neurons for rolling escape, while noxious light sensed by C4da neurons elicits avoidance behavior.

(B) For mechanonociception, Dp7 neuron-derived sNPF, but not Ilp7, enables mechanonociceptive rolling through feedback action on C4da neurons to facilitate output to A08n.[30]

(C) Developmental lethality due to exposure to blue light (470 nm), but not green light (525 nm), of the same intensity (2.5 μW/mm^2). Percentage of freshly hatched larvae placed on food plates at 25°C dying at stages, as indicated in the legend (n = 5 trials, 50 larvae each, ± SD; ***p < 0.0001, χ^2 test).

(D) Inactivation of Dp7 neurons using *LexAop-Kir2.1* under the control of *Dp7-LexA*, impairs larval light avoidance (n = 10 trials, **p < 0.01, ***p < 0.001, one-way ANOVA with Tukey's post hoc test).

(E) UVA light induces calcium transients in Dp7 neurons (*Ilp7-Gal4>UAS-GCaMP7s*, 365 nm, 60 μW/mm^2, means ± SEMs indicated by shaded area, n = 4).

(F) *Ilp7^{ko}*, but not *sNPF* mutant animals, showed decreased light avoidance (n = 10 trials, ***p < 0.001; n.s., non-significant; one-way ANOVA with Tukey's post hoc test).

(G) Dp7 neuron-specific UAS-Ilp7 expression (with *Dp7-Gal4*) in the *Ilp7^{ko}* background restores light avoidance (n = 10 trials, *p < 0.05, ****p < 0.0001, one-way ANOVA with Tukey's post hoc test, *Ilp7^{ko}* dataset same as in E).

(H) EM-reconstructed Dp7 neurons and their highest connected synaptic partners. Upstream partners are shown in magenta, downstream partners in green.

See also Figures S1 and S2 and Videos S1 and S2.

receive most of the synaptic input in the VNC and provide output mostly in the subesophageal zone (SEZ) and brain lobe region along its dorsally projecting axon (Figures 1H and S2C–S2F). Dp7 neurons receive input from several subtypes of sensory neurons in the VNC (Figures 1H and S2E), suggesting that they are a somatosensory hub. We confirmed connectivity of Dp7 neurons with somatosensory neurons (C2da, C3da, C4da) as well as with C4 da neuron-connected A08n neurons[30] at the EM level (Figure S2E). Moreover, we identified a subset of tracheal dendrite (called v'td2[44]) neurons as the sensory class with the highest Dp7 neuron connectivity (Figures S2D and S2E). In contrast, the anatomically similar subset of v'td1 neurons was only weakly connected to Dp7 neurons at the connectome level (Figures S2D and S2E; see also Figure 2A). Overall, four sensory circuits were found to converge on Dp7 neurons (Figures 2A and 2B): direct monosynaptic connections from C4da and v'td2 to Dp7 neurons and two 2-hop polysynaptic pathways. We identified a strong link via A08n neurons previously shown to receive numerous synaptic inputs from C4da neurons.[28,30,45] Furthermore, the v'td2 to Dp7 neuron link was strongly interconnected via so-far uncharacterized midline projection (MIP) neurons (Figures 2A and S3A–S3D).

As C4da neurons respond to UV and blue light and are involved in light avoidance,[36,37] we tested whether A08n neurons as a major downstream output connected to Dp7 neurons may play a role as well. Unlike silencing of C4da neurons or ablation of BO, A08n neuron silencing did not result in significantly decreased light avoidance (Figures S3E and S3F). However, we detected robust calcium transients in A08n neurons in response to UV light (Figure S3G). Therefore, A08n neurons may only play a minor role in larval light avoidance, suggesting that C4da neurons may contribute to noxious light avoidance via other pathways.

v'td2 neurons are the major presynaptic partner of Dp7 neurons and co-labeled with C4da neurons by a reporter line of the putative light sensor Gr28b,[37,44] suggesting a role in noxious light sensing. We confirmed synaptic and functional connectivity between v'td2 and Dp7 neurons using a v'td2-specific Gal4 line (*73B01-Gal4*,[44] called *v'td2-Gal4* hereafter). Synapse-specific GFP reconstitution across synaptic partners (SybGRASP[46]) showed that v'td2s form synaptic contacts with Dp7 neuron lateral dendritic arbors and along the proximal axonal segment (Figure S3H). Consistently, we also detected robust Dp7 neuron calcium responses upon optogenetic activation of v'td2 neurons

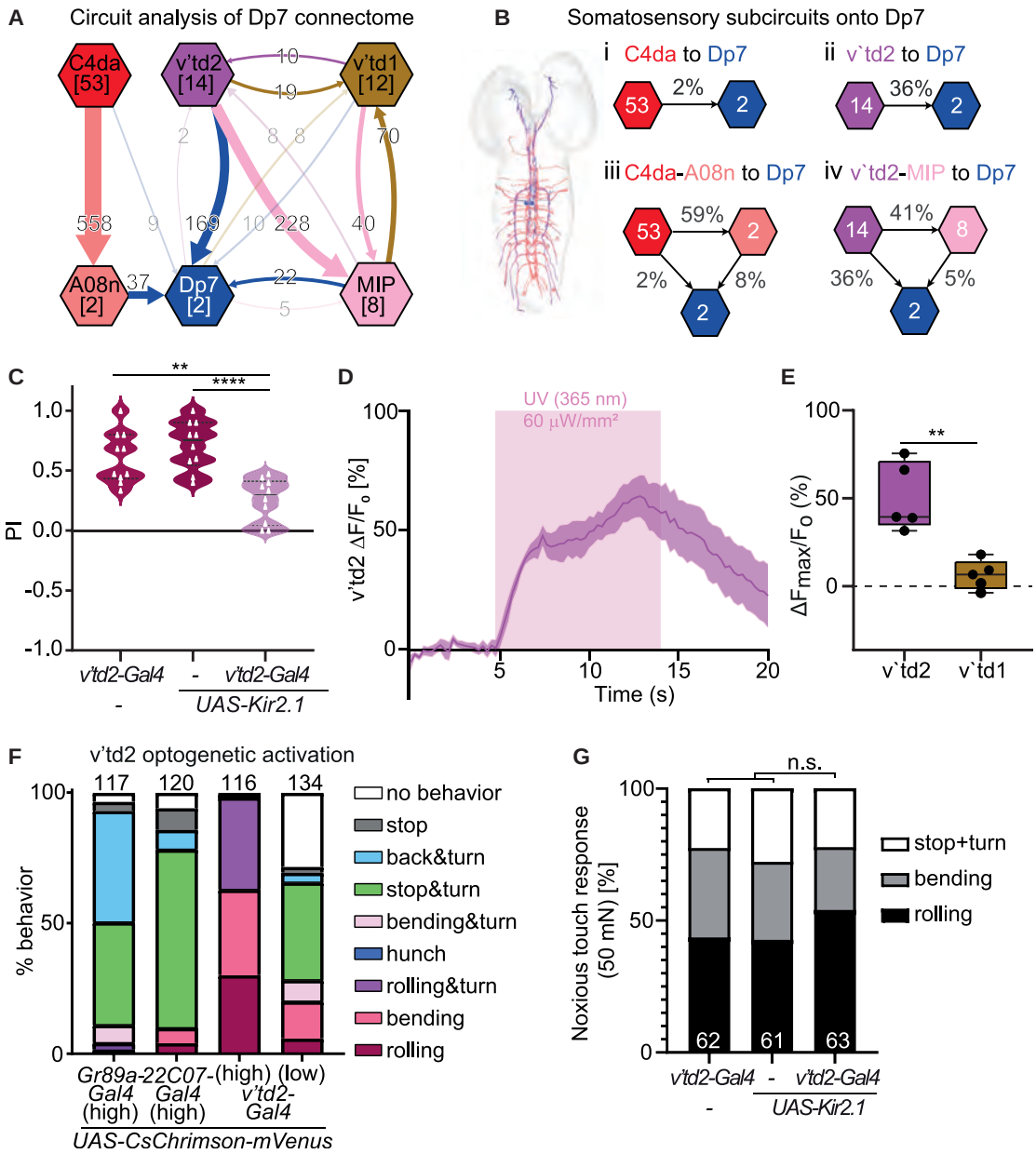

Figure 2. Dp7 integrates noxious light input from multiple somatosensory circuits

(A) Dp7 neuron presynaptic connectivity analysis showing the highest input from sensory v'td2 neurons. C4da to Dp7 neuron direct connectivity is weak, but additional indirect connections were found via A08n neurons. v'td2 neurons are additionally strongly connected to Dp7 neurons via MIP neurons, while v'td1 neurons display weak connectivity with Dp7 neurons and other circuit elements. Numbers in brackets indicate the number of neurons of the respective subtype; the numbers on the arrows indicate synapses from each neuronal subset forming direct connections.

(B) Inputs onto Dp7 neurons originating from either C4da or v'td2 neurons create 2 direct and 2 indirect subcircuits. The percentages of overall synaptic input of the target cells are shown.

(C) Silencing of v'td2 neurons using *Kir2.1* impairs light avoidance (*v'td2-Gal4* > *UAS-Kir2.1*, n = 10 trials, **p < 0.01, ****p < 0.0001, one-way ANOVA with Tukey's post hoc test).

(D) UV light-induced calcium transients in v'td2 neurons (*v'td2-Gal4* > *GCaMP6s*, means ± SEMs, n = 8).

(E) Quantitative comparison of calcium responses (GCaMP6s) of v'td2 and v'td1 neurons to UV light using *R35B01-Gal4*, which labels both subtypes ($\Delta F_{max}/F_0$ boxplot, n = 5, **p < 0.01, unpaired two-tailed t test).

(F) Optogenetic activation of CsChrimson (635 nm, high: 8.13 µW/mm^2, low: 1.33 µW/mm^2) using different previously characterized Gal4 driver lines expressing in v'td2 neurons.[44] Behavioral responses included avoidance (stop, backward, turn, hunch) and nocifensive behaviors (bending and rolling), as well as different combinations (n as indicated for each genotype). Note that all of the lines showed high prevalence for stop and turn or backward behavior depending on the activation level.

(G) Mechanonociceptive behavior (rolling and bending) is not affected by silencing of v'td2 neurons (*v'td2-Gal4* > *UAS-Kir2.1*, n = number of animals as indicated in graph, χ^2 test).

See also Figures S2 and S3 and Videos S3 and S4.

with CsChrimson (Figure S3I). We then tested whether v'td2 neurons are required for larval light avoidance. Similar to Dp7 neurons, Kir2.1-mediated silencing of v'td2 neurons significantly impaired light avoidance (Figure 2C). We further carried out calcium imaging of v'td2 neurons in intact larvae, which showed, similar to C4da neurons, acute responses to UV light stimulation (Figure 2D; Video S3). v'td1 sensory neurons, however, did not show calcium responses to UV stimulation (Figure 2E; Video S3), which is in line with the low connectivity to the Dp7 network (Figure 2A). We then tested whether v'td2 neurons could mediate acute avoidance behavior in response to optogenetic activation. We expressed and activated CsChrimson using different lines labeling v'td2 neurons, which resulted mostly in stop and turn or backward locomotion responses (Figure 2F; Video S4). At high, but not low, activation intensities, one of the three v'td2 lines used also induced significant rolling responses, likely due to the strong expression of CsChrimson. While we cannot rule out that v'td2 neuron activation can result in nociceptive rolling, Kir2.1-mediated silencing with the same driver line did not affect mechanonociceptive behavior, including rolling escape responses (Figure 2G). Thus, in contrast to C4da or A08n neurons, which are required for nociceptive rolling responses toward noxious touch,[30] v'td2 neuron activation induces acute avoidance behavior and is required for noxious light avoidance but not mechanonociception. Together with our connectome analysis, these findings show that at least two sensory subcircuits, C4da-A08n and v'td2 neurons, converge on Dp7 neurons and are involved in somatosensory UV light sensing, with v'td2, but not A08n neurons, strongly contributing to noxious light-avoidance behavior.

Compartmental organization of Dp7 hub neurons

To identify members of the noxious light-avoidance circuit downstream of Dp7 neurons, we analyzed the reconstructed synaptic wiring diagram. We identified abdominal leucokinin (ABLK) neurons, which receive direct input from Dp7, plus strong 2-hop synaptic connections from v'td2 via MIP neurons (Figure 3A). We inspected the topographical relationship of the mapped neurons and found that v'td2, MIP, and ABLK neurons anatomically converge on the ventrolateral dendritic arbor of Dp7 neurons (Figure 3B), which extends along the ventrolateral neuropil (Figure S4A). MIP and v'td2 neurons further extend mediodorsally along the axonal arbor of Dp7 neurons in the thoracic segments of the larval VNC and SEZ (Figures S3C and S3D). However, 75%–100% of synapses of v'td2 to MIP or Dp7 and MIP to ABLK neurons reside on the Dp7 ventrolateral dendrite (Figures 3B and 3C). This suggests the convergence of noxious light inputs and outputs within this Dp7 domain. In contrast, the mechanonociceptive circuit comprising C2da, C3da, C4da, and A08n neurons,[30] of which C4da and A08n also process noxious light information, primarily provides synaptic inputs on the medioventral dendritic arbor of Dp7 neurons (Figures 3D and S4A). Within the lateral region, Dp7 neurons receive extensive synaptic input from v'td2 neurons, which form concurrent (polyadic) synapses with MIP neurons. MIP neurons, in turn, innervate adjoining ABLK neuron processes also extending along the ventrolateral neuropil (Figures 3E, S4B, and S4C). This suggests that v'td2-MIP-ABLK neurons form a functional unit with the Dp7 ventrolateral arbor and that processing of mechanonociceptive and noxious light information may preferentially occur in distinct Dp7 arbor domains.

Interestingly, the synaptic contact region of v'td2-MIP-ABLK neurons on the lateral arbor of Dp7 neurons also coincides with Ilp7 neuropeptide localization (Figures 3B and 4A), suggesting that this could be a site of local peptide release. Analysis of Dp7 neurons in the EM volume revealed in total five putative fusion events of large dense-core vesicles (LDCVs), one of them occurring from Dp7 neurons to neighboring ABLK neurons (Figure 3F, arrow, from region marked with asterisk in Figure 3B). This indicated the possibility that Ilp7 is released from Dp7 neurons in direct vicinity of ABLK neurons.

Dp7- and Ilp7-dependent output to ABLK neurons in response to noxious light

Based on their converging input from the noxious light-sensing circuit, we next asked whether ABLK neurons are relevant downstream outputs. We silenced leukokinin (Lk)-expressing neurons (*Lk-Gal4*[47]) by expressing Kir2.1 and performed light-avoidance assays, which resulted in a strongly decreased dark preference (Figure 4B). As Lk is expressed in additional neurons in the SEZ (SELK) and brain lobes (ALK and LHLK), we genetically suppressed the expression of Kir2.1 only in ABLK neurons (*tsh-Gal80*; Figure S4H). Silencing of the remaining Lk^+ neurons did not result in light-avoidance defects, suggesting a specific dependence on ABLK neuron function. We also tested Hugin-VNC neuron function in light avoidance, which are downstream partners of Dp7 neurons, but receive major sensory input from non-UV responsive v'td1 neurons (Figure 3A). Consistent with our connectome and functional analysis, we did not detect any significant defects when silencing Hugin-VNC neurons with a specific Gal4 line[48] (Figure 4B). Our results show that ABLK neurons, but not Hugin-VNC neurons, are specifically involved in noxious light avoidance.

We analyzed potential light-dependent locomotion changes when silencing v'td2, Ilp7, or ABLK neurons. The average locomotion speed in the dark or during noxious blue light illumination was comparable to that of the control (Figure S4D), but overall turning rates of the animals, particularly during noxious light exposure, were reduced (Figure S4E). This indicated impaired reorientation/turning behavior under noxious light conditions. However, loss of *Ilp7* or silencing of v'td2, Ilp7, or ABLK neurons did not impair chemotaxis toward ethyl butyrate (Figures S4F and S4G), suggesting that complex navigational behavior is not generally affected. We next attempted to dissect ABLK neuron-dependent acute behavior by optogenetic activation of different Lk^+ subsets (Figures S4H and S4I). While we could selectively block expression in ABLK or brain lobe (ALK and LHLK) neurons using different genetic approaches, we could not suppress expression in SELK neurons. Optogenetic activation resulted in consistently strong rolling responses, suggesting that SELK neurons are likely involved in nociceptive rolling (Video S5).

We then assayed ABLK neuron responses to UV light using GCaMP6s and found prominent calcium transients upon stimulation (Figures 4C and S5A; Video S2). In contrast, SELK neurons did not respond to UV light, strongly suggesting that they are not involved in noxious light avoidance (Figure S5B; Video S2). We further assessed the activation of ABLK neurons by different light

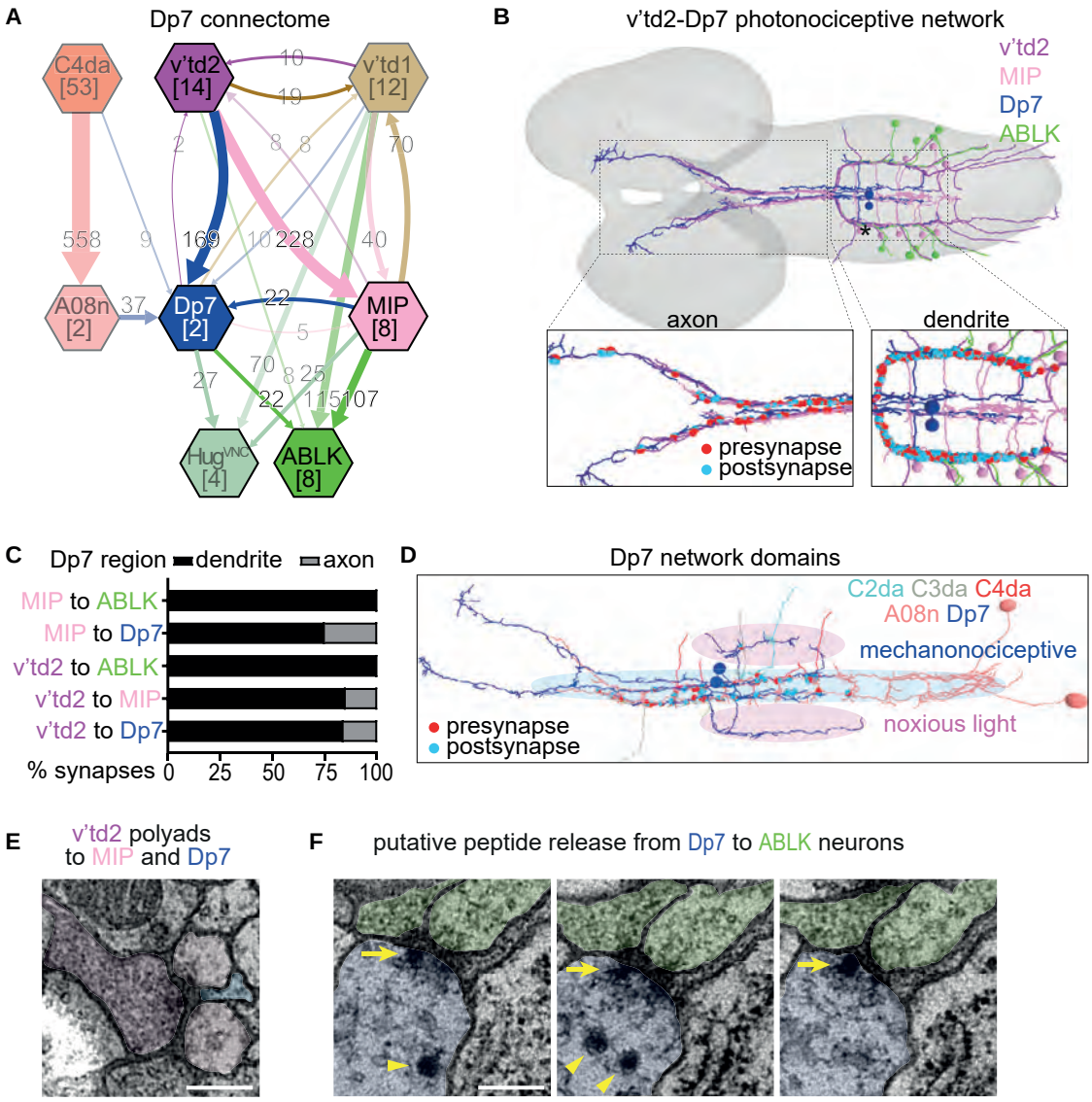

Figure 3. Domain-specific organization of the noxious light-avoidance network

(A) Connectivity graph of Dp7 neurons shows overlapping but distinct subcircuits. The major outputs of v'td2 neurons are Dp7 and MIP neurons, while v'td1 neurons strongly connect to ABLK and Hugin-VNC neurons. The numbers on the arrows indicate synapses from each neuronal subset forming direct connections.

(B) Overview of reconstructed Dp7, v'td2, MIP, and ABLK neuron innervation. Enlarged axon and dendrite regions of Dp7 neurons show local v'td2-Dp7, v'td2-MIP, and MIP-ABLK synapses on the lateral dendrite and anterior axon of Dp7 neurons.

(C) Relative synapse numbers in Dp7 dendritic and axonal arbor regions are shown for each partner.

(D) Synaptic connectivity of mechanosensory (C2da, C3da, C4da) and A08n neurons with Dp7. Most synapses are located on Dp7 medial dendrites providing mechanonociceptive input (indicated by shaded blue area). Except for C4da and A08n synapses, noxious light inputs (as shown in B) are mainly found on Dp7 lateral dendrites (indicated by shaded magenta area).

(E) v'td2 forms polyadic synapses with MIP and Dp7 neurons. Scale bar, 200 nm.

(F) Putative peptide release by docked LDCV (indicated by arrow) from Dp7 (blue) to adjacent ABLK neurons (green) in consecutive EM sections (region indicated by asterisk in B); additional LDCVs indicated by arrowheads. Scale bar, 200 nm.

See also Figure S4.

intensities and wavelengths using the red-shifted calcium sensor jRCaMP1b.[49] We could detect strong and acute calcium transients in ABLK neurons at UV light intensities ranging from 20 to 60 $\mu W/mm^2$ (Figure S5C). We then illuminated with different wavelengths in a range from 365 to 525 nm with the same intensity (60 $\mu W/mm^2$), revealing strong responses up to 470 nm, but not at 525 nm (Figure S5D). These data show that ABLK neurons are responding only to light within the noxious UV and blue wavelength range and that they are a part of a noxious light-sensing circuit.

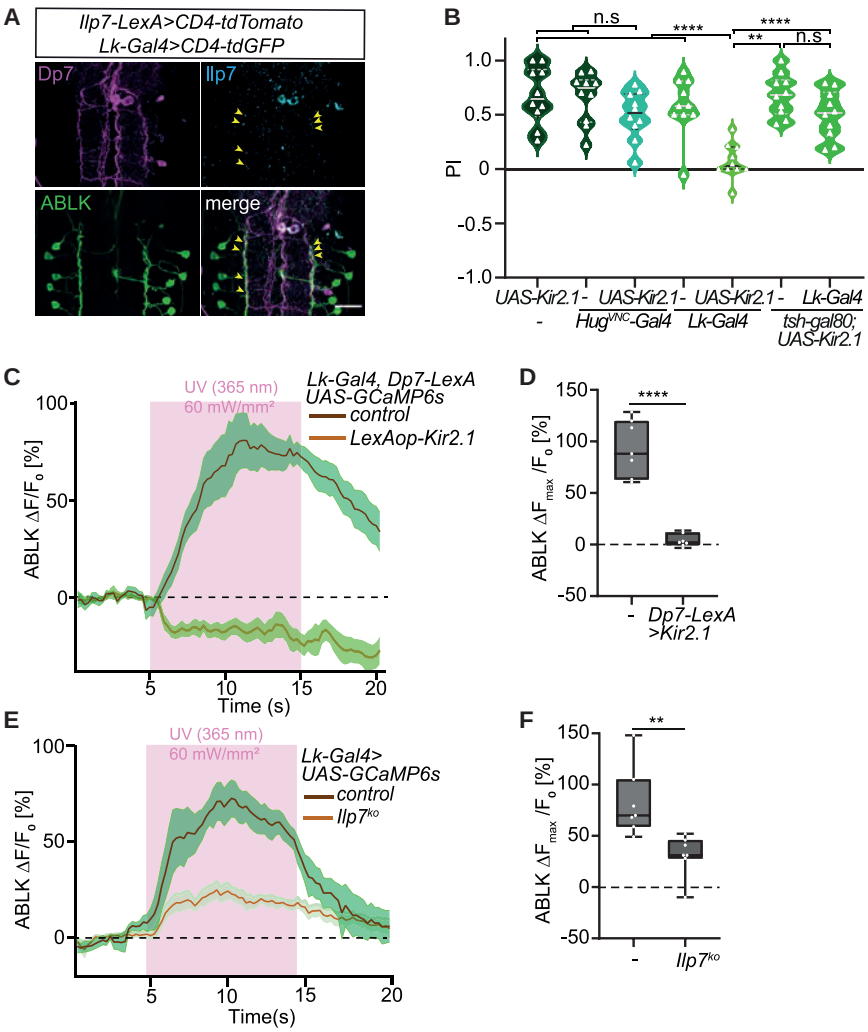

Figure 4. Dp7 neuron activity and Ilp7 peptide are required for noxious light information flow to ABLK neurons

(A) Confocal image stack (maximum projection) showing anatomical overlap of ABLK (*LK-Gal4 > UAS-CD4-tdGFP*) and Ilp7 neuropeptide puncta (cyan) along the lateral dendritic region of Dp7 neurons (*Ilp7-LexA > LexAop-CD4spGFP11-td-Tomato)*. Scale bar, 50 μm.

(B) Silencing of LK neurons (*Lk-Gal4 > UAS-Kir2.1*), but not when precluding ABLK expression (*tsh-Gal80, Lk-Gal4 > UAS-Kir2.1)*, abolishes light avoidance. Silencing Hugin-VNC neurons (*Hug^{VNC}-Gal4 > UAS-Kir2.1)* does not affect light avoidance (n = 10 trials/genotype, ****p < 0.0001, **p < 0.01, one-way ANOVA with Tukey's post hoc test).

(C) ABLK neuron calcium transients evoked by UV light with or without Dp7 neuron silencing (*Dp7-LexA*, *LexAop-Kir2.1*, means ± SEMs, n = 7).

(D) Boxplot quantification (% $\Delta F_{max}/F_0$) showing ABLK neuron response to UV light *(Lk-Gal4 > UAS-GCaMP6s*) with or without Ilp7 neuron silencing (*Ilp7-LexA > LexAopKir2.1*, n = 7 larvae/genotype, ****p < 0.0001, unpaired t test).

(E) ABLK neuron calcium transients evoked by UV light in control and *Ilp7^{ko}* animals (means ± SEMs, n = 7).

(F) % $\Delta F_{max}/F_0$ boxplots (n = 7 larvae/genotype, unpaired t test,**p < 0.01).

See also Figures S4 and S5 and Videos S2 and S5.

We next examined whether ABLK neuron responses to noxious light depend on Dp7 neuron function. To this end, we silenced Dp7 neurons using Kir2.1 expression and monitored ABLK neuron responses to UV light, which were absent under these conditions (Figures 4C and 4D). To assay whether Dp7-derived Ilp7 was required for ABLK activation, we performed calcium imaging in *Ilp7^{ko}* animals and detected a 70% decrease in ABLK neuron responses after UV light stimulation (Figures 4E and 4F). In contrast, the expression of tetanus toxin light chain (TNT) in Dp7 neurons did not affect ABLK neuron responses to UV light (Figure S5E), suggesting that synaptic transmission from Dp7 to ABLK neurons does not play a major role in this context. However, we cannot exclude the involvement of other neuropeptides contributing to ABLK responses. To test for a contribution to ABLK neuron activation by other light-sensing pathways, including C4da neurons or BO, we blocked their function by TNT expression or genetic ablation (*GMR-hid*), respectively. In both cases, ABLK neuron responses to UV light were not significantly impaired (Figure S5E). Similarly, the optogenetic activation of Dp7, BO, or C4da neurons using CsChrimson did not result in a significant activation of ABLK neurons, suggesting that neither Dp7 nor BO or C4da neurons are sufficient to activate ABLK neurons (Figures S5F–S5H). Consistently, we did not find a connectomic link between the BO network with Dp7 or ABLK neurons or a link between C4da and ABLK other than Dp7 neurons. These data strongly suggest that Dp7 neurons exert Ilp7-dependent control of ABLK neuron activation by noxious light, which likely involves the v'td2-MIP-Dp7 circuit rather than C4da neurons or BO.

Acute Ilp7 release from Dp7 neurons in response to noxious light

We next investigated the peptidergic link between Dp7 and ABLK neurons in more detail by asking whether Ilp7 release from Dp7 neurons can be acutely induced by UV light stimulation. We generated an Ilp7 release reporter by fusing Ilp7 to GCaMP6s (NPRR^{Ilp7}), analogous to previously characterized neuropeptide reporters.[50] NPRR^{Ilp7} expressed in Dp7 neurons localized in a punctate pattern similar to the endogenous pattern of Ilp7, and colocalized completely with the LDCV-specific Synaptotagmin Sytα[51] (Figures S6A and S6B). We next imaged NPRR^{Ilp7} responses to UV light in Dp7 neurons in live larvae. NPRR^{Ilp7} puncta in the proximal axon and ventrolateral dendrite region of Dp7 neurons displayed low baseline fluorescence consistent with low LDCV calcium levels, which increased rapidly upon UV light illumination, indicating peptide release (Figures 5A and 5B; Video S6). Repeated UV- light stimulation resulted in consistent NPRR^{Ilp7} responses in LDCV puncta (Figures 5C and 5D). These data are compatible with acute and rapid

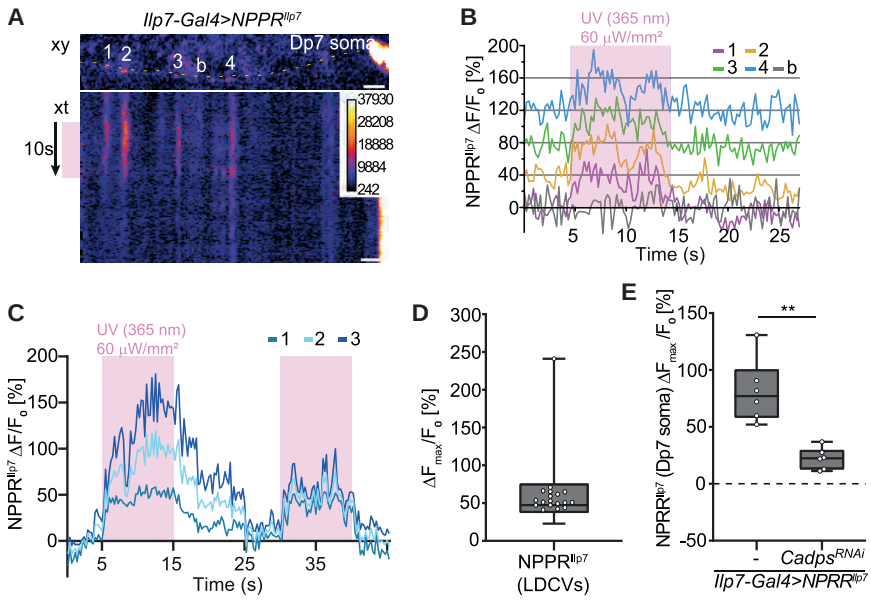

Figure 5. Acute Ilp7 peptide release from Dp7 neurons in response to UV light

(A) *NPRR*^{Ilp7}-labeled LDCVs (numbers 1–4; b, background) located along the Dp7 proximal axon. Time series (xt) along the dotted line showing acute evoked NPRR^{Ilp7} fluorescence increase in response to a 10-s UV light exposure (365 nm, 60 µW/mm^2). Scale bars, 10 µm.

(B) Stacked individual traces of *NPRR*^{Ilp7}-labeled LDCVs (numbered 1–4, individual responses are stacked by 20% each for clarity) and background (b) shown in (A).

(C) Repeated UV light-induced responses of individual NPRR^{Ilp7} puncta located along the proximal axon or lateral dendrite of Dp7 neurons (from 3 representative experiments).

(D) $\Delta F_{max}/F_0$ boxplot of Dp7 NPRR^{Ilp7} responses to UV light (n = 18 LDCVs from 6 animals).

(E) Boxplot quantification (% $\Delta F_{max}/F_0$) of maximum NPRR^{Ilp7} fluorescence change in Dp7 somata upon UV light stimulation without or with Cadps-RNAi. Cadps knockdown significantly reduces NPRR^{Ilp7} responses (n = 6 larvae/genotype, $^{**}p < 0.001$, unpaired t test).

See also Figure S6 and Video S6.

peptide release by partial LDCV fusion with the plasma membrane in the millisecond-to-second range, similarly to kiss-and-run-type peptide release upon electrical stimulation.[50,52] Imaging of NPPR^{Ilp7} in the Dp7 soma showed similar responses, also suggesting somatic release (Figure S6C). In contrast, posterior Ilp7$^+$ neurons, which innervate the gut, did not show UV light-induced somatic NPPR^{Ilp7} responses (Figure S6C). To further confirm that NPPR^{Ilp7} is reporting LDCV fusion with the plasma membrane, we used RNAi to knock down calcium-dependent secretion activator (Cadps), a conserved protein required for LDCV release, but not biogenesis.[53,54] UV light-induced NPPR^{Ilp7} responses in the Dp7 soma were strongly diminished upon Cadps-RNAi, showing that the observed responses are LDCV release dependent (Figure 5E). Our data thus show that LDCVs containing Ilp7 are acutely released from Dp7 in response to UV light, thereby acting directly on neighboring ABLK neurons, reminiscent of small-molecule neurotransmitter action.

Neuropeptidergic decoding of circuit responses and behavior for noxious light

As the noxious light and mechanonociceptive circuits overlap extensively at the sensory C4da and Dp7 neuron level, we asked whether Ilp7-dependent output of Dp7 to ABLK neurons is specific for UV light. Kir2.1-mediated silencing of LK neurons, with or without the inclusion of ABLK neurons, did not significantly impair mechanonociceptive escape responses resulting in nocifensive rolling behavior (Figure 6A). Instead, silencing all LK neurons mildly facilitated mechanonociceptive behavior, which is in line with a similar effect described for *Ilp7* deletion.[30] Moreover, in sharp contrast to UV light stimulation, we did not detect calcium responses in ABLK neurons after mechanonociceptive stimulation (Figure 6B). Divergence of the mechanonociceptive and noxious light circuits thus occurs downstream of Dp7 neurons through Ilp7-mediated actions on ABLK neurons.

While no cognate Ilp7 receptor has been identified so far, the relaxin family receptor Lgr4 has coevolved with Ilp7 across arthropod species, suggesting a receptor-ligand relationship.[55,56] A Gal4 reporter incorporated in the endogenous Lgr4 mRNA (*Lgr4*^{T2AGal4}) displayed expression in ABLK neurons, suggesting the presence of Lgr4 (Figure 6C). We further analyzed the localization of an ABLK-expressed hemagglutinin (HA)-tagged Lgr4, which localized along ABLK neuron projections close to endogenous Ilp7 puncta present on the ventrolateral branch of Dp7 neurons (Figure 6D). In addition, we biochemically confirmed Ilp7 and Lgr4 interaction in S2 cells in co-immunoprecipitation assays showing that Ilp7 and Lgr4 are capable of binding *in vitro* (Figure S6D). Binding was dependent on the presence of the extracellular leucine-rich repeat (LRR) domain of Lgr4, but not a conserved residue (I263) required for interaction of the mammalian orthologs RXFP1 and relaxin (Figure S6E).

To find out whether Lgr4 is physiologically relevant for noxious light avoidance, we tested *Lgr4*^{T2AGal4} larvae, which carry a T2A-Gal4 exon, resulting in the loss of *Lgr4* as confirmed by qPCR analysis (Figure S6F). *Lgr4*^{T2AGal4} animals showed significantly reduced light avoidance, which could be fully rescued by the overexpression of Lgr4 in its endogenous pattern (Figure 6E). We then imaged calcium responses of ABLK neurons using a confirmed *Lgr4* knockout (KO) allele (*Lgr4*^{ko57}) showing reduced light avoidance as well (Figures 6F, 6G, S6G, and S6H). Similar to *Ilp7*^{ko} animals, we detected a 3-fold decrease in calcium transients, which was rescued upon the expression of Lgr4 only in LK$^+$ neurons, including ABLKs (Figures 6F and 6G). Collectively, these results suggest that Lgr4 acts downstream of Ilp7 in ABLK neurons to promote their UV light responses and light-avoidance behavior.

DISCUSSION

Noxious light processing in *Drosophila* larvae for sustained avoidance responses

All animals must detect noxious stimuli and engage in appropriate escape actions to avoid injury or death. Consistent with previous reports,[58,59] extended exposure to blue, but not green,

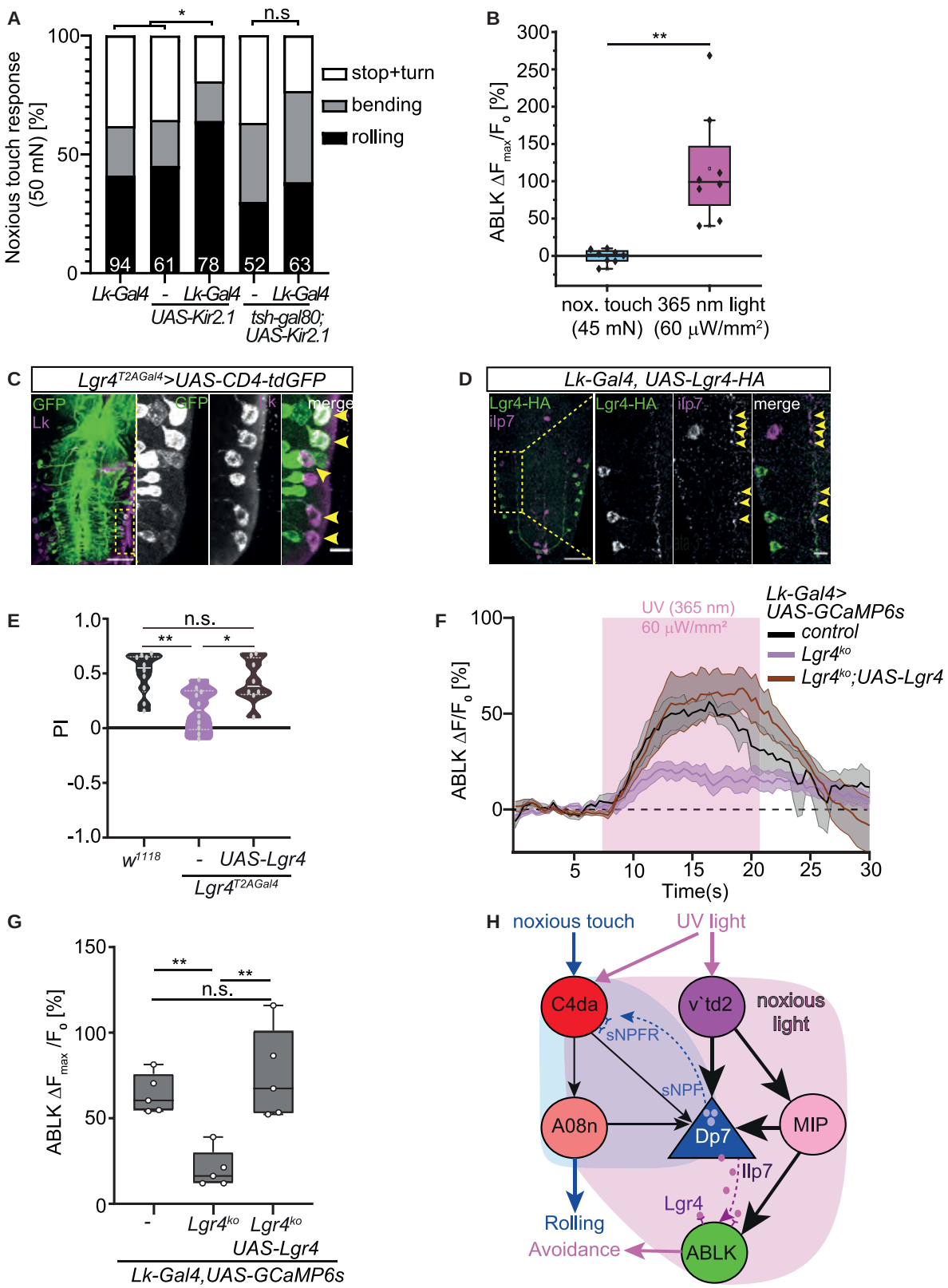

Figure 6. Neuromodulatory decoding of nociceptive escape behaviors

(A) Mechanonociceptive responses upon silencing of Lk neurons (*Lk-Gal4 UAS-Kir2.1*), with or without ABLK silencing (*Lk-Gal4;tsh-Gal80,UAS-Kir2.1*; n = total number of larvae indicated in graphs, *p < 0.05, χ^2 test).

(legend continued on next page)

light is noxious and lethal for developing *Drosophila* larvae. This suggests a strong need to efficiently detect and avoid short-wavelength light. Extraocular UV/blue light sensors expressed in body wall neurons have been identified in several invertebrates, including *Caenorhabditis elegans*[60] and *Drosophila*,[37,61,62] and the underlying circuits seem to aid in the detection and avoidance of noxious light qualities and intensities. Previous work in *Drosophila* larva showed that besides BO, C4da neurons are involved in acute UV or blue light-avoidance responses,[37,63,64] likely via independent circuits. Here, we provide evidence that v'td2 neurons represent an additional set of larval body wall neurons sensing noxious light and inducing avoidance responses via peptidergic Dp7 neuron action and ABLK neuron activation. Of note, ABLK neurons have been proposed to gate binary escape decisions in response to optogenetic activation of C4da neurons using a blue light-activated channelrhodopsin.[65] Our connectomic, functional, and behavioral data show that ABLK neurons are actually part of a UV and blue light-sensing circuit promoting acute and sustained noxious light-avoidance behavior. While ABLK neurons have known additional functions in stress response pathways[66,67] and blue light-induced rearing behavior,[68] the lack of major connectivity and functional activation of ABLK by C4da neurons as shown in our work will require further investigation of their role in computing binary escape decisions.

Why do *Drosophila* larvae need three seemingly independent sensory circuits (BO, C4 da, and v'td2) to sense and avoid noxious light? BO is located in the larval head region, while v'td2 and C4 da neurons reside in abdominal segments (A1–A7) or tile the entire body wall,[38,44,69] respectively. For acute noxious light responses after exposure on the larval head region, BO and C4da neurons seem to be jointly required.[37,63] However, as shown for our v'td2-Dp7-ABLK circuit here and previously for BO[40] and C4da neurons,[36] each of these sensory units is necessary for efficient light avoidance in choice assays. Under such chronic conditions, the combined action of these sensory systems covering different larval body regions may enable a sustained behavioral mode for continuous avoidance of extended periods of noxious light exposure of any body part. Although we could not identify a connectomic or functional link between BO and the circuit described here, C4da neurons may still contribute to Dp7 neuron-dependent Ilp7 release based on their ability to promote Dp7 neuron activation in mechanonociception.[30] We cannot rule out additional outputs of v'td2 neurons besides ABLK neurons, which may reside within the MIP connectome. However, it is also possible that these light-sensing circuits are connected via long-range peptidergic/hormonal regulation, as BO-dependent release of PTTH (prothoracicotropic hormone) has been suggested to control C4da neuron function in light-avoidance behavior.[36] This indicates that global hormonal signals may additionally coordinate the action of these circuits.

Neuromodulatory hub-mediated sensory processing

The challenge of a nervous system is to generate the correct behavioral output, such as specific escape responses, based on the received sensory input. Emerging connectomic data from *Drosophila* illustrates that sensory networks fan out extensively, adding numerous partners at each subsequent level.[14,28,70] As a result, the relevant output path of any given sensory input is often difficult to identify, indicating that physical connection is not a sufficient predictor for function.[22,71] This suggests specific circuit mechanisms for selective gating of action-specific network components. Along these lines, a hub-and-spoke-like circuit has been identified in *C. elegans*, where the RMG neuron forms a hub that receives spoke-like input from several sensory neurons regulating aggregation behavior via neuromodulatory signaling.[72,73] Similarly, somatostatin$^+$ neurons in the spinal cord receive converging input from different mechanosensory pathways[74] and play a pivotal role in mechanical pain processing. Such convergence of multiple sensory inputs allows the integration and regulation of behavioral output, suggesting that neuropeptide-expressing neurons are local network hubs. In our work, Dp7 neurons act as a regulatory hub that gates the activation of specific network responses. This may be particularly important in sensory processing, in which peptidergic action can increase the computational power by organizing circuit function to generate alternative behaviors.[22,27,75] In mice, alternative escape behaviors are regulated by competitive and mutually inhibitory circuits of corticotropin-releasing factor and somatostatin$^+$ neurons in the central amygdala, which mediate conditioned flight or passive freezing, respectively.[10] While direct involvement of these neuromodulators has not yet been shown, oxytocin release from presynaptic terminals of hypothalamic neurons in the central amygdala attenuates fear responses in mice,[76,77] suggesting extensive neuromodulatory regulation of escape and related behaviors across species. Our work revealed that discrete escape pathways are controlled by Dp7 hub neurons through input-specific neuropeptide function. Rolling in response to noxious mechanical touch[6,78] requires feedback signaling from Dp7 neurons via

(B) Maximum ABLK neuron responses (boxplot, % $\Delta F_{max}/F_0$) to noxious mechanical or UV light stimulations in semi-intact live larval preparations (n = 8, unpaired t test, $^{**}p < 0.01$).
(C) Endogenous Lgr4 reporter expression (*Lgr4^{T2AGal4},UAS-CD4-tdGFP*) in ABLK neurons detected by colocalized anti-Lk immunostaining. Overview and magnified lateral VNC region (boxed region) with ABLK neuron somata (GFP: green, Lk: magenta). Scale bars, 50 μm, 10 μm for enlarged view.
(D) Lgr4-HA localization in ABLK neurons (*Lk-Gal4,UAS-Lgr4-HA*) with anti-Ilp7 immunostaining. Overview and magnified lateral VNC region (boxed region) showing ABLK neuron somata and dendrites with proximity of Lgr4 (green) and Ilp7 (magenta) puncta on the Dp7 neuron lateral arbor. Scale bars, 50 and 10 μm.
(E) *Lgr4^{T2AGal4}* animals display reduced light avoidance, which was rescued by *UAS-Lgr4* expression (n = 10, 10, and 8 trials/genotype; $^*p < 0.05$, $^{**}p < 0.01$, one-way ANOVA with Tukey's post hoc test).
(F) GCaMP6s-expressing ABLK neuron responses to UV light in control and *Lgr4^{ko}* animals, with and without UAS-Lgr4 expression (*Lk-Gal4 > GCaMP6s*, n = 5 animals/genotype, means ± SEMs).
(G) Quantitative $\Delta F_{max}/F_0$ boxplots of (F) (n = 5, $^{**}p < 0.01$, one-way ANOVA, with Tukey's post hoc test).
(H) Model depicting neural and molecular elements shaping the larval somatosensory escape circuit, with specific action of sNPF or Ilp7 on mechanonociception versus noxious light resulting in rolling or avoidance, respectively.
See also Figure S6.

sNPF, but not Ilp7 peptide.[30] In contrast, noxious light-avoidance behavior requires Dp7 neuron-derived Ilp7, but not sNPF, and acts via a feedforward mechanism. Circuit-specific neuropeptide action thus generates discrete escape behaviors in this system by creating divergent networks, despite the extensive overlap between mechanonociceptive and noxious light avoidance circuits (Figure 6H). This may raise the question of why these circuits are converging on hub neurons in the first place. First, sensory integration can facilitate escape responses as vibration[14] or blue light[79] enhance nociceptive rolling in *Drosophila* larvae. Second, escape responses may have to be tuned depending on the overall environmental context as well as the state of the animal, for which peptidergic regulation is known to be a key factor.[22]

Compartmentalized modality-specific circuits and neuromodulatory action

Specific compartmentalization of sensory inputs and outputs can increase the efficiency of network computation at hub neurons through combined local synaptic and neuropeptide domains. In *C. elegans*, peptide release from the PVD neuron dendrites provides local proprioceptive feedback to motor neurons.[80] Discrete functional domains have also been described for *Drosophila* mushroom body Kenyon cells displaying compartmentalized activity, which encodes context-specific functions by local dopaminergic modulation.[81–83] Here, we show the convergence of UV light-responsive inputs and outputs with Ilp7 release sites on the Dp7 lateral dendritic arbor, which likely form a computational unit of the noxious light-avoidance circuit. Analogous compartmental organization is likely found in the somatosensory system of adult flies[84] and also in vertebrates displaying modality-specific laminar organization of sensory inputs and corresponding outputs.[16,17,85] This suggests that integrating neuropeptide-expressing neurons receiving sensory input linked to distinct modalities, such as Dp7 neurons in *Drosophila* or somatostatin-expressing neurons in the vertebrate spinal cord,[74] play a pivotal role in processing sensory stimuli. Dendrites can act as independent computational units,[86] as shown in the vertebrate retina.[87] Although we could identify physical compartmentalization of input and output domains, most of the physiological responses, including peptide release, seem to occur globally across the entire neuron. We currently lack the tools and resolution to investigate region-specific differences in calcium levels or peptide release efficiency. Nonetheless, neuromodulatory signals can still aid local processing due to circuit-specific expression of cognate receptors, as shown here by noxious light-specific responses of Lgr4-expressing ABLK neurons. In line with this notion, neuropeptide overexpression studies in zebrafish have shown that sensory responsiveness can be regulated in a peptide- and modality-specific manner[88] suggesting that their signaling still acts on selective circuits to enhance respective innate behaviors. Thus, compartmentalized circuits with broad yet functional unit-specific neuromodulatory action may be a widespread mechanism to generate context-specific behaviors.

Neuropeptide-mediated co-transmission selects network action and behavior

Co-transmission of small-molecule neurotransmitters and neuropeptides has been described in vertebrates and invertebrates;[20,22,27,89] however, the acute signaling function of neuropeptides in sensory behavior is not well understood. In general, neuropeptide release has been described to occur upon neuronal activity,[25,50,90–92] although their action is considered slow and broad,[20,22] with the ability to regulate targets distant from release sites (e.g., opioid receptor signaling in stress-induced analgesia)[93] and long-lasting behavioral states, including sleep, foraging, and social behavior.[72,94,95]

Here, we show that Ilp7 is acutely released from Dp7 neurons in response to noxious light and required for full ABLK neuron activation. Residual ABLK neuron calcium transients in the absence of Ilp7, likely due to small neurotransmitter activity in this network, are not sufficient for noxious light-avoidance behavior. This suggests that Ilp7 can act as a co-transmitter required for selective network activation and behavior. Ilp7 presumably acts via Lgr4 to enable noxious light-avoidance responses and behavior. Lgr4 belongs to the conserved family of relaxin receptors.[55,96–100] Recent work indicates a role for relaxin-3 in escape behavior through the inhibition of oxytocin-producing neurons in the hypothalamus, a brain region implicated in the modulation of escape responses of vertebrates.[76,101] This suggests a conserved role of relaxin signaling in escape responses.

Overall, our data suggest that neuropeptidergic signals can act acutely on the physical neuronal network to promote selective network activity and specific innate behaviors. Based on the widespread expression of neuropeptides and cognate G protein-coupled receptors (GPCRs), including in escape circuits,[20–23,102] further studies must determine whether local neuromodulatory hubs with compartmentalized circuits as described here may be a general motif for the computation of modality-specific sensory responses.

STAR★METHODS

Detailed methods are provided in the online version of this paper and include the following:

- KEY RESOURCES TABLE
- RESOURCE AVAILABILITY
  - Lead contact
  - Materials availability
  - Data and code availability
- EXPERIMENTAL MODEL AND SUBJECT DETAILS
  - Fly stocks
  - S2-DRSC cell line
- METHOD DETAILS
  - Generation of plasmids and transgenes
  - Neuronal reconstruction and circuit mapping
  - Immunohistochemistry and confocal imaging
  - Developmental toxicity assay
  - Light avoidance assays
  - Mechanonociception assays
  - Locomotion and chemotaxis assays
  - Optogenetic behavioral assays
  - Calcium imaging in intact larvae
  - Calcium imaging in semi-intact larvae
  - Cell culture and co-immunoprecipitation assay
  - qRT-PCR

- Light avoidance pupariation assay
- Developmental time assay

- QUANTIFICATION AND STATISTICAL ANALYSIS
  - Statistics
  - Analysis of network synaptic counts
  - Developmental toxicity assay
  - Light avoidance analysis
  - Mechanonociception analyses
  - Locomotion and chemotaxis analysis
  - Analysis of calcium imaging

SUPPLEMENTAL INFORMATION

Supplemental information can be found online at https://doi.org/10.1016/j.cub.2021.10.069.

ACKNOWLEDGMENTS

We would like to thank M. Petersen and A.R.M. Dias for excellent technical assistance; C. Wegener, T. Oertner, F. Morellini, J. Parrish, and Q. Yuan for comments on the manuscript; B. Ye, B. Hofbauer, and C. Wegener for communicating results prepublication; P. Herrero, C. Wegener, M. Wernet, and D. Anderson for fly stocks; T. Kazimier for advice and troubleshooting with CATMAID; and L. Herren for supervising Dp7 connectome reconstruction. P. Soba, B.N.I., and A.C. thank the visiting scientist program at HHMI Janelia, and HHMI Janelia for funding. Stocks obtained from the Bloomington Drosophila Stock Center (NIH grant P40OD018537) and Vienna Drosophila Resource Center (VDRC; http://stockcenter.vdrc.at) were used in this study. cDNA and cells obtained from the Drosophila Genomics Resource Center (NIH grant 2P40OD010949) were used in this study. This work was supported by the Deutsche Forschungsgemeinschaft (DFG; SO1337/4-1, SO1337/2-1/2-2, and SO1337/ 7-1 to P. Soba; WI4485/2-2 and WI4485/3-2 to J.S.W.), the DFG Heisenberg program (SO1337/6-1 to P. Soba), an Alexander von Humboldt Research Fellowship (to A.F.), an EMBO Short-Term Fellowship (to E.M.V.), the European Commission FP7 (PCIG13-GA-2013-618847 to A.M.G.), the European Research Council Horizon 2020 (ERC2016-StG-714762 to J.S.W.), the FCT (IF/00022/2012; Congento LISBOA-01-0145-FEDER-022170, co-financed by FCT/Lisboa2020; UID/Multi/04462/2019, PTDC/BEXBCM/1370/2014, and PTDC/BIA-BID/31071/2017 to A.M.G.; PTDC/MED-NEU/30753/2017 to F.H. and A.M.G.; and SFRH/BPD/94112/2013 to A.M.), PD/BD/52421/2013 to F.H., and SFRH/BD/135263/2017 via PGCD (Programa Pós-Graduação Ciência Para o Desenvolvimento) to E.M.V.

AUTHOR CONTRIBUTIONS

B.N.I. performed and analyzed most of the experiments, including connectome reconstruction and analysis, phototoxicity assays, light-avoidance behavior analysis, calcium imaging, and morphological analysis, and wrote the manuscript. A.W and F.Z. performed a subset of the light-avoidance assays. F.Z. and A.F. performed the locomotion and chemotaxis assays and analysis. A.F. wrote the custom analysis scripts and code. C.H. performed and analyzed experiments in semi-intact larval preparations. F.M.T. performed and analyzed the mechanonociceptive and optogenetic behavior assays. K.S. made the reagents and performed the co-immunoprecipitation experiments. E.M.V. performed and analyzed the pupariation assays. E.M.V., A.P.C., A.M., F.H., and A.M.G. developed Lgr4 transgenes and performed qPCR assays. P. Schlegel and M.J.P. performed the connectome reconstruction and analyses. C.-H.Y. and I.M.-A. developed the critical reagents. J.S.W. contributed to and supervised the behavioral analyses and custom code. A.C. performed and supervised the connectome reconstruction. P. Soba made the reagents, contributed to the circuit and behavioral analyses, supervised the work, and wrote the manuscript.

DECLARATION OF INTERESTS

The authors declare no competing interests.

Received: February 12, 2021
Revised: October 5, 2021
Accepted: October 29, 2021
Published: November 18, 2021

REFERENCES

1. Branco, T., and Redgrave, P. (2020). The neural basis of escape behavior in vertebrates. Annu. Rev. Neurosci. *43*, 417–439.
2. Im, S.H., and Galko, M.J. (2012). Pokes, sunburn, and hot sauce: Drosophila as an emerging model for the biology of nociception. Dev. Dyn. *241*, 16–26.
3. Hesselson, D., Walker, D.S., Massingham, J.N., Schafer, W.R., Neely, G.G., and Chew, Y.L. (2020). Invertebrate models of nociception. In The Oxford Handbook of the Neurobiology of Pain, J.N. Wood, ed. (Oxford University Press), pp. 60–100.
4. Basbaum, A.I., Bautista, D.M., Scherrer, G., and Julius, D. (2009). Cellular and molecular mechanisms of pain. Cell *139*, 267–284.
5. Chatzigeorgiou, M., Yoo, S., Watson, J.D., Lee, W.H., Spencer, W.C., Kindt, K.S., Hwang, S.W., Miller, D.M., 3rd, Treinin, M., Driscoll, M., and Schafer, W.R. (2010). Specific roles for DEG/ENaC and TRP channels in touch and thermosensation in C. elegans nociceptors. Nat. Neurosci. *13*, 861–868.
6. Tracey, W.D., Jr., Wilson, R.I., Laurent, G., and Benzer, S. (2003). painless, a Drosophila gene essential for nociception. Cell *113*, 261–273.
7. Julius, D. (2013). TRP channels and pain. Annu. Rev. Cell Dev. Biol. *29*, 355–384.
8. Barik, A., Thompson, J.H., Seltzer, M., Ghitani, N., and Chesler, A.T. (2018). A brainstem-spinal circuit controlling nocifensive behavior. Neuron *100*, 1491–1503.e3.
9. Tovote, P., Esposito, M.S., Botta, P., Chaudun, F., Fadok, J.P., Markovic, M., Wolff, S.B.E., Ramakrishnan, C., Fenno, L., Deisseroth, K., et al. (2016). Midbrain circuits for defensive behaviour. Nature *534*, 206–212.
10. Fadok, J.P., Krabbe, S., Markovic, M., Courtin, J., Xu, C., Massi, L., Botta, P., Bylund, K., Müller, C., Kovacevic, A., et al. (2017). A competitive inhibitory circuit for selection of active and passive fear responses. Nature *542*, 96–100.
11. Dunn, T.W., Gebhardt, C., Naumann, E.A., Riegler, C., Ahrens, M.B., Engert, F., and Del Bene, F. (2016). Neural circuits underlying visually evoked escapes in larval zebrafish. Neuron *89*, 613–628.
12. Kupfermann, I., Castellucci, V., Pinsker, H., and Kandel, E. (1970). Neuronal correlates of habituation and dishabituation of the gill-withdrawal reflex in Aplysia. Science *167*, 1743–1745.
13. Bezares-Calderón, L.A., Berger, J., Jasek, S., Verasztó, C., Mendes, S., Gühmann, M., Almeda, R., Shahidi, R., and Jékely, G. (2018). Neural circuitry of a polycystin-mediated hydrodynamic startle response for predator avoidance. eLife *7*, 1–28.
14. Ohyama, T., Schneider-Mizell, C.M., Fetter, R.D., Aleman, J.V., Franconville, R., Rivera-Alba, M., Mensh, B.D., Branson, K.M., Simpson, J.H., Truman, J.W., et al. (2015). A multilevel multimodal circuit enhances action selection in Drosophila. Nature *520*, 633–639.
15. Jovanic, T., Schneider-Mizell, C.M., Shao, M., Masson, J.-B., Denisov, G., Fetter, R.D., Mensh, B.D., Truman, J.W., Cardona, A., and Zlatic, M. (2016). Competitive disinhibition mediates behavioral choice and sequences in Drosophila. Cell *167*, 858–870.e19.
16. Abraira, V.E., and Ginty, D.D. (2013). The sensory neurons of touch. Neuron *79*, 618–639.
17. Koch, S.C., Acton, D., and Goulding, M. (2018). Spinal circuits for touch, pain, and itch. Annu. Rev. Physiol. *80*, 189–217.
18. Kaupp, U.B. (2010). Olfactory signalling in vertebrates and insects: differences and commonalities. Nat. Rev. Neurosci. *11*, 188–200.
19. Haverkamp, A., Hansson, B.S., and Knaden, M. (2018). Combinatorial codes and labeled lines: how insects use olfactory cues to find and judge

food, mates, and oviposition sites in complex environments. Front. Physiol. *9*, 49.

20. van den Pol, A.N. (2012). Neuropeptide transmission in brain circuits. Neuron *76*, 98–115.
21. Taghert, P.H., and Nitabach, M.N. (2012). Peptide neuromodulation in invertebrate model systems. Neuron *76*, 82–97.
22. Bargmann, C.I., and Marder, E. (2013). From the connectome to brain function. Nat. Methods *10*, 483–490.
23. Jékely, G., Melzer, S., Beets, I., Kadow, I.C.G., Koene, J., Haddad, S., and Holden-Dye, L. (2018). The long and the short of it - a perspective on peptidergic regulation of circuits and behaviour. J. Exp. Biol. *221*, jeb166710.
24. Schlegel, P., Texada, M.J., Miroschnikow, A., Schoofs, A., Hückesfeld, S., Peters, M., Schneider-Mizell, C.M., Lacin, H., Li, F., Fetter, R.D., et al. (2016). Synaptic transmission parallels neuromodulation in a central food-intake circuit. eLife *5*, 462–465.
25. Shakiryanova, D., Tully, A., Hewes, R.S., Deitcher, D.L., and Levitan, E.S. (2005). Activity-dependent liberation of synaptic neuropeptide vesicles. Nat. Neurosci. *8*, 173–178.
26. Nässel, D.R. (2009). Neuropeptide signaling near and far: how localized and timed is the action of neuropeptides in brain circuits? Invert. Neurosci. *9*, 57–75.
27. Nusbaum, M.P., Blitz, D.M., and Marder, E. (2017). Functional consequences of neuropeptide and small-molecule co-transmission. Nat. Rev. Neurosci. *18*, 389–403.
28. Gerhard, S., Andrade, I., Fetter, R.D., Cardona, A., and Schneider-Mizell, C.M. (2017). Conserved neural circuit structure across *Drosophila* larval development revealed by comparative connectomics. eLife *6*, 1–17.
29. Schneider-Mizell, C.M., Gerhard, S., Longair, M., Kazimiers, T., Li, F., Zwart, M.F., Champion, A., Midgley, F.M., Fetter, R.D., Saalfeld, S., and Cardona, A. (2016). Quantitative neuroanatomy for connectomics in Drosophila. eLife *5*, 1133–1145.
30. Hu, C., Petersen, M., Hoyer, N., Spitzweck, B., Tenedini, F., Wang, D., Gruschka, A., Burchardt, L.S., Szpotowicz, E., Schweizer, M., et al. (2017). Sensory integration and neuromodulatory feedback facilitate Drosophila mechanonociceptive behavior. Nat. Neurosci. *20*, 1085–1095.
31. Burgos, A., Honjo, K., Ohyama, T., Qian, C.S., Shin, G.J., Gohl, D.M., Silies, M., Tracey, W.D., Zlatic, M., Cardona, A., and Grueber, W.B. (2018). Nociceptive interneurons control modular motor pathways to promote escape behavior in *Drosophila*. eLife *7*, e26016.
32. Takagi, S., Cocanougher, B.T., Niki, S., Miyamoto, D., Kohsaka, H., Kazama, H., Fetter, R.D., Truman, J.W., Zlatic, M., Cardona, A., and Nose, A. (2017). Divergent connectivity of homologous command-like neurons mediates segment-specific touch responses in Drosophila. Neuron *96*, 1373–1387.e6.
33. Niu, J., Ding, L., Li, J.J., Kim, H., Liu, J., Li, H., Moberly, A., Badea, T.C., Duncan, I.D., Son, Y.-J., et al. (2013). Modality-based organization of ascending somatosensory axons in the direct dorsal column pathway. J. Neurosci. *33*, 17691–17709.
34. Osseward, P.J., 2nd, and Pfaff, S.L. (2019). Cell type and circuit modules in the spinal cord. Curr. Opin. Neurobiol. *56*, 175–184.
35. Dubin, A.E., and Patapoutian, A. (2010). Nociceptors: the sensors of the pain pathway. J. Clin. Invest. *120*, 3760–3772.
36. Yamanaka, N., Romero, N.M., Martin, F.A., Rewitz, K.F., Sun, M.M., O'Connor, M.B., Léopold, P., Connor, M.B.O., Léopold, P., O'Connor, M.B., et al. (2013). Neuroendocrine control of Drosophila larval light preference. Science *341*, 1113–1116.
37. Xiang, Y., Yuan, Q., Vogt, N., Looger, L.L., Jan, L.Y., and Jan, Y.N. (2010). Light-avoidance-mediating photoreceptors tile the Drosophila larval body wall. Nature *468*, 921–926.
38. Sprecher, S.G., Cardona, A., and Hartenstein, V. (2011). The Drosophila larval visual system: high-resolution analysis of a simple visual neuropil. Dev. Biol. *358*, 33–43.
39. Miguel-Aliaga, I., Thor, S., and Gould, A.P. (2008). Postmitotic specification of Drosophila insulinergic neurons from pioneer neurons. PLoS Biol. *6*, e58.
40. Mazzoni, E.O., Desplan, C., and Blau, J. (2005). Circadian pacemaker neurons transmit and modulate visual information to control a rapid behavioral response. Neuron *45*, 293–300.
41. Dana, H., Sun, Y., Mohar, B., Hulse, B.K., Kerlin, A.M., Hasseman, J.P., Tsegaye, G., Tsang, A., Wong, A., Patel, R., et al. (2019). High-performance calcium sensors for imaging activity in neuronal populations and microcompartments. Nat. Methods *16*, 649–657.
42. Linneweber, G.A., Jacobson, J., Busch, K.E., Hudry, B., Christov, C.P., Dormann, D., Yuan, M., Otani, T., Knust, E., de Bono, M., and Miguel-Aliaga, I. (2014). Neuronal control of metabolism through nutrient-dependent modulation of tracheal branching. Cell *156*, 69–83.
43. Nicolaï, L.J., Ramaekers, A., Raemaekers, T., Drozdzecki, A., Mauss, A.S., Yan, J., Landgraf, M., Annaert, W., and Hassan, B.A. (2010). Genetically encoded dendritic marker sheds light on neuronal connectivity in Drosophila. Proc. Natl. Acad. Sci. USA *107*, 20553–20558.
44. Qian, C.S., Kaplow, M., Lee, J.K., and Grueber, W.B. (2018). Diversity of internal sensory neuron axon projection patterns is controlled by the POU-domain protein Pdm3 in Drosophila larvae. J. Neurosci. *38*, 2081–2093.
45. Kaneko, T., Macara, A.M., Li, R., Hu, Y., Iwasaki, K., Dunnings, Z., Firestone, E., Horvatic, S., Guntur, A., Shafer, O.T., et al. (2017). Serotonergic modulation enables pathway-specific plasticity in a developing sensory circuit in Drosophila. Neuron *95*, 623–638.e4.
46. Macpherson, L.J., Zaharieva, E.E., Kearney, P.J., Alpert, M.H., Lin, T.-Y., Turan, Z., Lee, C.-H., and Gallio, M. (2015). Dynamic labelling of neural connections in multiple colours by trans-synaptic fluorescence complementation. Nat. Commun. *6*, 10024.
47. de Haro, M., Al-Ramahi, I., Benito-Sipos, J., López-Arias, B., Dorado, B., Veenstra, J.A., and Herrero, P. (2010). Detailed analysis of leucokinin-expressing neurons and their candidate functions in the Drosophila nervous system. Cell Tissue Res. *339*, 321–336.
48. Schoofs, A., Hückesfeld, S., Schlegel, P., Miroschnikow, A., Peters, M., Zeymer, M., Spieß, R., Chiang, A.-S., and Pankratz, M.J. (2014). Selection of motor programs for suppressing food intake and inducing locomotion in the Drosophila brain. PLoS Biol. *12*, e1001893.
49. Dana, H., Mohar, B., Sun, Y., Narayan, S., Gordus, A., Jeremy, P., Tsegaye, G., Holt, G.T., Hu, A., Walpita, D., et al. (2016). Sensitive red protein calcium indicators for imaging neural activity. eLife *5*, e12727.
50. Ding, K., Han, Y., Seid, T.W., Buser, C., Karigo, T., Zhang, S., Dickman, D.K., and Anderson, D.J. (2019). Imaging neuropeptide release at synapses with a genetically engineered reporter. eLife *8*, e46421.
51. Park, D., Li, P., Dani, A., and Taghert, P.H. (2014). Peptidergic cell-specific synaptotagmins in Drosophila: localization to dense-core granules and regulation by the bHLH protein DIMMED. J. Neurosci. *34*, 13195–13207.
52. Wong, M.Y., Cavolo, S.L., and Levitan, E.S. (2015). Synaptic neuropeptide release by dynamin-dependent partial release from circulating vesicles. Mol. Biol. Cell *26*, 2466–2474.
53. Farina, M., van de Bospoort, R., He, E., Persoon, C.M., van Weering, J.R.T., Broeke, J.H., Verhage, M., and Toonen, R.F. (2015). CAPS-1 promotes fusion competence of stationary dense-core vesicles in presynaptic terminals of mammalian neurons. eLife *4*, e05438.
54. Renden, R., Berwin, B., Davis, W., Ann, K., Chin, C.-T., Kreber, R., Ganetzky, B., Martin, T.F.J., and Broadie, K. (2001). Drosophila CAPS is an essential gene that regulates dense-core vesicle release and synaptic vesicle fusion. Neuron *31*, 421–437.
55. Gontijo, A.M., and Garelli, A. (2018). The biology and evolution of the Dilp8-Lgr3 pathway: a relaxin-like pathway coupling tissue growth and developmental timing control. Mech. Dev. *154*, 44–50.
56. Veenstra, J.A., Rombauts, S., and Grbić, M. (2012). In silico cloning of genes encoding neuropeptides, neurohormones and their putative

G-protein coupled receptors in a spider mite. Insect Biochem. Mol. Biol. *42*, 277–295.

57. Deng, B., Li, Q., Liu, X., Cao, Y., Li, B., Qian, Y., Xu, R., Mao, R., Zhou, E., Zhang, W., et al. (2019). Chemoconnectomics: mapping chemical transmission in Drosophila. Neuron *101*, 876–893.e4.
58. Hori, M., Shibuya, K., Sato, M., and Saito, Y. (2014). Lethal effects of short-wavelength visible light on insects. Sci. Rep. *4*, 7383.
59. Shibuya, K., Onodera, S., and Hori, M. (2018). Toxic wavelength of blue light changes as insects grow. PLoS ONE *13*, e0199266.
60. Gong, J., Yuan, Y., Ward, A., Kang, L., Zhang, B., Wu, Z., Peng, J., Feng, Z., Liu, J., and Xu, X.Z.S. (2016). The C. elegans taste receptor homolog LITE-1 is a photoreceptor. Cell *167*, 1252–1263.e10.
61. Guntur, A.R., Gu, P., Takle, K., Chen, J., Xiang, Y., and Yang, C.-H. (2015). *Drosophila* TRPA1 isoforms detect UV light via photochemical production of H_2O_2. Proc. Natl. Acad. Sci. USA *112*, E5753–E5761.
62. Lazopulo, S., Lazopulo, A., Baker, J.D., and Syed, S. (2019). Daytime colour preference in Drosophila depends on the circadian clock and TRP channels. Nature *574*, 108–111.
63. Omamiuda-Ishikawa, N., Sakai, M., and Emoto, K. (2020). A pair of ascending neurons in the subesophageal zone mediates aversive sensory inputs-evoked backward locomotion in Drosophila larvae. PLoS Genet. *16*, e1009120.
64. Keene, A.C., Mazzoni, E.O., Zhen, J., Younger, M.A., Yamaguchi, S., Blau, J., Desplan, C., and Sprecher, S.G. (2011). Distinct visual pathways mediate Drosophila larval light avoidance and circadian clock entrainment. J. Neurosci. *31*, 6527–6534.
65. Hu, Y., Wang, C., Yang, L., Pan, G., Liu, H., Yu, G., and Ye, B. (2020). A neural basis for categorizing sensory stimuli to enhance decision accuracy. Curr. Biol. *30*, 4896–4909.e6.
66. Zandawala, M., Marley, R., Davies, S.A., and Nässel, D.R. (2018). Characterization of a set of abdominal neuroendocrine cells that regulate stress physiology using colocalized diuretic peptides in Drosophila. Cell. Mol. Life Sci. *75*, 1099–1115.
67. Zandawala, M., Yurgel, M.E., Texada, M.J., Liao, S., Rewitz, K.F., Keene, A.C., and Nässel, D.R. (2018). Modulation of Drosophila post-feeding physiology and behavior by the neuropeptide leucokinin. PLoS Genet. *14*, e1007767.
68. Okusawa, S., Kohsaka, H., and Nose, A. (2014). Serotonin and downstream leucokinin neurons modulate larval turning behavior in Drosophila. J. Neurosci. *34*, 2544–2558.
69. Grueber, W.B., Jan, L.Y., and Jan, Y.N. (2002). Tiling of the Drosophila epidermis by multidendritic sensory neurons. Development *129*, 2867–2878.
70. Miroschnikow, A., Schlegel, P., Schoofs, A., Hueckesfeld, S., Li, F., Schneider-Mizell, C.M., Fetter, R.D., Truman, J.W., Cardona, A., and Pankratz, M.J. (2018). Convergence of monosynaptic and polysynaptic sensory paths onto common motor outputs in a *Drosophila* feeding connectome. eLife *7*, 1–23.
71. Swanson, L.W., and Lichtman, J.W. (2016). From Cajal to connectome and beyond. Annu. Rev. Neurosci. *39*, 197–216.
72. Chen, C., Itakura, E., Nelson, G.M., Sheng, M., Laurent, P., Fenk, L.A., Butcher, R.A., Hegde, R.S., and de Bono, M. (2017). IL-17 is a neuromodulator of Caenorhabditis elegans sensory responses. Nature *542*, 43–48.
73. Macosko, E.Z., Pokala, N., Feinberg, E.H., Chalasani, S.H., Butcher, R.A., Clardy, J., and Bargmann, C.I. (2009). A hub-and-spoke circuit drives pheromone attraction and social behaviour in C. elegans. Nature *458*, 1171–1175.
74. Duan, B., Cheng, L., Bourane, S., Britz, O., Padilla, C., Garcia-Campmany, L., Krashes, M., Knowlton, W., Velasquez, T., Ren, X., et al. (2014). Identification of spinal circuits transmitting and gating mechanical pain. Cell *159*, 1417–1432.
75. Bentley, B., Branicky, R., Barnes, C.L., Chew, Y.L., Yemini, E., Bullmore, E.T., Vértes, P.E., and Schafer, W.R. (2016). The multilayer connectome of Caenorhabditis elegans. PLoS Comput. Biol. *12*, e1005283.
76. Knobloch, H.S., Charlet, A., Hoffmann, L.C., Eliava, M., Khrulev, S., Cetin, A.H., Osten, P., Schwarz, M.K., Seeburg, P.H., Stoop, R., and Grinevich, V. (2012). Evoked axonal oxytocin release in the central amygdala attenuates fear response. Neuron *73*, 553–566.
77. Viviani, D., Charlet, A., Van Den Burg, E., Robinet, C., Hurni, N., Abatis, M., Magara, F., and Stoop, R. (2011). Oxytocin selectively gates fear responses through distinct outputs from the central amygdala. Science *333*, 104–107.
78. Hwang, R.Y., Zhong, L., Xu, Y., Johnson, T., Zhang, F., Deisseroth, K., and Tracey, W.D. (2007). Nociceptive neurons protect Drosophila larvae from parasitoid wasps. Curr. Biol. *17*, 2105–2116.
79. Wietek, J., Rodriguez-Rozada, S., Tutas, J., Tenedini, F., Grimm, C., Oertner, T.G., Soba, P., Hegemann, P., and Wiegert, J.S. (2017). Anion-conducting channelrhodopsins with tuned spectra and modified kinetics engineered for optogenetic manipulation of behavior. Sci. Rep. *7*, 14957.
80. Tao, L., Porto, D., Li, Z., Fechner, S., Lee, S.A., Goodman, M.B., Xu, X.Z.S., Lu, H., and Shen, K. (2019). Parallel processing of two mechanosensory modalities by a single neuron in C. elegans. Dev. Cell *51*, 617–631.e3.
81. Cohn, R., Morantte, I., and Ruta, V. (2015). Coordinated and compartmentalized neuromodulation shapes sensory processing in Drosophila. Cell *163*, 1742–1755.
82. Boto, T., Louis, T., Jindachomthong, K., Jalink, K., and Tomchik, S.M. (2014). Dopaminergic modulation of cAMP drives nonlinear plasticity across the Drosophila mushroom body lobes. Curr. Biol. *24*, 822–831.
83. Bilz, F., Geurten, B.R.H., Hancock, C.E., Widmann, A., and Fiala, A. (2020). Visualization of a distributed synaptic memory code in the Drosophila brain. Neuron *106*, 963–976.e4.
84. Tsubouchi, A., Yano, T., Yokoyama, T.K., Murtin, C., Otsuna, H., and Ito, K. (2017). Topological and modality-specific representation of somatosensory information in the fly brain. Science *358*, 615–623.
85. Choi, S., Hachisuka, J., Brett, M.A., Magee, A.R., Omori, Y., Iqbal, N.U., Zhang, D., DeLisle, M.M., Wolfson, R.L., Bai, L., et al. (2020). Parallel ascending spinal pathways for affective touch and pain. Nature *587*, 258–263.
86. Branco, T., and Häusser, M. (2010). The single dendritic branch as a fundamental functional unit in the nervous system. Curr. Opin. Neurobiol. *20*, 494–502.
87. Euler, T., Detwiler, P.B., and Denk, W. (2002). Directionally selective calcium signals in dendrites of starburst amacrine cells. Nature *418*, 845–852.
88. Woods, I.G., Schoppik, D., Shi, V.J., Zimmerman, S., Coleman, H.A., Greenwood, J., Soucy, E.R., and Schier, A.F. (2014). Neuropeptidergic signaling partitions arousal behaviors in zebrafish. J. Neurosci. *34*, 3142–3160.
89. Hökfelt, T., Barde, S., Xu, Z.D., Kuteeva, E., Rüegg, J., Le Maitre, E., Risling, M., Kehr, J., Ihnatko, R., Theodorsson, E., et al. (2018). Neuropeptide and small transmitter coexistence: fundamental studies and relevance to mental illness. Front. Neural Circuits *12*, 106.
90. Persoon, C.M., Hoogstraaten, R.I., Nassal, J.P., van Weering, J.R.T., Kaeser, P.S., Toonen, R.F., and Verhage, M. (2019). The RAB3-RIM pathway is essential for the release of neuromodulators. Neuron *104*, 1065–1080.e12.
91. Duggan, A.W., Morton, C.R., Zhao, Z.Q., and Hendry, I.A. (1987). Noxious heating of the skin releases immunoreactive substance P in the substantia gelatinosa of the cat: a study with antibody microprobes. Brain Res. *403*, 345–349.
92. Jan, L.Y., and Jan, Y.N. (1982). Peptidergic transmission in sympathetic ganglia of the frog. J. Physiol. *327*, 219–246.

93. Fields, H. (2004). State-dependent opioid control of pain. Nat. Rev. Neurosci. *5*, 565–575.
94. Nichols, A.L.A., Eichler, T., Latham, R., and Zimmer, M. (2017). A global brain state underlies C. elegans sleep behavior. Science *356*, eaam6851.
95. Flavell, S.W., Pokala, N., Macosko, E.Z., Albrecht, D.R., Larsch, J., and Bargmann, C.I. (2013). Serotonin and the neuropeptide PDF initiate and extend opposing behavioral states in C. elegans. Cell *154*, 1023–1035.
96. Garelli, A., Heredia, F., Casimiro, A.P., Macedo, A., Nunes, C., Garcez, M., Dias, A.R.M., Volonte, Y.A., Uhlmann, T., Caparros, E., et al. (2015). Dilp8 requires the neuronal relaxin receptor Lgr3 to couple growth to developmental timing. Nat. Commun. *6*, 8732.
97. Vallejo, D.M., Juarez-Carreño, S., Bolivar, J., Morante, J., and Dominguez, M. (2015). A brain circuit that synchronizes growth and maturation revealed through Dilp8 binding to Lgr3. Science *350*, aac6767.
98. Bathgate, R.A.D., Halls, M.L., van der Westhuizen, E.T., Callander, G.E., Kocan, M., and Summers, R.J. (2013). Relaxin family peptides and their receptors. Physiol. Rev. *93*, 405–480.
99. Jaszczak, J.S., Wolpe, J.B., Bhandari, R., Jaszczak, R.G., and Halme, A. (2016). Growth coordination during Drosophila melanogaster imaginal disc regeneration is mediated by signaling through the relaxin receptor Lgr3 in the prothoracic gland. Genetics *204*, 703–709.
100. Colombani, J., Andersen, D.S., Boulan, L., Boone, E., Romero, N., Virolle, V., Texada, M., and Léopold, P. (2015). Drosophila Lgr3 couples organ growth with maturation and ensures developmental stability. Curr. Biol. *25*, 2723–2729.
101. Kania, A., Gugula, A., Grabowiecka, A., de Ávila, C., Blasiak, T., Rajfur, Z., Lewandowski, M.H., Hess, G., Timofeeva, E., Gundlach, A.L., and Blasiak, A. (2017). Inhibition of oxytocin and vasopressin neuron activity in rat hypothalamic paraventricular nucleus by relaxin-3-RXFP3 signalling. J. Physiol. *595*, 3425–3447.
102. Smith, S.J., Sümbül, U., Graybuck, L.T., Collman, F., Seshamani, S., Gala, R., Gliko, O., Elabbady, L., Miller, J.A., Bakken, T.E., et al. (2019). Single-cell transcriptomic evidence for dense intracortical neuropeptide networks. eLife *8*, 1–35.
103. Yang, C.-H., Belawat, P., Hafen, E., Jan, L.Y., and Jan, Y.-N. (2008). Drosophila egg-laying site selection as a system to study simple decision-making processes. Science *319*, 1679–1683.
104. Grönke, S., Clarke, D.-F., Broughton, S., Andrews, T.D., and Partridge, L. (2010). Molecular evolution and functional characterization of Drosophila insulin-like peptides. PLoS Genet. *6*, e1000857.
105. Karuppudurai, T., Lin, T.-Y., Ting, C.-Y., Pursley, R., Melnattur, K.V., Diao, F., White, B.H., Macpherson, L.J., Gallio, M., Pohida, T., and Lee, C.H. (2014). A hard-wired glutamatergic circuit pools and relays UV signals to mediate spectral preference in Drosophila. Neuron *81*, 603–615.
106. Baines, R.A., Uhler, J.P., Thompson, A., Sweeney, S.T., and Bate, M. (2001). Altered electrical properties in Drosophila neurons developing without synaptic transmission. J. Neurosci. *21*, 1523–1531.
107. Watanabe, K., Chiu, H., Pfeiffer, B.D., Wong, A.M., Hoopfer, E.D., Rubin, G.M., and Anderson, D.J. (2017). A circuit node that integrates convergent input from neuromodulatory and social behavior-promoting neurons to control aggression in Drosophila. Neuron *95*, 1112–1128.e7.
108. Sancer, G., Kind, E., Plazaola-Sasieta, H., Balke, J., Pham, T., Hasan, A., Münch, L.O., Courgeon, M., Mathejczyk, T.F., and Wernet, M.F. (2019). Modality-specific circuits for skylight orientation in the fly visual system. Curr. Biol. *29*, 2812–2825.e4.
109. Saalfeld, S., Cardona, A., Hartenstein, V., and Tomancak, P. (2009). CATMAID: collaborative annotation toolkit for massive amounts of image data. Bioinformatics *25*, 1984–1986.
110. Thévenaz, P., Ruttimann, U.E., and Unser, M. (1998). A pyramid approach to subpixel registration based on intensity. IEEE Trans. Image Process. *7*, 27–41.
111. Risse, B., Thomas, S., Otto, N., Löpmeier, T., Valkov, D., Jiang, X., and Klämbt, C. (2013). FIM, a novel FTIR-based imaging method for high throughput locomotion analysis. PLoS ONE *8*, e53963.
112. Groth, A.C., Fish, M., Nusse, R., and Calos, M.P. (2004). Construction of transgenic Drosophila by using the site-specific integrase from phage phiC31. Genetics *166*, 1775–1782.
113. Tenedini, F.M., Sáez González, M., Hu, C., Pedersen, L.H., Petruzzi, M.M., Spitzweck, B., Wang, D., Richter, M., Petersen, M., Szpotowicz, E., et al. (2019). Maintenance of cell type-specific connectivity and circuit function requires Tao kinase. Nat. Commun. *10*, 3506.
114. Ingles-Prieto, A., Furthmann, N., Crossman, S.H., Tichy, A.-M., Hoyer, N., Petersen, M., Zheden, V., Biebl, J., Reichhart, E., Gyoergy, A., et al. (2021). Optogenetic delivery of trophic signals in a genetic model of Parkinson's disease. PLoS Genet. *17*, e1009479.
115. Hoyer, N., Petersen, M., Tenedini, F., and Soba, P. (2018). Assaying mechanonociceptive behavior in *Drosophila* larvae. Bio Protoc. *8*, e2736.
116. Soba, P., Han, C., Zheng, Y., Perea, D., Miguel-Aliaga, I., Jan, L.Y., and Jan, Y.N. (2015). The Ret receptor regulates sensory neuron dendrite growth and integrin mediated adhesion. eLife *4*, e05491.

STAR★METHODS

KEY RESOURCES TABLE

REAGENT or RESOURCE	SOURCE	IDENTIFIER
Antibodies		
Rabbit polyclonal anti-Ilp7	[39]	N/A
Rabbit polyclonal anti-Leucokinin	Dr. Dick Nässel, Stockholm University, Sweden	N/A
Chicken polyclonal anti-GFP	Abcam	Cat# ab13970; RRID: AB_300798
Rat monoclonal anti-HA	Roche	Cat# ROAHAHA; RRID: AB_2687407
Mouse monoclonal anti-Fas2 (1D4)	DSHB	RRID: AB_528235
Mouse monoclonal anti-myc (9E10)	Sigma-Aldrich	Cat# M4439; RRID: AB_439694
Mouse monoclonal anti-Flag M2	Sigma-Aldrich	Cat# P2983; RRID: AB_439685
Alexa Fluor 488 Donkey anti-mouse	Jackson Immunoresearch	Cat# 715-545-150; RRID: AB_2340846
Cy3 polyclonal Goat anti-Rabbit	Jackson Immunoresearch	Cat# 111-165-003; RRID: AB_2338000
Cy5 polyclonal Donkey anti-Chicken	Jackson Immunoresearch	Cat# 703-175-155; RRID: AB_2340365
Dylight 649 monoclonal mouse anti-Rabbit	Jackson immunoresearch	Cat# 211-492-171; RRID: AB_2339164
Chemicals, peptides, and recombinant proteins		
All-trans Retinal	Sigma-Aldrich	Cat# R2500
Schneider's Drosophila medium	Thermo-Fisher	Cat# 21720024
Ethyl butyrate	Sigma-Aldrich	Cat# E15701
Critical commercial assays		
High Pure RNA Tissue Kit	Roche	Cat# 12033674001
Maxima First Strand cDNA Synthesis Kit for RT–quantitative PCR	Thermo Scientific	Cat# K1641
High Pure PCR template preparation kit	Roche	Cat# 11796828001
Deposited data		
Catmaid neuronal reconstructions	This paper	https://l1em.catmaid.virtualflybrain.org/?pid=1
Experimental models: Cell lines		
D. melanogaster: Cell line S2: S2-DRSC	DGRC	RRID: CVCL_Z992
Experimental models: Organisms/strains		
D. melanogaster: w^{1118}	Bloomington Drosophila Stock Center	BDSC:3605
D. melanogaster: w[1118]; P{y[+t7.7] w[+mC] = GMR35B01-GAL4}attP2	Bloomington Drosophila Stock Center	BDSC: 49898
D. melanogaster: w[1118]; P{y[+t7.7] w[+mC] = GMR73B01-GAL4}attP2	Bloomington Drosophila Stock Center	BDSC: 39809
D. melanogaster: w[*]; wg[Sp-1]/CyO; P{w[+mC] = Gr28b.c-GAL4.6.5}3	Bloomington Drosophila Stock Center	BDSC: 57619
D. melanogaster: w[*]; P{w[+mC] = Gr89a-GAL4.2}11/CyO	Bloomington Drosophila Stock Center	BDSC: 57676
D. melanogaster: w[1118]; P{y[+t7.7] w[+mC] = GMR22C07-GAL4}attP2	Bloomington Drosophila Stock Center	BDSC: 48975
D. melanogaster: w[1118]; P{y[+t7.7] w[+mC] = GMR27H06-lexA}attP40	Bloomington Drosophila Stock Center	BDSC: 54751
D. melanogaster: w[1118]; P{y[+t7.7] w[+mC] = 20XUAS-IVS-GCaMP6s}attP40	Bloomington Drosophila Stock Center	BDSC: 42746
D. melanogaster: w1118; P{20XUAS-IVS-GCaMP6m}attP40	Bloomington Drosophila Stock Center	BDSC: 42748

(*Continued on next page*)

Continued

REAGENT or RESOURCE	SOURCE	IDENTIFIER
D. melanogaster: w[1118]; P{y[+t7.7] w[+mC] = 20XUAS-IVS-jGCaMP7s}VK00005	Bloomington Drosophila Stock Center	BDSC: 79032
D. melanogaster: w[1118]; P{y[+t7.7] w[+mC] = 20XUAS-IVS-CsChrimson. mVenus}attP2	Bloomington Drosophila Stock Center	BDSC: 55136
D. melanogaster: w[1118]; P{y[+t7.7] w[+mC] = 13XLexAop2-IVS-CsChrimson.mVenus}attP2	Bloomington Drosophila Stock Center	BDSC: 55139
D. melanogaster: w[*]; PBac{y[+mDint2] w[+mC] = 20XUAS-IVS-NES-jRCaMP1b-p10}VK00005	Bloomington Drosophila Stock Center	BDSC: 63793
D. melanogaster: P{w[+mC] = GMR-hid}G1/CyO, P{ry[+t7.2] = sevRas1.V12}FK1	Bloomington Drosophila Stock Center	BDSC: 5771
D. melanogaster: w[1118]; PBac{y[+mDint2] w[+mC] = UAS-CD4-tdGFP}VK00033	Bloomington Drosophila Stock Center	BDSC: 35836
D. melanogaster: y[1] w[*] Mi{Trojan-GAL4.1}Lgr4[MI06794-TG4.1]	Bloomington Drosophila Stock Center	BDSC: 77775
D. melanogaster: w Tl{Tl}Lgr4attP (Lgr4^{ko})*	Bloomington Drosophila Stock Center	BDSC: 84478
D. melanogaster: w[1118]; PBac{y[+mDint2] w[+mC] = UAS-CD4-tdTom}VK00033	Bloomington Drosophila Stock Center	BDSC: 35837
D. melanogaster: w[1118]; PBac{y[+mDint2] w[+mC] = UAS-CD4-tdGFP}VK00033	Bloomington Drosophila Stock Center	BDSC: 35836
D. melanogaster: w[1118]; P{w[+mC] = UAS-DenMark}3	Bloomington Drosophila Stock Center	BDSC: 33061
D. melanogaster: w[*]; P{w[+mC] = lexAop-nSyb-spGFP1-10}2, P{w[+mC] = UAS-CD4-spGFP11}2; MKRS/TM6B (Syb-GRASP)	Bloomington Drosophila Stock Center	BDSC: 64315
D. melanogaster: w[*]; wg[Sp-1]/CyO; P{w[+mC] = tubP(FRT.stop)GAL80}3	Bloomington Drosophila Stock Center	BDSC: 39213
D. melanogaster: UAS-spGFP1-10-Syb	M. Gallio, Northwestern University, Evanston, USA	N/A
D. melanogaster: UAS-Sytα-myc	[51]	N/A
D. melanogaster: w*;*tsh-Gal80/CyO*	J. Simpson, UCSB, Santa Barbara, USA	N/A
D. melanogaster: LexAop-CD4-sp11-CD4-tdTomato	[30]	N/A
D. melanogaster: A08n-Gal4 (82E12-Gal4AD, 6.14.3-Gal4DBD)	[30]	N/A
D. melanogaster: Dp7(4-3)-LexA	[30]	N/A
D. melanogaster: sNPF^{c00448}	[30]	N/A
D. melanogaster: sNPF^{MI01807}	[30]	N/A
D. melanogaster: Ilp7-LexA	[103]	N/A
D. melanogaster: Ilp7^{ko}	[104]	N/A
D. melanogaster: w[1118]; LexAop-Kir2.1	[30]	N/A
D. melanogaster: w[1118]; LexAop-TnT-HA	[105]	N/A
D. melanogaster: Hugin^{VNC} -Gal4	[48]	N/A
D. melanogaster: UAS-Kir2.1	[106]	N/A
D. melanogaster: Otd-Flp	[107]	N/A
D. melanogaster: Dp7(4-3)-Gal4	This paper	N/A
D. melanogaster: UAS-NPRR^{ilp7}	This paper	N/A
D. melanogaster: UAS-Ilp7	This paper	N/A
D. melanogaster: UAS-Lgr4-HA-flag	This paper	N/A

(*Continued on next page*)

Continued		
REAGENT or RESOURCE	SOURCE	IDENTIFIER
D. melanogaster: Lk-Gal4	[47]	N/A
D. melanogaster: GMR-LexA	[108]	N/A
D. melanogaster: UAS-Cadps-RNAi	Vienna Drosophila Stock Center	VDRC: KK110055
Oligonucleotides		
Primers for HA-tagged Ilp7 and Lgr4 cloning, see Table S2	This paper	N/A
Primers for Lgr4 qRT-PCR, see Table S2	This paper	N/A
Software and algorithms		
Collaborative annotation toolkit for massive amount of image data (CATMAID)	Janelia research campus, USA,[109]	RRID: SCR_006278
Ethovision XT-X2	Noldus Information Technology, Wageningen, Netherlands	RRID: SCR_000441
Pylon Camera Software Suite	Basler, Switzerland	N/A
StreamPix 6	Norpix, Montreal, Quebec, Canada	RRID: SCR_015773
Fiji/ImageJ	NIH, Bethesda	RRID: SCR_002285
Prism	Graphpad, San Diego, CA, USA	RRID: SCR_00279
StackReg, ImageJ plugin	EPFL, Lausanne, Switzerland[110]	N/A
Time Series analyzer V3, ImageJ plugin	UCLA, California, USA	RRID: SCR_014269
FimTrack	University of Münster, Germany[111]	https://github.com/kostasl/FIMTrack
Temporal larval distribution analysis scripts	This paper	https://github.com/formozov/larva_tracking_Imambocus_et_al
Other		
CoolLED pE-4000	CoolLED, Andover, UK	N/A
RGB-LED plate	Phlox, Provence, France	N/A
Custom incubator with RGB LEDs	[111]	N/A

RESOURCE AVAILABILITY

Lead contact

Further information and requests for resources and reagents should be directed to and will be fulfilled by the Lead Contact, Peter Soba (psoba@uni-bonn.de).

Materials availability

Lines generated and described in this study are available on request from the Lead Contact.

Data and code availability

- All data reported in this paper is available from the lead contact upon request.
- All neurons reconstructed from volume EM were archived in the Virtual Fly Brain server, and are accessible via CATMAID software at this address: https://l1em.catmaid.virtualflybrain.org/?pid=1
- Code and scripts used to analyze larval distribution in two choice assays are available at this address: https://github.com/formozov/larva_tracking_Imambocus_et_al
- Any additional information required to reanalyze the data reported in this paper is available from the lead contact upon request.

EXPERIMENTAL MODEL AND SUBJECT DETAILS

Fly stocks

Drosophila melanogaster were reared at 25°C and 70% humidity with a 12 light/dark cycle on standard fly food. Transgenic lines were maintained in either *white* mutant (w^-) or yellow-white (y^-, w^-) backgrounds. For analysis, 3rd instar foraging stage larvae of both sexes were used in this study (94h ± 2h AEL unless stated otherwise). No sex-specific effects were part of this study. For fly line details see Key resources table. Lines were obtained from the Bloomington *Drosophila* Stock Center or the Vienna *Drosophila* Stock Center

unless stated otherwise. *UAS-CsChrimson* was used as an optogenetic actuator to stimulate specific neurons. *UAS-Kir2.1* or *UAS-TNT* were used to block activity/function of specific neurons. Experimental genotypes for quantitative comparisons are listed in Table S1.

S2-DRSC cell line

Drosophila S2-DRSC cells (sex: male) were cultured in Schneider's *Drosophila* medium supplemented with 10% fetal calf serum, glutamine and Penicilin/Streptomycin (ThermoFisher, Carlsbad, CA,USA). Cells were passaged every 3-5 days and maintained in as semi-adherent cultures.

METHOD DETAILS

Generation of plasmids and transgenes

Dp7-Gal4 is a 2nd chromosome insertion and was generated analogously to *Dp7-LexA*[30] using a 1,099 bp fragment of the Ilp7 enhancer region at the 5′ end of the Ilp7 gene (starting from –1,131 to –33, where the ATG for Ilp7 starts at position 0). The genomic region was amplified by PCR and cloned into pCasper-AUG-GAL4. Transgenes were generated using P-element-mediated transformation. The UAS-Ilp7 transgene was generated by cloning Ilp7 cDNA via EcoRI into the pUAST vector and P-element mediated transformation. A UAS-Ilp7 insertion on the 3rd chromosome was used in this study. The Ilp7 neuropeptide release reporter (NPRR^{Ilp7}) was designed analogously to Ding et al.,[50] by fusing GCaMP6s to the C terminus of the Ilp7 neuropeptide. Ilp7 cDNA was obtained from the *Drosophila* Genetics Resource Center (DGRC) and amplified from clone FI18537 by PCR with specific primers carrying NotI and NdeI restriction sites, and fused in frame with GCaMP6s (Addgene) via NdeI/XbaI into the pUAST-AttB vector. Transgenes were made by phiC31-mediated genomic integration[112] into the AttP2 landing site (BestGene, Chino Hills, CA, USA). HA-tagged Ilp7 was generated by inserting the HA sequence after the signal peptide sequence at position 34 of the Ilp7 cDNA using overlap-PCR. Primers containing the HA-tag sequence were used for amplification and cloning into the pUAST-AttB vector via NotI/XhoI.

Lgr4 cDNA was amplified from DGRC clone UFO07708 (BDGP Tagged ORF collection) by PCR using specific primers and inserted into a pUAST-AttB vector containing a C-terminal 3xflag-6xHis-tag via NotI/XhoI. The Lgr4^{I263A} mutation was introduced using overlap-PCR with specific primers for the codon change and cloned via internal EcoRI/StuI sites into the original Lgr4 cDNA. To remove the Leucine-rich repeats (LRRs), Lgr4 cDNA was synthesized lacking amino acids 81-426 (Lgr4$^{\Delta 81\text{-}426}$, GeneArt, ThermoFisher) and subcloned into pUAST-AttB vector containing a C-terminal 3xflag-6xHis-tag via NotI/XhoI. All constructs were verified by sequencing. Primers used for cloning are listed in Table S2.

Transgenic flies carrying UAS-Lgr4-HA (pUAST-Lgr4-CFLAGHA-BD-PHI, consisting of full length Lgr4 cDNA dually-tagged with a Flag-HA C-terminal fusion (UFO07708, BDGP Tagged ORF collection)) where made using phiC31-mediated genomic integration by injection into *y^1 M{vas-int.Dm}ZH-2A w*; M{3xP3-RFP.attP'}ZH-51C* (BestGene, Chino Hills, CA, USA).

Neuronal reconstruction and circuit mapping

Neuronal reconstruction was performed on ssTEM images of the first instar larvae using the web-based software CATMAID.[109] Dp7 neurons and its partners were manually reconstructed similarly as described[14,29] and the location of pre- and post-synapses were identified. Synapses were annotated using the following 4 criteria: (1) the presence of a highly visible T-bar, (2) the presence of numerous synaptic vesicles close to the T-bars, (3) contact of pre- and post-synaptic membranes in at least 2 consecutive sections (4) the presence of a synaptic cleft. We then reconstructed the pre- and postsynaptic partners of Dp7 from the synaptic sites and identified the v'td2 sensory neurons. Neuronal reconstruction validation was done as previously described[14,29] by using the iterative method. Pre- and post-synaptic illustrations between 2 neurons were extracted using CATMAID's 3D-visualization tools. All reconstructed neurons from the EM volume are accessible via CATMAID software (https://l1em.catmaid.virtualflybrain.org/?pid=1).

Immunohistochemistry and confocal imaging

Larval brains from genotypes labeling Dp7 (*Dp7-Gal4, Ilp7-LexA, Ilp7-Gal4*) or ABLK (*Lk-Gal4*) neurons with a reporter (*LexAop-CD4-spGFP11-tdTomato*, *UAS-CD4-tdGFP,UAS-DenMARK, UAS-Lgr4-HA, UAS-Sytα-myc*) were dissected in PBS, fixed in 4% formaldehyde with PBS for 15 min at room temperature, washed in PBST (PBS with 0.3% Triton X-100 (Roth Karlsruhe, Germany), incubated with primary antibodies at room temperature overnight, washed in PBST and incubated with corresponding fluorescent dye-coupled secondary antibodies for 1 hour (Cy3, Cy5 or Dylight 649-coupled secondary antibodies, Jackson Immunoresearch, Ely, UK). Samples were mounted either on poly-L-lysine (Sigma) coated coverslips or on Superfrost slides in Slow Fade Gold (Thermo Fisher, Carlsbad, CA,USA). For anatomical inspection of Dp7 and ABLK neurons, native reporter fluorescence was sufficiently bright to be visualized together with antibody immunostaining by confocal microscopy (Zeiss LSM700 or LSM900). Primary antibodies used: rabbit anti-Ilp7 (1:5000), rabbit anti-Lk (1:1000), mouse anti-Fas2 (1:100, DSHB), rat anti-HA (1:100), mouse anti-myc: (1:100). Corresponding fluorescent dye-coupled secondary antibodies were used at 1:300. Confocal Z stacks were processed in Fiji (ImageJ, NIH, Bethesda).

Labeling of synapses between Dp7 and v'td2 neurons using Syb-GRASP[46] was performed as described.[113] Larval brains (*UAS-spGFP1-10-Syb, LexAop-spGFP11;73B01-Gal4/Ilp7-LexA*) were dissected in 5 mM dissection buffer (108 mM NaCl, 5 mM KCl, 4 mM NaHCO3, 1 mM NaH_2PO_4, 5 mM Trehalose, 10mM Sucrose, 5 mM HEPES, 8.2 mM MgCl2, 2 mM $CaCl_2$, pH 7.4), washed 3 times/5 s alternating between dissection buffer containing 5 mM KCl and 70 mM KCl, respectively, followed by 10 minutes

incubation in 5 mM dissection buffer. Brains were then fixed in 4% formaldehyde/PBS for 15 minutes, followed by immunohistochemistry (rabbit anti-Ilp7: 1:5000, chicken anti-GFP: 1:500, corresponding fluorescent dye-coupled secondary antibodies: 1:300) and mounting as described above. Z stacks were obtained using confocal microscopy and processed in Fiji (ImageJ, NIH, Bethesda).

Developmental toxicity assay

Wild-type flies (w^{1118}) were staged for 4 to 6 hours. After 1 day, 50 freshly hatched L1 larvae were transferred to a grape agar Petri dish supplemented with yeast paste. Yeast paste was replaced daily to prevent decay. The larvae were then incubated either under green light (2.5μW/mm^2) or blue light (2.5μW/mm^2) for at least 9 days at 25°C in a custom incubator (described in Ingles-Prieto et al.[114]). The temperature of the substrate or larvae was measured after 1h, 6h and 16h of blue or green light incubation and remained within the nominal temperature of the incubator (25.15 ± 1.75°C). After 9 days, the number of eclosed flies and the numbers of dead animals (pharate adults, white pupae, 2nd and 3rd instar larvae, 1st instar or lost upon transfer) were counted. The assay was repeated 5 times for each condition.

Light avoidance assays

After pre-staging, crosses of adult flies with the appropriate genotype were allowed to lay eggs on grape agar plates supplemented with fresh yeast paste within a fixed time frame (Zeitgeber (ZT) 4-6) for 1-3 h depending on the number of fertilized eggs to minimize overcrowding.

Third instar foraging larvae (94 h ± 1.5h AEL) were subjected to a 15 min light avoidance assay as described[36,40] with modifications. The experimental setup consisted of a dark chamber with a white light source (365-580 nm, intensity 6.9-3.3 μW/mm^2 on light side, respectively, < 0.01 μW/mm^2 on dark side) illuminating one half of a 10 cm agar plate (12 mL of 2% agar dissolved in ddH_2O (Roth, Karlsruhe, Germany)). An infrared LED source surrounding the plates allowed live recording of larval distribution in darkness with a digital camera (Basler ace-2040 gm, Basler, Switzerland).

For each trial, 20 larvae were preincubated in darkness for 15 min. The animals were placed in the middle of each Petri dish at the light /dark junction. Each trial was run for at least 15 min, recorded by a camera at the top of the chamber using Ethovision XT, Pylon (Basler) or StreamPix 6 (Norpix, Montreal, Canada). For each genotype, typically 10 trials consisting of 20 larvae each were performed. If more than 3 larvae were lost, the trial was excluded.

Mechanonociception assays

Mechanonociception experiments were performed on staged 96h old 3rd instar larvae as described[30,115] using a calibrated 50 mN *von Frey* filament. Larvae were stimulated on mid-abdominal segments (A3–A5) twice within 2 s and the behavioral response to the 2nd stimulus was scored (no response, stop, or stop and turn as non-nociceptive, bending and rolling as nociceptive). Each genotype was tested multiple times on different days in a blinded fashion.

Locomotion and chemotaxis assays

Larvae were staged on grape juice agar plates and fed with yeast paste. Third instar larvae (94 h ± 2 h after egg laying) were used for all experiments. For locomotion analysis under dark or blue light conditions, animals were carefully transferred to a 2% agar film on a FTIR (frustrated total internal reflection) based tracking system (FIM, University of Münster)[111] using a Basler ac2040-25 gm camera (Basler, Ahrensburg, Germany). Five freely moving larvae per trial were recorded for 1 min in the dark, or for 1 min with 4.5 μW/mm^2 470 nm light illumination from a LED light source (RGB-BL-S-Q-1R, Phlox, Aix-en-Provence, France). Locomotion was tracked with 10 frames per second.

For chemotaxis assays, 10 μl of 125mM Ethyl butyrate (Sigma-Aldrich) diluted in paraffin oil were placed in an odor container on one side of a 10 cm agar plate. Experiments were performed under minimum light conditions as for locomotion assays. Five freely moving larvae per trial were video-captured for 5min.

Optogenetic behavioral assays

Staged third instar larvae (96 h ± 3 h AEL) expressing CsChrimson in specific neuronal subsets (v'td2: *22C07-Gal4, 73B01-Gal4, Gr89a-Gal4*, Lk neuron subsets: *Lk-Gal4* without or with *tsh-Gal80* or *otd-Flp; tub-FRT-STOP-FRT-Gal80*) were grown in darkness on grape agar plates with yeast paste containing 5 mM all-*trans*-retinal. Larvae were carefully transferred under low red light conditions to 2% agar plates with a 1 ml water film. CsChrimson was activated with 625 nm light (high: 8.13 μW/mm^2 or low: 1.13 μW/mm^2) for 5 s. Videos were taken during the experiment and analyzed using the Fiji cell counter plugin (ImageJ, NIH, Bethesda). Rolling was defined as at least one complete 360° roll along the body axis. Bending was defined as a c-shape like twitching, typically seen before rolling behavior, and not to be confused with other described bending behavior.[15] Turning behavior describes head turning and thereby a direction changes of locomotion. Backward behavior describes at least one wave of backward crawling. Stop behavior describes a stop of locomotion. Hunch behavior describes a full body contraction. No behavior describes the absence of a change in larval behavior. Staging, behavioral assays and analyses were performed in a blinded and randomized fashion.

Calcium imaging in intact larvae

Calcium responses were recorded from the soma of specific neurons labeled with *UAS-GCaMP(6 s* or *7 s)* or *UAS-jRCaMP1b* under the control of specific neuronal Gal4-drivers (v'td2: *73B01-Gal4*; v'td1/2: 35B01-Gal4; v'td2/Ca4 da: *Gr28b.c-GAL4*; Dp7: *Ilp7-Gal4*;

ABLK: *Lk-Gal4*), . Live third instar larvae (94 ± 2 h) were mounted in 90% glycerol and immobilized with a coverslip. The neuronal somata were live imaged by confocal microscopy with a 40x/NA1.3 oil objective (Zeiss LSM700 or LSM900AS2). 400 frame times series were acquired at a frame rate of 0.24 s or 0.34 s (240 × 240 pixels) and the larva was subjected to UV light for 10 s (365-525 nm, 10-60 μW/mm^2 CoolLED). Each larva was subjected to at least 2 pulses of UV light during the 400 frame time series with an interval of at least 15 s between pulses. For each genotype, 5-10 larvae were assayed between ZT 3 to 6. Calcium imaging was performed with identical confocal microscope settings imaging a single plane (approx. 2 μm thickness). Only datasets without significant Z-drift (stable baseline, return to original baseline levels after stimulation) were retained for analysis.

Optogenetic activation of C4 da (*27H06-LexA*), BO (*GMR-LexA*) or Dp7 (*Ilp7-LexA*) neurons with CsChrimson (*LexAop-CsChrimson*), or inhibition/ablation (C4 da/Dp7: *LexAop-TnT*, BO: *GMR-hid*) and calcium imaging in ABLK neurons (*Lk-Gal4, UAS-GCaMP6s*), were also performed in intact 3rd instar larvae. For optogenetic activation experiments, animals were reared in grape agar plates supplemented with all-trans retinal in the dark. Imaging was performed under low light conditions. Larvae were mounted and imaged as described above. A red light pulse for CsChrimson activation (635nm, intensity: 700 μW/mm^2) or UV light pulse for native stimulation (365 nm, 60 μW/mm^2) was given using an optical fiber-coupled to CoolLED Pe4000 light source. For each genotype, 5 larvae were assayed with identical confocal settings.

To visualize NPPR^{Ilp7} release, we imaged either Dp7 soma or lateral dendrite (*Ilp7-Gal4, UAS-NPPR^{Ilp7}*) that features NPPR^{Ilp7} puncta as well as synaptic input and output of v'td2 and ABLK neurons, respectively. Time series with 500 frames were acquired at 0.24 s/frame (Zeiss LSM700).

Calcium imaging in semi-intact larvae

For comparison of noxious light versus mechanonociception, ABLK neuron calcium responses were assayed in semi-intact larval preparations essentially as described.[30] Staged 94 ± 2 h old larvae were partially dissected on a Sylgard (Dow Corning) plate in physiological saline[37] (120 mM NaCl, 3 mM KCl, 1.5 mM $CaCl_2$, 4 mM $MgCl_2$, 10 mM NaH_2CO_3, 10 mM Glucose, 10 mM Trehalose, 10 mM Sucrose, 5 mM TES, 10 mM HEPES). ABLK neuron somata expressing GCaMP6m were imaged by confocal microscopy with a 40×/NA 1.0 water objective (Olympus FV1000MP). A micromanipulator-mounted *von Frey* filament (45 mN) was used to provide a mechanonociceptive stimulus to midabdominal segments (A3–A5). For noxious light stimulation, the larval preparation was subjected to UV light for 10 s (365 nm, 60 μW/mm^2 CoolLED).

Cell culture and co-immunoprecipitation assay

Biochemical interaction of Lgr4 and Ilp7 in S2 cells was assayed by transient co-transfection using a previously established protocol.[116] For S2 cell expression the following constructs were used: pUAST-AttB-Lgr4-3xflag-6xHis (wildtpype, I264A and ΔLRR variants), pUAST-AttB-Ilp7-HA, pActin-Gal4. Cells were seeded in 6 well plates and transfected at 50% density in an adherent state using Effectene (QIAGEN, Venlo, Netherlands). Cells were harvested 48 h post-transfection and lysed in 500 μL lysis buffer (50 mM Tris pH7.4, 150 mM NaCl, 1% Triton X-100, protease inhibitor mix (Roche)) for 20 min on ice. After centrifugation (10 min/4°C/10.000 × g), the supernatant was incubated with mouse IgG-agarose (Sigma–Aldrich, St. Louis, MO) for 30 min at 4°C, and subsequently with anti-flag M2 agarose beads (Sigma–Aldrich, St. Louis, MO) or anti-HA Sepharose beads (Roche) for 4 h at 4°C. Samples were washed with lysis buffer three times, denatured and analyzed on Bis-Tris gels (ThermoFischer) and by western blotting against Ilp7-HA (rat anti-HA, 1:5000, Roche) and Lgr4-3xflag (anti-flag M2, 1:10.000, Sigma). Experiments were repeated three times.

qRT-PCR

The material used for each qRT–PCR sample (n = 3 per genotype) was obtained from 5 synchronized L3 males 94-96 h after egg-laying for 2 h in apple plates. 48 h after the egg laying, 30 larvae were transferred from the apple plates into a vial with fly food to avoid competition. The genotypes used were *y[1] w[*] Mi{Trojan-GAL4.1}Lgr4[MI06794-TG4.1]* or *P{w[+mW.hs] = GawB}109C1, y[1] w[*]*, which served as a *yw* background control for the *Lgr4* TROJAN insertion. Male larvae were selected under the stereoscope and immediately put into dry ice and either stored in −80°C or processed for RNA extraction immediately. Each sample was macerated using pellet pestles, homogenized in 800 μL TriPure Isolation Reagent (Roche), and centrifuged at 12000 g for 1 min, to remove tissue debris. We added 0.5 volume of absolute ethanol (400 μl) to the supernatant and then followed manufacturer's instructions from the kit High Pure RNA Tissue Kit (Roche). An extra DNase treatment (Turbo DNA-free kit, Ambion, Life Technologies) was performed to reduce gDNA contamination. 1 μg of RNA was used for the cDNA synthesis using the Maxima First Strand cDNA Synthesis Kit for RT–quantitative PCR (Thermo Scientific), following manufacturer's instructions but for a final volume of 10 μl.

qRT-PCR primers were designed and their specificity tested using Primer BLAST or Primer3. Primer efficiencies were determined to be between 90%–100% using qPCR standard curves using serial dilutions (1x, 0,1X, and 0.01x) of gDNA extracted from the genome reference stock #2057 (BDSC) extracted using the High Pure PCR template preparation kit (Roche). The resulting melting curves did not present primer dimers in any concentration or in water.

Briefly, the experiments were performed in a Lightcycler 96 (Roche) using the FastStart Essential DNA Green Master dye and polymerase (Roche). The final volume for each reaction was 10 μl, consisting of 5 μl of dye and polymerase (master mix), 2 μl of 10 × diluted cDNA sample and 3 μl of the specific primer pairs (1 μM each). qRT-PCR primers used are listed in Table S2.

Light avoidance pupariation assay

w^{1118} and $Ilp7^{ko}$ flies (3–6-days-old) were crossed and after 1–2 days transferred to laying pots with grape juice agar plates for 48 h. The next morning, the animals were allowed to lay eggs in fresh plates with yeast within a fixed time-frame (Zeitgeber (ZT) 4-6) for 1-2 h depending on the number of fertilized eggs to minimize the risk of overcrowding (the first plate was discarded). 3rd instar foraging larvae (94 h ± 1.5 h AEL) were then collected and placed in a tube containing standard medium. This tube was mounted in a T-shape glass device designed as described previously,[36] where half of the horizontal glass tube is covered by black electrical tape. This allows larvae to wander and pupariate either in the dark or in the light side. Larvae were kept for 3 days under constant white light (2.9-4.5 $\mu W/mm^2$) at 25°C. The numbers of pupae in both dark and light sides were then counted. The Preference Index (PI) was calculated as: (number of puparia in dark- number of puparia in light)/total number of puparia.

Developmental time assay

w^{1118} and $Ilp7^{ko}$ flies (2-9 days old) were crossed and maintained at 25°C in laying pots with grape juice agar plates for 48 h. Flies were then transferred to a fresh plate to lay eggs for 1–2 h. To control for overcrowding, 20-30 2nd instar larvae (48 h AEL) were transferred to vials containing normal *Drosophila* food at 25°C. The number and timing of pupariation was assessed 3 times/day every 6-8 h until all larvae pupariated or died. Pupariation was defined as cessation of movement with evaginated spiracles and a darker color of the puparium.

QUANTIFICATION AND STATISTICAL ANALYSIS

Statistics

Sample sizes were chosen similar to previous publications and commonly used in the field.[14,15,30,48,113] For comparison of two groups, unpaired Student's t test with Welch's correction was used, or nonparametric Mann-Whitney U test in case of non-normal distribution of the data. For analysis of mechanonociceptive behavior, the $\chi 2$ test was used. For multiple comparisons, one-way ANOVA with Tukey's post hoc analysis was performed. All tests were two-tailed and differences were considered significant for $p < 0.05$ (*$p < 0.05$, **$p < 0.01$, ***$p < 0.001$, ****$p < 0.0001$). Statistical testing was performed using Prism (GraphPad). Exact P values for all quantitative data comparisons are listed in Table S1.

Analysis of network synaptic counts

Network graphs were built by using the customized graph tools on CATMAID, where the interactions between a pair of nodes (neurons) was generated based on the absolute number of synaptic counts, using a synapse cutoff above 2[14]. The network was build starting with the first processing layer (sensory neurons) consisting of 3 nodes, each representing a subset of sensory neurons (C4 da, v'td1 and v'td2) connected to Dp7 neurons (second processing layer). Intermediate nodes from the sensory neurons to Dp7 were also extracted. The third processing layer consisted of output nodes of Dp7 neurons with a) VNC projections and b) being interconnected with sensory neurons (Hugin-VNC and ABLK). The thickness of the arrow between 2 nodes was determined automatically in CATMAID as a function of synaptic counts. Analysis of synaptic counts between different neurons connected on the lateral Dp7 domain was done using Graph Pad Prism (GraphPad, San Diego, CA, USA).

Developmental toxicity assay

Bar charts displaying percentages of animals were plotted with Excel, whiskers depict standard deviation. Statistical significance was calculated using the χ^2 test (GraphPad, San Diego, CA, USA).

Light avoidance analysis

Preference index (PI) was calculated at 15 mins as: (number of larvae in dark-number of larvae in light)/total number of larvae. PI data are shown as violin plots, where the middle line shows the median. If more than 3 larvae escaped during the trial, it was discarded. Statistical analysis was performed using one-way ANOVA and Tukey's post hoc test (GraphPad, San Diego, CA, USA).

Analysis of temporal larval distribution was performed by keeping only every 200th frame, cropping and converting mp4 files to avi using a custom script and ffmpeg (https://www.ffmpeg.org). Reduced avi files were processed and analyzed in Fiji (ImageJ, NIH) using a custom macro script to create background-corrected masked images retaining intensity-based signals from larvae only. Total intensities on the dark and light side were measured over time and plotted as a preference index (PI = (intensity in dark- intensity in light)/total intensity) analogously to larval distribution. All scripts and code used are available at https://github.com/formozov/larva_tracking_Imambocus_et_al.

Mechanonociception analyses

Statistical significance was calculated using the χ^2 test (GraphPad, San Diego, CA, USA).

Locomotion and chemotaxis analysis

For locomotion analysis, velocity and bending angles were analyzed using the FIMtrack software (https://github.com/kostasl/FIMTrack). For analysis, only animals displaying continuous locomotion and uninterrupted tracking were kept. Other animals were excluded from analysis. Average locomotion speed and cumulative bending angles were analyzed and plotted for the first 30 s under

dark or blue light conditions. Graphs of mean ± s.d. were plotted and analyzed using one-way ANOVA and Tukey's post hoc test (GraphPad, San Diego, CA, USA).

For chemotaxis, the locomotion tracks were generated using the FIMTrack software. All reconstructed tracks were considered in the analysis. The plate was virtually divided into four equidistant regions along x axis. The first and the last regions were further restricted along the y axis (to take only a central band with a width equal to the radius of the plate) to set a "no-odor" and "odor" zone, respectively. The area surrounding the odor was defined as the "odor" zone, while the same area on the opposite side of the plate was defined as the "no-odor" zone. To quantify chemotaxis we used a performance index (PI), defined as $(t_{odor}-t_{noodor})/(t_{odor}+t_{noodor})$, where t_{odor} and t_{noodor} are total time that larvae spent in the odor and no-odor zones, respectively, in the time window between 3 and 5 min of a given video recording. Graphs of mean ± s.d. were plotted and analyzed using one-way ANOVA and Tukey's post hoc test (GraphPad, San Diego, CA, USA).

Analysis of calcium imaging

Time series analysis was performed using image registration with the StackReg plugin (using translation function, Fiji, ImageJ) to correct for internal movement. GCaMP6 signal intensity was then quantified using a region of interest defining the neuronal soma and the Time Series Analyzer V3 plugin (Fiji, ImageJ). The calcium response ($\Delta F/F_0$ (%)) was calculated by subtracting the amplitude of pre-stimulation baseline (average of 19 frames) from the stimulation evoked amplitude. $\Delta F/F_0$ (%) = $(F-F_0)/F_0$ x100. Maximum fluorescence was calculated as $F_{max}-F_0/F_0$ x 100 (($F_{max,}$ maximum fluorescence observed during the stimulation; F_0 (average of 19 frames)). Graphs of mean ± s.e.m were plotted using Prism (GraphPad, San Diego, CA, USA). Comparison of maximum responses ($\Delta F_{max}/F_0$ (%)) were plotted as boxplots (box showing median and 25th and 75th percentile, whiskers 1st and 99th percentile), and analyzed using one-way ANOVA and Tukey's post hoc test (GraphPad, San Diego, CA, USA).

Analysis for calcium imaging data upon optogenetic activation of C4 da, BO and Dp7 neurons were performed as described above.

To analyze NPPR^{llp7} release, the baseline signal was calculated from 19 frames before 40 frames of UV illumination, with 100 frames between stimulations. NPPR^{llp7} release events were calculated for each puncta using the formula $\Delta F/F_0$ (%) = $(F-F_0)/F_0$ x100. The n number refers to individual LDCV puncta from 5 different larvae.

For calcium responses in semi-intact larval preparations, baseline (F_0) and the relative maximum intensity change (ΔF_{max}) of GCaMP6m fluorescence was analyzed. $\Delta F_{max}/F_0$ values of mechanonociceptive versus noxious light ABLK neuron responses were plotted and compared, with the centerline representing median values, upper and lower whiskers representing SEM. Statistical significance was analyzed using a Mann-Whitney U test. Analysis of Somatic Dp7 calcium responses upon optogenetic activation of v'td2 neurons was performed described above. Comparison of maximum responses ($\Delta F_{max}/F_0$ (%)) were plotted as boxplots (box showing median and 25th and 75th percentile, whiskers 1st and 99th percentile) and analyzed with the Mann-Whitney U test.

Current Biology, Volume *32*

Supplemental Information

A neuropeptidergic circuit gates selective escape behavior of *Drosophila* larvae

Bibi Nusreen Imambocus, Fangmin Zhou, Andrey Formozov, Annika Wittich, Federico M. Tenedini, Chun Hu, Kathrin Sauter, Ednilson Macarenhas Varela, Fabiana Herédia, Andreia P. Casimiro, André Macedo, Philipp Schlegel, Chung-Hui Yang, Irene Miguel-Aliaga, J. Simon Wiegert, Michael J. Pankratz, Alisson M. Gontijo, Albert Cardona, and Peter Soba

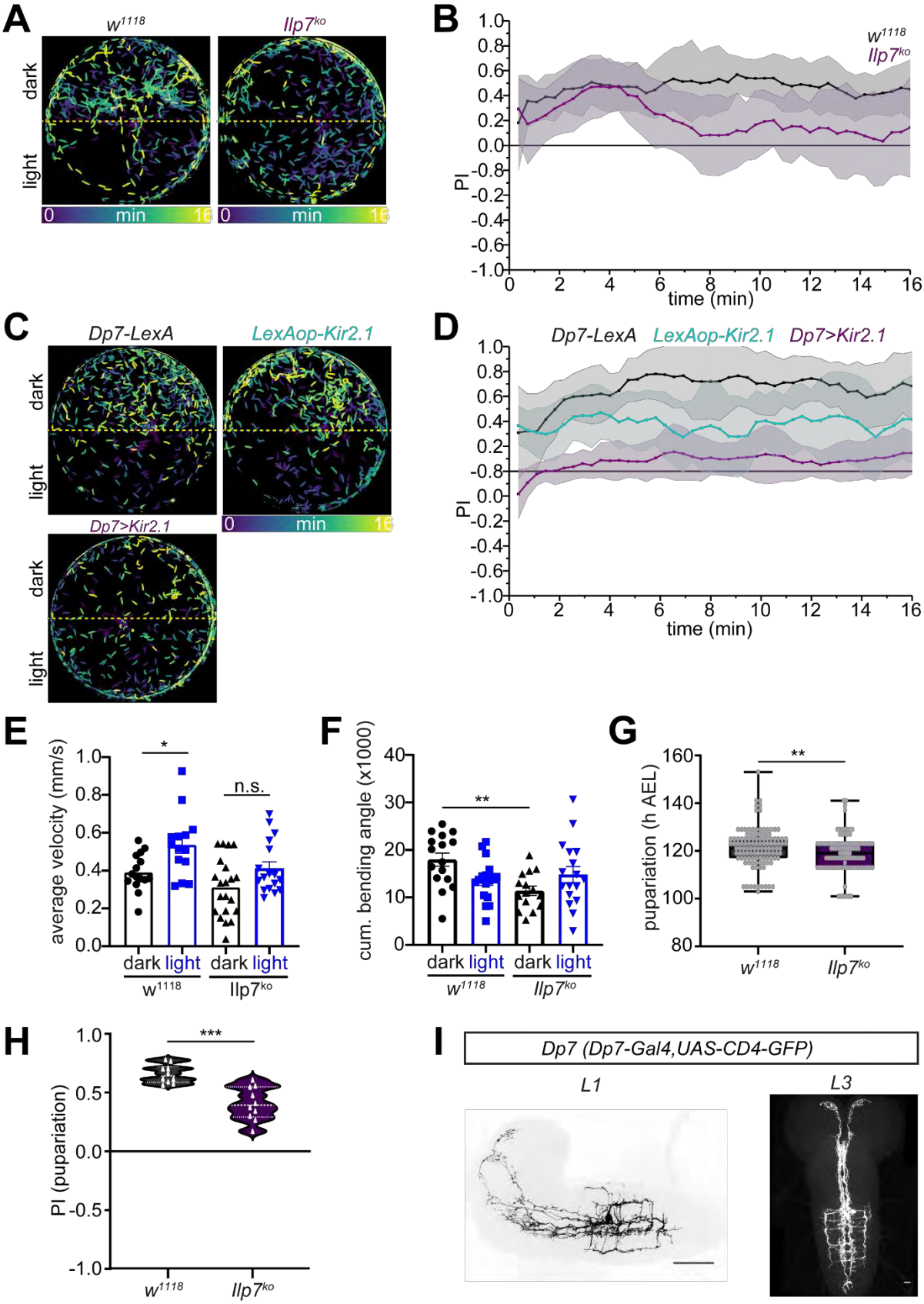
A
w1118
Ilp7ko
dark
light
0 min 16
B
w1118
Ilp7ko
PI
time (min)
C
Dp7-LexA
LexAop-Kir2.1
Dp7>Kir2.1
D
Dp7-LexA LexAop-Kir2.1 Dp7>Kir2.1
E
average velocity (mm/s)
n.s.
dark light dark light
w1118 Ilp7ko
F
cum. bending angle (x1000)
G
pupariation (h AEL)
H
PI (pupariation)
I
Dp7 (Dp7-Gal4,UAS-CD4-GFP)
L1
L3

Figure S1. Dp7 and Ilp7-dependent noxious light avoidance, Related to Figure 1.

A. Time-dependent redistribution of *w*^{1118} and *Ilp7*^{ko} larvae in light avoidance assays. Temporal color code indicates larval position at the different time points, dotted line represents light/dark boundary. **B.** Analysis of time-dependent larval distribution of *w*^{1118} and *Ilp7*^{ko} larvae during light avoidance assays. Preference index (PI) is based on intensities of larval signals on the dark or light side (see STAR methods). Stable dark preference is reached within the first 5 min for *w*^{1118}, but not *Ilp7*^{ko} larvae, which fail to maintain light avoidance. **C.** Time-dependent redistribution of control (*Dp7-LexA* and *LexAop*-Kir2.1) or animals, where Dp7 neurons were silenced (*Dp7-LexA>LexAop-Kir2.1*), in light avoidance assays. Temporal color code indicates larval position at the different time points, dotted line represents light/dark boundary. **D.** Analysis of time-dependent larval distribution in controls and upon Dp7 neuron silencing as indicated. Dp7 neuron function is required for establishing significant light avoidance during the entire assay. **E.** Average velocity and **F.** cumulative bending angle of *w*^{1118} and *Ilp7*^{ko} larvae in dark or noxious blue light (4.5 μW/mm^2) conditions. (n=14-21/genotype, non-significant, *P<0.05, **P<0.01 one-way-ANOVA with Tukey's *post-hoc* test). **G.** Pupariation timing of *w*^{1118} (median: 121h AEL, n=118) and *Ilp7*^{ko} larvae (median: 119h AEL, n=103, **P<0.01 Mann-Whitney test). **H.** Dark vs. white light (2.9-4.6 μW/mm^2) preference index (PI) of pupariation of *w*^{1118} and *Ilp7*^{ko} larvae (n=10 trials/genotype, ***P<0.001 two-tailed unpaired *t*-test). Note that control *w*^{1118} larvae preferentially enter puparium formation in darkness, which is reduced in *Ilp7*^{ko} animals. **I.** Light microscopic Dp7 neuron morphology at the L1 and L3 stage (*Dp7-Gal4>UAS-CD4-tdGFP*). Dp7 neurons display dendritic arbor extension to the posterior at the L3 stage. In L1, Dp7 neuron dendrites extend to segments A3-A4, while in L3, they extend to the A8 segment. Scale bar=10 μm (L1) and 50 μm (L3).

A

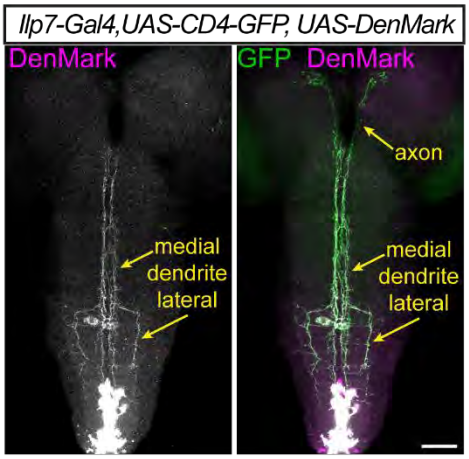

B

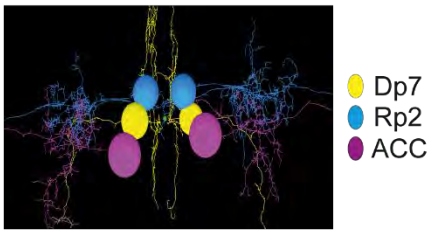

C

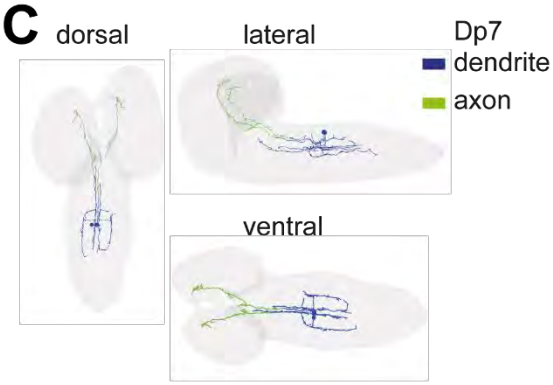

D

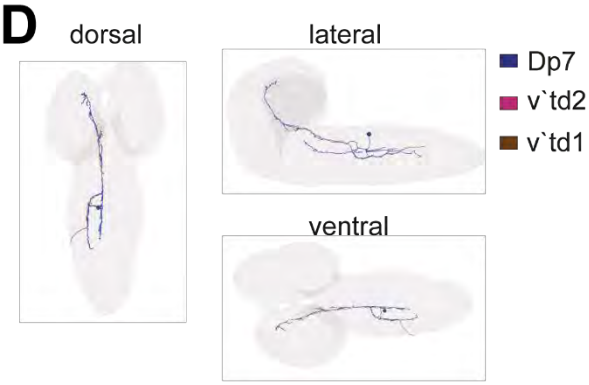

E Dp7 presynaptic connectome

Presynaptic neuron	skeleton ID	synapses Dp7_l	synapses Dp7_r
v`td2	891237		18
v`td2	3915835	21	
v`td2	4061049		14
v`td2	5638694		16
v`td2	7012280	15	
v`td2	12178825		14
v`td2	16303262	4	
v`td2	16911458	15	
v`td2	19017854	17	
v`td2	19037563		14
v`td2	19120772	15	
C2da	3827179		3
C3da	110633	4	
C3da	2777891		4
C3da	7792781	4	
C3da	16307065	4	
C3da	17237088	3	
C4da	18303100	5	1
v`td1	10852875		2
A08n	1927577	1	16
A08n	14899172	19	
MIP	7340664		4
MIP	11291634		3
MIP	11434579		6
MIP	13985838		3
MIP	19040382	3	1
TePn05	2558717		6
TePn05	18981220	18	
	2585319	8	
	2123393	3	
	3629633	3	
	4249897	3	
	6988490	3	
	13674287	3	
	19157404	3	
	2697511		7
	9428865		4
	11512247		4
	4179669		4
	2513992		4
	327601		3
	12617501		2

F Dp7 postsynaptic connectome

Postsynpatic neuron	skeleton ID	synapses Dp7_l	synapses Dp7_r
ABLK	429906	4	
ABLK	3985549	3	
ABLK	10844198	3	
ABLK	19037553		3
ABLK	19166763	5	
Hugin-VNC	6795358	2	5
Hugin-VNC	2613540	4	4
Hugin-VNC	3594705	10	
Hugin-RG	5601924	1	3
Hugin-RG	2138427	7	2
Hugin-RG	5038703	1	2
Hugin-PC	9805520	3	
Bamas	17176866		15
Bamas	17176882	15	
Af6	3946364	3	
BC	3801211		4
DPLm1 contralatera 1 left	6011278		4
DPMm1	3595837		3
DPMpm1	3944626	9	
IPC 6	2357110		3
MIP to the brain	9503414	9	
SN motor neuron	4050398	3	
	5644800	13	5
	8008617	13	5
	3793760	11	
	9524538	10	
	16500055	8	
	6445994	5	
	7345403	5	
	17019327	5	
	18694063	3	5
	16018440	3	1
	3918937	3	
	3945394	3	
	6568902	3	
	14839446	3	
	17415439	3	
	6802553	2	5
	19912140	2	5
	5071140	1	6
	5349961	1	3
	9424902		8
	4411688		6
	11946903		6
	161195633		6
	8546775		5
	15732471		5
	6300434		4
	11278919		4
	3729504		3
	5532548		3
	5613777		3
	6597872		3
	7340664		3
	14162492		3
	15304721		3
	10768709		2
	5378683		2

Figure S2. Dp7 connectome analysis, Related to Figure 1 and 2.

A. Light microscopic Dp7 neuron morphology and dendritic compartment marked by DenMark at the L3 stage (*Ilp7-Gal4>UAS-CD4-tdGFP, UAS-DenMark*). Dp7 neurons display dendritic arbor extensions within the medial and ventral VNC neuropil. The axon extends anteriorly to the brain lobe region. Scale bar= 50 μm (L3). **B.** Dp7 was identified based on its soma location in abdominal segment A1 on the dorsal side of the VNC in between the two motor neurons Rp2 and ACC and based on the trajectory of its emerging neurites**.** **C.** Reconstruction of Dp7 neurons illustrated from different angles, Dp7 neuron dendrites shown in blue and axon in green. **D.** V`td1 and v`td2 sensory neurons are anatomically similar and project alongside the lateral and proximal dendritic arbour of Dp7 neurons. **E.** Dp7 presynaptic connectome and **F.** Dp7 postsynaptic connectome from the reconstructed L1 larval EM volume. Numbers indicate synapses with the respective Dp7 neuron (L: left, R: right hemisphere).

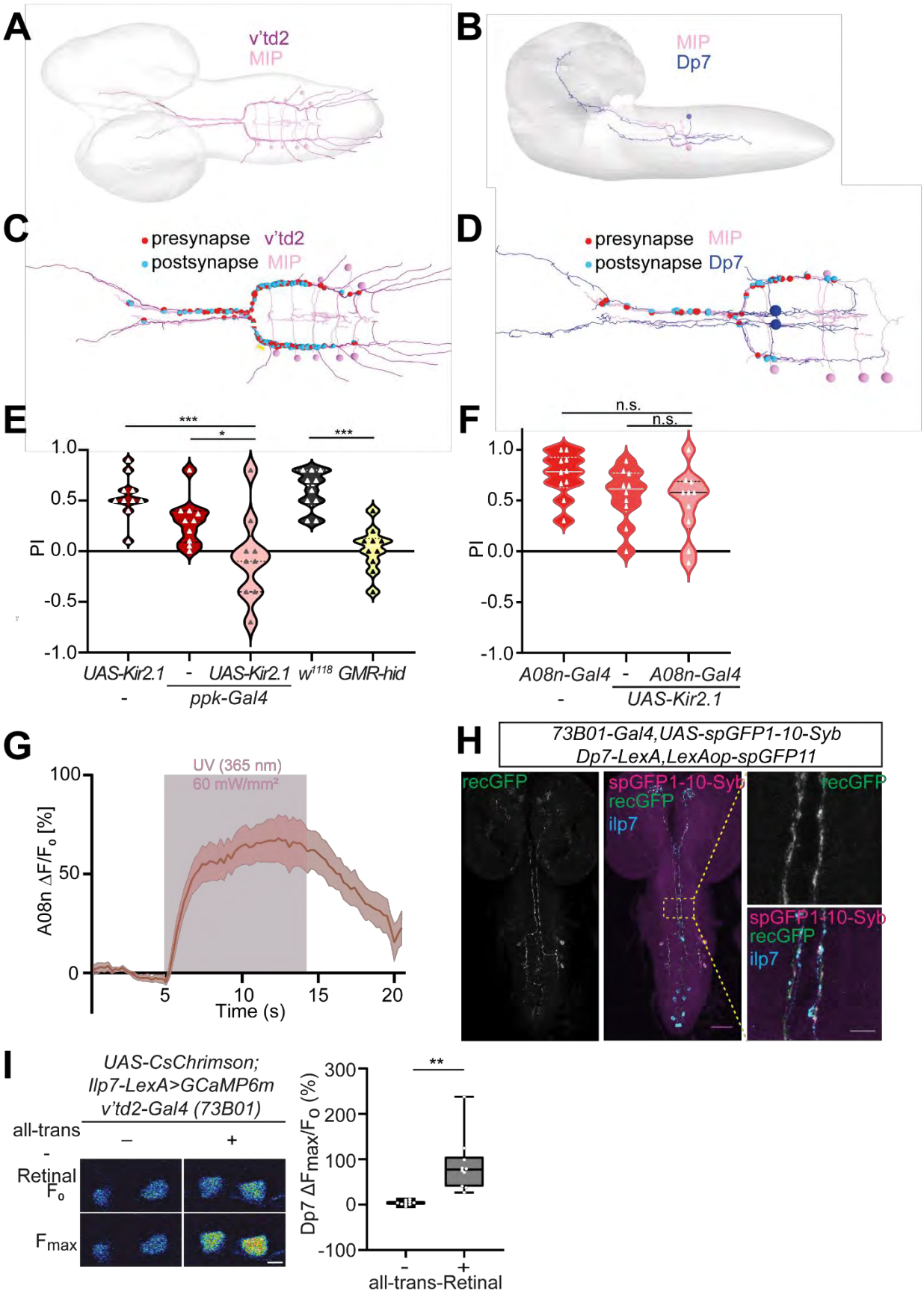
A
v'td2
MIP
B
MIP
Dp7
C
presynapse v'td2
postsynapse MIP
D
presynapse MIP
postsynapse Dp7
E
***
*
***
PI
1.0
0.5
0.0
-0.5
-1.0
UAS-Kir2.1
-
UAS-Kir2.1
w1118
GMR-hid
ppk-Gal4
F
n.s.
n.s.
A08n-Gal4
-
A08n-Gal4
UAS-Kir2.1
G
UV (365 nm)
60 mW/mm²
A08n ΔF/Fo [%]
100
50
0
5
10
15
20
Time (s)
H
73B01-Gal4,UAS-spGFP1-10-Syb
Dp7-LexA,LexAop-spGFP11
recGFP
spGFP1-10-Syb
recGFP
ilp7
recGFP
spGFP1-10-Syb
recGFP
ilp7
I
UAS-CsChrimson;
Ilp7-LexA>GCaMP6m
v'td2-Gal4 (73B01)
all-trans
-
+
Retinal
Fo
Fmax
Dp7 ΔFmax/Fo (%)
300
200
100
0
-100
**
-
+
all-trans-Retinal

Figure S3. Dp7 neuron upstream network and light sensing circuit, Related to Figure 2.

A. Reconstruction of MIP and v'td2 neurons and **B**. anatomical overlap of MIP (representative member) with Dp7 neurons, lateral view. **C**. Reconstructed synaptic connections between v'td2 and MIP neurons. **D**. Reconstructed synaptic connections between MIP and Dp7 neurons. **E.** Kir2.1 expression in C4da neurons significantly reduces light avoidance responses (*UAS-Kir2.1*, *ppk-Gal4*, *ppk-Gal4>UAS-Kir2.1,* n=10,10,9 trials/genotype, *P<0.05, ***P<0.001, one-way-ANOVA with Tukey's *post-hoc* test). Similarly, genetic ablation of BO by expression of the proapoptotic factor hid strongly impairs light avoidance (*w^{1118} vs. GMR-hid,* n=10 trials/genotype, ***P<0.001, one-way-ANOVA with Tukey's *post-hoc* test). **F.** Kir2.1 expression in A08n neurons does not significantly reduce light avoidance responses (*A08n-Gal4>UAS-Kir2.1,* n=10 trials/genotype, non-significant, one-way-ANOVA with Tukey's *post-hoc* test). **G.** Calcium response to UV light in A08n neuron somata (*82E12-Gal4>UAS-GCaMP6s*, mean ± s.e.m. n=5). **H.** Confocal image showing Syb-GRASP-labelled v`td2 to Dp7 neuron synapses. Presynaptic spGFP1-10-Syb is expressed in v`td2 neurons (*v'td2-Gal4*, magenta), postsynaptic spGFP11-CD4 in Dp7 neurons (*Dp7-LexA*). Reconstituted GFP signal (recGFP, green) labelling v`td2-Dp7 neuron synapses, and Ilp7 neuropeptide immunostaining (cyan). Enlarged boxed area shows proximity of Ilp7 peptide and v'td2-Dp7 neuron synapses along the proximal axon of Dp7 neurons. Scale bars=10 μm. **I.** GCaMP6m signal in Dp7 neurons (using *Ilp7-LexA*) before (F_0) and during (F_{max}) CsChrimson-mediated optogenetic activation of v`td2 neurons (*v'td2-Gal4, UAS-CsChrimson; Ilp7-LexA, LexAop-GCaMP6m*). Maximum responses ($\Delta F_{max}/F_0$) in Dp7 neurons after CsChrimson activation in v`td2 neurons with and without all-trans-retinal (**P<0.01, Mann-Whitney test). Scale bar=10 μm**.**

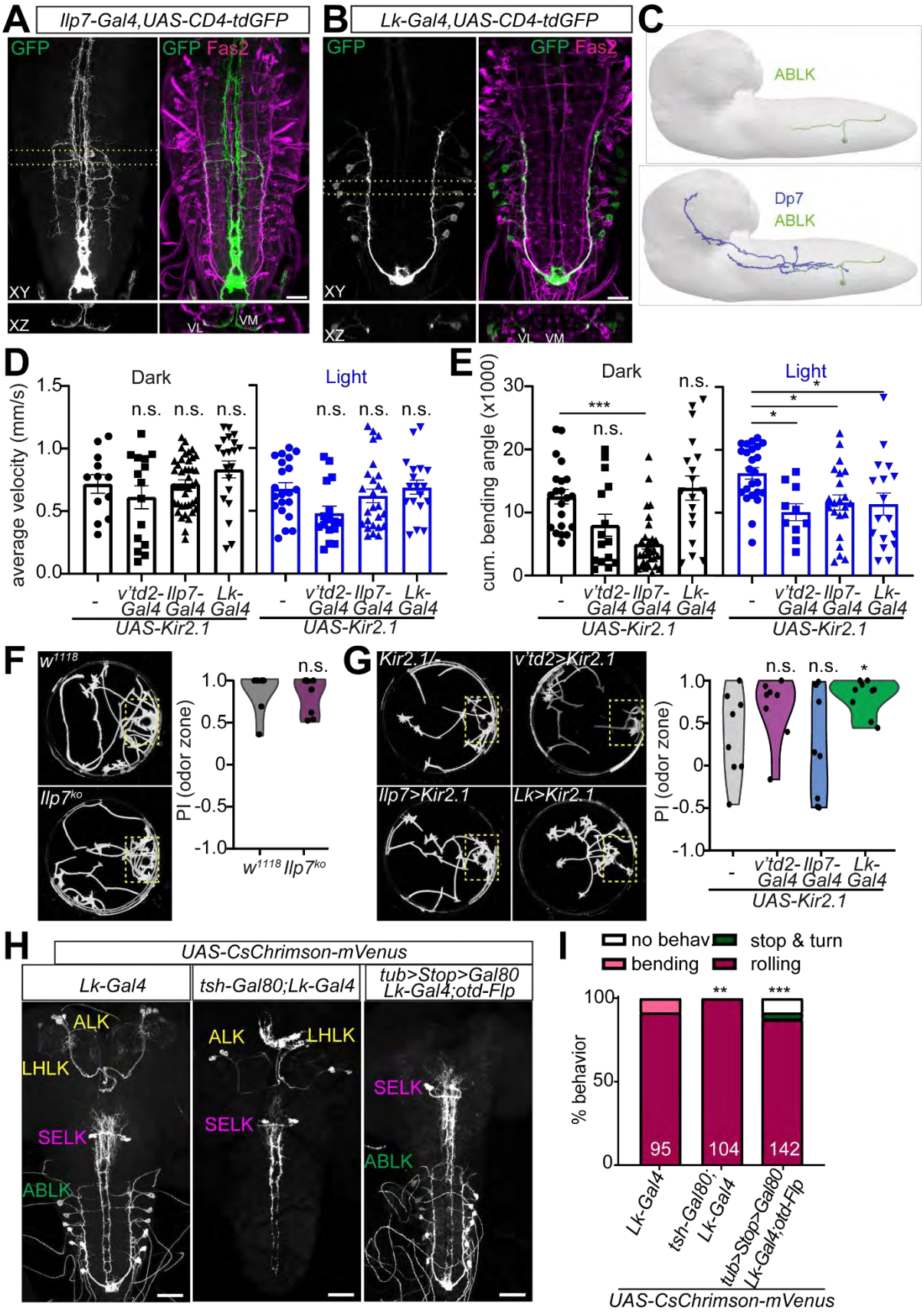
A
Ilp7-Gal4,UAS-CD4-tdGFP
GFP
GFP Fas2
XY
XZ
VL
VM
B
Lk-Gal4,UAS-CD4-tdGFP
C
ABLK
Dp7
D
average velocity (mm/s)
Dark
Light
n.s.
UAS-Kir2.1
E
cum. bending angle (x1000)
***
*
F
w1118
Ilp7ko
PI (odor zone)
G
Kir2.1/-
v'td2>Kir2.1
Ilp7>Kir2.1
Lk>Kir2.1
H
UAS-CsChrimson-mVenus
Lk-Gal4
tsh-Gal80;Lk-Gal4
tub>Stop>Gal80 Lk-Gal4;otd-Flp
ALK
LHLK
SELK
ABLK
I
no behav
stop & turn
bending
rolling
% behavior
**
***
95
104
142
Lk-Gal4
tsh-Gal80; Lk-Gal4
tub>Stop>Gal80 Lk-Gal4;otd-Flp
UAS-CsChrimson-mVenus

Figure S4. Behavioral functions of noxious light circuit components, Related to Figure 3 and 4.

A. Anatomical localization of Dp7 neuron arbors in relation to Fas2-labelled axon tracts in the larval neuropil. CD4-tdGFP-expression in Dp7 (*Ilp7-Gal4, UAS-CD4tdGFP*) in maximal projection (XY) and a XZ cross-section of the Dp7 soma region (shown region indicated by dotted lines). The primary Dp7 neurite projects from the dorsally located soma (segment A1) to the ventral neuropil forming medial and lateral dendritic branches localizing next to the ventromedial (VM) and ventrolateral (VL) Fas2-positive fascicle, respectively. Scale bar = 50 μm. **B.** Anatomical localization of ABLK neuron arbors in relation to Fas2-labelled axon tracts in the larval neuropil. CD4-tdGFP-expression in ABLK (*Lk-Gal4, UAS-CD4tdGFP*) in maximal projection (XY) and a XZ cross-section of shown region (indicated by dotted lines). ABLK neurons are located in the lateral cortex area (segment A1-A7) and project an axon to body wall muscles, while the resumed dendrites are targeted to the posterior terminal plexus area along the ventromedial (VM) Fas2-positive fascicle. Scale bar = 50 μm. **C.** Reconstruction of ABLK neurons (representative member) and anatomical overlap with Dp7 neurons, lateral view. **D.** Average velocity and **E.** cumulative bending angle of control (*UAS-Kir2.1*) and Kir2.1 expression with different Gal4 lines silencing v'td2 (*v'td2-Gal4*), Dp7 (*Ilp7-Gal4*) or ABLK (*Lk-Gal4*) neurons. Larvae of respective genotypes were tracked in dark or noxious blue light (470 nm, 4.5 $\mu W/mm^2$) conditions. No significant differences were found for average velocity, while cumulative bending angles were significantly reduced under blue light conditions for all groups compared to control (n=15-42, non-significant, *P<0.05, ***P<0.001 one-way-ANOVA with Tukey's *post-hoc* test). **F.** Chemotaxis experiments with a 125mM ethyl butyrate odor source comparing w^{1118} and $Ilp7^{ko}$ larvae. Representative larval tracks are shown, defined odor zone is indicated by dotted yellow box. Both genotypes displayed a high preference index for the odor zone with no significant differences (n=8 trials with 6 larvae each, non-significant, one-way-ANOVA) **G.** Chemotaxis of control (*UAS-Kir2.1*) and Kir2.1 expressing larvae using different Gal4 lines to silence v'td2 (*v'td2-Gal4*), Dp7 (*Ilp7-Gal4*) or ABLK (*Lk-Gal4*) neurons.**.** Representative larval tracks are shown for each genotype, defined odor zone is indicated by dotted yellow box. Preference index for odor zone during the last 2 min of all recorded animals is shown (n=8 trials with 6 larvae each, non-significant, *P<0.05 one-way-ANOVA with Tukey's *post-hoc* test) **H.** CsChrimson-GFP expression with Lk-Gal4 labels ALK and LHLK brain lobe neurons, SELK in the SEZ and ABLK neurons in the VNC. Addition of *tsh-Gal80* (middle panel) selectively eliminates ABLK neuron expression. Otd-Flp-mediated excision of a stop cassette allows brain lobe-specific Gal80 expression (*otd-Flp;tub>Stop>Gal80*), which selectively eliminates ALK an LHLK neuron expression. **I.** Optogenetic activation of CsChrimson in respective genotypes shown in G results in strong rolling responses without significant differences, indicating an involvement of SELK neurons in nociceptive rolling (n= number of animals as indicated in graph, **P<0.01, ***P<0.001, X^2-test).

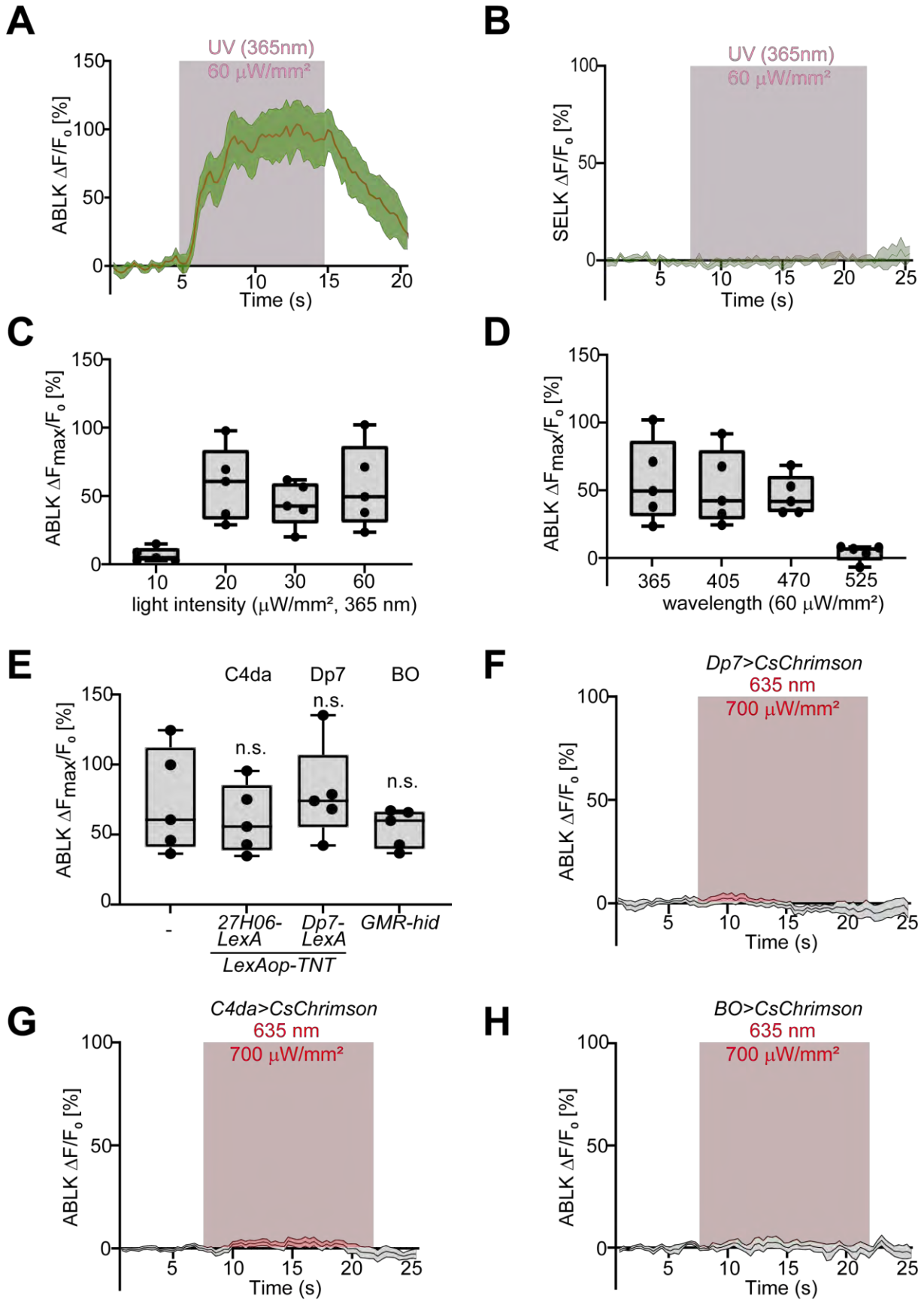
A
UV (365nm)
60 µW/mm²
ABLK ΔF/F$_o$ [%]
Time (s)
B
UV (365nm)
60 µW/mm²
SELK ΔF/F$_o$ [%]
Time (s)
C
ABLK ΔF$_{max}$/F$_o$ [%]
light intensity (µW/mm², 365 nm)
D
ABLK ΔF$_{max}$/F$_o$ [%]
wavelength (60 µW/mm²)
E
C4da
Dp7
BO
n.s.
n.s.
n.s.
ABLK ΔF$_{max}$/F$_o$ [%]
-
27H06-LexA
Dp7-LexA
GMR-hid
LexAop-TNT
F
Dp7>CsChrimson
635 nm
700 µW/mm²
ABLK ΔF/F$_o$ [%]
Time (s)
G
C4da>CsChrimson
635 nm
700 µW/mm²
ABLK ΔF/F$_o$ [%]
Time (s)
H
BO>CsChrimson
635 nm
700 µW/mm²
ABLK ΔF/F$_o$ [%]
Time (s)

Figure S5. Noxious light dependent activation of ABLK neurons, Related to Figure 4.

A. Evoked calcium transients in ABLK neurons by UV-A light (n=5, mean ± s.e.m.). **B**. SELK neurons expressing GCaMP6s do not show UV light-evoked calcium responses light (n=5, mean ± s.e.m.). **C.** Boxplot quantification (% $\Delta F_{max}/F_0$) of ABLK neuron somatic calcium responses (*Lk-Gal4>jRCaMP1b*) in dependence of the UV light intensity (365nm). Strong responses were observed between 20-60 $\mu W/mm^2$ (n=5 larvae/genotype). **D.** ABLK neuron somatic calcium responses (*Lk-Gal4>jRCaMP1b*) to different wavelengths of the same intensity (365nm-525nm, 60 $\mu W/mm^2$). Boxplots of maximum responses (% $\Delta F_{max}/F_0$) show strong activation up to 470nm, but not at 525nm (n=5 larvae/genotype, dataset for 365nm same as in C). **E.** ABLK neuron somatic calcium responses (*Lk-Gal4>GCaMP6s*) to UV light (365nm, 60$\mu W/mm^2$) and synaptic silencing of C4da (*27H06-LexA*) and Dp7 (*Dp7-LexA*) neurons using Tetanus toxin light chain (*LexAop-TNT*) or genetic ablation of BO (*GMR-hid*). Strong ABLK neuron responses without significant differences were observed for all genotypes indicating no major effect of C4da or Dp7 neuron synaptic inactivation or BO ablation (n=5/genotype, non-significant, one-way-ANOVA with Tukey's *post-hoc* test). **F-H**. Expression and activation of CsChrimson (700 $\mu W/mm^2$) for 15s in **F.** C4da (*27H06-LexA*), **G.** Dp7 (*Dp7-LexA*) or **H.** BO (*GMR-LexA*) does not evoke significant somatic ABLK neuron calcium responses (*Lk-Gal4>GCaMP6s,* n=5/genotype).

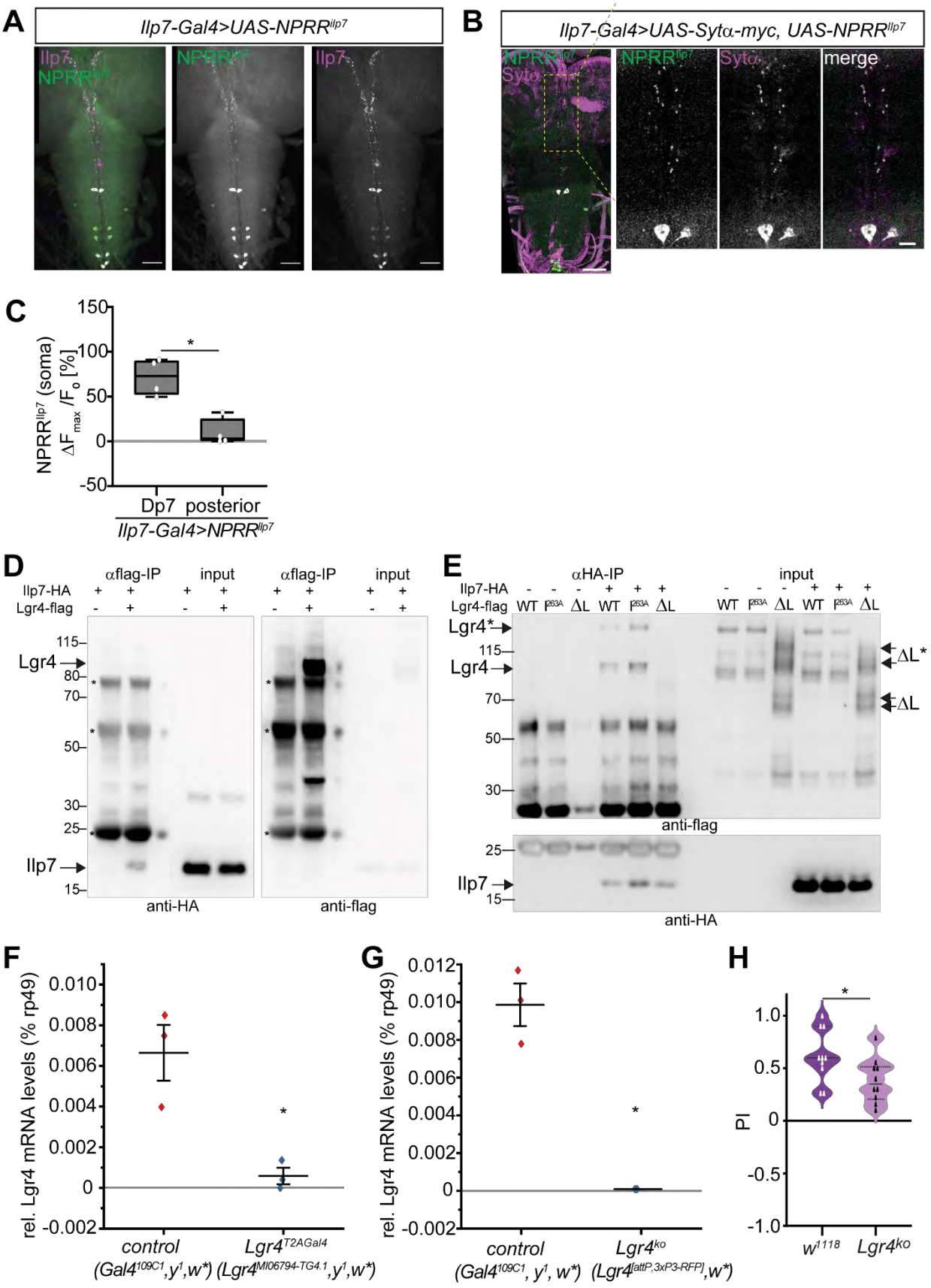
A
Ilp7-Gal4>UAS-NPRR^ilp7
Ilp7
NPRR^Ilp7
B
Ilp7-Gal4>UAS-Sytα-myc, UAS-NPRR^Ilp7
Sytα
merge
C
NPRR^Ilp7 (soma) ΔF_max /F_o [%]
Dp7 posterior
Ilp7-Gal4>NPRR^Ilp7
D
αflag-IP
input
Ilp7-HA
Lgr4-flag
Lgr4
Ilp7
anti-HA
anti-flag
E
αHA-IP
input
Lgr4*
ΔL*
ΔL
anti-flag
anti-HA
F
rel. Lgr4 mRNA levels (% rp49)
control
Lgr4^T2AGal4
(Gal4^109C1,y^1,w*) (Lgr4^MI06794-TG4.1,y^1,w*)
G
rel. Lgr4 mRNA levels (% rp49)
control
Lgr4^ko
(Gal4^109C1, y^1, w*) (Lgr4^[attP,3xP3-RFP],w*)
H
PI
w^1118
Lgr4^ko

Figure S6. *NPRR^{Ilp7}* characterization and biochemical interaction of Lgr4 and Ilp7, Related to Figure 5 and 6.

A. Immunohistochemical analysis of Ilp7 neuropeptide release reporter in Ilp7-expressing neurons (*Ilp7-Gal4>UAS-NPRR^{Ilp7}*, anti-Ilp7 and anti-GFP). Scale bar=50μm. **B**. Immunohistochemical analysis of Ilp7 neuropeptide reporter (NPRR^{Ilp7}, anti-GFP, green) and Sytα-myc (anti-myc, magenta) localization expressed in Ilp7 neurons (*Ilp7-Gal4>UAS-Sytα-myc,UAS-NPRR^{Ilp7}*). Boxed area in overview image is showing enlarged Dp7 neuron proximal dendrite and axon region. Scale bar=50μm, 10μm. **C**. Boxplot quantification (% $\Delta F_{max}/F_0$) of NPRR^{Ilp7} fluorescence changes in Dp7 and posterior Ilp7 neuron somata upon UV light stimulation. Dp7 neurons, but not posterior Ilp7 expressing neurons (A6-A8) show significant responses (n=4 larvae/genotype,*P<0.05, Mann Whitney test). **D-E.** Co-immunoprecipitation of Lgr4 and Ilp7. S2 cells were transfected with flag-tagged Lgr4 and HA-tagged Ilp7, immunoprecipitated with either **D**. anti-flag or **E**. anti-HA antibody beads and detected with antibodies against the coprecipitated Lgr4 or Ilp7, respectively (anti-flag or anti-HA). Specific interaction between Lgr4 and Ilp7 was found under both conditions. In **E**, we also tested interaction with a point mutation (Lgr4-I^{263}A) or deletion (Lgr4$^{\Delta L}$) of the LRR repeats. Lgr4 lacking LRR repeats did not interact with Ilp7 suggesting specific binding of Ilp7 to the Lgr4 extracellular LRR domain. Signals specific for Lgr4 (and ΔL form) and multimeric forms (Lgr4*, ΔL*) are indicated by arrows. Asterisks indicate IP antibody signal. **F**. Quantitative RT-PCR of Lgr4 mRNA comparing *Lgr4^{T2AGal4}* allele to control (n=3, unpaired t-test,**P<0.05*). **G**. Quantitative RT-PCR of Lgr4 mRNA comparing *Lgr4^{ko}* allele to control (n=3, unpaired t-test,**P<0.05*). **H**. *Lgr4^{ko}* animals display reduced light avoidance compared to controls (n=10 trials/genotype, **P<0.05*, unpaired *t*-test).

Figure	Genotypes compared	Statistical test	Signif-icance	P values	post-hoc test
Figure 1C	*w*^{1118} blue vs. green light	Chi-Square	***	0.001	
Figure 1D	*Dp7-LexA/- vs. Dp7-LexA:LexAop-Kir2.1*	One-way Anova	**	0.001	Tukey
	LexAopKir2.1/- vs. Dp7-LexA:LexAopKir2.1	One-way Anova	***	0.0006	Tukey
Figure 1F	*w*^{1118} vs. *Ilp7*^{ko}	One-way Anova	***	0.001	Tukey
	w ^{1118} vs. *sNPF*^{C00448}	One-way Anova	n.s.	>0.999	Tukey
	w ^{1118} vs. *sNPF* ^{Mi01807}	One-way Anova	n.s.	0.6046	Tukey
Figure 1G	*Dp7-GAL4*;*UAS-Ilp7* vs. *Ilp7*^{ko}	One-way Anova	****	<0.0001	Tukey
	Dp7-GAL4;*UAS-Ilp7* vs. Ilp7ko;*Dp7Gal4*;*UAS-Ilp7*	One-way Anova	n.s.	0.1083	Tukey
	Ilp7^{ko} vs. Ilp7^{ko};*Dp7-Gal4*;*UAS-Ilp7*	One-way Anova	**	0.0011	Tukey
Figure 2C	*73B01-GAL4/- vs. 73B01-GAL4;UAS-Kir2.1*	One-way Anova	**	0.0014	Tukey
	UAS-Kir2.1/- vs. *73B01-GAL4;UAS-Kir2.1*	One-way Anova	****	<0.0001	Tukey
Figure 2E	*35BO1-Gal4, UAS-GCaMP6s*	unpaired t test, two tailed with Welch`s correction	**	0.0044	
Figure 2G	*73BO1-GAL4*/- vs. *73B01-GAL4; UAS-Kir2.1*	Chi-Square	n.s.	0.5598	
	UAS-Kir2.1/- vs. 73B01-GAL4; UAS-Kir2.1	Chi-Square	n.s.	0.5598	
Figure 4B	*UAS-Kir2.1*/- vs. *HuginVNC-GAL4; UAS-Kir2.1*	One-way Anova	n.s.	0.5546	Tukey
	HuginVNC-Gal4/- vs. *HuginVNC-GAL4;UAS-Kir2.1*	One-way Anova	n.s.	0.6569	Tukey
	UAS-Kir2.1/- vs. *Lk-Gal4;UAS-Kir2.1*	One-way Anova	****	<0.0001	Tukey
	Lk-Gal4/- vs. *Lk-Gal4;UAS-Kir2.1*	One-way Anova	****	<0.0001	Tukey
	Lk-Gal4;*UAS-Kir2.1 vs. -/tsh-gal80; UAS-Kir2.1*	One-way Anova	**	0.0013	Tukey
	Lk-Gal4;*UAS-Kir2.1 vs. Lk-Gal4; tsh-gal80;UAS-Kir2.1*	One-way Anova	****	<0.0001	Tukey
Figure 4D	*LK-Gal4,UAS-GCamP6s; ilp7-LexA* vs. *LK-Gal4,UAS-GCamP6s; Ilp7-LexA, LexAop-Kir2.1*	unpaired t test, two tailed with Welch`s correction	****	<0.0001	

Figure 4F	*LK-Gal4,UAS-GCaMP6s* vs. *Ilp7^{ko}*; *LK-Gal4,UAS-GCaMP6s*	unpaired t test, two tailed with Welch`s correction	**	0.0064	
Figure 5E	*ilp7-Gal4,UAS-NPRR^{ilp7}, CapdsRNAi*	unpaired t test, two tailed with Welch`s correction	**	0.0026	
Figure 6A	*Lk-Gal4/- vs. Lk-Gal4;UAS-Kir2.1*	Chi-Square	*	0.0167	
	UAS-Kir2.1/- vs. Lk-Gal4;UAS-Kir2.1	Chi-Square	*	0.0167	
	Lk-Gal4/- vs. -/tsh-gal80;UAS-Kir2.1	Chi-Square	n.s.	0.1873	
Figure 6B	*LK-Gal4,UAS-GCaMP6, mechano vs. UV light*	unpaired t test, two tailed with Welch`s correction	**	0.00295	
Figure 6E	*W^{1118}*vs. *Lgr4$^{T2A-Gal4}$*	One-way Anova	**	0.0023	Tukey
	Lgr4$^{T2A-Gal4}$ vs. *Lgr4$^{T2A-Gal4}$*;UAS-Lgr4	One-way Anova	*	0.0239	Tukey
	W^{1118} vs. *Lgr4$^{T2A-Gal4}$*;UAS-Lgr4	One-way Anova	n.s.	0.7338	Tukey
Figure 6G	*Lgr4ko; LK-Gal4,UAS-GCaMP6s vs. LK-Gal4,UAS-GCaMP6s*	One-way Anova	**	0.0011	Tukey
	Lgr4ko; LK-Gal4,UAS-GCaMP6s vs. Lgr4ko; LK-Gal4,UAS-GCaMP6s/UASLgr4	One-way Anova	**	0.0058	Tukey
	LK-Gal4,UAS-GCaMP6s vs. Lgr4ko; LK-Gal4,UAS-GCaMP6s/UASLgr4	One-way Anova	n.s.	0.6186	Tukey
Figure S1E	*w^{1118} dark vs. light*	One-way Anova	*	0.03858	Tukey
	Ilp7^{ko} dark vs. light	One-way Anova	n.s.	0.1457	Tukey
	w^{1118} dark vs. Ilp7^{ko} dark	One-way Anova	n.s.	0. 3687	Tukey
	w^{1118} light vs. Ilp7^{ko} light	One-way Anova	n.s	0.0869	Tukey
Figure S1F	*w^{1118} dark vs. light*	One-way Anova	n.s.	0.0978	Tukey
	w^{1118} dark vs. Ilp7^{ko} dark	One-way Anova	**	0.0061	Tukey
	w^{1118}light vs. Ilp7^{ko} light	One-way Anova	n.s.	0.8988	Tukey
	Ilp7^{ko} dark vs. light	One-way Anova	n.s.	0.2715	Tukey
Figure S1G	*w^{1118} vs. Ilp7^{ko}*	Mann-Whitney test, two tailed	**	0.0080	
Figure S1H	*w^{1118} vs. Ilp7^{ko}*	unpaired t test, two tailed with Welch`s	***	0.0002	

		correction			
Figure S3E	*ppk-GAL4/-* vs. *ppk-GAL4>UAS-Kir2.1*	One-way Anova	*	0.0439	Tukey
	UAS-Kir2.1/- vs. *ppk-GAL4>UAS-Kir2.1*	One-way Anova	***	0.0001	Tukey
	W^{1118} vs. GMR-hid	One-way Anova	***	0.0002	Tukey
Figure S3F	*A08n-GAL4/-* vs. *A08n-GAL4;UAS-Kir2.1*	One-way Anova	n.s.	0.0883	Tukey
	UAS-Kir2.1/- vs. *A08n-GAL4;UAS-Kir2.1*	One-way Anova	n.s.	0.8282	Tukey
Figure S3I	*73B01-Gal4, UAS-Chrimson; Ilp7-LexA,LexAop-GCaMP6m*	Mann-Whitney test, two tailed	**	0.0015	
FigureS4D	*UAS-Kir2.1/- vs. 73B01-Gal4>UAS-Kir2.1 (dark)*	One-way Anova	n.s.	0.7290	Tukey
	UAS-Kir2.1/- vs. Ilp7-Gal4>UAS-Kir2.1 (dark)	One-way Anova	n.s.	>0.9999	Tukey
	UAS-Kir2.1/- vs. Lk-Gal4>UAS-Kir2.1(dark)	One-way Anova	n.s.	0.6197	Tukey
	UAS-Kir2.1/- vs. 73B01-Gal4>UAS-Kir2.1 (light)	One-way Anova	n.s.	0.0862	Tukey
	UAS-Kir2.1/- vs. Ilp7-Gal4>UAS-Kir2.1 (light)	One-way Anova	n.s.	0.863	Tukey
	UAS-Kir2.1/- vs. Lk-Gal4>UAS-Kir2.1(light)	One-way Anova	n.s.	0.9985	Tukey
FigureS4E	*UAS-Kir2.1/- vs. v'td2-Gal4>UAS-Kir2.1 (dark)*	One-way Anova	n.s.	0.1264	
	UAS-Kir2.1/- vs. Ilp7-Gal4>UAS-Kir2.1 (dark)	One-way Anova	***	0.0002	
	UAS-Kir2.1/- vs. Lk-Gal4>UAS-Kir2.1(dark)	One-way Anova	n.s.	0.8929	
	UAS-Kir2.1/- vs. 73B01-Gal4>UAS-Kir2.1 (light)	One-way Anova	*	0.022	
	UAS-Kir2.1/- vs. Ilp7-Gal4> UAS-Kir2.1 (light)	One-way Anova	*	0.0308	
	UAS-Kir2.1/- vs. Lk-Gal4> UAS-Kir2.1(light)	One-way Anova	*	0.0354	
Figure S4F	*W1118 vs Ilp7ko*	One-way Anova	n.s.	0.6167	
Figure S4G	*UAS-Kir2.1/- vs. 73B01-GAL4;UAS-Kir2.1*	One-way Anova	n.s.	0.1857	
	UAS-Kir2.1/- vs. ilp7-Gal4;UAS-Kir2.1	One-way Anova	n.s.	0.5927	
	UAS-Kir2.1/- vs. Lk-Gal4;UAS-Kir2.1	One-way Anova	*	0.0247	
Figure S4I	*Lk-Gal4 ; UAS-ChrimsonGFP vs. Lk-*	Chi-Square	***	0.0001	

	Gal4;tub>STOP>Gal80xotdFlp;UAS-ChrimsonGFP				
	Lk.Gal4 ; UAS-ChrimsonGFP vs. LkGAl4+ tshGal80; UAS-ChrimsonGFP	Chi-Square	**	0.0025	
Figure S5E	*ctrl vs. Lk-Gal4>UAS-GCaMP6s ; 27H06-LexA >LexAop-TNT*	One-way Anova	n.s.	0.899	Tukey
	ctrl vs. Lk-Gal4>UAS-GCaMP6s; Ilp7-LexA >LexAop-TNT	One-way Anova	n.s.	0.9859	Tukey
	ctrl vs. Lk-Gal4>UAS-GCaMP6s; GMR-hid	One-way Anova	n.s.	0.7331	Tukey
Figure S6C	*Ilp7-Gal4>UAS-NPRRilp7*	Mann-Whitney test, two tailed	*	0.0286	
Figure S6F	*ctl vs. Lgr4-T2A-Gal4*	unpaired t test, two tailed with Welch`s correction	*	0.03858	
Figure S6G	*ctl vs. Lgr4ko*	unpaired t test, two tailed with Welch`s correction	*	0.01311	
Figure S6H	*Lgr4ko vs. W1118*	unpaired t test, two tailed with Welch`s correction	*	0.0361	

Table S1. Exact *P* values and genotypes, Related to STAR Methods

Primers:	
Ilp7-NotI-c (Ilp7-HA)	aaGCGGCCGCATGACCAGAATGATAATAC
Ilp7-HA-nc (Ilp7-HA)	This paper
ILP7-Nde_nc (Ilp7-GCaMP6s) agaCATATGGTAGTGATTGCGTCGCTTG	AGCATCTCGAGACCCTCCTCGGTGTGCTGCAGcagagatgcgtagtctggcacgtcgtatgggtagctCTGCAGTGCCTC
GCaMP6s-Nde-c (Ilp7-GCaMP6s)	tggCATATGggttctcatcatcatcatc
GCaMP6s-Xba-nc (Ilp7-GCaMP6s)	atctagattacttcgctgtcatcatttgtac
Lgr4-Not-c	acGCGGCCGCATGTGTATAGCTCACCTGC
Lgr4-Xho-nc (Lgr4-flag)	TTGCCTCGAGCAGATAGCTCATCTGCCGGTg
Lgr4-over-c (Lgr4-I263A)	ATTGAGTATTCTCgccTTGGCACGCAACCACCTGCACC
Lgr4-over-nc (Lgr4-I263A)	TGGTTGCGTGCCAAggcGAGAATACTCAATTGATTGC
Lgr4^{T2AGal4} forward	TCACCTCGACAGGGACAGGAA
Lgr4^{T2AGal4} reverse	ACTGCGTGAACGAGGTGGAC
Lgr4^{ko} forward	TGCAGCGATAAGCAGACACCAT
Lgr4^{ko} reverse	GTCCTACGCCTTCTGCTGTTGT
rp49 forward	TTGAGAACGCAGGCGACCGT
rp49 reverse	CGTCTCCTCCAAGAAGCGCAAG

Table S2. Primer sequences, Related to STAR Methods

4 Discussion

4.1 Optimized design and *in vivo* application of optogenetically modified *Drosophila* Dopamine receptors

G protein-coupled receptors (GPCRs) play a critical role in coordinating multicellular physiology and are implicated in various pathological dysfunctions. They rely on diverse extracellular signals to control specific downstream signaling pathways, thereby regulating essential physiological processes. Thus, understanding the molecular function of GPCRs is crucial for assessing their contributions to physiological functions nd their potential as drug targets.

To achieve spatio-temporal precision in controlling GPCR signaling, researchers have developed and utilized chimeric light-activated optoXRs, in conjunction with repurposed naturally occurring opsins (Eichel & von Zastrow, 2018; van Wyk et al., 2015). The design of most published optoXRs has relied on domain boundaries proposed in a seminal study (Kim et al., 2005). Despite extensive efforts, the design of light activated chimeric GPCRs has remained a challenge, in particular to mimic the downstream signaling of endogenous GPCRs. In recent years, this approach has been used to develop a functionalized receptor library, in which secondary structure elements associated with downstream signaling and trafficking of 63 human Class A GPCRs were incorporated into a rhodopsin backbone (Morri et al., 2018). However, they have not been validated *in vivo* so far. In my study, I used an optimized chimeric design combining the signaling function of *Drosophila* dopamine (DA) receptors with the light sensitivity of Rho for *in vivo* application in functional assays (learning, locomotion etc.).

4.1.1 Characterization of optoDopRs activation profiles *in vitro*

In this project, we generated an optogenetically functionalized *Drosophila* receptor library (including the DA and serotonin receptor family) based on previous strategies (Kim et al., 2005; Morri et al 2018). However, most optoXRs displayed different or no signaling compared to wildtype receptors in the cellular assays. We evaluated structure-based alignments and identified receptor residues that are proximal to the Gα-subunits enabling us to better position the domain boundaries in modified chimeric receptors (Tichy et al., 2022).

We successfully generated highly light-sensitive and specific optoDopRs via the optimization of the chimeric optoXR, involving the replacement of the intracellular loop 2-3 (ICL 2-3) of Rho and extending the C-terminus of the target receptor into the transmembrane domain. These optoDopRs exhibit light dose-dependent activation properties, resembling DA-dose dependent activation of the wildtype receptors. Notably, optoDop1R1^{V2} displays efficient activation across a broad spectral range (430 to 595 nm) in cellular assays, which is however still compatible with red-shifted optogenetic tools, such as Chrimson (Klapoetke et al., 2014). This offers a potential for all-optical access to investigate neuronal network function *in vivo,* which involves the control of neuronal activity through ion channels and neuromodulatory pathways.

In my experiments, as well as across the literature, testing the same GPCR in various established signaling assays can lead to different results. I observed that the data from our Gsx assay did not fully reflect the previously reported activity of Dop1R2 (Himmelreich et al., 2017a), which is mostly coupled to G_q and G_s signaling. However, in our Gsx and TRUPATH assays I observed mainly coupling to G_{15} and G_s, the latter showing only minor induction in TRUPATH assay. This might suggest that the chimeric G_q proteins employed in the Gsx and TRUPATH assays may not efficiently bind to Dop1R2 thus not properly reporting its activity. While Gsx and TRUPATH assays monitor $G\alpha_s$ induced cAMP increases or loss of BRET signal upon Gβ/γ dissociation from Gα, respectively, G protein fingerprinting measures the BRET signal increase between Venus-tagged Gβ/γ and Nanoluc-tagged GRK after G protein activation (Masuho et al., 2015). In all of these assays the differential abundance of intracellular signaling modulators may alter signaling outcomes in a cell-specific manner. Moreover, it's important to note that G_{15} belongs to the G_q family and also triggers signaling through the release of intracellular calcium stores (Yang et al., 2021). Similar to DopRs, many GPCRs are promiscuous regarding their G protein selectivity. Thus, the signaling outcome *in vivo* largely depends on the specific cell type and the expressed subsets of G proteins, which cannot be assayed *in vitro*.

4.1.2 Characterization of optoDopR localization and functionality *in vivo*

The proper subcellular localization and cell type-specific signaling is crucial for endogenous GPCR signaling (Lobingier & von Zastrow, 2019; Lohse & Hofmann, 2015; Muntean et al., 2018). Recent findings have demonstrated that second messenger signaling (such as cAMP) can occur in nanodomains with receptor-specific profiles (Anton et al., 2022), suggesting that proper subcellular localization is crucial for the

cellular signaling outcome. The improved optoDopR^{V2}s exhibit localization patterns to somatodendritic and axonal compartments similar to their endogenous counterparts (Kondo et al.,2020). Furthermore, the localization of optoDop1R1^{V2} in MBONs at the single-cell level also resembles the endogenous localization of Dop1R1. In contrast, optoDop1R1^{V1} based on the previous design strategy (Morri et al., 2018) mostly localized to the somatic (or cell body) compartment with a signaling profile different from the wildtype receptor. This suggests that improving the chimeric design, especially of ICL transitions and at the C-terminus is necessary to mimic endogenous receptor localization and function.

I observed that optoDopR activation in larval nociceptive neurons was able to induce escape responses with similarity to cAMP and calcium-induced behavior (Stierl et al., 2011; Dannhäuser et al., 2020). optoDop1R1^{V2} induced a rolling response comparable to the employed positive control using a photoactivated adenylyl cyclase from Beggiatoa (bPAC), which can mediate light-dependent cAMP increase and behavioral changes in freely moving animals (Stierl et al., 2011). Moreover, cAMP imaging (Gflamp1) and calcium imaging (GCaMP6s) to monitor the light-induced cAMP or calcium changes, respectively, showed that activation of optoDop1R1^{V2} preferentially resulted in cAMP responses. Conversely, activation of optoDop1R2^{V2} resulted in robust calcium but not cAMP responses in the mushroom body medial lobe and KC soma region. These results indicate that despite their promiscuous signaling *in vitro*, these optoDopRs can induce receptor-specific signaling *in vivo.*

In the mushroom body of *Drosophila*, each compartment serves as a pivotal site where dopaminergic reinforcement converges. The spatial distribution of dopamine release and the dopamine receptor signaling pathways cascades adhere to the segmented structure of the lobes (Boto et al., 2014), which allows different synapses along the same Kenyon cells (KCs) axon to be regulated independently (Cohn et al., 2015). Dop1R1 has previously been shown to be necessary for cAMP responses in KCs, while Dop1R2 is required for calcium store release during olfactory conditioning (Handler et al., 2019). Thus, precise manipulation of DopR signaling in specific KC compartments would be key for precise functional and behavioral studies. As the optoDopRs localize throughout the entire MB, it is not trivial to mimic compartment specific activation without inadvertently activating additional regions. Consequently, imaging and local activation of optoDopRs could be used for compartment-specific effects in KCs. If

successful, such experiments could further elucidate the temporal activation requirements of DA signaling that are required to induce functional associations *in vivo*.

4.1.3 Behavioral analysis of dopaminergic signaling in *Drosophila*

OptoDopRs can be used for experiments that require modulation during a longer time frame, from minutes to hours. My behavioral experiments showed the functionality of both optoDopR^{V2} variants, demonstrating their ability to partially substitute for endogenous DopRs in various assays, including innate odor preference (Selcho et al., 2009), locomotion (Silva et al., 2020), and learning (Himmelreich et al., 2017). Interestingly, in the locomotion assay, the activation of Dop1R1^{V2} significantly enhanced larval velocity and reduced turning behavior in animals with toxin-induced dopaminergic impairment. However, this effect was not fully replicated in the group using optoDop1R2^{V2}. These results suggest that cAMP but not calcium signaling might play a vital role in modulating locomotion behavior. Moreover, the activation of optoDop1R1^{V2}, but not optoDop1R2^{V2}, promoted adult fly arousal if activated in central circadian clock neurons, consistent with the finding that downregulation of Dop1R1 affects daytime sleep (Fernandez-Chiappe et al., 2020). Conversely, activation of optoDop1R2^{V2}, but not optoDop1R1^{V2}, controlled feeding behavior of adult flies when activated in a valence-encoding subset MBONs. This strongly suggests the cell type-specific requirement of receptor-specific dopamine receptor (DopR) signaling in these behaviors.

DA plays a dual role in learning and forgetting in flies. Dop1R1 expressed in the mushroom body (MB) is essential for memory acquisition, while Dop1R2 is vital for the process of forgetting (Berry et al., 2012). During odor-reward learning in *Drosophila* larvae, odors are detected by olfactory receptor neurons (ORNs), and then forming olfactory preferences through odor-fructose association (Saumweber et al., 2018; Schleyer et al., 2020). The MB plays a central role in this process: Kenyon cells (KCs) receive specific dopaminergic input and in conjunction with MB output neurons (MBONs), form a tripartite circuit that is able to reinforce specific preference behaviors (Saumweber et al., 2018). Furthermore, my findings indicate that acute optoDop1R1^{V2} activation during learning can effectively substitute for endogenous DA signaling in MBONs, which is crucial for odor association reward learning. While DopR function has been extensively studied in KCs, it has not been previously explored in MBONs. Hence, my results strongly suggest that DA signaling also regulates corresponding MB outputs. Consequently, optoDopRs should be valuable tools for gaining insights into the

temporal and cell type-specific requirements of DA signaling in *Drosophila* learning and feeding behavior.

4.1.4 Outlook and future directions

Taken together, I demonstrated that optoDopRs exhibit highly light sensitivity, receptor specific and endogenous-like localization and signaling. In addition, with activation time constants in the seconds range and suitability for repeated light activation, optoDopRs could be a potential tool for the investigation of dopamine dependent behaviors.

Structural biology has had a significant impact on optogenetics by facilitating the rational design of light-activated ion channels and protein-protein interactions (Ziegler et al., 2015, Dagliyan & Hahn 2019). My results demonstrate that the exchange of dopamine (DA) receptor domains, including intracellular loops (ICLs) and C-terminus of transmembrane domain 7 (TM7), yields more potent optoDopRs, enabling their functionality *in vivo*. Nevertheless, due to the complexity of GPCR signaling and the limited examples of demonstrating structure-guided engineering of optoXRs, further studies are necessary to evaluate the universality of this approach. Opto-β2AR-2.0, a recently developed optoXRs using structure-based design of β2AR has led to notable enhancements in the functionality, resulting in a significant improved of its light-induced signaling properties (Tichy et al., 2022). Furthermore, the implementation of spectrally tuned or bistable rhodopsin backbones into chimeric designs shows promise for further expanding the optoXR toolbox. Various studies employing chimeric approaches used mouse Opn4 as a light sensitive opsin (Spoida, Eickelbeck, Karapinar, Eckhardt, Mark, Jancke, Ehinger, König, Dalkara, & Herlitze, 2016; van Wyk et al., 2015). Additionally, native opsins including lamprey parapinopsin (PPO; Copits et al., 2021), mosquito Opn3 (Mahn et al., 2021) and *platynereis dumerilii* ciliary opsin (*Pd*CO; Wietek et al., 2023) have been applied *in vivo*. It is important to notice that optoXRs, cannot entirely replicate the native receptor behavior; nevertheless, combinations of these complementary methods and continually improving the design as well as the functionality of optoXRs should enable efficient chimera generation and native opsins applications, thus allowing *in vivo* studies of other receptors in the future.

4.2 BiPOLES as new tool for bidirectional control of neuronal activity

The optogenetic manipulation of neuronal activity, has evolved into an essential and invaluable experimental approach in the field of neuroscience research. Effective combination of excitatory and inhibitory optogenetic tool allows precise activation or inhibition of genetically targetable neuronal populations. However, there are very few optogenetic tools for achieving bidirectional control over the neuronal activity of the same neurons within a single experiment (Carus-Cadavieco et al., 2017; Gradinaru et al., 2010; Kleinlogel et al., 2011). Additionally, among these available tools, only the combination of a channelrhodopsin 2 variant (ChR2-HR) and microbial halorhodopsin eNpHR3.0 (known as eNPAC2.0) has been successfully applied in mice to investigate neuroscientific questions (Carus-Cadavieco et al., 2017; Gradinaru et al., 2010; Vesuna et al., 2020).

In the newly developed optogenetic tool termed BiPOLES (for Bidirectional Pair of Opsins for Light-induced Excitation and Silencing), a blue-light sensitive anion-conducting channelrhodopsin (ACR, GtACR2) was combined with a red-shifted cation-conducting channelrhodopsin (CCR, Chrimson). BiPOLES introduces a novel optogenetic solution for manipulating excitation or inhibition of the same neurons with red or blue light, respectively. This fusion protein covalently links the two opsins (ACR and CCR) in a 1:1 ratio, allowing excitatory or inhibitory conductance to occur at the cell membrane. BiPOLES has been optimized for efficient membrane trafficking, and with improved expression and enables reliable and potent optogenetic stimulation or suppression *in vivo* (Vierock et al., 2021).

Together with our colleagues, we demonstrated that BiPOLES has a reliable performance in both invertebrate and vertebrate model systems, showing powerful bidirectional modulation in the *C. elegans* motor system, the *D. melanogaster* motor and nociceptive systems, as well as the ferret visual cortex (Vierock et al., 2021). In *Drosophila* larvae, BiPOLES expressed in glutamatergic neurons enables bidirectional control of body contraction and relaxation. Moreover, BiPOLES-dependent manipulation of dorsal pair Ilp7 neurons (Dp7 neurons) in the brain can bidirectionally regulate the nociceptive escape behavior These results suggest that BiPOLES is a suitable tool for investigating locomotion and nociceptive circuits in the fly model (Dason et al., 2020). It's worth noting that the silencing ability of anion channels relies on the extra- and intracellular Cl^- concentration. Therefore, BiPOLES may not be suitable for

achieving bidirectional control over developing neurons or presynaptic boutons (Wiergert et al.,2017). Nonetheless, BiPOLES contributes to the expanding optogenetic toolbox and has the potential to become the tool for investigating a variety of specific behaviors or a cognitive task in living organisms.

4.3 Precise presynaptic silencing with a bistable rhodopsin

Optogenetic silencing serves as a robust tool for functionally dissecting neural circuits and gaining insights into the role of specific neuronal populations in behavioral processes. Nevertheless, effectively silencing long-range axonal projections has presented a formidable challenge. Together with our colleagues, I jointly demonstrated that an optimized mosquito rhodopsin Opn3 (eOPN3) can selectively recruit $G_{i/o}$ signaling in mammalian neurons and showed improved membrane targeting and enhanced expression in long-range axons (Mahn et al., 2021). Furthermore, activation of eOPN3 triggers the $G_{i/o}$ pathway and reduces calcium channel activity, leading to the suppression of neurotransmitter release, suggesting its potential for modulating locomotion behavior in *Drosophila*. However, it is worth noting that the efficacy of $G_{i/o}$-mediated inhibition may vary among cell types and subcellular compartments, and it is influenced by the intrinsic firing patterns and short-term synaptic plasticity of the targeted neurons (Brenowitz et al., 1998). Therefore, electrophysiological characterization of eOPN3 effects is likely required before applying this tool in behavioral experiments.

Optogenetic silencing serves as a robust tool for functionally dissecting neural circuits and gaining insights into the role of specific neuronal populations in behavioral processes. Nevertheless, effectively silencing long-range axonal projections has presented a formidable challenge. Together with our colleagues, I demonstrated that an optimized mosquito rhodopsin Opn3 (eOPN3) can selectively recruit $G_{i/o}$ signaling in mammalian neurons and showed improved membrane targeting and enhanced expression in long-range axons (Mahn et al., 2021). Furthermore, activation of eOPN3 triggers the $G_{i/o}$ pathway and reduces calcium channel activity, leading to the suppression of neurotransmitter release, suggesting its potential for modulating locomotion behavior in *Drosophila*. However, it is worth noting that the efficacy of $G_{i/o}$-mediated inhibition may vary among cell types and subcellular compartments, and it is influenced by the intrinsic firing patterns and short-term synaptic plasticity of the targeted neurons (Brenowitz et al., 1998). Therefore, electrophysiological

characterization of eOPN3 effects are likely required before applying this tool in behavioral experiments.

Similarly, lamprey parapinopsin (PPO) is bistable nonvisual rhodopsins that was recently used for efficient light-gated silencing of synaptic transmission (Copits et al., 2021). Both eOPN3 and PPO have unique spectral features that may enable dual-channel optogenetic control of intracellular signaling. These rhodopsins belong to a family of nonvisual rhodopsins, suggesting the potential for further development of similar tools for controlling presynaptic terminal activity. In summary, eOPN3-mediated silencing of transmitter release offers a valuable approach for light-triggered suppression of neuronal communication in the target area of long-range projections, promising to facilitate various neurobiological studies.

4.4 A neuropeptidergic circuit modulating escape behavior of *Drosophila* larvae

Animals display selective escape behaviors when their nervous system receives a noxious stimulus. How the nociceptive pathways are modulated to elicit appropriate escape behaviors is still not well understood. Hub neurons have the potential to be involved in the computation of several behaviors (Macosko et al., 2009). Mechanonociception in *Drosophila* larvae requires the integration of three mechanosensory neuron subtypes (namely C2da, C3da, and C4da) by dorsal pair insulin-like peptide 7 (Dp7) neurons (Miguel-Aliaga et al., 2008), which provide neuropeptidergic feedback via short neuropeptide F (sNPF) (Hu et al.,2017) . In this study, we showed the role of Dp7 neurons that acts as a regulatory hub in gating specific network responses. These hub neurons facilitate the integration and regulation of behavioral responses to mechanosensitive and nociceptive input, modulating alternative escape behaviors based on input-specific neuropeptide function (Imambocus et al., 2022). In addition, we identified specific sensory neurons, C4da neurons and v'td2 neurons, playing key roles in the response to noxious light. These neurons transmit the light signal to ABLK neurons via Dp7 neurons and MIP interneurons (Figure 5).

The co-release of small-molecule neurotransmitters and neuropeptides has been well-documented in both vertebrates and invertebrates (Hökfelt et al., 2018; Nusbaum et al., 2017; van den Pol, 2012). However, the acute signaling function of neuropeptides in sensory behavior has remained unclear. We showed that noxious light triggers the

acute release of insulin-like peptide 7 (Ilp7) in a local region of Dp7 neurons, which acts on downstream neurons expressing the Lgr4 receptor. This suggests that Ilp7 can serve as a co-transmitter, playing a critical role in network activation and behavioral responses. In summary, our findings strongly indicate that neuropeptidergic signals can have an acute impact on the physical neuronal network, promoting specific network activities to elicit innate behaviors such as escape behavior.

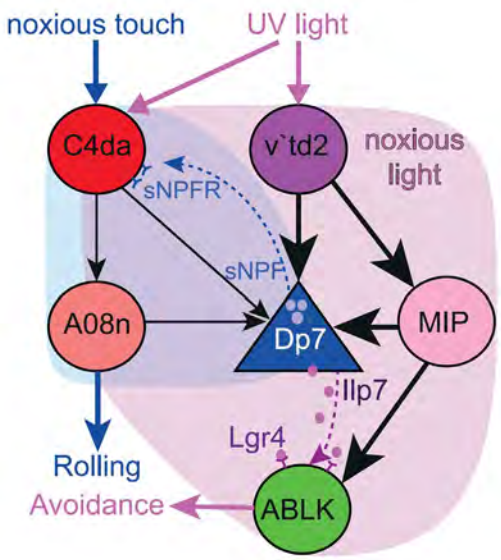

Figure 5. Neuromodulatory decoding of nociceptive escape behaviors. Model depicting neural and molecular elements shaping the larval somatosensory escape circuit, with specific action of sNPF or Ilp7 on mechanonociception versus noxious light resulting in rolling or avoidance, respectively. Figure and legend adapted from Imambocus et al., 2022.

4.5 Concluding remarks

In this thesis, I characterized a number of novel optogenetic tools for optical control of neuronal activity and modulating related behaviors (Figure 6). Firstly, I generated and optimized chimeric OptoDopRs for functional studies in *Drosophila melanogaster.* I showed the specific and light dose dependent activity of optoDopRs by cellular assay. Moreover, I also showed that optoDopRs can at least partially replace endogenous DA signaling in various behaviors, including locomotion, odor preference, and reward learning. Secondly, I used locomotion assays to functionally characterize BiPOLES, which combines in a single fusion protein with the blue-light-sensitive ACR and the red-light-sensitive cation CCR. BiPOLES enables reliable bidirectional control of neuronal activity with red and blue light. Thirdly, I showed that eOPN3, which is a mosquito rhodopsin, couples specifically to $G_{i/o}$ signaling. eOPN3 was introduced as a novel

optogenetic tool for achieving rapid and reversible light-induced suppression of neurotransmitter release. Lastly, I also investigated the Dp7 neurons as regulatory hubs in gating escape behavior responses. Taken together, the present thesis brings together new strategies to develop and characterize specific optogenetic tools that could help facilitating various neurobiological studies.

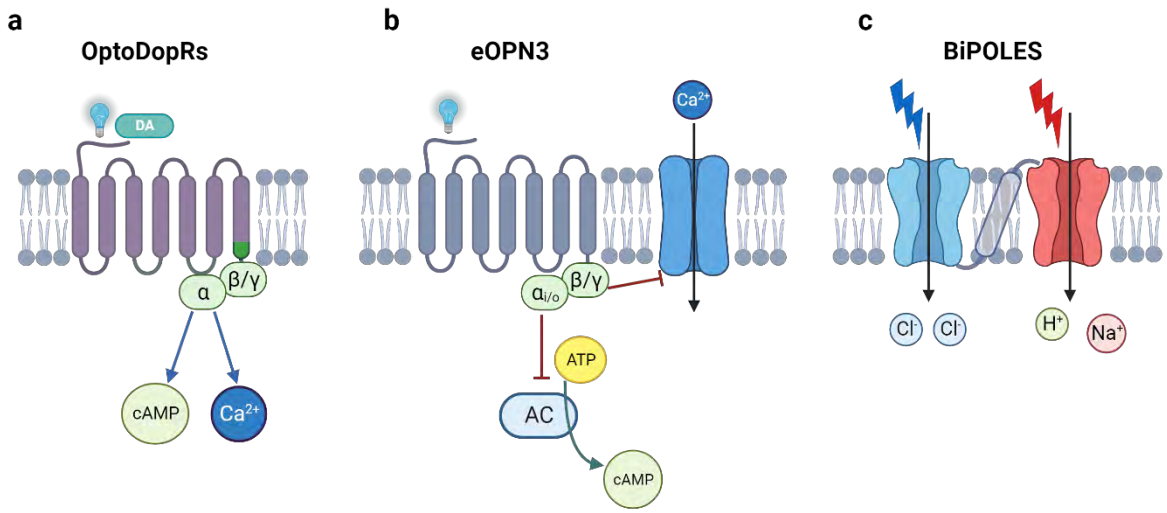

Figure 6. Schematic of optogenetic tools used in this thesis. a. An activation of optoDopRs mediate downstream signaling via different G protein family (cAMP: $G\alpha_s$; Ca^{2+}: $G\alpha_q$). **b.** Light activated eOPN3 leads to inhibition of voltage-gated Ca^{2+} channels as well as reduced cAMP levels (red arrow). The $G_{i/o}$ signaling able to reduces the synaptic vesicle release probability. ATP: adenosine triphosphate; AC: Adenylate cyclase; cAMP: cyclic adenosine monophosphate. **c.** By pairing a blue-light-sensitive ACR (GtACR2) with a red-shifted CCR (Chrimson), BiPOLES allows dual-color bidirectional control of the same neurons.

5 General Summary

5.1 English summary

Precise control over G-protein-coupled receptors (GPCRs) signaling is key to understanding their role in physiology and potential as drug targets. Light-activated chimeric GPCRs (optoXRs) combining naturally occurring opsins with the desired signaling properties have been developed to study the function of target GPCRs. Despite extensive efforts however, achieving functional optoXRs has remained a challenge.

In this thesis, I investigated newly designed optogenetically modified dopamine receptors (optoDopRs) to study Dopaminergic signaling and receptor-specific function in *Drosophila*. *In vitro*, I characterized optoDopR signaling and found that the optimized design resulted in improved signaling specificity and light sensitivity. These optimized optoDopRs offer a broad range of activation wavelengths, making them compatible with other optogenetic tools, such as the cation channelrhodopsin Chrimson. *In vivo*, I observed that optimized optoDopRs exhibited a localization pattern and signaling responses similar to the endogenous dopamine receptors. Second, I showed that the optoDopR variants could functionally replace endogenous DopRs in various behavioral experiments, including odor preference, locomotion, and odor-reward learning. Furthermore, specific behaviors such as arousal and feeding were influenced by cell type-specific optoDopR activation. Taken together, I demonstrated that optoDopRs display high light sensitivity, cell type specificity, and endogenous-like dopaminergic signaling. Future strategies like structure-based design and the use of spectrally tuned or bistable rhodopsin backbones could provide further strategies to extend the optogenetic toolbox. The improved design of optoDopRs as shown here should thus offer a valuable tool for studying DA signaling *in vitro* and *in vivo*.

5.2 German summary

Die genaue Kontrolle der Signalübertragung von G-Protein-gekoppelten Rezeptoren (GPCRs) ist der Schlüssel zum Verständnis ihrer Rolle in der Physiologie und ihres pharmakologischen Potenzials. Lichtaktivierte chimäre GPCRs (optoXRs), die natürlich vorkommende Opsine mit den gewünschten Signaleigenschaften kombinieren, wurden entwickelt, um die Funktion von Ziel-GPCRs zu untersuchen. Trotz umfangreicher Bemühungen ist es jedoch eine Herausforderung geblieben, funktionale optoXRs zu entwickeln.

In dieser Arbeit untersuchte ich neu entwickelte optogenetisch modifizierte Dopaminrezeptoren (optoDopRs), um die dopaminerge Signalübertragung und rezeptorspezifische Funktionen in *Drosophila* zu untersuchen. *In vitro* habe ich die optoDopR-Signalübertragung charakterisiert und festgestellt, dass das optimierte Design zu einer verbesserten Signalspezifität und Lichtempfindlichkeit führt. Diese optimierten optoDopRs bieten ein breites Spektrum an Aktivierungswellenlängen, sind aber dennoch mit anderen optogenetischen Werkzeugen, wie dem Kationenkanalrhodopsin Chrimson, kompatibel. *In vivo* konnte ich beobachten, dass die optimierten optoDopRs ein ähnliches Lokalisierungsmuster und ähnliche Signaltransduktion wie die endogenen Dopaminrezeptoren aufweisen. Zweitens konnte ich zeigen, dass die optoDopR-Varianten die endogenen DopRs in verschiedenen Verhaltensexperimenten funktionell ersetzen können, z. B. bei der Geruchspräferenz, der Fortbewegung und dem Lernen von Geruchsbelohnungen. Darüber hinaus wurden bestimmte Verhaltensweisen wie Erregung und Fütterung durch zelltypspezifische optoDopR-Aktivierung beeinflusst. Insgesamt konnte ich zeigen, dass optoDopRs eine hohe Lichtempfindlichkeit, Zelltypspezifität und eine endogen-ähnliche dopaminerge Signalübertragung aufweisen. Zukünftige Strategien wie strukturbasiertes Design und die Verwendung von spektral abgestimmten oder bistabilen Rhodopsin-Rückgraten könnten weitere Strategien zur Erweiterung des optogenetischen Instrumentariums bieten. Das verbesserte Design von optoDopRs, wie hier gezeigt, sollte daher ein wertvolles Werkzeug für die Untersuchung der DA-Signalübertragung *in vitro* und *in vivo* darstellen.

6 Bibliography

1. Airan, R. D., Thompson, K. R., Fenno, L. E., Bernstein, H., & Deisseroth, K. (2009). Temporally precise *in vivo* control of intracellular signalling. Nature, 458(7241), 1025–1029.
2. Andersen, P. H., Gingrich, J. A., Bates, M. D., Dearry, A., Falardeau, P., Senogles, S. E., & Caron, M. G. (1990). Dopamine receptor subtypes: beyond the D1/D2 classification. Trends in Pharmacological Sciences, 11(6), 231–236. https://doi.org/10.1016/0165-6147(90)90249-8
3. Anton, S. E., Kayser, C., Maiellaro, I., Nemec, K., Möller, J., Koschinski, A., Zaccolo, M., Annibale, P., Falcke, M., & Lohse, M. J. (2022). Receptor-associated independent cAMP nanodomains mediate spatiotemporal specificity of GPCR signaling. Cell, 185(7), 1130–1142.
4. Aso, Y., Sitaraman, D., Ichinose, T., Kaun, K. R., Vogt, K., Belliart-Guérin, G., Plaçais, P.-Y., Robie, A. A., Yamagata, N., & Schnaitmann, C. (2014). Mushroom body output neurons encode valence and guide memory-based action selection in *Drosophila*. Elife, 3, e04580.
5. Ayano, G. (2016). Dopamine: receptors, functions, synthesis, pathways, locations and mental disorders: review of literatures. J Ment Disord Treat, 2(120), 2.
6. Baik, J.-H. (2013). Dopamine signaling in reward-related behaviors. Frontiers in Neural Circuits, 7, 152.
7. Baines, R. A., Uhler, J. P., Thompson, A., Sweeney, S. T., & Bate, M. (2001). Altered electrical properties in *Drosophila*neurons developing without synaptic transmission. Journal of Neuroscience, 21(5), 1523–1531.
8. Ballister, E. R., Rodgers, J., Martial, F., & Lucas, R. J. (2018). A live cell assay of GPCR coupling allows identification of optogenetic tools for controlling Go and Gi signaling. BMC Biology, 16(1). https://doi.org/10.1186/s12915-017-0475-2
9. Bargmann, C. I., & Marder, E. (2013). From the connectome to brain function. Nature Methods, 10(6), 483–490. https://doi.org/10.1038/nmeth.2451
10. Bellmann-Sickert, K., & Beck-Sickinger, A. G. (2010). Peptide drugs to target G protein-coupled receptors. Trends in Pharmacological Sciences, 31(9), 434–441.
11. Berridge, M. J. (2009). Inositol trisphosphate and calcium signalling mechanisms. Biochimica et Biophysica Acta (BBA)-Molecular Cell Research, 1793(6), 933–940.
12. Berridge, M. J. (2016). The inositol trisphosphate/calcium signaling pathway in health and disease. Physiological Reviews, 96(4), 1261–1296.
13. Berry, B. J., Trewin, A. J., Milliken, A. S., Baldzizhar, A., Amitrano, A. M., Lim, Y., Kim, M., & Wojtovich, A. P. (2020). Optogenetic control of mitochondrial protonmotive force

to impact cellular stress resistance. EMBO Reports, 21(4). https://doi.org/10.15252/embr.201949113

14. Berry, J. A., Cervantes-Sandoval, I., Nicholas, E. P., & Davis, R. L. (2012). Dopamine Is Required for Learning and Forgetting in *Drosophila*. Neuron, 74(3), 530–542. https://doi.org/10.1016/j.neuron.2012.04.007
15. Boto, T., Louis, T., Jindachomthong, K., Jalink, K., & Tomchik, S. M. (2014). Dopaminergic modulation of cAMP drives nonlinear plasticity across the *Drosophila* mushroom body lobes. Current Biology, 24(8), 822–831. https://doi.org/10.1016/j.cub.2014.03.021
16. Brenowitz, S., David, J., & Trussell, L. (1998). Enhancement of Synaptic Efficacy by Presynaptic GABAB Receptors. Neuron, 20(1), 135–141. https://doi.org/10.1016/s0896-6273(00)80441-9
17. Bulenger, S., Marullo, S., & Bouvier, M. (2005). Emerging role of homo- and heterodimerization in G-protein-coupled receptor biosynthesis and maturation. Trends in Pharmacological Sciences, 26(3), 131–137. https://doi.org/10.1016/j.tips.2005.01.004
18. Čapek, D., Smutny, M., Tichy, A.-M., Morri, M., Janovjak, H., & Heisenberg, C.-P. (2019). Light-activated Frizzled7 reveals a permissive role of non-canonical wnt signaling in mesendoderm cell migration. Elife, 8, e42093.
19. Carus-Cadavieco, M., Gorbati, M., Ye, L., Bender, F., van der Veldt, S., Kosse, C., Börgers, C., Lee, S. Y., Ramakrishnan, C., & Hu, Y. (2017). Gamma oscillations organize top-down signalling to hypothalamus and enable food seeking. Nature, 542(7640), 232–236.
20. Cehajic-Kapetanovic, J., Eleftheriou, C., Allen, A. E., Milosavljevic, N., Pienaar, A., Bedford, R., Davis, K. E., Bishop, P. N., & Lucas, R. J. (2015). Restoration of Vision with Ectopic Expression of Human Rod Opsin. Current Biology, 25(16), 2111–2122. https://doi.org/10.1016/j.cub.2015.07.029
21. Chen, T.-W., Wardill, T. J., Sun, Y., Pulver, S. R., Renninger, S. L., Baohan, A., Schreiter, E. R., Kerr, R. A., Orger, M. B., & Jayaraman, V. (2013). Ultrasensitive fluorescent proteins for imaging neuronal activity. Nature, 499(7458), 295–300.
22. Christenson, J. G., Dairman, W., & Udenfriend, S. (1970). Preparation and properties of a homogeneous aromatic L-amino acid decarboxylase from hog kidney. Archives of Biochemistry and Biophysics, 141(1), 356–367.
23. Cohn, R., Morantte, I., & Ruta, V. (2015). Coordinated and Compartmentalized Neuromodulation Shapes Sensory Processing in *Drosophila*. Cell, 163(7), 1742–1755. https://doi.org/10.1016/j.cell.2015.11.019
24. Copits, B. A., Gowrishankar, R., O'Neill, P. R., Li, J.-N., Girven, K. S., Yoo, J. J., Meshik, X., Parker, K. E., Spangler, S. M., & Elerding, A. J. (2021). A photoswitchable GPCR-

based opsin for presynaptic inhibition. Neuron, 109(11), 1791–1809.

25. Dagliyan, O. & Hahn, K.M. (2019). Controlling protein conformation with light. Curr Opin Struct Biol 57, 17-22 .
26. Dannhäuser, S., Lux, T. J., Hu, C., Selcho, M., Chen, J. T. C., Ehmann, N., Sachidanandan, D., Stopp, S., Pauls, D., & Pawlak, M. (2020). Antinociceptive modulation by the adhesion GPCR CIRL promotes mechanosensory signal discrimination. Elife, 9, e56738.
27. Dason, J. S., Cheung, A., Anreiter, I., Montemurri, V. A., Allen, A. M., & Sokolowski, M. B. (2020). *Drosophila* melanogaster foraging regulates a nociceptive-like escape behavior through a developmentally plastic sensory circuit. Proceedings of the National Academy of Sciences, 117(38), 23286–23291.
28. Deisseroth, K. (2011). Optogenetics. Nature Methods, 8(1), 26–29.
29. Deisseroth, K. (2015). Optogenetics: 10 years of microbial opsins in neuroscience. Nature Neuroscience, 18(9), 1213–1225.
30. Deisseroth, K., & Hegemann, P. (2017). The form and function of channelrhodopsin. Science, 357(6356). https://doi.org/10.1126/science.aan5544
31. Deng, B., Li, Q., Liu, X., Cao, Y., Li, B., Qian, Y., Xu, R., Mao, R., Zhou, E., Zhang, W., Huang, J., & Rao, Y. (2019). Chemoconnectomics: Mapping Chemical Transmission in *Drosophila*. Neuron, 101(5), 876-893.e4. https://doi.org/10.1016/j.neuron.2019.01.045
32. Edgar, R. C. (n.d.). MUSCLE: multiple sequence alignment with improved accuracy and speed. In Proceedings. 2004 IEEE Computational Systems Bioinformatics Conference, 2004. CSB 2004. IEEE. https://doi.org/10.1109/csb.2004.1332560
33. Eichel, K., & von Zastrow, M. (2018). Subcellular Organization of GPCR Signaling. Trends in Pharmacological Sciences, 39(2), 200–208. https://doi.org/10.1016/j.tips.2017.11.009
34. Eickelbeck, D., Karapinar, R., Jack, A., Suess, S. T., Barzan, R., Azimi, Z., Surdin, T., Grömmke, M., Mark, M. D., Gerwert, K., Jancke, D., Wahle, P., Spoida, K., & Herlitze, S. (2019). CaMello-XR enables visualization and optogenetic control of Gq/11 signals and receptor trafficking in GPCR-specific domains. Communications Biology, 2(1). https://doi.org/10.1038/s42003-019-0292-y
35. Fernandez-Chiappe, F., Hermann-Luibl, C., Peteranderl, A., Reinhard, N., Senthilan, P. R., Hieke, M., Selcho, M., Yoshii, T., Shafer, O. T., Muraro, N. I., & Helfrich-Förster, C. (2020). Dopamine signaling in wake-promoting clock neurons is not required for the normal regulation of sleep in *Drosophila*. Journal of Neuroscience, 40(50), 9617–9633. https://doi.org/10.1523/JNEUROSCI.1488-20.2020
36. Flock, T., Hauser, A. S., Lund, N., Gloriam, D. E., Balaji, S., & Babu, M. M. (2017). Selectivity determinants of GPCR–G-protein binding. Nature, 545(7654), 317–322. https://doi.org/10.1038/nature22070

37. Franco, R., Lluis, C., Canela, E. I., Mallol, J., Agnati, L., Casadó, V., Ciruela, F., Ferré, S., & Fuxe, K. (2006). Receptor–receptor interactions involving adenosine A1 or dopamine D1 receptors and accessory proteins. Journal of Neural Transmission, 114(1), 93–104. https://doi.org/10.1007/s00702-006-0566-7
38. Fredriksson, R., Lagerström, M. C., Lundin, L.-G., & Schiöth, H. B. (2003). The G-Protein-Coupled Receptors in the Human Genome Form Five Main Families. Phylogenetic Analysis, Paralogon Groups, and Fingerprints. Molecular Pharmacology, 63(6), 1256–1272. https://doi.org/10.1124/mol.63.6.1256
39. Gao, S., Nagpal, J., Schneider, M. W., Kozjak-Pavlovic, V., Nagel, G., & Gottschalk, A. (2015). Optogenetic manipulation of cGMP in cells and animals by the tightly light-regulated guanylyl-cyclase opsin CyclOp. Nature Communications, 6(1), 8046.
40. Gardner, B. R., Hall, D. A., & Strange, P. G. (1997). Agonist action at D2 (short) dopamine receptors determined in ligand binding and functional assays. Journal of Neurochemistry, 69(6), 2589–2598.
41. Gardner, B., Hall, D. A., & Strange, P. G. (1996). Pharmacological analysis of dopamine stimulation of [35S]-GTPγS binding via human D2short and D2long dopamine receptors expressed in recombinant cells. British Journal of Pharmacology, 118(6), 1544–1550.
42. Gerber, B., Biernacki, R., & Thum, J. (2013). Odor–Taste Learning Assays in *Drosophila* Larvae. Cold Spring Harbor Protocols, 2013(3), pdb.prot071639. https://doi.org/10.1101/pdb.prot071639
43. Gilman, A. G. (1987). G proteins: transducers of receptor-generated signals. Annual Review of Biochemistry, 56(1), 615–649.
44. Girault, J.-A., & Greengard, P. (2004). The Neurobiology of Dopamine Signaling. Archives of Neurology, 61(5), 641. https://doi.org/10.1001/archneur.61.5.641
45. Gradinaru, V., Zhang, F., Ramakrishnan, C., Mattis, J., Prakash, R., Diester, I., Goshen, I., Thompson, K. R., & Deisseroth, K. (2010). Molecular and Cellular Approaches for Diversifying and Extending Optogenetics. Cell, 141(1), 154–165. https://doi.org/10.1016/j.cell.2010.02.037
46. Greengard, P. (2001). The neurobiology of slow synaptic transmission. Science, 294(5544), 1024–1030.
47. Grönke, S., Clarke, D.-F., Broughton, S., Andrews, T. D., & Partridge, L. (2010). Molecular evolution and functional characterization of *Drosophila* insulin-like peptides. PLoS Genetics, 6(2), e1000857.
48. Gurevich, E. V, Benovic, J. L., & Gurevich, V. V. (2002). Arrestin2 and arrestin3 are differentially expressed in the rat brain during postnatal development. Neuroscience, 109(3), 421–436. https://doi.org/10.1016/s0306-4522(01)00511-5
49. Guru, A., Post, R. J., Ho, Y.-Y., & Warden, M. R. (2015). Making sense of optogenetics. International Journal of Neuropsychopharmacology, 18(11), pyv079.

50. Han, C., Jan, L. Y., & Jan, Y.-N. (2011). Enhancer-driven membrane markers for analysis of nonautonomous mechanisms reveal neuron–glia interactions in *Drosophila*. Proceedings of the National Academy of Sciences, 108(23), 9673–9678. https://doi.org/10.1073/pnas.1106386108
51. Han, K.-A., Millar, N. S., Grotewiel, M. S., & Davis, R. L. (1996). DAMB, a novel dopamine receptor expressed specifically in *Drosophila* mushroom bodies. Neuron, 16(6), 1127–1135.
52. Handler, A., Graham, T. G. W., Cohn, R., Morantte, I., Siliciano, A. F., Zeng, J., Li, Y., & Ruta, V. (2019). Distinct Dopamine Receptor Pathways Underlie the Temporal Sensitivity of Associative Learning. Cell, 178(1), 60-75.e19. https://doi.org/10.1016/j.cell.2019.05.040
53. Heisenberg, M. (2003). Mushroom body memoir: from maps to models. Nature Reviews Neuroscience, 4(4), 266-275.
54. Herve, D., Le Moine, C., Corvol, J.-C., Belluscio, L., Ledent, C., Fienberg, A. A., Jaber, M., Studler, J.-M., & Girault, J.-A. (2001). Gαolf levels are regulated by receptor usage and control dopamine and adenosine action in the striatum. Journal of Neuroscience, 21(12), 4390–4399.
55. Himmelreich, S., Masuho, I., Berry, J. A., MacMullen, C., Skamangas, N. K., Martemyanov, K. A., & Davis, R. L. (2017). Dopamine Receptor DAMB Signals via Gq to Mediate Forgetting in *Drosophila*. Cell Reports, 21(8), 2074–2081. https://doi.org/10.1016/j.celrep.2017.10.108
56. Hisahara, S., & Shimohama, S. (2011). Dopamine receptors and Parkinson's disease. International Journal of Medicinal Chemistry, 2011.
57. Hökfelt, T., Barde, S., Xu, Z.-Q. D., Kuteeva, E., Rüegg, J., Le Maitre, E., Risling, M., Kehr, J., Ihnatko, R., & Theodorsson, E. (2018). Neuropeptide and small transmitter coexistence: fundamental studies and relevance to mental illness. Frontiers in Neural Circuits, 12, 106.
58. Hu, C., Petersen, M., Hoyer, N., Spitzweck, B., Tenedini, F., Wang, D., Gruschka, A., Burchardt, L. S., Szpotowicz, E., Schweizer, M., Guntur, A. R., Yang, C. H., & Soba, P. (2017). Sensory integration and neuromodulatory feedback facilitate *Drosophila* mechanonociceptive behavior. Nature Neuroscience. https://doi.org/10.1038/nn.4580
59. Hwang, R. Y., Zhong, L., Xu, Y., Johnson, T., Zhang, F., Deisseroth, K., & Tracey, W. D. (2007). Nociceptive neurons protect *Drosophila* larvae from parasitoid wasps. Current Biology, 17(24), 2105–2116.
60. Imambocus, B. N., Zhou, F., Formozov, A., Wittich, A., Tenedini, F. M., Hu, C., Sauter, K., Varela, E. M., Herédia, F., & Casimiro, A. P. (2022). A neuropeptidergic circuit gates selective escape behavior of *Drosophila* larvae. Current Biology, 32(1), 149–163.
61. Jennings, B. H. (2011). *Drosophila* – a versatile model in biology & medicine.

Materials Today, 14(5), 190–195. https://doi.org/10.1016/s1369-7021(11)70113-4

62. Jose, P. A., Yu, P.-Y., Yamapchi, I., Eisner, G. M., Mouradian, M. M., Felder, C. C., & Felder, R. A. (1995). Dopamine D1 receptor regulation of phospholipase C. Hypertension Research, 18(SupplementI), S39–S42.
63. Karunarathne, W. K. A., Giri, L., Kalyanaraman, V., & Gautam, N. (2013). Optically triggering spatiotemporally confined GPCR activity in a cell and programming neurite initiation and extension. Proceedings of the National Academy of Sciences, 110(17). https://doi.org/10.1073/pnas.1220697110
64. Kaun, K. R., & Rothenfluh, A. (2017). Dopaminergic rules of engagement for memory in *Drosophila*. Current Opinion in Neurobiology, 43, 56–62. https://doi.org/10.1016/j.conb.2016.12.011
65. Kebabian, J. W., & Calne, D. B. (1979). Multiple receptors for dopamine. Nature, 277(5692), 93–96.
66. Kebabian, J. W., & Greengard, P. (1971). Dopamine-sensitive adenyl cyclase: possible role in synaptic transmission. Science, 174(4016), 1346–1349.
67. Kim, J. M., Hwa, J., Garriga, P., Reeves, P. J., RajBhandary, U. L., & Khorana, H. G. (2005). Light-driven activation of β2-adrenergic receptor signaling by a chimeric rhodopsin containing the β2-adrenergic receptor cytoplasmic loops. Biochemistry, 44(7), 2284–2292. https://doi.org/10.1021/bi048328i
68. Kim, Y.-C., Lee, H.-G., Seong, C.-S., & Han, K. (2003). Expression of a D1 dopamine receptor dDA1/DmDOP1 in the central nervous system of *Drosophila* melanogaster. Gene Expression Patterns : GEP, 3, 237–245. https://doi.org/10.1016/S1567-133X(02)00098-4
69. Klapoetke, N. C., Murata, Y., Kim, S. S., Pulver, S. R., Birdsey-Benson, A., Cho, Y. K., Morimoto, T. K., Chuong, A. S., Carpenter, E. J., & Tian, Z. (2014). Independent optical excitation of distinct neural populations. Nature Methods, 11(3), 338–346.
70. Klein, M. O., Battagello, D. S., Cardoso, A. R., Hauser, D. N., Bittencourt, J. C., & Correa, R. G. (2018). Dopamine: Functions, Signaling, and Association with Neurological Diseases. Cellular and Molecular Neurobiology, 39(1), 31–59. https://doi.org/10.1007/s10571-018-0632-3
71. Kleinlogel, S. (2016). Optogenetic user s guide to Opto-GPCRs. Frontiers in Bioscience, 21(4), 794–805. https://doi.org/10.2741/4421
72. Kleinlogel, S., Terpitz, U., Legrum, B., Gökbuget, D., Boyden, E. S., Bamann, C., Wood, P. G., & Bamberg, E. (2011). A gene-fusion strategy for stoichiometric and co-localized expression of light-gated membrane proteins. Nature Methods, 8(12), 1083–1088. https://doi.org/10.1038/nmeth.1766
73. Kondo, S., Takahashi, T., Yamagata, N., Imanishi, Y., Katow, H., Hiramatsu, S., Lynn, K., Abe, A., Kumaraswamy, A., & Tanimoto, H. (2020). Neurochemical Organization of

the *Drosophila* Brain Visualized by Endogenously Tagged Neurotransmitter Receptors. Cell Reports, 30(1), 284-297.e5. https://doi.org/10.1016/j.celrep.2019.12.018

74. Landayan, D., Feldman, D. S., & Wolf, F. W. (2018). Satiation state-dependent dopaminergic control of foraging in *Drosophila*. Scientific Reports, 8(1), 5777.
75. Lefkowitz, R. J. (2004). Historical review: a brief history and personal retrospective of seven-transmembrane receptors. Trends in Pharmacological Sciences, 25(8), 413–422.
76. Levesque, D., Diaz, J., Pilon, C., Martres, M. P., Giros, B., Souil, E., Schott, D., Morgat, J.-L., Schwartz, J.-C., & Sokoloff, P. (1992). Identification, characterization, and localization of the dopamine D3 receptor in rat brain using 7-[3H] hydroxy-N, N-di-n-propyl-2-aminotetralin. Proceedings of the National Academy of Sciences, 89(17), 8155–8159.
77. Lobingier, B. T., & von Zastrow, M. (2019). When trafficking and signaling mix: How subcellular location shapes G protein-coupled receptor activation of heterotrimeric G proteins. Traffic, 20(2), 130–136. https://doi.org/10.1111/tra.12634
78. Lohse, M. J., & Hofmann, K. P. (2015). Spatial and Temporal Aspects of Signaling by G-Protein–Coupled Receptors. Molecular Pharmacology, 88(3), 572–578. https://doi.org/10.1124/mol.115.100248
79. Lou, H. C., Rosa, P., Pryds, O., Karrebæk, H., Lunding, J., Cumming, P., & Gjedde, A. (2004). ADHD: increased dopamine receptor availability linked to attention deficit and low neonatal cerebral blood flow. Developmental Medicine and Child Neurology, 46(3), 179–183.
80. Luttrell, L. M., & Lefkowitz, R. J. (2002). The role of β-arrestins in the termination and transduction of G-protein-coupled receptor signals. Journal of Cell Science, 115(3), 455–465.
81. Macosko, E. Z., Pokala, N., Feinberg, E. H., Chalasani, S. H., Butcher, R. A., Clardy, J., & Bargmann, C. I. (2009). A hub-and-spoke circuit drives pheromone attraction and social behaviour in C. elegans. Nature, 458(7242), 1171–1175. https://doi.org/10.1038/nature07886
82. Mahn, M., Saraf-Sinik, I., Patil, P., Pulin, M., Bitton, E., Karalis, N., Bruentgens, F., Palgi, S., Gat, A., & Dine, J. (2021). Efficient optogenetic silencing of neurotransmitter release with a mosquito rhodopsin. Neuron, 109(10), 1621–1635.
83. Margolis, B., Rhee, S. G., Felder, S., Mervic, M., Lyall, R., Levitzki, A., Ullrich, A., Zilberstein, A., & Schlessinger, J. (1989). EGF induces tyrosine phosphorylation of phospholipase C-II: a potential mechanism for EGF receptor signaling. Cell, 57(7), 1101–1107.
84. Masuho, I., Ostrovskaya, O., Kramer, G. M., Jones, C. D., Xie, K., & Martemyanov, K. A. (2015). Distinct profiles of functional discrimination among G proteins determine the actions of G protein–coupled receptors. Science Signaling, 8(405), ra123–ra123.

85. Miguel-Aliaga, I., Thor, S., & Gould, A. P. (2008). Postmitotic specification of *Drosophila* insulinergic neurons from pioneer neurons. PLoS Biology, 6(3), e58.
86. Milner, B., Squire, L. R., & Kandel, E. R. (1998). Cognitive neuroscience and the study of memory. Neuron, 20(3), 445–468. https://doi.org/10.1016/S0896-6273(00)80987-3
87. Missale, C., NASH, S. R., ROBINSON, S. W., JABER, M., & CARON, M. G. (1998). Dopamine Receptors: From Structure to Function. Physiological Reviews, 78(1), 189–225. https://doi.org/10.1152/physrev.1998.78.1.189
88. Morri, M., Sanchez-Romero, I., Tichy, A. M., Kainrath, S., Gerrard, E. J., Hirschfeld, P. P., Schwarz, J., & Janovjak, H. (2018). Optical functionalization of human Class A orphan G-protein-coupled receptors. Nature Communications, 9(1), 1950. https://doi.org/10.1038/s41467-018-04342-1
89. Muntean, B. S., Zucca, S., MacMullen, C. M., Dao, M. T., Johnston, C., Iwamoto, H., Blakely, R. D., Davis, R. L., & Martemyanov, K. A. (2018). Interrogating the Spatiotemporal Landscape of Neuromodulatory GPCR Signaling by Real-Time Imaging of cAMP in Intact Neurons and Circuits. Cell Reports, 22(1), 255–268. https://doi.org/10.1016/j.celrep.2017.12.022
90. Nagel, G., Ollig, D., Fuhrmann, M., Kateriya, S., Musti, A. M., Bamberg, E., & Hegemann, P. (2002). Channelrhodopsin-1: A Light-Gated Proton Channel in Green Algae. Science, 296(5577), 2395–2398. https://doi.org/10.1126/science.1072068
91. Nässel, D. R. (2018). Substrates for Neuronal Cotransmission With Neuropeptides and Small Molecule Neurotransmitters in *Drosophila*. Frontiers in Cellular Neuroscience, 12. https://doi.org/10.3389/fncel.2018.00083
92. Nässel, D. R., & Zandawala, M. (2019). Recent advances in neuropeptide signaling in *Drosophila*, from genes to physiology and behavior. Progress in Neurobiology, 179, 101607. https://doi.org/10.1016/j.pneurobio.2019.02.003
93. Noyes, N. C., Walkinshaw, E., & Davis, R. L. (2020). Ras acts as a molecular switch between two forms of consolidated memory in *Drosophila*. Proceedings of the National Academy of Sciences of the United States of America, 117(4), 2133–2139. https://doi.org/10.1073/pnas.1819925117
94. Nusbaum, M. P., Blitz, D. M., & Marder, E. (2017). Functional consequences of neuropeptide and small-molecule co-transmission. Nature Reviews Neuroscience, 18(7), 389–403. https://doi.org/10.1038/nrn.2017.56
95. Olsen, R. H. J., DiBerto, J. F., English, J. G., Glaudin, A. M., Krumm, B. E., Slocum, S. T., Che, T., Gavin, A. C., McCorvy, J. D., & Roth, B. L. (2020). TRUPATH, an open-source biosensor platform for interrogating the GPCR transducerome. Nature Chemical Biology, 16(8), 841–849.
96. Peeters, M. C., Van Westen, G. J. P., Li, Q., & IJzerman, A. P. (2011). Importance of the extracellular loops in G protein-coupled receptors for ligand recognition and receptor

activation. Trends in Pharmacological Sciences, 32(1), 35–42.

97. Pulver, S. R., Pashkovski, S. L., Hornstein, N. J., Garrity, P. A., & Griffith, L. C. (2009). Temporal dynamics of neuronal activation by Channelrhodopsin-2 and TRPA1 determine behavioral output in *Drosophila* larvae. Journal of Neurophysiology, 101(6), 3075–3088.
98. Reiter, E., & Lefkowitz, R. J. (2006). GRKs and β-arrestins: roles in receptor silencing, trafficking and signaling. Trends in Endocrinology & Metabolism, 17(4), 159–165.
99. Rosenbaum, D. M., Rasmussen, S. G. F., & Kobilka, B. K. (2009). The structure and function of G-protein-coupled receptors. Nature, 459(7245), 356–363.
100. Rost, B. R., Wietek, J., Yizhar, O., & Schmitz, D. (2022). Optogenetics at the presynapse. Nature Neuroscience, 25(8), 984–998. https://doi.org/10.1038/s41593-022-01113-6
101. Sahu, A., Tyeryar, K. R., Vongtau, H. O., Sibley, D. R., & Undieh, A. S. (2009). D5 dopamine receptors are required for dopaminergic activation of phospholipase C. Molecular Pharmacology, 75(3), 447–453.
102. Saumweber, T., Rohwedder, A., Schleyer, M., Eichler, K., Chen, Y., Aso, Y., Cardona, A., Eschbach, C., Kobler, O., & Voigt, A. (2018). Functional architecture of reward learning in mushroom body extrinsic neurons of larval *Drosophila*. Nature Communications, 9(1), 1104.
103. Scanziani, M., & Häusser, M. (2009). Electrophysiology in the age of light. Nature, 461(7266), 930–939.
104. Scheib, U., Broser, M., Constantin, O. M., Yang, S., Gao, S., Mukherjee, S., Stehfest, K., Nagel, G., Gee, C. E., & Hegemann, P. (2018). Rhodopsin-cyclases for photocontrol of cGMP/cAMP and 2.3 Å structure of the adenylyl cyclase domain. Nature Communications, 9(1), 2046.
105. Schleyer, M., Weiglein, A., Thoener, J., Strauch, M., Hartenstein, V., Weigelt, M. K., Schuller, S., Saumweber, T., Eichler, K., Rohwedder, A., Merhof, D., Zlatic, M., Thum, A. S., & Gerber, B. (2020). Identification of dopaminergic neurons that can both establish associative memory and acutely terminate its behavioral expression. Journal of Neuroscience, 40(31), 5990–6006. https://doi.org/10.1523/JNEUROSCI.0290-20.2020
106. Schoofs, A., Hückesfeld, S., Surendran, S., & Pankratz, M. J. (2014). Serotonergic pathways in the *Drosophila* larval enteric nervous system. Journal of Insect Physiology, 69, 118–125.
107. Schroll, C., Riemensperger, T., Bucher, D., Ehmer, J., Völler, T., Erbguth, K., Gerber, B., Hendel, T., Nagel, G., & Buchner, E. (2006). Light-induced activation of distinct modulatory neurons triggers appetitive or aversive learning in *Drosophila* larvae. Current Biology, 16(17), 1741–1747.

108. Seeman, P. (2013). Schizophrenia and dopamine receptors. European Neuropsychopharmacology, 23(9), 999–1009.
109. Selcho, M., Pauls, D., Han, K. A., Stocker, R. F., & Thum, A. S. (2009). The role of dopamine in *Drosophila* larval classical olfactory conditioning. PLoS ONE, 4(6). https://doi.org/10.1371/journal.pone.0005897
110. Siju, K. P., De Backer, J.-F., & Grunwald Kadow, I. C. (2021). Dopamine modulation of sensory processing and adaptive behavior in flies. Cell and Tissue Research, 383(1), 207–225. https://doi.org/10.1007/s00441-020-03371-x
111. Silva, B., Hidalgo, S., & Campusano, J. M. (2020a). Dop1R1, a type 1 dopaminergic receptor expressed in Mushroom Bodies, modulates *Drosophila* larval locomotion. Plos One, 15(2), e0229671.
112. Silva, B., Hidalgo, S., & Campusano, J. M. (2020b). Dop1R1, a type 1 dopaminergic receptor expressed in Mushroom Bodies, modulates *Drosophila* larval locomotion. PLoS ONE, 15(2). https://doi.org/10.1371/journal.pone.0229671
113. Spangler, S. M., & Bruchas, M. R. (2017). Optogenetic approaches for dissecting neuromodulation and GPCR signaling in neural circuits. Current Opinion in Pharmacology, 32, 56–70. https://doi.org/10.1016/j.coph.2016.11.001
114. Spoida, K., Eickelbeck, D., Karapinar, R., Eckhardt, T., Mark, M. D., Jancke, D., Ehinger, B. V., König, P., Dalkara, D., & Herlitze, S. (2016). Melanopsin variants as intrinsic optogenetic on and off switches for transient versus sustained activation of G protein pathways. Current Biology, 26(9), 1206–1212.
115. Stevens, C. F. (2015). What the fly's nose tells the fly's brain. Proceedings of the National Academy of Sciences, 112(30), 9460-9465.
116. Stierl, M., Stumpf, P., Udwari, D., Gueta, R., Hagedorn, R., Losi, A., Gärtner, W., Petereit, L., Efetova, M., & Schwarzel, M. (2011). Light Modulation of Cellular cAMP by a Small Bacterial Photoactivated Adenylyl Cyclase, bPAC, of the Soil Bacterium Beggiatoa*♦. Journal of Biological Chemistry, 286(2), 1181–1188.
117. Sun, H., Nishioka, T., Hiramatsu, S., Kondo, S., Amano, M., Kaibuchi, K., Ichinose, T., & Tanimoto, H. (2020). Dopamine Receptor Dop1R2 Stabilizes Appetitive Olfactory Memory through the Raf/MAPK Pathway in*Drosophila*. The Journal of Neuroscience, 40(14), 2935–2942. https://doi.org/10.1523/jneurosci.1572-19.2020
118. Svenningsson, P., Nishi, A., Fisone, G., Girault, J.-A., Nairn, A. C., & Greengard, P. (2004). DARPP-32: an integrator of neurotransmission. Annu. Rev. Pharmacol. Toxicol., 44, 269–296.
119. Tiberi, M., Jarvie, K. R., Silvia, C., Falardeau, P., Gingrich, J. A., Godinot, N., Bertrand, L., Yang-Feng, T. L., Fremeau, R. T., & Caron, M. G. (1991). Cloning, molecular characterization, and chromosomal assignment of a gene encoding a second D1 dopamine receptor subtype: differential expression pattern in rat brain compared with

the D1A receptor. Proceedings of the National Academy of Sciences, 88(17), 7491–7495. https://doi.org/10.1073/pnas.88.17.7491

120. Tichy, A. M., Gerrard, E. J., Sexton, P. M., & Janovjak, H. (2019). Light-activated chimeric GPCRs: limitations and opportunities. Current Opinion in Structural Biology, 57, 196–203. https://doi.org/10.1016/j.sbi.2019.05.006
121. Tichy, A. M., So, W. L., Gerrard, E. J., & Janovjak, H. (2022). Structure-guided optimization of light-activated chimeric G-protein-coupled receptors. Structure, 30(8), 1075-1087.e4. https://doi.org/10.1016/j.str.2022.04.012
122. van den Pol, A. N. (2012). Neuropeptide Transmission in Brain Circuits. Neuron, 76(1), 98–115. https://doi.org/10.1016/j.neuron.2012.09.014
123. van Wyk, M., Pielecka-Fortuna, J., Löwel, S., & Kleinlogel, S. (2015). Restoring the ON Switch in Blind Retinas: Opto-mGluR6, a Next-Generation, Cell-Tailored Optogenetic Tool. PLOS Biology, 13(5), e1002143. https://doi.org/10.1371/journal.pbio.1002143
124. Vesuna, S., Kauvar, I. V, Richman, E., Gore, F., Oskotsky, T., Sava-Segal, C., Luo, L., Malenka, R. C., Henderson, J. M., & Nuyujukian, P. (2020). Deep posteromedial cortical rhythm in dissociation. Nature, 586(7827), 87–94.
125. Vierock, J., Rodriguez-Rozada, S., Dieter, A., Pieper, F., Sims, R., Tenedini, F., Bergs, A. C. F., Bendifallah, I., Zhou, F., & Zeitzschel, N. (2021). BiPOLES is an optogenetic tool developed for bidirectional dual-color control of neurons. Nature Communications, 12(1), 1–20.
126. Waddell, S. (2013). Reinforcement signalling in *Drosophila*; dopamine does it all after all. Current Opinion in Neurobiology, 23(3), 324–329. https://doi.org/10.1016/j.conb.2013.01.005
127. Wan, Q., Okashah, N., Inoue, A., Nehme, R., Carpenter, B., Tate, C. G., & Lambert, N. A. (2018). Mini G protein probes for active G protein– coupled receptors (GPCRs) in live cells. Journal of Biological Chemistry, 293(19), 7466–7473. https://doi.org/10.1074/jbc.RA118.001975
128. Wang, L., Wu, C., Peng, W., Zhou, Z., Zeng, J., Li, X., Yang, Y., Yu, S., Zou, Y., Huang, M., Liu, C., Chen, Y., Li, Y., Ti, P., Liu, W., Gao, Y., Zheng, W., Zhong, H., Gao, S., … Chu, J. (2022). A high-performance genetically encoded fluorescent indicator for *in vivo* cAMP imaging. Nature Communications, 13(1), 1–81. https://doi.org/10.1038/s41467-022-32994-7
129. Wietek, J., Nozownik, A., Pulin, M., Saraf-Sinik, I., Matosevich, N., Malan, D., Brown, B. J., Dine, J., Levy, R., Litvin, A., Regev, N., Subramaniam, S., Bitton, E., Benjamin, A., Copits, B. A., Sasse, P., Rost, B. R., Schmitz, D., Soba, P., … Yizhar, O. (2023). A bistable inhibitory OptoGPCR for multiplexed optogenetic control of neural circuits. BioRxiv, 2023.07.01.547328. http://biorxiv.org/content/early/2023/07/02/2023.07.01.547328.abstract

130. Wietek, J., Rodriguez-Rozada, S., Tutas, J., Tenedini, F., Grimm, C., Oertner, T. G., Soba, P., Hegemann, P., & Simon Wiegert, J. (2017). Anion-conducting channelrhodopsins with tuned spectra and modified kinetics engineered for optogenetic manipulation of behavior. Scientific Reports, 7(1), 1–18. https://doi.org/10.1038/s41598-017-14330-y
131. Xiang, Y., Yuan, Q., Vogt, N., Looger, L. L., Jan, L. Y., & Jan, Y. N. (2010). Light-avoidance-mediating photoreceptors tile the *Drosophila* larval body wall. Nature, 468(7326), 921–926. https://doi.org/10.1038/nature09576
132. Yang, S., Constantin, O. M., Sachidanandan, D., Hofmann, H., Kunz, T. C., Kozjak-Pavlovic, V., Oertner, T. G., Nagel, G., Kittel, R. J., & Gee, C. E. (2021). PACmn for improved optogenetic control of intracellular cAMP. BMC Biology, 19, 1–17.
133. Yizhar, O., Fenno, L. E., Davidson, T. J., Mogri, M., & Deisseroth, K. (2011). Optogenetics in Neural Systems. Neuron, 71(1), 9–34. https://doi.org/10.1016/j.neuron.2011.06.004
134. Zhang, F., Vierock, J., Yizhar, O., Fenno, L. E., Tsunoda, S., Kianianmomeni, A., Prigge, M., Berndt, A., Cushman, J., & Polle, J. (2011). The microbial opsin family of optogenetic tools. Cell, 147(7), 1446–1457.
135. Zhang, F., Wang, L.-P., Brauner, M., Liewald, J. F., Kay, K., Watzke, N., Wood, P. G., Bamberg, E., Nagel, G., & Gottschalk, A. (2007). Multimodal fast optical interrogation of neural circuitry. Nature, 446(7136), 633–639.
136. Zhou, F., Tichy, A. M., Imambocus, B. N., Rodriguez Jimenez, F. J., Gonzalez Martinez, M., Jahan, I., ... & Soba, P. (2023). Optimized design and *in vivo* application of optogenetically functionalized *Drosophila* dopamine receptors. bioRxiv, 2023-05.
137. Ziegler, T. & Moglich, A. (2015).Photoreceptor engineering. Front Mol Biosci 2, 30 .
138. Zolin, A., Cohn, R., Pang, R., Siliciano, A. F., Fairhall, A. L., & Ruta, V. (2021). Context-dependent representations of movement in *Drosophila* dopaminergic reinforcement pathways. Nature Neuroscience, 24(11), 1555–1566. https://doi.org/10.1038/s41593-021-00929-y.

7 List of abbreviations

3-OCT	3-octanol
4-MCH	4-methylcyclohexanol
AC	Adenylate cyclase
ACRs	Anion-conducting ChRs
ADHD	Attention deficit hyperactivity disorder
AEL	After egg laying
AM	n-amylacetate
AMPA	α-amino-3-hydroxy-5-methyl-4-isoxazolepropionic acid
ATP	Adenosine triphosphate
BDSC	Bloomington *Drosophila* Stock Center
BiPOLES	Bidirectional Pair of Opsins for Light-induced Excitation and Silencing
bPAC	Photoactivated adenylyl cyclase from Beggiatoa
C1da	Class I dendritic arborization (neuron)
C2da	Class II dendritic arborization (neuron)
C3da	Class III dendritic arborization (neuron)
C4da	Class IV dendritic arborization (neuron)
CaMKII	Calcium/calmodulin-dependent kinase II
cAMP	Cyclic 3,5 adenine-monophosphate
CCRs	Cation-conducting ChRs
cGMP	Cyclic guanosine monophosphate
ChRs	Channelrhodopsins
CREB	cAMP response element-binding protein
CS	Conditioned stimulus
DA	Dopamine
DAG	Diacylglycerol
DARPP-32	Dopamine and cAMP-regulated phosphoprotein 32-kDa
Dp7	Dorsal pair insulin-like peptide 7
DopRs	Dopamine receptors
eOPN3	Enhanced mosquito rhodopsin
Epac	Exchange proteins directly activated by cAMP
ERK	Extracellular-signal regulated kinase 1 and 2
GABA	γ-Aminobutyrate

Gal4	Gal4 transcription factor
GC	Guanylyl cyclase;
GFP	Green fluorescent protein
GIRK	G protein-coupled inwardly rectifying potassium channel
GPCRs	G protein-coupled receptors
GRKs	G protein-coupled receptor kinases
GTP	Guanosine triphosphate;
HEK	Human embryonic kidney
HL3	Hemolymph-like saline
ICLs	Intracellular loops
Ilp7	Insulin-like peptide 7
IP3	Inositol trisphosphate
KCs	Kenyon cells
KO	Knockout
L-DOPA	L-3,4-dihydroxyphenylalanine
MAP	Mitogen-activated protein
MB	Mushroom body
MBONs	Mushroom body out neurons
MEK	MAP/ERK kinase
MSN	Medium spiny neuron
NMDA	N-methyl-D-aspartate
OPN4	Melanopsin
Opto-DopRs	Optogenetically modified Dopamine receptors
OptoXRs	Light-activated chimeric GPCRs
Opto-β2AR	Optogenetically modified β2-adrenergic receptor
ORNs	Olfactory receptor neurons
P	Phosphorylation site
PBS	Phosphate-buffered saline
PBST	Phosphate-buffered saline with 0.3% Triton X-100
PD	Parkinson's disease
PdCO	Platynereis dumerilii ciliary opsin
PDE	Phosphodiesterase
PKA	Protein kinase A

PKC	Protein kinase C
PLC	Phospholipase C
PPO	Lamprey parapinopsin
RGS	Regulators of G protein signaling
RhGCs	Rhodopsin-coupled guanylyl cyclases
Rho	Bovine Rhodopsin
SD	Standard deviation
SEM	Standard error of the mean
sNPF	Short neuropeptide F
WT	Wild type
α1AR	α1-adrenergic receptor
β2AR	β2-adrenergic receptor
μm	micro meter
μW	micro watts

8 Acknowledgments

Firstly, I would like to express my sincere gratitude to my supervisor, Prof. Dr. Peter Soba, for giving me the opportunity to do my PhD research in his lab. His dynamic guidance and unwavering support, which have played a pivotal role in shaping my scientific career and persona development. His wealth of experience and extensive knowledge have ignited my own passion and curiosity for neuroscience. I am thankful for the numerous opportunities he provided, including attendance at conferences and practical courses like the EMBO course and the next-generation optogenetic meeting. I would also like to express my deep appreciation to my co-supervisor, Prof. Dr. J. Simon Wiegert, for the chance to collaborate with his group and for learning valuable techniques, such as two photon microscopy. His insightful suggestions, brilliant ideas, and enduring dedication to scientific research have been a constant source of motivation for me. Furthermore, I appreciated China Scholarship Council (CSC) for the funding support for my PhD.

I would like to thank Prof. Dr. Stefan Bonn, Prof. Dr. Dietmar Kuhl and Prof. Dr. Thomas G. Oertner for very helpful discussion and valuable advice. I always appreciate their time and kind help throughout those years.

I would also like to express my gratitude to all the members in Soba lab, Wiegert lab and Pankratz lab, Who shared their knowledge, experience and many unforgettable moments.In particular, they are Chun Hu, Federico Tenedini, Kathrin Sauter, Meike Petersen, Nusreen Imambocus, Tatjana Binzenbach, Yan Tang, Peiyun Yu, Neena Dhiman, Shreyas Sakharwade, Ingo Zinke, Anne Jansen, Damian Demarest, Nicole Kolosnjaji. Special thanks Dr. Andreas Schoofs for excellent technical support and insightful comments of thesis. Outside of the lab, I would like to express my deepest gratitude to Xiaoyan, Linzhen, Wei, Yu and Shuai, for they sharing knowledge of research and life tips in Germany.

Thanks also to all the fantastic collaborators, Prof. Dr. Harald Janovjak, Prof. Dr. Ilona C. Grunwald Kadow, Prof. Dr. Jan Pielage, Prof. Dr. Charlotte Helfrich-Förster, Dr. Alexandra-Madelaine Tichy, Dr. Andrey Formozov; in particular, with whom I had the pleasure to work with and learned a lot from over the past few years.

Finally, I extend my heartfelt gratitude to my parents for their unwavering love and support, which I have been fortunate to receive throughout my life. I would also like to express my appreciation to all of my friends who have stood with me, offering their support over the years.

9 Curriculum Vitae

Fangmin Zhou

EDUCATION

PhD in Neuroscience
University of Hamburg, Hamburg, Germany 09/2018 -present

MSc in Pharmacology
Sun Yat-sen University, Guangzhou, China 08/2015- 07/2018

BSc in Pharmacy
Fujian Medical University, Fuzhou, China 09/2011-06/2015

INTERESTS AND AREA OF EXPERTISE

- Improved optogenetic tools for the precise manipulation of GPCR signaling
- Dopamine receptor functional in learning and locomotion behavior
- The role of ion channel (TRPM7, chloride channel) in the disease

PROFESSIONAL SKILLS

Proficient with: Cell cultivation, Molecular cloning, Western Blot, Primer Design, PCR, Agarose Gel Electrophoresis, ELISA, Confocal microscopy, Tissue Harvest, Oil-red O staining, Animal learning behavior

Familiar with: Enzyme assaying, Reagent preparation, Animal breeding

PUBLICATIONS

1) **Zhou, F.,** Tichy, A.-M., Imambocus, B. N., Sakharwade, S., Rodriguez Jimenez, F. J., Gonzalez Martinez, M., Jahan, I., … Soba P. (2023). Optimized design and *in vivo* application of optogenetically functionalized *Drosophila* dopamine receptors. **Nat Commun**.,14, 8434 DOI: 10.1038/s41467-023-43970-0.
2) **Zhou, F. M.**, Huang, Y. Y., Tian, T., Li, X. Y., & Tang, Y. B. (2018). Knockdown of chloride channel-3 inhibits breast cancer growth *in vitro* and *in vivo*. **Journal of Breast Cancer**, 21(2), 103–111.
3) Imambocus BN, **Zhou F**, Formozov A, Wittich A, Tenedini F, Hu C, Sauter K, Macarenhas Varela E, Herédia F, Casimiro AP, Macedo A, Schlegel P, Yang C-H, Miguel-Aliaga I, Wiegert JS, Pankratz MJ, Gontijo AM, Cardona A, Soba P (2022) A neuropeptidergic circuit gates selective escape behavior of *Drosophila* larvae**. Curr Biol** 32:149-163.e8. doi: 10.1016/j.cub.2021.10.069.
4) Mahn M, Saraf-Sinik I, Patil P, Pulin M, Bitton E, Karalis N, Bruentgens F, Palgi S, Gat A, Dine J, Wietek J, Davidi I, Levy R, Litvin A, **Zhou F,** Sauter K, Soba P, Schmitz D, Lüthi A, Rost BR, Wiegert JS, Yizhar O. (2021) Efficient optogenetic silencing of neurotransmitter release with a mosquito rhodopsin. **Neuron** 109:1621-1635.e8. doi:10.1016/j.neuron.2021.03.013
5) Vierock J, Rodriguez-Rozada S, Dieter A, Pieper F, Sims R, Tenedini F, Bergs A, Bendifallah I, **Zhou F**, Zeitzschel N, Ahlbeck J, Augustin S, Sauter K, Papagiakoumou E, Gottschalk A, Soba P, Emiliani V, Engel A, Hegemann P, Wiegert JS. (2021) BiPOLES: a tool for bidirectional dual-color optogenetic control of neurons. **Nat Commun** 12(1):4527. doi: 10.1038/s41467-021-24759-5
6) Imambocus, B. N., Formozov, A., **Zhou, F.**, & Soba, P. (2022). A two-choice assay for noxious light avoidance with temporal distribution analysis in *Drosophila* melanogaster larvae. **STAR Proctocl**., *3*(4), 101787.

10 Eidesstattliche Versicherung

Ich versichere ausdrücklich, dass ich die Arbeit selbständig und ohne fremde Hilfe verfasst, andere als die von mir angegebenen Quellen und Hilfsmittel nicht benutzt und die aus den benutzten Werken wörtlich oder inhaltlich entnommenen Stellen einzeln nach Ausgabe (Auflage und Jahr des Erscheinens), Band und Seite des benutzten Werkes kenntlich gemacht habe.

Ferner versichere ich, dass ich die Dissertation bisher nicht einem Fachvertreter an einer anderen Hochschule zur Überprüfung vorgelegt oder mich anderweitig um Zulassung zur Promotion beworben habe. Ich erkläre mich einverstanden, dass meine Dissertation vom Dekanat der Medizinischen Fakultät mit einer gängigen Software zur Erkennung von Plagiaten überprüft werden kann.